Experimental Study of Heat Release Effects in Exothermically Reacting Turbulent Shear Flows

by

Zachary William Nagel

A dissertation submitted in partial fulfillment
of the requirements for the degree of
Doctor of Philosophy
(Aerospace Engineering)
in The University of Michigan
2007

Doctoral Committee:

Professor Werner J. A. Dahm, Chair
Professor David R. Dowling
Professor James F. Driscoll
Associate Professor Luis P. Bernal

Dedicated to my loving and devoted wife, Ginelle. For all her sacrifices and her trust in me as we travel life together.

ACKNOWLEDGEMENTS

I would like to thank many people for supporting me in unnumberable ways, both tangible and intangible. This thesis would not have been possible without their collective support.

First and foremost, my parents, Bill and Jane, deserve as much credit as I do for this dissertation. Without their selflessness and sacrifice to instill many of life's lessons within their children, this work would never have begun. My sisters, Christy, Jessica, Jory, and Shona and my brother Greg; have been sources of inspiration and encouragement to me throughout these many years.

Life in the FXB would not have been the same without several important friends and colleagues. Sulabh and Chad have been there from the beginning and I am deeply thankful for their friendship over the years – as well as our handlebar moustaches. Individually, I am grateful to Chad for his challenging questions about research and life in general, morning and afternoon coffee, great musical hits such as "da data don' matta", and of course the patented triple flame and three-phase flow. Sulabh has provided numerous thoughtful discussions over coffee and otherwise, as well as many an evening with an Old Friend, trips to New York, Pierpont and various burrito establishments. Contra and Techmo bowl would not have been the same without you, S-diddy.

Within the LTC, I've been fortunate enough to work with a number of exceptional people. I will always be indebted to John Mullin for taking me under his wing and mentoring me. Andy, thank-you for morning coffee and spirited discussions regarding the supremacy of the Yankees over the red sox. Peter for his help with filtering and data processing, and enlightening hip-hop discussions. Just remember, that what happens in Huntsville stays in Huntsville...that goes for Alex 'G&T' Schumaker, as well.

I am thankful for Dave, Ryan, Courtney, who have been great friends throughout the past decade of college and throughout the potato gun competition. Your support and friendship means a great deal to me.

To Barb and Frank, thanks for your support during the Madison years and the Yankee camaraderie.

To my great friends Nate, Joe, Shawn, thanks for being the best of friends during most important times of my life.

To Samantha and Nicko, thanks for everything that you've meant to me. There are a hundred laughs that you gave me and I'll always be grateful for the times that we shared playing exciting games of naptathalon.

Pari, thanks for help with the figures, your kindness and general good cheer – and for hosting game nights.

I thank Professors Dowling, Driscoll and Bernal for graciously serving on my defense committee.

I am exceedingly thankful to my advisor, Professor Werner Dahm for his patience, vision and passion in advising my doctoral thesis. I have learned a great deal under his tutelage in all areas of research, science and life. Without his tireless efforts and unwavering belief in me, this work would never have been completed – and would have certainly been only 37 % as good.

Thanks to Prof. Dowling for his help with the filtering procedure and to Prof.

Bernal help for his knowledgable insight regarding PIV.

Thanks also to Jeff Sutton for his great sense of humor, conversations about college football and helpful advice regarding research.

I am grateful to the Aerospace Technical staff, specifically Dave McLean and Tom Griffin for their help and support in conducting my experiments. Their positive attitudes and commitment to supporting research are priceless.

I would also like to thank Terry Tate for teaching me to bring my *A*-game, all day, everyday.

Finally, I give thanks to the Heavenly Father for His many blessings and His Love. All things are possible through Christ who strengthens me.

TABLE OF CONTENTS

DEDICATION . . . . **ii**

ACKNOWLEDGEMENTS . . . . **iii**

LIST OF FIGURES . . . . **ix**

LIST OF TABLES . . . . **xxiv**

LIST OF APPENDICES . . . . **xxix**

NOMENCLATURE . . . . **xxx**

CHAPTER

I. Introduction **1**

1.1 Present Study 5

II. Theoretical Foundation **11**

2.1 Elementary Effects of Heat Release 13
2.2 Scaling Laws for Non-Reacting Coflowing Turbulent Jets 17
2.3 Heat Release: Inertial Effects of Density Variations 20
2.4 Heat Release: Body Force Effects of Density Variations 24
2.5 Heat Release: Dilatation Effects of Density Variations 25
2.6 Heat Release: Diffusive Effects of Viscosity Variations 29
2.7 Combined Effects of Heat Release 32

III. Experimental Facilities and Diagnostic **45**

3.1 LTC DSPIV Laboratory 46
3.2 Gas Delivery System 47
3.2.1 Fuel Board 48
3.2.2 PIV Seeders 49
3.2.3 PIV Seed 49
3.2.4 Jet Nozzle 50
3.3 Optical Layout 51

3.3.1 Light Sheet Generation 52
3.3.2 Particle Imaging 53
3.4 Experimental Conditions 53

IV. Outer Scale Effects of Heat Release 74

4.1 PIV Data and Analysis 75
4.2 Outer-Flow Scaling Results from Nonreacting Cases 77
4.3 Outer-Flow Scaling Results from Reacting Cases 78
4.4 Comparison with Prior Studies 80

V. Inner Scaling of Nonreacting Flows: Effects of Resolution . . 100

5.1 Inner-Scale PIV Measurements 101
5.2 Inner-Scale Velocities and Velocity Gradients 103
5.3 Isotropy Assessments 105
5.4 PIV Resolution Effects 107
5.4.1 Inertial-Range Correction 108
5.4.2 PIV Resolution: Spectra 111
5.4.3 PIV Resolution: Low Pass Filtering 111
5.4.4 PIV Resolution: Effective Length Scale $\Delta^{\star}$ 114
5.4.5 PIV Resolution: Viscous Roll-Off 116
5.5 Inner Scale Pdfs with Resolution-Corrected Inner Scaling 118
5.6 Inner Scale PIV: Corrected Moments 119
5.7 Comparison to Existing Data 119

VI. Inner-Scale Effects of Heat Release 169

6.1 Inner-Scale PIV Measurements 169
6.2 Inner-Scale Velocities and Velocity Gradients 170
6.2.1 Resolution-Corrected Pdfs 172
6.2.2 Comparisons with Nonreacting Inner-Scale Results 174
6.2.3 Inner-Scale Effects of Heat Release 175
6.2.4 Effects of Heat Release on Isotropy 180

VII. Inner-Scaling of Nonreacting Flows: Effects of Shear 230

7.1 Inner Scale PIV: Off-Axis Experiments 231
7.2 Inner-Scale Velocity Gradients 232
7.3 Data Conditioning 234
7.4 Conditioned Inner-Scale Velocity Gradient Statistics 235
7.5 Effects of Shear on Inner-Scale Statistics 237

VIII. Inner-Scaling of Nonreacting Flows: Effects of Shear and Heat Release **274**

8.1 Inner Scale PIV: Off-Axis Reacting Flow Experiments 275
8.2 Inner Scale Velocity Gradients 275
8.3 Inner Scale, Off-Axis: Reacting & Nonreacting 276
8.4 Effects of Shear and Exothermicity on Local Isotropy 279

IX. Conclusions **302**

APPENDICES **306**

BIBLIOGRAPHY **328**

LIST OF FIGURES

Figure

2.1 Schematics indicating proper definition of local outer length and velocity scales δ and u_c from local mean velocity profiles for typical coflowing jet profile shape *(top)* so that $(\partial u/\partial u)_{\max} \approx (u_c/\delta)$ where $u_c \equiv U_c - U_\infty$ is centerline excess velocity and typical mixing layer profile shape *(bottom)* where $u_c \equiv (U_1 - U_2)$. 34

2.2 Schematic of strained diffusion and reaction layer separating fuel-rich and oxidizer-rich regions in mixture fraction field $\zeta(\mathbf{x}, t)$, shown in local Lagrangian frame moving with point P at center of layer. . 35

2.3 Schematic indicating basic layout and nomenclature for axisymmetric coflowing turbulent jets as used for experimental measurements presented herein. 36

2.4 Decrease in local outer velocity u_c with downstream coordinate x in coflowing turbulent jets for three different values of jet-to-ambient velocity ratios U_0/U_∞, showing naïve jet scaling with jet exit diameter d_E *(top)* and proper coflowing jet scaling with jet momentum radius θ *(bottom)*. Adapted from Dahm and Dibble (1988); symbols defined therein. 37

2.5 Increase in local outer length scale δ with downstream coordinate x in coflowing turbulent jets for three different values of jet-to-ambient velocity ratios U_0/U_∞, showing naïve jet scaling with jet exit diameter d_E *(top)* and proper coflowing jet scaling with jet momentum radius θ *(bottom)*. Adapted from Dahm and Dibble (1988); symbols defined therein. 38

2.6 Decrease in local outer velocity u_c with downstream coordinate x in coflowing turbulent jets from Fig. 2.4 *(top)*. Increase in local outer length scale δ with downstream coordinate x in coflowing turbulent jets from Fig. 2.5 *(bottom)*. Both panels include for comparison data from Davidson and Wang (2002) spanning a large range in x/θ (grey squares). 39

2.7 State relation for temperature in terms of conserved scalar ζ *(top)* and mole fraction X *(bottom)* from OPPDIF computations for strain rates $\mathcal{S}$ ranging from equilibrium limit to deep nonequilibrium. Note bilinear form of $T(X)$ in equilibrium regime at $\mathcal{S} < 1/20$ s^{-1}. 40
2.8 Equilibrium temperature state relation function from Fig. 2.7 shown in terms of mole fraction X. Departures from strict bilinear form of $T(X)$ for $X \neq X_s$ *(top)* are due to small variations in molar specific heat $\widetilde{c}_p$. Linear approximation of $T(X)$ for $X > X_s$ leads to effective ambient temperature T_∞^{eff} *(bottom)* in a corresponding nonreacting flow. 41
2.9 Schematic of equivalence principle, showing implications for mean temperature (*top*) and density (*middle*) profiles in an exothermically reacting jet. Solid lines show profiles in exothermic reacting flow; dashed lines show profiles in nonreacting flow produced by simple mixing between the actual source values T_0 and ρ_∞ effective ambient values T_∞^{eff} and ρ_∞^{eff}. Heavy line shows resulting agreement for $X > X_s$, where velocity (*bottom*) is large, ensuring proper accounting for the dominant inertial effects of heat release, from Diez and Dahm (2007). 42
2.10 Equilibrium temperature state relation $T(\zeta)$ for $H_2 -$ air chemistry, showing variation in temperature T with mixture fraction ζ (*left axis*), and corresponding relative dilation $\mathcal{R}_\nabla(\zeta)$ (*right axis*). Results are shown for $0 \leq \zeta \leq 1$ *(top)*, and near stoichiometric value ζ_s *(bottom)*. 43
2.11 Kinematic viscosity state relationship as a function of conserved scalar *(top)* and mole fraction *(bottom)*. Results obtained via OPPDIF computations for a wide range of strain conditions ranging from 1/10 to 1/5000 s^{-1}. 44

3.1 Photograph of LTC DSPIV laboratory. See corresponding schematic of overall layout in Fig. 3.2, and schematic of optical layout in Fig. 3.12. 55
3.2 Plan view schematic of LTC DSPIV laboratory layout, corresponding to Fig. 3.1. 56
3.3 Schematic of vertical induced-draft wind tunnel, with flow conditioning elements shown on the right. Laboratory air is drawn through the bottom into the seeding section, where seed particles are introduced, then passes through the flow conditioning section and proceeds into the test section, from which it exits into the exhaust system. 57
3.4 Photograph of the test section portion of the vertical draft wind tunnel. The optical path is visible on the far right and the large FOV camera is seen in the background on the left. On the near left side, the small FOV camera is shown. 58

3.5 Photographs of the flow conditioning section. Upper panel: section containing only the porous plate element. Lower panel: screens, honeycomb and jet apparatus have been mounted. 59
3.6 Typical cradle consisting of twelve compressed gas cylinders providing the hydrogen fuel used in the reacting flow experiments. Flame arrestor is visible to left of regulator. 60
3.7 Photograph of fuel mixing board. The three independent gas lines are identifiable by vertical alignment of pressure gauge pairs. Fine and coarse flow metering valves are located near bottom of mixing board. 61
3.8 Photograph of the jet seeder *(left)* and coflow seeder *(right)*. 62
3.9 Details of jet nozzles and entrance tube, showing entrance tube dimensions with threaded fittings *(top)*, with typical jet nozzle attached *(middle)*, and precise shapes of inner and outer wall profiles for $d_E = 5.5$ mm nozzle *(lower left)* and $d_E = 4.0$ mm nozzle *(lower right)*. 63
3.10 Photograph of jet nozzles and entrance tube, showing entrance tube with threaded end visible and disassembled nozzles *(top)*, and nozzle fitted to entrance tube with view to mating internal threads in the remaining nozzle *(bottom)*. 64
3.11 Photograph of the optical table setup. The principal optical path is in the center of the image. The two Nd:YAG lasers used for this study are at the upper right of the image, the large FOV camera is on the left of the test section, and the small FOV camera is near the bottom of the image. 65
3.12 Schematic of the optical table arrangement in Fig. 3.11. Mirrors are labeled *MX*, beam-splitting optics *BSX*, beam dumps *BDX*, mechanical shutters *SX* and cylindrical lenses *CX*. The optical arrangement used for this study is discussed in §3.3.1. 66
3.13 Motorized mounts for laser sheet positioning. PC-controlled servo motors provide positioning for mirror traverse (a), kinematic mirror adjustments (b) and combined system (c) for accurate, repeatable beam alignment. 67

4.1 Sample PIV results for instantaneous streamwise velocity field $U(\mathbf{x}, t)$ *(top)* and transverse velocity field $V(\mathbf{x}, t)$ *(bottom)* from nonreacting case *ONR5* in Table 3.1 at $Re_\delta = 173\,500$. The FOV is 46.5×58.1 mm and located at a distance of 100 mm from the jet nozzle. 83
4.2 Ensemble-averaged PIV results for mean streamwise velocity field $\langle U \rangle$ *(top)* and transverse velocity field $\langle V \rangle$ *(bottom)* from nonreacting case *ONR5* in Table 3.1 at $Re_\delta = 173\,500$. 84

4.3 Sample PIV results for instantaneous streamwise velocity field $U(\mathbf{x}, t)$ *(top)* and transverse velocity field $V(\mathbf{x}, t)$ *(bottom)* from reacting case *OR3* in Table 3.2 at $Re_\delta = 299\,300$. 85
4.4 Ensemble-averaged PIV results for mean streamwise velocity field $\langle U \rangle$ *(top)* and transverse velocity field $\langle V \rangle$ *(bottom)* from nonreacting case *OR3* in Table 3.2 at $Re_\delta = 173\,500$. 86
4.5 Mean velocity profile from case *ONR1* in Table 3.1 at $Re_\delta = 22\,600$, showing the mean normalized streamwise velocity $\overline{u}/u_c$ *(top)* and Reynolds stress $\overline{u'v'}/u_c^2$ *(bottom)* versus radial similarity coordinate $\eta \equiv r/\delta_{1/2}$. 87
4.6 Results for local outer length scale $\delta_{1/2}$ versus downstream distance x, normalized by momentum radius θ, for all nonreacting cases in Table 3.1. Solid line corresponds to (4.4); dashed line gives jet-limit scaling. Note $\delta_{1/2}$ is the half-width at half-maximum of the mean excess velocity profile $u(x)$. 88
4.7 Results for local outer velocity scale u_c versus downstream distance x, normalized by momentum radius θ, for all nonreacting cases in Table 3.1. Solid line corresponds to (4.5); dashed line gives jet-limit scaling. 89
4.8 Results for local outer length scale $\delta_{1/2}$ versus downstream distance x, normalized by momentum radius θ, for all reacting cases in Table 3.2. 90
4.9 Centerline scaling of centerline velocity decay u_c normalized by coflow velocity U_∞ in terms of x/θ for all reacting cases in Table 3.2. . . . 91
4.10 Results for local outer length scale $\delta_{1/2}$ versus downstream distance x, normalized by extended momentum radius θ^+, for all reacting cases in Table 3.2. Solid line gives scaling for nonreacting flow in (4.4); dashed line gives jet-limit scaling. 92
4.11 Results for local outer velocity scale u_c versus downstream distance x, normalized by extended momentum radius θ^+, for all reacting cases in Table 3.2. Solid line gives scaling for nonreacting flow in (4.5); dashed line gives jet-limit scaling. 93
4.12 Results for local outer length scale $\delta_{1/2}$ versus downstream distance x, normalized by extended momentum radius θ^+, showing all nonreacting cases in Table 3.1 and all reacting cases in Table 3.2. Solid line gives scaling for nonreacting flow in (4.4); dashed line gives jet-limit scaling. 94
4.13 Results for local outer velocity scale u_c versus downstream distance x, normalized by extended momentum radius θ^+, showing all nonreacting cases in Table 3.1 and all reacting cases in Table 3.2. Solid line gives scaling for nonreacting flow in (4.5); dashed line gives jet-limit scaling. 95

4.14 Results from Muñiz and Mungal (2001) for local outer length scale $\delta_{1/2}$ versus downstream distance x *(top)*, with reacting and nonreacting cases denoted R and NR, respectively. Same results are shown normalized by extended momentum radius θ^+ *(bottom)*, where reacting and nonreacting cases both follow solid line giving scaling in (4.4); dashed line gives jet-limit scaling. 96
4.15 Results for local outer length scale $\delta_{1/2}$ versus downstream distance x, normalized by extended momentum radius θ^+, showing all nonreacting cases in Table 3.1 and all reacting cases in Table 3.2 as well as data from Muñiz and Mungal (2001) from Fig. 4.14. Solid line gives scaling for nonreacting flow in (4.4); dashed line gives jet-limit scaling. 97
4.16 Results for local outer velocity scale u_c versus downstream distance x, normalized by extended momentum radius θ^+, showing all nonreacting cases in Table 3.1 and all reacting cases in Table 3.2 as well as data from Muñiz and Mungal (2001), Biringen (1975) and Wang and Davidson (2001). Solid line gives scaling for nonreacting flow in (4.5); dashed line gives jet-limit scaling. 98
4.17 Results for local outer length scale $\delta_{1/2}$ versus downstream distance x, normalized by extended momentum radius θ^+, showing all nonreacting cases in Table 3.1 and all reacting cases in Table 3.2 as well as data from Muñiz and Mungal (2001), Biringen (1975) and Wang and Davidson (2001). Solid line gives scaling for nonreacting flow in (4.4); dashed line gives jet-limit scaling. 99

5.1 Sample velocity fields at $Re_\delta = 45\,500$. Instantaneous velocity fluctuations u *(top)* and v *(bottom)*, normalized by the centerline velocity u_c. 121
5.2 Sample velocity gradient fields at $Re_\delta = 45\,500$. Instantaneous velocity gradients $\partial u/\partial x$ *(top)* and $\partial u/\partial y$ *(bottom)*, normalized by inner variables ν/λ_ν^2 122
5.3 Sample velocity gradient fields at $Re_\delta = 45\,500$. Instantaneous velocity gradients $\partial v/\partial x$ *(top)* and $\partial v/\partial y$ *(bottom)*, normalized by inner variables ν/λ_ν^2 123
5.4 Sample velocity gradient fields at $Re_\delta = 45\,500$. Instantaneous strain rate components S_{xx} *(top)* and S_{yy} *(bottom)*, normalized by inner variables ν/λ_ν^2 124
5.5 Sample velocity gradient fields at $Re_\delta = 45\,500$. Instantaneous strain rate component S_{xy} *(top)* and $\mathrm{Log}_{10}(S_{ij}S_{ij})$ *(bottom)*, normalized respectively by classical inner scaling ν/λ_ν^2 and $(\nu/\lambda_\nu^2)^2$. Here $S_{ij}S_{ij} \equiv S_{xx}^2 + S_{yy}^2 + 2\,S_{xy}^2$. 125
5.6 Sample velocity gradient fields at $Re_\delta = 45\,500$. Instantaneous vorticity ω_z *(top)* and enstrophy $\mathrm{Log}_{10}(\vartheta_z)$ *(bottom)*, normalized respectively by classical inner scaling ν/λ_ν^2 and $(\nu/\lambda_\nu^2)^2$. Here $\vartheta_z \equiv 3/2\,\omega_z^2$. 126

5.7 Sample velocity gradient fields at $Re_\delta = 45\,500$, showing contraction of instantaneous velocity gradient tensor $\mathrm{Log}_{10}(\boldsymbol{\nabla}\mathbf{u} : \boldsymbol{\nabla}\mathbf{u})$ *(top)* and two-dimensional divergence $-\partial w/\partial z$ *(bottom)*, normalized respectively by classical inner scaling $(\nu/\lambda_\nu^2)^2$ and ν/λ_ν^2 127

5.8 Pdfs from all nonreacting cases *INR1 – INR6* for velocity gradient $\partial u/\partial x$ normalized by outer variables u_c/δ *(top)* and $\partial u/\partial x$ normalized by inner variables ν/λ_ν^2 *(bottom)*. 128

5.9 Pdfs from all nonreacting cases *INR1 – INR6* for velocity gradient $\partial u/\partial y$ normalized by outer variables u_c/δ *(top)* and $\partial u/\partial y$ normalized by inner variables ν/λ_ν^2 *(bottom)*. 129

5.10 Pdfs from all nonreacting cases *INR1 – INR6* for velocity gradient $\partial v/\partial x$ normalized by outer variables u_c/δ *(top)* and $\partial v/\partial x$ normalized by inner variables ν/λ_ν^2 *(bottom)*. 130

5.11 Pdfs from all nonreacting cases *INR1 – INR6* for velocity gradient $\partial v/\partial y$ normalized by outer variables u_c/δ *(top)* and $\partial v/\partial y$ normalized by inner variables ν/λ_ν^2 *(bottom)*. 131

5.12 Pdfs from all nonreacting cases *INR1 – INR6* for strain rate components S_{xx} *(top)* and S_{yy} *(bottom)* normalized by inner variables ν/λ_ν^2. 132

5.13 Pdfs from all nonreacting cases *INR1 – INR6* for strain rate components S_{xy} *(top)* and $\mathrm{Log}_{10}\,(S_{ij}S_{ij})$ *(bottom)* normalized by inner variables ν/λ_ν^2 and $(\nu/\lambda_\nu^2)^2$. 133

5.14 Pdfs from all nonreacting cases *INR1 – INR6* for vorticity ω_z *(top)* and enstrophy $\mathrm{Log}_{10}\,(\vartheta_z)$ *(bottom)* normalized by inner variables ν/λ_ν^2 and $(\nu/\lambda_\nu^2)^2$. 134

5.15 Pdfs from all nonreacting cases *INR1 – INR6* for contraction of the instantaneous velocity gradient tensor $\boldsymbol{\nabla}\mathbf{u} : \boldsymbol{\nabla}\mathbf{u}$ *(top)* and two-dimensional divergence $-\partial w/\partial z$ *(bottom)* normalized by inner variables $(\nu/\lambda_\nu^2)^2$ and ν/λ_ν^2. 135

5.16 Schematic indicating procedure for obtaining resolution length scale $\Delta^\star$ from artificially-degraded experimental data via successive, spectrally sharp, low-pass filtering. 136

5.17 Results from low-pass filtering to determine effective length scale $\Delta^\star$ for case *INR1*, $Re_\delta = 7200$. 137

5.18 Results from low-pass filtering to determine effective length scale $\Delta^\star$ for case *INR2*, $Re_\delta = 11\,000$. 138

5.19 Results from low-pass filtering to determine effective length scale $\Delta^\star$ for case *INR3*, $Re_\delta = 21\,400$. 139

5.20 Results from low-pass filtering to determine effective length scale $\Delta^\star$ for case *INR4*, $Re_\delta = 31\,400$. 140

5.21 Results from low-pass filtering to determine effective length scale $\Delta^\star$ for case *INR5*, $Re_\delta = 45\,500$. 141

5.22 Results from low-pass filtering to determine effective length scale $\Delta^\star$ for case *INR6*, $Re_\delta = 50\,200$. 142
5.23 Spectral roll-off parameter p *(top)* and normalized length scale Δ_R/δ with associated $\Delta^\star/\delta$ *(bottom)* obtained from three strain rate components S_{xx}, S_{yy}, S_{xy} and vorticity ω_z at Re_δ corresponding to each case in Table 3.3. 143
5.24 Schematic diagram indicating inertial-range overshoot correction of the $D(p)$ contribution to resolution-corrected inner scaling. Here the $D(p)$ function compensates for the overprediction of the inertial-range scaling in the dissipative scales. 144
5.25 Unscaled *rms* of the vorticity $(\omega_z')_{rms}$ plotted against Re_δ *(top)*. Vorticity *rms* $(\omega_z')_{rms}$ normalized by resolution-corrected inner scaling $\mathcal{N}^\star$ *(bottom)*. 146
5.26 Pdfs from all nonreacting cases *INR1* – *INR6* for velocity gradient $\partial u/\partial x$ normalized by resolution-corrected inner scaling, shown in linear axes *(top)* and semilogarithmic axes *(bottom)*. 147
5.27 Pdfs from all nonreacting cases *INR1* – *INR6* for velocity gradient $\partial u/\partial y$ normalized by resolution-corrected inner scaling, shown in linear axes *(top)* and semilogarithmic axes *(bottom)*. 148
5.28 Pdfs from all nonreacting cases *INR1* – *INR6* for velocity gradient $\partial v/\partial x$ normalized by resolution-corrected inner scaling, shown in linear axes *(top)* and semilogarithmic axes *(bottom)*. 149
5.29 Pdfs from all nonreacting cases *INR1* – *INR6* for velocity gradient $\partial v/\partial y$ normalized by resolution-corrected inner scaling, shown in linear axes *(top)* and semilogarithmic axes *(bottom)*. 150
5.30 Pdfs from all nonreacting cases *INR1* – *INR6* for strain rate component S_{xx} normalized by resolution-corrected inner scaling, shown in linear axes *(top)* and semilogarithmic axes *(bottom)*. 151
5.31 Pdfs from all nonreacting cases *INR1* – *INR6* for strain rate component S_{yy} normalized by resolution-corrected inner scaling, shown in linear axes *(top)* and semilogarithmic axes *(bottom)*. 152
5.32 Pdfs from all nonreacting cases *INR1* – *INR6* for strain rate component S_{xy} normalized by resolution-corrected inner scaling, shown in linear axes *(top)* and semilogarithmic axes *(bottom)*. 153
5.33 Pdfs from all nonreacting cases *INR1* – *INR6* for dissipation normalized by resolution-corrected inner scaling, shown in linear axes *(top)* and semilogarithmic axes *(bottom)*. 154
5.34 Pdfs from all nonreacting cases *INR1* – *INR6* for vorticity ω_z normalized by resolution-corrected inner scaling, shown in linear axes *(top)* and semilogarithmic axes *(bottom)*. 155
5.35 Pdfs from all nonreacting cases *INR1* – *INR6* for enstrophy normalized by resolution-corrected inner scaling, shown in linear axes *(top)* and semilogarithmic axes *(bottom)*. 156

5.36 Pdfs from all nonreacting cases *INR1 – INR6* for contraction of the velocity gradient tensor $\boldsymbol{\nabla}\mathbf{u} : \boldsymbol{\nabla}\mathbf{u}$ normalized by resolution-corrected inner scaling, shown in linear axes *(top)* and semilogarithmic axes *(bottom)*. 157
5.37 Pdfs from all nonreacting cases *INR1 – INR6* for two-dimensional divergence $-\partial w/\partial z$ normalized by resolution-corrected inner scaling, shown in linear axes *(top)* and semilogarithmic axes *(bottom)*. . . . 158
5.38 Pdfs from nonreacting cases *INR1 – INR6*, normalized by resolution-corrected inner scaling. On-diagonal velocity gradients *(top)*, where the black symbols represent the $\partial u/\partial x$ component while the grey display $\partial v/\partial y$. Off-diagonal velocity gradients *(bottom)*, where the black symbols represent the $\partial u/\partial y$ component while the grey display $\partial v/\partial x$. 165

6.1 Sample velocity fields at $Re_\delta = 200\,100$. Instantaneous velocity fluctuations u *(top)* and v *(bottom)*, normalized by the centerline velocity u_c. 181
6.2 Sample velocity gradient fields at $Re_\delta = 200\,100$. Instantaneous velocity gradients $\partial u/\partial x$ *(top)* and $\partial u/\partial y$ *(bottom)*, normalized by inner variables ν/λ_ν^2 182
6.3 Sample velocity gradient fields at $Re_\delta = 200\,100$. Instantaneous velocity gradients $\partial v/\partial x$ *(top)* and $\partial v/\partial y$ *(bottom)*, normalized by inner variables ν/λ_ν^2 183
6.4 Sample velocity gradient fields at $Re_\delta = 200\,100$. Instantaneous strain rate components S_{xx} *(top)* and S_{yy} *(bottom)*, normalized by inner variables ν/λ_ν^2 184
6.5 Sample velocity gradient fields at $Re_\delta = 200\,100$. Instantaneous strain rate component S_{xy} *(top)* and $\mathrm{Log}_{10}(S_{ij}S_{ij})$ *(bottom)*, normalized respectively by classical inner scaling ν/λ_ν^2 and $(\nu/\lambda_\nu^2)^2$. Here $S_{ij}S_{ij} \equiv S_{xx}^2 + S_{yy}^2 + 2\,S_{xy}^2$. 185
6.6 Sample velocity gradient fields at $Re_\delta = 200\,100$. Instantaneous in-plane vorticity ω_z *(top)* and enstrophy $\mathrm{Log}_{10}(\vartheta_z)$ *(bottom)*, normalized respectively by classical inner scaling ν/λ_ν^2 and $(\nu/\lambda_\nu^2)^2$. Here $\vartheta_z \equiv 3/2\,\omega_z^2$. 186
6.7 Sample velocity gradient fields at $Re_\delta = 200\,100$, showing contraction of instantaneous velocity gradient tensor $\mathrm{Log}_{10}(\boldsymbol{\nabla}\mathbf{u} : \boldsymbol{\nabla}\mathbf{u})$ *(top)* and two-dimensional divergence $(-\partial w/\partial z + \boldsymbol{\nabla}\cdot\mathbf{u})$ *(bottom)*, normalized respectively by classical inner scaling $(\nu/\lambda_\nu^2)^2$ and ν/λ_ν^2 . . . 187
6.8 Pdfs from all reacting cases *IR1 – IR7* for velocity gradient $\partial u/\partial x$ *(top)* and $\partial u/\partial y$ *(bottom)* normalized by inner variables ν/λ_ν^2. . . . 188
6.9 Pdfs from all reacting cases *IR1 – IR7* for velocity gradient $\partial v/\partial x$ *(top)* and $\partial v/\partial y$ *(bottom)* normalized by inner variables ν/λ_ν^2. . . . 189

6.10 Pdfs from all reacting cases *IR1* − *IR7* for strain rate components S_{xx} *(top)* and S_{yy} *(bottom)* normalized by inner variables ν/λ_ν^2. 190
6.11 Pdfs from all reacting cases *IR1* − *IR7* for strain rate components S_{xy} *(top)* and $\mathrm{Log}_{10}\left(S_{ij}S_{ij}\right)$ *(bottom)* normalized by inner variables ν/λ_ν^2 and $\left(\nu/\lambda_\nu^2\right)^2$. 191
6.12 Pdfs from all reacting cases *IR1* − *IR7* for in-plane vorticity ω_z *(top)* and enstrophy $\mathrm{Log}_{10}\left(\vartheta_z\right)$ *(bottom)* normalized by inner variables ν/λ_ν^2 and $\left(\nu/\lambda_\nu^2\right)^2$. 192
6.13 Pdfs from all reacting cases *IR1* − *IR7* for contraction of the instantaneous velocity gradient tensor $\mathbf{\nabla u : \nabla u}$ *(top)* and two-dimensional divergence $\left(-\partial w/\partial z + \mathbf{\nabla \cdot u}\right)$ *(bottom)* normalized by inner variables $\left(\nu/\lambda_\nu^2\right)^2$ and ν/λ_ν^2. 193
6.14 Results from low-pass filtering to determine effective length scale $\Delta^\star$ for case *IR1*, $Re_\delta = 18\,300$. 194
6.15 Results from low-pass filtering to determine effective length scale $\Delta^\star$ for case *IR2*, $Re_\delta = 25\,900$. 195
6.16 Results from low-pass filtering to determine effective length scale $\Delta^\star$ for case *IR3*, $Re_\delta = 60\,600$. 196
6.17 Results from low-pass filtering to determine effective length scale $\Delta^\star$ for case *IR4*, $Re_\delta = 81\,900$. 197
6.18 Results from low-pass filtering to determine effective length scale $\Delta^\star$ for case *IR5*, $Re_\delta = 93\,700$. 198
6.19 Results from low-pass filtering to determine effective length scale $\Delta^\star$ for case *IR6*, $Re_\delta = 145\,300$. 199
6.20 Results from low-pass filtering to determine effective length scale $\Delta^\star$ for case *IR7*, $Re_\delta = 200\,100$. 200
6.21 Pdfs from all reacting cases *IR1* − *IR7* for velocity gradient $\partial u/\partial x$ normalized by resolution-corrected inner scaling, shown in linear axes *(top)* and semilogarithmic axes *(bottom)*. 202
6.22 Pdfs from all reacting cases *IR1* − *IR7* for velocity gradient $\partial u/\partial y$ normalized by resolution-corrected inner scaling, shown in linear axes *(top)* and semilogarithmic axes *(bottom)*. 203
6.23 Pdfs from all reacting cases *IR1* − *IR7* for velocity gradient $\partial v/\partial x$ normalized by resolution-corrected inner scaling, shown in linear axes *(top)* and semilogarithmic axes *(bottom)*. 204
6.24 Pdfs from all reacting cases *IR1* − *IR7* for velocity gradient $\partial v/\partial y$ normalized by resolution-corrected inner scaling, shown in linear axes *(top)* and semilogarithmic axes *(bottom)*. 205
6.25 Pdfs from all on-axis cases, reacting (open, red symbols) and nonreacting (closed, black symbols) for velocity gradient $\partial u/\partial x$ normalized by resolution-corrected inner scaling, shown in linear axes *(top)* and semilogarithmic axes *(bottom)*. 206

6.26 Pdfs from all on-axis cases, reacting (open, red symbols) and nonreacting (closed, black symbols) for velocity gradient $\partial u/\partial y$ normalized by resolution-corrected inner scaling, shown in linear axes *(top)* and semilogarithmic axes *(bottom)*. 207
6.27 Pdfs from all on-axis cases, reacting (open, red symbols) and nonreacting (closed, black symbols) for velocity gradient $\partial v/\partial x$ normalized by resolution-corrected inner scaling, shown in linear axes *(top)* and semilogarithmic axes *(bottom)*. 208
6.28 Pdfs from all on-axis cases, reacting (open, red symbols) and nonreacting (closed, black symbols) for velocity gradient $\partial v/\partial y$ normalized by resolution-corrected inner scaling, shown in linear axes *(top)* and semilogarithmic axes *(bottom)*. 209
6.29 Pdfs from all reacting cases *IR1* – *IR7*, normalized by resolution-corrected inner scaling. On-diagonal velocity gradients *(top)*, where the black symbols represent the $\partial u/\partial x$ component while the grey display $\partial v/\partial y$. Off-diagonal velocity gradients *(bottom)*, where the black symbols represent the $\partial u/\partial y$ component while the grey display $\partial v/\partial x$. 210
6.30 Pdfs from all on-axis cases, reacting (open, red symbols) and nonreacting (closed, black symbols) for strain rate S_{xx} normalized by resolution-corrected inner scaling, shown in linear axes *(top)* and semilogarithmic axes *(bottom)*. 213
6.31 Pdfs from all on-axis cases, reacting (open, red symbols) and nonreacting (closed, black symbols) for strain rate S_{yy} normalized by resolution-corrected inner scaling, shown in linear axes *(top)* and semilogarithmic axes *(bottom)*. 214
6.32 Pdfs from all on-axis cases, reacting (open, red symbols) and nonreacting (closed, black symbols) for strain rate S_{xy} normalized by resolution-corrected inner scaling, shown in linear axes *(top)* and semilogarithmic axes *(bottom)*. 215
6.33 Pdfs from all on-axis cases, reacting (open, red symbols) and nonreacting (closed, black symbols) for pseudo-dissipation normalized by resolution-corrected inner scaling, shown in linear axes *(top)* and semilogarithmic axes *(bottom)*. 216
6.34 Pdfs from all on-axis cases, reacting (open, red symbols) and nonreacting (closed, black symbols) for vorticity normalized by resolution-corrected inner scaling, shown in linear axes *(top)* and semilogarithmic axes *(bottom)*. 217
6.35 Pdfs from all on-axis cases, reacting (open, red symbols) and nonreacting (closed, black symbols) for enstrophy normalized by resolution-corrected inner scaling, shown in linear axes *(top)* and semilogarithmic axes *(bottom)*. 218

6.36 Pdfs from all on-axis cases, reacting (open, red symbols) and nonreacting (closed, black symbols) for contraction of the velocity gradient tensor normalized by resolution-corrected inner scaling, shown in linear axes *(top)* and semilogarithmic axes *(bottom)*. 219

6.37 Pdfs from all on-axis cases, reacting (open, red symbols) and nonreacting (closed, black symbols) for two-dimensional divergence normalized by resolution-corrected inner scaling, shown in linear axes *(top)* and semilogarithmic axes *(bottom)*. 220

6.38 Reduced *rms* values for the four $\partial u_i/\partial x_j$ components, S_{xy}, ω_z and $(-\partial w/\partial z + \boldsymbol{\nabla}\cdot\mathbf{u})$. Here σ_q is normalized by $\mathcal{N}^\star$ and by the nonreacting ensemble value $\langle\sigma_q\rangle_{NR}$ for each of the aforementioned gradients q. Results for nonreacting gradient data *(top)* and reacting gradients *(bottom)*. 228

6.39 Data from Fig. 6.38 replotted according to relative magnitude. The global average of all nonreacting data (black symbols), is $\sigma_q/\langle\sigma_q\rangle_{NR} = 1$. Each reacting cases is represented schematically above it by to-scale sketches of flames depicting the PIV FOV (green rectangles) and averaged stoichiometric centerline location s. The influence of buoyancy is diminished moving from left-to-right, as jet momentum flux J_0 is increased. 229

7.1 Pdfs from all nonreacting, off-centerline cases *RN0* – *RN5* for velocity gradient $\partial u/\partial x$ normalized by resolution-corrected inner scaling, shown in linear axes *(top)* and semilogarithmic axes *(bottom)*. . . . 241

7.2 Pdfs from all nonreacting, off-centerline cases *RN0* – *RN5* for velocity gradient $\partial u/\partial y$ normalized by resolution-corrected inner scaling, shown in linear axes *(top)* and semilogarithmic axes *(bottom)*. . . . 242

7.3 Pdfs from all nonreacting, off-centerline cases *RN0* – *RN5* for velocity gradient $\partial v/\partial x$ normalized by resolution-corrected inner scaling, shown in linear axes *(top)* and semilogarithmic axes *(bottom)*. . . . 243

7.4 Pdfs from all nonreacting, off-centerline cases *RN0* – *RN5* for velocity gradient $\partial v/\partial y$ normalized by resolution-corrected inner scaling, shown in linear axes *(top)* and semilogarithmic axes *(bottom)*. . . . 244

7.5 Pdfs from all nonreacting, off-centerline cases *RN0* – *RN5* for strain rate component S_{xx} normalized by resolution-corrected inner scaling, shown in linear axes *(top)* and semilogarithmic axes *(bottom)*. . . . 245

7.6 Pdfs from all nonreacting, off-centerline cases *RN0* – *RN5* for strain rate component S_{yy} normalized by resolution-corrected inner scaling, shown in linear axes *(top)* and semilogarithmic axes *(bottom)*. . . . 246

7.7 Pdfs from all nonreacting, off-centerline cases *RN0* – *RN5* for strain rate component S_{xy} normalized by resolution-corrected inner scaling, shown in linear axes *(top)* and semilogarithmic axes *(bottom)*. . . . 247

7.8 Pdfs from all nonreacting, off-centerline cases *RN0* − *RN5*, for dissipation normalized by resolution-corrected inner scaling, shown in linear axes *(top)* and semilogarithmic axes *(bottom)*. 248
7.9 Pdfs from all nonreacting, off-centerline cases *RN0* − *RN5* for vorticity ω_z normalized by resolution-corrected inner scaling, shown in linear axes *(top)* and semilogarithmic axes *(bottom)*. 249
7.10 Pdfs from all nonreacting, off-centerline cases *RN0* − *RN5*, for enstrophy normalized by resolution-corrected inner scaling, shown in linear axes *(top)* and semilogarithmic axes *(bottom)*. 250
7.11 Pdfs from all nonreacting, off-centerline cases *RN0* − *RN5*, for contraction of the velocity gradient tensor $\mathbf{\nabla u} : \mathbf{\nabla u}$ normalized by resolution-corrected inner scaling, shown in linear axes *(top)* and semilogarithmic axes *(bottom)*. 251
7.12 Pdfs from all nonreacting, off-centerline cases *RN0* − *RN5* for two-dimensional divergence $-\partial w/\partial z$ normalized by resolution-corrected inner scaling, shown in linear axes *(top)* and semilogarithmic axes *(bottom)*. 252
7.13 Pdfs from conditioned data for all nonreacting, off-centerline cases *RN0* − *RN5* for velocity gradient $\partial u/\partial x$ normalized by resolution-corrected inner scaling, shown in linear axes *(top)* and semilogarithmic axes *(bottom)*. 254
7.14 Pdfs from conditioned data for all nonreacting, off-centerline cases *RN0* − *RN5* for velocity gradient $\partial u/\partial y$ normalized by resolution-corrected inner scaling, shown in linear axes *(top)* and semilogarithmic axes *(bottom)*. 255
7.15 Pdfs from conditioned data for all nonreacting, off-centerline cases *RN0* − *RN5* for velocity gradient $\partial v/\partial x$ normalized by resolution-corrected inner scaling, shown in linear axes *(top)* and semilogarithmic axes *(bottom)*. 256
7.16 Pdfs from conditioned data for all nonreacting, off-centerline cases *RN0* − *RN5* for velocity gradient $\partial v/\partial y$ normalized by resolution-corrected inner scaling, shown in linear axes *(top)* and semilogarithmic axes *(bottom)*. 257
7.17 Pdfs from conditioned data for all nonreacting, off-centerline cases *RN0* − *RN5* for strain rate component S_{xx} normalized by resolution-corrected inner scaling, shown in linear axes *(top)* and semilogarithmic axes *(bottom)*. 258
7.18 Pdfs from conditioned data for all nonreacting, off-centerline cases *RN0* − *RN5* for strain rate component S_{yy} normalized by resolution-corrected inner scaling, shown in linear axes *(top)* and semilogarithmic axes *(bottom)*. 259

7.19 Pdfs from conditioned data for all nonreacting, off-centerline cases *RN0 – RN5* for strain rate component S_{xy} normalized by resolution-corrected inner scaling, shown in linear axes *(top)* and semilogarithmic axes *(bottom)*. 260
7.20 Pdfs from conditioned data for all nonreacting, off-centerline cases *RN0 – RN5*, for the pseudo-dissipation normalized by resolution-corrected inner scaling, shown in linear axes *(top)* and semilogarithmic axes *(bottom)*. 261
7.21 Pdfs from conditioned data for all nonreacting, off-centerline cases *RN0 – RN5* for the vorticity ω_z normalized by resolution-corrected inner scaling, shown in linear axes *(top)* and semilogarithmic axes *(bottom)*. 262
7.22 Pdfs from conditioned data for all nonreacting, off-centerline cases *RN0 – RN5*, for pseudo-enstrophy normalized by resolution-corrected inner scaling, shown in linear axes *(top)* and semilogarithmic axes *(bottom)*. 263
7.23 Pdfs from conditioned data for all nonreacting, off-centerline cases *RN0 – RN5*, for contraction of the velocity gradient tensor $\boldsymbol{\nabla}\mathbf{u} : \boldsymbol{\nabla}\mathbf{u}$ normalized by resolution-corrected inner scaling, shown in linear axes *(top)* and semilogarithmic axes *(bottom)*. 264
7.24 Pdfs from conditioned data for all nonreacting, off-centerline cases *RN0 – RN5* for two-dimensional divergence $-\partial w/\partial z$ normalized by resolution-corrected inner scaling, shown in linear axes *(top)* and semilogarithmic axes *(bottom)*. 265
7.25 *Rms* values of the strain rate components as a function of shear $\mathcal{S}$ nondimensionalized on outer variables. The ratio of the *rms* of the on-diagonal strain rates S_{xx}/S_{yy}, *(top)*, is shown with the ratio $(\sigma_{S_{xx}} + \sigma_{S_{xx}})^{1/2}/\sigma_{S_{xy}}$, *(bottom)*. The black circles are data from the present study, the red squares are from the data of Mullin and Dahm (2005b). 272
7.26 *Rms* values of the velocity fluctuation ratio $\sigma_{v'}/\sigma_{u'}$ as a function of shear $\mathcal{S}$ nondimensionalized on outer variables, *(top)*. The *rms* of the divergence, normalized by its centerline (*RN0*) value, is also plotted against the dimensionless shear, *(bottom)*. The black circles are data from the present study, the red squares are the data of Mullin and Dahm (2005b). 273

8.1 Pdfs from conditioned data for all reacting, off-centerline cases *RR0 – RR5* for velocity gradient $\partial u/\partial x$ normalized by resolution-corrected inner scaling, shown in linear axes *(top)* and semilogarithmic axes *(bottom)*. 280

8.2 Pdfs from conditioned data for all reacting, off-centerline cases *RR0* – *RR5* for velocity gradient $\partial u/\partial y$ normalized by resolution-corrected inner scaling, shown in linear axes *(top)* and semilogarithmic axes *(bottom)*. . . . 281

8.3 Pdfs from conditioned data for all reacting, off-centerline cases *RR0* – *RR5* for velocity gradient $\partial v/\partial x$ normalized by resolution-corrected inner scaling, shown in linear axes *(top)* and semilogarithmic axes *(bottom)*. . . . 282

8.4 Pdfs from conditioned data for all reacting, off-centerline cases *RR0* – *RR5* for velocity gradient $\partial v/\partial y$ normalized by resolution-corrected inner scaling, shown in linear axes *(top)* and semilogarithmic axes *(bottom)*. . . . 283

8.5 Pdfs from conditioned data for all reacting, off-centerline cases *RR0* – *RR5* for strain rate component S_{xx} normalized by resolution-corrected inner scaling, shown in linear axes *(top)* and semilogarithmic axes *(bottom)*. . . . 284

8.6 Pdfs from conditioned data for all reacting, off-centerline cases *RR0* – *RR5* for strain rate component S_{yy} normalized by resolution-corrected inner scaling, shown in linear axes *(top)* and semilogarithmic axes *(bottom)*. . . . 285

8.7 Pdfs from conditioned data for all reacting, off-centerline cases *RR0* – *RR5* for strain rate component S_{xy} normalized by resolution-corrected inner scaling, shown in linear axes *(top)* and semilogarithmic axes *(bottom)*. . . . 286

8.8 Pdfs from conditioned data for all reacting, off-centerline cases *RR0* – *RR5*, for pseudo-dissipation normalized by resolution-corrected inner scaling, shown in linear axes *(top)* and semilogarithmic axes *(bottom)*. . . . 287

8.9 Pdfs from conditioned data for all reacting, off-centerline cases *RR0* – *RR5* for vorticity ω_z normalized by resolution-corrected inner scaling, shown in linear axes *(top)* and semilogarithmic axes *(bottom)*. . . . 288

8.10 Pdfs from conditioned data for all reacting, off-centerline cases *RR0* – *RR5*, for pseudo-enstrophy normalized by resolution-corrected inner scaling, shown in linear axes *(top)* and semilogarithmic axes *(bottom)*. . . . 289

8.11 Pdfs from conditioned data for all reacting, off-centerline cases *RR0* – *RR5*, for contraction of the velocity gradient tensor $\nabla \mathbf{u} : \nabla \mathbf{u}$ normalized by resolution-corrected inner scaling, shown in linear axes *(top)* and semilogarithmic axes *(bottom)*. . . . 290

8.12 Pdfs from conditioned data for all reacting, off-centerline cases *RR0* – *RR5* for two-dimensional divergence $(-\partial w/\partial z + \nabla \cdot \mathbf{u})$ normalized by resolution-corrected inner scaling, shown in linear axes *(top)* and semilogarithmic axes *(bottom)*. . . . 291

8.13 Results from nonreacting *and* reacting, off-centerline cases: *RN0 – RN5 (top)*, and *RR0 – RR5 (bottom)*, spanning the entire range of shear values $\mathcal{S}$ investigated. Pdfs of dissipation $\text{Log}_{10}(S_{ij}S_{ij})$ normalized by $(\mathcal{N}^\star)^2$. Statistics are shown *with* application of the enstrophy rejection strategy. 299
8.14 Results from nonreacting *and* reacting, off-centerline cases: *RN0 – RN5 (top)*, and *RR0 – RR5 (bottom)*, spanning the entire range of shear values $\mathcal{S}$ investigated. Pdfs of enstrophy $\text{Log}_{10}(\vartheta_z)$ normalized by $(\mathcal{N}^\star)^2$. Statistics are shown *with* application of the enstrophy rejection strategy. 300
8.15 Results from nonreacting *and* reacting, off-centerline cases: *RN0 – RN5 (top)*, and *RR0 – RR5 (bottom)*, spanning the entire range of shear values $\mathcal{S}$ investigated. Pdfs of the two-dimensional divergence $(-\partial w/\partial z + \mathbf{\nabla} \cdot \mathbf{u})$ normalized by $\mathcal{N}^\star$. Statistics are shown *with* application of the enstrophy rejection strategy. 301

A.1 Spherical coordinate system. 309
A.2 Nomenclature for Snell's law applied to randomly oriented index of refraction interface. 310
A.3 Differential surface element in spherical coordinates. 311
A.4 von Neumann's Golden Rule for sampling a distribution. 314
A.5 Projection of ϕ and θ onto ψ_x and ψ_y. 315
A.6 Sampling of $\beta(\phi)$ and $\beta(\theta)$: $N = 1000$, bins $= 100$. 317
A.7 Sampling of $\beta(\phi)$ and $\beta(\theta)$: $N = 1 \times 10^6$, bins $= 100$. 318
A.8 Sampling of $\beta(\phi)$ and $\beta(\theta)$: $N = 1 \times 10^6$, bins $= 1000$. 319
A.9 Sampling of $\beta(\phi)$ and $\beta(\theta)$: $N = 900$, $\text{bins}_{\phi,\theta} = 10$, $\text{bins}_{\epsilon_{x,y}} = 100$. . 320
A.10 Sampling of $\beta(\epsilon_x)$ and $\beta(\epsilon_y)$ for $N = 2000$, $\text{bins}_{\phi,\theta} = 50$, $\text{bins}_{\epsilon_{x,y}} = 1000$. 321
A.11 History of running average plotted against sample size for a record length of $n = 10^7$ samples. 322
A.12 Geometric origin of Cauchy distribution. 323

B.1 Profiles of the beam position uncertainty and the analytical Cauchy fit using the experimentally determined parameters. Upper panel: positional uncertainty for a reacting jet flame; lower panel: uncertainty for nonreacting Nitrogen jet. 325
B.2 Reynolds number scaling of beam position uncertainty. Plotted on linear axes in the upper panel and log-log in the lower panel. The squares and circles indicate experimental data and the red triangles are the results from corresponding MC simulations. 326

LIST OF TABLES

Table

3.1 Flow conditions and relevant parameters for each of the outer-scale nonreacting measurement cases, identified as *ONR*X, in this study. . . 68

3.2 Flow conditions and relevant parameters for each of the outer-scale reacting measurement cases, identified as *OR*X, in this study. 69

3.3 Flow conditions and relevant parameters for each of the inner-scale nonreacting on-centerline measurement cases, identified as *INR*X, in this study. 70

3.4 Flow conditions and relevant parameters for each of the inner-scale reacting on-centerline measurement cases, identified as *IR*X, in this study. 71

3.5 Flow conditions and relevant parameters for the off-centerline (radial) nonreacting inner-scale measurement cases, identified as *RN*X, in this study. 72

3.6 Flow conditions and relevant parameters for each of the off-centerline (radial) reacting inner-scale measurement cases, identified as *RR*X, in this study. 73

5.1 Averaged spectral parameters $\langle p \rangle$, $\langle \Delta_R \rangle$ and $\langle \Delta^\star \rangle$ for all cases in Table 3.3 obtained by averaging over results in Fig. 5.23 from ω_z, S_{xx}, S_{yy} and S_{xy}. Here Λ_ν and $\Lambda^\star$ values are from $\Lambda_i \equiv (\Delta_i/\delta) Re_\delta^{3/4}$. 145

5.2 Normalized central moments computed from pdfs for $Re = 7200$ case. The mean is μ, σ is the *rms* fluctuation, $\gamma = \mu_3/\sigma^3$ is the skewness and $\beta = \mu_4/\sigma^4$ is the kurtosis. All quantities normalized by resolution-corrected inner scaling $\mathcal{N}^\star$. 159

5.3 Normalized central moments computed from pdfs for $Re = 11\,000$ case. The mean is μ, σ is the *rms* fluctuation, $\gamma = \mu_3/\sigma^3$ is the skewness and $\beta = \mu_4/\sigma^4$ is the kurtosis. All quantities normalized by resolution-corrected inner scaling $\mathcal{N}^\star$. 160

5.4 Normalized central moments computed from pdfs for $Re = 21\,400$ case. The mean is μ, σ is the *rms* fluctuation, $\gamma = \mu_3/\sigma^3$ is the skewness and $\beta = \mu_4/\sigma^4$ is the kurtosis. All quantities normalized by resolution-corrected inner scaling $\mathcal{N}^\star$. 161

5.5 Normalized central moments computed from pdfs for $Re = 31\,400$ case. The mean is μ, σ is the *rms* fluctuation, $\gamma = \mu_3/\sigma^3$ is the skewness and $\beta = \mu_4/\sigma^4$ is the kurtosis. All quantities normalized by resolution-corrected inner scaling $\mathcal{N}^\star$. 162
5.6 Normalized central moments computed from pdfs for $Re = 45\,500$ case. The mean is μ, σ is the *rms* fluctuation, $\gamma = \mu_3/\sigma^3$ is the skewness and $\beta = \mu_4/\sigma^4$ is the kurtosis. All quantities normalized by resolution-corrected inner scaling $\mathcal{N}^\star$. 163
5.7 Normalized central moments computed from pdfs for $Re = 50\,200$ case. The mean is μ, σ is the *rms* fluctuation, $\gamma = \mu_3/\sigma^3$ is the skewness and $\beta = \mu_4/\sigma^4$ is the kurtosis. All quantities normalized by resolution-corrected inner scaling $\mathcal{N}^\star$. 164
5.8 Ratios of the variances of the on-diagonal gradient components over the off-diagonal components. The analytical value obtained via the assumption of homogeneous isotropic turbulence is 2. The final two conditions adorned with a † are presented for comparison, and are from the data given by Mullin and Dahm (2005b). 166
5.9 Ratios of the variances of the on-diagonal gradient components over the off-diagonal components. The analytical value obtained via the assumption of homogeneous isotropic turbulence is 2. The final conditions indicated by † are from Mullin and Dahm (2005b), shown for comparison. 167
5.10 Comparison of present measured velocity gradient skewness γ and kurtosis β with corresponding results from DNS studies of periodic homogeneous isotropic turbulence from Gotoh et al. (2002) and Jiménez et al. (1993), along with measured values from Mullin (2004) at similar Re_λ values. 168

6.1 Averaged spectral parameters $\langle p \rangle$, $\langle \Delta_R \rangle$ and $\langle \Delta^\star \rangle$ for all cases in Table 3.4 obtained by averaging over results from ω_z, S_{xx}, S_{yy} and S_{xy}. Here Λ_ν and $\Lambda^\star$ values are from $\Lambda_i \equiv (\Delta_i/\delta) Re_\delta^{3/4}$. 201
6.2 Ratios of the variances of the on-diagonal gradient components over the off-diagonal components. The analytical value obtained via the assumption of homogeneous isotropic turbulence is 2. 211
6.3 Ratios of the variances of the on-diagonal gradient components over the off-diagonal components. The analytical value obtained via the assumption of homogeneous isotropic turbulence is 2. 212
6.4 Normalized central moments computed from pdfs for $Re = 18\,300$ case. The mean is μ, σ is the *rms* fluctuation, $\gamma = \mu_3/\sigma^3$ is the skewness and $\beta = \mu_4/\sigma^4$ is the kurtosis. All quantities normalized by resolution-corrected inner scaling $\mathcal{N}^\star$. 221

6.5 Normalized central moments computed from pdfs for $Re = 25\,900$ case. The mean is μ, σ is the *rms* fluctuation, $\gamma = \mu_3/\sigma^3$ is the skewness and $\beta = \mu_4/\sigma^4$ is the kurtosis. All quantities normalized by resolution-corrected inner scaling $\mathcal{N}^\star$. 222
6.6 Normalized central moments computed from pdfs for $Re = 60\,600$ case. The mean is μ, σ is the *rms* fluctuation, $\gamma = \mu_3/\sigma^3$ is the skewness and $\beta = \mu_4/\sigma^4$ is the kurtosis. All quantities normalized by resolution-corrected inner scaling $\mathcal{N}^\star$. 223
6.7 Normalized central moments computed from pdfs for $Re = 81\,900$ case. The mean is μ, σ is the *rms* fluctuation, $\gamma = \mu_3/\sigma^3$ is the skewness and $\beta = \mu_4/\sigma^4$ is the kurtosis. All quantities normalized by resolution-corrected inner scaling $\mathcal{N}^\star$. 224
6.8 Normalized central moments computed from pdfs for $Re = 93\,700$ case. The mean is μ, σ is the *rms* fluctuation, $\gamma = \mu_3/\sigma^3$ is the skewness and $\beta = \mu_4/\sigma^4$ is the kurtosis. All quantities normalized by resolution-corrected inner scaling $\mathcal{N}^\star$. 225
6.9 Normalized central moments computed from pdfs for $Re = 145\,300$ case. The mean is μ, σ is the *rms* fluctuation, $\gamma = \mu_3/\sigma^3$ is the skewness and $\beta = \mu_4/\sigma^4$ is the kurtosis. All quantities normalized by resolution-corrected inner scaling $\mathcal{N}^\star$. 226
6.10 Normalized central moments computed from pdfs for $Re = 200\,100$ case. The mean is μ, σ is the *rms* fluctuation, $\gamma = \mu_3/\sigma^3$ is the skewness and $\beta = \mu_4/\sigma^4$ is the kurtosis. All quantities normalized by resolution-corrected inner scaling $\mathcal{N}^\star$. 227

7.1 Averaged spectral parameters $\langle p \rangle$, $\langle \Delta_R \rangle$ and $\langle \Delta^\star \rangle$ for all cases in Table 3.5 obtained by averaging over results from ω_z, S_{xx}, S_{yy} and S_{xy}. Here Λ_ν and $\Lambda^\star$ values are from $\Lambda_i \equiv (\Delta_i/\delta) Re_\delta^{3/4}$. The quantity $r/\delta_{1/2}$ is the radius normalized by the half width at the half-maximum point. The mean outer shear is $\mathcal{S} \equiv \sqrt{2}\,|\partial\langle u \rangle/\partial r|$. For all cases, $Re_\delta = 19\,000$ and $\delta = 0.202$ m. The final two cases, indicated by a †, are the cases reprocessed with the data conditioning strategy. 253
7.2 Normalized central moments computed from pdfs of conditioned data for *RN0* case. The mean is μ, σ is the *rms* fluctuation, $\gamma = \mu_3/\sigma^3$ is the skewness and $\beta = \mu_4/\sigma^4$ is the kurtosis. All quantities normalized by resolution-corrected inner scaling $\mathcal{N}^\star$. 266
7.3 Normalized central moments computed from pdfs of conditioned data for *RN1* case. The mean is μ, σ is the *rms* fluctuation, $\gamma = \mu_3/\sigma^3$ is the skewness and $\beta = \mu_4/\sigma^4$ is the kurtosis. All quantities normalized by resolution-corrected inner scaling $\mathcal{N}^\star$. 267

7.4 Normalized central moments computed from pdfs of conditioned data for *RN2* case. The mean is μ, σ is the *rms* fluctuation, $\gamma = \mu_3/\sigma^3$ is the skewness and $\beta = \mu_4/\sigma^4$ is the kurtosis. All quantities normalized by resolution-corrected inner scaling $\mathcal{N}^\star$. 268
7.5 Normalized central moments computed from pdfs of conditioned data for *RN3* case. The mean is μ, σ is the *rms* fluctuation, $\gamma = \mu_3/\sigma^3$ is the skewness and $\beta = \mu_4/\sigma^4$ is the kurtosis. All quantities normalized by resolution-corrected inner scaling $\mathcal{N}^\star$. 269
7.6 Normalized central moments computed from pdfs of conditioned data for *RN4* case. The mean is μ, σ is the *rms* fluctuation, $\gamma = \mu_3/\sigma^3$ is the skewness and $\beta = \mu_4/\sigma^4$ is the kurtosis. All quantities normalized by resolution-corrected inner scaling $\mathcal{N}^\star$. 270
7.7 Normalized central moments computed from pdfs of conditioned data for *RN5* case. The mean is μ, σ is the *rms* fluctuation, $\gamma = \mu_3/\sigma^3$ is the skewness and $\beta = \mu_4/\sigma^4$ is the kurtosis. All quantities normalized by resolution-corrected inner scaling $\mathcal{N}^\star$. 271

8.1 Averaged spectral parameters $\langle p \rangle$, $\langle \Delta_R \rangle$ and $\langle \Delta^\star \rangle$ for all cases in Table 3.6 obtained by averaging over results from ω_z, S_{xx}, S_{yy} and S_{xy}. Here Λ_ν and $\Lambda^\star$ values are from $\Lambda_i \equiv (\Delta_i/\delta) Re_\delta^{3/4}$. The quantity $r/\delta_{1/2}$ is the radius normalized by the half width at the half-maximum point. The mean outer shear is $\mathcal{S} \equiv \sqrt{2}\, |\partial \langle u \rangle / \partial r|$. For all cases, $Re_\delta = 65\,000$ and $\delta = 0.226$ m. The final two cases, indicated by a †, are the cases reprocessed with the data conditioning strategy. 292
8.2 Normalized central moments computed from pdfs of conditioned data for *RR0* case. The mean is μ, σ is the *rms* fluctuation, $\gamma = \mu_3/\sigma^3$ is the skewness and $\beta = \mu_4/\sigma^4$ is the kurtosis. All quantities normalized by resolution-corrected inner scaling $\mathcal{N}^\star$. 293
8.3 Normalized central moments computed from pdfs of conditioned data for *RR1* case. The mean is μ, σ is the *rms* fluctuation, $\gamma = \mu_3/\sigma^3$ is the skewness and $\beta = \mu_4/\sigma^4$ is the kurtosis. All quantities normalized by resolution-corrected inner scaling $\mathcal{N}^\star$. 294
8.4 Normalized central moments computed from pdfs of conditioned data for *RR2* case. The mean is μ, σ is the *rms* fluctuation, $\gamma = \mu_3/\sigma^3$ is the skewness and $\beta = \mu_4/\sigma^4$ is the kurtosis. All quantities normalized by resolution-corrected inner scaling $\mathcal{N}^\star$. 295
8.5 Normalized central moments computed from pdfs of conditioned data for *RR3* case. The mean is μ, σ is the *rms* fluctuation, $\gamma = \mu_3/\sigma^3$ is the skewness and $\beta = \mu_4/\sigma^4$ is the kurtosis. All quantities normalized by resolution-corrected inner scaling $\mathcal{N}^\star$. 296

8.6 Normalized central moments computed from pdfs of conditioned data for *RR4* case. The mean is μ, σ is the *rms* fluctuation, $\gamma = \mu_3/\sigma^3$ is the skewness and $\beta = \mu_4/\sigma^4$ is the kurtosis. All quantities normalized by resolution-corrected inner scaling $\mathcal{N}^\star$. 297

8.7 Normalized central moments computed from pdfs of conditioned data for *RR5* case. The mean is μ, σ is the *rms* fluctuation, $\gamma = \mu_3/\sigma^3$ is the skewness and $\beta = \mu_4/\sigma^4$ is the kurtosis. All quantities normalized by resolution-corrected inner scaling $\mathcal{N}^\star$. 298

A.1 Sampling functions for ϕ and θ: $\beta(\phi)$ and $\beta(\theta)$. 313

LIST OF APPENDICES

Appendix

A. Index of Refraction Effects in a Reacting Flow 307

A.1 Concept 308
A.2 Formulation 308
A.3 Index of Refraction Interface Deflections 315
A.4 First-Order Approximation Results 316
A.5 Random Number Generator 317
A.6 Probability Distribution of Individual Interfaces 319
A.6.1 Geometric Interpretation 322
A.7 Probability Distribution of a Sum over $\mathcal{N}$ Individual Interfaces . . 324

B. Experimental Results for Index of Refraction Effects in a Reacting Flow325

B.1 Conclusions 326

NOMENCLATURE

Symbol	Description
A_E	Nozzle area
b	Gradient order parameter from (5.18)
$(c_\delta)_j$	≈ 0.36, Growth rate constant for jets
$(c_\delta)_w$	Growth rate constant for wakes
$(c_u)_j$	≈ 7.2, Velocity decay constant for jets
$(c_u)_w$	Velocity decay constant for wakes
d^+	Extended momentum diameter
d^*	Far-field equivalent source diameter
d_E	Nozzle diameter
D	Drag force
$D(p)$	Viscous roll off function
$\boldsymbol{\nabla} \cdot \mathbf{u}$	$\approx \partial u/\partial x + \partial v/\partial y$, Measured 2D divergence
$\boldsymbol{\nabla}\mathbf{u}$	Velocity gradient tensor
$\boldsymbol{\nabla}\mathbf{u} : \boldsymbol{\nabla}\mathbf{u}$	$\approx (\partial u/\partial x)^2 + (\partial u/\partial y)^2 + (\partial v/\partial x)^2 +$ $(\partial v/\partial y)^2 + (-\partial w/\partial z)^2$, Velocity gradient contraction
J_0	Jet momentum flux
k	Wavenumber
k_R	Δ_R wavenumber

k_δ	Outer length scale wavenumber
k_ν	Viscous length scale wavenumber
k_{PIV}	PIV wavenumber cutoff frequency
ℓ	Length of potential core region
M	Molecular weight
N	Number of samples
$\mathcal{N}^\star$	Normalization quantity (5.23)
p	Exponent parameter from (5.18)
$E_P(k)$	Pao spectrum
$q(\mathbf{x})$	Generic gradient quantity
$Q(\mathbf{k})$	Generic gradient spectra
Q_E	Volumetric flow rate of jet fluid
r	Radial distance from jet axis
Re_δ	$\equiv u_c\delta/\nu$, Local Reynolds number
Re_λ	$\equiv u'_{rms}\lambda_g/\nu$, Taylor scale Reynolds number
$\widetilde{R}$	Molar gas constant
$\mathcal{S}$	$\equiv \sqrt{2}\ \lvert\partial\overline{u}/\partial r\rvert$, Mean shear parameter
S_{xx}	$\equiv 1/2\,(\partial u/\partial x + \partial u/\partial x)$, Strain-rate component
S_{yy}	$\equiv 1/2\,(\partial v/\partial y + \partial v/\partial y)$, Strain-rate component
S_{xy}	$\equiv 1/2\,(\partial v/\partial x + \partial u/\partial y)$, Strain-rate component
U_E	Jet exit velocity
U_∞	Coflow velocity
u_c	$\equiv U_c - U_\infty$ Local outer scale excess centerline velocity
U	Absolute streamwise velocity
u	$\equiv U - U_\infty$, Excess streamwise velocity

u'_{rms}, v'_{rms}	*rms* velocity fluctuation values
V	Mean transverse velocity
x	Streamwise coordinate
x_E	Virtual origin
(x/θ)	Dimensionless streamwise coordinate
y	Transverse coordinate
y_{CL}	Fitted velocity profile centerline

Greek

β	$\equiv \mu_4/\sigma^4$, Dimensionless kurtosis
γ	$\equiv \mu_3/\sigma^3$, Dimensionless skewness
Δ	Arbitrary length scale
Δ_{IW}	PIV interrogation window (vector) spacing
Δ_R	Length scale parameter from (5.18)
$\Delta^\star$	Effective length scale obtained from (5.18)
Δt	PIV temporal resolution
δ	Local outer scale full-width where u reaches 5% of u_c
$\delta_{1/2}$	Local half-width at half-maximum of velocity profile
ε	$\equiv 2\,\nu\left[\frac{3}{2}\left(S_{xx}^2 + S_{yy}^2\right) + 6\,S_{xy}^2\right]$, Kinetic energy dissipation
η	$\equiv r/\delta$, Dimensionless radial coordinate
Λ	Viscous length scale constant ≈ 11.2
λ_K	Kolmogorov length scale
λ_ν	Local inner (viscous) length scale
μ	Mean value of a sample set
μ_n	Central moments, with $n = 2$ as the variance

ν	Kinematic viscosity
ω_z	$\equiv 1/2\,(\partial v/\partial x - \partial u/\partial y)$, vorticity vector component
ρ_E	Source/jet fluid density
ρ_∞	Coflow density
$\rho_\infty^{\mathit{eff}}$	Coflow density
σ	$\equiv \mu_2^{1/2}$, Root mean square (*rms*)
σ_q	*Rms* of the q-th gradient
σ_q	$\equiv \sigma_q/\mathcal{N}^\star$ normalized *rms*
θ	Momentum radius
θ^+	Extended momentum radius
ϑ_z	$\equiv \omega_z^2$, Pseudo-enstrophy
ξ	$\equiv x - x_E$, Ideal point source streamwise coordinate

<u>Mathematical</u>

$\overline{(\cdot)}$	Averaged quantity
$\langle\cdot\rangle$	Ensemble averaged quantity
$(\cdot)'$	Fluctuating quantity, e.g. mean subtracted
$(\cdot)''$	Fluctuation obtained by local field mean subtracted
$\langle\cdot\rangle_\Delta$	Under resolved at scale Δ
$\langle\cdot\rangle_\infty$	Infinitely-resolved or true value
$\sim$	Proportional to
$\mathrm{var}\{\cdot\}$	Variance

<u>Initializations & Acronyms</u>

DNS	Direct numerical simulation

FFT	Fast Fourier transform
FOV	Field of view
K41	Kolmogorov's 1941 theorem
pdf	Probability density function
PIV	Particle image velocimetry
PSD	Power spectrum density
rms	Root mean square
SLPM	Standard liters per minute

CHAPTER I

Introduction

Studies of the flow and mixing processes in nonreacting turbulent shear flows, such as mixing layers, jets, wakes, plumes and other canonical configurations, have represented a substantial fraction of the research efforts devoted to fluid dynamics over the past 50 years. This has produced a substantial body of results in the literature on the large-scale and small-sale turbulence in such nonreacting shear flows and the resulting entrainment and mixing properties of such flows. In principle, one of the most significant areas of potential application for these results is in nonpremixed or partially-premixed combustion, where turbulent shear flows are routinely used to rapidly mix a fuel and oxidizer together and allow them to react. Yet for most fuel-oxidizer combinations of practical interest, the resulting reactions release considerable heat on a volume or mass basis, and as a consequence the turbulent shear flow itself is substantially modified from its original nonreacting form by the effects of heat release. If the heat release effects are large enough, then the reacting flow might bear little resemblance to its nonreacting counterpart, and the large body of research results on nonreacting turbulent shear flows would then be of limited utility in understanding combustion in such flows. On the other hand, if the effects of heat release are sufficiently small that they can be considered as corrections to the original nonreacting flow, then it may even be possible to predict most of the properties of mixing-limited combustion occurring within the flow from the entrainment and mixing properties of the underlying turbulent shear flow itself.

Indeed, in combustion science, studies of nonreacting turbulent shear flows such as jets and plumes without heat release were used in early investigations to gain insights into the flow and mixing processes that may be at work in corresponding reacting flows (e.g., Hottel and Hawthorne 1949; Hawthorne and Hottel 1949). However, it was widely observed in subsequent experimental studies that the heat release produced by exothermic chemical reactions occurring in turbulent shear flows can dramatically alter the resulting flow and mixing processes relative to a corresponding nonreacting version of the same flow (e.g., Ricou and Spalding 1961; Kremer 1967; Chigier and Strokin 1974; Takagi et al. 1981; Beér and Chigier 1983; Muñiz and Mungal 1995; Rehm and Clemens 1998; Tacina and Dahm 2000; Han and Mungal 2001). Often, among the most obvious of such changes are those produced by buoyancy effects that result from the reduced density. These can produce large changes in the velocity field and greatly increase the associated entrainment and mixing rates in the flow (e.g., Steward 1970; Chen and Rodi 1980; Cetegen et al. 1984; Peters and Göttgens 1991; Delichatsios 1993; Blake and McDonald 1995; Blake and Coté 1999). However, even under conditions for which buoyancy effects are negligible, heat release occurring within turbulent shear flows is known to produce potentially large changes in the flow, which in turn can create substantial changes the resulting entrainment and mixing rates relative to an otherwise identical nonreacting turbulent shear flow (e.g., Wallace 1981; Hermanson and Dimotakis 1989; Tacina and Dahm 2000; Dahm 2005). In general, results from turbulent shear flows without heat release are today widely viewed as having limited relevance to exothermically reacting turbulent shear flows with substantial heat release (e.g., Beér and Chigier 1983; Muñiz and Mungal 1995; Han and Mungal 2001).

One approach to understanding how heat release affects the flow and mixing processes in turbulent shear flows is to address individual canonical flow configurations one at a time, and then conduct comparative studies of nonreacting and reacting versions of otherwise identical versions of each flow. This is the approach that has been used almost exclusively to date in studies of heat release effects on turbulent shear flows. Thus, for instance, there have been numerous such comparative studies for fundamental configurations such as mixing layers (e.g., Wallace 1981; Hermanson and Dimotakis 1989), axisymmetric jets (e.g., Ricou and Spalding 1961; Chigier and Strokin 1974; Takagi et al. 1981; Muñiz and Mungal 1995), planar jets (e.g., Rehm and Clemens 1998;), and many other canonical flows. Studies of this type have focused primarily on reporting observations of various differences in measurable quantities from nonreacting and reacting versions of the same flow.

Collectively, comparitive studies of this type have served to clearly demonstrate that there are widely differing effects produced by heat release among these flows, but they have provided little general understanding of the physical mechanisms that produce these differences. Even considering any one of these canonical flows alone, there is to date no real understanding of the origins of the heat release effects seen in that flow, and across the broad class of turbulent shear flows there is certainly no widely accepted, fundamentally-based, physical understanding for how heat release produces the changes that it does. Consistent with this, methods to date for predicting the effects of heat release on any given turbulent shear flow are almost entirely *ad hoc*, and are based heavily on empiricism. Lacking an understanding of the dominant physical mechanisms that cause heat release effects, there has to date been little basis from which to develop any broadly applicable method for predicting heat release effects in turbulent shear flows in general.

In principle, though, it should be possible to develop a fundamentally-based and broadly applicable understanding of how heat release alters the flow and mixing properties of essentially any turbulent shear flow. While studies to date have focused almost entirely on highly exothermic reacting flows relevant to practical combustion with hydrocarbon fuels in air, where the heat release effects are necessarily large, it is conceptually productive to first consider the limit of a fuel with asymptotically low heat release. In that case, when the level of exothermicity produced by the reaction is essentially zero, the flow properties must return to those of the corresponding nonreacting flow. With increasing but still small levels of exothermicity, the effects of heat release should in principle be deducible from the flow and mixing properties of the nonreacting flow. Moreover, for such small levels of exothermicity, the connection between the properties of the nonreacting flow and the heat release effects they imply in the reacting flow should be expressible in general terms that could be applied to essentially any other shear flow. As the level of exothermicity increases further, specific physical mechanisms should be identifiable that lead to the increasing effects seen in the flow due to the heat release.

Such an approach is closely related to that taken in this study. While the level of exothermicity is fixed in this study, the objective is to understand the specific physical mechanisms that lead to changes in the velocity fields $\mathbf{u}(\mathbf{x}, t)$ in turbulent shear flows due to heat release occurring in the flow. However, the objective is not simply to report empirical observations of changes due to heat release in various measurable quantities associated with the velocity field in a particular turbulent shear flow. Instead, this study seeks to develop a physically-based understanding of the underlying mechanisms by which heat release produces changes $\mathbf{u}(\mathbf{x},t)$ in essentially any turbulent shear flow.

1.1 Present Study

The objective of this study is to develop a substantially improved understanding of how heat release effects alter the velocity field $\mathbf{u}(\mathbf{x},t)$ in turbulent shear flows. In particular, it seeks to clarify which of the physical mechanisms that can potentially produce heat release effects dominate the actual changes that occur at the outer (large) scales of the flow and at the inner (small) scales of the flow. It also seeks to understand how the effects of heat release produced by each of these mechanisms vary with flow conditions, or from one location to another in any particular turbulent shear flow, and even from one turbulent shear flow to another.

The study is based on experimental measurements, using particle image velocimetry (PIV), to obtain velocity and velocity gradient fields on both outer and inner scales over a wide range of conditions in both nonreacting and reacting versions of the same turbulent shear flow. These include measurements on the flow centerline, where the mean shear is zero, over a wide range of outer-scale Reynolds numbers Re_δ, as well as measurements at a fixed Re_δ over a range of radial locations, and thereby over a range of local shear rates. The particular turbulent shear flow considered here is an axisymmetric coflowing turbulent jet, though the data are interpreted in scaled terms that allow the results to be applied in essentially any other turbulent shear flow.

The approach used here is based on scaling and similarity. Identifying the dominant physical mechanisms that lead to heat release effects on either the outer or inner range of scales in turn results in implied scaling laws for the measured quantities. These scaling laws can be tested to determine if they provide similarity in results obtained at widely differing conditions, meaning that the results reduce to a single universal form in the appropriately scaled variables. Such similarity, if achieved, is exceedingly strong evidence that the presumed physical mechanisms are in fact the dominant ones controlling the heat release effects on the flow. This principle is used here to determine the separate physical mechanisms that produce the dominant heat release effects on the outer flow scales, and thus on quantities such as the mean velocities and the Reynolds stresses, as well as on the inner flow scales, and thus on quantities such as distributions of velocity gradients. Moreover, the resulting similarity and scaling – if successfully achieved – allows quantities measured at essentially any location in essentially any turbulent shear flow to be rescaled to any other location or any other flow.

This dissertation is organized as follows. Chapter II first develops key theoretical concepts that are essential for interpreting the experimental results obtained in the particular turbulent shear flow used for this study, and for extending these experimental results to other flow conditions and to flows other than those used in this study. It begins with the governing equations for the velocity field $\mathbf{u}(\mathbf{x}, t)$ and from these identifies the specific physical mechanisms that can lead to direct changes in the velocity field due to heat release. It then examines each of these mechanisms individually, and proposes specific methods by which the effects of each can be related to the local inner or outer variables associated with any particular turbulent shear flow. Subsequent chapters then use experimental measurements to test these proposed methods, and show that even highly sensitive measures of heat release effects in turbulent shear flows, such as distributions of velocity gradient quantities based on

$\overline{(\partial u_i/\partial x_j)^n}$, when scaled in the manner suggested by these methods, become similar in both reacting and nonreacting flows.

In particular, Chapter III describes the experimental facility and measurement methods used for this study. Following this, Chapter IV examines the outer-scale effects of heat release on the mean velocity field, specifically on the velocity u_c and the width δ that characterize the local mean shear profile in the particular turbulent shear flow. It shows that the changes in these quantities due to heat release can be predicted from the scaling laws for the nonreacting flow via a "general equivalence principle" outlined in Chapter II. It also shows that previous measurements in the same flow, by Muñiz and Mungal 1995, that have been interpreted as showing fundamental differences between reacting and nonreacting versions of the flow, are in fact consistent with the present measurements and can be rescaled in the same manner as were the present results to match the nonreacting flow using the same equivalence principle. In effect, Chapter IV shows that the effects of heat release on the outer-scale properties of turbulent shear flows – namely those that are dominated by the large scales of motion, such as the mean velocities $\overline{u}_i$ and the Reynolds stresses $\overline{u_i' u_j'}$ – are dominated by the inertial effects due to the reduced densities $\rho(\mathbf{x}, t)$, and that these inertial effects can be accounted for via the general equivalence principle.

Chapter V then presents results from measurements of inner-scale properties of turbulent shear flows – namely those that are dominated by the small scales of motion, such as the velocity gradients $\partial u_i/\partial x_j$ – on the centerline of a nonreacting flow over a wide range of Reynolds numbers Re_δ. It first shows that classical inner scaling (Kolmogorov 1941) in terms of the viscosity ν and the inner (viscous) length scale λ_ν successfully removes most of the differences in distributions measured at different Reynolds numbers, but that there are remaining differences due to the incomplete resolution of the inner scale λ_ν at the higher Re_δ. It then uses the inertial- and dissipation-range spectra to determine the actual measurement resolution and develop the proper resolution-corrected inner scaling for velocity gradient fields. For the same distributions as before, it shows essentially perfect similarity via this scaling among the results for all Re_δ for each of the velocity gradient quantities. This provides the basis for using this scaling and similarity in subsequent chapters to look for heat release effects at the inner scales of turbulent shear flow.

Chapter VI first presents results from inner-scale measurements similar to those in Chapter V, but from the centerline of an exothermically reacting flow over a range of Re_δ from 18 000 to 200 000. It also shows that the classical inner-scale normalization in terms of a corrected viscosity ν and the corresponding inner length scale λ_ν removes most of the differences in the distributions from the different Re_δ. It then determines the measurement resolution at each Re_δ using the method from Chapter V, and shows that the resolution-corrected inner scaling again gives near-ideal similarity in the results for all Re_δ for each of the velocity gradient quantities. Finally, it compares the resolution-corrected inner-scaled self-similar forms of the distributions from the nonreacting and reacting flows for each velocity gradient quantity. The differences are thus the true inner-scale effects of heat release, and these are shown and quantified. In effect, Chapters V and VI together show that, once the inertial effects of heat release on the local outer variables u_c and δ of the turbulent shear flow have been accounted for via the equivalence principle, and the viscous effects of heat release have been accounted for via the corrected viscosity, and the resolution limits of the measurement have been rigorously accounted for via the resolution-corrected inner scaling, then the remaining true effects of heat release on inner-scale properties of turbulent shear flows are remarkably small.

Chapters VII and VIII then extend the results obtained on the flow centerline in Chapters V and VI, where the mean shear is zero, to numerous radial locations across the flow, where the mean shear is no longer zero. The effect of the local shear is to induce anisotropy in the turbulent shear flow, which in turn can lead to departures from the inner scaling used here to identify the effects of heat release on the small scales of the flow. Chapter VII first considers the nonreacting flow, and considers the value of the classical Corrsin-Uberoi parameter $\mathcal{S}_c^\star$ – believed to determine whether the shear-induced large-scale anisotropy extends to the smallest scales - that corresponds to the local shear at each radial location. It then determines the measurement resolution at each radial location using the same spectral procedure as above, and presents the resolution-corrected inner-scaled distributions at each radial location for various velocity gradient quantities. By comparing the departures from perfect similarity with the relative shear values that correspond to each location, it shows that there is no direct effect of shear on the scaled distributions, but that there is a subtle yet noticeable effect of the radial location that is not directly connected with the shear value. Chapter VIII then presents corresponding results from measurements at the same radial locations in the exothermically reacting flow. As a last step, it compares the resulting resolution-corrected inner-scaled distributions at each radial location in the reacting flow with the correspondingly scaled distributions in the nonreacting flow. Consistent with the findings from the flow centerline in Chapters V and VI, the remaining true effects of heat release at all radial locations are seen to be small when – using the methods above – proper account has been taken of the inertial effects on the outer variables, and the viscous effects and measurement resolution effects on the inner variables.

Chapter IX then summarizes the overarching conclusion from this study, and notes several additional major conclusions implied by the findings in this study.

CHAPTER II

Theoretical Foundation

The objective of this study is not simply to report miscellaneous empirical observations of changes due to heat release in various measurable quantities associated with the velocity field $\mathbf{u}(\mathbf{x}, t)$ in a particular turbulent shear flow. Instead, this study seeks to develop a physically based understanding of the underlying mechanisms by which heat release produces changes $\mathbf{u}(\mathbf{x}, t)$ in essentially any turbulent shear flow, and to clarify:

(i) which of the numerous plausible physical mechanisms that could potentially produce heat release effects in turbulent shear flows are in fact significant,

(ii) which of these are the dominant mechanisms controlling heat release effects under practical conditions, and

(iii) how the effects of heat release produced by each of these mechanisms vary with flow conditions, or from one location to another in any particular turbulent shear flow, and even from one turbulent shear flow to another.

This chapter therefore develops key theoretical concepts that are essential for interpreting the experimental results obtained in the particular turbulent shear flow used for this study, and for extending these experimental results to flow conditions other than those used in this study. The chapter is organized as follows:

- Section 2.1 first uses the governing equations and associated scaling laws to identify individual physical mechanisms that can lead to heat release effects on $\mathbf{u}(\mathbf{x}, t)$ in turbulent shear flows.

- Section 2.2 then develops the scaling laws for the particular class of non-reacting turbulent shear flows that are used in this study to assess how these individual physical mechanisms contribute to the heat release effects in shear flows.

- Section 2.3 addresses the inertial effects of heat release produced by density changes in the flow. It uses the mole-fraction-based equivalence principle Tacina and Dahm (2000) to obtain the outer-scale changes that should occur in the flow as a result of the purely inertial effects of heat release. Measurements of outer-scale flow properties presented in Chapter IV and inner-scale flow properties presented in Chapters V – VIII will compare the extent to which the predicted inertial effects of heat release account for the observed changes due to heat release in the flow.

- Section 2.4 addresses the body force (buoyancy) effects produced by density changes due to heat release in the flow, and discusses the outer-scale changes that occur in the flow as a result of buoyancy effects.

- Section 2.5 then addresses dilatational effects that result from the density changes due to heat release in the flow. It develops a general theoretical framework that determines the magnitude of such dilatational effects and obtains quantitative estimates of the relative importance of dilatation effects due to heat release on the inner-scale flow properties. Measurement results presented in Chapters V – VIII assess the extent to which these predicted dilatational effects of heat release are consistent with the observed changes due to heat release in the flow.

- Section 2.6 addresses the diffusive effects of heat release produced by viscosity changes that result from variations in temperature and species composition in the flow. It develops an extension of the mole-fraction-based equivalence principle that provides an effective viscosity to allow these diffusive effects on the inner-scale flow properties to be determined.

- Section 2.7 discusses how the relative magnitude of each of these elementary heat release effects can vary depending on the flow conditions, or from one location to another in any given turbulent shear flow, or from one class of turbulent shear flows to another.

2.1 Elementary Effects of Heat Release

This study investigates the changes produced in the velocity fields $\mathbf{u}(\mathbf{x}, t)$ in turbulent shear flows due to heat released by exothermic chemical reactions occurring within the flow. In this section, the specific physical mechanisms that can create such changes in $\mathbf{u}(\mathbf{x}, t)$ are identified.

The governing equations for conservation of mass and momentum in any flow with spatial and temporal variations in the density ρ and in the first and second viscosities μ and λ can be written as

$$\frac{D\rho}{Dt} \equiv \frac{\partial \rho}{\partial t} + \mathbf{u} \cdot \boldsymbol{\nabla} \rho = -\rho \left(\boldsymbol{\nabla} \cdot \mathbf{u} \right) \qquad (2.1)$$

$$\frac{D\mathbf{u}}{Dt} \equiv \frac{\partial \mathbf{u}}{\partial t} + \mathbf{u} \cdot \boldsymbol{\nabla}\mathbf{u} =$$
$$-\frac{1}{\rho}\left\{ \boldsymbol{\nabla} p - \left[\boldsymbol{\nabla} \cdot \mu \left(\boldsymbol{\nabla}\mathbf{u} + \boldsymbol{\nabla}\mathbf{u}^T \right) + \boldsymbol{\nabla} \left(\lambda \boldsymbol{\nabla} \cdot \mathbf{u} \right) \right] - \mathbf{f}_B \right\} + \mathbf{u} \left(\boldsymbol{\nabla} \cdot \mathbf{u} \right) \tag{2.2}$$

where $\mathbf{u}$ is the fluid velocity, p is the hydrodynamic pressure, and $\mathbf{f}_B \equiv (\rho - \rho_\infty)\mathbf{g}$ is the buoyancy body force per unit volume, with $\mathbf{g}$ the gravitational acceleration. The form of the momentum equation in (2.2) and is obtained using (2.1) from

$$\frac{D}{Dt}\left(\rho \mathbf{u}\right) = \mathbf{f}_{net}$$

where

$$\mathbf{f}_{net} = \mathbf{f}_B + \boldsymbol{\nabla} \cdot \boldsymbol{\sigma}$$

is the net force per unit volume and

$$\sigma_{ij} = -p\, \delta_{ij} + \left[\mu \left(\boldsymbol{\nabla}\mathbf{u} + \boldsymbol{\nabla}\mathbf{u}^T \right)_{ij} + \lambda \left(\boldsymbol{\nabla} \cdot \mathbf{u} \right) \delta_{ij} \right]$$

is the stress tensor. Additional equations for conservation of energy and chemical species account for the heat release produced by the exothermic chemical reactions occurring in the flow, however these equations couple to (2.1) and (2.2) only *indirectly* through their effect on the density and viscosity fields $\rho(\mathbf{x}, t)$ and $\nu(\mathbf{x}, t)$. As a result, the physical mechanisms that can *directly* produce heat release effects in $\mathbf{u}(\mathbf{x}, t)$ are limited to those found on the right-hand side of (2.2). These consist of:

(1) the inertial effect produced by the changes in the density field $\rho(\mathbf{x}, t)$,

(2) the body force effect produced by the buoyancy force $\mathbf{f}_B$,

(3) the diffusive effect produced by changes in the viscosity field $\nu(\mathbf{x}, t)$, and

(4) the dilatation effect produced by the divergence field $\boldsymbol{\nabla} \cdot \mathbf{u}$ in (2.2) that results from variations in the density field $\rho(\mathbf{x}, t)$ via (2.1).

Theoretical considerations relevant to each of these physical mechanisms above will be considered separately in §§ 2.2 – 2.5. Note that the pressure gradient appears on the right-hand side in (2.2), but it does not produce a *direct* effect of heat release on $\mathbf{u}(\mathbf{x}, t)$. Instead, the pressure changes due to heat release, but only as a consequence of the direct changes that occur in the velocity field due to heat release.

While (2.1) and (2.2) apply to any flow, this study is concerned solely with heat release effects in turbulent shear flows. Such flows typically vary far more slowly along their downstream direction than along the lateral directions, and for this reason can be treated as quasi-one-dimensional. Thus mean-flow properties of turbulent shear flows scale with local outer variables $\delta(x)$ and $u_c(x)$, namely the local length and velocity scales that characterize the local mean shear profile that sustains the turbulence at any downstream location x, as indicated in Fig. 2.1. Appropriate choices of δ and u_c depend on the shape of the mean velocity profile for the particular turbulent shear flow at hand, but the local peak mean shear is $\mathcal{O}(u_c/\delta)$. Scaling laws for $\delta(x)$ and $u_c(x)$ can often be determined by simple dimensional reasoning, and in general depend on the fluid densities even in flows without heat release. As a result, when heat release is present the resulting density changes will therefore affect the mean-flow properties through the density that appears in these outer-variable scaling laws. Outer-scale properties of the flow – namely quantities that are dominated by the large scales of motion, such as the mean velocities $\overline{u_i'}$ and the Reynolds stress components $\overline{u_i'u_j'}$ – will be altered primarily by the effects that heat release has on the local outer variables $\delta(x)$ and $u_c(x)$.

While the largest scales of motion in the turbulent flow field $\mathbf{u}(\mathbf{x}, t)$ are of the order of the local *outer* scale δ, the smallest scales are set by the inertial-diffusive balance that occurs at the local *inner* scale $\lambda_\nu \sim \delta Re_\delta^{-3/4}$. Here $Re_\delta \equiv u_c\delta/\nu$ is the local outer-scale Reynolds number, which determines the outer-to-inner length scale ratio in the flow field. Inner-scale properties of turbulent shear flows – namely quantities that are dominated by the smallest-scale motions, such as the velocity gradient moments $\overline{(\partial u_i/\partial x_j)^n}$ – scale with the local inner variables ν and λ_ν. Thus, for instance, $\overline{(\partial u_i/\partial x_j)^n} \sim (\nu/\lambda_\nu^2)^n$, and from the outer-to-inner length scale relation this inner scaling can be equivalently written in the local outer variables u_c and δ as $\overline{(\partial u_i/\partial x_j)^n} \sim (u_c/\delta)^n Re_\delta^{n/2}$. As a consequence, when heat release is present then such inner-scale flow properties will be affected by the changes that occur in both the viscosity and the density. The viscosity effect enters explicitly through the ν that appears in these inner-variable scaling relations, as well as implicitly through its effect on Re_δ in the λ_ν scaling. The density effect enters implicitly through its influence on u_c and δ, and thus its further effect on Re_δ.

A similar inertial-diffusive balance determines the smallest scale λ_D of the gradients in the mixture fraction field that governs the heat-releasing chemical reactions. As indicated in Fig. 2.2, the peak strain rate $S \sim (\nu/\lambda_\nu^2)$ in the strain-diffusion competition produces a scalar dissipation layer thickness $\lambda_D \sim \lambda_\nu Sc^{-1/2}$, where the Schmidt number $Sc \equiv \nu/\mathcal{D}$ is the ratio of the viscosity and scalar diffusivities. Density changes produced by heat releasing reactions occurring within this locally two-dimensional scalar dissipation layer create a dilatation field $\boldsymbol{\nabla} \cdot \mathbf{u}(\mathbf{x}, t)$ via (2.1), which in turn produces a dilatationally induced flow via the Poisson integral that opposes the strain field. If this effect is sufficiently strong, it could in principle disrupt the strain-diffusion balance that establishes the diffusion-reaction layer. The magnitude of the dilatation field is obtained theoretically in § 2.5, and examined experimentally in Chapters VI and VIII.

2.2 Scaling Laws for Non-Reacting Coflowing Turbulent Jets

While the considerations in § 2.1 apply to any exothermically reacting turbulent shear flow, the experimental measurements in this study were necessarily obtained in a particular flow, in this case an axisymmetric coflowing turbulent jet diffusion flame. Such coflowing jets are convenient for particle-based measurements of $\mathbf{u}(\mathbf{x}, t)$, since they readily allow introduction and removal of seed particles in the flow field. In order to present the results for heat release effects measured in this flow in general forms that can be applied to other turbulent shear flows, this section develops the scaling laws for the local outer variables $\delta(x)$ and $u_c(x)$ in nonreacting axisymmetric coflowing turbulent jets. All results in Chapters IV – VIII are then presented in terms of these outer variables, or together with ν in terms of the inner length scale λ_ν implied by u_c and δ, allowing these results to be rescaled to other flow conditions and to other turbulent shear flows.

The basic configuration for an axisymmetric coflowing turbulent jet is indicated in Fig. 2.3. A jet fluid, in this case a fuel, issues from a nozzle at bulk velocity U_0 into a surrounding coflowing fluid, in this case air, moving in the same direction at the coflow speed U_∞. Unlike a "simple" jet issuing into a quiescent surrounding fluid, the coflowing jet is a "compound" shear flow, in the sense that it undergoes a transition with increasing downstream distance from one power-law scaling regime to another. The proper scaling laws for such coflowing jets can be obtained from dimensional reasoning, as first shown by Maczyński (1962) and subsequently verified experimentally by Biringen (1975), Nickels and Perry (1996), and Davidson and Wang (2002).

At any downstream location x, the local streamwise velocity profile U is used to define the "excess velocity" profile $u \equiv U - U_\infty$, from which the local u_c and δ characterizing the local peak mean shear are obtained, as indicated in Fig. 2.3. In the absence of buoyancy, the momentum flux J_0 issuing from the jet source is an invariant of the flow. This allows defining an invariant length scale, termed the "jet momentum radius", as

$$\theta \equiv \left(\frac{J_0}{\pi \rho_\infty U_\infty^2} \right)^{\frac{1}{2}}, \tag{2.3}$$

On dimensional grounds, the resulting scalings for δ and u_c must then be

$$\left(\frac{\delta}{\theta} \right) = f_\delta \left(\frac{x}{\theta} \right), \tag{2.4a}$$

$$\left(\frac{u_c}{U_\infty} \right) = f_u \left(\frac{x}{\theta} \right). \tag{2.4b}$$

where f_δ and f_u are universal scaling functions for all axisymmetric coflowing turbulent jets. The scaling achieved in this form is demonstrated in Figs. 2.4 and 2.5, adapted from Dahm and Dibble (1988) using data originally published by Biringen (1975). In each figure, the upper panel presents the data scaled by the jet nozzle diameter for various U_0 and U_∞, for which no collapse to a universal scaling is seen. The lower panel in each figure shows the same data properly scaled as in (2.4a),(2.4b), and a good collapse of the data is seen to the two universal scaling functions f_δ and f_u.

The two scaling functions f_δ and f_u do not have simple power-law forms, but must approach power-law scalings in the limits as the normalized downstream distance (x/θ) becomes small or large. In particular, when $(x/\theta) \to 0$, then u_c is much larger than U_∞ and thus the distinction between u_c and U_c is lost. As a consequence, the flow in this limit must become identical to a simple non-coflowing jet, which requires $f_\delta(x/\theta) = (c_\delta)_j(x/\theta)$ and $f_u(x/\theta) = \pi^{1/2}(c_u)_j(x/\theta)^{-1}$. In the opposite limit, as $(x/\theta) \to \infty$ then u_c becomes sufficiently small relative to U_∞ that the momentum conservation in terms of the excess velocity becomes identical to that in terms of the "deficit velocity" for a wake, which requires $f_\delta(x/\theta) = (c_\delta)_w(x/\theta)^{1/3}$ and $f_u(x/\theta) = (c_u)_w(x/\theta)^{-2/3}$. The log-log form in Fig. 2.6 verifies these two power-law limit scalings, where the data from Figs. 2.4 and 2.5 are shown together with the more extensive data of Davidson and Wang (2002). The transition between the jet-like and wake-like limits can be seen to occur around $(x/\theta) \approx 10$.

In these scalings, x is the downstream distance measured from an ideal point source that introduces momentum flux J_0 but has zero mass flux m_0. Practical jets, however, issue from finite-diameter nozzles that introduce a nonzero exit mass flux m_E when producing the exit momentum flux J_E. The distinction between the ideal and actual configurations is typically accounted for by an empirically defined virtual origin. However, Diez and Dahm (2007) have shown that the actual flow is formally equivalent to that produced by a point source having $J_0 = J_E$ located upstream of the actual source at a distance

$$x_E = \frac{\sqrt{\pi}/2}{I_1\,(c_u)_j\,(c_\delta)_j^2}\underbrace{\left[\frac{2m_E}{(\pi\rho_\infty J_E)^{1/2}}\right]}_{d^*}, \tag{2.5}$$

where the term in square brackets is the classical far-field equivalent source diameter d^*. Here $I_1 = \pi/a_f \approx 0.262$ is an integral invariant of the flow, the value of which depends only on the definition of the outer length scale δ. The value $a_f = 12.0$ corresponds to the choice of δ as the full width where the mean streamwise velocity profile has decreased to 5% of its centerline value u_c. From Papanicolaou and List (1988), $(c_u)_j \approx 7.2$ and $(c_\delta)_j \approx 0.36$. When, as is common in practice, x is used to denote the downstream distance from the jet nozzle, then it is necessary to calculate the virtual origin x_E from (2.5) and replace x in (2.4a) and (2.4b) with

$$\xi \equiv x + x_E. \tag{2.6}$$

Note also that the momentum deficit produced by the boundary layers on the outer surface of a practical nozzle in a coflowing stream must be subtracted from the momentum excess produced by the flow issuing from the nozzle to determine the *net* momentum flux J_E introduced by the nozzle. For small J_E, this correction can be significant. In the present study, the wake flow produced by the nozzle with $U_0 = 0$ was measured directly for each coflow speed U_∞. The resulting drag for each U_∞ was subtracted from the nominal outflow momentum flux for each measurement condition to determine the net J_E.

Use of the outer variables δ and u_c allows the experimentally measured heat release effects obtained at the particular measurement locations and flow conditions for the particular turbulent shear flow used in this study to be presented in general forms that allows these results to then be applied to any other location, any other flow conditions, or even any other turbulent shear flow.

2.3 Heat Release: Inertial Effects of Density Variations

The reduction due to heat release in the fluid density field $\rho(\mathbf{x}, t)$ appearing on the right-hand side of (2.2) will lead to a purely inertial effect of reaction exothermicity on the velocity field $\mathbf{u}(\mathbf{x}, t)$. This inertial effect of heat release can, in concept, be quantitatively accounted for by the "general equivalence principle" of Tacina and Dahm (2000), which provides a completely general way of predicting the inertial effects of heat release on the outer variables δ and u_c in any turbulent shear flow. This section applies this equivalence principle to the axisymmetric coflowing turbulent jet configuration used in the present study, to obtain the theoretical changes due to heat release in the local outer variables δ and u_c in (2.4a) and (2.4b) and the virtual origin x_E in (2.5). In Chapter IV these predictions will be compared with the experimentally measured changes, where it will be seen that this equivalence principal in coflowing jets accurately predicts the inertial effects due to heat release.

The equivalence principle is based on the bilinear form of the equilibrium temperature $T(X)$ with jet-fluid elemental mole fraction $X(\mathbf{x},t)$ as required by enthalpy conservation. This can be seen in Fig. 2.7, where as the strain rate S is decreased the temperature $T(X)$ approaches the bilinear form for mole fraction values X sufficiently far from the stoichiometric value X_s. Since a linear $T(X)$ reflects simple fluid mixing without reaction, in Fig. 2.8 on either side of X_s the temperature field $T(X)$ in the reacting flow is equivalent to that which would occur in a corresponding non-reacting flow with the temperature $T_\infty \equiv T(X=0)$ of the surrounding fluid raised to a fictitious elevated value T_∞^{eff}, where

$$T_\infty^{\mathit{eff}} = T_0 + (T_s - T_0)\frac{X_0 - X_\infty}{X_0 - X_s} \tag{2.7}$$

with T_s denoting the stoichiometric temperature, as indicated in Fig. 2.8. This is equivalent to replacing the density ρ_∞ in the outer-variable scaling laws for the non-reacting flow with the effective value that corresponds to this elevated temperature, namely

$$\rho_\infty^{\mathit{eff}} = \rho_\infty \left(\frac{T_\infty}{T_\infty^{\mathit{eff}}}\right) \tag{2.8}$$

The density field $\rho(\mathbf{x},t)$ in the equivalent nonreacting flow is then identical to that in the exothermic reacting flow wherever the jet-fluid mole fraction field $X(\mathbf{x},t)$ is above the stoichiometric value X_s. In this manner, the inertial effects of density changes due to heat release in the exothermic flow are obtained from the density scaling of the equivalent non-reacting flow.

This equivalence in mole-fraction space in Fig. 2.8 is shown in physical space in Fig. 2.9 via the mean temperature, density and velocity profiles. Where $X > X_s$ as indicated by the heavy line, the temperature and density profiles in the reacting flow (solid line) are the same as those in a nonreacting flow (dashed line) produced by simple mixing between the actual jet exit values and the effective ambient values T_∞^{eff} and $\rho_\infty^{\mathit{eff}}$. The equivalence thus ensures the correct density changes in those parts of the flow where the velocity profile (shown by the bottommost profile in Fig. 2.9) is highest, and thus where the inertial effects of heat release are most important.

Tacina and Dahm (2000) have shown that this general equivalence principle accurately predicts the heat release effects in both the near and far fields of planar and axisymmetric turbulent jet flames over a wide range of fuels and dilutions. In the jet far field, it leads to a generalized momentum diameter d^+ that extends the classical Thring and Newby (1953) and Ricou and Spalding (1961) momentum diameter d^* in (2.5) to exothermic jet flames. The equivalence principle accurately predicts the reduced entrainment rate due to heat release, as well as the resulting effect of heat release on jet flame lengths. When applied to planar turbulent jet flames, the equivalence principle leads to an extended momentum width h^+ that similarly gives correct predictions for the much stronger effect of heat release on the scaling laws in that flow. The equivalence principle also correctly predicts effects of heat release on the near-field lengths of both planar and axisymmetric turbulent jets. In particular, it indicates a much larger increase in near-field length due to heat release in planar turbulent jets than in axisymmetric jets, in good agreement with observations and measurements. Dahm (2005) has further shown that this same general equivalence principle, when applied to turbulent mixing layers, leads to an extended density ratio s^+ that correctly predicts the reduction in growth rate and change in entrainment ratio due to heat release. These predicted effects are in good agreement with experimentally measured values, and reveal an important additional influence of stochiometry that had previously gone unnoticed in the experimental results.

The equivalence principle is valid within the range over which its physical assumptions apply (Tacina and Dahm 2000). Violating these constraints invalidates the predictions of the equivalence principle, such as in flames where buoyancy due to heat release is large. The equivalence principle also fails near the flame tip where mole fractions are close to the stoichiometric value – here neither the rich nor lean branches of $T(X)$ dominate and the equivalence principle does not apply. Furthermore, if the temperature is no longer determined solely by the mole fraction, the equivalence principle is not to be applied – such as in strongly radiating flows or where differential diffusion effects are non-trivial. However, many practical combustion applications are within the assumptions of the equivalence principle and it captures the dominant effects of heat release on the outer flow variables u_c and δ.

This equivalence principle can be applied to the scaling laws in (2.4a), (2.4b) for nonreacting axisymmetric coflowing turbulent jets to obtain outer-variable scaling laws for the corresponding exothermically reacting version of this flow. In particular, note that the density ρ_∞ appears in (2.4a), (2.4b) only via the momentum radius θ from (2.3). The equivalence principle implies that the scaling laws for the exothermically reacting flow are the same as those for the corresponding non-reacting flow, but with ρ_∞ replaced by $\rho_\infty^{\mathit{eff}}$ from (2.7) and (2.8). This defines the "extended momentum radius" θ^+, namely

$$\theta^+ \equiv \left(\frac{J_0}{\pi \rho_\infty^{\mathit{eff}} U_\infty^2} \right)^{\frac{1}{2}}, \tag{2.9}$$

in terms of which the scaling laws for the outer length and velocity, δ and u_c, in exothermically reacting coflowing turbulent jets should be

$$\left(\frac{\delta}{\theta^+} \right) = f_\delta \left(\frac{\xi}{\theta^+} \right) \tag{2.10a}$$

$$\left(\frac{u_c}{U_\infty} \right) = f_u \left(\frac{\xi}{\theta^+} \right) \tag{2.10b}$$

where, from (2.6), $\xi \equiv x + x_E$ and f_δ and f_u are the same universal scaling functions shown in Fig. 2.6. The ability of (2.10a), (2.10b) to account for the experimentally measured heat release effects on δ and u_c in exothermic reacting axisymmetric coflowing turbulent jets will be assessed in Chapter IV.

2.4 Heat Release: Body Force Effects of Density Variations

In addition to the inertial effect of heat release in § 2.3, the buoyancy body force term $\mathbf{f}_B$ on the right-hand side of (2.2) will lead to an additional heat release effect on $\mathbf{u}(\mathbf{x}, t)$. Owing to the volumetric nature of the buoyancy body force, its effects are greatest at the largest flow scales. In practice, it is extremely difficult to produce a fully buoyancy-free flame, and as a result this "buoyancy effect" has been the most widely investigated heat release effect. Numerous studies have proposed various approximate ways to account for its influence on the outer variables δ and u_c (e.g., Steward, 1970; Becker and Yamazaki 1978; Heskestad 1981; Zukoski et al. 1981; Cetegen et al. 1984; Peters and Göttgens 1991; Delichatsios 1993; Blake and McDonald 1995; Blake and Coté 1999). Most of these approaches have been based on an approximation referred to as the Morton entrainment hypothesis (Morton 1959), and lead to various ad hoc expressions in terms of Froude or Richardson numbers. Diez and Dahm (2007) have developed an integral approach that avoids this approximation altogether. Their approach, based in part on the general equivalence principle noted in § 2.3, leads to two parameters that determine the complete buoyancy effects on the outer variables. Comparisons of the resulting predicted heat release effects on δ and u_c over a wide range of conditions show good agreement with measured values.

Because the buoyancy effects of heat release have been widely addressed in prior studies, and numerous methods exist for understanding and predicting the effect of buoyancy on $\mathbf{u}(\mathbf{x}, t)$, the present study is focused primarily on heat release effects other than buoyancy. Thus in this investigation, the outer variables δ and u_c are measured directly at each flow condition, and as a consequence the effects of buoyancy on them are directly accounted for independent of any theoretical formulation. By presenting results normalized with these outer variables and the accompanying outer-scale Reynolds number Re_δ, or equivalently normalized on the inner variables ν and λ_ν, this study is able to go beyond the comparatively simple heat release effects produced by buoyancy at the large flow scales, and can thereby investigate the heat release effects produced at the intermediate and small scales of turbulent shear flows by each of the terms on the right-hand side of (2.2).

2.5 Heat Release: Dilatation Effects of Density Variations

An additional effect of heat release on $\mathbf{u}(\mathbf{x}, t)$ comes from the dilatation term on the right-hand side of (2.2). The dilatation field $\boldsymbol{\nabla} \cdot \mathbf{u}$ is produced by density variations via (2.1) as

$$\boldsymbol{\nabla} \cdot \mathbf{u} = -\frac{1}{\rho}\frac{\mathrm{D}\rho}{\mathrm{D}t}. \tag{2.11}$$

From the ideal gas equation of state

$$p = \rho \left(\frac{\widetilde{R}}{M}\right) T, \tag{2.12}$$

where $\widetilde{R}$ is the universal (molar) gas constant and M is the molecular weight, and taking the pressure to be essentially constant in the absence of compressibility effects, the dilatation in (2.11) becomes

$$\boldsymbol{\nabla} \cdot \mathbf{u} = \frac{1}{T}\frac{\mathrm{D}T}{\mathrm{D}t} - \frac{1}{M}\frac{\mathrm{D}M}{\mathrm{D}t}. \tag{2.13}$$

As evident in Fig. 2.7, in the chemical equilibrium limit that applies as the strain rate $S \to 0$, the temperature and chemical composition become independent of S and are functions only of the mixture fraction ζ. Thus $T = T(\zeta)$ and $M = M(\zeta)$, and consequently the dilatation in (2.13) becomes

$$\boldsymbol{\nabla} \cdot \mathbf{u} = \left[\frac{1}{T}\frac{\mathrm{d}T}{\mathrm{d}\zeta} - \frac{1}{M}\frac{\mathrm{d}M}{\mathrm{d}\zeta}\right]\frac{\mathrm{D}\zeta}{\mathrm{D}t}. \tag{2.14}$$

Since the mixture fraction ζ is a conserved scalar, it satisfies the advection-diffusion equation

$$\frac{\mathrm{D}\zeta}{\mathrm{D}t} \equiv \frac{\partial\zeta}{\partial t} + \mathbf{u} \cdot \boldsymbol{\nabla}\zeta = \mathcal{D}\boldsymbol{\nabla}^2\zeta \tag{2.15}$$

where $\mathcal{D}$ is the scalar diffusivity. As a result, the dilatation in (2.14) becomes

$$\boldsymbol{\nabla} \cdot \mathbf{u} = \Big[F(\zeta)\Big]\mathcal{D}\boldsymbol{\nabla}^2\zeta, \tag{2.16a}$$

$$F(\zeta) \equiv \frac{1}{T}\frac{\mathrm{d}T}{\mathrm{d}\zeta} - \frac{1}{M}\frac{\mathrm{d}M}{\mathrm{d}\zeta} \tag{2.16b}$$

is an equilibrium state relation that can be readily evaluated via CHEMKIN or any other chemical equilibrium solver for any fuel and oxidizer combination. In general, the effect on $F(\zeta)$ in (2.16b) from $T(\zeta)$ is found to be far larger than that from $M(\zeta)$, consistent with Tacina and Dahm (2000).

The results in (2.16a), (2.16b) allow a comparison between the dilatation $\boldsymbol{\nabla}\cdot\mathbf{u}$ due to heat release and the velocity gradients $\boldsymbol{\nabla}\mathbf{u} \equiv \partial u_i/\partial x_j$ that occur in a turbulent shear flow even in the absence of any heat release. As noted in § 2.1, the velocity gradients scale on inner variables and thus their characteristic magnitude is

$$\left[\overline{(\boldsymbol{\nabla}\mathbf{u} : \boldsymbol{\nabla}\mathbf{u})}\right]^{\frac{1}{2}} \equiv \left[\overline{\left(\frac{\partial u_i}{\partial x_j}\right)^2}\right]^{\frac{1}{2}} \sim \left(\frac{\nu}{\lambda_\nu^2}\right). \tag{2.17}$$

From Mullin and Dahm (2005b), the proportionality constant in (2.17) is approximately 10 (see their Fig. 5 and Tables III and IV). The corresponding characteristic dilatation magnitude from (2.16a) requires an estimate of the characteristic magnitude of $\boldsymbol{\nabla}^2\zeta$, which scales as

$$\left[\overline{(\boldsymbol{\nabla}^2\zeta)^2}\right]^{\frac{1}{2}} \sim \left(\frac{\zeta'_{rms}}{\lambda_{\mathcal{D}}}\right), \tag{2.18}$$

with $\lambda_{\mathcal{D}}$ the scalar dissipation layer thickness in Fig. 2.2. From the scalar gradient measurements in Southerland (1994), the proportionality constant in (2.18) is found to be approximately 0.67. Since $Sc \approx 1$ in gaseous reacting flows, $\lambda_{\mathcal{D}} \approx \lambda_\nu$ and thus the ratio of the characteristic dilatation magnitude to the characteristic velocity gradient magnitude is

$$\mathcal{R}_{\nabla}(\zeta) \equiv \frac{\left[\overline{(\boldsymbol{\nabla}\cdot\mathbf{u})}\right]^{\frac{1}{2}}}{\left[\overline{(\boldsymbol{\nabla}\mathbf{u} : \boldsymbol{\nabla}\mathbf{u})}\right]^{\frac{1}{2}}} \approx 0.067\Big[F(\zeta)\Big]\zeta'_{rms} \tag{2.19}$$

Since $0 \leq \zeta \leq 1$, by definition $\zeta'_{rms} \leq 1/2$, and in practice throughout most turbulent shear flows $\zeta'_{rms} \ll 1$.

Figure 2.10 shows a representative computation of $\mathcal{R}_\nabla(\zeta)$ for the far-field of a reacting jet, at $x/d^* = 100$ where $\zeta'_{rms} \approx 0.01$, from adiabatic chemical equilibrium calculations using the NASA CEA solver (McBride et al. 1994) for hydrogen-air chemistry. Also shown in each panel is the corresponding $T(\zeta)$, from which the stoichiometric mixture fraction $\zeta_s = 0.028$ can be readily identified. In the top panel, it is apparent that this estimate of the relative dilatation magnitude $\mathcal{R}_\nabla(\zeta)$ is essentially zero wherever the composition is fuel-rich ($\zeta > \zeta_s$). In the lower panel, it can be seen that for fuel-lean compositions ($\zeta < \zeta_s$) the dilatation magnitude remains negligible except possibly as $\zeta \to 0$. The relative dilatation values in Fig. 2.10 are representative values for practical shear flows. These results thus indicate that the dilatation $\boldsymbol{\nabla} \cdot \mathbf{u}$ appearing on the right-hand side of (2.2) should have no significant *direct* dynamical effect in altering the gradients $\partial u_i/\partial x_j$ in the velocity field $\mathbf{u}(\mathbf{x}, t)$.

The above finding that the velocity gradients induced by dilatation due to heat release are negligible in comparison with the naturally occurring velocity gradients in turbulent shear flows is independent of the Reynolds number and applies to all turbulent shear flows. Moreover, it not unique to the hydrogen-air chemistry in Fig. 2.10, and applies to all other common hydrocarbon-air reactants as well.

As a measure of the overall levels of heat release, the present hydrogen-air chemistry is $T_s/T_\infty = 7.95$, where T_s is the adiabatic flame temperature and T_∞ is the temperature of the reactants. By comparison, most hydrocarbon systems such as methane-air ($T_s/T_\infty = 7.42$) are lower. Thus the use of hydrogen-air represents an upper bound of heat release for most practical combustion systems – with the notable exception of oxygen-enriched combustion where the levels of heat release are much larger, such as hydrogen-oxygen , $T_s/T_\infty = 10.3$.

Of course, it is the dilatation itself that produces the reductions in the density field

$\rho(\mathbf{x}, t)$ due to heat release, as can be seen in (2.1), and in this way the dilatation has an *indirect* effect on $\mathbf{u}(\mathbf{x}, t)$. That indirect effect occurs via the explicit appearance of the density ρ on the right-hand side of (2.2), which produces the purely inertial effect on $\mathbf{u}(\mathbf{x}, t)$ discussed in § 2.3, and via the implicit appearance of the density ρ in the body force $\mathbf{f}_B$ on the right-hand side of (2.2), which produces the buoyancy effect on $\mathbf{u}(\mathbf{x}, t)$ discussed in § 2.4. However the present section indicates that the appearance of the dilatation $\boldsymbol{\nabla} \cdot \mathbf{u}$ on the right-hand side of (2.2) has no direct effect on $\mathbf{u}(\mathbf{x}, t)$. In Chapters V – VIII, results from experimental measurements will be used to assess the validity of this finding.

2.6 Heat Release: Diffusive Effects of Viscosity Variations

Additional direct effects of heat release on $\mathbf{u}(\mathbf{x}, t)$ can result from changes in the viscosities μ and λ that appear on the right-hand side of (2.2). The viscous terms in this equation can be written as

$$\frac{1}{\rho}\Big[\boldsymbol{\nabla} \cdot \mu \left(\boldsymbol{\nabla}\mathbf{u} + \boldsymbol{\nabla}\mathbf{u}^T\right) - \boldsymbol{\nabla}\left(\lambda \boldsymbol{\nabla} \cdot \mathbf{u}\right)\Big] =$$
$$\nu \boldsymbol{\nabla}^2 \mathbf{u} + \frac{1}{\rho}\Big[\boldsymbol{\nabla}\mu \cdot \left(\boldsymbol{\nabla}\mathbf{u} + \boldsymbol{\nabla}\mathbf{u}^T\right) + \boldsymbol{\nabla}\lambda \left(\boldsymbol{\nabla} \cdot \mathbf{u}\right)\Big] - \frac{\lambda}{\rho}\boldsymbol{\nabla}\left(\boldsymbol{\nabla} \cdot \mathbf{u}\right) \qquad (2.20)$$

where $\nu \equiv \mu/\rho$. The first term on the right-hand side of (2.20) accounts for the classical diffusion of momentum that sets the local inner length scale $\lambda_\nu \sim \delta Re_\delta^{-3/4}$ as discussed in § 2.1. In nonreacting turbulent shear flows, the constant viscosity μ and the resulting λ_ν then determines the values of all inner-scale quantities. In the presence of heat release, however, the viscosity will increase over its corresponding nonreacting value, and this acts to increase the inner length scale in the flow and thereby alters the values of all such inner-scale quantities. In addition, $\nu(\mathbf{x}, t)$ will no longer be constant, and this introduces significant complications in the inner scaling of various turbulence quantities. While the remaining terms on the right-hand side of (2.20) include the effects of spatial variations in the viscosities, such nonuniformities in $\nu(\mathbf{x},t)$ also affects the otherwise simple strain-diffusion balance that sets the inner length scale λ_ν via the first term of (2.20) in nonreacting flows. In reacting flows, lacking a uniform ν the notion of a single inner length scale and the inner scaling based on it is, strictly speaking, no longer valid. Nevertheless, owing to the enormous success that the "Kolmogorov 1941 theory" of inner scaling via ν and λ_ν (or, equivalently, via ν and ε) has had in understanding and predicting velocity gradients and other inner-scale properties in nonreacting turbulent shear flows, current extensions to reacting flows are largely based on preserving the notion of inner scaling in terms of some appropriately-defined effective viscosity.

A common approximation is to ignore the spatial variations in the viscosity altogether and assign a constant *ad hoc* "hot" value for ν. Often, this is chosen as the viscosity ν_s that corresponds to the chemical equilibrium temperature and composition at the stoichiometric mixture fraction. This produces an increase in λ_ν due to heat release, and allows classical scaling of inner-scale flow properties based on this ν_s and λ_{ν_s}. However, since ν_s is generally the highest viscosity in $\nu(\mathbf{x},t)$ this will overestimate the diffusive effects of heat release.

A more accurate approach is possible by first computing the viscosity state relation $\nu(\zeta)$ from the chemical equilibrium temperature and composition over the entire range of mixture fractions $0 \leq \zeta \leq 1$. This can be done with any equilibrium calculator, or preferably with OPPDIF in the limit as the strain rate $S \to 0$, since the latter accounts for differential diffusion in the fundamentally layer-like gradient regions shown in Fig. 2.2. The top panel in Fig. 2.11 shows the result of such calculations for hydrogen-air chemistry over a wide range of strain rates S. At sufficiently low S, the chemistry approaches an S-independent equilibrium limit $\nu(\zeta)$; this can be seen clearly in the lower panel of Fig. 2.11, where the ν variations are shown in mole-based mixture fraction. The average viscosity can then be computed from $\nu(\zeta)$ as

$$\overline{\nu}(\mathbf{x}) \equiv \int_0^1 \nu(\zeta) P(\zeta;\mathbf{x})\,\mathrm{d}\zeta, \tag{2.21}$$

where $P(\zeta;\mathbf{x})$ is the mixture-fraction probability density function at the particular location $\mathbf{x}$ of interest in the turbulent shear flow. In the interior of the flow, $P(\zeta)$ can often be approximated as Gaussian, namely

$$P(\zeta;\mathbf{x}) \approx \frac{1}{\sqrt{2\pi\overline{(\zeta')^2}}} \exp\left[-\frac{\left(\zeta-\overline{\zeta}\right)^2}{2\overline{(\zeta')^2}}\right] \tag{2.22}$$

where $\overline{\zeta}(\mathbf{x})$ is the local mean mixture fraction and $\overline{(\zeta')^2}(\mathbf{x})$ is the local mixture-fraction variance. In turbulent shear flows, the local mean and variance of the conserved-scalar mixture fraction can be obtained from the outer variable scaling laws for δ and u_c, as noted in §§ 2.2 and 2.3, allowing $\overline{\nu}(\mathbf{x})$ to be readily calculated.

This approach is used at each measurement location $\mathbf{x}$ in the present study to provide a single value of the average local viscosity $\overline{\nu}(\mathbf{x})$ that partially accounts for the viscous effect of heat release. From this, a single local inner length scale is obtained as $\lambda_\nu \sim \delta Re_\delta^{-3/4}$, with $Re_\delta \equiv u_c\delta/\overline{\nu}$. All inner-scale flow properties are then scaled with this $\overline{\nu}$ and λ_ν. This provides a simple way of extending the classical Kolmogorov (1941) inner scaling for nonreacting flows to exothermically reacting flows. It retains the conceptual simplicity of a single local "hot" value for ν in the first term on the right-hand side of (2.20), while providing greater accuracy than simply choosing this to be the stoichiometric value ν_s.

2.7 Combined Effects of Heat Release

In an exothermically reacting turbulent shear flow, all of the heat release effects in §§ 2.2 – 2.6 act to produce *direct* changes in the velocity field $\mathbf{u}(\mathbf{x}, t)$ and the associated velocity gradient fields $\partial u_i/\partial x_j(\mathbf{x}, t)$ via the terms on the right-hand side in (2.2). Because outer-scale properties of the flow such as the mean velocities $\overline{u_i}$ and the Reynolds stress components $\overline{u_i' u_j'}$ are dominated by the large scales of motion, they will be altered primarily by the effects that heat release has on the local outer variables $u_c(x)$ and $\delta(x)$. From § 2.2, scaling laws for the axisymmetric coflowing turbulent jet configuration used in the present experiments allow the local u_c and δ to be determined at each flow condition. From the general equivalence principle in § 2.3 and the extended scaling laws it provides for u_c and δ in reacting version of this flow, the inertial effects of heat release on the outer-scale flow properties can be determined via (2.9) and (2.10a), (2.10b). As noted in § 2.4, the additional effects of buoyancy on u_c and δ are relatively well understood and will not be investigated here; since u_c and δ are measured directly in this study, the effects of buoyancy on them are accounted for in all results presented herein. The dilatation effects in § 2.5 and the viscous effects in § 2.6 act at the inner (diffusive) flow scales, and thus these should not directly affect outer-scale flow properties. As a result, the principal effect of heat release on the outer-scale flow properties should be the inertial effect on $u_c(x)$ and $\delta(x)$ via $\rho_\infty^{\mathit{eff}}$ from the general equivalence principle. One of the goals of this experimental study is to determine the extent to which the resulting theoretically predicted heat release effects on $u_c(x)$ and $\delta(x)$ are supported by results from velocity measurements in an exothermically reacting turbulent shear flow.

Inner-scale flow properties, such as the velocity gradients $\partial u_i/\partial x_j$, are dominated by the smallest scales of motion. As a result, in addition to the inertial and buoyancy effects on them from $u_c(x)$ and $\delta(x)$ via the inner-scaling $\overline{(\partial u_i/\partial x_j)^n} \sim (u_c/\delta)^n Re_\delta^{n/2}$, the dilatation effects in § 2.5 and the viscous effects in § 2.6 can potentially produce additional direct inner-scale heat release effects. However, $\mathcal{R}_\nabla(\zeta)$ in Fig. 2.10 from (2.19) of § 2.5 suggests that the direct effects of dilatation in altering the velocity gradients from their values in the corresponding nonreacting flow will be negligible. One of the goals of this experimental study is to determine the extent to which this theoretical prediction is supported by results from velocity gradient measurements in an exothermically reacting turbulent shear flow. With regard to direct viscous effects of heat release on inner-scale flow quantities, the considerations in § 2.6 suggest that these can be accounted for by retaining the classical inner scaling from Kolmogorov (1941) theory, but using the local mixture-fraction averaged viscosity $\overline{\nu}(\mathbf{x})$ from (2.21) and (2.22) and the corresponding local inner scale λ_ν. One of the further goals of this experimental study is to determine the extent to which such classical inner scaling correlates measured velocity gradients in an exothermically reacting turbulent shear flow. This latter objective is made more difficult by the fact that, at high Reynolds numbers, the diffusive scale λ_ν may be beyond the resolution limit of the measurements. This study thus develops methods for objectively determining the measurement resolution, and for assessing the validity of inner scaling even when the viscous scale λ_ν is only partially resolved.

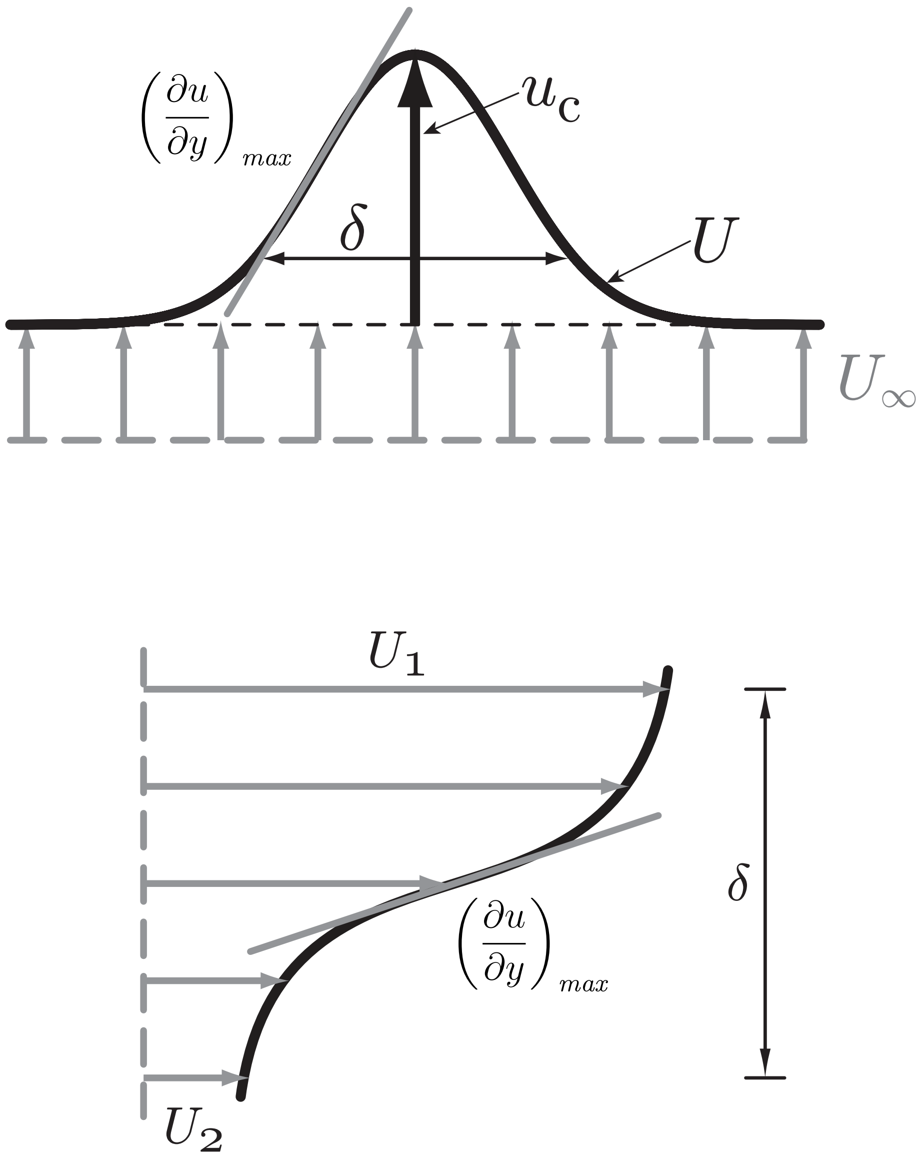

Figure 2.1: Schematics indicating proper definition of local outer length and velocity scales δ and u_c from local mean velocity profiles for typical coflowing jet profile shape *(top)* so that $(\partial u/\partial u)_{\max} \approx (u_c/\delta)$ where $u_c \equiv U_c - U_\infty$ is centerline excess velocity and typical mixing layer profile shape *(bottom)* where $u_c \equiv (U_1 - U_2)$.

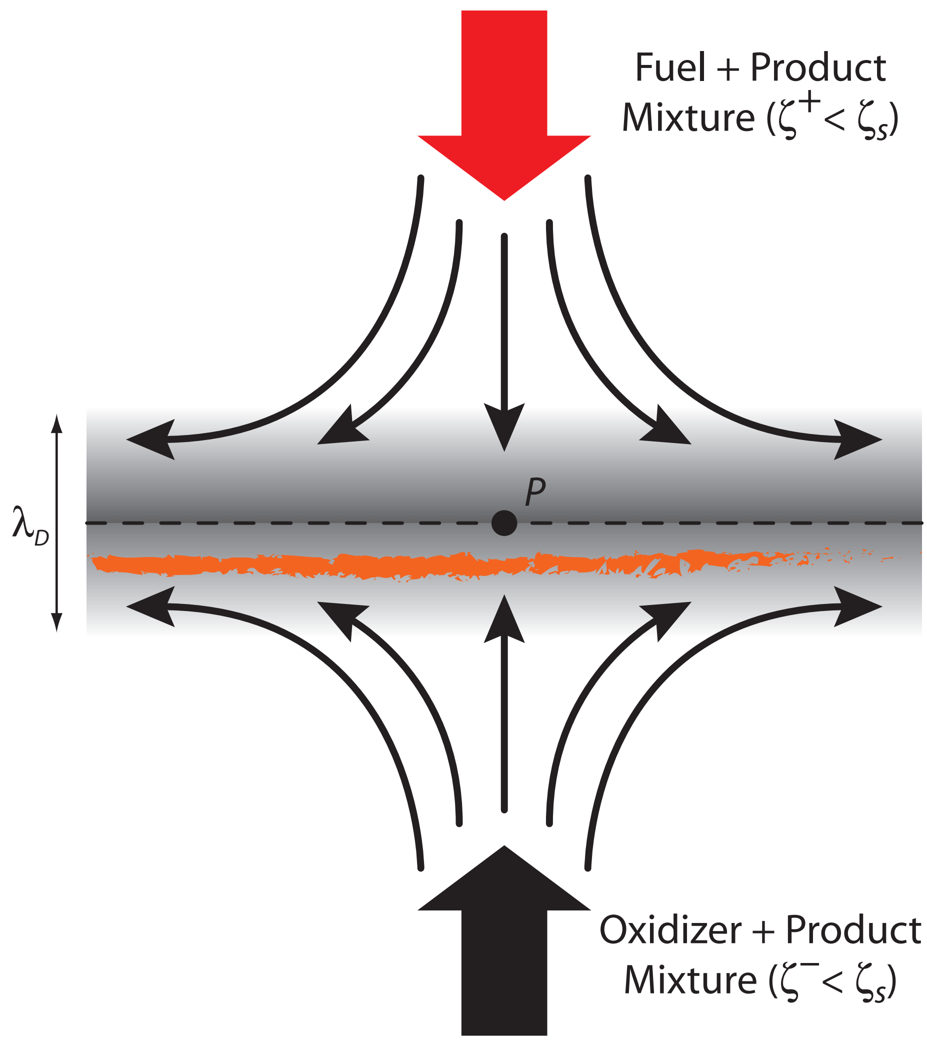

Figure 2.2: Schematic of strained diffusion and reaction layer separating fuel-rich and oxidizer-rich regions in mixture fraction field $\zeta(\mathbf{x}, t)$, shown in local Lagrangian frame moving with point P at center of layer.

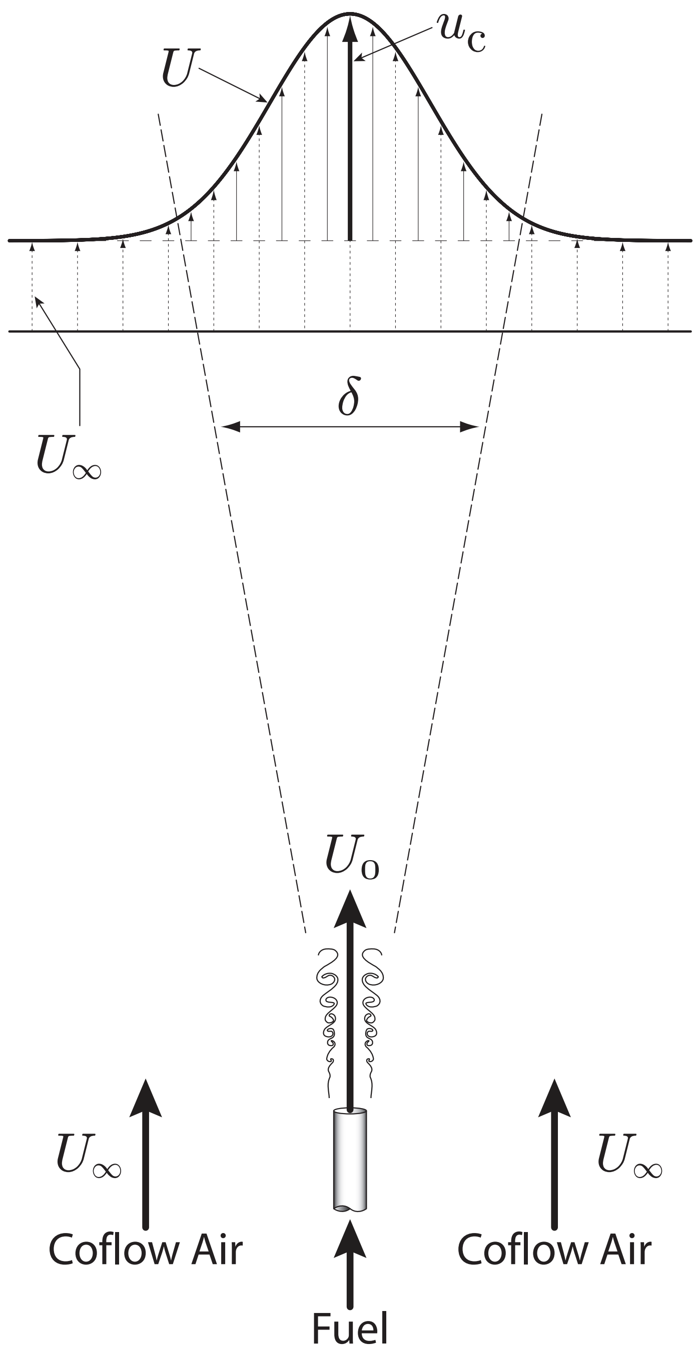

Figure 2.3: Schematic indicating basic layout and nomenclature for axisymmetric coflowing turbulent jets as used for experimental measurements presented herein.

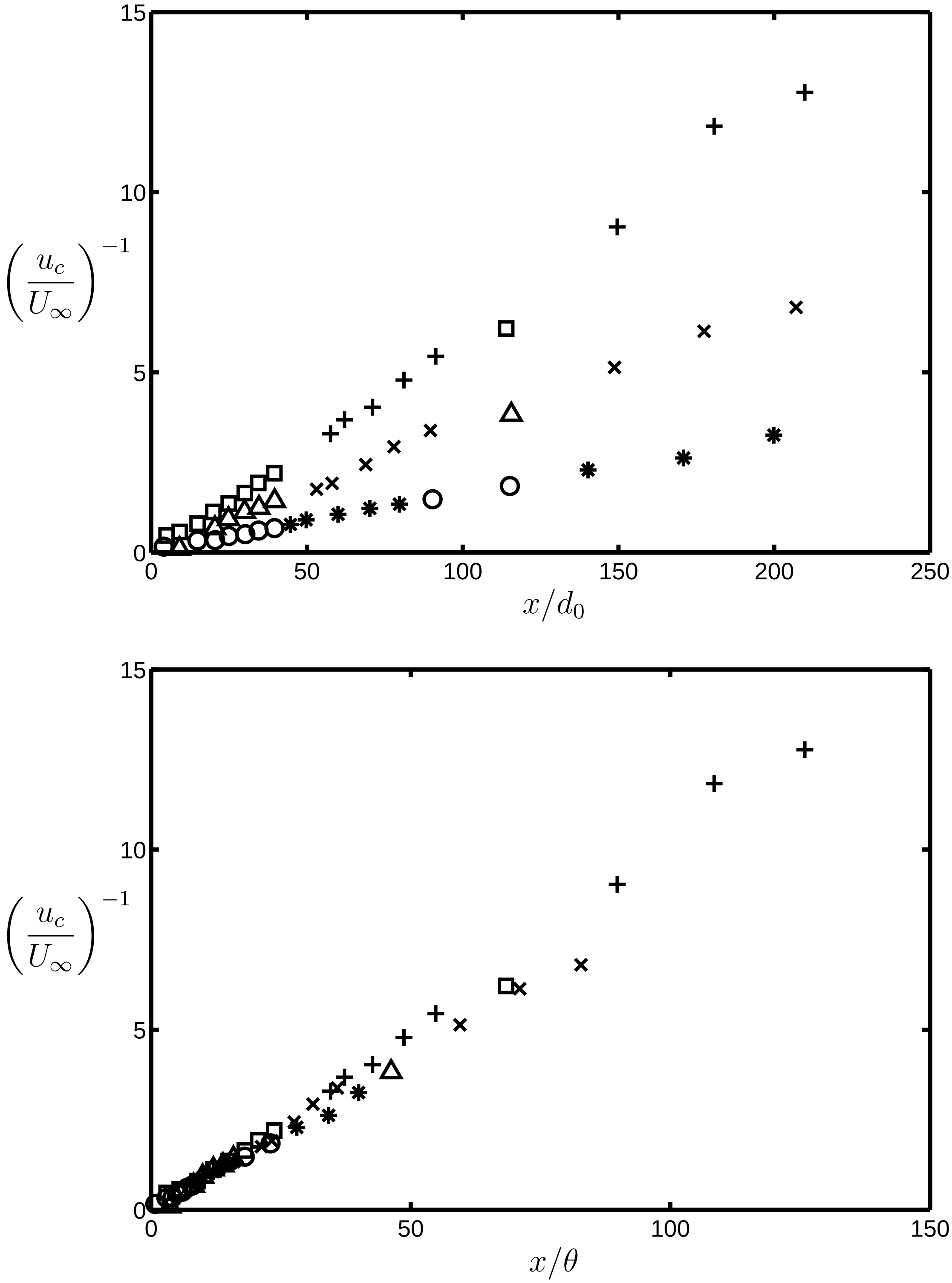

Figure 2.4: Decrease in local outer velocity u_c with downstream coordinate x in coflowing turbulent jets for three different values of jet-to-ambient velocity ratios U_0/U_∞, showing naïve jet scaling with jet exit diameter d_E *(top)* and proper coflowing jet scaling with jet momentum radius θ *(bottom)*. Adapted from Dahm and Dibble (1988); symbols defined therein.

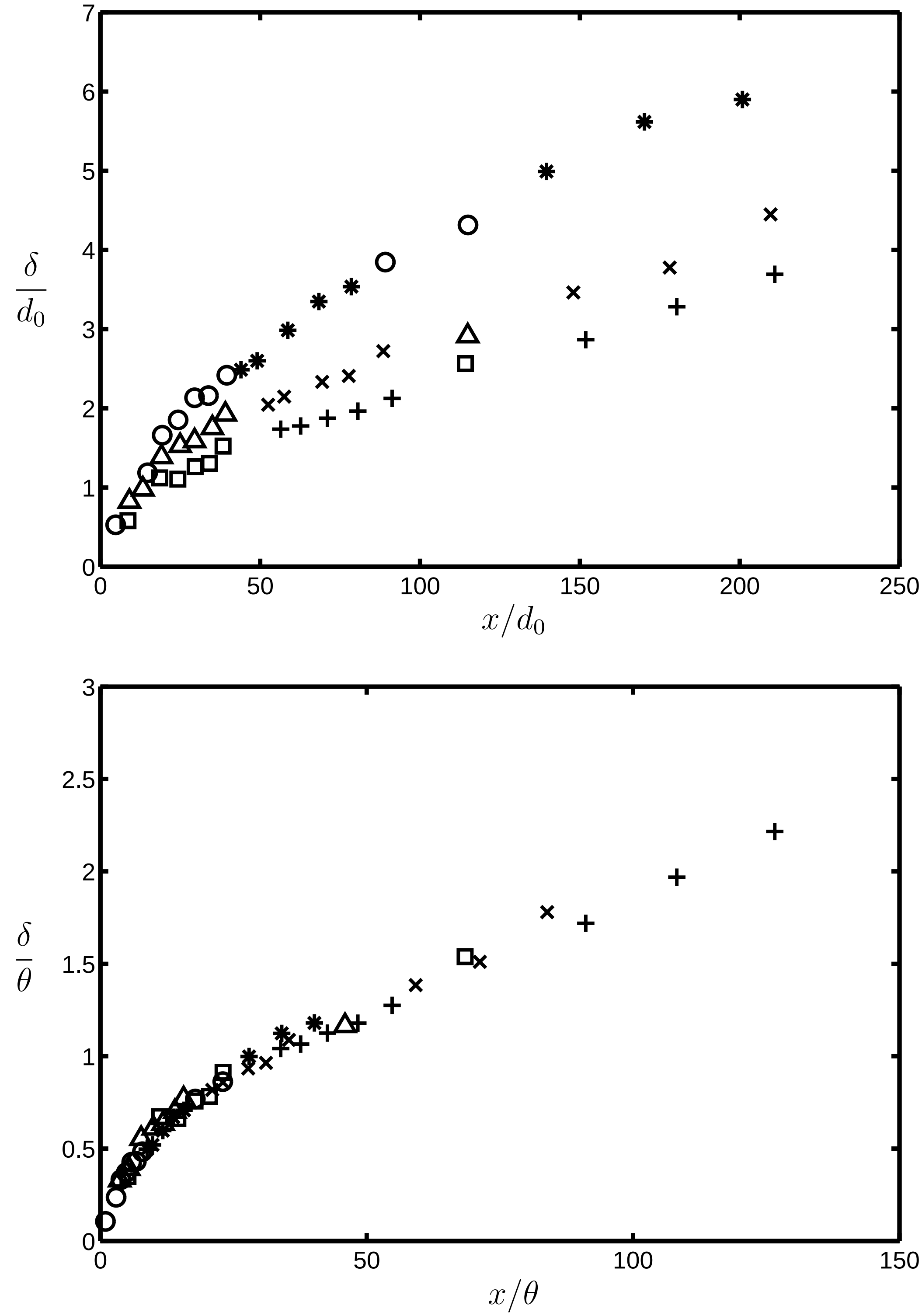

Figure 2.5: Increase in local outer length scale δ with downstream coordinate x in coflowing turbulent jets for three different values of jet-to-ambient velocity ratios U_0/U_∞, showing naïve jet scaling with jet exit diameter d_E *(top)* and proper coflowing jet scaling with jet momentum radius θ *(bottom)*. Adapted from Dahm and Dibble (1988); symbols defined therein.

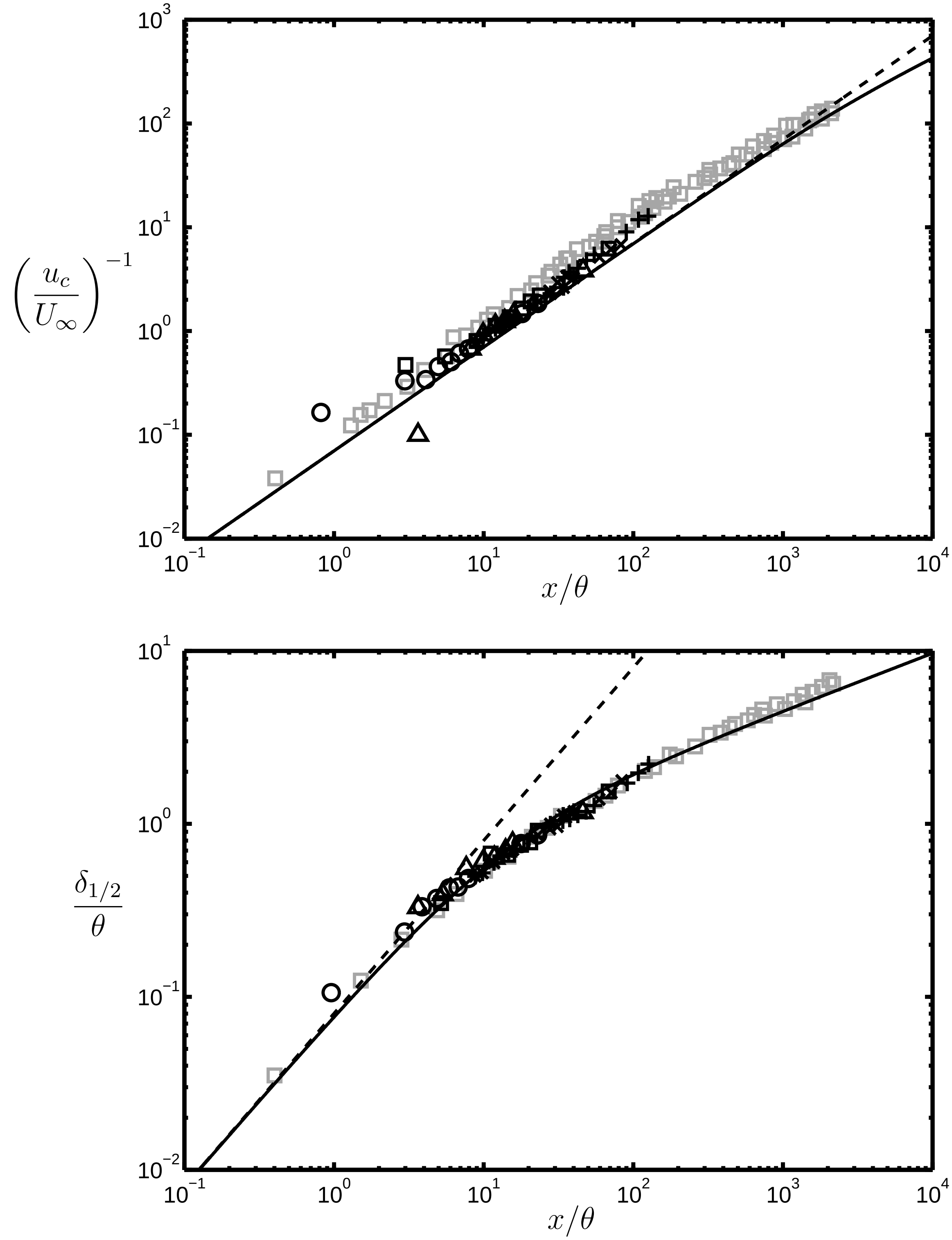

Figure 2.6: Decrease in local outer velocity u_c with downstream coordinate x in coflowing turbulent jets from Fig. 2.4 *(top)*. Increase in local outer length scale δ with downstream coordinate x in coflowing turbulent jets from Fig. 2.5 *(bottom)*. Both panels include for comparison data from Davidson and Wang (2002) spanning a large range in x/θ (grey squares).

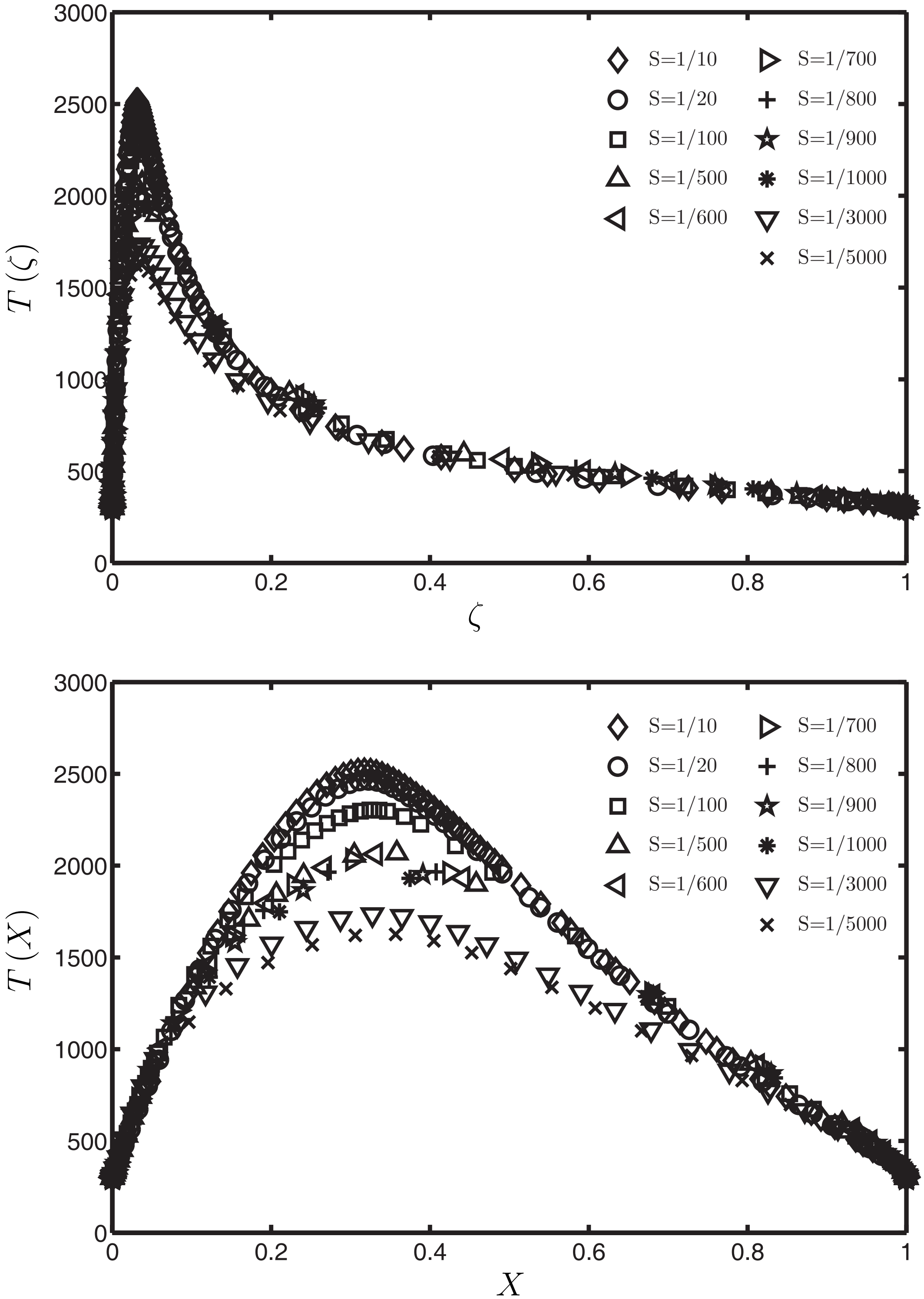

Figure 2.7: State relation for temperature in terms of conserved scalar ζ *(top)* and mole fraction X *(bottom)* from OPPDIF computations for strain rates $\mathcal{S}$ ranging from equilibrium limit to deep nonequilibrium. Note bilinear form of $T(X)$ in equilibrium regime at $\mathcal{S} < 1/20\ \mathrm{s}^{-1}$.

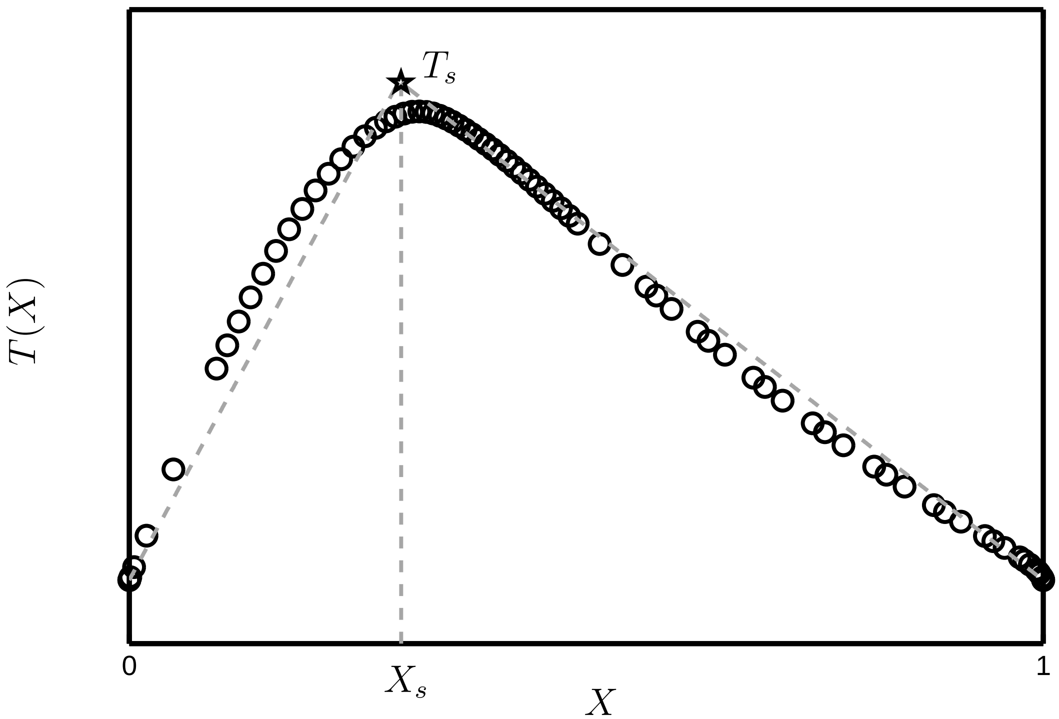

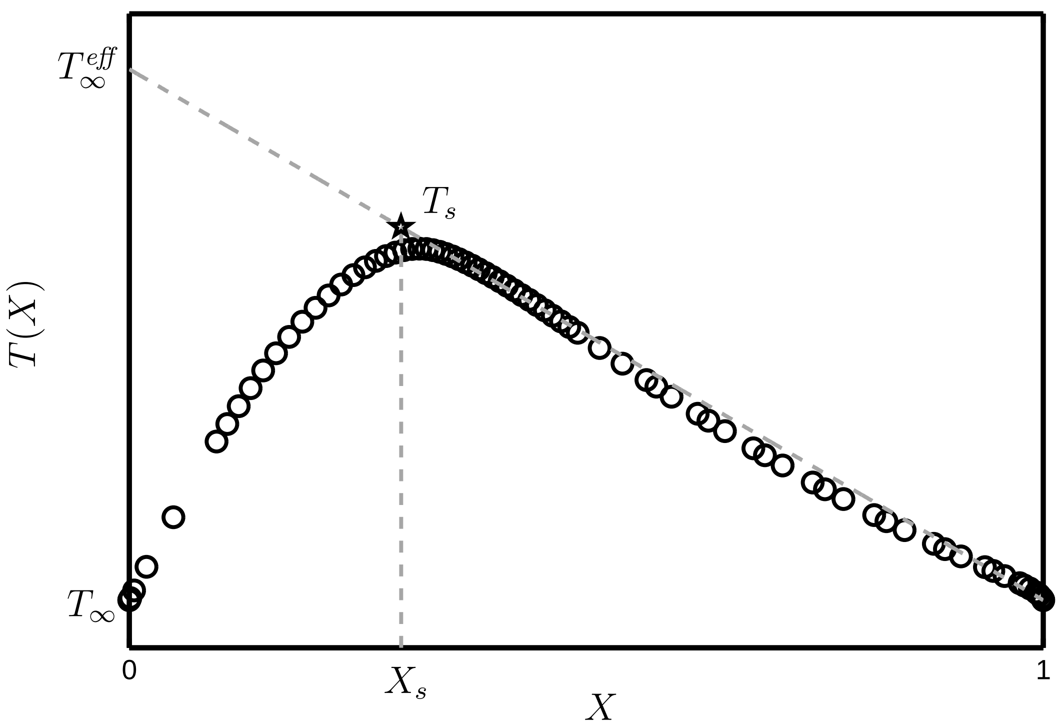

Figure 2.8: Equilibrium temperature state relation function from Fig. 2.7 shown in terms of mole fraction X. Departures from strict bilinear form of $T(X)$ for $X \neq X_s$ *(top)* are due to small variations in molar specific heat $\widetilde{c}_p$. Linear approximation of $T(X)$ for $X > X_s$ leads to effective ambient temperature T_∞^{eff} *(bottom)* in a corresponding nonreacting flow.

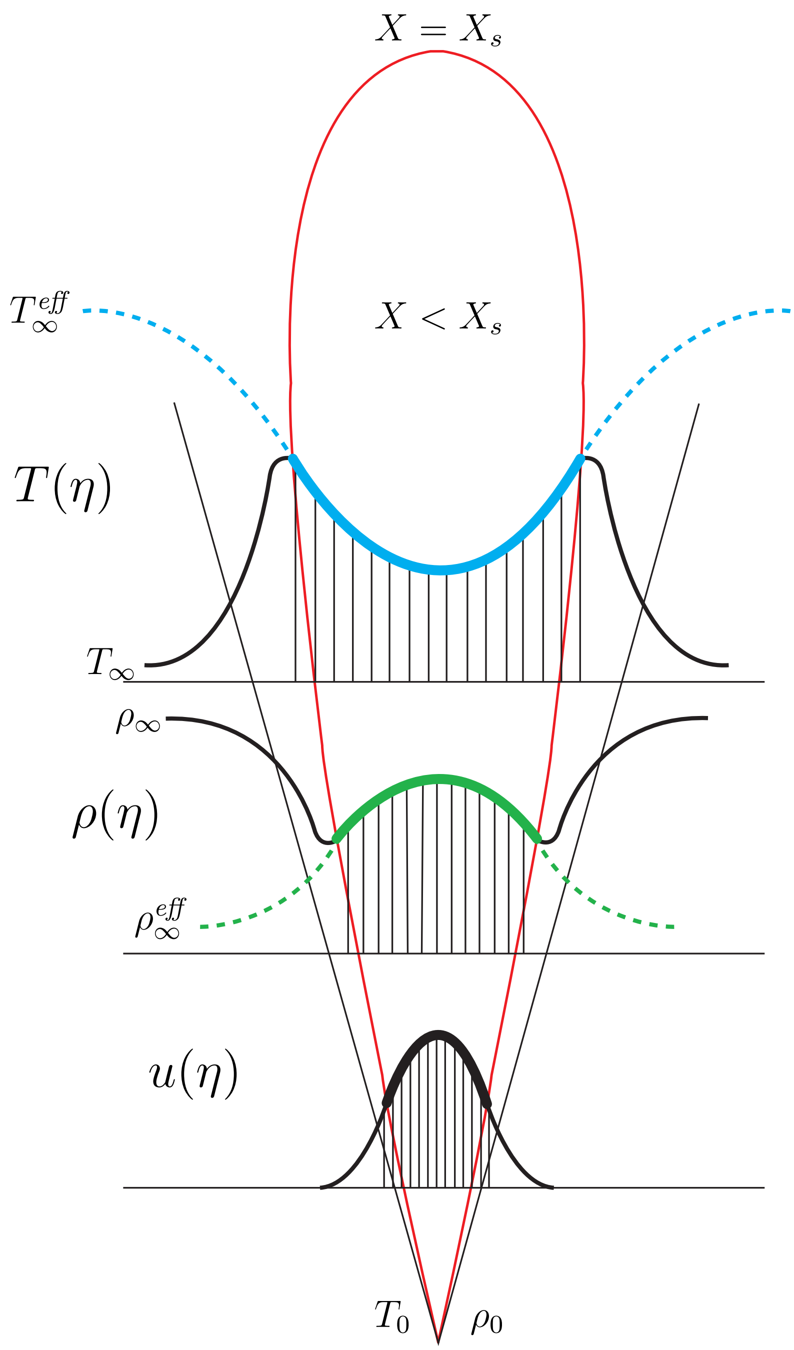

Figure 2.9: Schematic of equivalence principle, showing implications for mean temperature (*top*) and density (*middle*) profiles in an exothermically reacting jet. Solid lines show profiles in exothermic reacting flow; dashed lines show profiles in nonreacting flow produced by simple mixing between the actual source values T_0 and ρ_∞ effective ambient values T_∞^{eff} and ρ_∞^{eff}. Heavy line shows resulting agreement for $X > X_s$, where velocity (*bottom*) is large, ensuring proper accounting for the dominant inertial effects of heat release, from Diez and Dahm (2007).

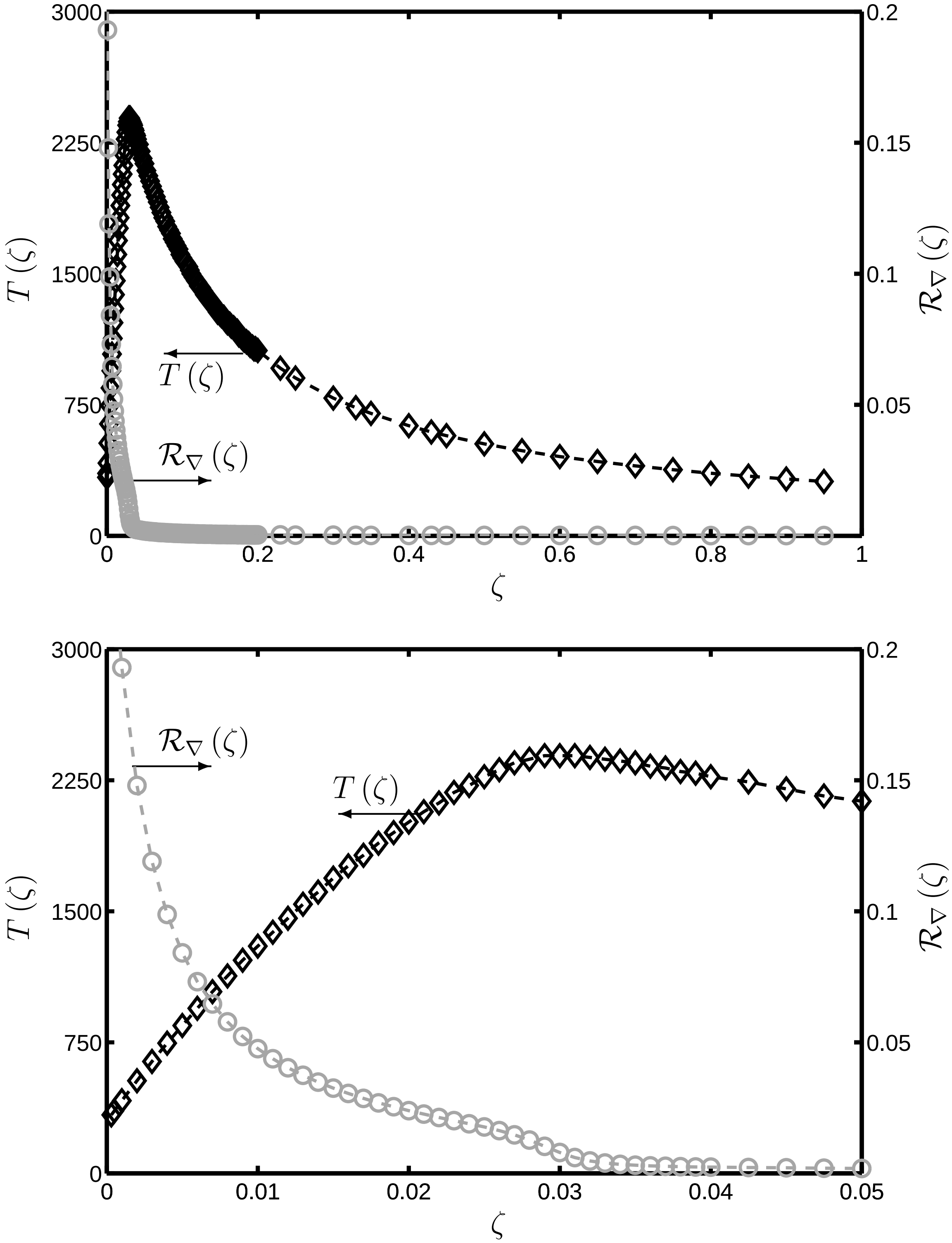

Figure 2.10: Equilibrium temperature state relation $T(\zeta)$ for $\mathrm{H_2} - \mathrm{air}$ chemistry, showing variation in temperature T with mixture fraction ζ (*left axis*), and corresponding relative dilation $\mathcal{R}_\nabla(\zeta)$ (*right axis*). Results are shown for $0 \leq \zeta \leq 1$ *(top)*, and near stoichiometric value ζ_s *(bottom)*.

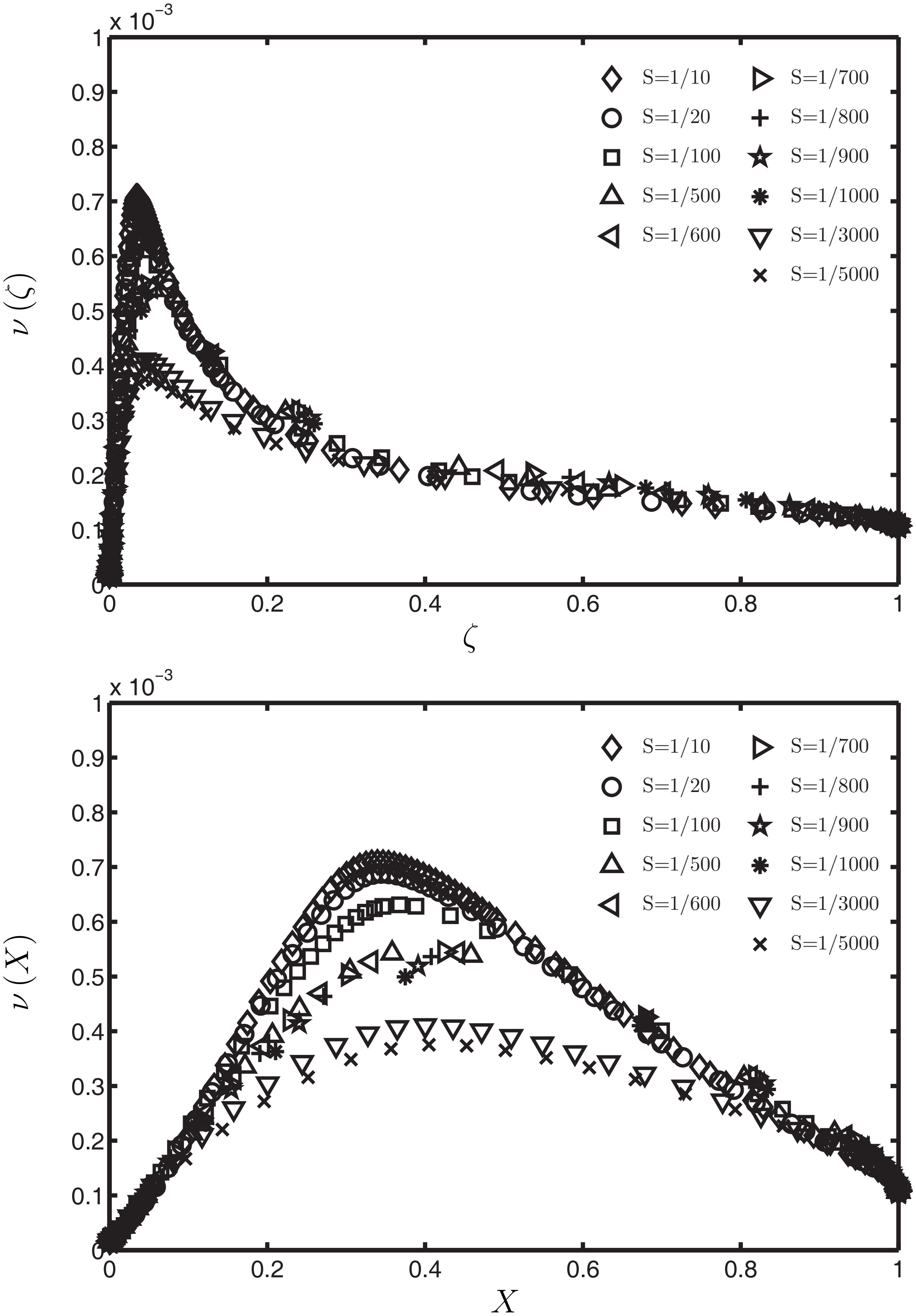

Figure 2.11: Kinematic viscosity state relationship as a function of conserved scalar *(top)* and mole fraction *(bottom)*. Results obtained via OPPDIF computations for a wide range of strain conditions ranging from 1/10 to 1/5000 s^{-1}.

CHAPTER III

Experimental Facilities and Diagnostic

The particular flow used in this study of heat release effects on the velocity field $\mathbf{u}(\mathbf{x}, \mathbf{t})$ in turbulent shear flows is an axisymmetric coflowing turbulent jet configuration. Such coflowing jets readily allow introduction and removal of seed particles needed for particle image velocimetry (PIV) measurements of the velocity field. This chapter describes the LTC DSPIV reacting turbulent shear flow facility designed and assembled for this study. This facility was specifically developed to provide high-resolution instantaneous velocity gradient fields via Particle Image Velocimetry (PIV). The facility can be readily modified to acquire large field of view (FOV) images spanning the full extent of the jet width δ in order to accurately characterize the outer flow quantities. Herein "small FOV" imaging refers to experiments conducted at the inner scales of the jet where the PIV resolution is comparable to λ_ν, the local viscous length scale. Conversely, "large FOV" experiments refer to data acquired where the overall PIV FOV is comparable to $\delta(x)$ the local outer length scale.

The LTC DSPIV laboratory was designed, fabricated and assembled to be capable of sustaining large heat loads while remaining readily configurable for various types of measurements. The basic facility is a vertical draft wind tunnel that can sustain a 1 kW jet flame. The entire test section assembly can be removed in a matter of minutes to readily permit changes between experimental configurations.

3.1 LTC DSPIV Laboratory

The LTC DSPIV facility is shown in its current experimental arrangement in Fig. 3.1. The major components shown include: the fuel mixing board on the left, the optical table in the center, the vertical induced draft wind tunnel, the four Nd:YAG lasers, and the data acquisition computer and data processing PC. A schematic of the equipment layout is shown in plan view in Fig. 3.2. The current layout was arrived at by optimization of several constraints: laboratory safety, ease of access to bottled gases, experiment flexibility and reconfigurability, laboratory maintenance and experimental objectives.

The vertical induced-draft test section is shown schematically in Fig. 3.3 and photographically in Fig. 3.4. The first of the two main components of the test section is the flow conditioning section at the base of the tunnel, where the ambient room air enters the apparatus. A flow conditioning section (shown in Fig. 3.5) consists of a porous plate, two screens and a layer of aluminum honeycomb. The latter removes the unwanted large-scale motions in the induced laboratory air flow and yields a uniform coflow with low turbulence intensity ($4\% - 5\%$ as measured by PIV) for the test section. The flow conditioner was designed according to "Roshko's Rules" detailed in Appendix B of Mullin (2004).

Briefly, the design parameters employed in the flow conditioning section assume a target coflow velocity of $U_\infty \approx 2.5$ m/s. A porous plate with 12.7 mm holes on

25.4 mm centers is the first element encountered by the flow. This is closely followed by a screen 6 mm downstream. The screen consists of a mesh of wires 0.81 mm in diameter with 2.36 mm square openings. The honeycomb section follows 62 mm downstream. The honeycomb is 31.8 mm in length with cells 3.18 mm in width. A second screen of the same type as the first is the final flow conditioning element. This arrangement yields a coflow in the test section with a turbulence intensity of approximately 5%.

Following the flow conditioning section, the test section is the second component of the wind tunnel. Shown in Fig. 3.4, the test section consists of a constant cross-section duct, 457 mm square, with ample optical access. Tempered glass windows 6.35 mm in thickness, 300 mm in width and 810 mm in height occupy both sides of the test section and the rear wall. The front wall is a door with a 285 $\times$ 825 mm tempered glass window. The tempered glass provides an inexpensive solution to the problem of maximizing optical access while resisting fracture due to heat load. The 6.35 mm thick tempered glass was found to produce only about 10 % transmission loss at near-UV (355 nm) wavelengths. The test section door enables rapid access to the tunnel for routine tasks: cleaning windows, alignment of PIV camera targets, positioning of laser sheet targets, jet nozzle alignment and jet nozzle changes.

3.2 Gas Delivery System

The laboratory schematic in Fig. 3.2 shows the key components of the gas delivery system: the fuel mixing board and the compressed gas cylinders for both fuel and inerts/oxidizers. For the benefit of safety and ease of laboratory access, the gas delivery lines are routed either overhead or beneath the raised flooring. The fuel cylinders (shown in Fig. 3.6) are located along the south wall of the laboratory while the oxidizers and inerts are placed along the north wall. The delivery lines are all routed to the fuel mixing board where the gases are metered and, if appropriate, are also mixed. The mixing board (shown in Fig. 3.7) is capable of blending three independent gases streams to produce a wide variety of fuel mixtures. Immediately following the fuel board, the PIV seeders (see Fig. 3.8) are located to introduce seed particles in both the jet fluid and the coflow fluid before they enter the test section.

3.2.1 Fuel Board

The fuel mixing board provides flow metering for up to three independent lines by use of O'Keefe calibrated choked orifices to control the flow rates. The pressure is monitored both upstream and downstream of the orifices to determine the flow rates within each of the delivery lines. The flow board is equipped with both coarse and fine valve controls to provide accurate and repeatable flow rates. All delivery lines are joined together to pass through an emergency shut-off valve before entering the jet fluid seeder.

The mixing board also provides carrier air metering for the coflow seeder. Owing to the much higher flow rates required by the coflow seed carrier fluid, a high volume King rotometer capable of measuring up to 2600 SLPM of air was used to meter the flow. The supply for this carrier gas was provided by the FXB shop air lines. The air was filtered twice to remove both water vapor and residual oil from the shop air compressor. Typically $200-300$ SLPM of carrier air was required for most experimental conditions.

3.2.2 PIV Seeders

The seeders, shown in Fig. 3.8, are fashioned from stainless steel vacuum chambers manufactured by MDC industries. Before entering the seeders, the gas lines are split to allow a bypass which can control the seeding level in the gas lines. The lines entering the seeders terminate inside the seeders with highly supple flexible tubing. This tubing oscillates wildly inside the seeders, providing a highly unsteady and chaotic flow field to fluidize the seed particles. The seed-laden gas then exits the seeders and is routed directly into the test section. The jet fluid proceeds to the jet apparatus, and the coflow seed is introduced into the flow conditioning section via seed rakes. The rakes (indicated schematically in Fig. 3.3) are oriented such that the holes create small jets issuing fluid in the streamwise direction. The rakes are created from thin-walled 19 mm OD tubing with 1.6 mm holes drilled 25.4 mm apart. The numerous small-diameter holes provide a uniform distribution of seed delivery into the flow conditioning section.

3.2.3 PIV Seed

The application of PIV to a reacting flow has been demonstrated numerous times (e.g. Stella et al. 2001; Muñiz and Mungal 2001). Successful application of the technique rests upon judicious selection of tracer particles capable of faithfully following the flow while surviving a flame. Consequently, solid refractory ceramic particles have become the customary flow tracer for an exothermically reacting flow. Typical materials include aluminum oxide, titanium oxide, zirconium dioxide and magnesium oxide, (Reuss and Rosalik, 1998).

The seed particle sizing criterion is usually expressed in terms of the particle Stokes number (e.g. Raffel et al. 1998; Clemens and Mungal 1991; Melling 1997) as

$$St \equiv \frac{\tau_p}{\tau_f}, \tag{3.1}$$

where τ_p and τ_f are the particle and flow time scales, respectively. Following Mullin (2004) aluminum oxide Al_2O_3 particles nominally 0.5 μm in diameter have been demonstrated to satisfy the particle Stokes criteria for the expected conditions in the present work.

Under exothermically reacting conditions, two additional considerations arise: thermophoretic effects and index of refraction gradients. Thermophoresis accounts for tendency of a particle suspended in a fluid to drift towards the low temperature regions when a temperature gradient is present. The effects of beam steering and apparent particle displacement due to changes in the index of refraction field are discussed in Appendix A.

The effects of thermophoresis have been examined by Sung et al. (1994) and from a more applied perspective by Stella et al. (2001). Based on counterflow flame configurations, both these studies identified the upper bound of velocity error for particles similar to the present 0.5 μm aluminum oxide seed to be approximately 0.15 m/s. Estimates based on jet flames studied by Muñiz (2002) provided similarly small values, namely 0.08 m/s.

3.2.4 Jet Nozzle

The jet assembly used in the present study is shown in Figs. 3.9 and 3.10. The jet was designed with a large area ratio contraction to create a "top-hat" flow profile at the exit. The jet was fabricated from aluminum with interchangeable, threaded nozzles to allow various nozzle diameters to be used with minimal time required for change-over.

In order to assess the likelihood of flow separation on the outer surface of the jet nozzle, an axisymmetric Thwaites' Method laminar boundary layer calculation was conducted. The final nozzle designs were obtained by iterating over a family of profiles until a satisfactory shape was reached where the area ratio was maximized while preventing flow separation from the external wall of the nozzle.

Profiles of the two nozzles with diameters 4.0 and 5.5 mm are shown in the subpanels of Fig. 3.9. Coupled with an inner (entrance) tube diameter of 25.4 mm, these two nozzles yield area ratios of 40.3 and 21.3, respectively. The outer profiles were obtained by manipulating a family of error function profile shapes given by

$$\rho = S + \frac{A}{2}\mathrm{erfc}\left(-\frac{(\xi\sigma + \mu)}{\sqrt{2}}\right), \tag{3.2}$$

to produce the desired shape. The dimensionless axial and radial coordinates are given as $\xi \in [0, 1]$, $\xi \equiv x/L$ and $\rho \equiv r/L$. This leaves four free parameters available to create the desired profile shape, namely S, A, σ and μ.

3.3 Optical Layout

The optical arrangement is shown photographically in Fig. 3.11. Here the main components include the Nd:YAG lasers, the sheet generating optics, beam positioning equipment and image acquisition cameras.

3.3.1 Light Sheet Generation

The PIV particles are illuminated via two Nd:YAG lasers (one Spectra-Physics Quanta-Ray Pro-250 and one Spectra-Physics GCR 3) shown in Fig. 3.11 and schematically in Fig. 3.12. The lasers produce 400 mJ pulses 6 ns in duration at the frequency doubled wavelength of 532 nm. Typically, only 25-35 mJ are required for the small field of view (FOV) experiments, whereas the lasers are operated at full power for the large FOV PIV.

The time delay Δt between the laser pulses is controlled by a PC-based Programmable Timing Unit (PTU) operated by the DaVis software. This PTU also operates the mechanical shutter by way of a Stanford Systems Delay Generator model DG535 (*S2* in Fig. 3.12) which permits the Nd:YAG lasers to maintain their internal 10 Hz operation frequency. The two beams are combined using a 50/50 power-based beam splitter *BS1* and the alignment is controlled by mirror *M1*, shown in Fig. 3.13. The *M1* mirror provides precise computer-controlled actuation via Thor Labs 12 V DC servo-motors.

The motors are mounted to give control over three degrees of freedom in the beam positioning: two angular and one translational. The Thor Labs models *Z612* and *Z25B* servo motors are capable of a minimum increment of less than 0.20 μm. A kinematic mount, coupled with 50 mm diameter mirrors, yields a 14 μm beam position uncertainty over the 3.5 m path length of the laser sheets.

After combination, the laser beams pass through a CVI $f = -750$ mm high energy cylindrical lens *C1* to slowly expand the beams in the vertical plane. The resulting laser sheets then pass through an $f = 1000$ mm CVI cylindrical lens *C2* oriented to focus the sheets in the horizontal plane. The sheets arrive at the image field of view nearly 40 mm in height and 400 μm thick.

An optional mirror *M5* can be removed/positioned in the beam path to redirect the sheets for use in the large field of view PIV experiments. In this case, the beams avoid the *C2* lens and pass through an $f = -50$ mm which further increases the sheet height while the thickness remains unchanged from the nominal 6 mm beam diameter exiting the Nd:YAG lasers.

3.3.2 Particle Imaging

The PIV images are captured by PCO SensiCam interline transfer CCD cameras. The CCD is rated at 200 ns interframe timing with an array size of 1024×1280 ($h \times w$). The physical chip size is 6.8×8.6 mm with 12-bit digital depth and low noise due to electronic Peltier cooling.

The small field of view experiments use a Sigma 70−300 mm $f/4$−5.6 APO macro lens while the large FOV experiments employ a Sigma 24 − 70 mm $f/3.5$ aspherical lens. The reacting flow cases required a narrow-band filter to reject unwanted signal due to flame luminosity. An Andover Corp. Model 532FS10-50 bandpass filter was selected with 532 ± 5 nm bandwidth and 55% peak transmission.

3.4 Experimental Conditions

Tables 3.1 – 3.6 give the experimental conditions for all cases reported in the present study. Conditions for each of the "outer-scale nonreacting" cases, denoted *ONR*X, are listed in Table 3.1, and for the "outer-scale reacting" cases, denoted *OR*X, are in Table 3.2. The "inner-scale nonreacting" cases, denoted *INR*X, are in

Table 3.3, and the "inner-scale reacting" cases, denoted IRX, are in Table 3.4. All of these cases correspond to measurements obtained on the jet centerline. Additional measurements were obtained at various radial locations off the jet centerline. Conditions for each of the "radial nonreacting" cases, denoted RNX, are given in Table 3.5, and for the "radial reacting" cases denoted RRX are given in Table 3.6.

In these tables, the local outer length scale δ in Fig. 2.3 is defined as the full-width where the streamwise velocity drops to 5% of its centerline value; for any other choice of δ the values in these tables can be easily converted via the Gaussian shape of the mean velocity profile. This, together with the local centerline excess velocity $u_c \equiv U - U_\infty$ in Fig. 2.3, comprises the local outer flow variables. These values, together with the kinematic viscosity $\nu = 15(10^{-6})$ m^2/s, yield the local outer-scale Reynolds number Re_δ. From these, the local viscous (inner) length scale λ_ν can be deduced following

$$\frac{\lambda_\nu}{\delta} = \Lambda Re_\delta^{-\frac{3}{4}}, \tag{3.3}$$

where $\Lambda \approx 11.2$ is from Buch and Dahm (1996). The source conditions listed in Tables 3.1 – 3.6 include the jet nozzle diameter d_E, the exit density ρ_E of the jet fluid, and the coflow density ρ_∞, which is taken to be that of air at 294 K. The PIV interrogation window size is given as Δ_{IW} and the streamwise distance from the nozzle exit to the middle of the PIV FOV is denoted by x.

Figure 3.1: Photograph of LTC DSPIV laboratory. See corresponding schematic of overall layout in Fig. 3.2, and schematic of optical layout in Fig. 3.12.

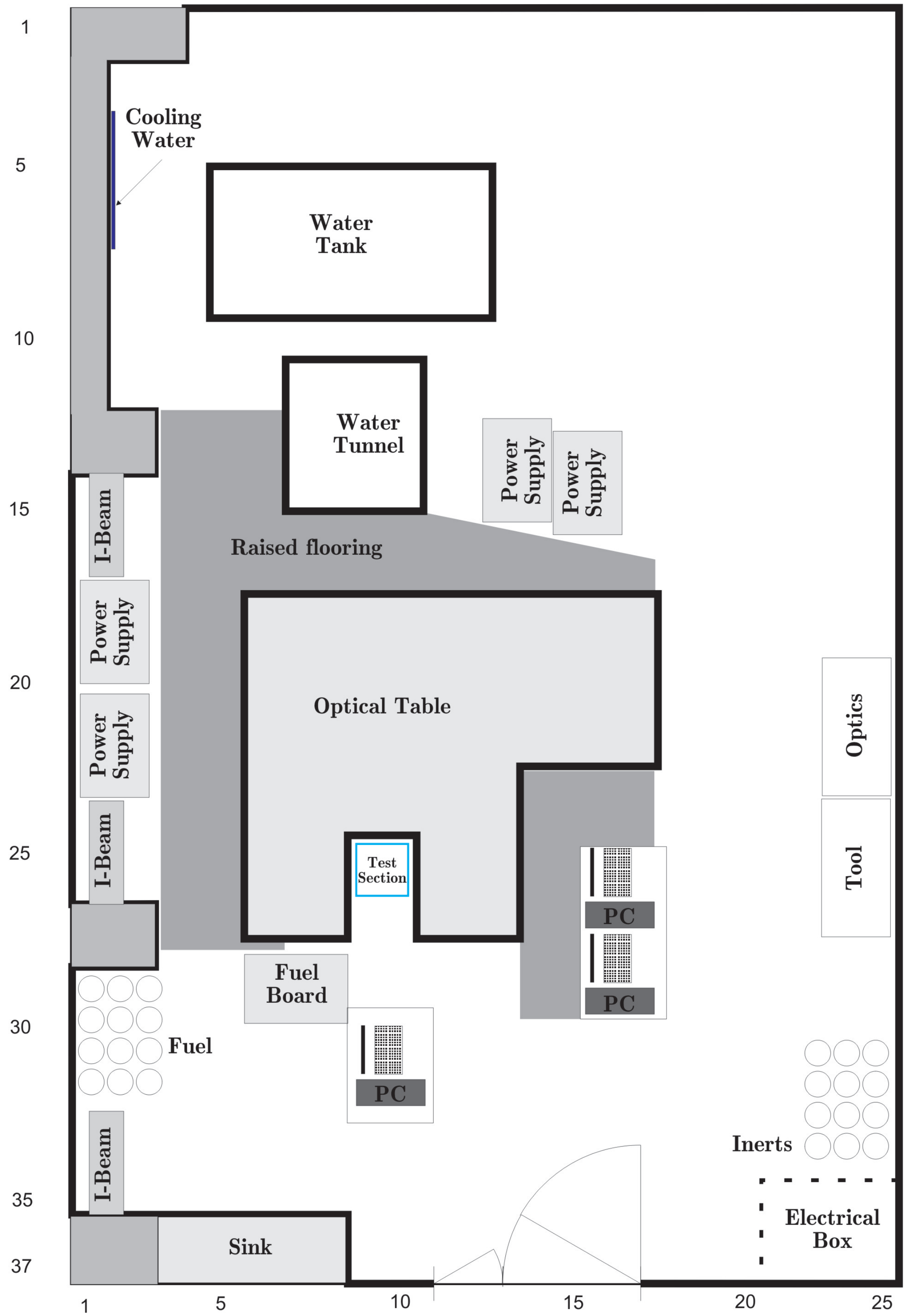

Figure 3.2: Plan view schematic of LTC DSPIV laboratory layout, corresponding to Fig. 3.1.

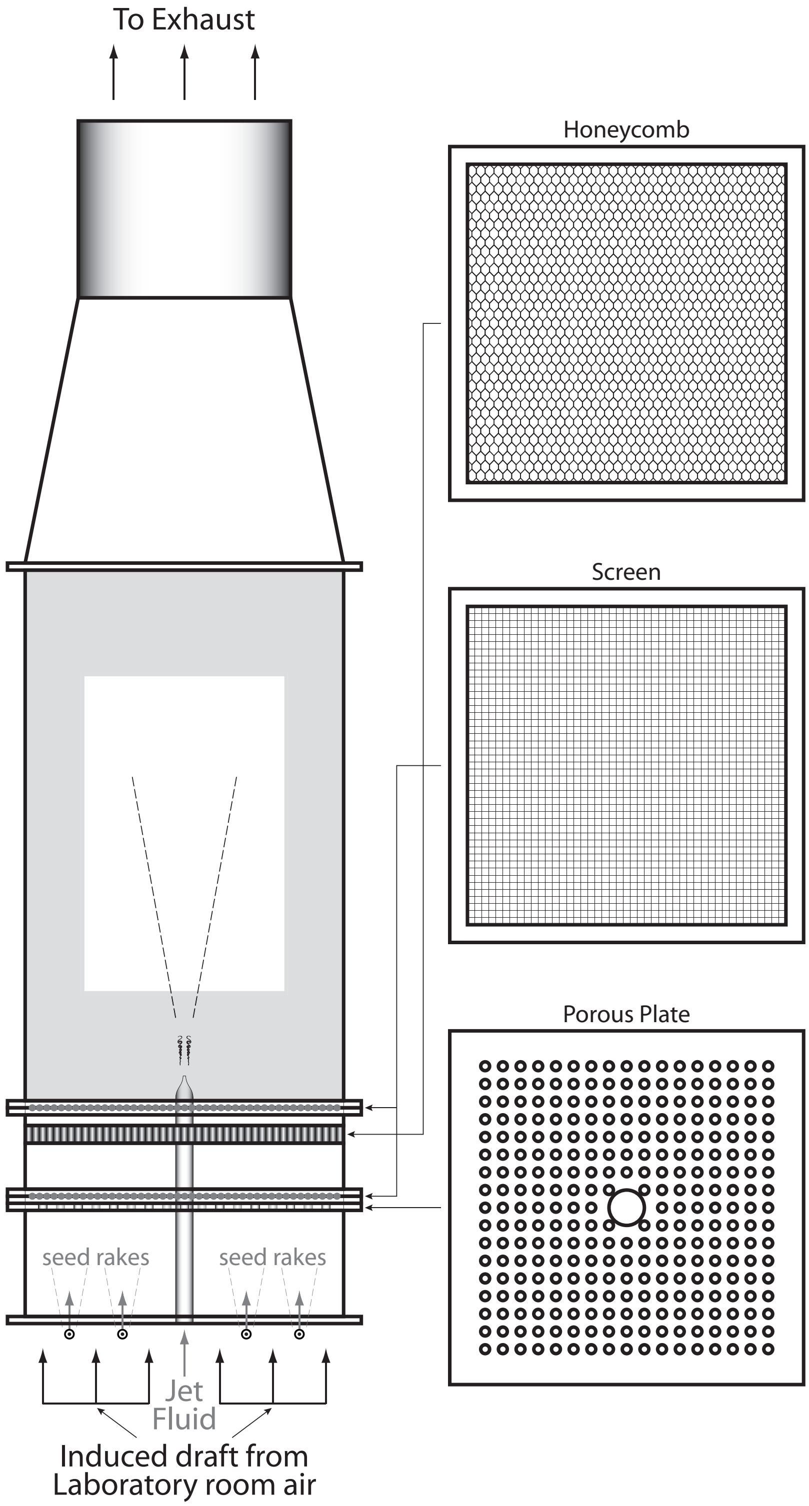

Figure 3.3: Schematic of vertical induced-draft wind tunnel, with flow conditioning elements shown on the right. Laboratory air is drawn through the bottom into the seeding section, where seed particles are introduced, then passes through the flow conditioning section and proceeds into the test section, from which it exits into the exhaust system.

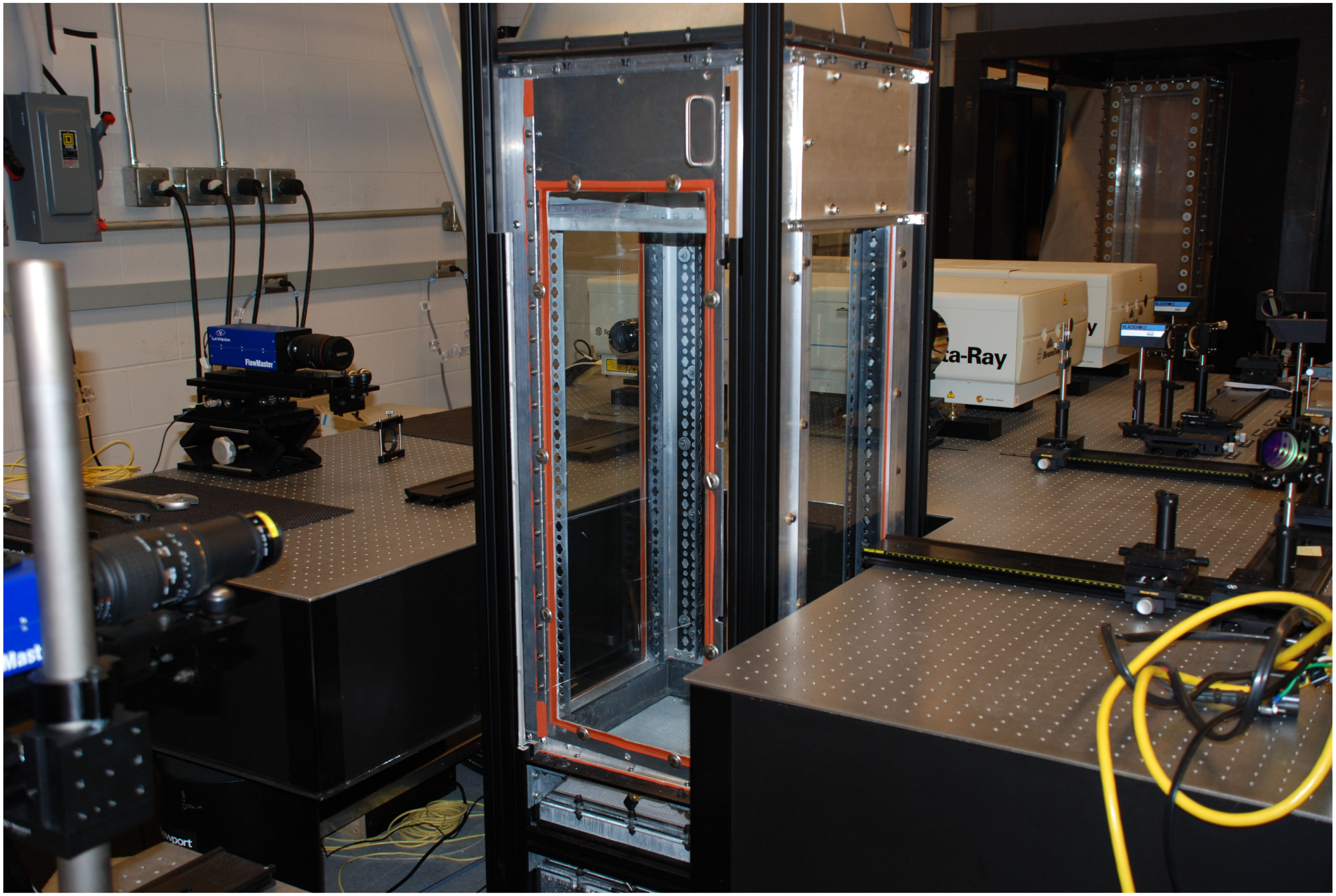

Figure 3.4: Photograph of the test section portion of the vertical draft wind tunnel. The optical path is visible on the far right and the large FOV camera is seen in the background on the left. On the near left side, the small FOV camera is shown.

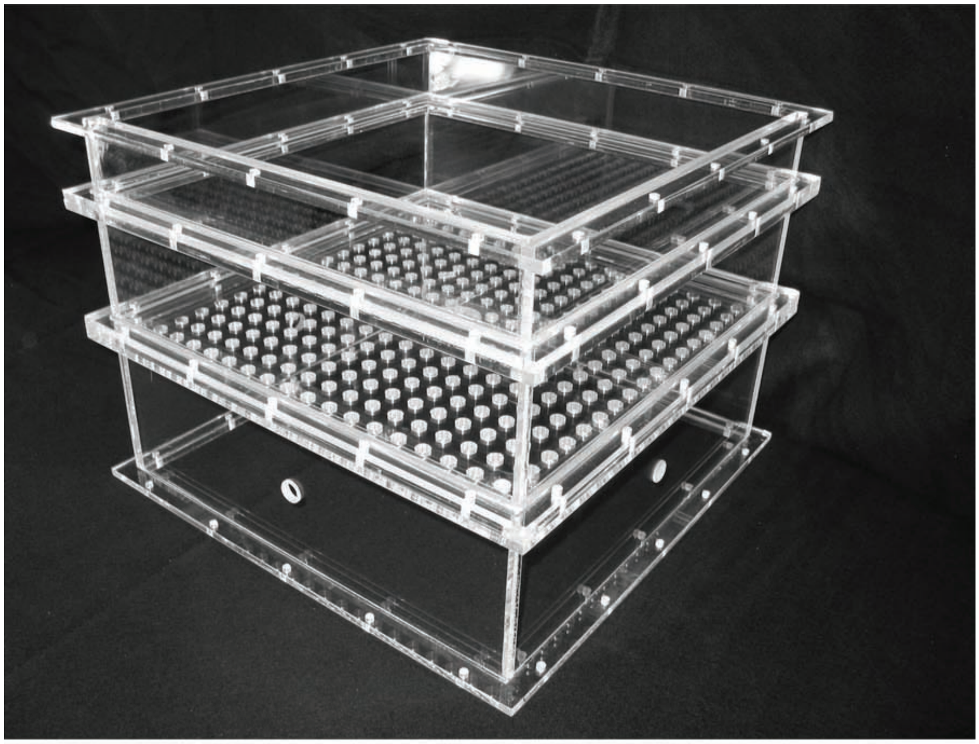

(a)

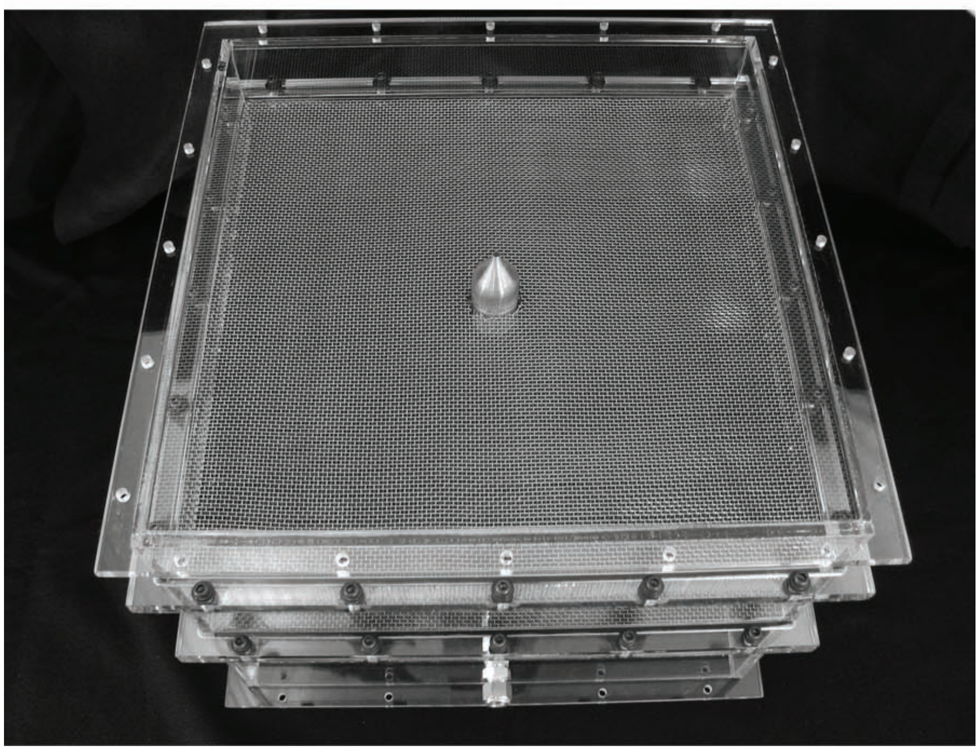

(b)

Figure 3.5: Photographs of the flow conditioning section. Upper panel: section containing only the porous plate element. Lower panel: screens, honeycomb and jet apparatus have been mounted.

Figure 3.6: Typical cradle consisting of twelve compressed gas cylinders providing the hydrogen fuel used in the reacting flow experiments. Flame arrestor is visible to left of regulator.

Figure 3.7: Photograph of fuel mixing board. The three independent gas lines are identifiable by vertical alignment of pressure gauge pairs. Fine and coarse flow metering valves are located near bottom of mixing board.

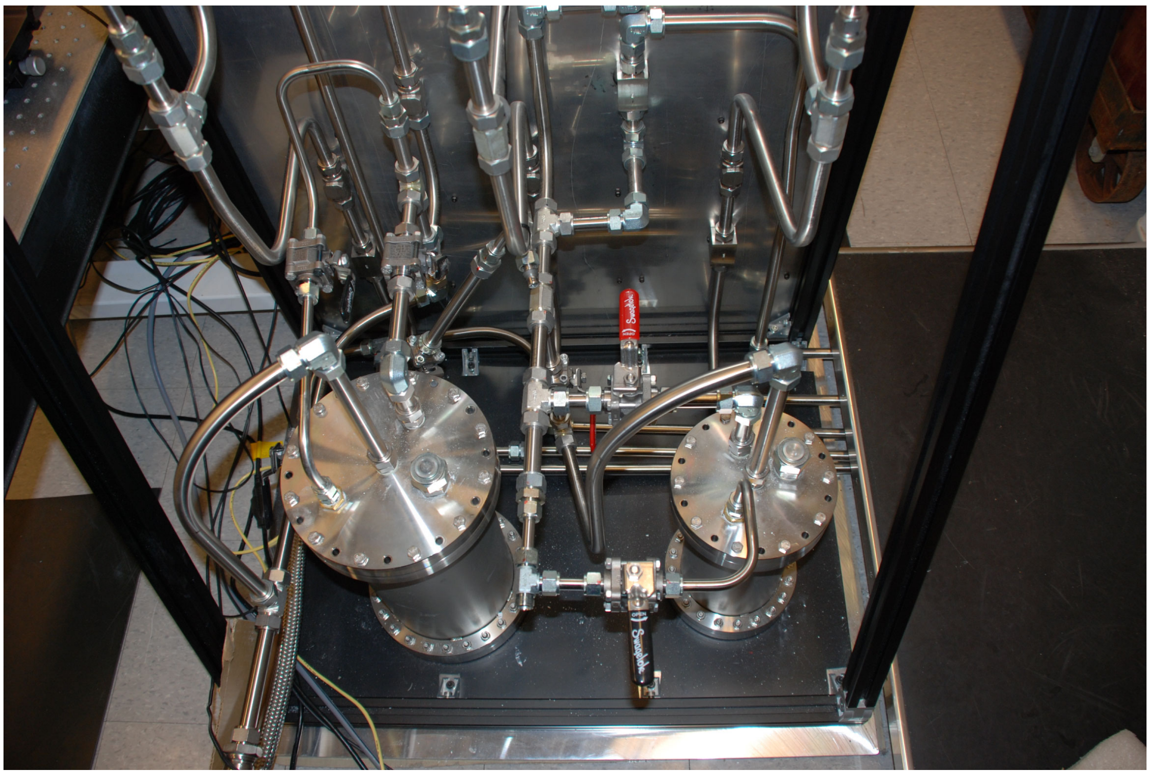

Figure 3.8: Photograph of the jet seeder *(left)* and coflow seeder *(right)*.

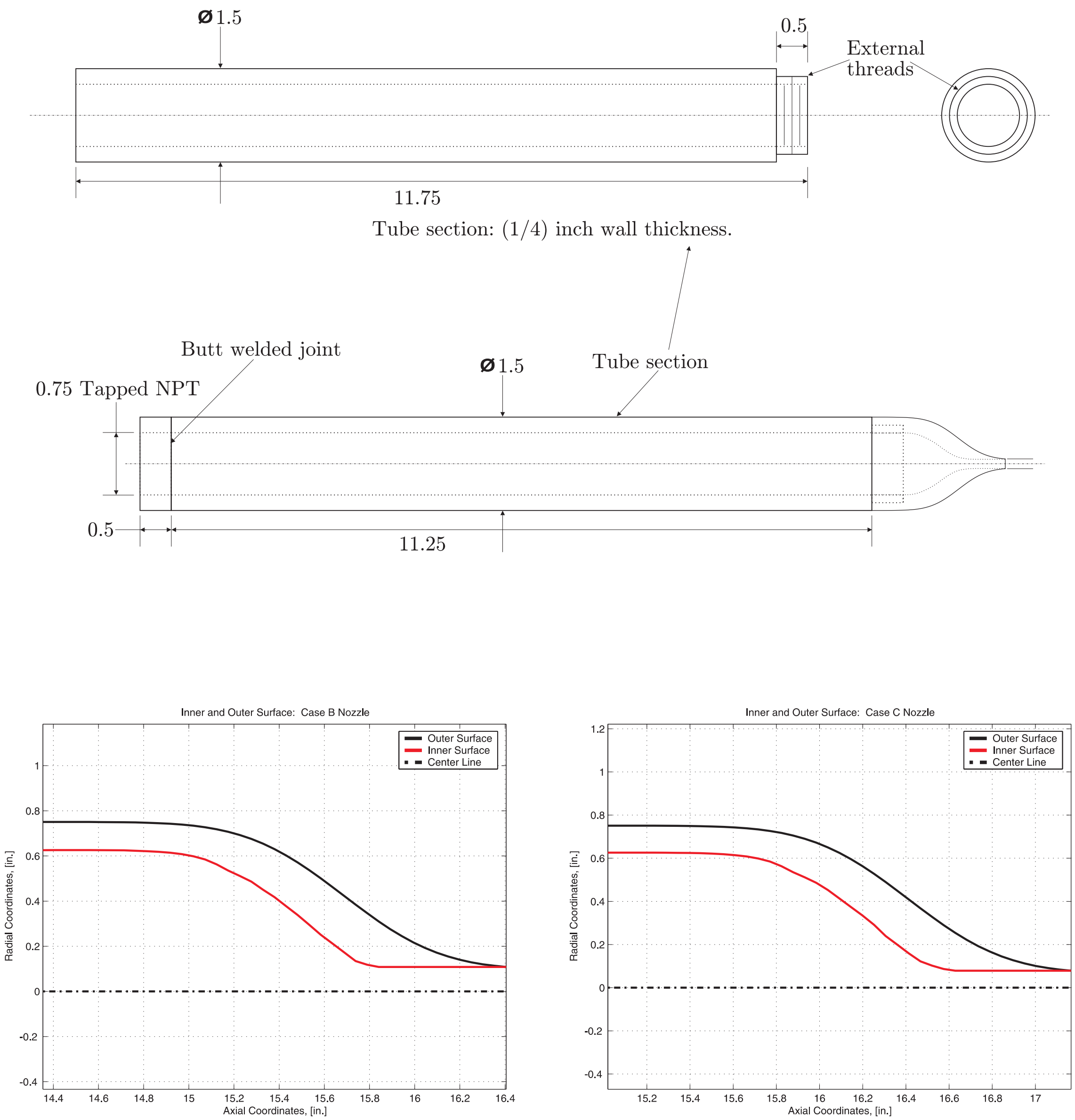

Figure 3.9: Details of jet nozzles and entrance tube, showing entrance tube dimensions with threaded fittings *(top)*, with typical jet nozzle attached *(middle)*, and precise shapes of inner and outer wall profiles for $d_E = 5.5$ mm nozzle *(lower left)* and $d_E = 4.0$ mm nozzle *(lower right)*.

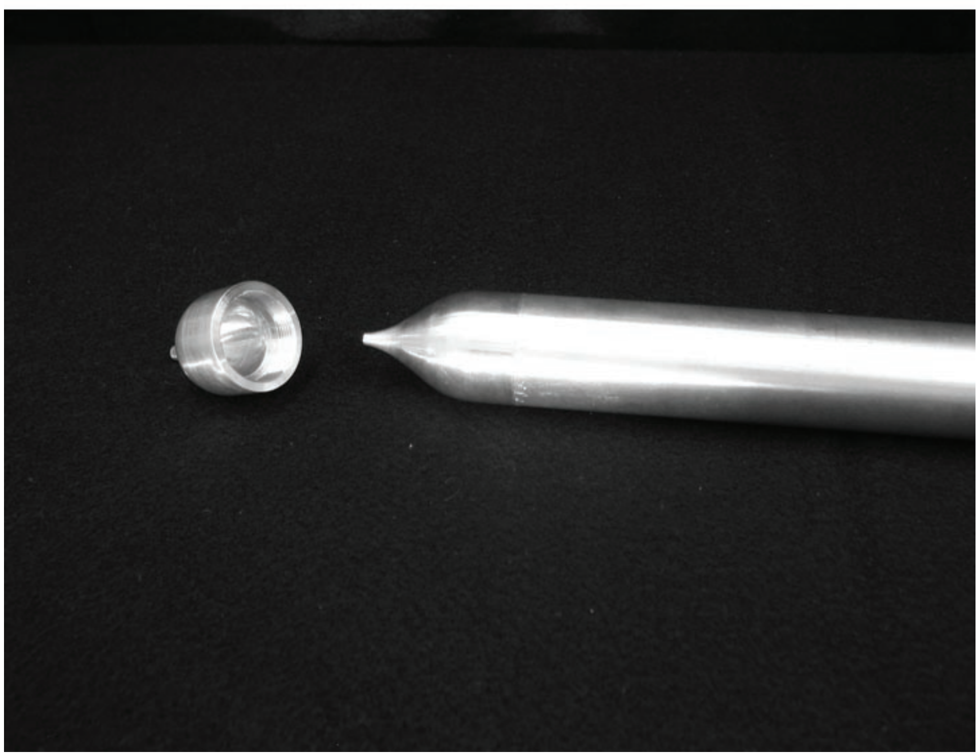

Figure 3.10: Photograph of jet nozzles and entrance tube, showing entrance tube with threaded end visible and disassembled nozzles *(top)*, and nozzle fitted to entrance tube with view to mating internal threads in the remaining nozzle *(bottom)*.

Figure 3.11: Photograph of the optical table setup. The principal optical path is in the center of the image. The two Nd:YAG lasers used for this study are at the upper right of the image, the large FOV camera is on the left of the test section, and the small FOV camera is near the bottom of the image.

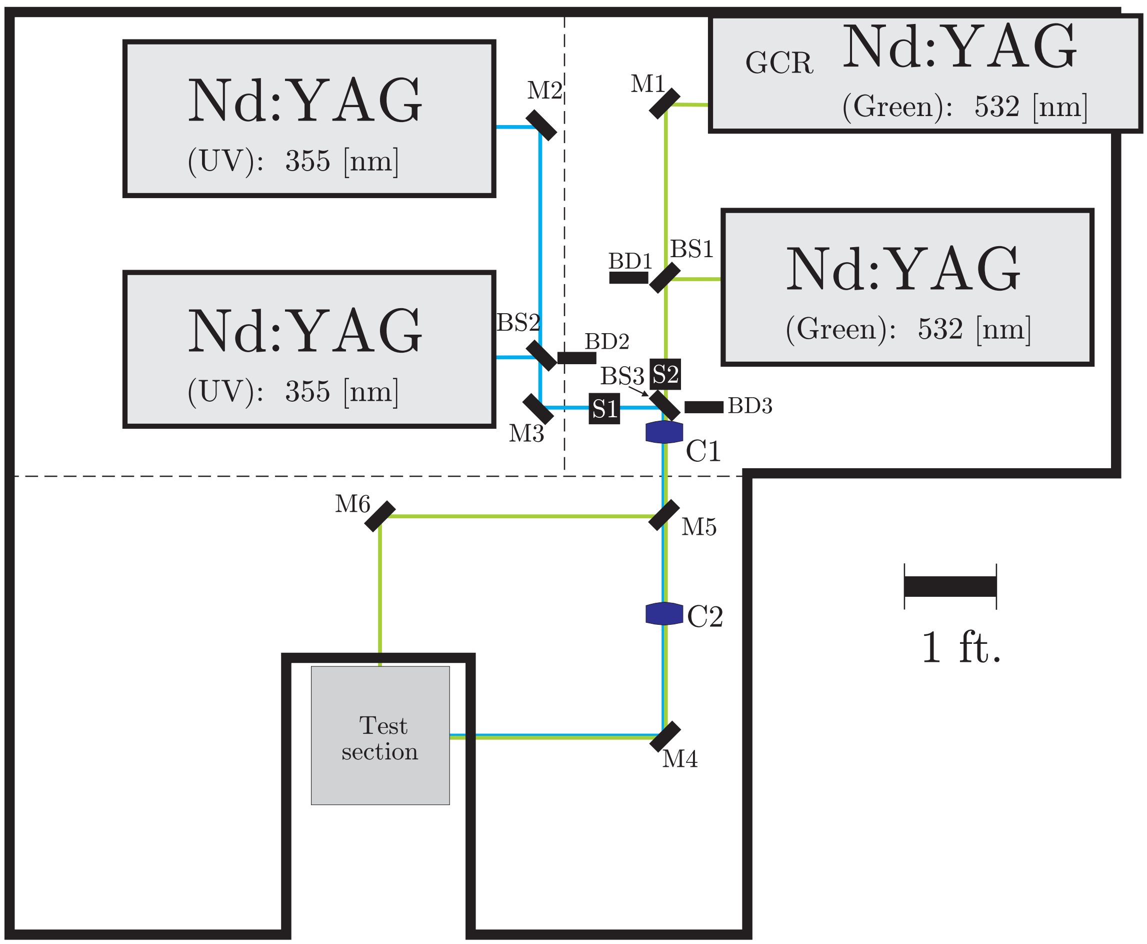

Figure 3.12: Schematic of the optical table arrangement in Fig. 3.11. Mirrors are labeled *MX*, beam-splitting optics *BSX*, beam dumps *BDX*, mechanical shutters *SX* and cylindrical lenses *CX*. The optical arrangement used for this study is discussed in §3.3.1.

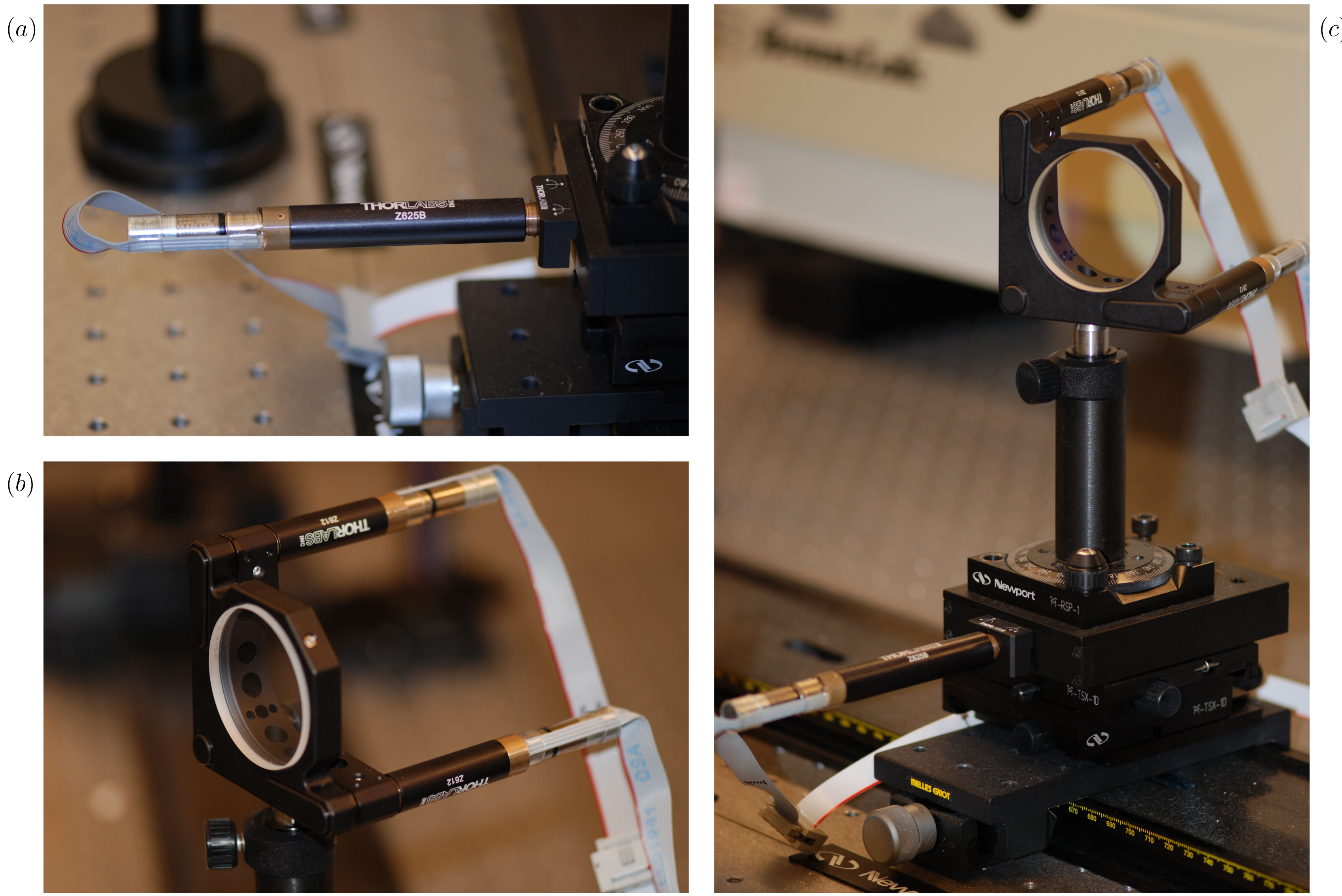

Figure 3.13: Motorized mounts for laser sheet positioning. PC-controlled servo motors provide positioning for mirror traverse (a), kinematic mirror adjustments (b) and combined system (c) for accurate, repeatable beam alignment.

Quantity	Units	*ONR1*	*ONR2*	*ONR3*	*ONR4*	*ONR5*	*ONR6*	*ONR7*
Re_δ	$[-]$	22 600	23 300	24 000	172 100	173 500	178 600	193 700
d_E	mm	4.00	4.00	4.00	4.00	4.00	4.00	4.00
x	m	0.397	0.399	0.401	0.107	0.100	0.100	0.107
u_c	m/s	3.29	3.33	3.44	80.02	81.34	82.19	92.74
δ	mm	103.1	104.8	104.8	32.3	32.0	32.6	31.3
$\delta_{1/2}$	mm	24.8	25.2	25.2	7.8	7.7	7.8	7.5
U_∞	m/s	2.04	2.19	2.16	0.53	2.19	0.79	2.67
Δ_{IW}	mm	2.00	3.57	2.36	0.73	0.73	0.73	0.73
ρ_E	kg/m^3	1.145	1.145	1.145	1.145	1.145	1.145	1.145
ρ_∞	kg/m^3	1.204	1.204	1.204	1.204	1.204	1.204	1.204
ρ_∞^{eff}	kg/m^3	1.204	1.204	1.204	1.204	1.204	1.204	1.204
J_0	N	0.057	0.065	0.063	1.012	0.996	1.012	1.012
D	N	0.031	0.035	0.035	0.000	0.037	0.000	0.035
θ	m	0.041	0.041	0.040	0.983	0.230	0.651	0.190
x/θ	$[-]$	9.74	9.72	9.98	0.11	0.44	0.15	0.56
N	$[-]$	500	500	500	500	500	500	500

Table 3.1: Flow conditions and relevant parameters for each of the outer-scale non-reacting measurement cases, identified as *ONR*X, in this study.

Quantity	Units	*OR1*	*OR2*	*OR3*
Re_δ	$[-]$	26 600	81 500	299 300
d_E	mm	4.00	4.00	4.00
x	m	0.545	0.556	0.544
u_c	m/s	3.47	7.71	27.92
δ	mm	115.0	158.5	160.8
$\delta_{1/2}$	mm	27.7	38.1	38.7
U_∞	m/s	2.14	2.12	3.02
Δ_{IW}	mm	3.02	3.09	3.01
ρ_E	kg/m^3	0.084	0.084	0.084
ρ_∞	kg/m^3	1.204	1.204	1.204
ρ_∞^{eff}	kg/m^3	0.111	0.111	0.111
J_0	N	0.006	0.056	0.623
D	N	0.000	0.037	0.040
θ	m	0.018	0.034	0.130
x/θ	$[-]$	29.52	16.54	4.18
N	$[-]$	1000	1000	1000

Table 3.2: Flow conditions and relevant parameters for each of the outer-scale reacting measurement cases, identified as *OR*X, in this study.

Quantity	Units	*INR1*	*INR2*	*INR3*	*INR4*	*INR5*	*INR6*
Re_δ	$[-]$	7200	11 000	21 400	31 400	45 500	50 200
d_E	mm	4.00	4.00	4.00	4.00	4.00	4.00
x	m	0.566	0.564	0.564	0.564	0.564	0.566
u_c	m/s	0.517	0.882	1.476	2.154	3.087	3.389
δ	m	0.208	0.187	0.217	0.219	0.221	0.222
$\delta_{1/2}$	m	0.050	0.045	0.052	0.053	0.053	0.053
U_∞	m/s	0.016	0.078	-0.018	-0.075	-0.114	0.009
λ_ν	mm	2.991	1.948	1.375	1.039	0.794	0.742
Δ_{IW}	mm	0.468	0.375	0.375	0.375	0.375	0.468
ρ_E	kg/m^3	1.140	1.140	1.140	1.140	1.140	1.140
ρ_∞	kg/m^3	1.180	1.180	1.180	1.180	1.180	1.180
N	$[-]$	300	300	300	297	297	300

Table 3.3: Flow conditions and relevant parameters for each of the inner-scale nonreacting on-centerline measurement cases, identified as *INR*X, in this study.

Quantity	Units	*IR1*	*IR2*	*IR3*	*IR4*	*IR5*	*IR6*	*IR7*
Re_δ	[−]	18 300	25 900	60 600	81 900	93 700	145 300	200 100
d_E	mm	4.00	4.00	4.00	4.00	4.00	4.00	4.00
x	m	0.613	0.613	0.614	0.614	0.614	0.614	0.614
u_c	m/s	1.194	1.687	4.127	5.868	7.199	11.413	15.553
δ	m	0.230	0.230	0.247	0.216	0.197	0.191	0.193
$\delta_{1/2}$	m	0.055	0.055	0.059	0.052	0.047	0.046	0.046
U_∞	m/s	0.224	0.226	0.175	0.608	0.940	1.387	1.551
λ_ν	mm	1.636	1.263	0.657	0.488	0.409	0.287	0.228
Δ_{IW}	mm	0.469	0.469	0.469	0.469	0.469	0.469	0.469
ρ_E	kg/m^3	0.081	0.081	0.081	0.081	0.081	0.081	0.081
ρ_∞	kg/m^3	1.180	1.180	1.180	1.180	1.180	1.180	1.180
N	[−]	300	289	253	295	297	253	292

Table 3.4: Flow conditions and relevant parameters for each of the inner-scale reacting on-centerline measurement cases, identified as *IR*X, in this study.

Quantity	Units	*RN0*	*RN1*	*RN2*	*RN3*	*RN4*	*RN5*
Re_δ	[−]	19 000	19 000	19 000	19 000	19 000	19 000
d_E	mm	4.00	4.00	4.00	4.00	4.00	4.00
x	m	0.614	0.614	0.614	0.614	0.614	0.614
u_c	m/s	1.407	1.407	1.407	1.407	1.407	1.407
δ	m	0.202	0.202	0.202	0.202	0.202	0.202
$\delta_{1/2}$	m	0.049	0.049	0.049	0.049	0.049	0.049
U_∞	m/s	0.277	0.277	0.277	0.277	0.277	0.277
λ_ν	mm	1.401	1.401	1.401	1.401	1.401	1.401
Δ_{IW}	mm	0.413	0.413	0.413	0.413	0.413	0.413
ρ_E	kg/m^3	1.140	1.140	1.140	1.140	1.140	1.140
ρ_∞	kg/m^3	1.180	1.180	1.180	1.180	1.180	1.180
r	m	0.000	0.008	0.024	0.039	0.055	0.071
$\mathcal{S}$	1/s	4.931	17.982	27.854	27.497	20.403	11.987
N	[−]	581	600	600	597	564/336	592/134

Table 3.5: Flow conditions and relevant parameters for the off-centerline (radial) nonreacting inner-scale measurement cases, identified as RNX, in this study.

Quantity	Units	*RR0*	*RR1*	*RR2*	*RR3*	*RR4*	*RR5*
Re_δ	[−]	65 000	65 000	65 000	65 000	65 000	65 000
d_E	mm	4.00	4.00	4.00	4.00	4.00	4.00
x	m	0.612	0.612	0.612	0.612	0.612	0.612
u_c	m/s	4.744	4.744	4.744	4.744	4.744	4.744
δ	m	0.206	0.206	0.206	0.206	0.206	0.206
$\delta_{1/2}$	m	0.049	0.049	0.049	0.049	0.049	0.049
U_∞	m/s	0.353	0.353	0.353	0.353	0.353	0.353
λ_ν	mm	0.566	0.566	0.566	0.566	0.566	0.566
Δ_{IW}	mm	0.421	0.421	0.421	0.421	0.421	0.421
ρ_E	kg/m^3	1.140	1.140	1.140	1.140	1.140	1.140
ρ_∞	kg/m^3	1.180	1.180	1.180	1.180	1.180	1.180
r	m	0.000	0.008	0.024	0.039	0.055	0.071
$\mathcal{S}$	1/s	16.078	58.494	91.638	91.765	69.537	42.078
N	[−]	507	467	514	563	517/267	481/125

Table 3.6: Flow conditions and relevant parameters for each of the off-centerline (radial) reacting inner-scale measurement cases, identified as *RR*X, in this study.

CHAPTER IV

Outer Scale Effects of Heat Release

Outer-scale properties of turbulent shear flows – namely quantities that are dominated by the large scales of motion, such as the mean velocities $\overline{u}_i$ and the Reynolds stress components $\overline{u_i'u_j'}$ – can be substantially different in nonreacting and reacting turbulent shear flows. However, as noted in Chapter II, these properties will be affected by heat release primarily through the changes that exothermicity induces in the local outer variables $\delta(x)$ and $u_c(x)$ in § 2.1. These changes due to heat release in the flow width δ and the centerline velocity u_c are *inertial* effects that result from the reduced densities $\rho(\mathbf{x}, t)$ in the flow. In theory, these changes can be predicted via (2.7) – (2.10) from the "general equivalence principle", which leads to the finding that the outer-variable scaling laws in an exothermically reacting turbulent shear flow should be identical to those in the corresponding nonreacting flow when the ambient density ρ_∞ is replaced by the effective value $\rho_\infty^{\mathit{eff}}$ from (2.7) – (2.8).

In this chapter, results from PIV measurements of mean velocity profiles in nonreacting and reacting versions of the axisymmetric coflowing turbulent jet in Chapter III are used obtain experimental values for $\delta(x)$ and $u_c(x)$ over a wide range of conditions. The resulting values, together with additional values from nonreacting studies of the same flow in the literature, are then compared via (2.9) and 2.10) from the general equivalence principle. It will be seen here that, consistent with the equivalence principle, the scalings of δ and u_c with downstream distance and flow conditions are *identical* in the reacting and nonreacting flows in terms of the effective ambient density ρ_∞^{eff}. As a consequence, the purely inertial effects of heat release – while impressive – follow from relatively simple principles and are completely predictable. In view of this, in the following chapters these inertial effects are taken into account via δ and u_c, and those chapters then examine the remaining inner-scale effects of heat release on quantities associated with the instantaneous velocity gradients $\partial u_i/\partial x_j$.

4.1 PIV Data and Analysis

The outer-scale PIV experiments were conducted at numerous downstream locations with different imaging fields of view (FOVs). Among the measurement cases listed in Tables 3.1 – 3.6, at the smallest downstream location ($x = 100$ mm) the FOV was as small as 46.5×58.1 mm, and at the largest downstream location ($x = 556$ mm) the FOV was 229×286 mm. In all large FOV measurements, the size of the FOV was adjusted to scale with the local outer jet width $\delta(x)$. In this respect the relative resolution was held approximately constant, since the PIV processing was identical all cases.

The PIV data processing used 32×32 pixel interrogation windows cross-correlated with a zero-padded FFT algorithm, producing a 32×40 vector field which was then overlapped by 50% – yielding a final vector image of 64×80 for the large FOV experiments. Owing to the very high seed densities, the DaVis PIV software obtained very high values ($\sim 99\%$) of acceptable vector correlations. After processing the PIV particle images to obtain the raw PIV vector fields, the data were effectively low-pass filtered using a 3×3 median filter to reduce high-frequency noise. The filtered data planes were then ensemble averaged and subtracted to produce fluctuating quantities.

Sample images obtained under nonreacting flow conditions are shown in Figs. 4.1 and 4.2. Figure 4.1 shows a sample instantaneous image of both the absolute streamwise component U and the transverse component V of the velocity field. Corresponding ensemble-averaged flow fields $\langle U \rangle$ and $\langle V \rangle$ are shown in Fig. 4.2. These particular example images are among those acquired closest to the jet nozzle, similarly, instantaneous and averaged large FOV images are shown for a hydrogen jet flame in Figs. 4.3 and 4.4. In this case, the reacting examples shown were obtained further downstream, nearly 136 jet diameters from the nozzle. It is worthwhile to compare the instantaneous images in Figs. 4.1 and 4.3, specifically the upper panels where the streamwise component U is shown. Here the classical large scale structure of the jet is observed in both the nonreacting and reacting flows.

Once the ensemble averaged and fluctuating quantities of interest were obtained, the data were fitted with a Gaussian profile based on the four parameters u_c, δ, U_∞ and y_{CL}, denoting the centerline excess velocity, outer scale jet width, coflow velocity and jet centerline coordinate, respectively. The fitting algorithm employs a Levenberg-Marquardt nonlinear regression; see Bard (1974) and Draper and Smith (1981). The algorithm takes each individual row (e.g. fixed streamwise position x) of ensemble averaged streamwise velocity $\langle U \rangle$ data and determines the four parameters. Thus each of the four parameters are given as a function of the streamwise coordinate x.

With the fitted parameters, the ensemble averaged data are then normalized by similarity quantities. The ensemble averaged fields can be further averaged to produce a single averaged profile for each of the quantities u, v, u'_{rms}, v'_{rms} and $\overline{u'v'}$. Figure 4.5 presents a sample profile of the excess streamwise velocity $u(\eta)$ and $\overline{u'v'}(\eta)$, where $\eta \equiv r/\delta$ and $r \equiv y - y_{CL}$. For comparison, the sample results are shown along with data from Antonia and Bilger (1973) and from Nickels and Perry (1996). The sample profiles are results from the nonreacting $Re_\delta = 22\,600$ case. Note that here the jet half-width $\delta_{1/2}$, specifically the half-width at the half-maximum point, is used for comparison with data from the literature.

4.2 Outer-Flow Scaling Results from Nonreacting Cases

Proper scaling of the local jet width $\delta(x)$ and local centerline excess velocity $u_c(x)$ as outlined in § 2.2 for the nonreacting flow involves the jet momentum radius θ, which in turn requires the jet *source* momentum flux J_0. To obtain this, the jet *exit* momentum flux $\widetilde{J}_0$ was first computed as

$$\widetilde{J}_0 = \rho_E U_E^2 A_E, \tag{4.1}$$

where A_E is the exit area of the nozzle, ρ_E is the density of the nozzle fluid and $U_E \equiv Q_E/A_E$ via the assumption of a "top-hat" flow profile produced by the large contraction ratio nozzle shown in Figs. 3.9 and 3.10. This exit profile was measured using laser Doppler velocimetry (LDV) and found to closely approximate a uniform exit profile, validating the "top-hat" assumption. The volumetric flow rate Q_E was determined by measuring the pressure drop across a choked orifice used to meter the flow rate of the jet fluid. The use of a large diameter contraction ratio jet nozzle allows calculation of the jet exit momentum flux $\widetilde{J}_0$ in this way, however the drag associated with the relatively large-diameter (38.1 mm) entrance tube in the jet nozzle assembly (see Fig. 3.9) is not insignificant and must be accounted for to obtain the *net* jet source momentum flux J_0. This was done by measuring the velocity profile in the coflowing stream without any jet fluid issuing from the nozzle, and integrating the resulting velocity deficit profile to obtain the drag D exerted on the flow. This was done for each case, and the resulting *net* jet source momentum flux J_0 was then obtained as

$$J_0 \equiv \widetilde{J}_0 - D. \tag{4.2}$$

Based on the J_0 value for each case, results obtained for the jet width $\delta_{1/2}(x)$ and centerline velocity $u_c(x)$ for the nonreacting cases (*ONR1* – *ONR7*) in Table 3.1, produced by a nitrogen jet issuing into a coflowing air stream, are shown in Figs. 4.6 and 4.7. The scaling functions f_δ and f_u in § 4.3 are shown for comparison with the experimental results in these figures. The data at small values of x/θ can be seen to be well within the jet-like scaling regime, and at the furthest downstream location (largest x/θ) just begin to enter the transition to the wake-like scaling regime. It is apparent that the outer-scale variables δ and u_c obtained for the nonreacting cases in the present study are in generally good agreement with the accepted scaling functions f_δ and f_u for nonreacting axisymmetric coflowing turbulent jets.

4.3 Outer-Flow Scaling Results from Reacting Cases

Corresponding results for $\delta_{1/2}$ and u_c obtained for each of the reacting flow cases in Table 3.2 are shown in Figs. 4.8 and 4.9. Here the jet momentum radius θ is based on the actual coflowing stream density ρ_∞. It is apparent in these figures that, unlike the nonreactng cases in Figs. 4.6 and 4.7, the results from the reacting flows do not collapse to universal scaling functions in terms of θ. However in accordance with the equivalence principle (Tacina and Dahm, 2000) summarized in § 2.3, the freestream density ρ_∞ in the momentum radius should be replaced by the effective density $\rho_\infty^{\mathit{eff}}$ to yield the extended momentum radius θ^+ as

$$\theta^+ \equiv \left(\frac{J_0}{\pi \rho_\infty^{\mathit{eff}} U_\infty^2} \right)^{\frac{1}{2}} . \tag{4.3}$$

For each case, the resulting extended momentum radius allows the dimensionless coordinate ξ/θ^+ to be formed, where $\xi \equiv x + x_E$ is the virtual origin in (2.5), and the same data can then be plotted as shown in Figs. 4.10 and 4.11. The scaling functions f_δ and f_u outlined in §2.3 are shown for comparison with the experimental results in these figures. It is apparent that, in terms of the extended momentum radius θ^+ from the general equivalence principle, the outer-variable scaling for the reacting flow cases is in generally good agreement with the accepted scaling for the corresponding nonreacting flows. In Figs. 4.10 and 4.11, the virtual origin x_E from (2.5) has been used for completeness, though the effect of x_E on the present data is small. It is primarily through the extended momentum radius θ^+ from the equivalence principle that the outer-flow scalings in the reacting flow become essentially identical to that for nonreacting flows.

The solid curves in Figs. 4.10 and 4.11 are fits to the scaling functions f_δ and f_u from § 2.3. These are here given by

$$\left(\frac{\delta}{\theta^+} \right) \equiv f_\delta \left(\frac{x}{\theta^+} \right) = \left(\frac{x}{\theta^+} \right) \left[(c_\delta)_j^{-\frac{3}{2}} + \left(\frac{x}{\theta^+} \right) (c_\delta)_w^{-\frac{3}{2}} \right]^{-\frac{2}{3}} , \tag{4.4}$$

where the constants $(c_\delta)_j \approx 0.08$ and $(c_\delta)_w \approx 0.45$ are the constants in the outer length scaling in the jet and the wake limits, respectively. Similarly for the centerline excess velocity decay, the fit is given by

$$\left(\frac{u_c}{U_\infty}\right)^{-1} \equiv f_u\left(\frac{x}{\theta^+}\right) = \left(\frac{x}{\theta^+}\right)\left[(c_u)_j^{-3} + \left(\frac{x}{\theta^+}\right)(c_u)_w^{-3}\right]^{-\frac{1}{3}}, \tag{4.5}$$

where $(c_u)_j \approx 0.07$ and $(c_u)_w \approx 1.0$ are the constants in the outer velocity scaling in the jet and the wake limits, respectively. Figures 4.12 and 4.13 demonstrate the unified scaling for both reacting and nonreacting coflowing jets from the present measurements. The local outer length scale δ is shown in Fig. 4.12 for all seven nonreacting flow cases (*ONR1 – ONR7*) in Table 3.1 as well as for the three reacting flow cases (*OR1 – OR3*) in Table 3.2. The dashed line shows the jet-limit scaling ($\delta \sim x$), from which the data begin to show a perceptible departure for $\xi/\theta^+ > 1$. The outer velocity scale is similarly plotted in Fig. 4.13 for all the nonreacting and reacting cases. For u_c, the onset of the transition from the jet-limit scaling to the wake-limit scaling is not seen over the range of x/θ in the present measurements. This is consistent with the results of Davidson and Wang (2002), where the transition region does not appear in the centerline excess velocity until nearly a decade later until $\xi/\theta^+ \approx 10$.

4.4 Comparison with Prior Studies

The present results for the local outer scale δ in Fig. 4.12 showed that, in terms of the effective density $\rho_\infty^{\mathit{eff}}$ from the general equivalence principle, the reacting and nonreacting flows followed identical scaling laws. This finding may appear to disagree with the earlier observation by Muñiz and Mungal (2001) that "…heat release accounts for a reduction in the jet growth rate by 20% …", based on their PIV measurements. Similarly, Chigier and Strokin (1974) state that the local flow width of δ is smaller in jet flames than in corresponding nonreacting jets, though they provide no data to support this observation, apart from referencing the work of Kremer (1967). That study consisted of dynamic pressure measurements obtained in and near the potential core region of a planar jet flame. Yet the elongation of the potential core region of reacting jets over their nonreacting counterparts has been known for some time, and follows naturally from the equivalence principle as shown by Tacina and Dahm (2000). This increase in the potential core length is taken into account in making direct comparisons between reacting and nonreacting flows in the downstream coordinate ξ.

To reconcile the results from Muñiz and Mungal (2001) with those from the present study, the measured jet growth data from Muñiz and Mungal have been reproduced in Fig. 4.14, where the cases denoted *R* and *NR* denote reacting and nonreacting flows, respectively. The upper panel presents their data in unscaled form, as they were originally reported, and the lower panel presents the same data scaled by the extended momentum radius θ^+ as suggested by the equivalence principle. It is apparent in the lower panel of Fig. 4.14 that, when properly scaled by the extended momentum radius, the data of Muñiz and Mungal show substantial agreement between the reacting and nonreacting cases. Here the solid curve again gives the scaling function $f_\delta(x/\theta^+)$, and the dashed line gives the jet-limit scaling. Indeed, when the data of Muñiz and Mungal are compared in this properly scaled form to the present results for the local outer length scale δ in Fig. 4.15, all of these data agree within the range of the scatter in the measurements. Thus when properly scaled via the equivalence principle to account for the inertial effects of heat release, the data of Muñiz and Mungal agree with the present finding that the outer-variable scalings in nonreacting and reacting jets become identical.

As a final step, the data from the present study and those from Muñiz and Mungal (2001) are presented together with the coflowing air jet data of Biringen (1975) and the coflowing water jet data of Wang and Davidson (2001) in Figs. 4.16 and 4.17. The Davidson & Wang data are distinguished by the exceedingly large values of ξ/θ^+ accessible in their experiments. The results for the outer length scale δ in Fig. 4.17 span nearly five orders of magnitude in ξ/θ^+, and clearly show both the jet-like and wake-like scaling regimes. The collapse of *all* these data from nonreacting and reacting flows onto a single curve f_u demonstrates that the inertial effects of heat release on the outer scales u_c and δ in turbulent shear flows can be properly accounted for by the equivalence principle in § 2.3.

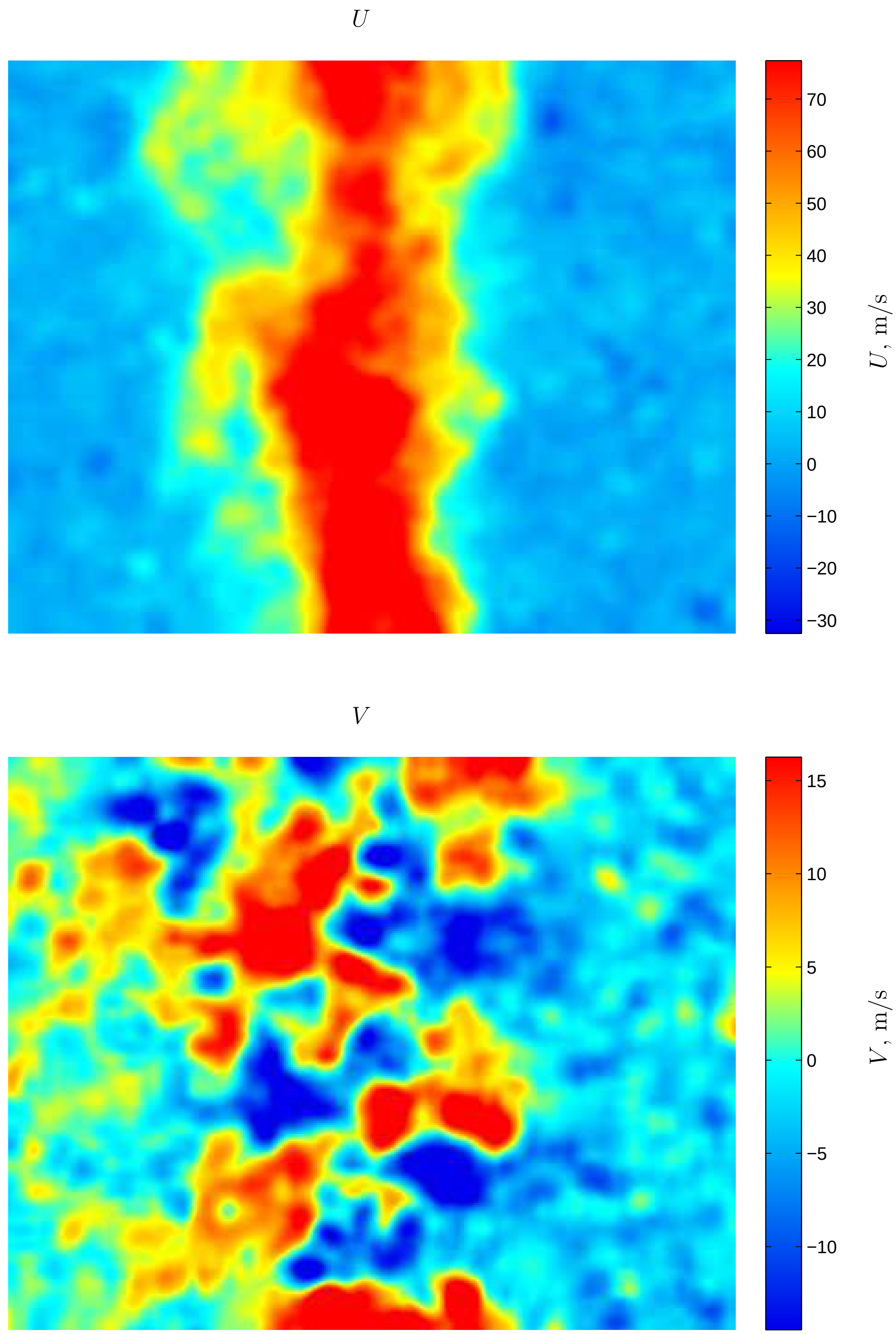

Figure 4.1: Sample PIV results for instantaneous streamwise velocity field $U(\mathbf{x}, t)$ *(top)* and transverse velocity field $V(\mathbf{x}, t)$ *(bottom)* from nonreacting case *ONR5* in Table 3.1 at $Re_\delta = 173\,500$. The FOV is 46.5×58.1 mm and located at a distance of 100 mm from the jet nozzle.

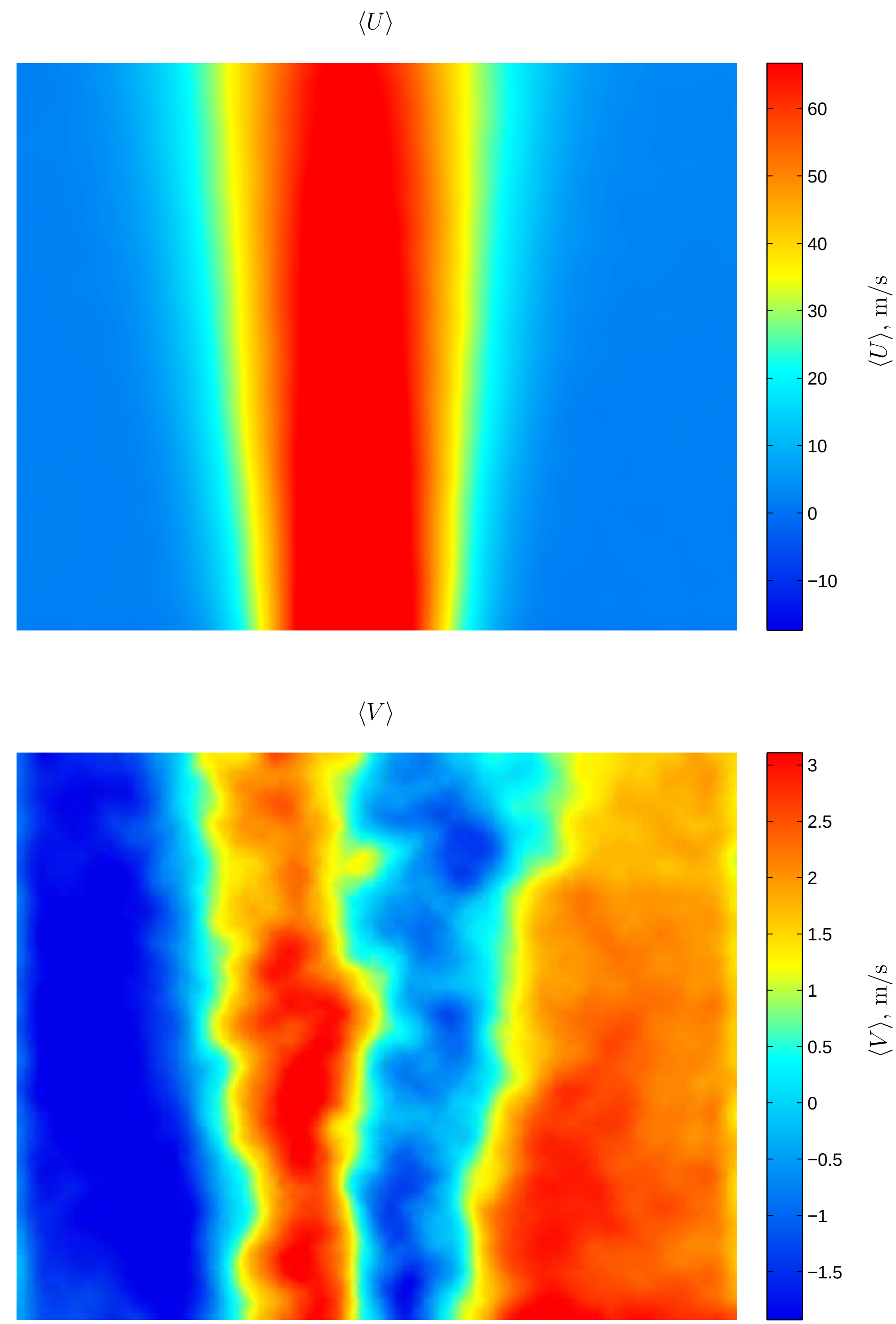

Figure 4.2: Ensemble-averaged PIV results for mean streamwise velocity field $\langle U \rangle$ *(top)* and transverse velocity field $\langle V \rangle$ *(bottom)* from nonreacting case *ONR5* in Table 3.1 at $Re_\delta = 173\,500$.

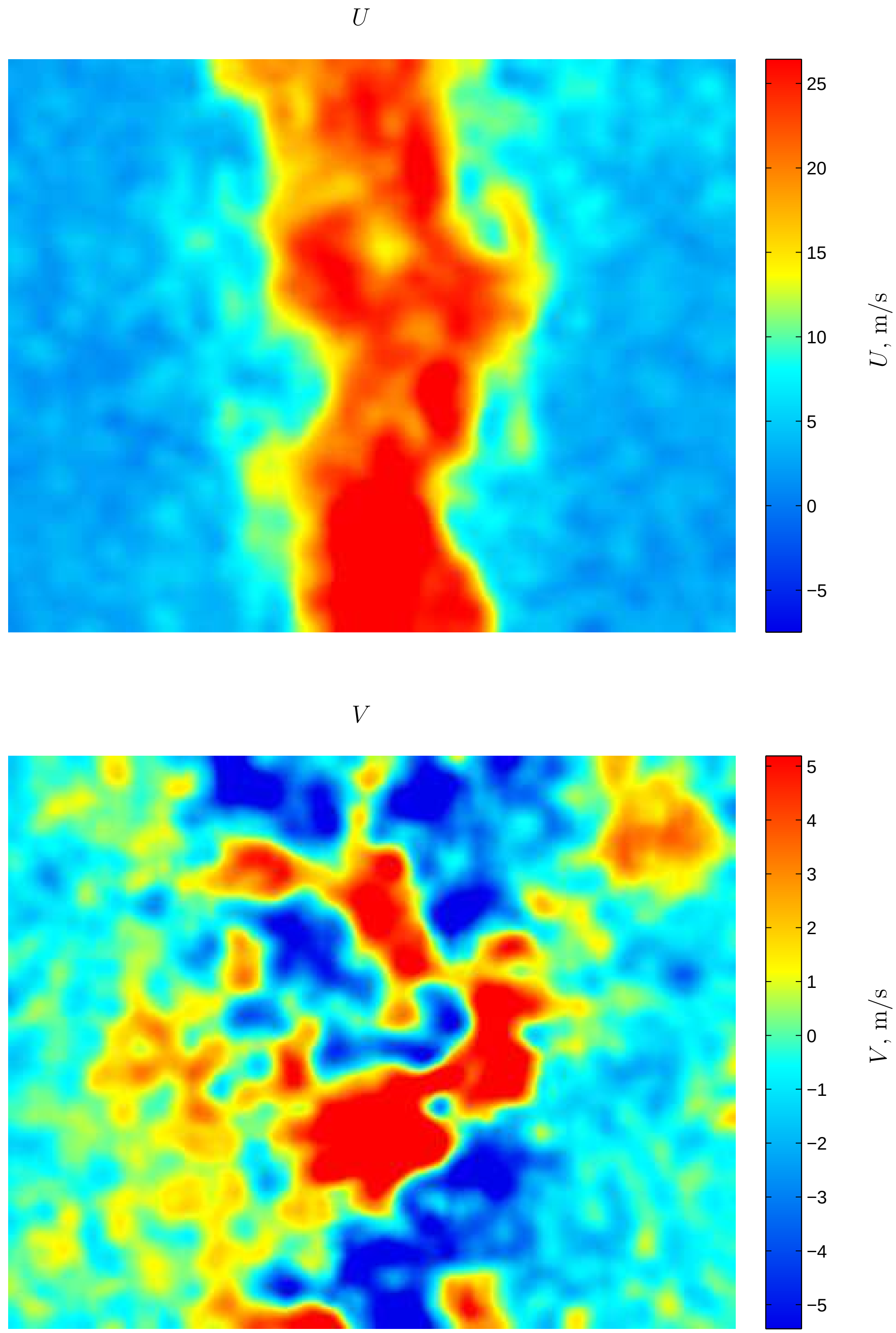

Figure 4.3: Sample PIV results for instantaneous streamwise velocity field $U(\mathbf{x}, t)$ *(top)* and transverse velocity field $V(\mathbf{x}, t)$ *(bottom)* from reacting case *OR3* in Table 3.2 at $Re_\delta = 299\,300$.

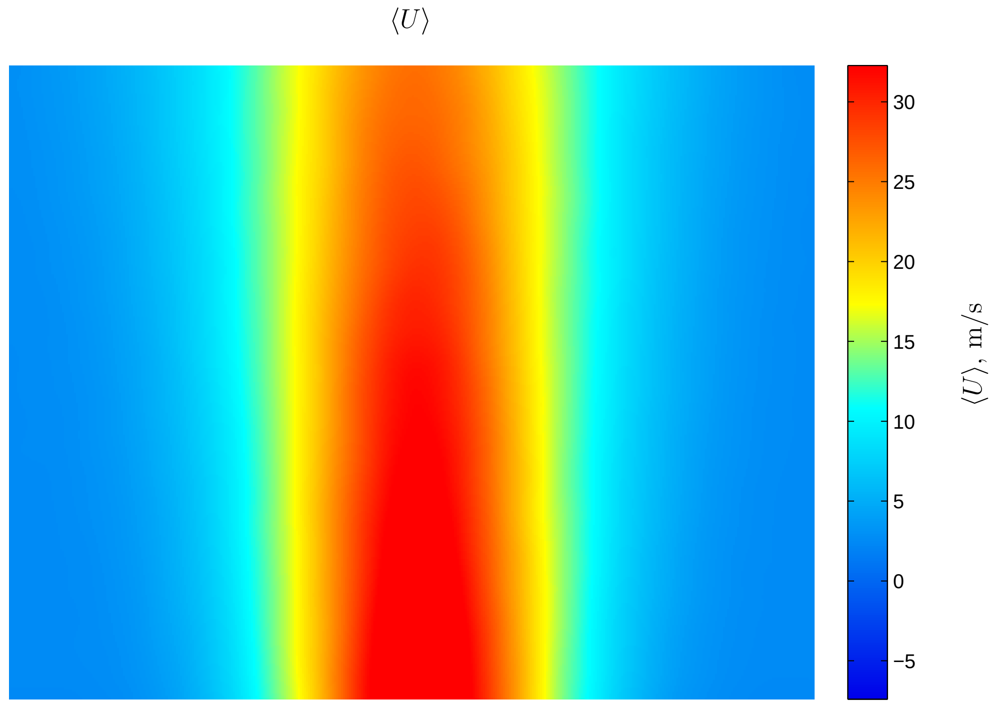

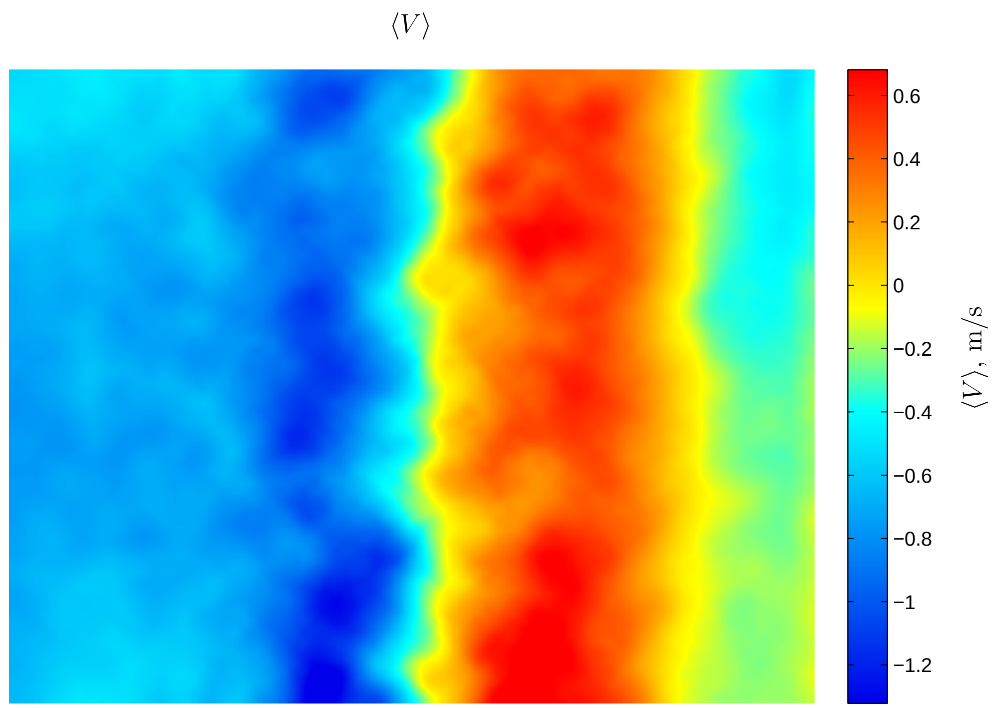

Figure 4.4: Ensemble-averaged PIV results for mean streamwise velocity field $\langle U \rangle$ *(top)* and transverse velocity field $\langle V \rangle$ *(bottom)* from nonreacting case *OR3* in Table 3.2 at $Re_\delta = 173\,500$.

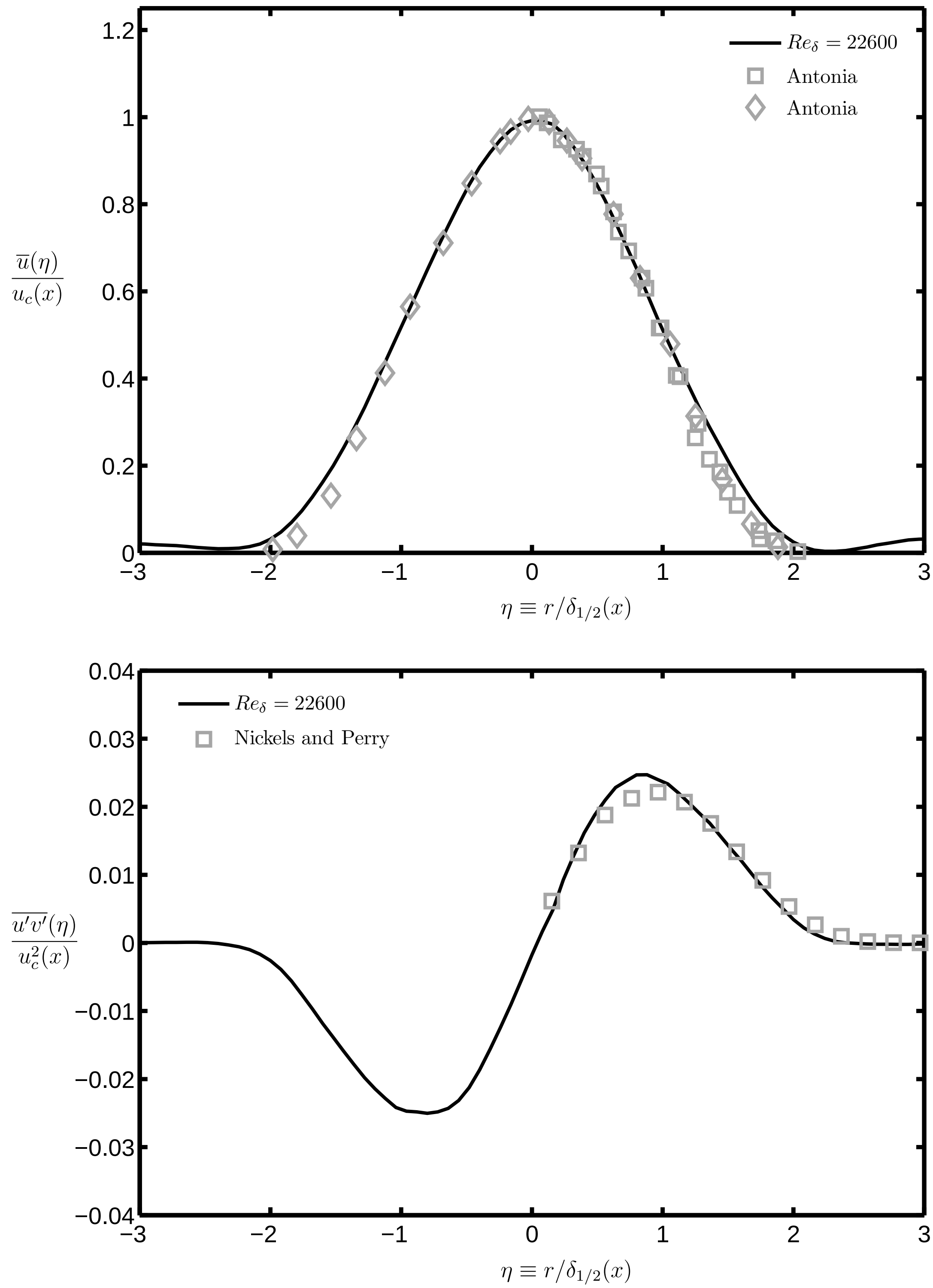

Figure 4.5: Mean velocity profile from case *ONR1* in Table 3.1 at $Re_\delta = 22\,600$, showing the mean normalized streamwise velocity $\overline{u}/u_c$ *(top)* and Reynolds stress $\overline{u'v'}/u_c^2$ *(bottom)* versus radial similarity coordinate $\eta \equiv r/\delta_{1/2}$.

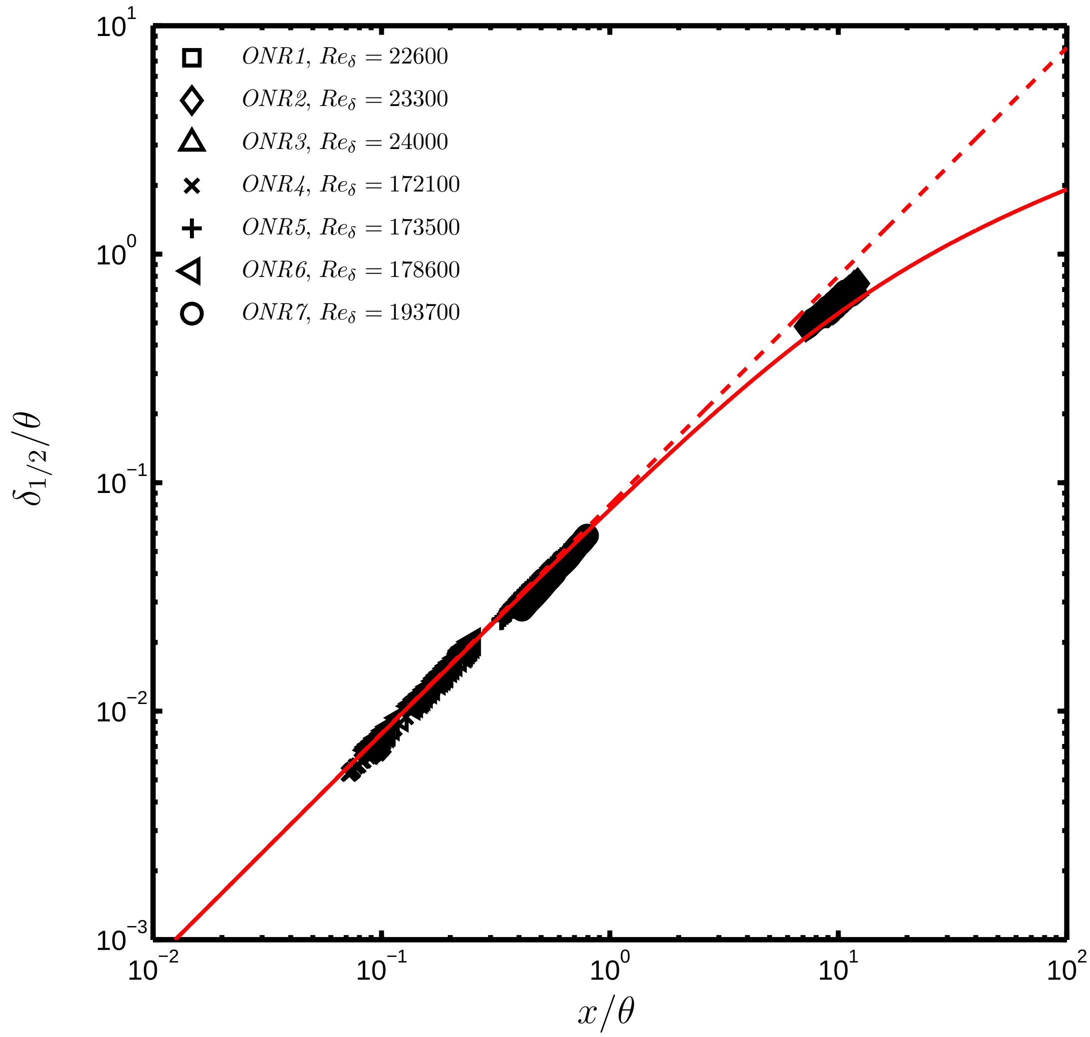

Figure 4.6: Results for local outer length scale $\delta_{1/2}$ versus downstream distance x, normalized by momentum radius θ, for all nonreacting cases in Table 3.1. Solid line corresponds to (4.4); dashed line gives jet-limit scaling. Note $\delta_{1/2}$ is the half-width at half-maximum of the mean excess velocity profile $u(x)$.

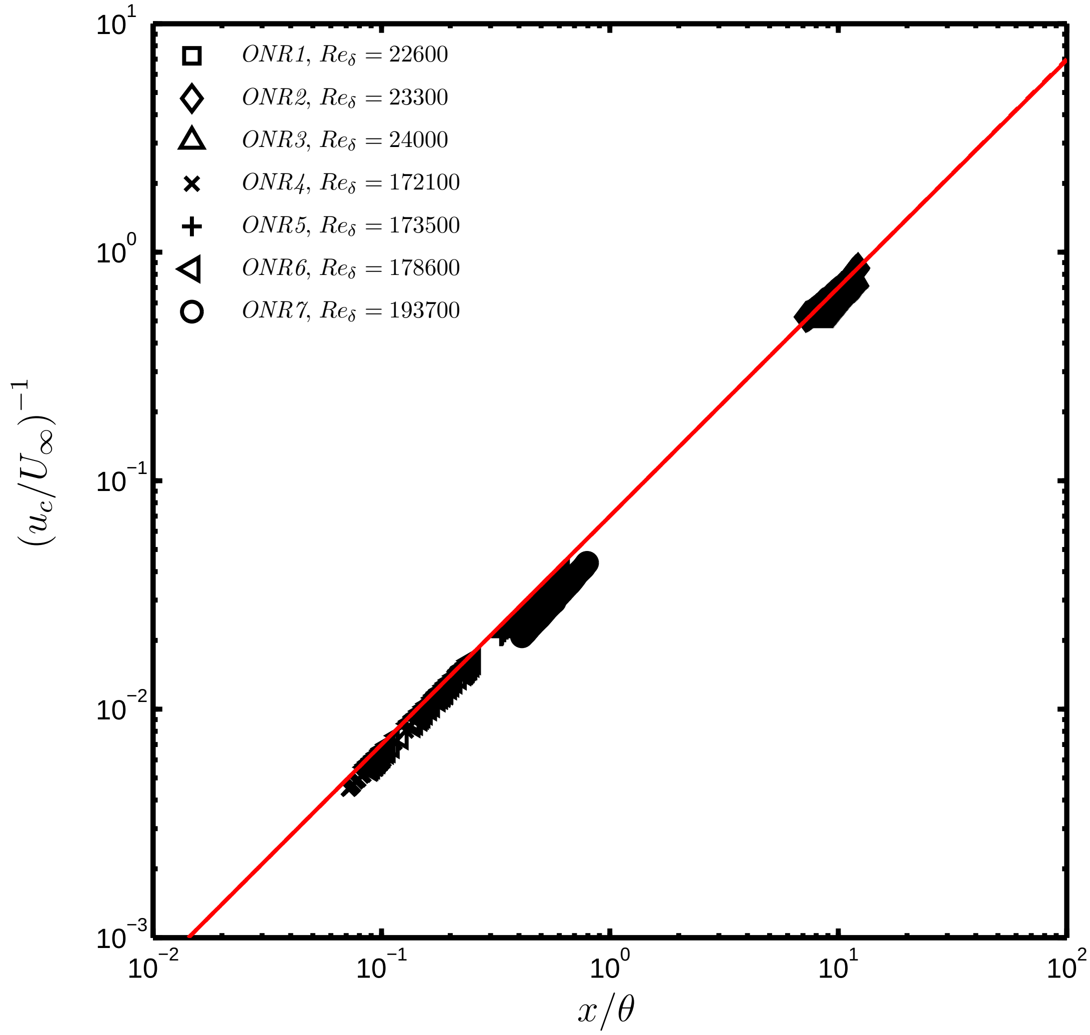

Figure 4.7: Results for local outer velocity scale u_c versus downstream distance x, normalized by momentum radius θ, for all nonreacting cases in Table 3.1. Solid line corresponds to (4.5); dashed line gives jet-limit scaling.

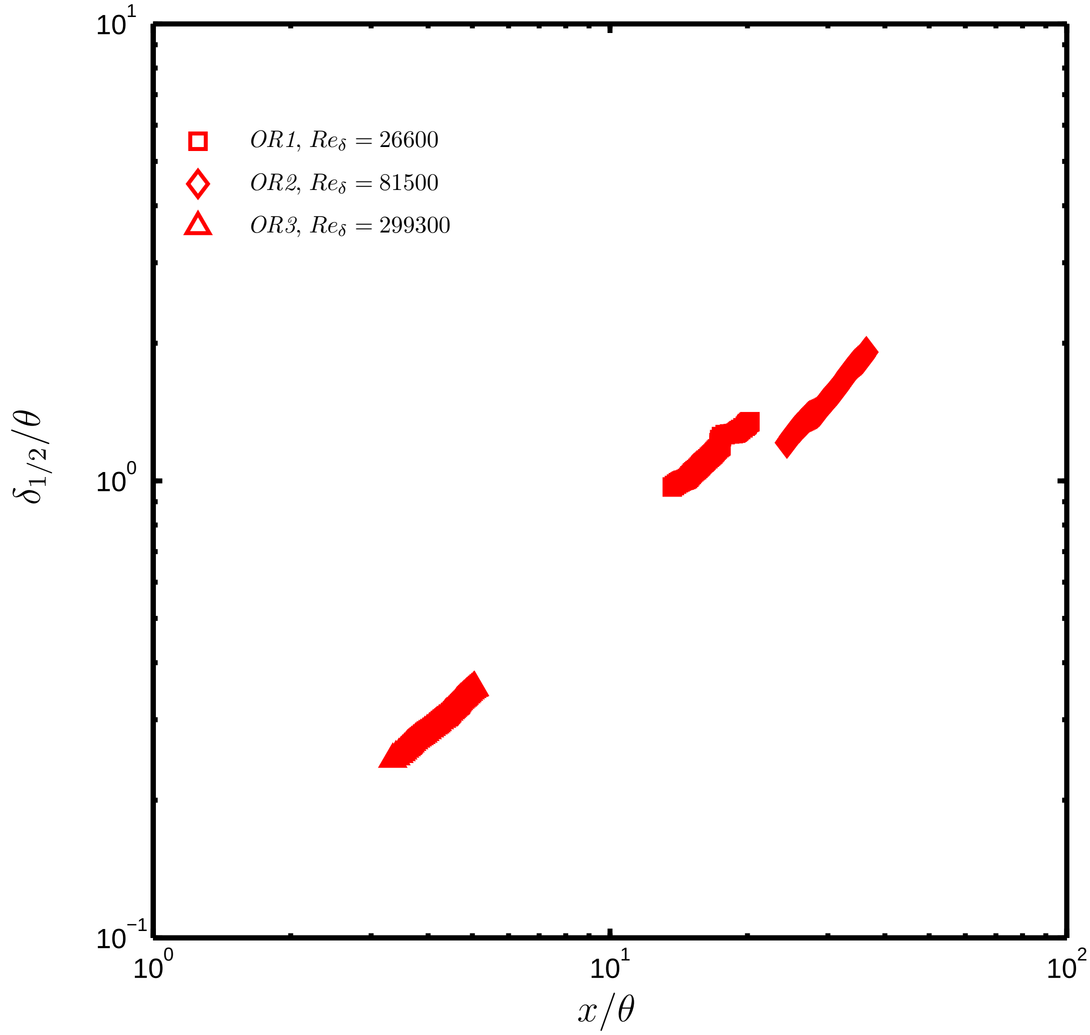

Figure 4.8: Results for local outer length scale $\delta_{1/2}$ versus downstream distance x, normalized by momentum radius θ, for all reacting cases in Table 3.2.

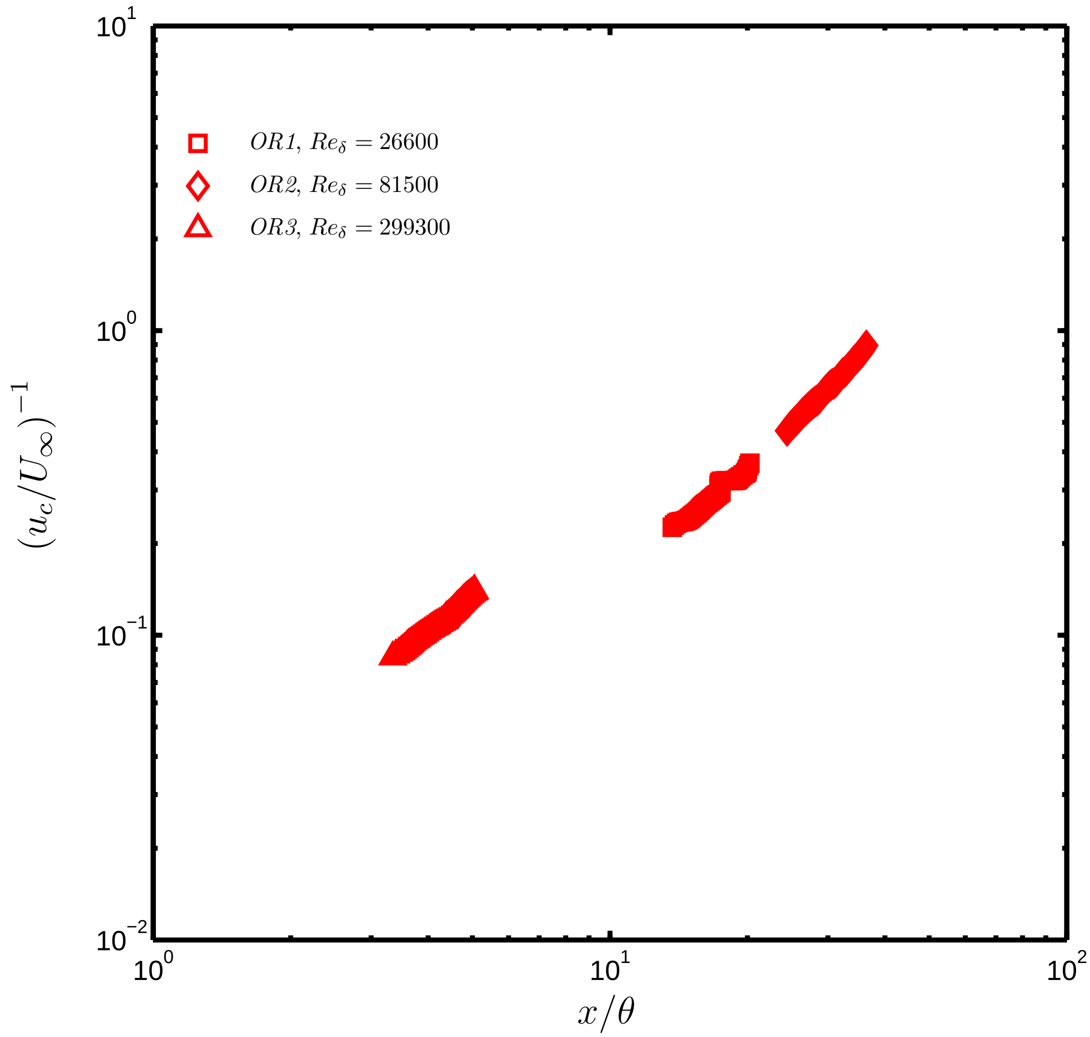

Figure 4.9: Centerline scaling of centerline velocity decay u_c normalized by coflow velocity U_∞ in terms of x/θ for all reacting cases in Table 3.2.

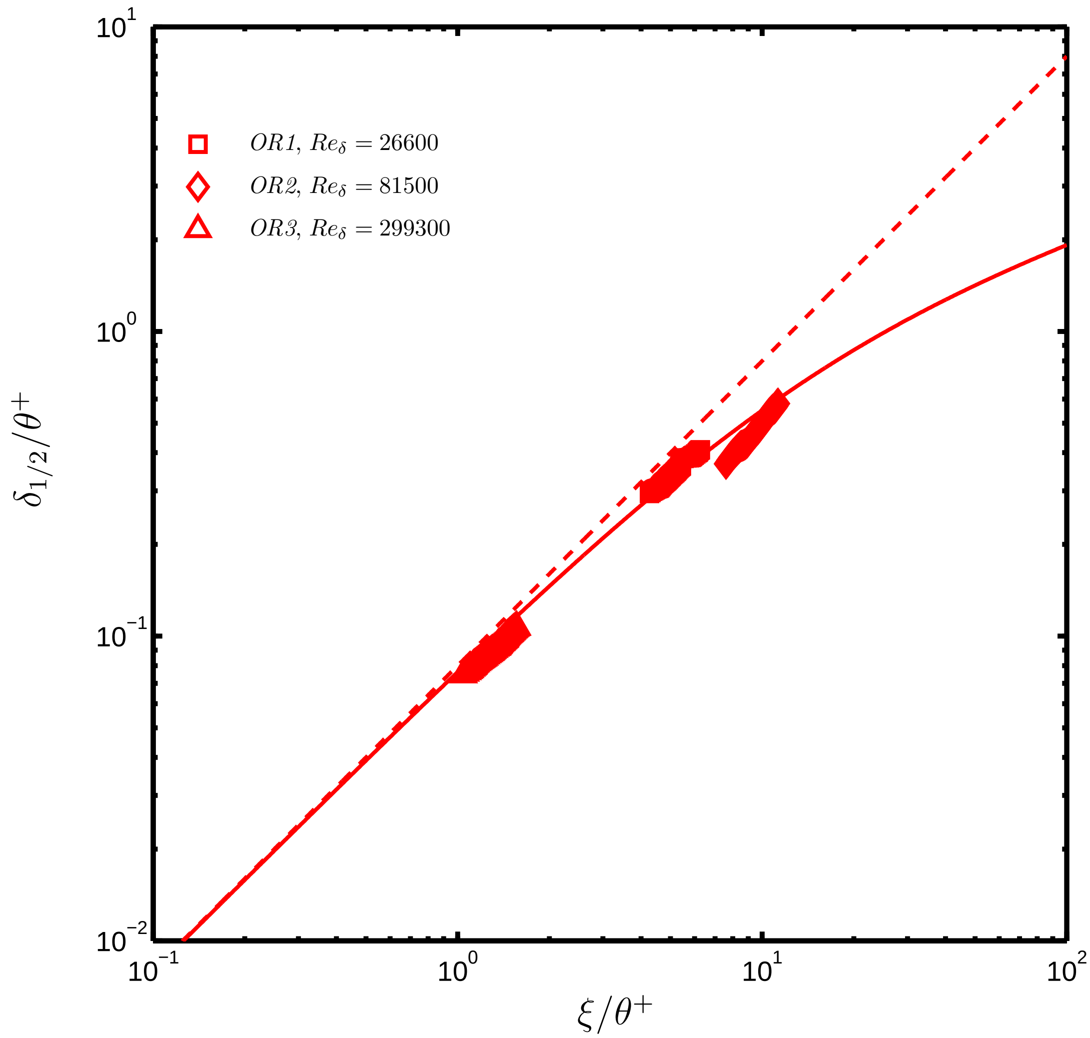

Figure 4.10: Results for local outer length scale $\delta_{1/2}$ versus downstream distance x, normalized by extended momentum radius θ^+, for all reacting cases in Table 3.2. Solid line gives scaling for nonreacting flow in (4.4); dashed line gives jet-limit scaling.

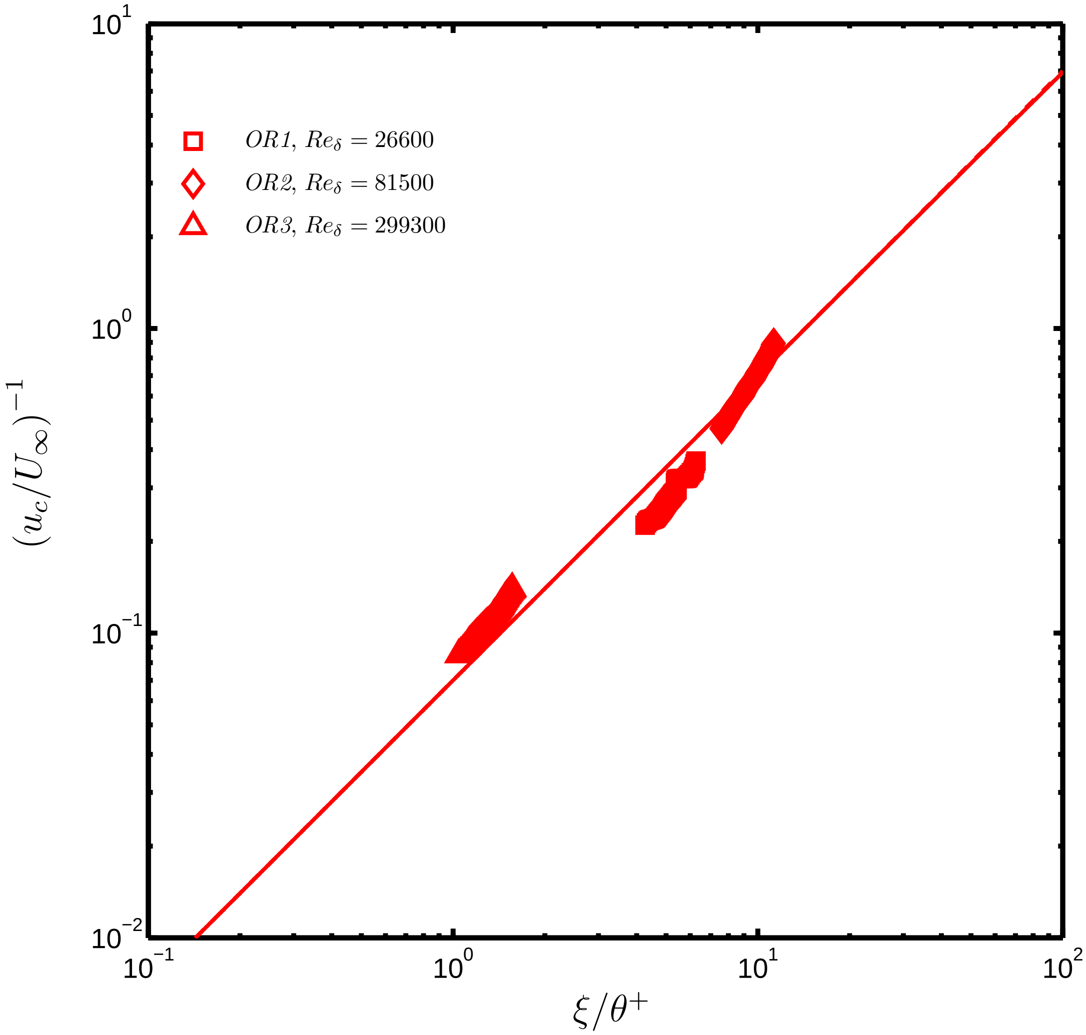

Figure 4.11: Results for local outer velocity scale u_c versus downstream distance x, normalized by extended momentum radius θ^+, for all reacting cases in Table 3.2. Solid line gives scaling for nonreacting flow in (4.5); dashed line gives jet-limit scaling.

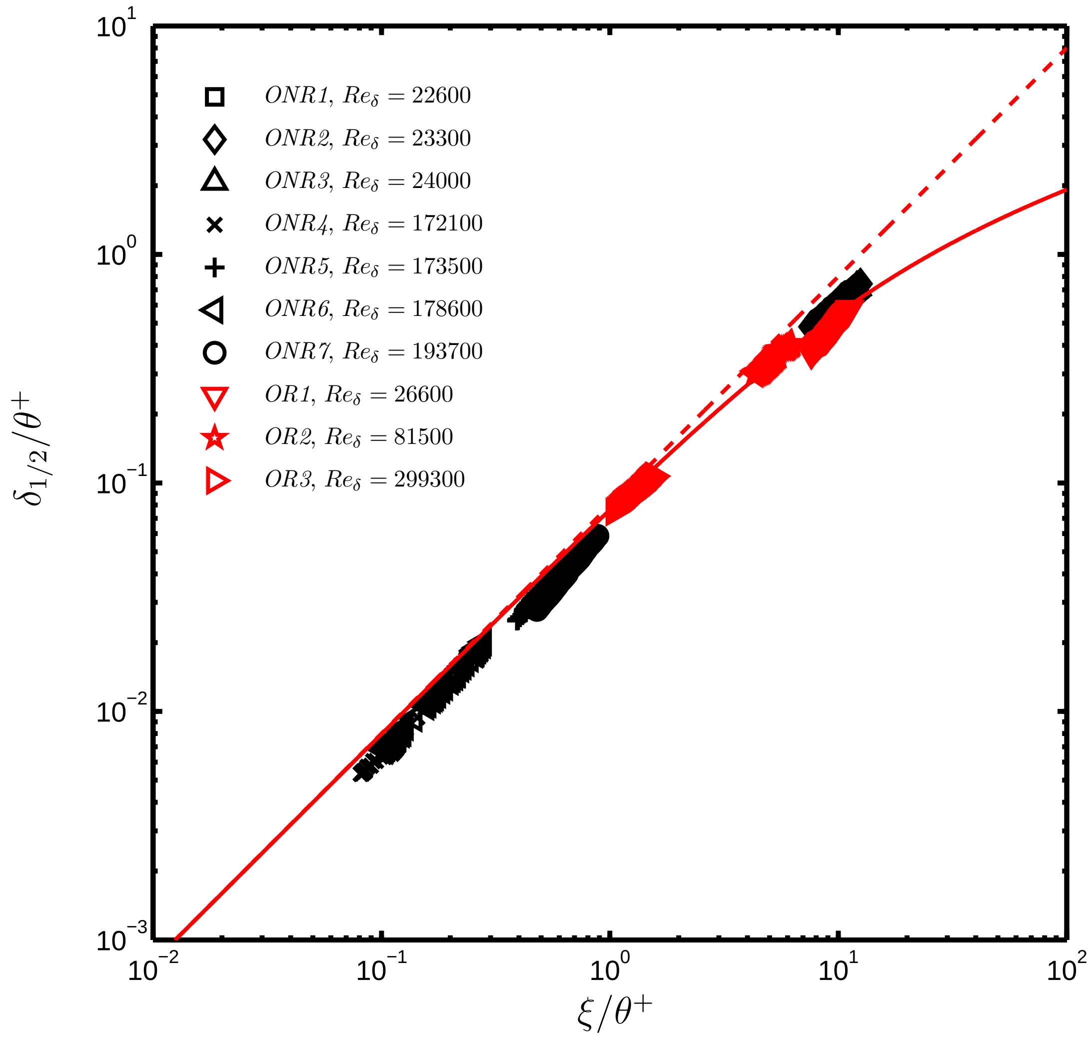

Figure 4.12: Results for local outer length scale $\delta_{1/2}$ versus downstream distance x, normalized by extended momentum radius θ^+, showing all nonreacting cases in Table 3.1 and all reacting cases in Table 3.2. Solid line gives scaling for nonreacting flow in (4.4); dashed line gives jet-limit scaling.

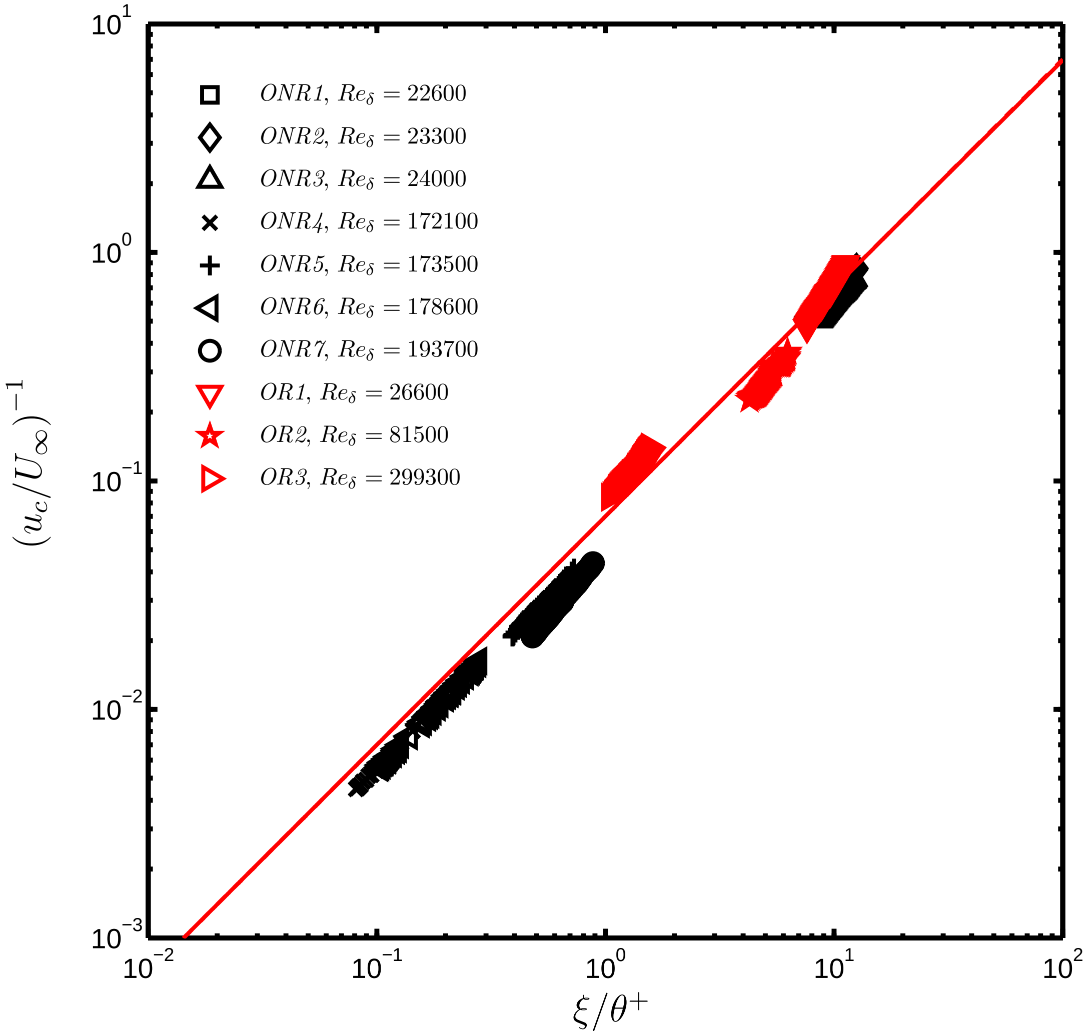

Figure 4.13: Results for local outer velocity scale u_c versus downstream distance x, normalized by extended momentum radius θ^+, showing all nonreacting cases in Table 3.1 and all reacting cases in Table 3.2. Solid line gives scaling for nonreacting flow in (4.5); dashed line gives jet-limit scaling.

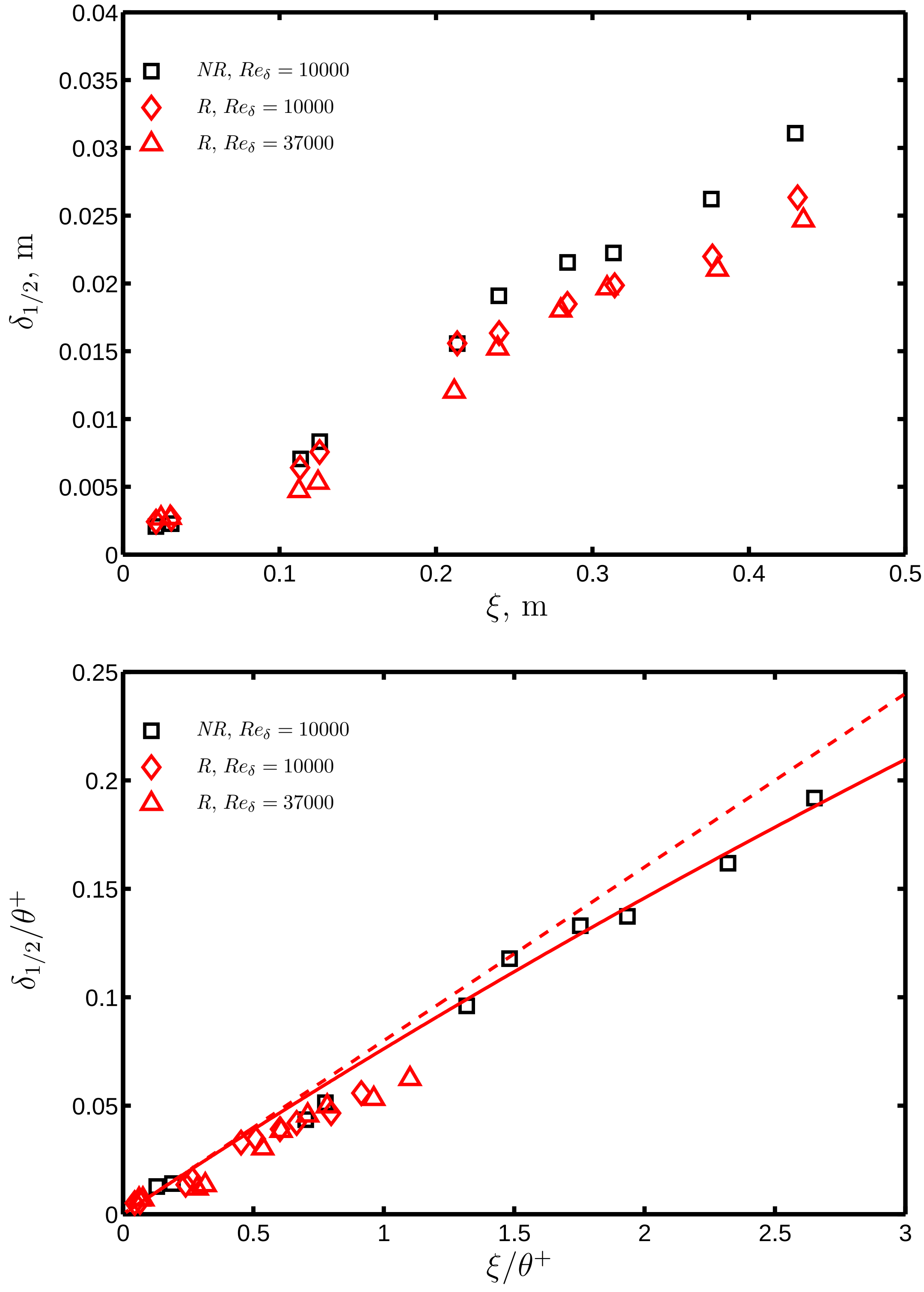

Figure 4.14: Results from Muñiz and Mungal (2001) for local outer length scale $\delta_{1/2}$ versus downstream distance x *(top)*, with reacting and nonreacting cases denoted R and NR, respectively. Same results are shown normalized by extended momentum radius θ^+ *(bottom)*, where reacting and nonreacting cases both follow solid line giving scaling in (4.4); dashed line gives jet-limit scaling.

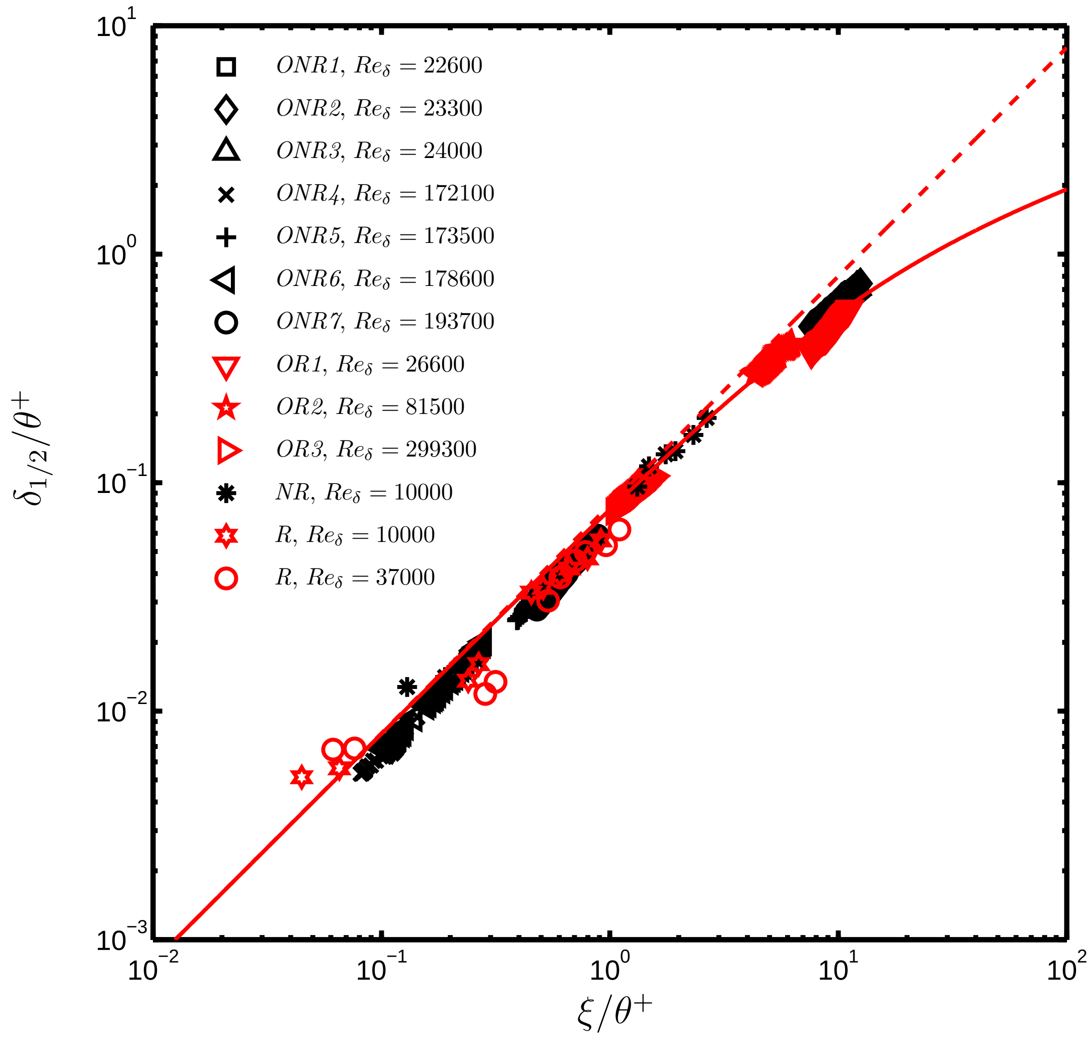

Figure 4.15: Results for local outer length scale $\delta_{1/2}$ versus downstream distance x, normalized by extended momentum radius θ^+, showing all nonreacting cases in Table 3.1 and all reacting cases in Table 3.2 as well as data from Muñiz and Mungal (2001) from Fig. 4.14. Solid line gives scaling for nonreacting flow in (4.4); dashed line gives jet-limit scaling.

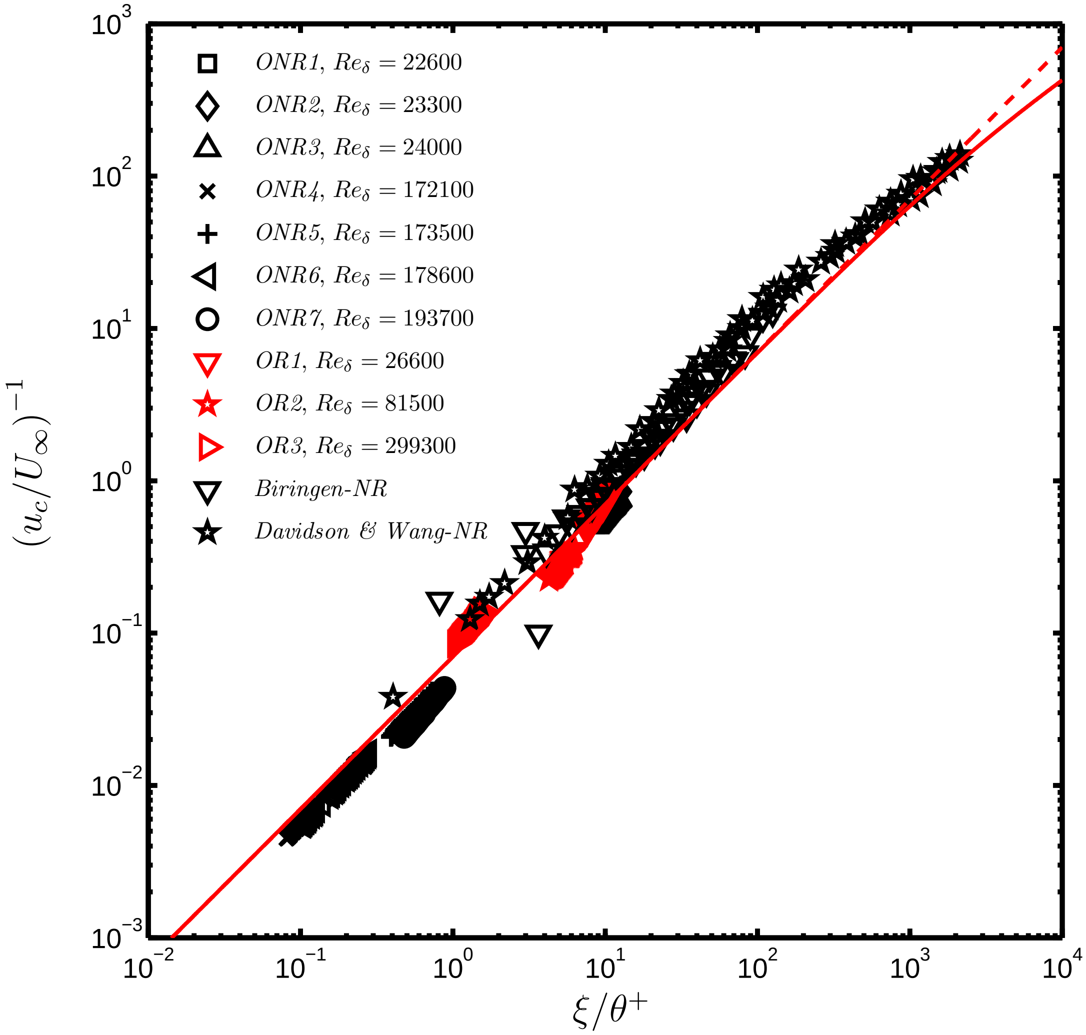

Figure 4.16: Results for local outer velocity scale u_c versus downstream distance x, normalized by extended momentum radius θ^+, showing all nonreacting cases in Table 3.1 and all reacting cases in Table 3.2 as well as data from Muñiz and Mungal (2001), Biringen (1975) and Wang and Davidson (2001). Solid line gives scaling for nonreacting flow in (4.5); dashed line gives jet-limit scaling.

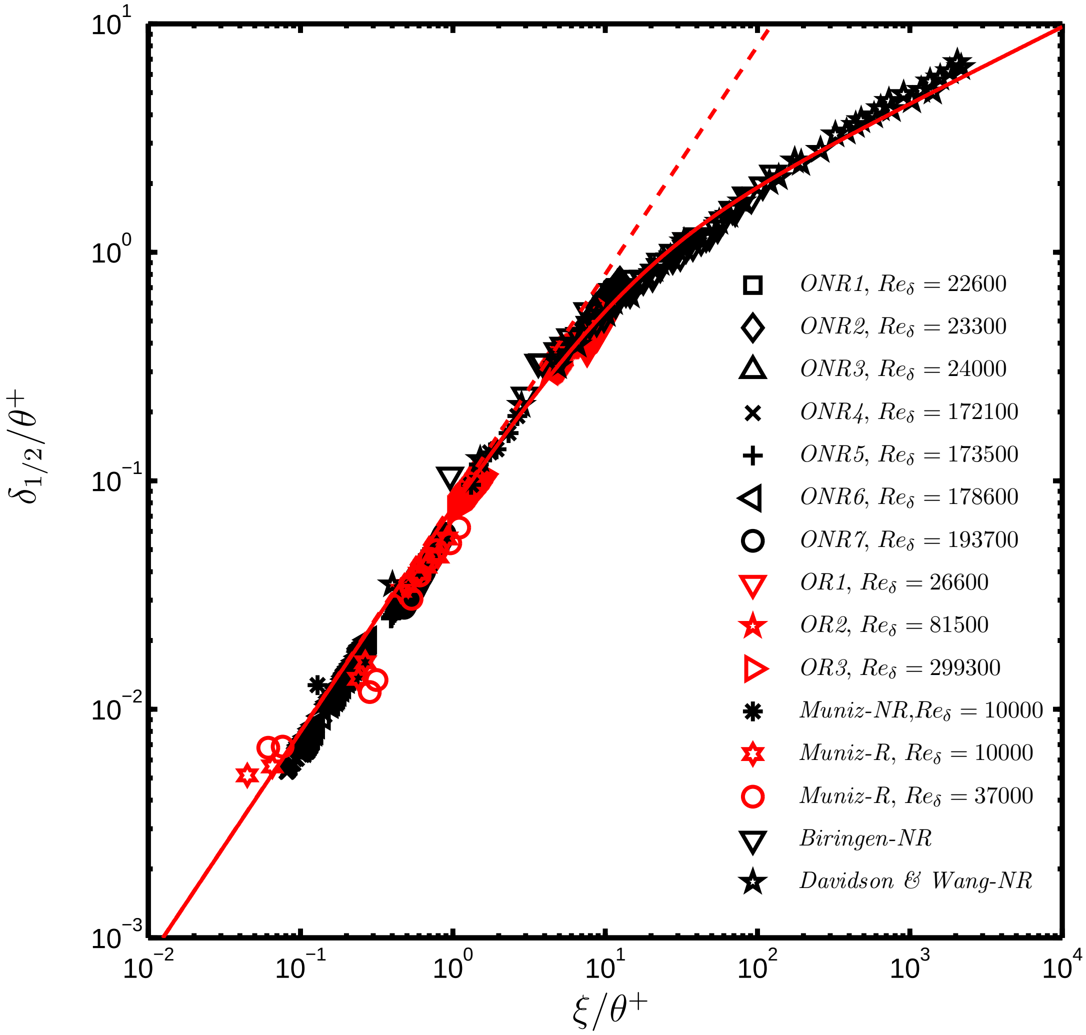

Figure 4.17: Results for local outer length scale $\delta_{1/2}$ versus downstream distance x, normalized by extended momentum radius θ^+, showing all nonreacting cases in Table 3.1 and all reacting cases in Table 3.2 as well as data from Muñiz and Mungal (2001), Biringen (1975) and Wang and Davidson (2001). Solid line gives scaling for nonreacting flow in (4.4); dashed line gives jet-limit scaling.

CHAPTER V

Inner Scaling of Nonreacting Flows: Effects of Resolution

Those properties of turbulent shear flows that are dominated by the smallest-scale motions, such as the velocity gradient moments $\overline{(\partial u_i/\partial x_j)^n}$ and other quantities derived from them, are referred to as "inner-scale quantities". Since the inner scales of turbulent flows become increasingly isotropic and locally homogeneous as the outer-scale Reynolds number Re_δ is increased, inner-scale quantities follow simple scalings (Kolmogorov 1941) in terms of the inner variables ν and λ_ν, where $\lambda_\nu \sim \delta Re_\delta^{-\frac{3}{4}}$ is the local inner (viscous) length scale. Thus, for instance, on purely dimensional grounds $\overline{(\partial u_i/\partial x_j)^n} \sim (\nu/\lambda_\nu^2)^n$. Such "inner scaling" of velocity gradient quantities in turbulent shear flows has been experimentally verified using PIV measurements that resolve essentially all the scales of motion in a nonreacting turbulent shear flow at relatively small values of Re_δ (*e.g.,* Mullin and Dahm 2005a; Mullin and Dahm 2005b)

In a reacting turbulent shear flow, departures from such simple inner scaling could in principle be used to experimentally determine the effects of heat release at the inner scales of motion. However, when Re_δ becomes large then PIV measurements can no longer resolve all the scales of motion, and this will lead to departures from the classical inner scaling due simply to resolution effects and not heat release effects. Separating these resolution effects from true heat release effects requires properly accounting for the effects of limited measurement resolution on the inner scaling. In this chapter, a method is developed that allows the measurement resolution scale Δ^* in any velocity gradient quantity to be objectively quantified, and the proper inner scaling in terms of the resolution scale $\Delta^\star$ is developed. PIV measurements of velocity gradients in a nonreacting turbulent shear flow over a wide range of Re_δ are then used to assess the ability of this modified inner scaling to account for resolution effects. It will be seen here that this modified inner scaling in terms of $\Delta^\star$ provides near-perfect similarity in the distributions of all velocity gradient quantities at all Re_δ in nonreacting turbulent shear flows. In following chapters, velocity gradient quantities from PIV measurements in exothermically reacting turbulent shear flows are then investigated with this modified inner scaling to remove the effects of resolution and allow the true inner-scale effects of heat release to be determined.

5.1 Inner-Scale PIV Measurements

The experimental conditions for the results presented in this chapter are given in Table 3.3. In contrast to the outer-scale PIV measurements in Chapter V, for these inner-scale measurements the field-of-view (FOV) for the PIV measurements is much smaller than the local outer scale of the coflowing jet, and is of the order of several local inner length scales in each direction. Two different FOVs, corresponding to 15×18.7 mm and 12×15 mm, were used for the six cases in Table 3.3. Over the range of downstream locations x and outer-scale Reynolds numbers Re_δ, the major dimension w_{FOV} of these FOVs ranged from 6 to 25 local λ_ν.

The CCD array of 1024×1280 pixels was divided into 32×32 pixel interrogation windows yielding a vector field of 32×40. The PIV interrogation windows were not overlapped in order to clearly define the resolution of the velocity data. A total of 300 PIV velocity fields were obtained in this manner for each measurement case. For each case, the resulting velocity fields were ensemble-averaged to obtain a mean velocity field across the FOV, and this mean field was subtracted from each individual instantaneous velocity field to produce velocity fluctuation fields. All subsequent processing and analysis was done on these velocity vector fluctuation fields.

The resulting velocity vector fluctuation fields were then differentiated to obtain the gradient fields $\partial u_i / \partial x_j$ via a second-order central differencing scheme. The second-order differencing template, in addition having a compact stencil that maintains high spatial resolution, is also well-matched to PIV data based on spectral analyses of the transfer functions associated with numerous differencing schemes (Foucaut and Stanislas 2002). Following Appendix A of Mullin (2004), a standard second-order central-differencing stencil used four of the eight adjacent vectors (north, south, east and west) to compute the four components of the velocity gradients, and a second stencil in a frame rotated by 45° used the remaining four adjacent vectors (NW, NE, SW and SE). The two resulting estimates of each gradient component were then averaged to provide a more accurate value that maintains high spatial resolution.

For each of the small-FOV inner-scale PIV measurements in Table 3.3, an accompanying large-FOV outer-scale PIV measurement was made to determine the local outer length and velocity scales δ and u_c at that measurement location and flow condition. For each case, the procedure was to first obtain 300 images of inner-scale

PIV data. The laser beams were then redirected and formed into larger sheets, and a second PIV camera was used to obtain an additional 300 images of large-FOV data. The much larger FOV for the outer-scale PIV measurements was sufficient to provide the mean velocity profile $U(y)$ across the entire jet, from which the local values for the outer length δ and outer velocity $u_c \equiv U_c - U_\infty$ could be obtained. From these, the local outer-scale Reynolds number $Re_\delta \equiv u_c\delta/\nu$ was calculated, and the corresponding inner length scale λ_ν was obtained as

$$\frac{\lambda_\nu}{\delta} = \Lambda Re_\delta^{-\frac{3}{4}}, \tag{5.1}$$

where $\Lambda \approx 11.2$, Buch and Dahm (1998). Since u_c and δ are measured directly for all cases in this study, any effects of buoyancy on these for the reacting flow cases in later chapters are directly accounted for, and thus such effects on λ_ν are also accounted for.

5.2 Inner-Scale Velocities and Velocity Gradients

A typical example of the resulting instantaneous velocity fluctuation fields $u(x,y)$ and $v(x,y)$ from these inner-scale measurements is given in Fig. 5.1, where the velocity fluctuations are normalized by the local outer velocity scale u_c. The particular example shown is from case *INR5* in Table 3.3, for which $Re_\delta = 45\,500$ and thus the FOV spans $15.1\,\lambda_\nu \times 18.9\,\lambda_\nu$. This FOV contains 32×40 independent values of each velocity component, since there was no overlap used in the PIV processing. The corresponding velocity gradient components fields $\partial u_i/\partial x_j$ accessible by these measurements, namely $\partial u/\partial x$, $\partial u/\partial y$, $\partial v/\partial x$ and $\partial v/\partial y$, obtained as described in § 5.1 are shown in Figs. 5.2 and 5.3. Since these gradient components are inner-scale quantities, they are shown normalized by the local inner velocity gradient scale (ν/λ_ν^2). Additional gradient fields associated with various physical processes in (2.1),(2.2) that result from these velocity gradient components are shown in Figs. 5.4 – 5.7. These include the strain rate component fields S_{xx}, S_{yy} and S_{xy}, together with the "pseudo" dissipation rate field $S_{ij}S_{ij} \approx S_{xx}^2 + S_{yy}^2 + 2S_{xy}^2$ (the full dissipation rate is $2\nu S_{ij}S_{ij}$), as well as the vorticity component field ω_z and the "pseudo" enstrophy field $\vartheta_z \equiv 3/2\,\omega_z^2$. Also shown are the square-magnitude of the velocity gradient tensor $\boldsymbol{\nabla}\mathbf{u} : \boldsymbol{\nabla}\mathbf{u} \approx (\partial u/\partial x)^2 + (\partial u/\partial y)^2 + (\partial v/\partial x)^2 + (\partial v/\partial y)^2 + (\partial w/\partial z)^2$ where the additional velocity gradient component $\partial w/\partial z \equiv -\left(\partial u/\partial x + \partial v/\partial y\right)$ is obtained from the $\boldsymbol{\nabla} \cdot \mathbf{u} \equiv 0$ requirement in the nonreacting flow, as well as the $\partial w/\partial z$ field itself.

Probability density functions (pdfs) for each of the quantities shown in Figs. 5.2 – 5.7 are given in Figs. 5.8 – 5.15, where a separate curve in each figure is given to each of the six nonreacting flow cases in Table 3.3. For the four velocity gradient components $\partial u/\partial x$, $\partial u/\partial y$, $\partial v/\partial x$ and $\partial v/\partial y$ in Figs. 5.8 – 5.11, the pdfs are shown with outer-variable normalization (u_c/δ) in the upper panel, and with inner-variable normalization (ν/λ_ν^2) in the lower panel. Consistent with the fact that the velocity gradients are inner-scale quantities, as expected considerably better collapse of the six curves is seen from the inner-variable normalization in the lower panels than from the outer-variable normalizations. Nevertheless, even with the inner-variable normalizations in the lower panels of these figures, there are still substantial differences apparent among the pdfs from the six cases. In following sections, it will be seen that these differences are due to incomplete resolution of the smallest-scale motions by the PIV measurements as the Reynolds number Re_δ increases. Those sections will show how these resolution effects can be rigorously accounted for to provide essentially complete similarity in the pdfs of such inner-scaled quantities among all six cases.

Pdfs for the additional derived gradient fields are shown in Figs. 5.12 – 5.15 with appropriate inner-variable normalization. Consistent with the results above for the individual velocity-gradient pdfs, it is apparent – despite the relatively wide range of Reynolds numbers represented in these data – that the inner-variable normalization largely accounts for the case-by-case differences among the six cases in Table 3.3. There are, however, remaining differences still apparent in these pdfs that should not be present if the data were fully resolved. These differences are most apparent in the results for $\mathbf{\nabla u : \nabla u}$ in Fig. 5.15, and will be seen to result from incomplete resolution of the measurements in the higher Re_δ cases.

5.3 Isotropy Assessments

The fact that the inner-variable normalizations in Figs. 5.2 – 5.15 suffice to largely rescale the pdfs from each of the six cases onto a single distribution for each quantity is a substantial validation of the measurements. Further assessment of the velocity gradients from these inner-scale PIV measurements is possible by comparing various quantities formed from them with corresponding theoretical values for perfectly homogeneous and isotropic turbulence. While the present measurements are from a turbulent shear flow, where effects of spatial inhomogeneity and anisotropy will necessarily lead to departures from these ideal theoretical values, the approach to local homogeneity and isotropy with increasingly smaller scales in such flows suggests that at sufficiently large values of Re_δ and sufficiently high resolution the measured values should approach these ideal values. Moreover, prior studies (*e.g.,* Mullin and Dahm 2005b) have reported values for various such quantities at Reynolds numbers comparable to those in the present study, which can be used for comparison.

One such isotropy test can be based on the ratio of mean-square values of the available off-diagonal ($i \neq j$) to on-diagonal ($i = j$) components of the velocity gradients $\partial u_i/\partial x_j$, for which the ideal theoretical value is

$$\frac{\overline{\left(\frac{\partial u}{\partial y}\right)^2} + \overline{\left(\frac{\partial v}{\partial x}\right)^2}}{\overline{\left(\frac{\partial u}{\partial x}\right)^2} + \overline{\left(\frac{\partial v}{\partial y}\right)^2}} = 2. \tag{5.2}$$

Values obtained from the present inner-scale measurements for each of the six cases are shown in Table 5.8. These can be compared with corresponding values from Mullin and Dahm (2005b) at comparable Re_δ. In particular, that study reported values of 1.915 at $Re_\delta = 6000$ and 1.856 at $Re_\delta = 30\,000$, which generally agree well the values ranging from 1.9-2.0 in Table 5.8.

Further comparisons are possible from ratios of the individual on- and off-diagonal velocity gradients components, for which the ideal theoretical values in homogeneous isotropic turbulence are

$$\frac{\left[\overline{\left(\frac{\partial u_i}{\partial x_j}\right)^2}\right]_{i\neq j}}{\left[\overline{\left(\frac{\partial u_i}{\partial x_j}\right)^2}\right]_{i=j}} = 2. \tag{5.3}$$

The corresponding results given in Table 5.9 from the present inner-scale measurements for each of the six cases are generally close to this value. Moreover, these values also agree well with those of Mullin and Dahm (2005b), who report a u-component ratio of 1.933 and a v-component ratio of 1.895 at $Re_\delta = 6000$, and at $Re_\delta = 30\,000$ report a u-component ratio of 1.931 and a v-component ratio of 1.774.

The values obtained for such isotropy ratios from the present measurements are thus in generally good agreement with ideal theoretical values that apply to homogeneous isotropic turbulence. Moreover, they agree well with previously reported values measured in a similar inhomogeneous, anisotropic turbulent shear flow. Deviations from strict inner-scale similarity in terms of ν and λ_ν in the velocity gradient pdfs in Figs. 5.2 – 5.15 are thus unlikely to be due to errors in the velocity gradient measurements themselves. Instead, it will be seen below that incomplete resolution of the inner-scale measurements at these Re_δ values is the origin of this incomplete similarity, and that these resolution effects can be rigorously accounted for obtain complete inner-scale similarity in these pdfs.

5.4 PIV Resolution Effects

Careful examination of the remaining departures from strict similarity in the inner-scaled velocity gradient pdfs in Figs. 5.8 – 5.11 shows a monotonic decrease in the width of the scaled pdfs with increasing Reynolds number. Such a decrease is consistent with the expected lower spatial resolution relative to λ_ν in the PIV data as Re_δ is increased. The outer scale $\delta(x)$ is essentially the same for all of the inner-scale cases, and thus with increasing Re_δ the viscous length scale λ_ν of the smallest-scale motions in the flow becomes increasingly smaller. Since the PIV interrogation window size is essentially the same for most of these cases, less of the spatial variations in velocity fields are resolved by the measurements as Re_δ increases.

The effect of the relative resolution in these measurements can be accounted for by a rigorous method based on integrating the spectral density of the quantity being considered. The approach developed here is, at least conceptually, somewhat similar to that originally proposed by Wyngaard (1968) and subsequently used by Antonia and Mi (1993), Elsner et al. (1993), Ewing et al. (1995), and Zhou et al. (2002) to account for resolution effects on measurements in turbulent shear flows. The present method is developed in this section, and in the following section is used to account for resolution effects on the inner scaling of the velocity gradient pdfs obtained from these measurements. The method is first described in the context of the simple inertial-range scaling of the spectral density of first-order velocity gradient quantities. A Pao-like rolloff is then incorporated to provide a higher-fidelity representation of the spectral density. The approach is then used to infer the actual measurement resolution for each of the six cases in Table 3.3, and this resolution scale is then subsequently used to correct the inner-scaling of the various quantities in Figs. 5.8 – 5.11.

5.4.1 Inertial-Range Correction

Examining the measurement resolution issue from a spectral perspective, the gradient quantity of interest, say q, can be represented in the Fourier domain by its spectral density $Q(k)$, where k is the wavenumber. The *true* average value of q is defined by integrating this spectral density over all wavenumbers as

$$\langle q \rangle_\infty \equiv \int_0^\infty Q(k)\mathrm{d}k, \tag{5.4}$$

where the notation $\langle \cdot \rangle_\infty$ implies the true, or infinitely resolved, average value of the quantity q. Here the effect of limited resolution will be examined in the context of the inertial-range form of $Q(k)$. Let $Q(k)$ denote the inertial-range portion of the spectrum for the variance of a first-order gradient quantity such that

$$\overline{q'^2} = \int_0^\infty Q(k)\mathrm{d}k, \tag{5.5}$$

where the left-hand side has dimensions of $1/T^2$, thus $Q(k) \sim L/T^2$. The physics of the turbulence constrain the limits on the integral to those wavenumbers associated with the inner-scales k_ν and outer-scales k_δ of the flow, giving

$$\overline{q'^2} = \int_{k_\delta}^{k_\nu} Q(k)\mathrm{d}k. \tag{5.6}$$

Kolmogorov's 1941 theory provides the following inertial range scaling for the right-hand side: $Q(k) \sim \varepsilon^{2/3}k^{1/3}$, where ε is the local averaged kinetic dissipation rate. Substituting this inertial range scaling into (5.6) and integrating, gives,

$$\overline{q'^2} \sim \varepsilon^{2/3}\left(k_\nu^{4/3} - k_\delta^{4/3}\right). \tag{5.7}$$

Recalling the definition of the Kolmogorov length scale

$$\lambda_K \equiv \left(\frac{\nu^3}{\varepsilon}\right)^{1/4}, \tag{5.8}$$

and its relationship with the viscous length scale ($6\,\lambda_K \approx \lambda_\nu$), combined with the wavenumber relationship $k \equiv 2\pi/\lambda$ gives

$$\overline{q'^2} \sim \left(\frac{\nu^3}{\lambda_\nu^4}\right)^{2/3}\left(\lambda_\nu^{-4/3} - \delta^{-4/3}\right). \tag{5.9}$$

For high Reynolds number turbulence, $\delta^{-4/3} \ll \lambda_\nu^{-4/3}$ and thus the δ term can be neglected, yielding the scaling relationship for inner-scale gradient moments with dimensions of $1/T^2$

$$\overline{q'^2} \sim \left(\frac{\nu}{\lambda_\nu^2}\right)^2. \tag{5.10}$$

This scaling relation holds when the true value of the moment is known, e.g. when the measurements are infinitely resolved.

However, practical measurement technique cannot provide infinite resolution, and are typically unable to provide fully-resolved measurements of high Reynolds number turbulent flows of practical interest. Considering this practical limitation, the previous analysis is retraced beginning with (5.6). Here the upper limit is recognized to not always be k_ν, but rather k_Δ, where Δ represents the spatial resolution limitations of the experimental apparatus. For the present data Δ scales with the PIV interrogation window size. Maintaining the assumption that $\delta^{-4/3} \ll \Delta^{-4/3}$ yields the result

$$\overline{q'^2} \sim \left(\frac{\nu^3}{\lambda_\nu^4}\right)^{2/3} \Delta^{-4/3}. \tag{5.11}$$

Rearranging the left-hand side gives rise to the "correction" factor: $(\lambda_\nu/\Delta)^{4/3}$,

$$\overline{q'^2} \sim \left(\frac{\nu}{\lambda_\nu^2}\right)^2 \left(\frac{\lambda_\nu}{\Delta}\right)^{4/3}. \tag{5.12}$$

The Reynolds number dependence in this relationship is seen by rearranging terms and employing the viscous length-scale Reynolds number scaling: $\lambda_\nu \sim \delta Re_\delta^{-3/4}$,

$$\frac{\overline{q'^2}}{\left(\frac{\nu}{\Delta^2}\right)^2} \sim \left(\frac{\Delta}{\delta}\right)^{8/3} Re_\delta^2. \tag{5.13}$$

Or, equivalently, for the *rms* value of the gradient

$$q'_{rms} \sim \left(\frac{\nu}{\Delta^2}\right) \left(\frac{\Delta}{\delta}\right)^{4/3} Re_\delta. \tag{5.14}$$

Thus for data that are acquired under the condition $k_\Delta < k_\nu$ and are under-resolving the flow in a spatial sense, the right-hand side of (5.14) provides the *K41* inertial-range scaling correction enabling the expected data collapse.

Hence, the problem has been reduced to a single question: "what is the relevant length scale Δ by which the data can be correctly scaled?"

5.4.2 PIV Resolution: Spectra

Determination of the length scale Δ in physical space is equivalent to ascertaining k_Δ in Fourier space. Knowledge of the spectra of the measured gradient quantities is then desirable to assess the extent to which the PIV measurements resolves the flow. The most straightforward manner by which to obtain the spectra or power spectrum density (PSD) is to compute the FFT of the data fields $q(\mathbf{x})$, to obtain the Fourier transform of the data $\widehat{Q}(k)$. This is then multiplied by its complex conjugate to form the spectrum of $q(\mathbf{x})$, $Q(k)$.

Unfortunately, this procedure is not well-suited to PIV data where the length of the data records (e.g. the length of the rows or columns of the PIV vector field) are relatively small. Thus this direct approach to obtaining the spectrum of the gradient data was abandoned.

5.4.3 PIV Resolution: Low Pass Filtering

Since the direct estimation of the PSD no longer a viable option, a more indirect approach was attempted. The method employed in the present study extracts information regarding the resolution of a given gradient quantity q by artificially degrading the data in successive measures. The statistics of the artificially degraded data are then used to determine the level of resolution achieved .

Conceptually, this is loosely similar to the methods of Mi and Nathan (2003), and Antonia and Mi (1993). However, the present work seeks to obtain resolution information on a case-by-case basis, allowing the data to dictate the form of the spectrum; as opposed to prescribing a shape for the spectra based upon present constraints from the archival literature, Antonia and Mi (1993). The present methodology follows these steps:

(i) Ensemble average PIV data to obtain fluctuating velocities u, v.

(ii) Smooth the u and v fields via explicit filtering (typically Gaussian).

(iii) Calculate gradient quantities q from smoothed fluctuating velocities $\widetilde{\mathbf{u}}$.

(iv) Before explicitly filtering each q field, the average is subtracted on an plane-by-plane basis, yielding q''.

(v) Directly filter the "fluctuating" gradient quantities q'' at various explicit filter scales Δ_i via a spectrally sharp, low-pass filter.

(vi) For explicit filter scale Δ_i, a new gradient field is produced q_i''. Statistics are then collected for each q_i'' field.

(vii) The moments from the statistics of the q_i'' fields are then plotted against the explicit filter scale Δ_i.

When statistics are collected, they are averaged over all points in the data image and over all images, thus the number of samples is typically $\sim 342\,000$.

Steps (v) – (vii) are shown schematically in Fig. 5.16, where the subpanels illustrate the successive low-pass filtering of the selected gradient quantity. Moving from left to right, the quantity q is artificially filtered with decreasing cutoff frequency k_{Δ_i}, corresponding to an effective spatial filter of size Δ_i. The data are filtered using a spectrally sharp FFT routine. The red data points in Fig. 5.16 represent the global variance of the gradient q – that is, the variance of q averaged over all points in each vector field, over all data planes. The results described in step (vii) are shown in Figs. 5.17 – 5.22, where the variance of the vorticity is selected as the filtered moment. Here, the abscissa is given in explicit spatial filter size Δ_i and is equivalent to the inverse of the cutoff wavenumber $\sim 1/k_{\Delta_i}$.

The left-hand side of the plots represents the highest resolved values of the gradients q and is unfiltered. Moving towards the right along the abscissa indicates increasing levels of explicit filtering (e.g. increasing the size of Δ_i), and thus the gradients are (artificially) less resolved. The ordinate represents the value of the $\mathrm{var}\{\omega_z\}_\Delta$ moment at a given explicit scale Δ_i normalized by the maximum value given by the data set (e.g. the unfiltered, initial data). Thus the first (unfiltered) moment (left-most point) is identically unity. As the level of filtering increases (moving left to right), the inertial range behavior becomes evident, especially for the cases at the highest Re_δ. In Fig. 5.16, as well as Figs. 5.17 – 5.22, the diagonal dashed line represents a $-4/3$ power law slope as (5.11) prescribes.

The zero-slope data appearing for the smallest levels of explicit filtering in the lowest Re_δ cases in Figs. 5.17 – 5.22 are evidence of the spectral signature of the viscous roll-off in the dissipative range of scales within the turbulence. At the higher Re_δ data, this zero slope is not expected to indicate the viscous roll-off, as the data are not fully resolved. Rather, this flat response is the result of the implicit spectral response due to the measurement technique – in this case the spectral character of the PIV system, (Foucaut and Stanislas 2002).

The intersection between the horizontal line set at unity (maximum measured moment value) and the inertial range scaling, projected backwards, defines a length scale in this diagram. This intersection is denoted with a ($\star$) in Figs. 5.17 – 5.22. This length scale is interpreted as the "effective resolution" length scale, where the data begin to exhibit significant inertial range behavior. This point is noted on all the aforementioned figures and is labeled as $\Delta^\star$. In order to extract this $\Delta^\star$ value from each data set, the set of filtered moments are spectrally modeled by a function in order to provide an unbiased projection for the inertial range slope. This method is addressed in the following section.

While Figs. 5.17 – 5.22 present the $\Delta^\star$ extraction results for the all the nonreacting cases for only the vorticity ω_z, three other gradients were also processed: the three in-plane strain rate components: S_{xx}, S_{yy}, S_{xy}. The results from all these four gradients were used in the present work to obtain aggregate values for $\Delta^\star$.

5.4.4 PIV Resolution: Effective Length Scale $\Delta^\star$

In order use the filtered moment data described in §5.4.3, a model was developed for the spectral behavior at wavenumbers beyond the inertial range, in the dissipative range. The Pao spectrum was chosen as a starting point for the dissipative range model due to its good agreement with existing data, Pao (1965), and Chapman (1979):

$$E_P(k) \sim k^{-\frac{5}{3}} \exp\left[-\frac{3}{2}\left(k\lambda_K\right)^{\frac{4}{3}}\right], \tag{5.15}$$

where λ_K is the Kolmogorov length scale. The exponential function modifying the $k^{-5/3}$ inertial range scaling in the Pao spectrum gives the model its dissipative range behavior. In similar fashion, the PSD for the gradient quantities of interest in the present work are modified.

For first order gradient quantities: S_{ij} and ω_z, the inertial range scaling is identical, recall §5.4.1,

$$Q(k) \sim \varepsilon^{2/3} k^{1/3}. \tag{5.16}$$

This spectrum can then be modified with the exponential function to create a dissipation range, or roll-off model:

$$Q(k) \sim \varepsilon^{2/3} k^{1/3} \exp\left[-\left(k\Delta_R\right)^p\right], \tag{5.17}$$

where the constants given by Pao (1965), have been generalized to Δ_R and p to allow flexibility. These are identified as a resolution length scale Δ_R (similar to the Kolmogorov scale in the Pao formulation) and the shape of the spectra p in the dissipation range.

This model spectrum in (5.17) can then be integrated over all wavenumbers $k \in \{0, k_\Delta\}$ to obtain the value of the moment at filter cutoff k_Δ,

$$\langle \widetilde{q''} \rangle_\Delta \sim \int_0^{k_\Delta} \varepsilon^a k^b \exp\left[-\left(k\Delta_R\right)^p\right] \mathrm{d}k. \tag{5.18}$$

The result in (5.18) gives the most general form for the model gradient spectrum. For the present work, where the variance of the first order gradients which have units of $1/T$ are the moments of interest, $a = 2/3$ and $b = 1/3$. This leaves two free parameters, Δ_R and p to fit the filtered moments obtained from the data.

$$\langle \widetilde{q''} \rangle_\Delta \sim \int_0^{k_\Delta} \varepsilon^{\frac{2}{3}} k^{-\frac{1}{3}} \exp\left[-\left(k\Delta_R\right)^p\right] \mathrm{d}k. \tag{5.19}$$

As a convenience, the expression in (5.19) is normalized by its unfiltered value $\langle q'' \rangle_{IW}$ (e.g. the value of the gradients at the implicitly filtered scale of the interrogation window, before the artificial data degradation filtering) given as,

$$\frac{\langle \widetilde{q''} \rangle_\Delta}{\langle q'' \rangle_{IW}} = \frac{\int_0^{k_\Delta} \varepsilon^{\frac{2}{3}} k^{-\frac{1}{3}} \exp\left[-\left(k\Delta_R\right)^p\right] \mathrm{d}k}{\langle q'' \rangle_{IW}}. \tag{5.20}$$

Equation 5.20 was integrated numerically using a Romberg scheme and the error between the filtered data points (red circles in Fig. 5.16) and the fitting function was minimized to obtain the optimum fit. The values for the two parameters were obtained by searching over a large parametric space with fine increments of 0.0035 for p and 0.005 mm for Δ_R.

Once the optimum value for the two parameters p and Δ_R were determined, the model spectrum was integrated out to exceedingly large wavenumbers to achieve the, power-law, inertial range behavior. This allowed for the inertial range scaling to be asymptotically matched and projected backwards to elucidate the value of $\Delta^\star$. The intersection point between the power law and the horizontal line set at unity was noted is dentoted by a ($\star$) in Figs. 5.17 – 5.22 The value of this point along the horizontal axis is $\Delta^\star$ and is noted in each of the figures.

The values for these parameters (p, Δ_R and $\Delta^\star$) are given in Table 5.1. Note that the $\langle\cdot\rangle$ notation for p, Δ_R and $\Delta^\star$ in the table indicates that the values for these parameters have been averaged over the four gradients, each processed independently: S_{xx}, S_{yy}, S_{xy} and ω_z. The values of the individual p, Δ_R and $\Delta^\star$ parameters for each of the four gradients is shown in Fig. 5.23.

5.4.5 PIV Resolution: Viscous Roll-Off

However, substituting $\Delta^\star$ for Δ in (5.14), did not give satisfactory results in terms of the expected data collapse. This correction neglects the effect of the viscous roll-off reaching to length scales as much ten times larger than λ_K, Chapman (1979). This viscous phenomenon was accounted for by adding a roll-off function $D(p)$ to the inertial-range correction.

The inertial-range correction term given in (5.14), assumes that the gradient moment is obtained by integrating under its spectrum to $k_{\Delta^\star}$, all the while following inertial range scaling. Thus as the spectrum nears the dissipative range and the roll-off begins to manifest itself, this inertial-range correction begins to overpredict the area under the spectrum – as shown schematically in Fig. 5.24. Since a model spectrum has been developed (5.19), complete with dissipative range model, correcting the overprediction is straightforward. For each data set, the following ratio was computed

$$D(p) \equiv \frac{\int_{k_\delta}^{k_{\Delta_R}} \varepsilon^{\frac{2}{3}} k^{-\frac{1}{3}} \exp\left[-\left(k\Delta_R\right)^p\right] \mathrm{d}k}{\int_{k_\delta}^{k_{\Delta_R}} \varepsilon^{\frac{2}{3}} k^{-\frac{1}{3}} \mathrm{d}k}. \tag{5.21}$$

When this $D(p)$ term is included with the inertial-range correction in (5.13), it gives the complete normalization factor that properly accounts for both the inner scaling and the effect of measurement resolution. This resolution-corrected inner-scale normalization is thus

$$\mathcal{N}^\star = \left(\frac{\nu}{(\Delta^\star)^2}\right)\left(\frac{\Delta^\star}{\delta}\right)^{\frac{4}{3}} Re_\delta \left[D(p)\right]^{\frac{1}{2}} \tag{5.22}$$

which can be rearranged to reveal that this is simply a correction to the classical inner-scale normalization (ν/λ_ν^2), namely

$$\mathcal{N}^\star \equiv \left(\frac{\nu}{\lambda_\nu^2}\right)\Lambda^2\left(\frac{\delta}{\Delta^\star}\right)^{\frac{2}{3}} Re_\delta^{-\frac{1}{2}} \left[D(p)\right]^{\frac{1}{2}}. \tag{5.23}$$

The normalization in (5.23) is appropriate for first-order gradient quantities, which have dimensions of $1/T$; higher-order gradient quantities with dimension $(1/T)^n$ are accordingly normalized with $(\mathcal{N}^\star)^n$. Values for the parameters that comprise (5.23) for each of the cases Table 3.3 are given in Table 5.1. Following the example of the vorticity, Fig. 5.25 plots the *rms* value of the vorticity for each of the six cases. The figure compares the difference between unscaled moments to the same moments normalized by $\mathcal{N}^\star$.

If $\Delta^\star$ is thought to loosely behave as an inner length scale of sorts, the following scaling relationship can be solved for its constant $\Lambda^\star$:

$$\left(\frac{\Delta^\star}{\delta}\right) \approx \Lambda^\star \, Re_\delta^{-\frac{3}{4}}. \tag{5.24}$$

This value is also recorded in Table 5.1.

5.5 Inner Scale Pdfs with Resolution-Corrected Inner Scaling

Application of the inertial-range correction given by (5.23) to the pdfs initially presented in Figs. 5.8 – 5.15 are shown in Figs. 5.26 – 5.37. By using $\mathcal{N}^\star$ in place of the viscous length scale λ_ν, an improvement in the expected collapse of the pdfs was observed. In these figure, all six of the inner scale, nonreacting data sets are shown simultaneously. The pdfs include the four accessible components of the velocity gradient tensor: $\partial u/\partial x$, $\partial u/\partial y$, $\partial v/\partial x$ and $\partial v/\partial y$, shown in Figs. 5.26 – 5.29. Figures 5.30 – 5.33 present the accessible strain rate components, S_{xx}, S_{yy}, S_{xy} and $S_{ij}S_{ij}$. The vorticity component ω_z and its subsequent enstrophy ϑ_z, are shown in Figs. 5.34 – 5.35. Lastly, the two-dimensional projection of the divergence, $\boldsymbol{\nabla} \cdot \mathbf{u}$ and velocity gradient contraction $\boldsymbol{\nabla}\mathbf{u} : \boldsymbol{\nabla}\mathbf{u}$ are given in Figs. 5.36 – 5.37.

All of the gradients presented here have dimensions of $1/T$, save for the quantities $\boldsymbol{\nabla}\mathbf{u} : \boldsymbol{\nabla}\mathbf{u}$, ϑ_z and $S_{ij}S_{ij}$, which scale as $1/T^2$. By inspection, these three gradients are normalized by $(\mathcal{N}^\star)^2$.

5.6 Inner Scale PIV: Corrected Moments

The first four moments of each of the data sets presented as pdfs in Figs. 5.26 – 5.37, are listed in Tables 5.2 – 5.7. The moments are listed as the mean μ, the *rms* value σ, the skewness γ and the kurtosis β, where they are defined as,

$$\mu_n = \frac{1}{N}\sum_{j=1}^{N}(x_j - \mu)^n\,, \qquad\qquad n = 2, 3, \ldots \tag{5.25}$$

From these central moments, $\sigma = \mu_2^{1/2}$ is the *rms* value and the third and fourth moments are non-dimensionalized by the *rms* value as $\gamma = \mu_3/\sigma^3$ with $\beta = \mu_4/\sigma^4$. Here N represents the total number of samples, typically 342 000 for the present data.

In tables 5.2 – 5.7, the fluctuating velocities u and v are normalized by the centerline velocity while the remaining quantities are normalized via $\mathcal{N}^\star$ defined in (5.23).

Returning to the topic of isotropy discussed in §5.3, Fig. 5.38 presents a comparison of the on-axis gradient components $\partial u/\partial x$ and $\partial v/\partial y$ for all data sets as well as the off-axis components $\partial u/\partial y$ and $\partial v/\partial x$. The gradients have all been normalized by $\mathcal{N}^\star$ and display a reasonable level of agreement.

5.7 Comparison to Existing Data

The present results are compared to Direct Numerical Simulations (DNS) studies of periodic homogeneous isotropic turbulence from Gotoh, Fukayama, and Nakano (2002) and Jiménez, Wray, Saffman, and Rogallo (1993), in Table 5.10. Here the third and fourth moments γ and β for $\partial u/\partial x$ are compared to the DNS results alongside measured values from Mullin (2004). The values of the Taylor scale Reynolds numbers are roughly comparable, $Re_\lambda = 58$ and 115 for the present study, $Re_\lambda = 45$ and 113 from the PIV data of Mullin (2004), $Re_\lambda = 54$ and 125 from the DNS results of Gotoh, Fukayama, and Nakano (2002) and $Re_\lambda = 61$ and 168 from the DNS study of Jiménez, Wray, Saffman, and Rogallo (1993). Bearing in mind that the present data are obtained from shear flow turbulence and the DNS results are obtained from homogeneous isotropic turbulence (HIT), the agreement appears to be fair in an overall sense.

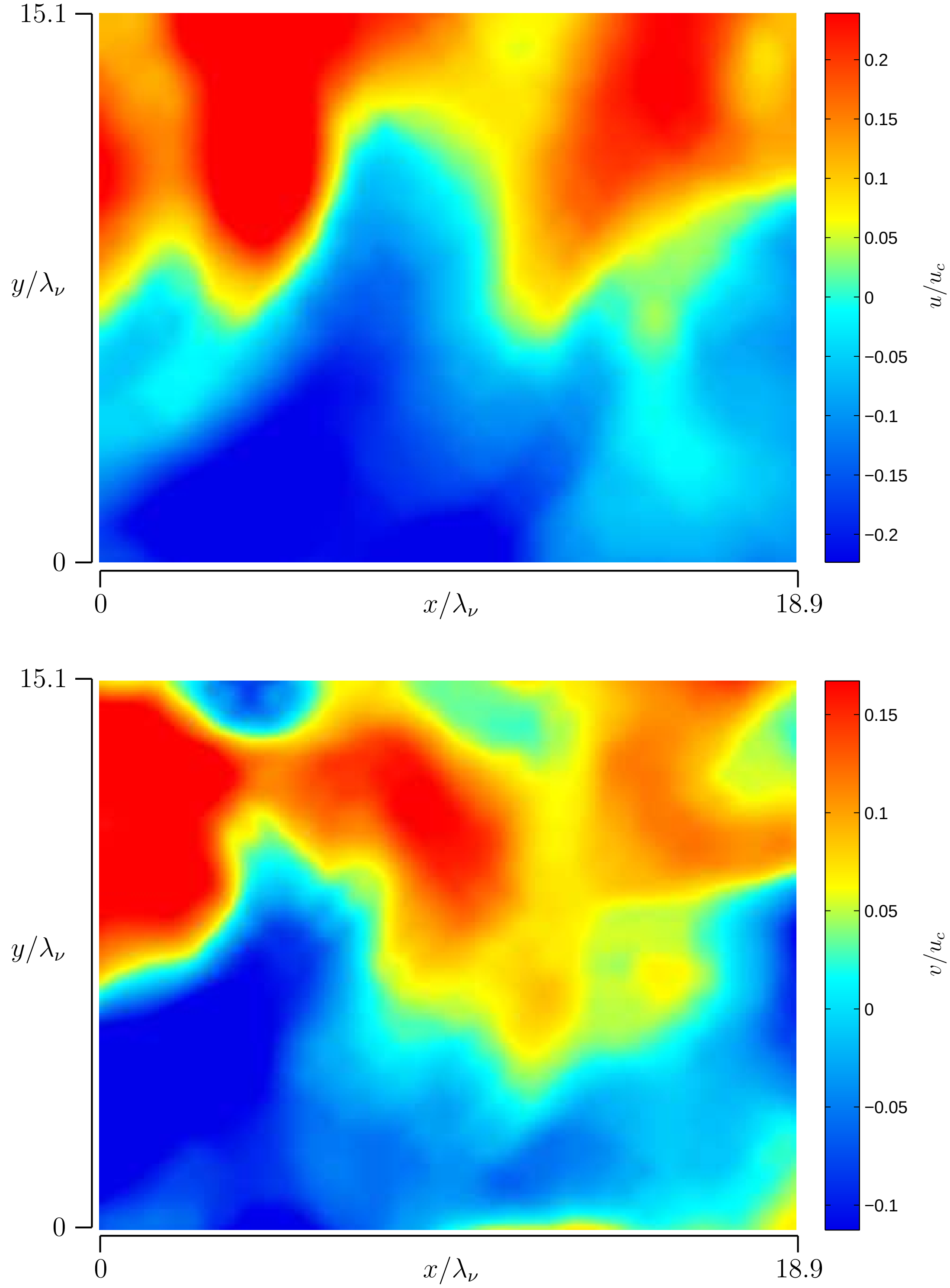

Figure 5.1: Sample velocity fields at $Re_\delta = 45\,500$. Instantaneous velocity fluctuations u *(top)* and v *(bottom)*, normalized by the centerline velocity u_c.

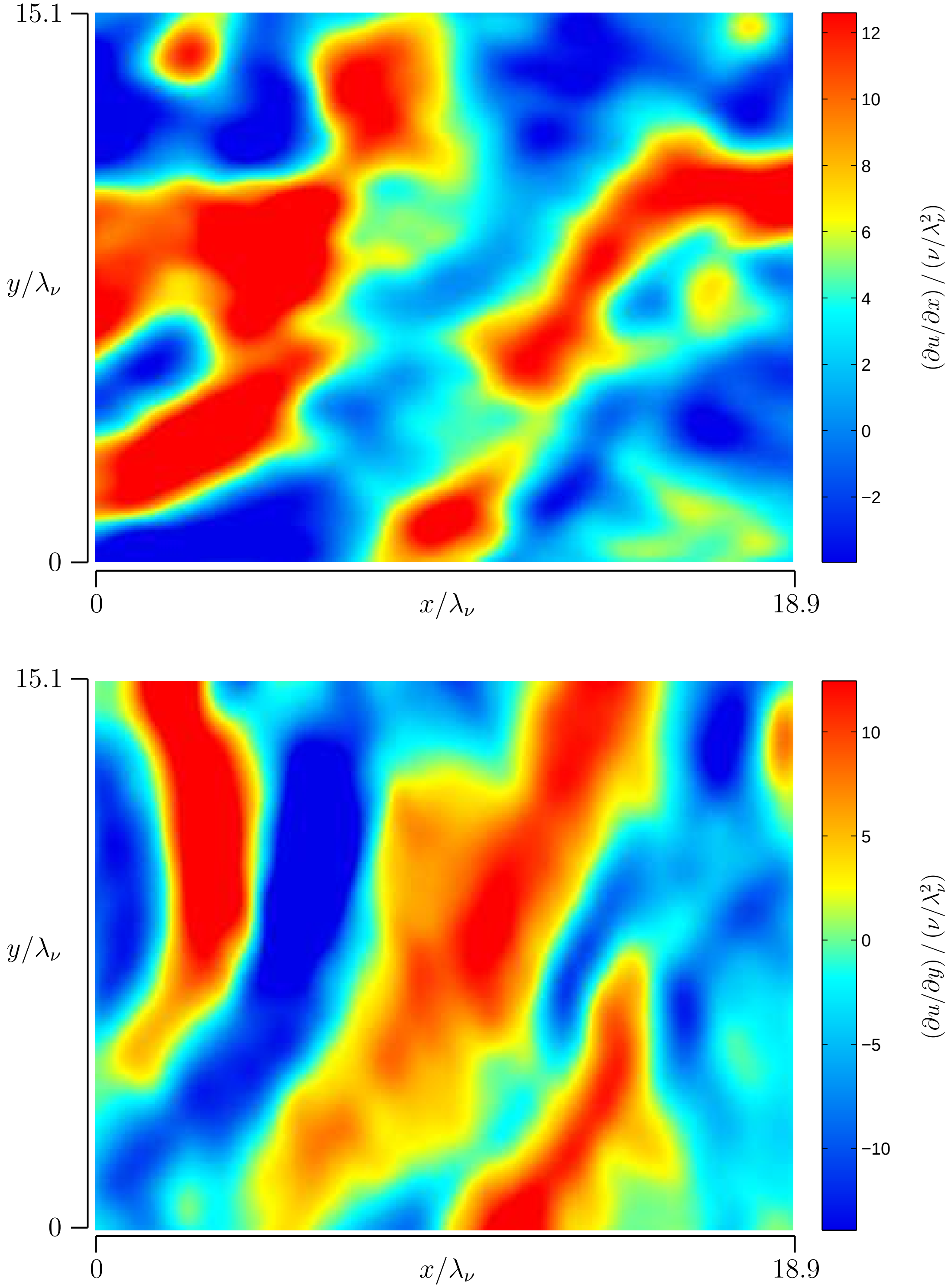

Figure 5.2: Sample velocity gradient fields at $Re_\delta = 45\,500$. Instantaneous velocity gradients $\partial u/\partial x$ *(top)* and $\partial u/\partial y$ *(bottom)*, normalized by inner variables ν/λ_ν^2 .

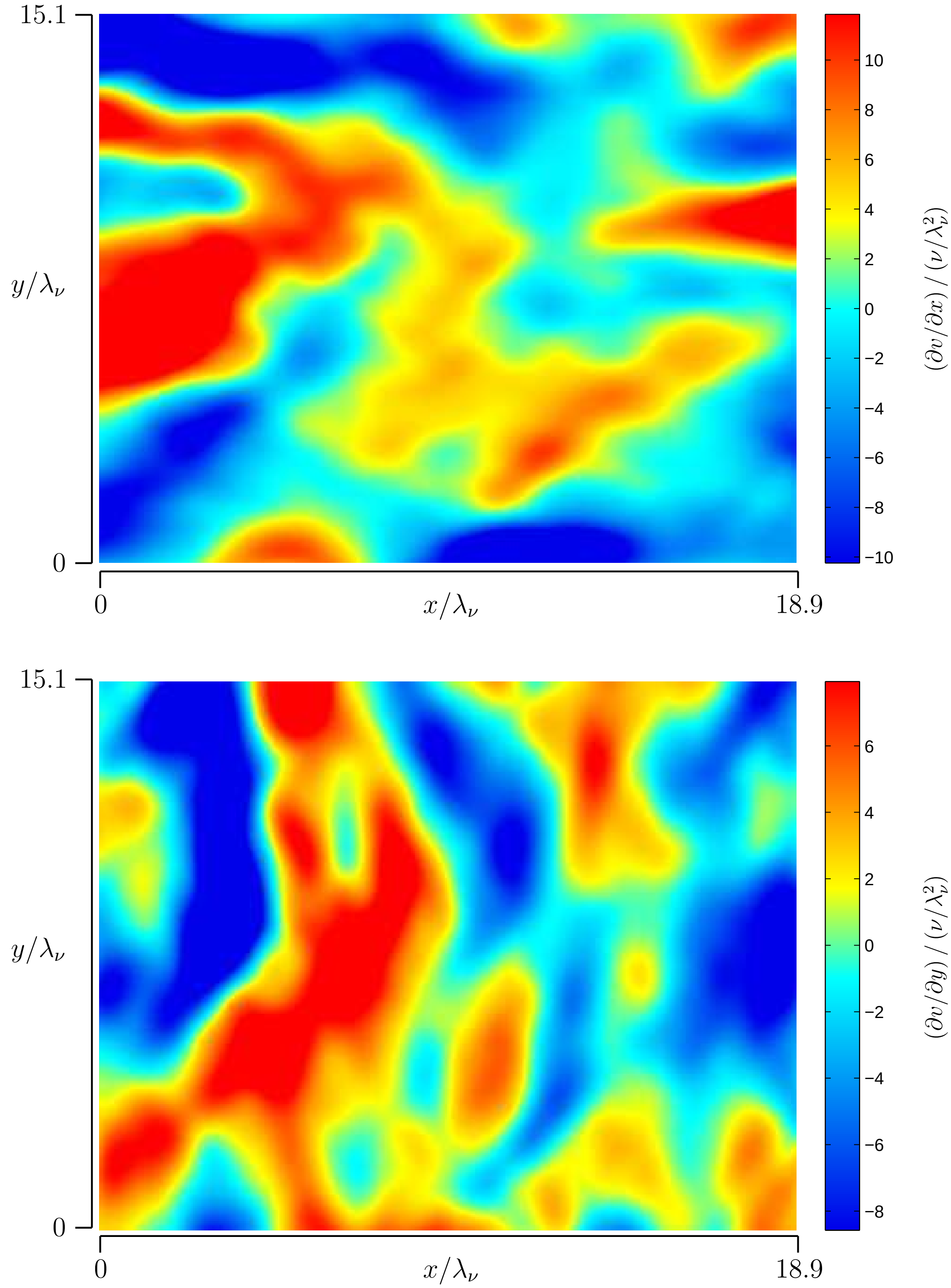

Figure 5.3: Sample velocity gradient fields at $Re_\delta = 45\,500$. Instantaneous velocity gradients $\partial v/\partial x$ *(top)* and $\partial v/\partial y$ *(bottom)*, normalized by inner variables ν/λ_ν^2 .

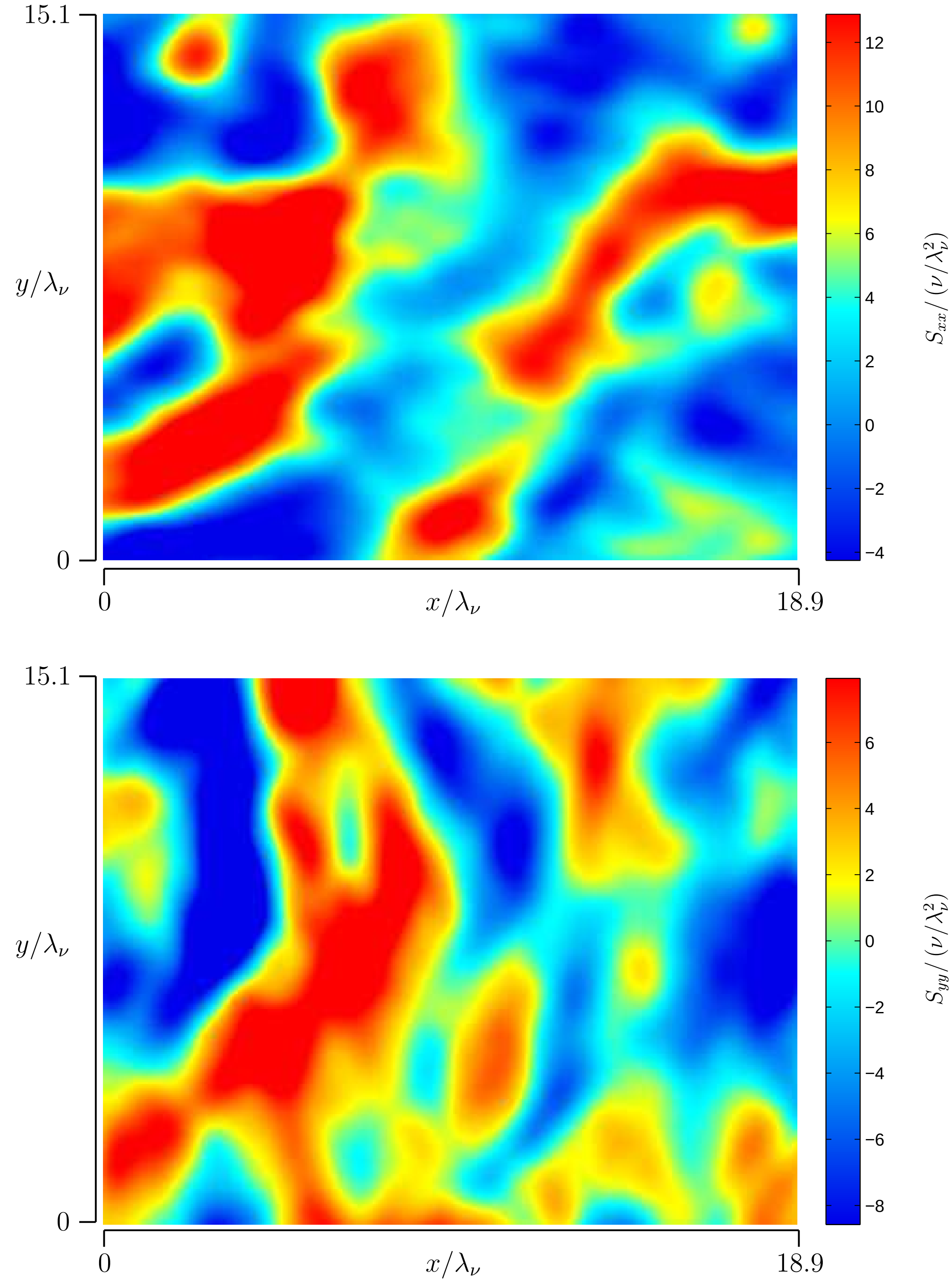

Figure 5.4: Sample velocity gradient fields at $Re_\delta = 45\,500$. Instantaneous strain rate components S_{xx} *(top)* and S_{yy} *(bottom)*, normalized by inner variables ν/λ_ν^2 .

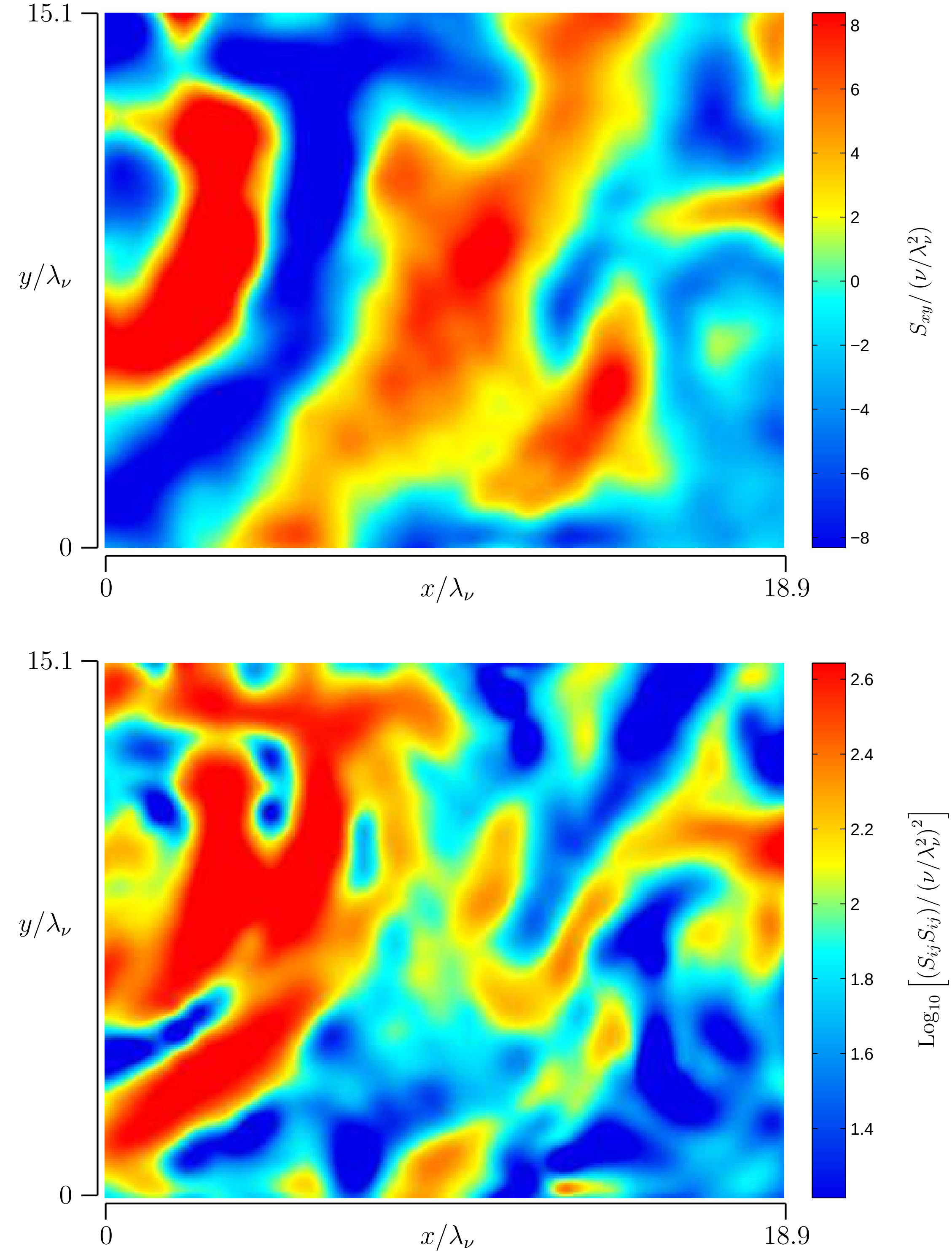

Figure 5.5: Sample velocity gradient fields at $Re_\delta = 45\,500$. Instantaneous strain rate component S_{xy} *(top)* and $\mathrm{Log}_{10}(S_{ij}S_{ij})$ *(bottom)*, normalized respectively by classical inner scaling ν/λ_ν^2 and $(\nu/\lambda_\nu^2)^2$. Here $S_{ij}S_{ij} \equiv S_{xx}^2 + S_{yy}^2 + 2\,S_{xy}^2$.

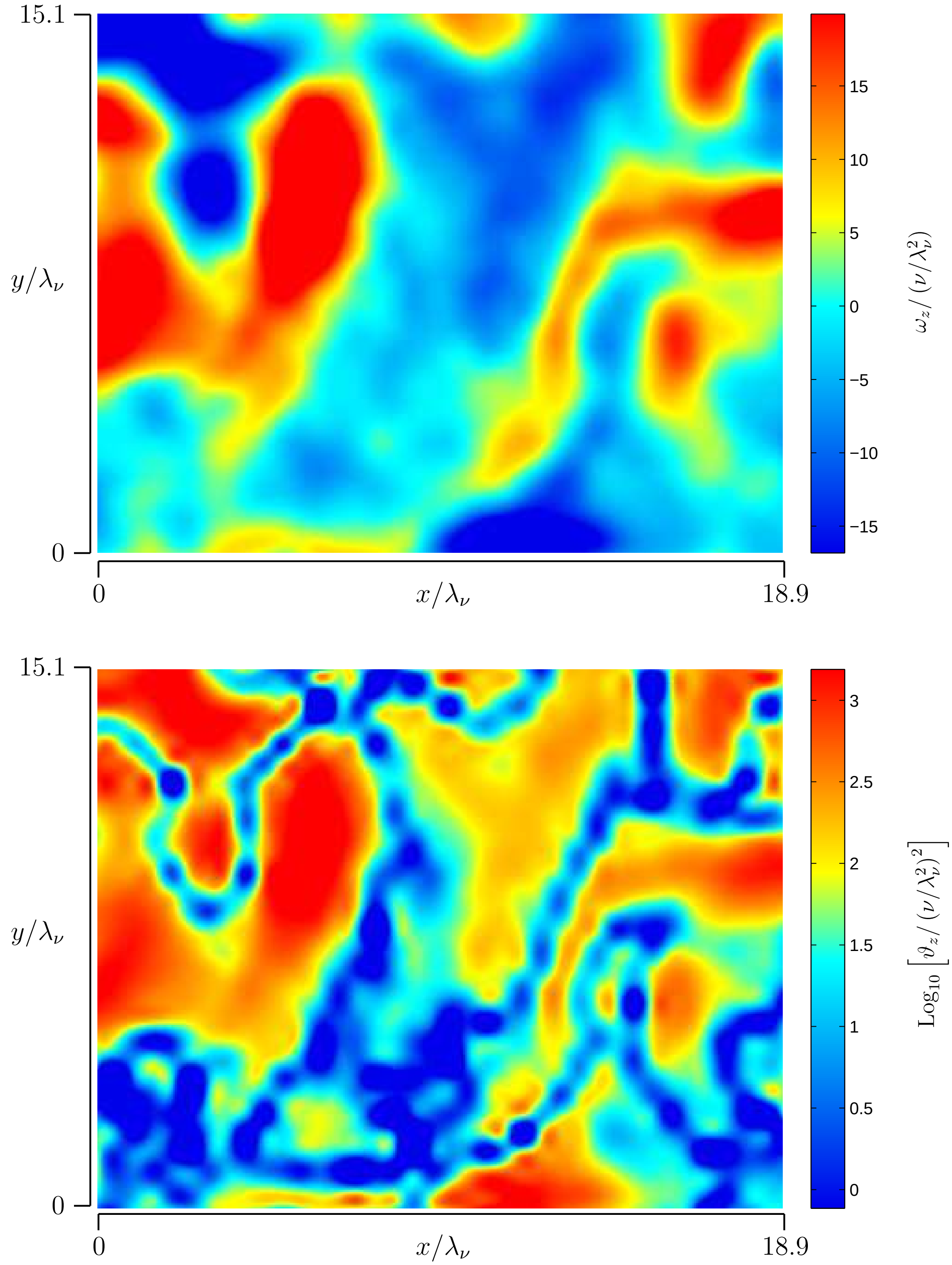

Figure 5.6: Sample velocity gradient fields at $Re_\delta = 45\,500$. Instantaneous vorticity ω_z *(top)* and enstrophy $\mathrm{Log}_{10}(\vartheta_z)$ *(bottom)*, normalized respectively by classical inner scaling ν/λ_ν^2 and $(\nu/\lambda_\nu^2)^2$. Here $\vartheta_z \equiv 3/2\,\omega_z^2$.

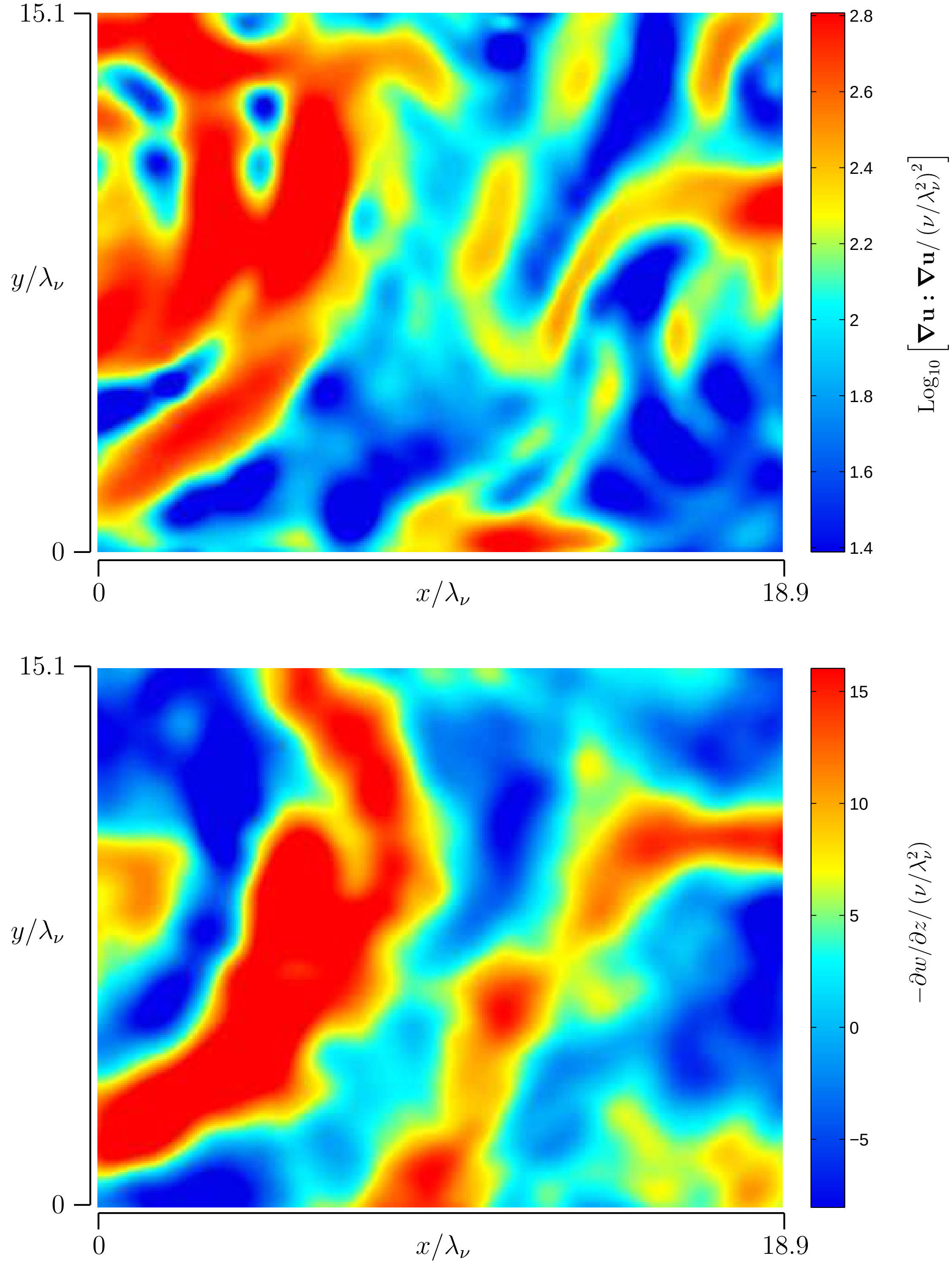

Figure 5.7: Sample velocity gradient fields at $Re_\delta = 45\,500$, showing contraction of instantaneous velocity gradient tensor $\mathrm{Log}_{10}(\boldsymbol{\nabla}\mathbf{u} : \boldsymbol{\nabla}\mathbf{u})$ *(top)* and two-dimensional divergence $-\partial w/\partial z$ *(bottom)*, normalized respectively by classical inner scaling $(\nu/\lambda_\nu^2)^2$ and ν/λ_ν^2.

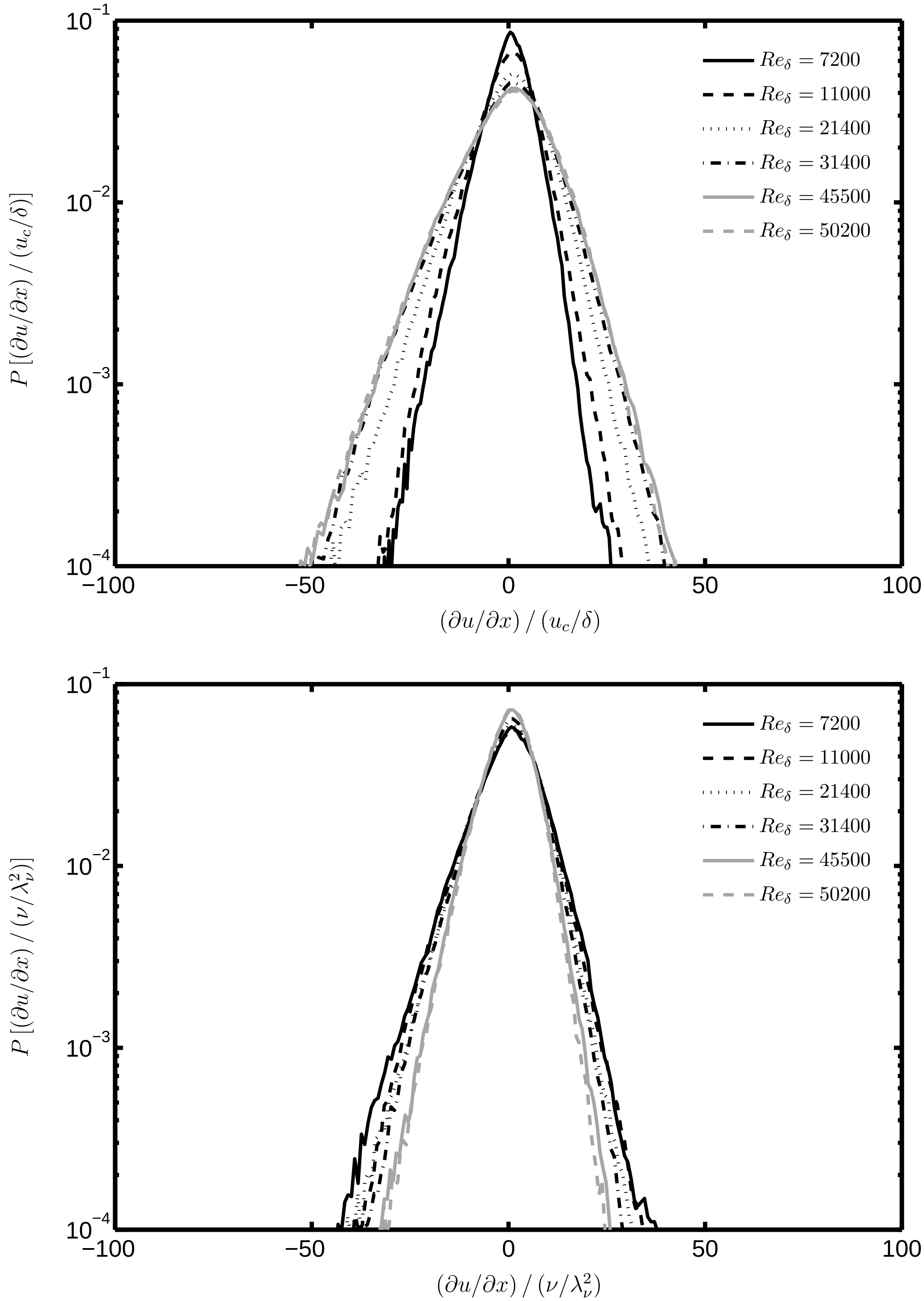

Figure 5.8: Pdfs from all nonreacting cases *INR1* − *INR6* for velocity gradient $\partial u/\partial x$ normalized by outer variables u_c/δ *(top)* and $\partial u/\partial x$ normalized by inner variables ν/λ_ν^2 *(bottom)*.

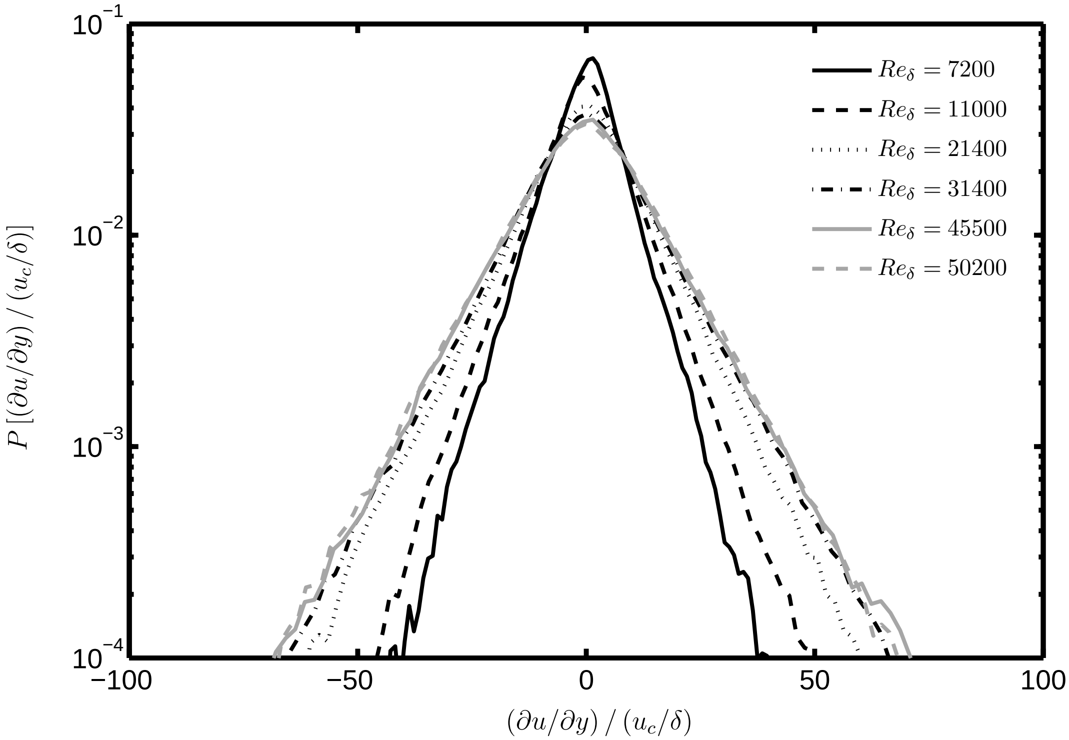

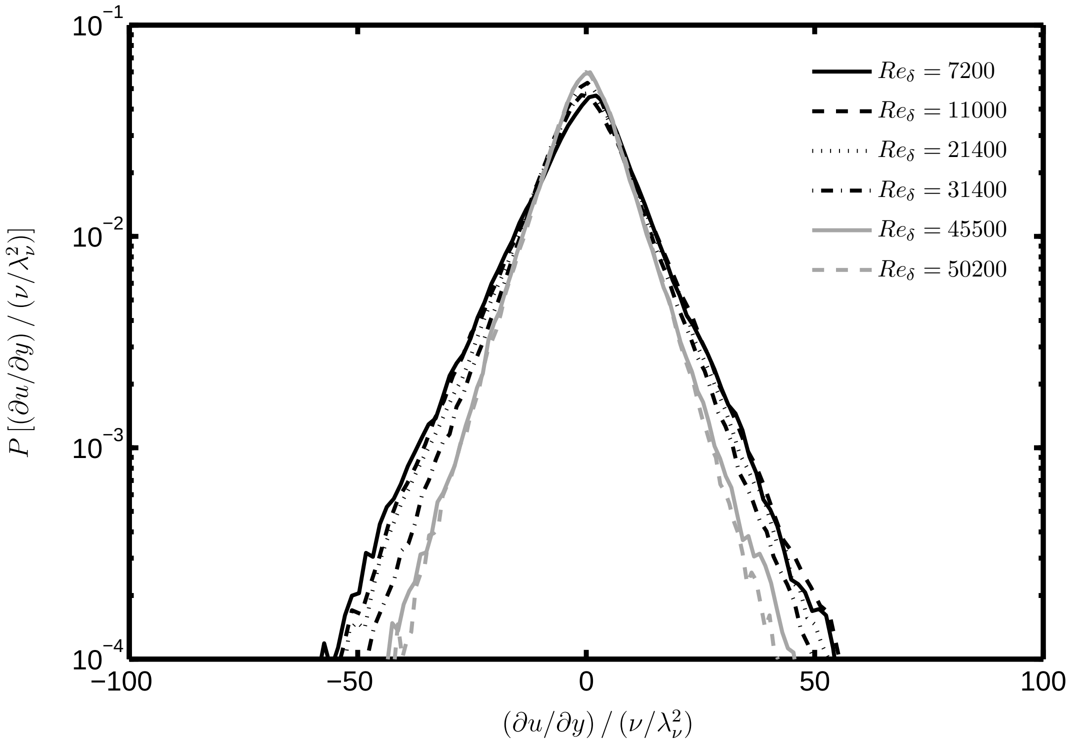

Figure 5.9: Pdfs from all nonreacting cases *INR1 – INR6* for velocity gradient $\partial u/\partial y$ normalized by outer variables u_c/δ *(top)* and $\partial u/\partial y$ normalized by inner variables ν/λ_ν^2 *(bottom)*.

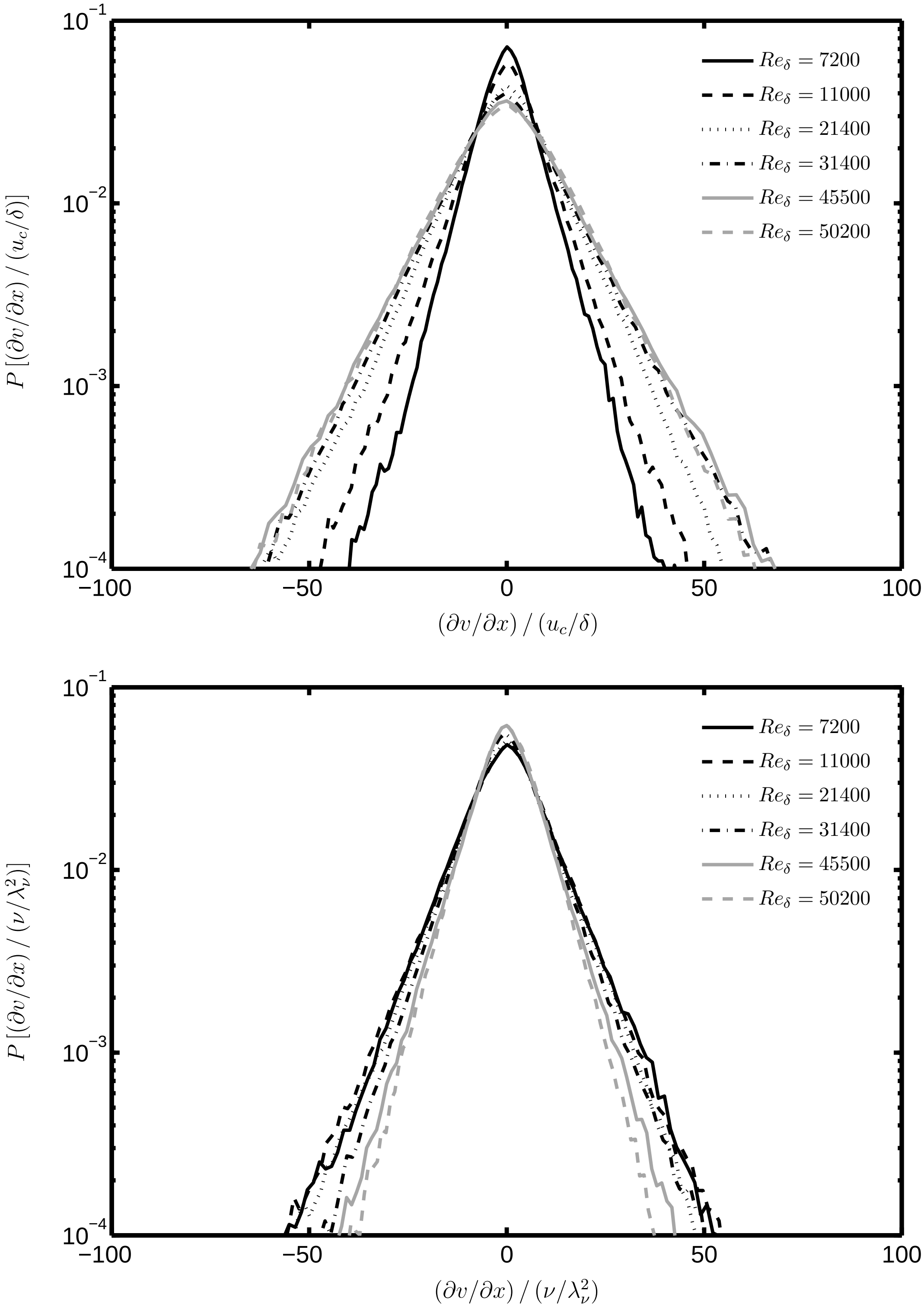

Figure 5.10: Pdfs from all nonreacting cases *INR1 – INR6* for velocity gradient $\partial v/\partial x$ normalized by outer variables u_c/δ *(top)* and $\partial v/\partial x$ normalized by inner variables ν/λ_ν^2 *(bottom)*.

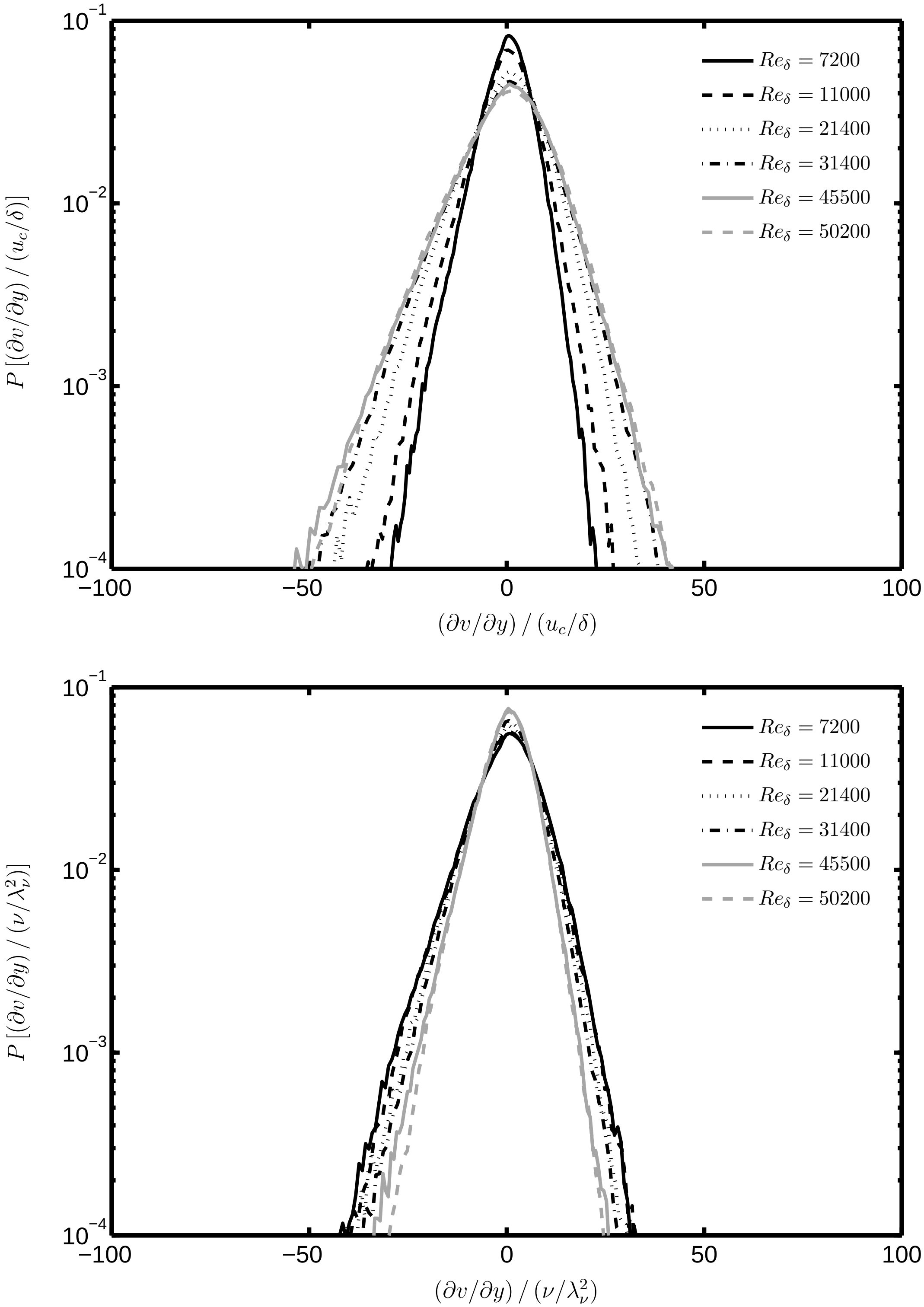

Figure 5.11: Pdfs from all nonreacting cases *INR1 – INR6* for velocity gradient $\partial v/\partial y$ normalized by outer variables u_c/δ *(top)* and $\partial v/\partial y$ normalized by inner variables ν/λ_ν^2 *(bottom)*.

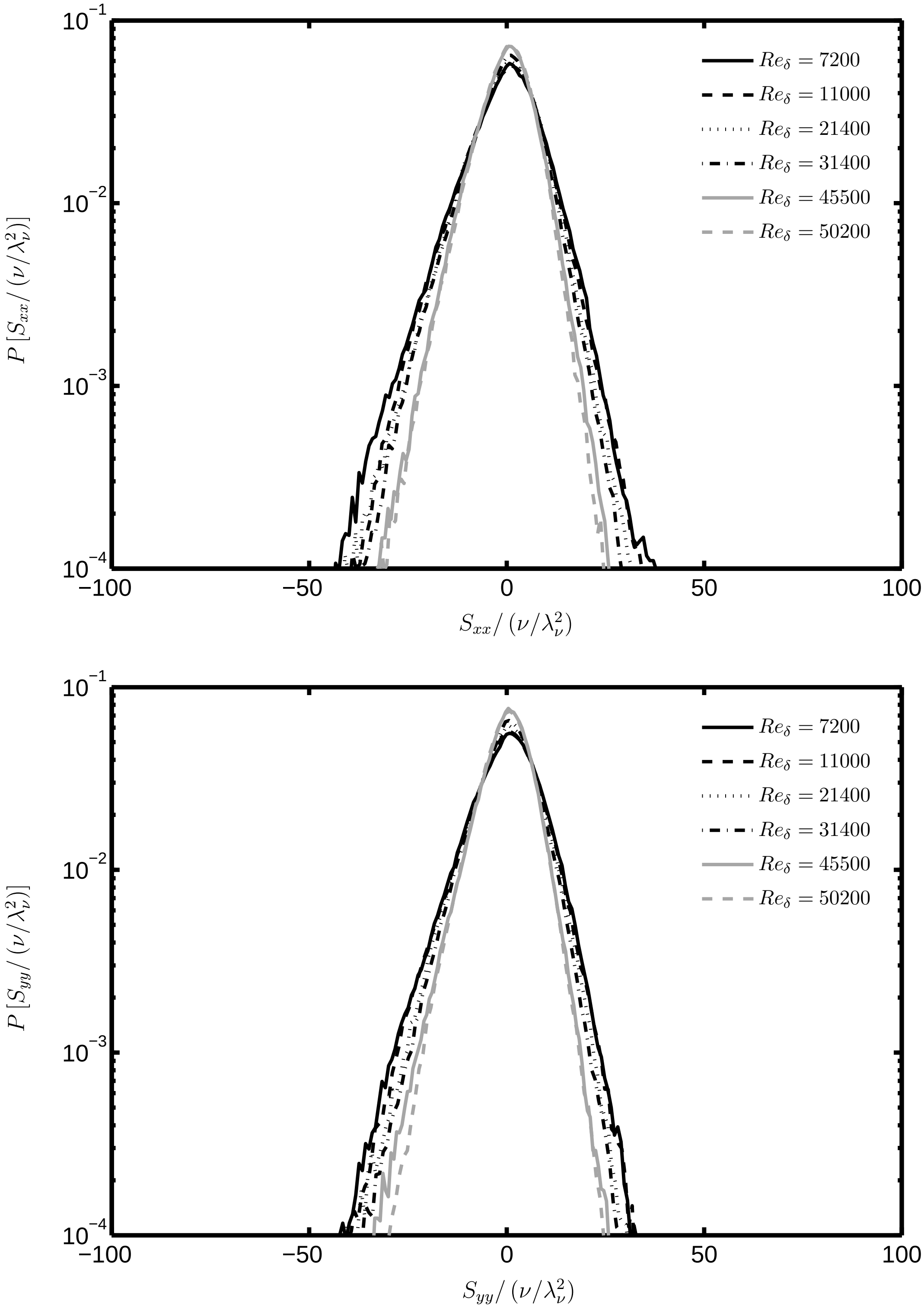

Figure 5.12: Pdfs from all nonreacting cases *INR1 – INR6* for strain rate components S_{xx} *(top)* and S_{yy} *(bottom)* normalized by inner variables ν/λ_ν^2.

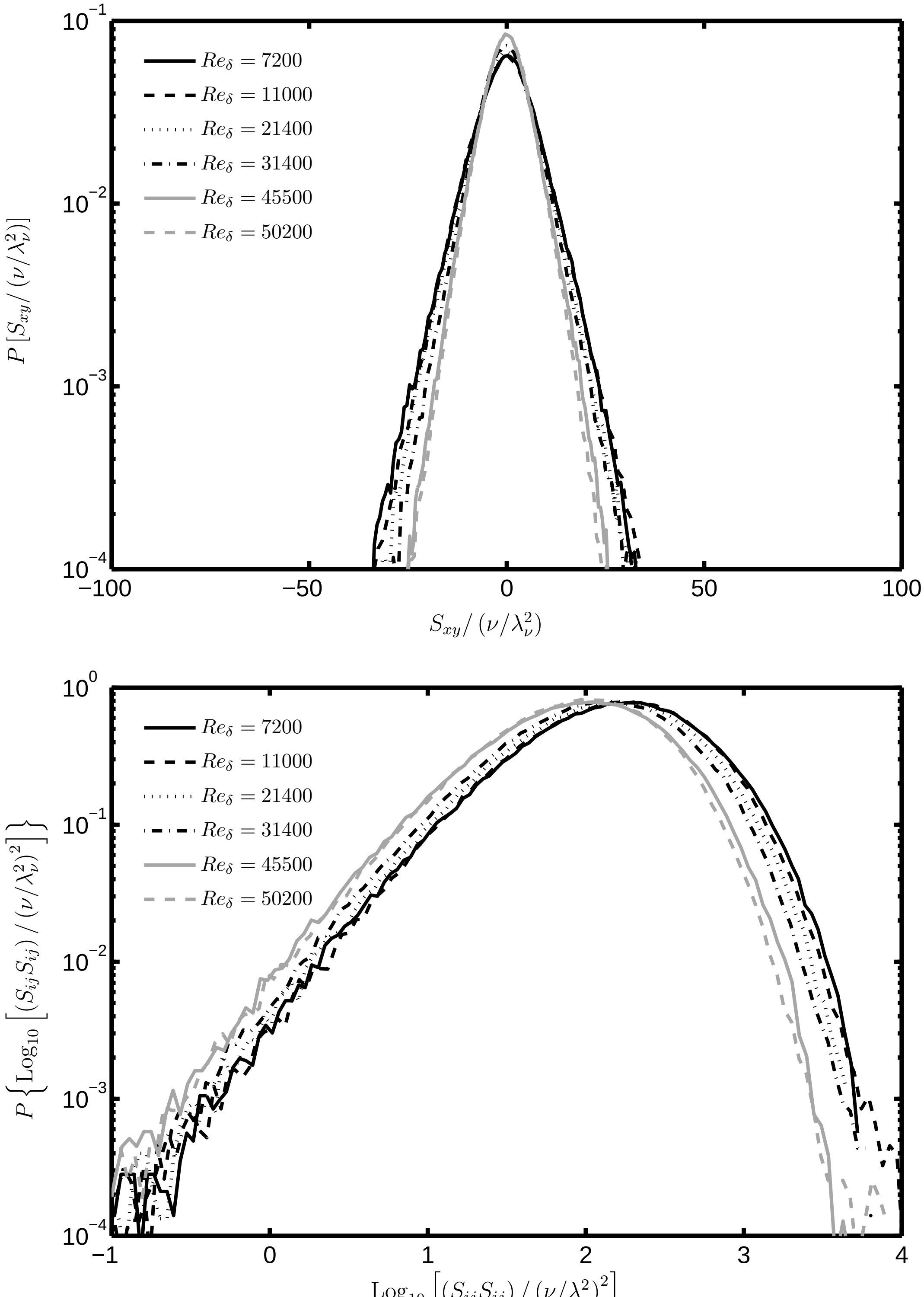

Figure 5.13: Pdfs from all nonreacting cases *INR1* − *INR6* for strain rate components S_{xy} *(top)* and $\mathrm{Log}_{10}\left(S_{ij}S_{ij}\right)$ *(bottom)* normalized by inner variables ν/λ_ν^2 and $\left(\nu/\lambda_\nu^2\right)^2$.

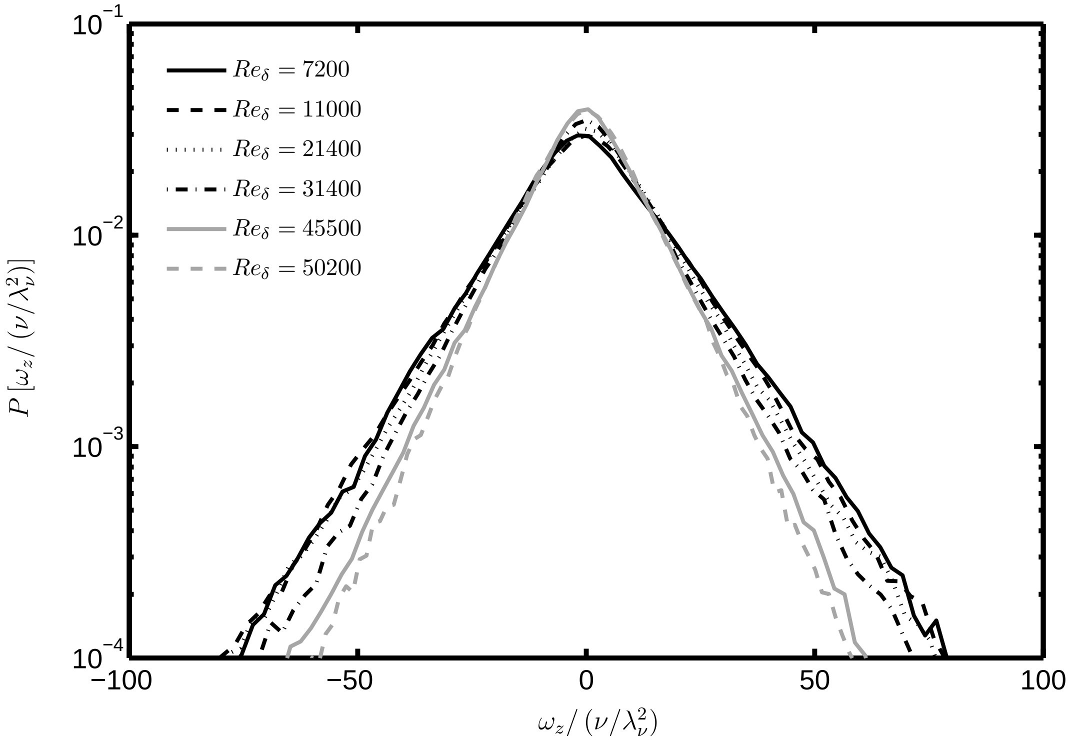

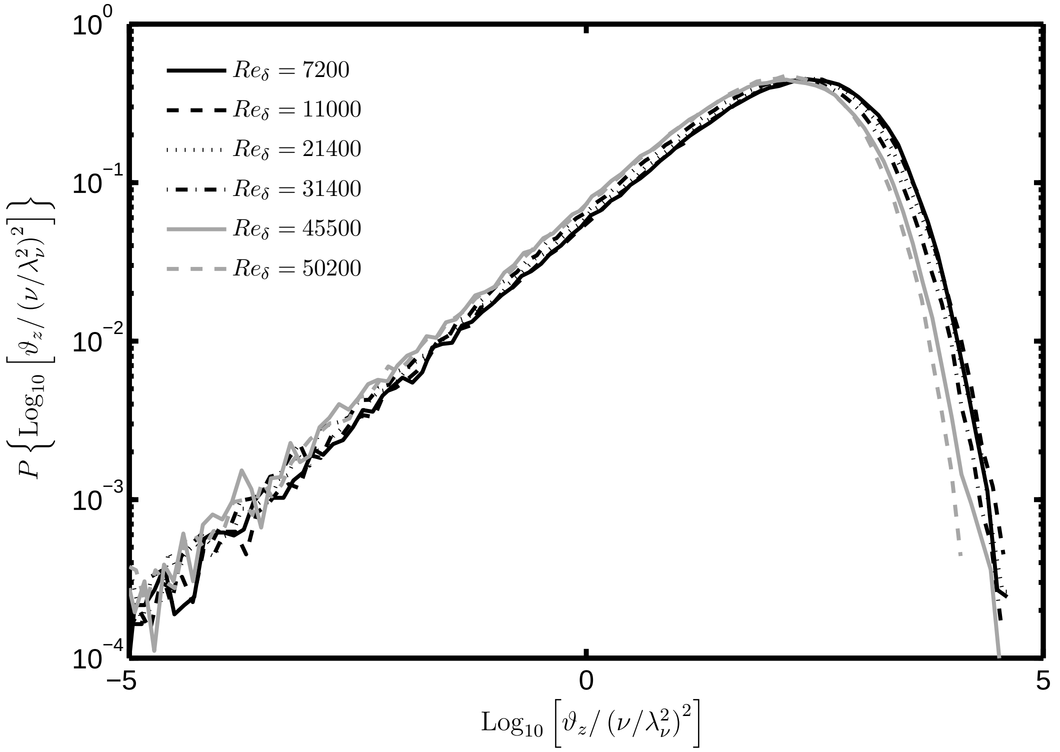

Figure 5.14: Pdfs from all nonreacting cases *INR1 − INR6* for vorticity ω_z *(top)* and enstrophy $\mathrm{Log}_{10}\left(\vartheta_z\right)$ *(bottom)* normalized by inner variables ν/λ_ν^2 and $\left(\nu/\lambda_\nu^2\right)^2$.

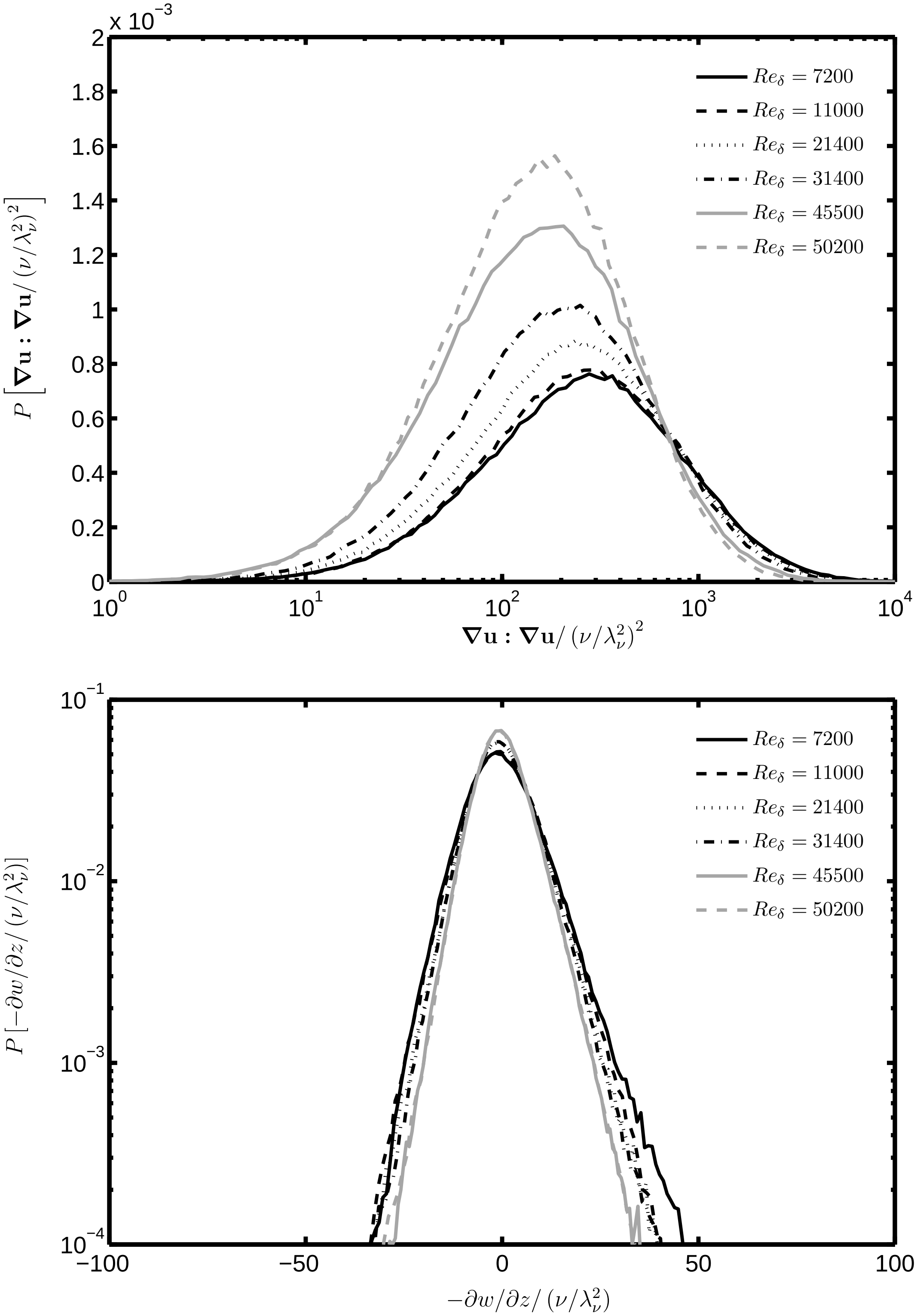

Figure 5.15: Pdfs from all nonreacting cases *INR1* – *INR6* for contraction of the instantaneous velocity gradient tensor $\nabla\mathbf{u} : \nabla\mathbf{u}$ *(top)* and two-dimensional divergence $-\partial w/\partial z$ *(bottom)* normalized by inner variables $\left(\nu/\lambda_\nu^2\right)^2$ and ν/λ_ν^2.

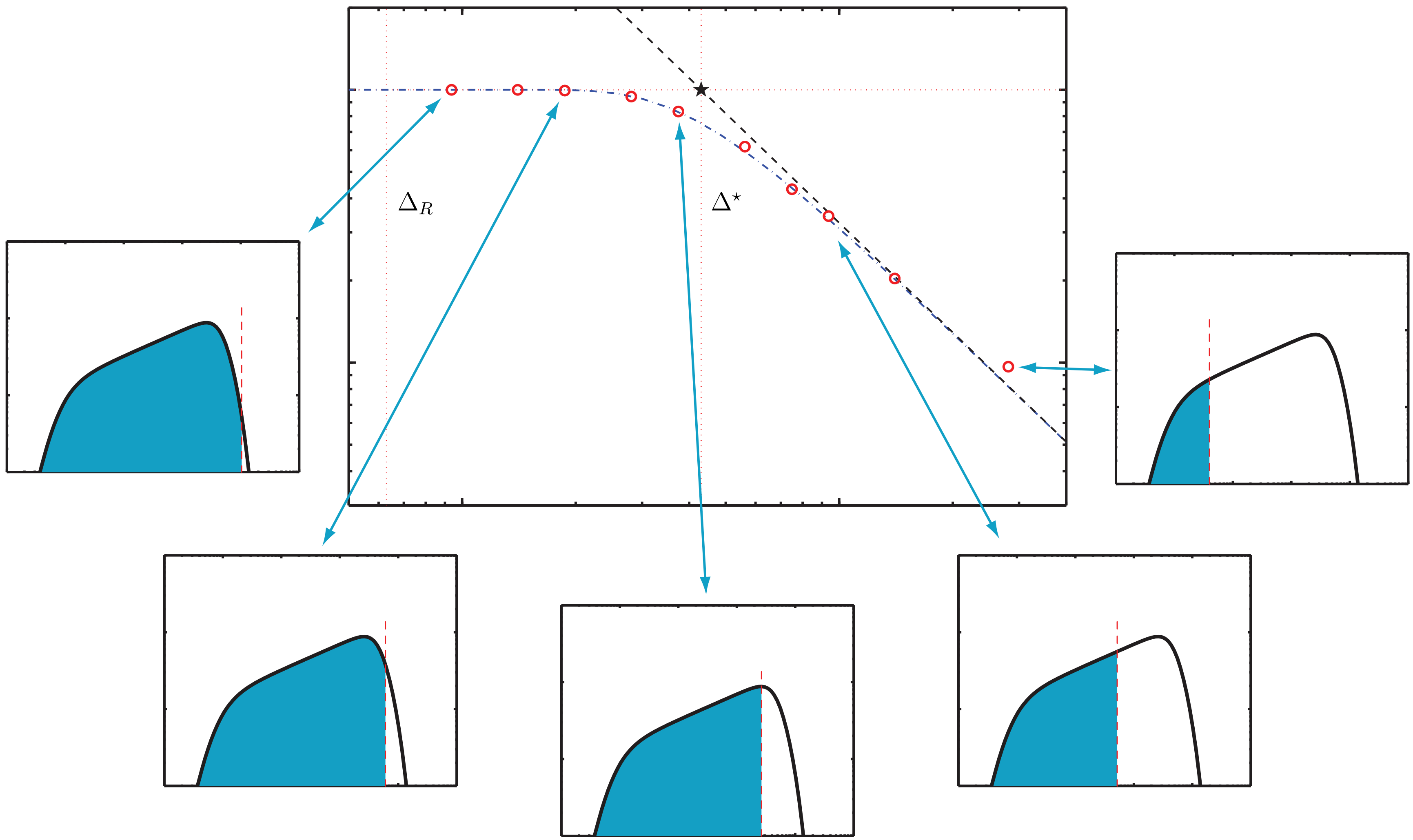

Figure 5.16: Schematic indicating procedure for obtaining resolution length scale $\Delta^\star$ from artificially-degraded experimental data via successive, spectrally sharp, low-pass filtering.

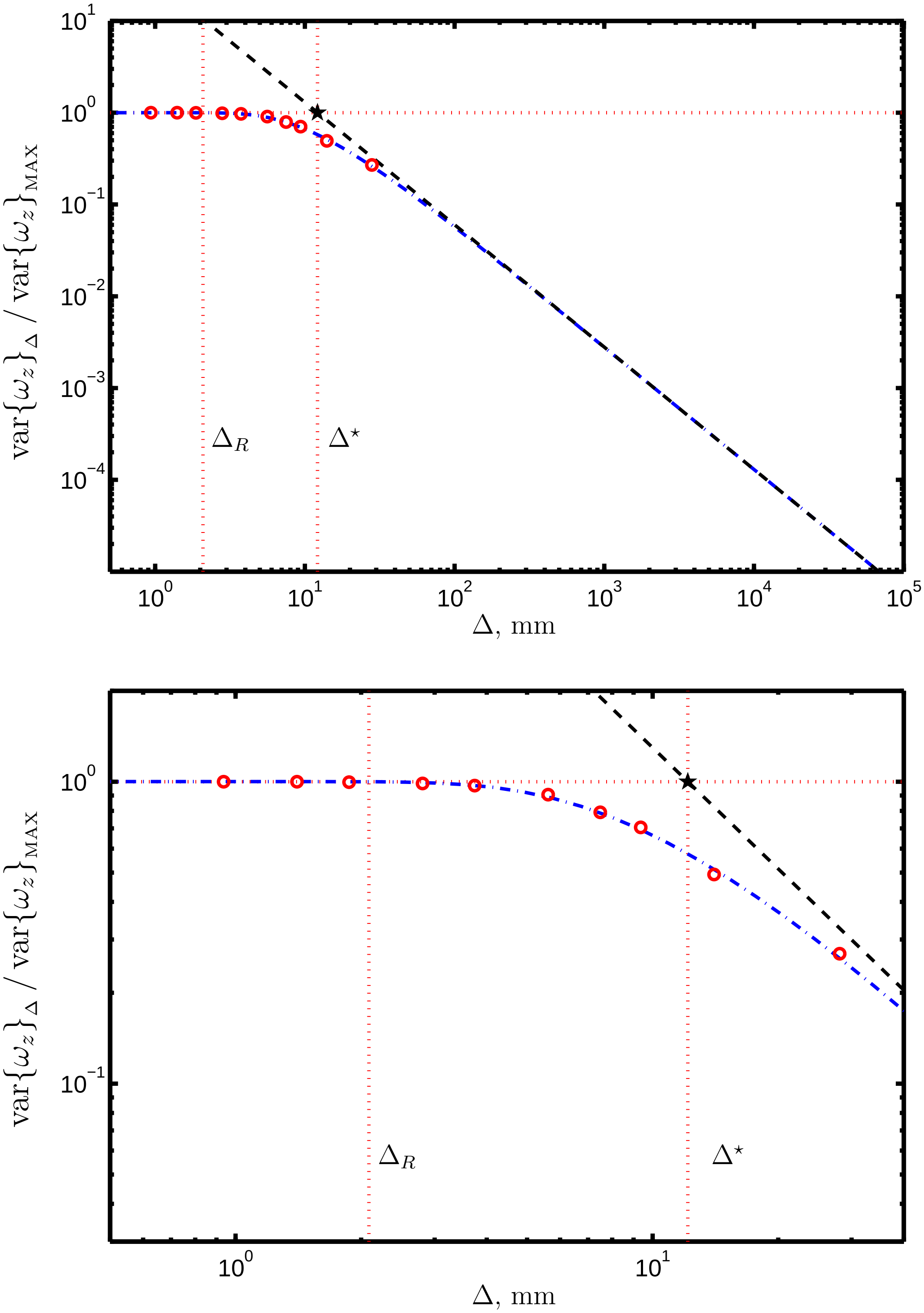

Figure 5.17: Results from low-pass filtering to determine effective length scale $\Delta^{\star}$ for case *INR1*, $Re_{\delta} = 7200$.

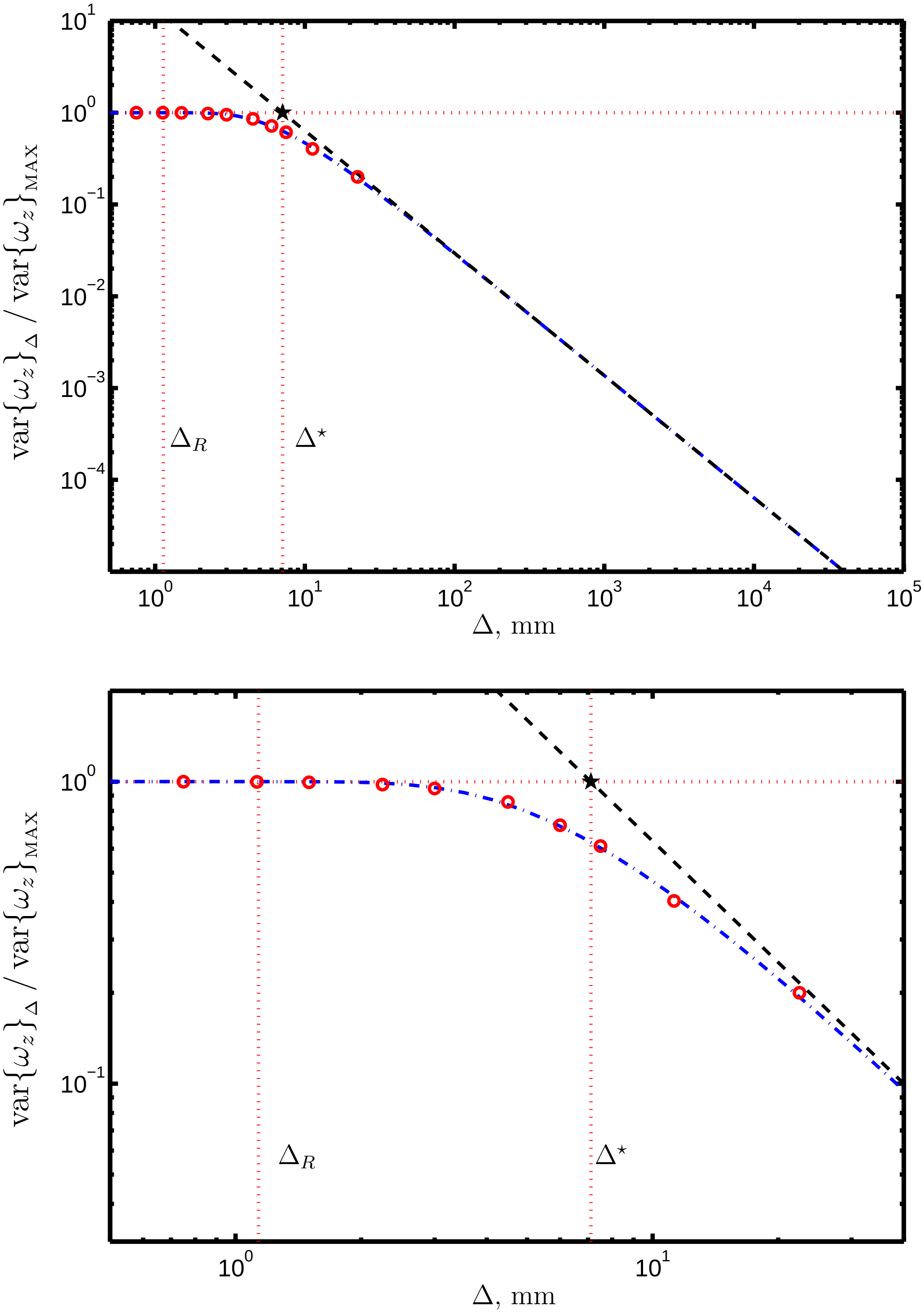

Figure 5.18: Results from low-pass filtering to determine effective length scale $\Delta^\star$ for case *INR2*, $Re_\delta = 11\,000$.

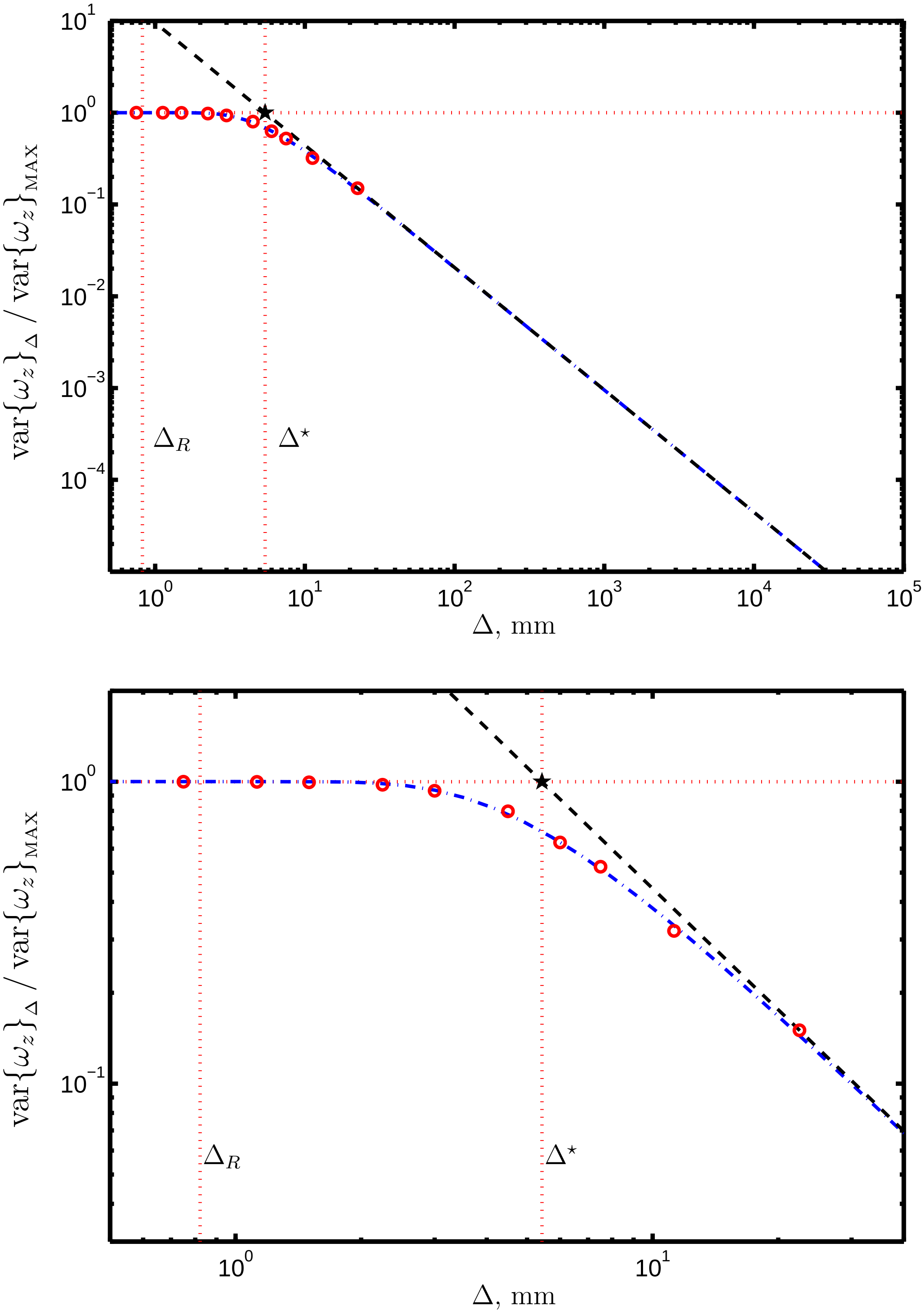

Figure 5.19: Results from low-pass filtering to determine effective length scale $\Delta^\star$ for case *INR3*, $Re_\delta = 21\,400$.

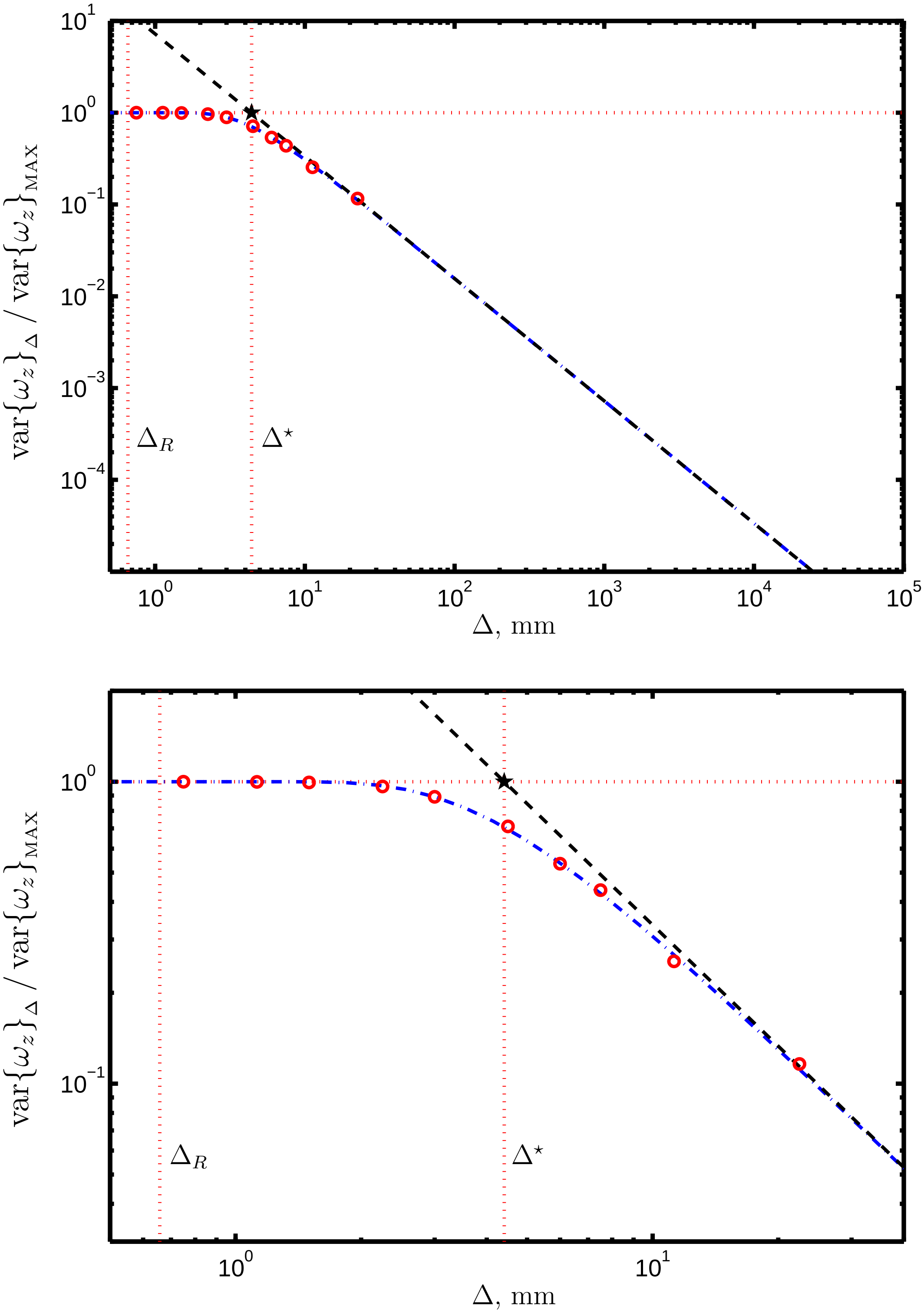

Figure 5.20: Results from low-pass filtering to determine effective length scale $\Delta^\star$ for case *INR4*, $Re_\delta = 31\,400$.

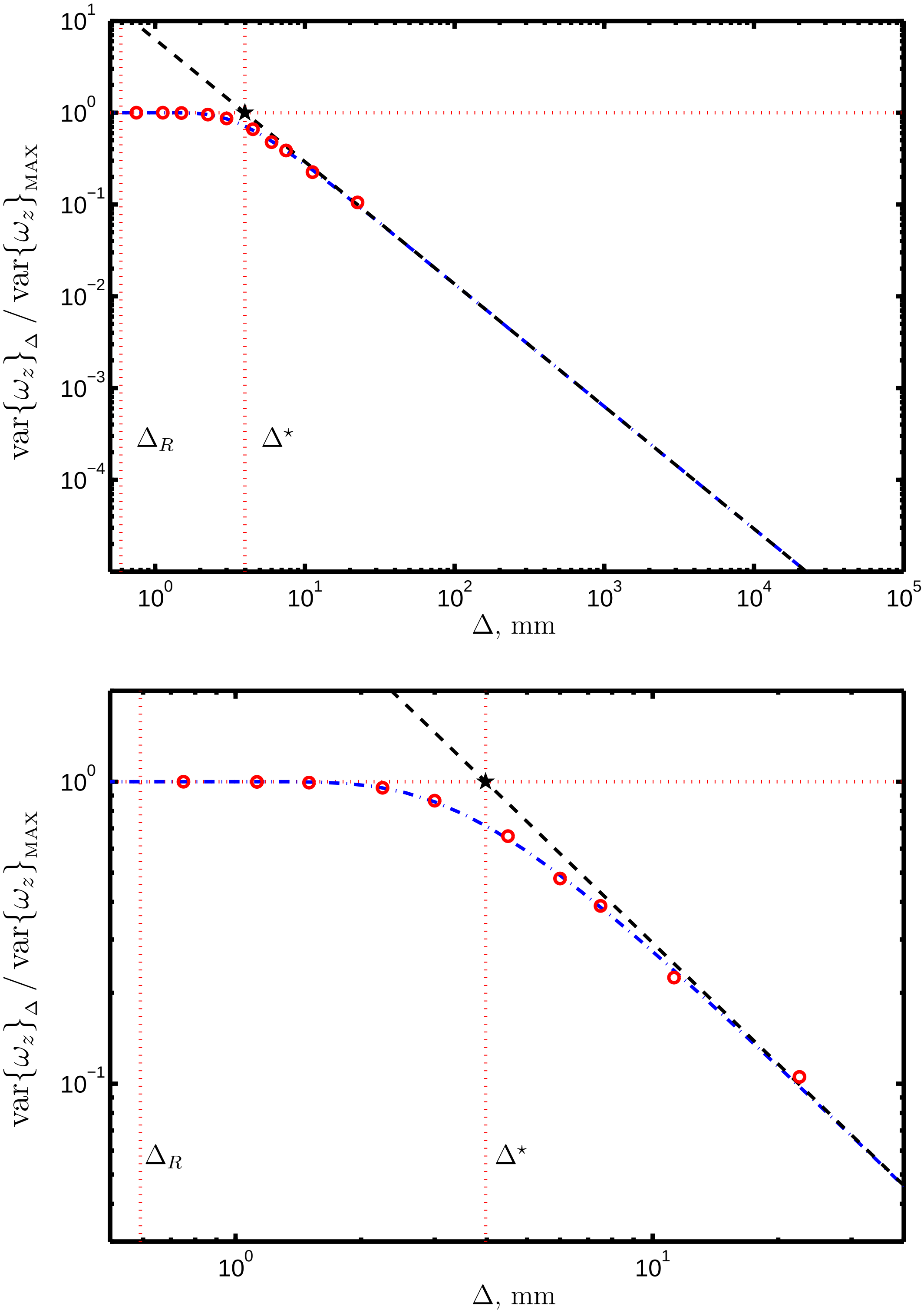

Figure 5.21: Results from low-pass filtering to determine effective length scale $\Delta^\star$ for case *INR5*, $Re_\delta = 45\,500$.

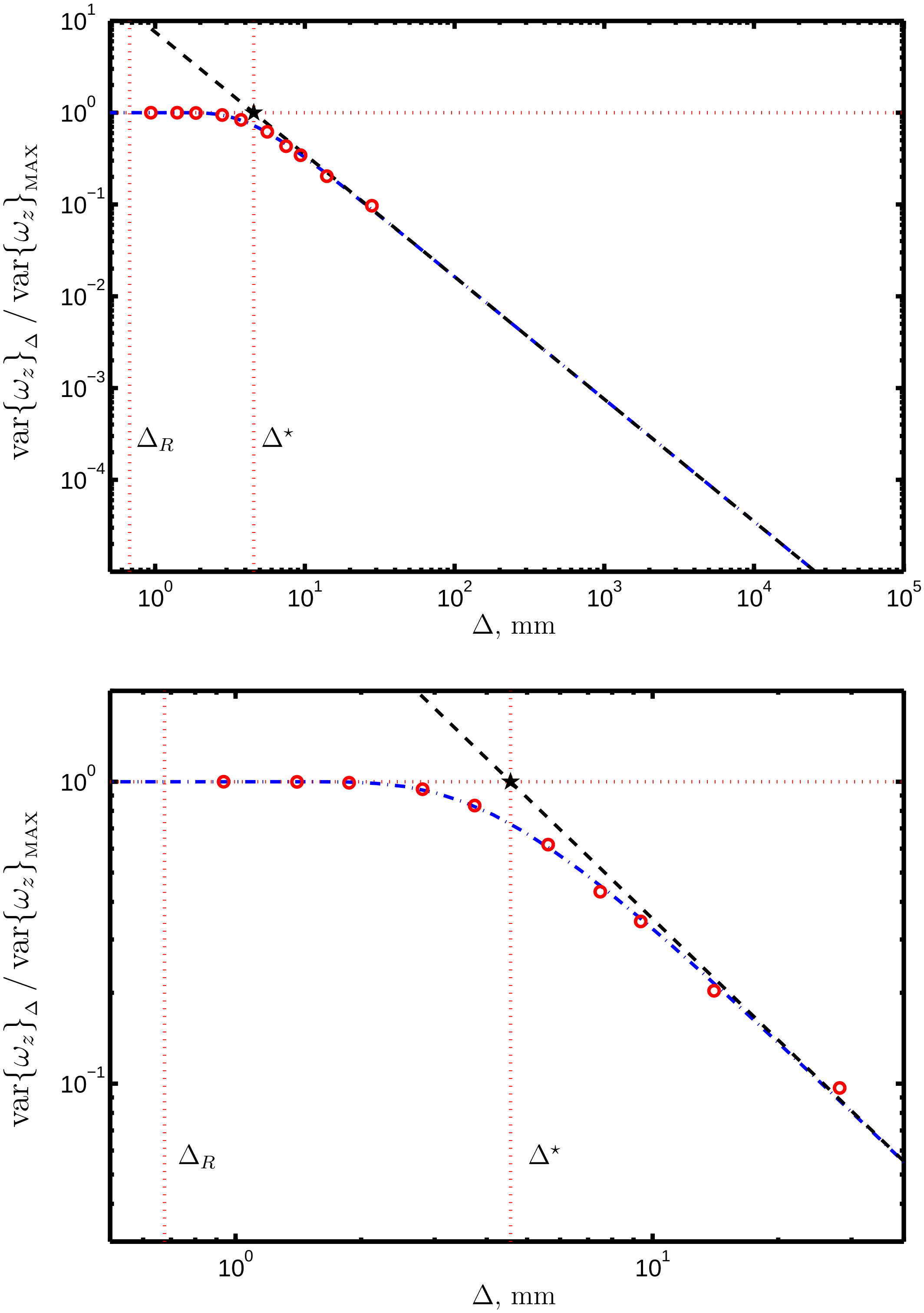

Figure 5.22: Results from low-pass filtering to determine effective length scale $\Delta^\star$ for case *INR6*, $Re_\delta = 50\,200$.

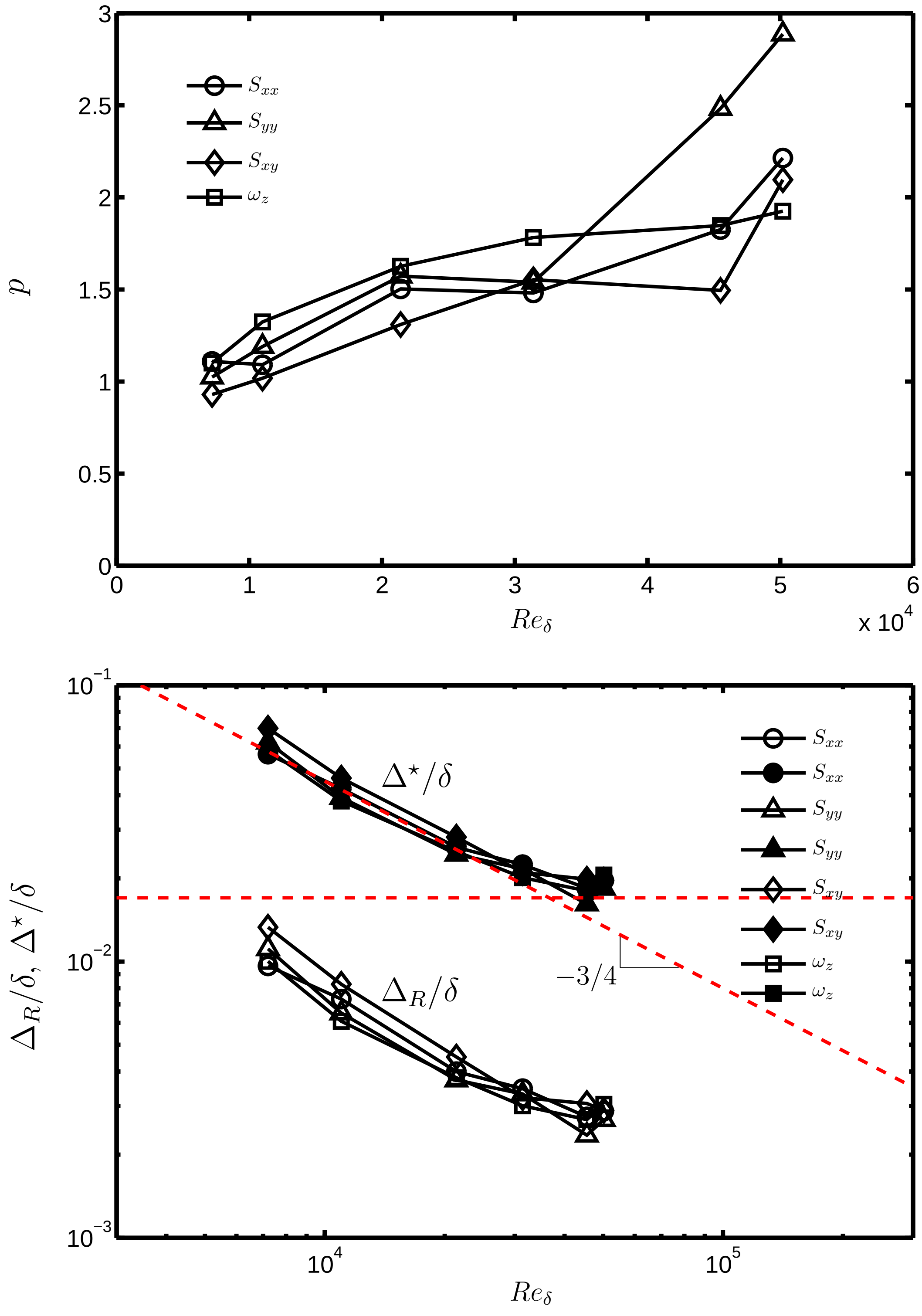

Figure 5.23: Spectral roll-off parameter p *(top)* and normalized length scale Δ_R/δ with associated $\Delta^\star/\delta$ *(bottom)* obtained from three strain rate components S_{xx}, S_{yy}, S_{xy} and vorticity ω_z at Re_δ corresponding to each case in Table 3.3.

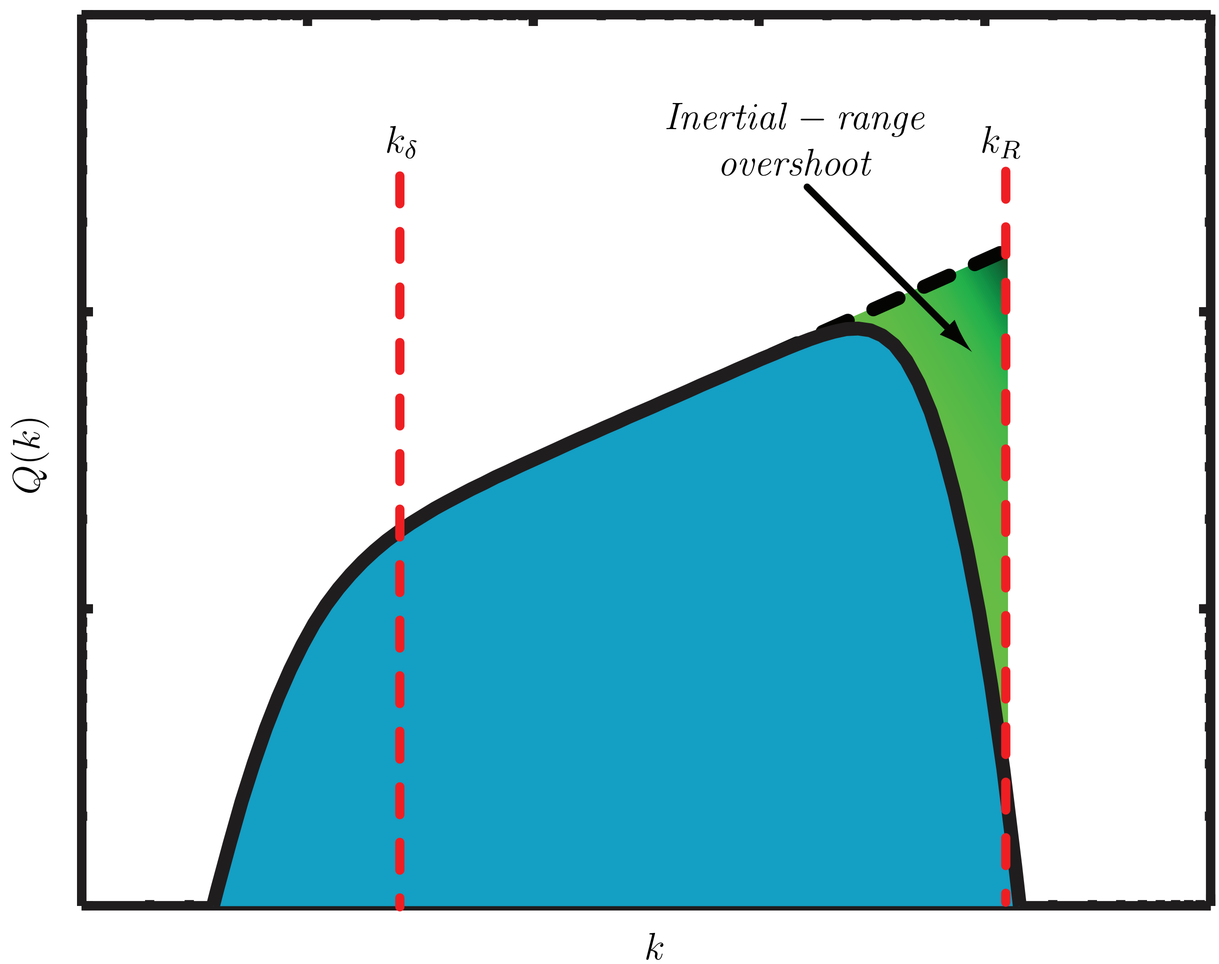

Figure 5.24: Schematic diagram indicating inertial-range overshoot correction of the $D(p)$ contribution to resolution-corrected inner scaling. Here the $D(p)$ function compensates for the overprediction of the inertial-range scaling in the dissipative scales.

Re_δ	δ, m	Δ_{IW}, mm	Inertial- and dissipation-range spectral parameters and resulting factors							
			$\langle p \rangle$, [-]	$\langle \Delta_R \rangle$, mm	Λ_ν, [-]	$\langle \Delta^\star \rangle$, mm	$\Lambda^\star$, [-]	$\langle \Delta^\star \rangle / \langle \Delta_R \rangle$	$D(p)$	$\mathcal{N}^\star$, s^{-1}
7200	0.208	0.468	1.041	2.297	8.599	12.845	48.095	5.59	0.0974	4.962
11000	0.187	0.375	1.156	1.314	7.556	7.734	44.458	5.88	0.0918	11.963
21400	0.217	0.375	1.503	0.868	7.072	5.611	45.704	6.46	0.0820	22.298
31400	0.219	0.375	1.589	0.712	7.676	4.666	50.307	6.55	0.0809	36.389
45500	0.221	0.375	1.912	0.598	8.430	3.998	56.366	6.69	0.0780	56.634
50200	0.222	0.468	2.280	0.637	9.620	4.346	65.604	6.82	0.0766	58.158

Table 5.1: Averaged spectral parameters $\langle p \rangle$, $\langle \Delta_R \rangle$ and $\langle \Delta^\star \rangle$ for all cases in Table 3.3 obtained by averaging over results in Fig. 5.23 from ω_z, S_{xx}, S_{yy} and S_{xy}. Here Λ_ν and $\Lambda^\star$ values are from $\Lambda_i \equiv (\Delta_i/\delta) Re_\delta^{3/4}$.

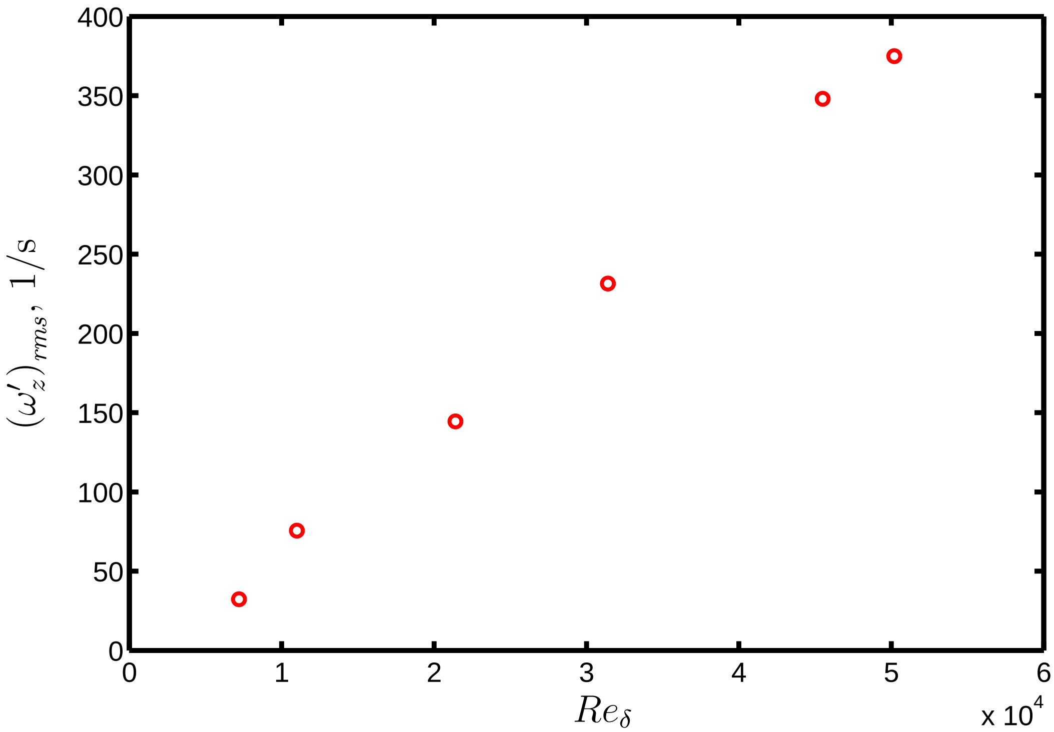

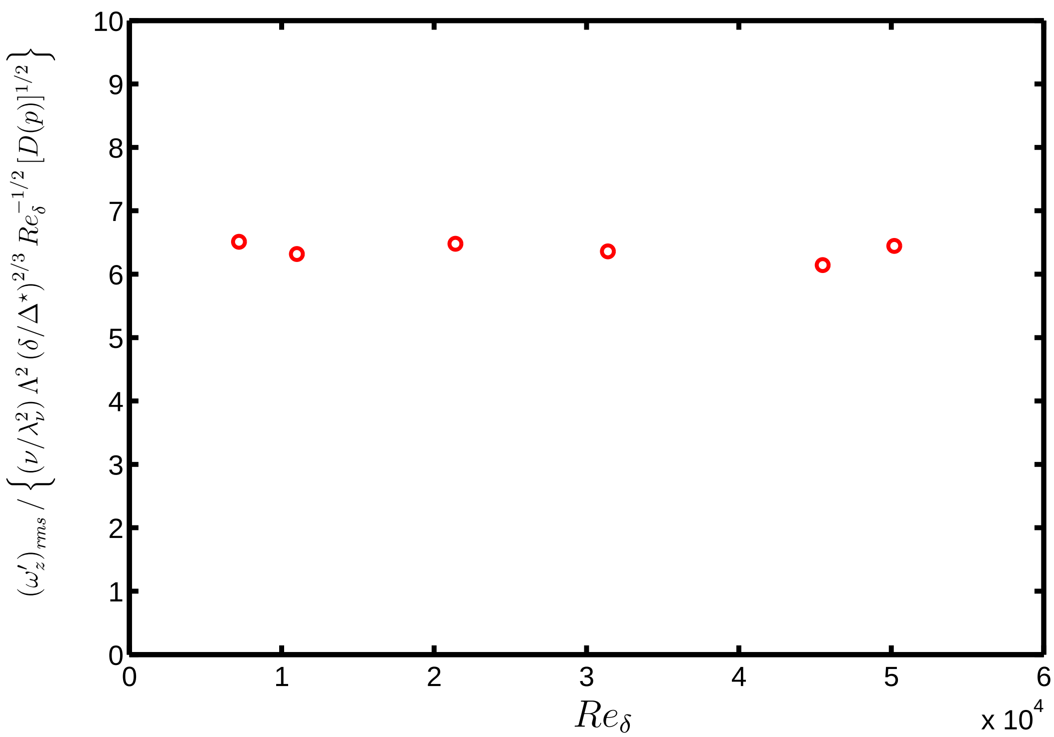

Figure 5.25: Unscaled *rms* of the vorticity $(\omega_z')_{rms}$ plotted against Re_δ *(top)*. Vorticity *rms* $(\omega_z')_{rms}$ normalized by resolution-corrected inner scaling $\mathcal{N}^\star$ *(bottom)*.

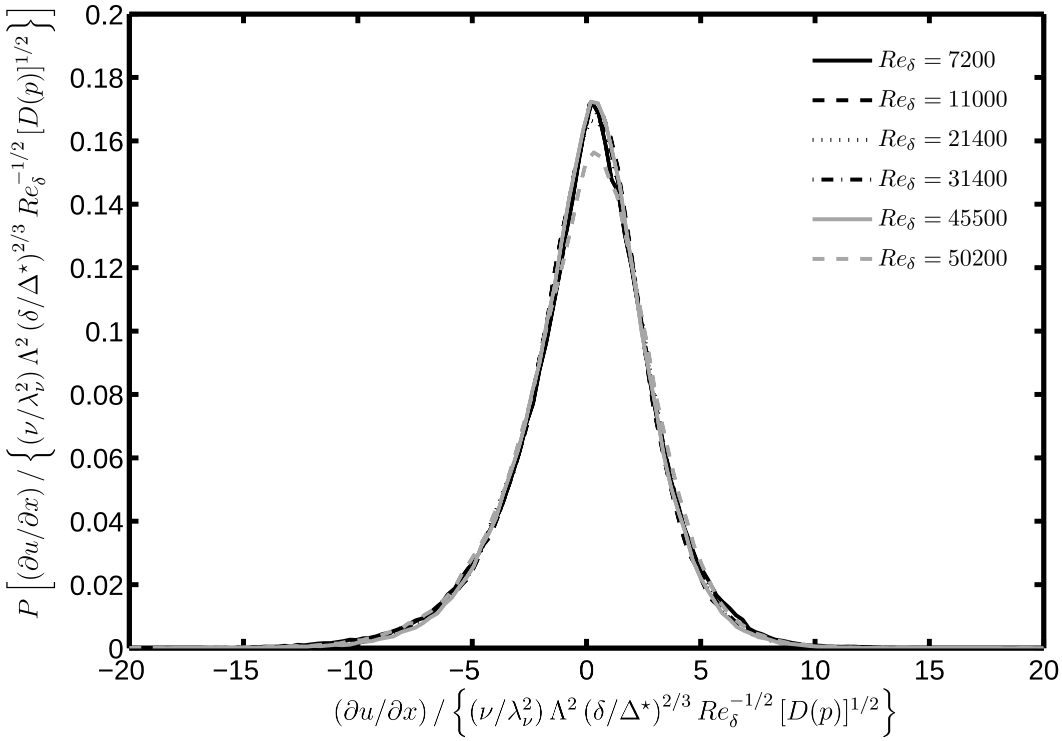

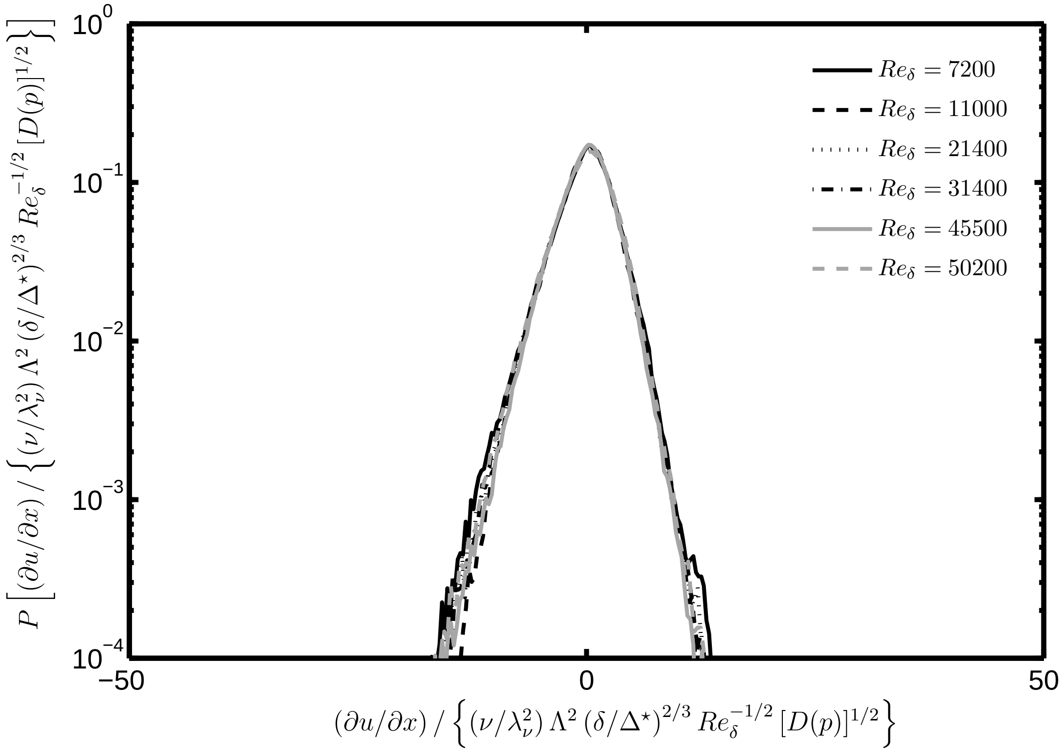

Figure 5.26: Pdfs from all nonreacting cases *INR1* – *INR6* for velocity gradient $\partial u/\partial x$ normalized by resolution-corrected inner scaling $(\nu/\lambda_\nu^2)\,\Lambda^2\,(\delta/\Delta^\star)^{2/3}\,Re_\delta^{-1/2}\,[D(p)]^{1/2}$, shown in linear axes *(top)* and semilogarithmic axes *(bottom)*.

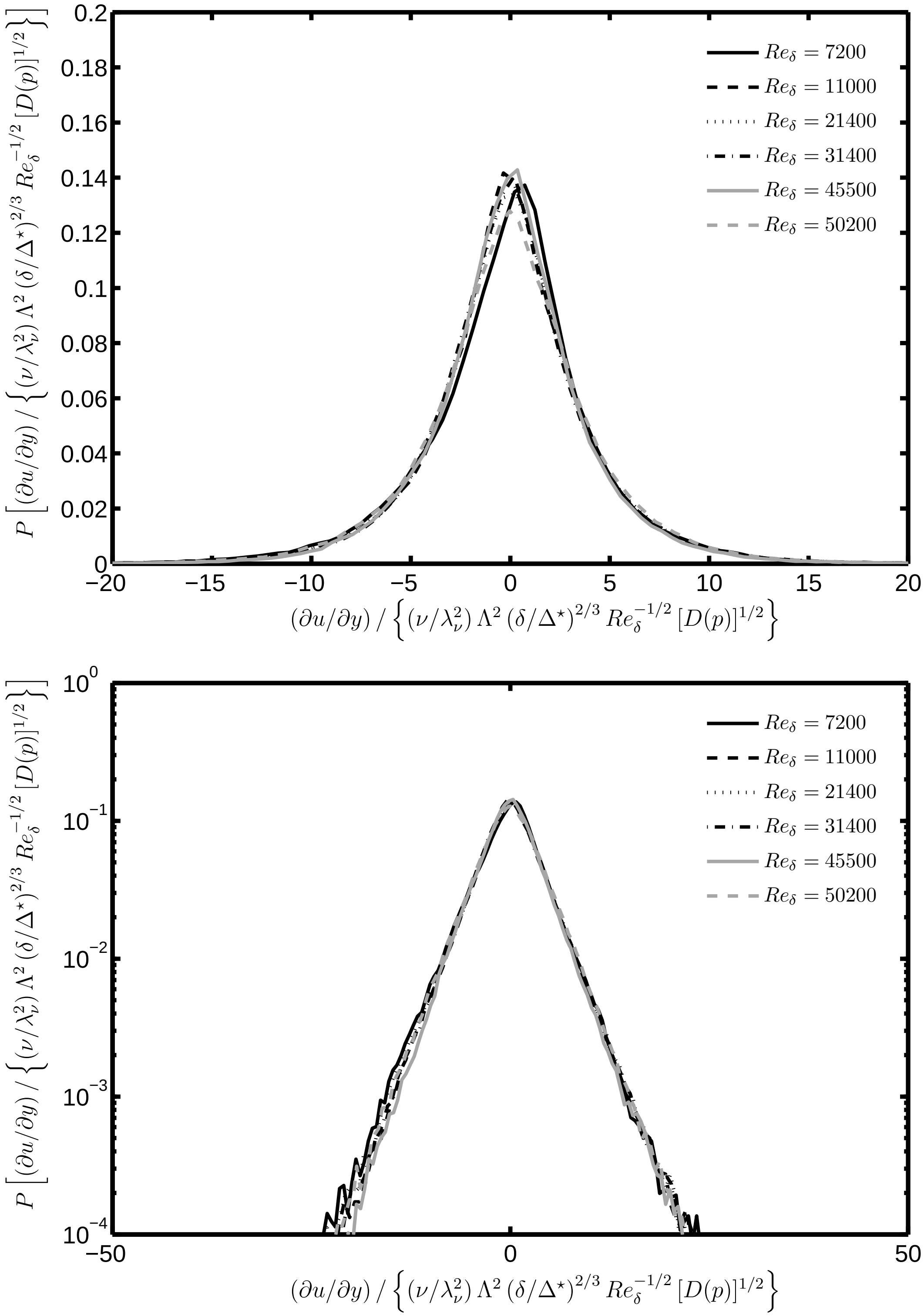

Figure 5.27: Pdfs from all nonreacting cases *INR1* – *INR6* for velocity gradient $\partial u/\partial y$ normalized by resolution-corrected inner scaling $(\nu/\lambda_\nu^2)\,\Lambda^2\,(\delta/\Delta^\star)^{2/3}\,Re_\delta^{-1/2}\,[D(p)]^{1/2}$, shown in linear axes *(top)* and semilogarithmic axes *(bottom)*.

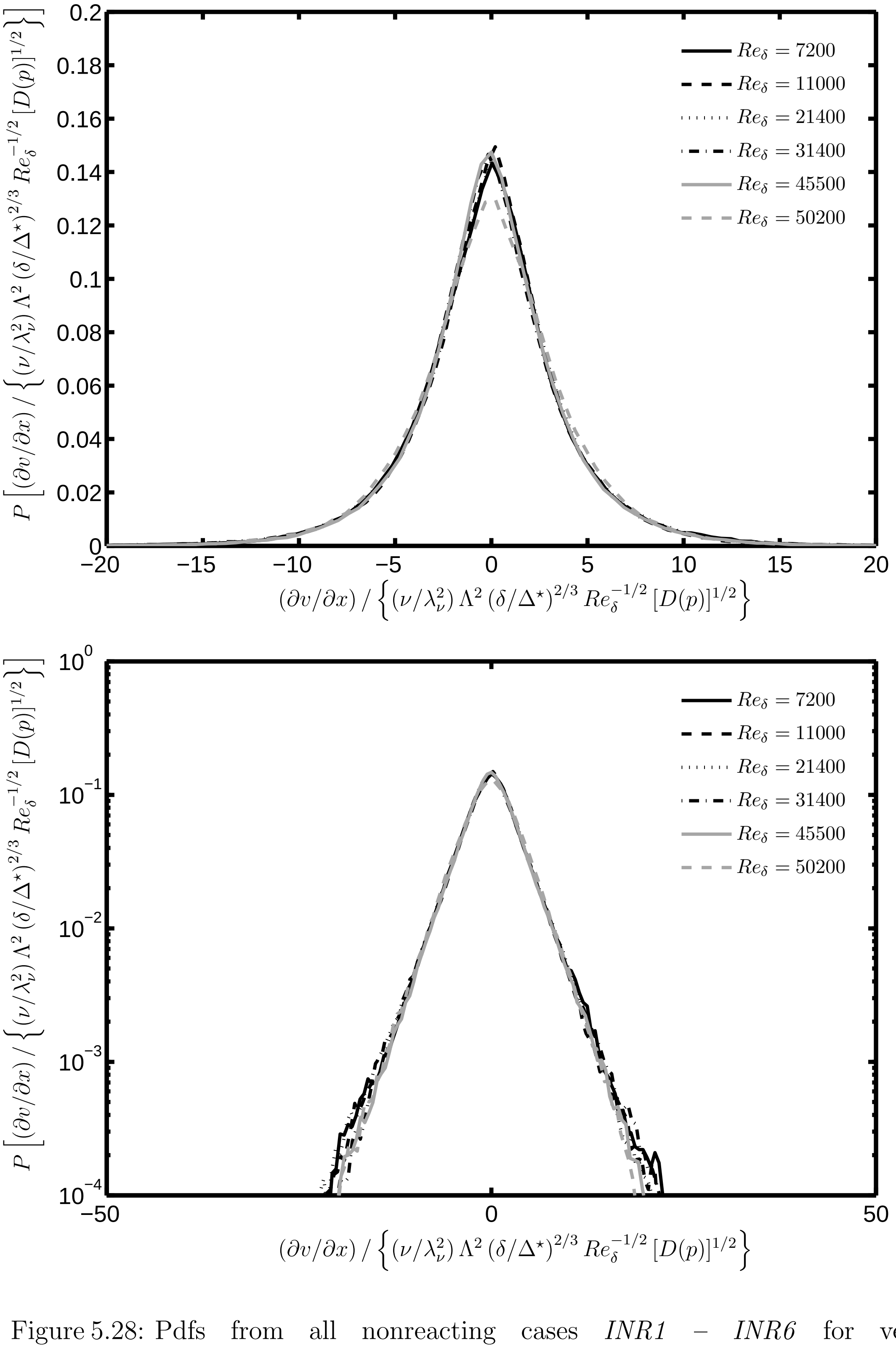

Figure 5.28: Pdfs from all nonreacting cases *INR1* – *INR6* for velocity gradient $\partial v/\partial x$ normalized by resolution-corrected inner scaling $(\nu/\lambda_\nu^2)\,\Lambda^2\,(\delta/\Delta^\star)^{2/3}\,Re_\delta^{-1/2}\,[D(p)]^{1/2}$, shown in linear axes *(top)* and semilogarithmic axes *(bottom)*.

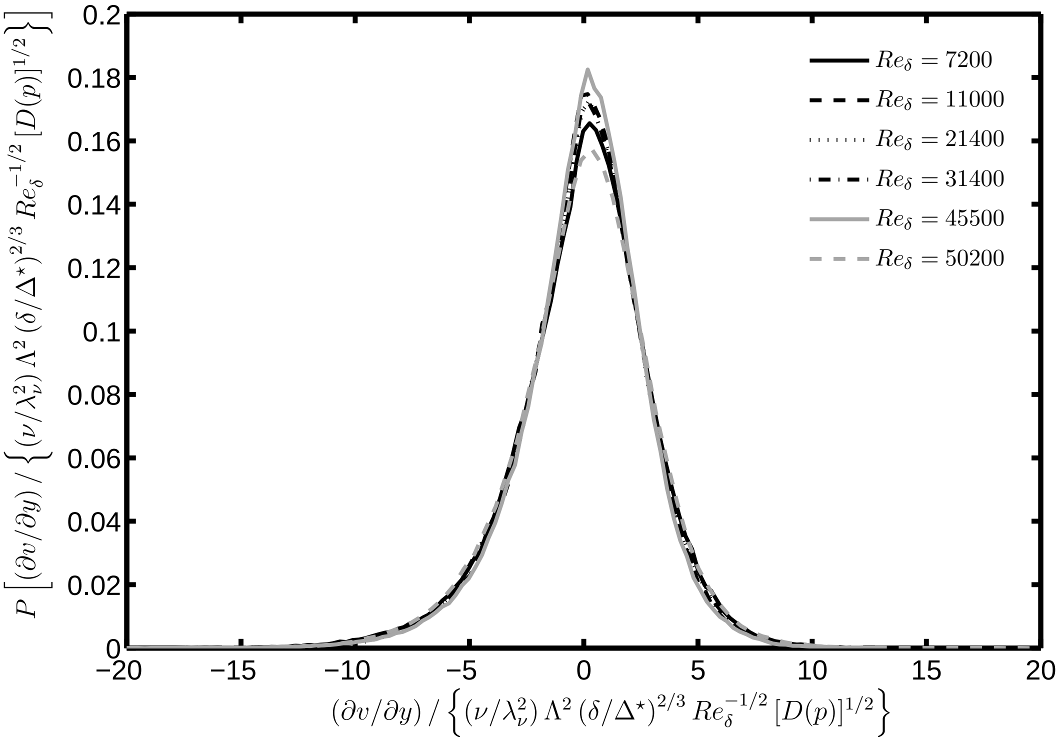

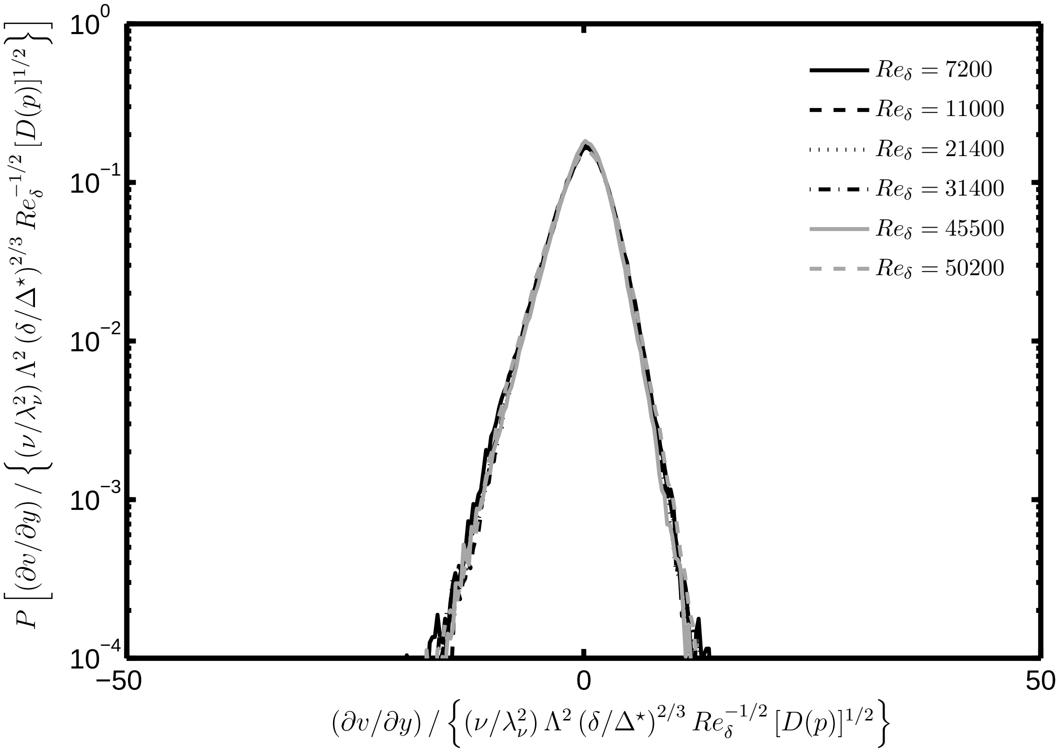

Figure 5.29: Pdfs from all nonreacting cases *INR1* – *INR6* for velocity gradient $\partial v/\partial y$ normalized by resolution-corrected inner scaling $(\nu/\lambda_\nu^2)\,\Lambda^2\,(\delta/\Delta^\star)^{2/3}\,Re_\delta^{-1/2}\,[D(p)]^{1/2}$, shown in linear axes *(top)* and semilogarithmic axes *(bottom)*.

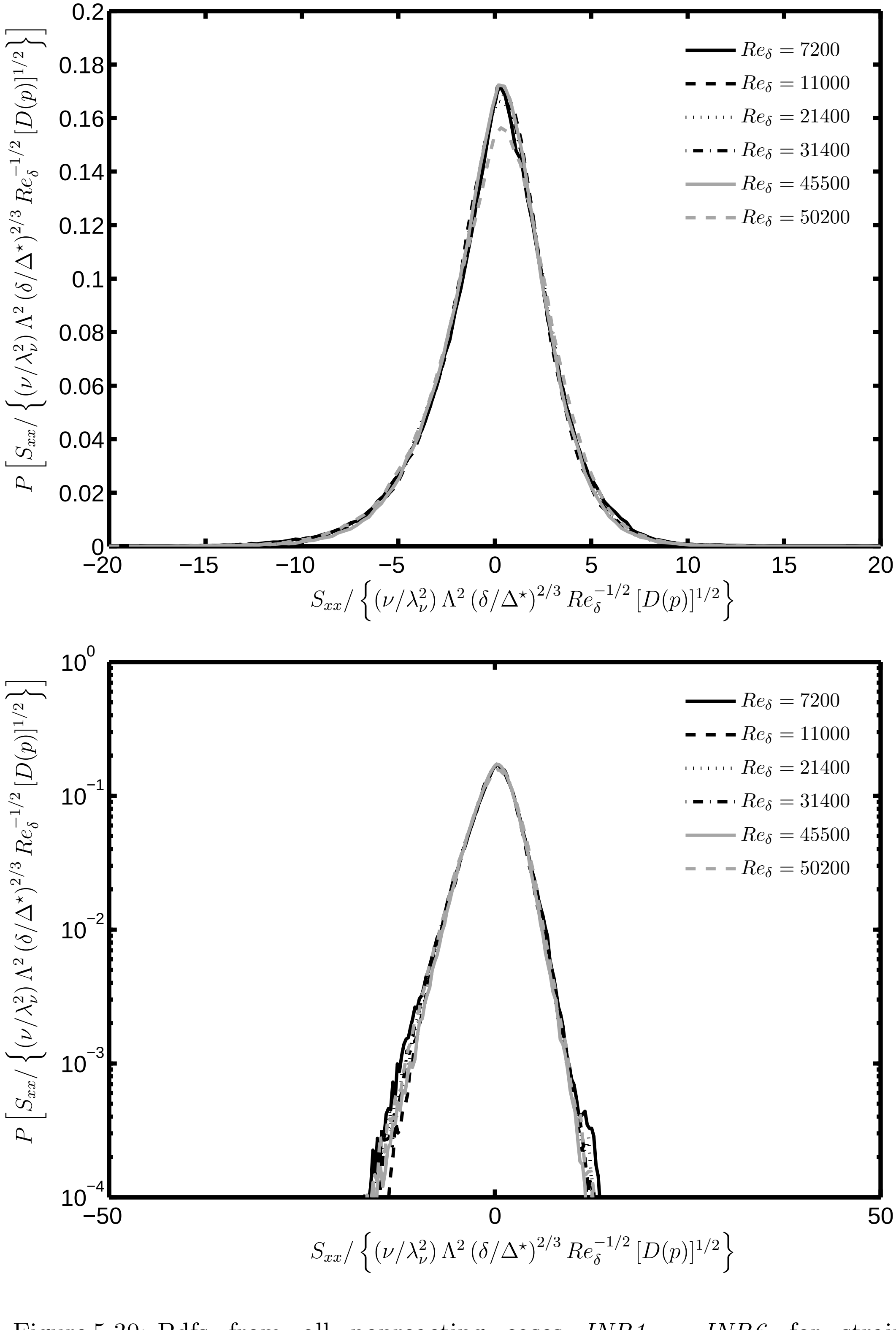

Figure 5.30: Pdfs from all nonreacting cases *INR1* – *INR6* for strain rate component S_{xx} normalized by resolution-corrected inner scaling $(\nu/\lambda_\nu^2)\,\Lambda^2\,(\delta/\Delta^\star)^{2/3}\,Re_\delta^{-1/2}\,[D(p)]^{1/2}$, shown in linear axes *(top)* and semilogarithmic axes *(bottom)*.

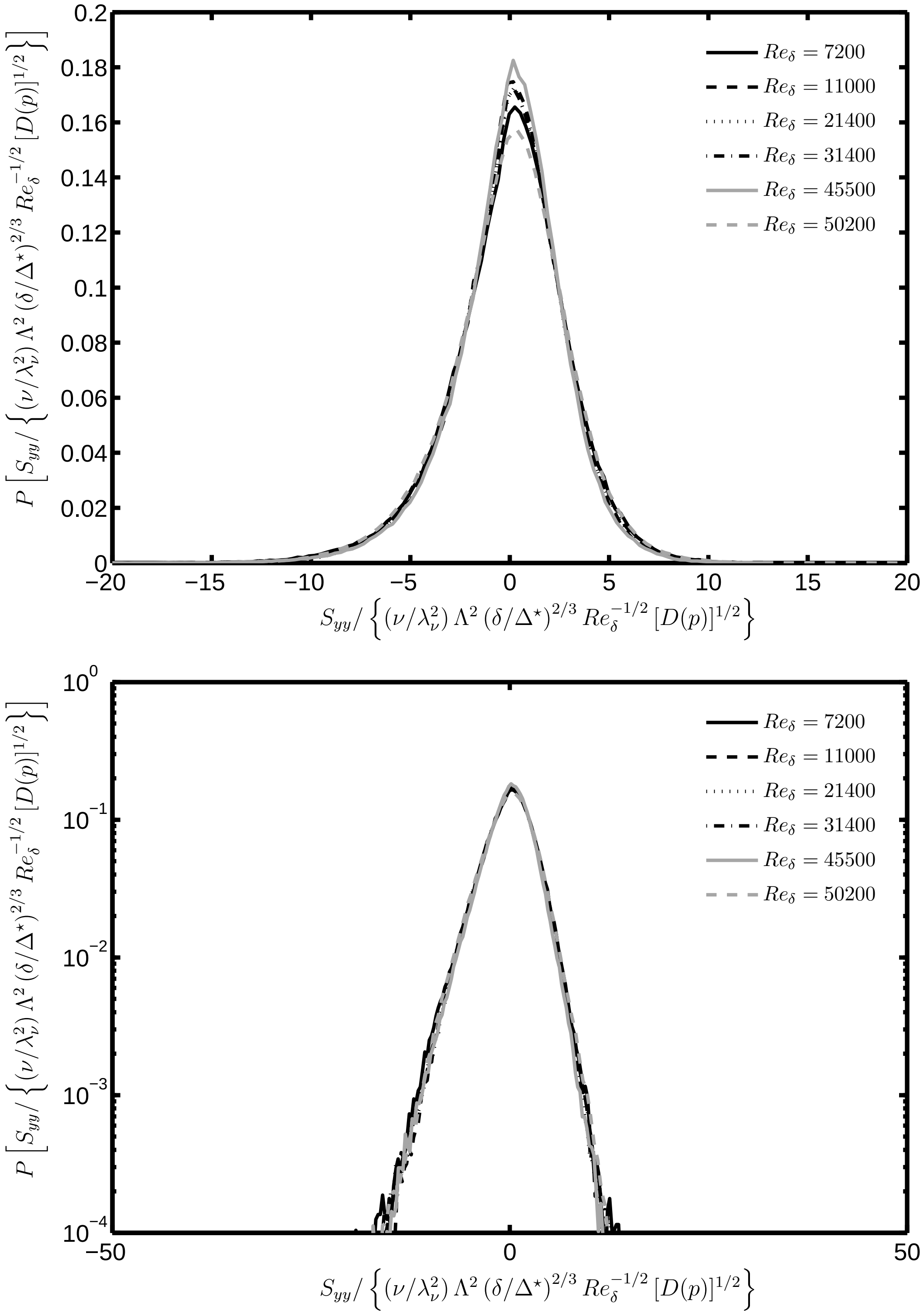

Figure 5.31: Pdfs from all nonreacting cases *INR1 – INR6* for strain rate component S_{yy} normalized by resolution-corrected inner scaling $(\nu/\lambda_\nu^2)\,\Lambda^2\,(\delta/\Delta^\star)^{2/3}\,Re_\delta^{-1/2}\,[D(p)]^{1/2}$, shown in linear axes *(top)* and semilogarithmic axes *(bottom)*.

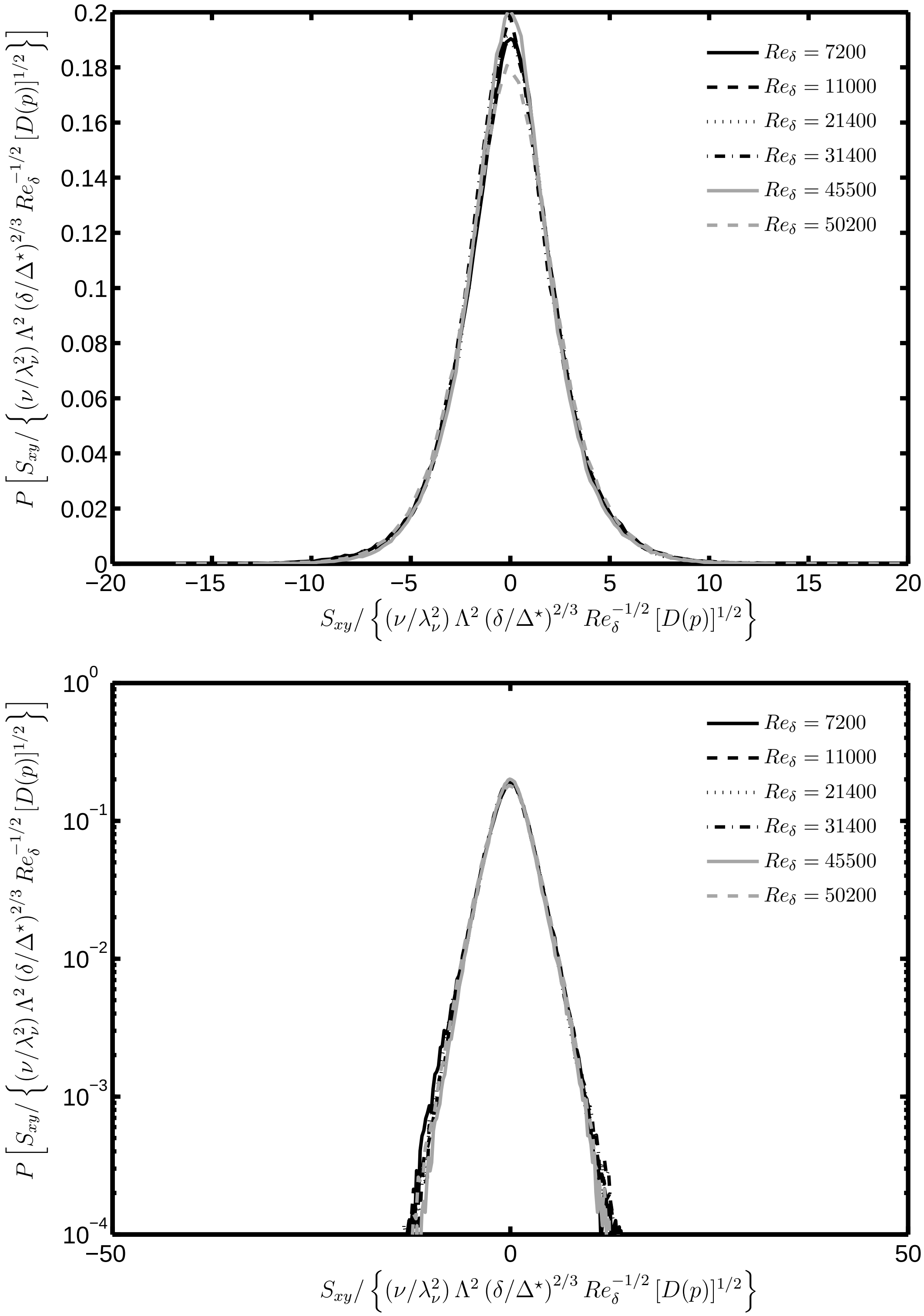

Figure 5.32: Pdfs from all nonreacting cases *INR1* – *INR6* for strain rate component S_{xy} normalized by resolution-corrected inner scaling $(\nu/\lambda_\nu^2)\,\Lambda^2\,(\delta/\Delta^\star)^{2/3}\,Re_\delta^{-1/2}\,[D(p)]^{1/2}$, shown in linear axes *(top)* and semilogarithmic axes *(bottom)*.

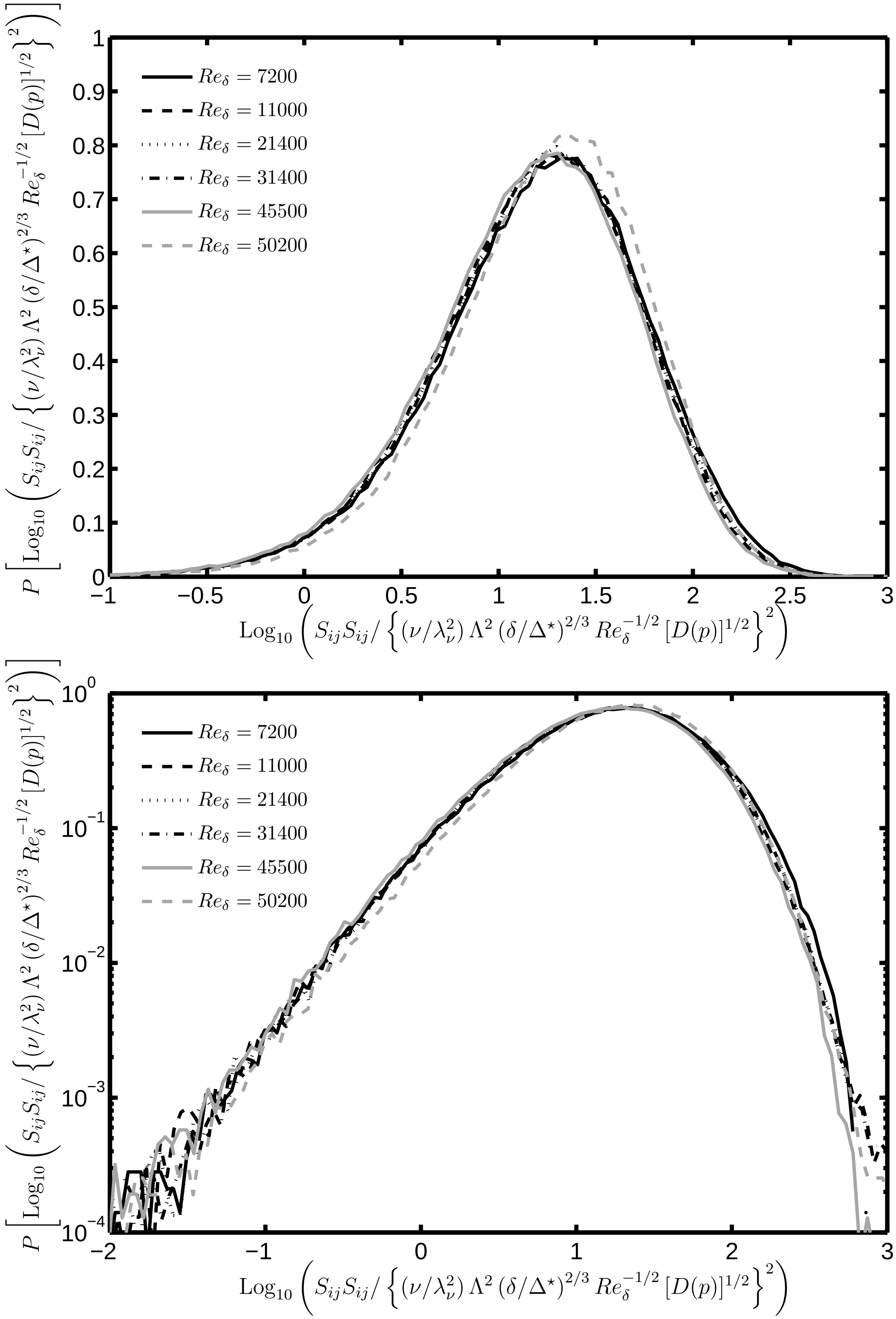

Figure 5.33: Pdfs from all nonreacting cases *INR1* – *INR6* for dissipation $\mathrm{Log}_{10}(S_{ij}S_{ij})$ normalized by resolution-corrected inner scaling $\{(\nu/\lambda_\nu^2)\,\Lambda^2\,(\delta/\Delta^\star)^{2/3}\,Re_\delta^{-1/2}\,[D(p)]^{1/2}\}^2$, shown in linear axes *(top)* and semilogarithmic axes *(bottom)*.

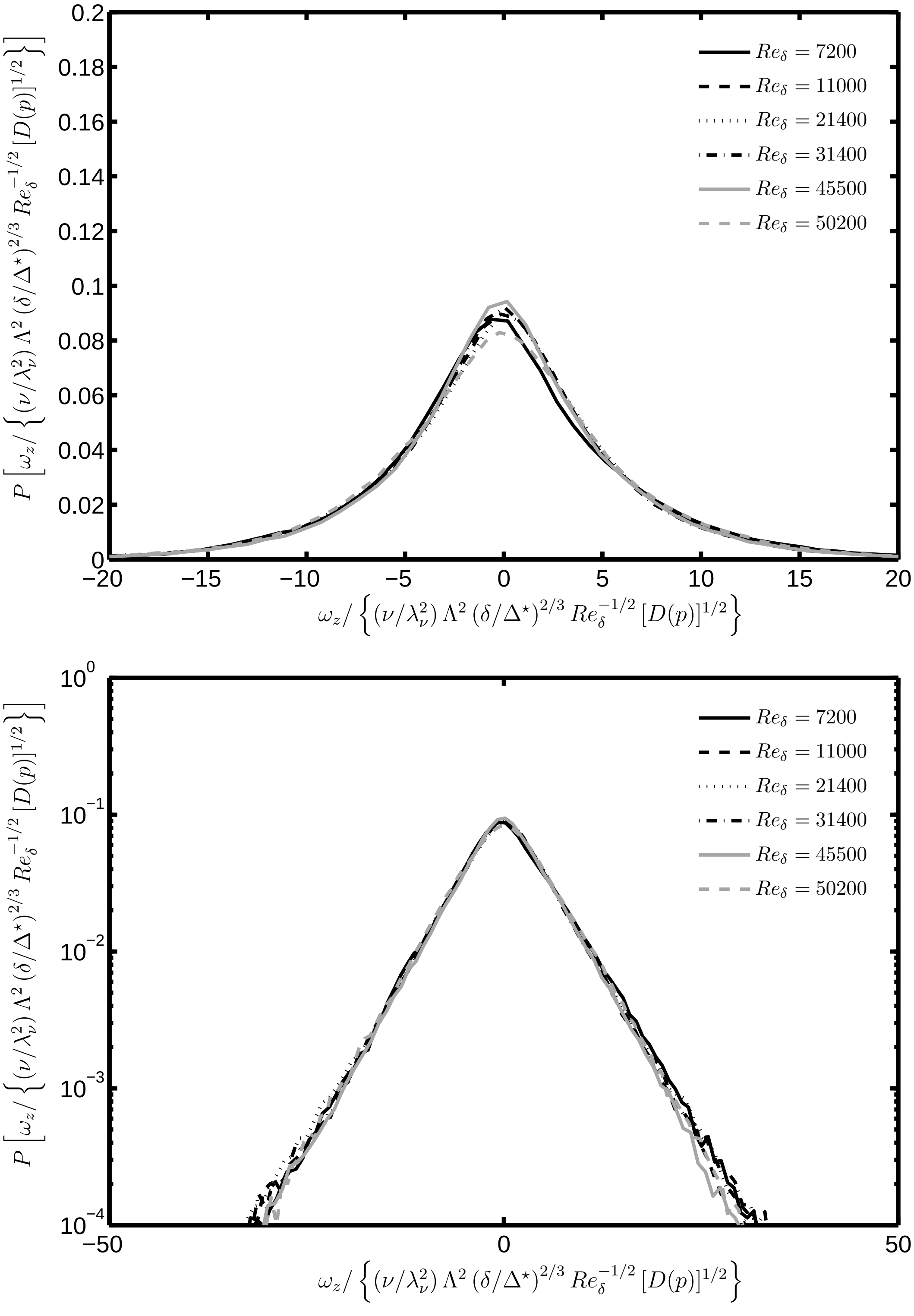

Figure 5.34: Pdfs from all nonreacting cases *INR1* – *INR6* for vorticity ω_z normalized by resolution-corrected inner scaling $(\nu/\lambda_\nu^2)\,\Lambda^2\,(\delta/\Delta^\star)^{2/3}\,Re_\delta^{-1/2}\,[D(p)]^{1/2}$, shown in linear axes *(top)* and semilogarithmic axes *(bottom)*.

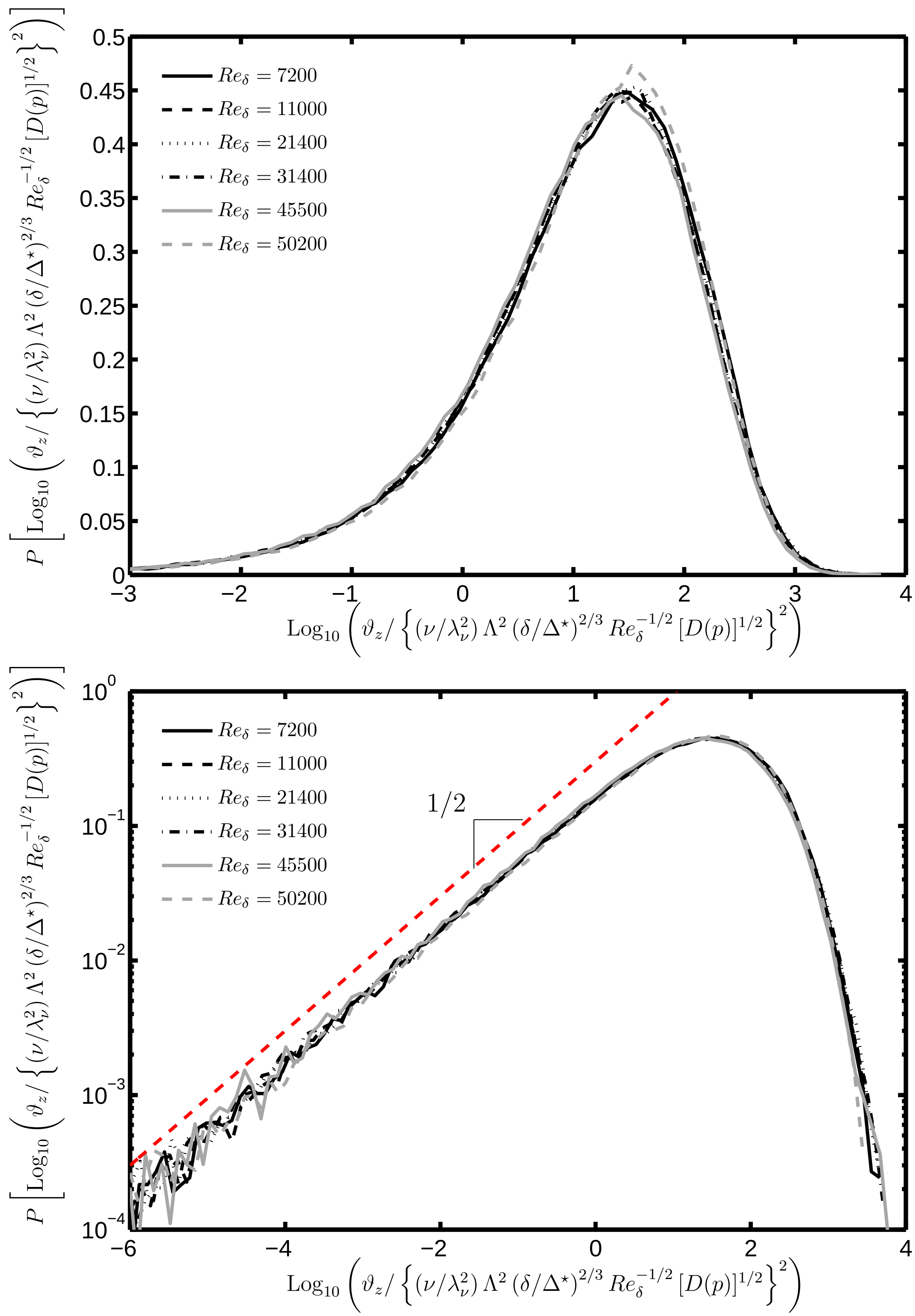

Figure 5.35: Pdfs from all nonreacting cases *INR1* – *INR6* for enstrophy $\mathrm{Log}_{10}(\vartheta_z)$ normalized by resolution-corrected inner scaling, $\{(\nu/\lambda_\nu^2)\,\Lambda^2\,(\delta/\Delta^\star)^{2/3}\,Re_\delta^{-1/2}\,[D(p)]^{1/2}\}^2$, shown in linear axes *(top)* and semilogarithmic axes *(bottom)*.

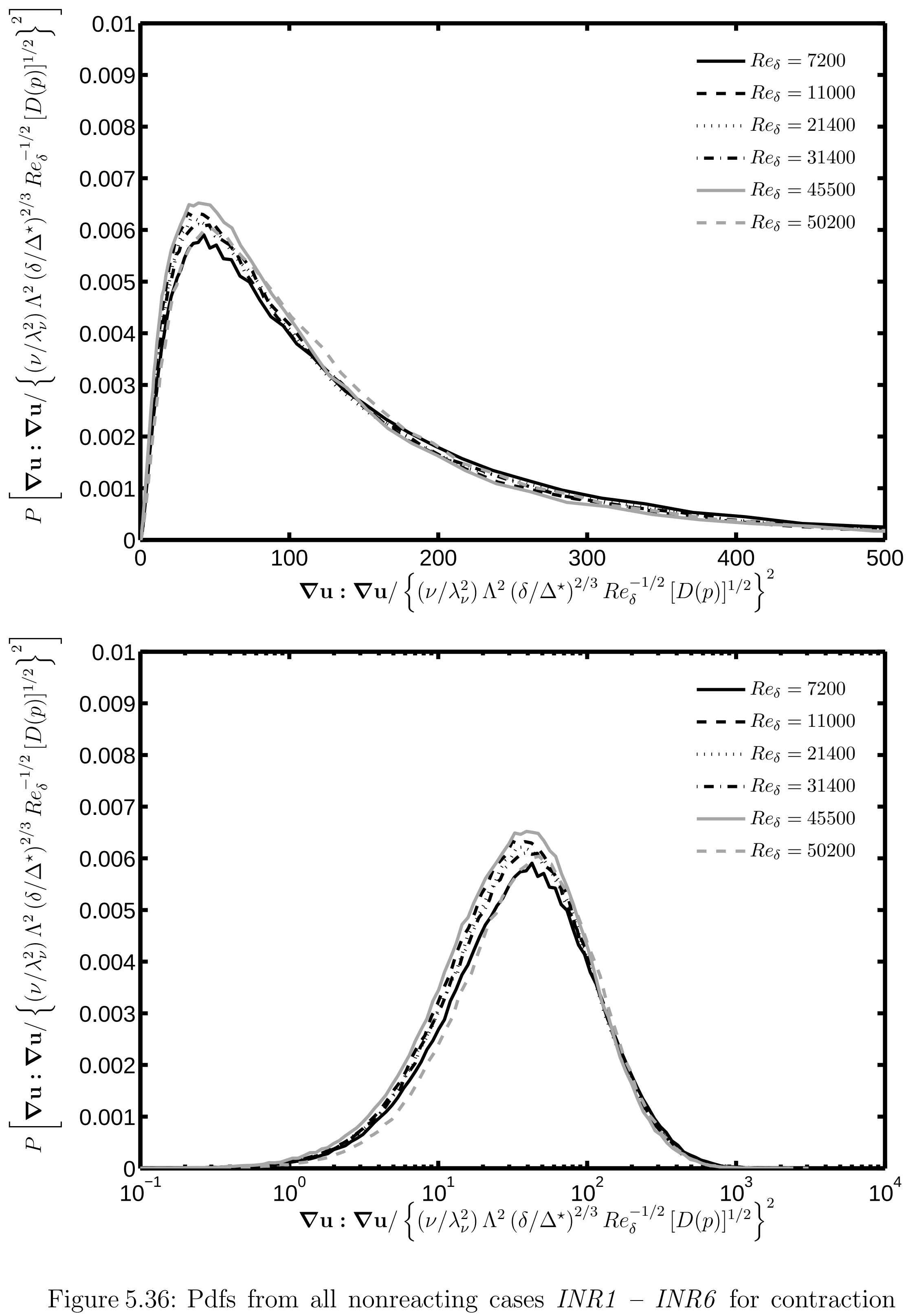

Figure 5.36: Pdfs from all nonreacting cases *INR1* – *INR6* for contraction of the velocity gradient tensor $\nabla\mathbf{u}:\nabla\mathbf{u}$ normalized by resolution-corrected inner scaling, $\{(\nu/\lambda_\nu^2)\,\Lambda^2\,(\delta/\Delta^\star)^{2/3}\,Re_\delta^{-1/2}\,[D(p)]^{1/2}\}^2$, shown in linear axes *(top)* and semilogarithmic axes *(bottom)*.

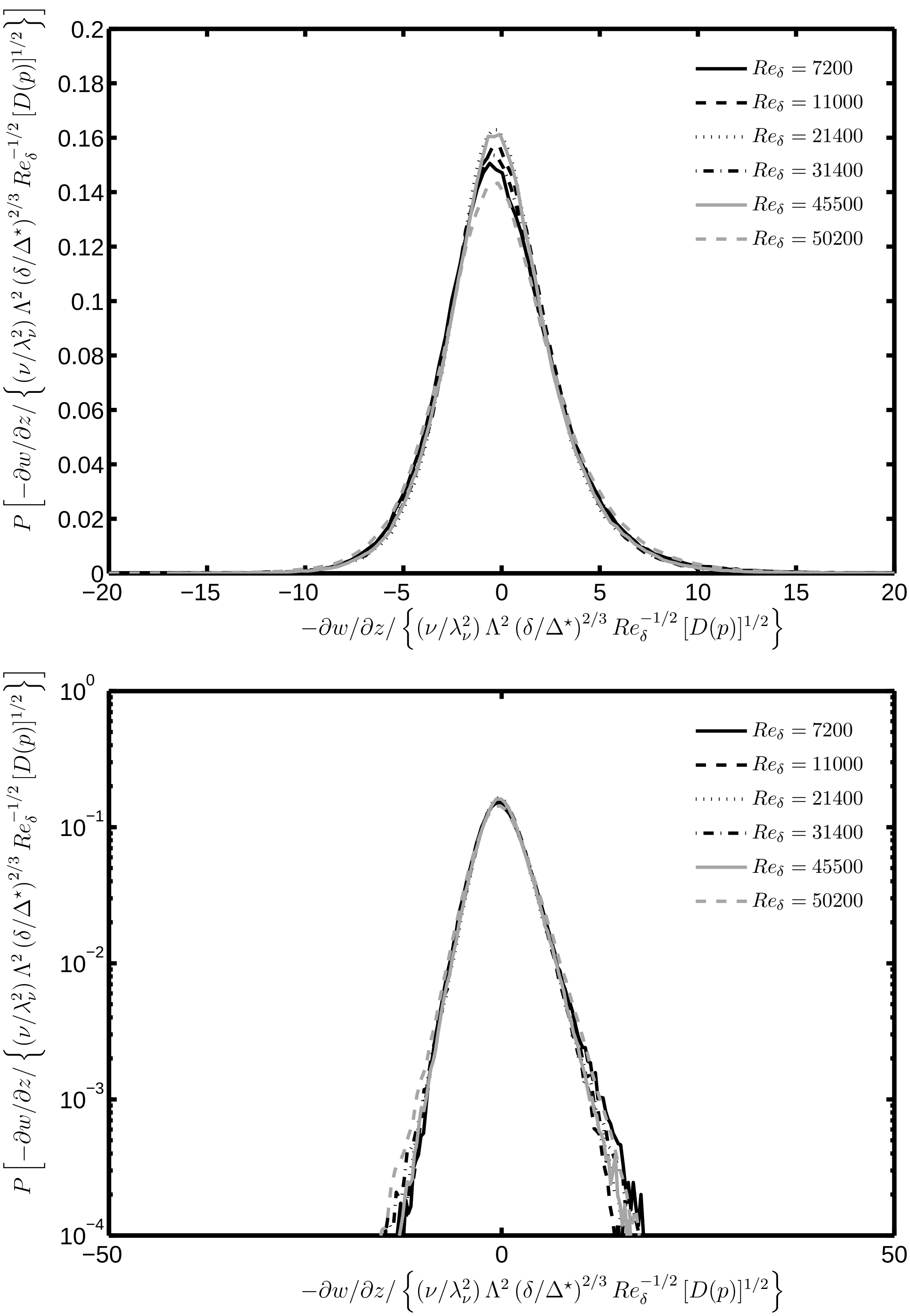

Figure 5.37: Pdfs from all nonreacting cases *INR1 – INR6* for two-dimensional divergence $-\partial w/\partial z$ normalized by resolution-corrected inner scaling $(\nu/\lambda_\nu^2)\,\Lambda^2\,(\delta/\Delta^\star)^{2/3}\,Re_\delta^{-1/2}\,[D(p)]^{1/2}$, shown in linear axes *(top)* and semilogarithmic axes *(bottom)*.

Quantity	μ	σ	γ	β
u/u_c	$1.744E-17$	$2.666E-01$	$2.676E-02$	$2.849E+00$
v/u_c	$6.645E-18$	$2.061E-01$	$1.641E-01$	$2.901E+00$
$\partial u/\partial x$	$-3.649E-16$	$3.051E+00$	$-4.599E-01$	$4.737E+00$
$\partial u/\partial y$	$-5.684E-16$	$4.288E+00$	$-1.269E-01$	$5.934E+00$
$\partial v/\partial x$	$4.195E-17$	$4.004E+00$	$1.105E-02$	$6.196E+00$
$\partial v/\partial y$	$-5.314E-17$	$2.989E+00$	$-5.032E-01$	$4.690E+00$
S_{xx}	$-3.649E-16$	$3.051E+00$	$-4.599E-01$	$4.737E+00$
S_{yy}	$-5.314E-17$	$2.989E+00$	$-5.032E-01$	$4.690E+00$
S_{xy}	$-3.622E-16$	$2.571E+00$	$-6.213E-02$	$4.492E+00$
ω_z	$5.258E-16$	$6.510E+00$	$8.246E-02$	$5.740E+00$
ε	$4.952E-02$	$6.830E-02$	$3.847E+00$	$2.675E+01$
$\mathrm{Log}_{10}[\varepsilon]$	$-1.611E+00$	$5.587E-01$	$-4.600E-01$	$3.515E+00$
$-\partial w/\partial z$	$-2.531E-16$	$3.161E+00$	$5.630E-01$	$4.917E+00$
$\boldsymbol{\nabla}\mathbf{u} : \boldsymbol{\nabla}\mathbf{u}$	$6.265E+01$	$8.006E+01$	$4.120E+00$	$3.571E+01$
$\left[\dfrac{-\partial w/\partial z}{(\boldsymbol{\nabla}\mathbf{u} : \boldsymbol{\nabla}\mathbf{u})^{1/2}}\right]$	$1.809E-02$	$4.206E-01$	$2.219E-01$	$1.965E+00$
$S_{ij} : S_{ij}$	$3.146E+01$	$4.124E+01$	$3.645E+00$	$2.442E+01$
$\mathrm{Log}_{10}[S_{ij} : S_{ij}]$	$1.212E+00$	$5.421E-01$	$-4.972E-01$	$3.593E+00$
$3/2\,(\omega_z)^2$	$6.357E+01$	$1.384E+02$	$7.124E+00$	$1.051E+02$
$\mathrm{Log}_{10}\left[3/2\;(\omega_z)^2\right]$	$1.060E+00$	$1.063E+00$	$-1.191E+00$	$5.769E+00$

Table 5.2: Normalized central moments computed from pdfs for $Re = 7200$ case. The mean is μ, σ is the *rms* fluctuation, $\gamma = \mu_3/\sigma^3$ is the skewness and $\beta = \mu_4/\sigma^4$ is the kurtosis. All quantities normalized by resolution-corrected inner scaling $(\nu/\lambda_\nu^2)\,\Lambda^2\,(\delta/\Delta^\star)^{2/3}\,Re_\delta^{-1/2}\,[D(p)]^{1/2}$ as shown in Figs. 5.26 – 5.37.

Quantity	μ	σ	γ	β
u/u_c	$2.159E-17$	$2.498E-01$	$7.533E-02$	$2.671E+00$
v/u_c	$-1.284E-17$	$2.008E-01$	$-8.459E-02$	$2.842E+00$
$\partial u/\partial x$	$-5.812E-16$	$2.829E+00$	$-3.599E-01$	$4.418E+00$
$\partial u/\partial y$	$2.906E-16$	$4.147E+00$	$1.043E-01$	$6.602E+00$
$\partial v/\partial x$	$5.626E-17$	$3.920E+00$	$-5.465E-02$	$5.999E+00$
$\partial v/\partial y$	$1.056E-16$	$2.823E+00$	$-4.552E-01$	$4.555E+00$
S_{xx}	$-5.812E-16$	$2.829E+00$	$-3.599E-01$	$4.418E+00$
S_{yy}	$1.056E-16$	$2.823E+00$	$-4.552E-01$	$4.555E+00$
S_{xy}	$5.788E-17$	$2.510E+00$	$2.522E-02$	$4.990E+00$
ω_z	$-3.295E-16$	$6.317E+00$	$-3.479E-02$	$6.334E+00$
ε	$2.652E-01$	$3.824E-01$	$6.300E+00$	$1.061E+02$
$\text{Log}_{10}[\varepsilon]$	$-8.765E-01$	$5.512E-01$	$-4.541E-01$	$3.528E+00$
$-\partial w/\partial z$	$-3.805E-16$	$2.952E+00$	$3.666E-01$	$4.819E+00$
$\boldsymbol{\nabla}\mathbf{u} : \boldsymbol{\nabla}\mathbf{u}$	$5.724E+01$	$7.515E+01$	$5.239E+00$	$6.418E+01$
$\left[\dfrac{-\partial w/\partial z}{(\boldsymbol{\nabla}\mathbf{u} : \boldsymbol{\nabla}\mathbf{u})^{1/2}}\right]$	$1.999E-02$	$4.151E-01$	$1.866E-01$	$1.975E+00$
$S_{ij} : S_{ij}$	$2.857E+01$	$3.763E+01$	$4.993E+00$	$6.432E+01$
$\text{Log}_{10}[S_{ij} : S_{ij}]$	$1.180E+00$	$5.315E-01$	$-5.021E-01$	$3.630E+00$
$3/2\,(\omega_z)^2$	$5.986E+01$	$1.382E+02$	$7.881E+00$	$1.167E+02$
$\text{Log}_{10}\left[3/2\ (\omega_z)^2\right]$	$1.029E+00$	$1.059E+00$	$-1.188E+00$	$5.809E+00$

Table 5.3: Normalized central moments computed from pdfs for $Re = 11\,000$ case. The mean is μ, σ is the *rms* fluctuation, $\gamma = \mu_3/\sigma^3$ is the skewness and $\beta = \mu_4/\sigma^4$ is the kurtosis. All quantities normalized by resolution-corrected inner scaling $(\nu/\lambda_\nu^2)\,\Lambda^2\,(\delta/\Delta^\star)^{2/3}\,Re_\delta^{-1/2}\,[D(p)]^{1/2}$ as shown in Figs. 5.26 – 5.37.

Quantity	μ	σ	γ	β
u/u_c	$-8.615E-18$	$2.493E-01$	$-3.642E-02$	$2.815E+00$
v/u_c	$-1.359E-18$	$2.062E-01$	$-1.175E-01$	$3.024E+00$
$\partial u/\partial x$	$-5.228E-16$	$2.899E+00$	$-4.352E-01$	$4.636E+00$
$\partial u/\partial y$	$-9.118E-17$	$4.207E+00$	$-8.245E-02$	$6.214E+00$
$\partial v/\partial x$	$7.344E-17$	$4.000E+00$	$-1.322E-01$	$6.161E+00$
$\partial v/\partial y$	$-1.834E-17$	$2.864E+00$	$-4.465E-01$	$4.589E+00$
S_{xx}	$-5.228E-16$	$2.899E+00$	$-4.352E-01$	$4.636E+00$
S_{yy}	$-1.834E-17$	$2.864E+00$	$-4.465E-01$	$4.589E+00$
S_{xy}	$7.892E-17$	$2.519E+00$	$-7.421E-02$	$4.478E+00$
ω_z	$9.709E-17$	$6.481E+00$	$-1.147E-02$	$6.589E+00$
ε	$9.397E-01$	$1.275E+00$	$4.029E+00$	$3.135E+01$
$\mathrm{Log}_{10}[\varepsilon]$	$-3.233E-01$	$5.503E-01$	$-4.720E-01$	$3.546E+00$
$-\partial w/\partial z$	$-4.693E-16$	$2.911E+00$	$3.681E-01$	$4.603E+00$
$\boldsymbol{\nabla}\mathbf{u} : \boldsymbol{\nabla}\mathbf{u}$	$5.878E+01$	$7.647E+01$	$4.804E+00$	$5.309E+01$
$\left[\dfrac{-\partial w/\partial z}{(\boldsymbol{\nabla}\mathbf{u} : \boldsymbol{\nabla}\mathbf{u})^{1/2}}\right]$	$2.210E-02$	$4.051E-01$	$2.265E-01$	$2.034E+00$
$S_{ij} : S_{ij}$	$2.931E+01$	$3.719E+01$	$3.585E+00$	$2.439E+01$
$\mathrm{Log}_{10}[S_{ij} : S_{ij}]$	$1.192E+00$	$5.324E-01$	$-5.167E-01$	$3.630E+00$
$3/2\,(\omega_z)^2$	$6.300E+01$	$1.489E+02$	$8.696E+00$	$1.575E+02$
$\mathrm{Log}_{10}\left[3/2\ (\omega_z)^2\right]$	$1.041E+00$	$1.067E+00$	$-1.178E+00$	$5.673E+00$

Table 5.4: Normalized central moments computed from pdfs for $Re = 21\,400$ case. The mean is μ, σ is the *rms* fluctuation, $\gamma = \mu_3/\sigma^3$ is the skewness and $\beta = \mu_4/\sigma^4$ is the kurtosis. All quantities normalized by resolution-corrected inner scaling $(\nu/\lambda_\nu^2)\,\Lambda^2\,(\delta/\Delta^\star)^{2/3}\,Re_\delta^{-1/2}\,[D(p)]^{1/2}$ as shown in Figs. 5.26 – 5.37.

Quantity	μ	σ	γ	β
u/u_c	$4.531E-18$	$2.526E-01$	$1.413E-01$	$2.996E+00$
v/u_c	$1.379E-17$	$2.046E-01$	$-3.306E-03$	$2.889E+00$
$\partial u/\partial x$	$4.119E-17$	$2.943E+00$	$-4.526E-01$	$4.484E+00$
$\partial u/\partial y$	$-7.627E-17$	$4.139E+00$	$9.692E-02$	$6.185E+00$
$\partial v/\partial x$	$3.671E-17$	$3.957E+00$	$2.080E-01$	$6.317E+00$
$\partial v/\partial y$	$1.888E-17$	$2.894E+00$	$-4.522E-01$	$4.777E+00$
S_{xx}	$4.119E-17$	$2.943E+00$	$-4.526E-01$	$4.484E+00$
S_{yy}	$1.888E-17$	$2.894E+00$	$-4.522E-01$	$4.777E+00$
S_{xy}	$-7.427E-17$	$2.506E+00$	$1.577E-01$	$4.646E+00$
ω_z	$7.055E-17$	$6.360E+00$	$7.566E-02$	$6.476E+00$
ε	$2.512E+00$	$3.488E+00$	$4.632E+00$	$4.532E+01$
$\mathrm{Log}_{10}\left[\varepsilon\right]$	$1.030E-01$	$5.497E-01$	$-4.669E-01$	$3.556E+00$
$-\partial w/\partial z$	$-7.856E-17$	$3.091E+00$	$4.190E-01$	$4.911E+00$
$\boldsymbol{\nabla}\mathbf{u}:\boldsymbol{\nabla}\mathbf{u}$	$5.938E+01$	$7.729E+01$	$4.715E+00$	$4.883E+01$
$\left[\dfrac{-\partial w/\partial z}{(\boldsymbol{\nabla}\mathbf{u}:\boldsymbol{\nabla}\mathbf{u})^{1/2}}\right]$	$1.953E-02$	$4.208E-01$	$2.094E-01$	$1.949E+00$
$S_{ij}:S_{ij}$	$2.960E+01$	$3.831E+01$	$4.107E+00$	$3.641E+01$
$\mathrm{Log}_{10}\left[S_{ij}:S_{ij}\right]$	$1.195E+00$	$5.328E-01$	$-5.093E-01$	$3.632E+00$
$3/2\,(\omega_z)^2$	$6.068E+01$	$1.420E+02$	$8.207E+00$	$1.372E+02$
$\mathrm{Log}_{10}\left[3/2\ (\omega_z)^2\right]$	$1.021E+00$	$1.068E+00$	$-1.167E+00$	$5.668E+00$

Table 5.5: Normalized central moments computed from pdfs for $Re = 31\,400$ case. The mean is μ, σ is the *rms* fluctuation, $\gamma = \mu_3/\sigma^3$ is the skewness and $\beta = \mu_4/\sigma^4$ is the kurtosis. All quantities normalized by resolution-corrected inner scaling $(\nu/\lambda_\nu^2)\,\Lambda^2\,(\delta/\Delta^\star)^{2/3}\,Re_\delta^{-1/2}\,[D(p)]^{1/2}$ as shown in Figs. 5.26 – 5.37.

Quantity	μ	σ	γ	β
u/u_c	$-1.454E-17$	$2.413E-01$	$4.491E-02$	$2.928E+00$
v/u_c	$4.214E-19$	$2.029E-01$	$7.160E-03$	$2.806E+00$
$\partial u/\partial x$	$2.588E-16$	$2.828E+00$	$-3.876E-01$	$4.517E+00$
$\partial u/\partial y$	$1.348E-16$	$3.963E+00$	$9.128E-02$	$5.901E+00$
$\partial v/\partial x$	$7.658E-17$	$3.840E+00$	$4.669E-02$	$5.945E+00$
$\partial v/\partial y$	$-2.254E-17$	$2.761E+00$	$-5.361E-01$	$4.822E+00$
S_{xx}	$2.588E-16$	$2.828E+00$	$-3.876E-01$	$4.517E+00$
S_{yy}	$-2.254E-17$	$2.761E+00$	$-5.361E-01$	$4.822E+00$
S_{xy}	$7.204E-17$	$2.405E+00$	$7.122E-02$	$4.248E+00$
ω_z	$2.450E-19$	$6.144E+00$	$-4.934E-02$	$6.355E+00$
ε	$5.594E+00$	$7.441E+00$	$3.686E+00$	$2.508E+01$
$\mathrm{Log}_{10}[\varepsilon]$	$4.526E-01$	$5.513E-01$	$-4.882E-01$	$3.550E+00$
$-\partial w/\partial z$	$3.284E-16$	$2.962E+00$	$3.825E-01$	$4.599E+00$
$\boldsymbol{\nabla}\mathbf{u} : \boldsymbol{\nabla}\mathbf{u}$	$5.484E+01$	$7.009E+01$	$5.323E+00$	$7.826E+01$
$\left[\dfrac{-\partial w/\partial z}{(\boldsymbol{\nabla}\mathbf{u} : \boldsymbol{\nabla}\mathbf{u})^{1/2}}\right]$	$2.178E-02$	$4.179E-01$	$2.088E-01$	$1.967E+00$
$S_{ij} : S_{ij}$	$2.719E+01$	$3.435E+01$	$3.674E+00$	$2.762E+01$
$\mathrm{Log}_{10}[S_{ij} : S_{ij}]$	$1.160E+00$	$5.337E-01$	$-5.331E-01$	$3.646E+00$
$3/2\,(\omega_z)^2$	$5.663E+01$	$1.310E+02$	$9.573E+00$	$2.161E+02$
$\mathrm{Log}_{10}\left[3/2\ (\omega_z)^2\right]$	$9.975E-01$	$1.067E+00$	$-1.170E+00$	$5.650E+00$

Table 5.6: Normalized central moments computed from pdfs for $Re = 45\,500$ case. The mean is μ, σ is the *rms* fluctuation, $\gamma = \mu_3/\sigma^3$ is the skewness and $\beta = \mu_4/\sigma^4$ is the kurtosis. All quantities normalized by resolution-corrected inner scaling $(\nu/\lambda_\nu^2)\,\Lambda^2\,(\delta/\Delta^\star)^{2/3}\,Re_\delta^{-1/2}\,[D(p)]^{1/2}$ as shown in Figs. 5.26 – 5.37.

Quantity	μ	σ	γ	β
u/u_c	$-1.235E-17$	$2.748E-01$	$-4.827E-03$	$2.725E+00$
v/u_c	$-1.424E-17$	$2.258E-01$	$-2.759E-02$	$2.801E+00$
$\partial u/\partial x$	$-3.412E-16$	$3.037E+00$	$-4.698E-01$	$4.473E+00$
$\partial u/\partial y$	$1.503E-16$	$4.274E+00$	$2.672E-03$	$5.252E+00$
$\partial v/\partial x$	$-4.522E-17$	$3.988E+00$	$-1.793E-02$	$5.228E+00$
$\partial v/\partial y$	$4.200E-17$	$3.006E+00$	$-4.270E-01$	$4.864E+00$
S_{xx}	$-3.412E-16$	$3.037E+00$	$-4.698E-01$	$4.473E+00$
S_{yy}	$4.200E-17$	$3.006E+00$	$-4.270E-01$	$4.864E+00$
S_{xy}	$4.391E-17$	$2.588E+00$	$2.309E-02$	$4.256E+00$
ω_z	$-3.341E-18$	$6.446E+00$	$-5.595E-03$	$5.110E+00$
ε	$6.856E+00$	$9.031E+00$	$5.289E+00$	$8.286E+01$
$\mathrm{Log}_{10}\,[\varepsilon]$	$5.606E-01$	$5.319E-01$	$-5.188E-01$	$3.659E+00$
$-\partial w/\partial z$	$-3.140E-16$	$3.340E+00$	$2.942E-01$	$5.451E+00$
$\boldsymbol{\nabla}\mathbf{u} : \boldsymbol{\nabla}\mathbf{u}$	$6.359E+01$	$7.614E+01$	$5.416E+00$	$9.864E+01$
$\left[\dfrac{-\partial w/\partial z}{(\boldsymbol{\nabla}\mathbf{u} : \boldsymbol{\nabla}\mathbf{u})^{1/2}}\right]$	$1.585E-02$	$4.213E-01$	$2.020E-01$	$1.957E+00$
$S_{ij} : S_{ij}$	$3.165E+01$	$3.916E+01$	$5.499E+00$	$1.072E+02$
$\mathrm{Log}_{10}\,[S_{ij} : S_{ij}]$	$1.245E+00$	$5.144E-01$	$-5.675E-01$	$3.748E+00$
$3/2\,(\omega_z)^2$	$6.233E+01$	$1.264E+02$	$5.575E+00$	$5.537E+01$
$\mathrm{Log}_{10}\left[3/2\ (\omega_z)^2\right]$	$1.087E+00$	$1.043E+00$	$-1.252E+00$	$6.066E+00$

Table 5.7: Normalized central moments computed from pdfs for $Re = 50\,200$ case. The mean is μ, σ is the *rms* fluctuation, $\gamma = \mu_3/\sigma^3$ is the skewness and $\beta = \mu_4/\sigma^4$ is the kurtosis. All quantities normalized by resolution-corrected inner scaling $(\nu/\lambda_\nu^2)\,\Lambda^2\,(\delta/\Delta^\star)^{2/3}\,Re_\delta^{-1/2}\,[D(p)]^{1/2}$ as shown in Figs. 5.26 – 5.37.

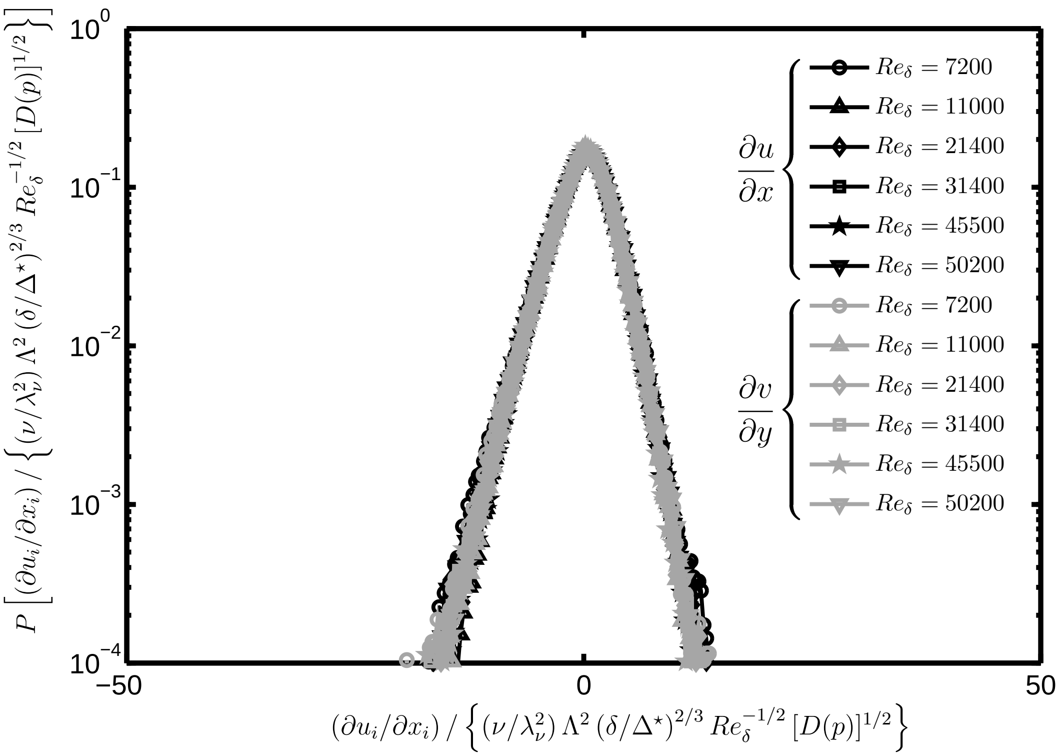

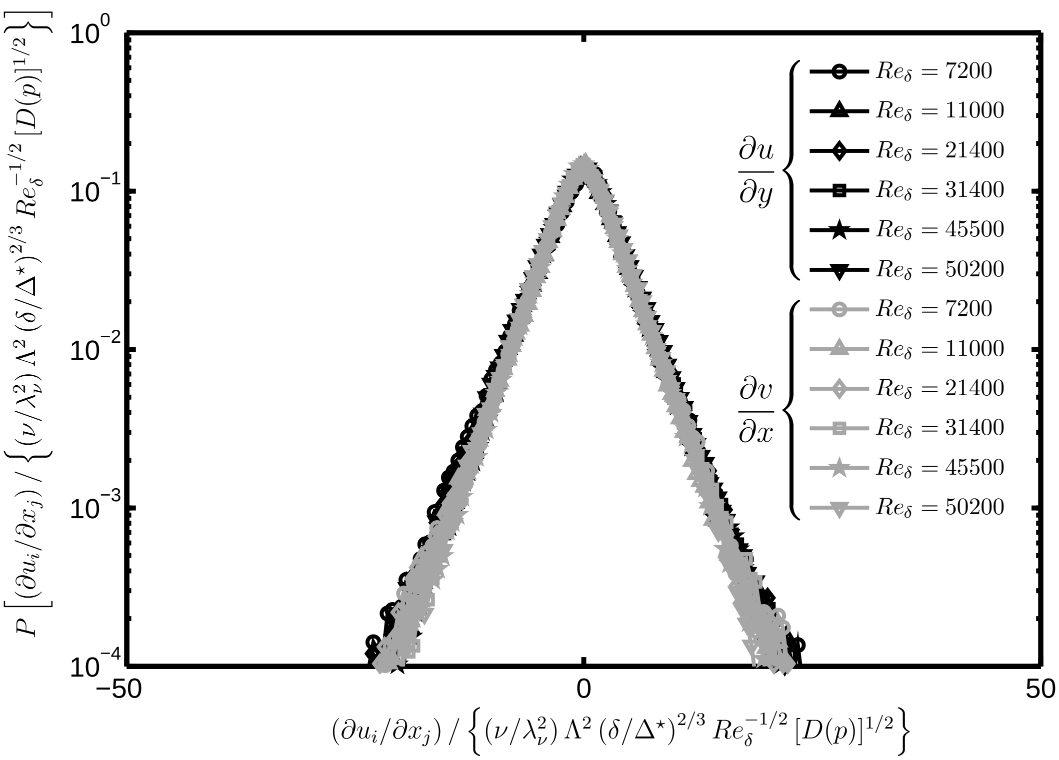

Figure 5.38: Pdfs from nonreacting cases *INR1 – INR6*, normalized by resolution-corrected inner scaling. On-diagonal velocity gradients *(top)*, where the black symbols represent the $\partial u/\partial x$ component while the grey display $\partial v/\partial y$. Off-diagonal velocity gradients *(bottom)*, where the black symbols represent the $\partial u/\partial y$ component while the grey display $\partial v/\partial x$.

Re_δ	$\dfrac{\overline{\left(\dfrac{\partial u}{\partial y}\right)^2} + \overline{\left(\dfrac{\partial v}{\partial x}\right)^2}}{\overline{\left(\dfrac{\partial u}{\partial x}\right)^2} + \overline{\left(\dfrac{\partial v}{\partial y}\right)^2}}$
7200	1.887
11000	2.039
21400	2.028
31400	1.925
45500	1.949
50200	1.872
$6000^\dagger$	1.915
$30000^\dagger$	1.856

Table 5.8: Ratios of the variances of the on-diagonal gradient components over the off-diagonal components. The analytical value obtained via the assumption of homogeneous isotropic turbulence is 2. The final two conditions adorned with a † are presented for comparison, and are from the data given by Mullin and Dahm (2005b).

Re_δ	$\dfrac{\mathrm{var}\left(\dfrac{\partial u}{\partial y}\right)}{\mathrm{var}\left(\dfrac{\partial u}{\partial x}\right)}$	$\dfrac{\mathrm{var}\left(\dfrac{\partial v}{\partial x}\right)}{\mathrm{var}\left(\dfrac{\partial v}{\partial y}\right)}$
7200	1.975	1.795
11000	2.149	1.928
21400	2.105	1.950
31400	1.978	1.870
45500	1.963	1.935
50200	1.981	1.760
$6000^\dagger$	1.933	1.895
$30000^\dagger$	1.931	1.774

Table 5.9: Ratios of the variances of the on-diagonal gradient components over the off-diagonal components. The analytical value obtained via the assumption of homogeneous isotropic turbulence is 2. The final conditions indicated by † are from Mullin and Dahm (2005b), shown for comparison.

Quantity	Present Data	Mullin	Gotoh	Jiménez
Re_λ	58	45	54	61
$\gamma\,(\partial u/\partial x)$	-0.456	-0.428	-0.517	-0.495
$\beta\,(\partial u/\partial x)$	4.74	4.22	4.47	4.60
Re_λ	115	113	125	168
$\gamma\,(\partial u/\partial x)$	-0.453	-0.355	-0.529	-0.525
$\beta\,(\partial u/\partial x)$	4.48	4.81	5.65	6.10

Table 5.10: Comparison of present measured velocity gradient skewness γ and kurtosis β with corresponding results from DNS studies of periodic homogeneous isotropic turbulence from Gotoh et al. (2002) and Jiménez et al. (1993), along with measured values from Mullin (2004) at similar Re_λ values.

CHAPTER VI

Inner-Scale Effects of Heat Release

Chapter V dealt with inner-scale velocity field data obtained on the centerline of a nonreacting turbulent shear flow. It showed how the resolution scale $\Delta^\star$ in such measurements could be objectively determined, and presented results that verified the proper inner scaling of various velocity gradient quantities in terms of $\Delta^\star$ to account for resolution effects in the measurements. In this chapter, this proper inner scaling methodology is used as the basis for separating effects of measurement resolution from effects of heat release in inner-scale velocity field data obtained on the centerline of an exothermically reacting turbulent shear flow. By comparing such inner-scaled pdfs of velocity gradient quantities from reacting and nonreacting versions of an otherwise identical turbulent shear flow, the effects of heat release on the inner scales of the velocity field $\mathbf{u}(\mathbf{x}, t)$ can be directly determined.

6.1 Inner-Scale PIV Measurements

Table 3.4 lists the flow conditions and other relevant parameters for each of the seven inner-scale reacting flow cases used in this part of the study. The fuel for all these cases was hydrogen (99.99% purity), which issued from the jet nozzle into the coflowing air stream. Both the jet and the coflow were seeded with the same 0.5 μm aluminum oxide particles used for the nonreacting cases in Chapter V. In all these reacting flow cases, the field-of-view (FOV) of the PIV measurements was 15 mm $\times$ 18.7 mm. The data from these reacting flow cases were processed in a manner identical to the nonreacting cases in Chapter V. The FOV was subdivided into a vector field of 32 $\times$ 40 vectors, with each vector corresponding to a final interrogation window size of (0.469 mm)^2. This interrogation window size for the reacting flow cases is similar to the (0.375 mm)^2 and (0.468 mm)^2 window sizes used for the nonreacting cases in Chapter V. As in Chapter V, for each of these inner-scale reacting flow cases a companion large-FOV measurement was also made to directly obtain the outer variables (u_c and δ) needed to properly scale the results. The procedure for acquiring 300 images for each of these inner- and outer-scale measurements is described in §5.1.

6.2 Inner-Scale Velocities and Velocity Gradients

In keeping with the presentation format of the previous chapter, an example of the typical instantaneous velocity fluctuation fields $u(x, y)$ and $v(x, y)$ from these inner-scale reacting flow measurements, corresponding to case *IR7* with $Re_\delta = 200\,100$ in Table 3.4, is shown in Fig. 6.1 normalized by the outer velocity scale u_c. The corresponding velocity gradient fields $\partial u/\partial x$, $\partial u/\partial y$, $\partial v/\partial x$ and $\partial v/\partial y$ are shown in Figs. 6.2 – 6.7, normalized with the measured values of the outer variables u_c and δ in the upper panel, and normalized with the classical inner variables ν and λ_ν in the lower panel. Here ν is the mixture-fraction averaged viscosity evaluated as described in § 2.6, and λ_ν is obtained from this, together with the measured values of u_c and δ, via (5.1).

Figures 6.4 – 6.5 give the corresponding strain rate components S_{xx}, S_{yy} and S_{xy}, together with the "pseudo" dissipation rate field $S_{ij}S_{ij}$, each shown normalized with classical inner variables. The corresponding out-of-plane vorticity component ω_z and its associated enstrophy ϑ_z are given in Fig. 6.6. Lastly, Fig. 6.7 gives the corresponding square-magnitude of the velocity gradient tensor $\boldsymbol{\nabla}\mathbf{u} : \boldsymbol{\nabla}\mathbf{u}$ formed from the above velocity gradient components, as well as the apparent two-dimensional divergence $(\boldsymbol{\nabla}\cdot\mathbf{u})_{2D}$, which in these reacting flow cases now includes both the additional velocity gradient component $\partial w/\partial z \equiv -(\partial u/\partial x + \partial v/\partial y)$ as well as the true divergence $\boldsymbol{\nabla}\cdot\mathbf{u}$ induced by heat release as described in § 2.5.

Probability density functions for each of the inner-scale quantities shown in Figs. 6.2 – 6.7 are given in Figs. 6.8 – 6.13, each normalized on the classical inner variables ν and λ_ν. A separate curve in each of these figures corresponds to each of the seven cases denoted by *IR1* – *IR7* in Table 3.4, with corresponding outer-scale Reynolds numbers Re_δ ranging from 18 300 to 200 100 based on the cold air viscosity. As was seen in Chapter V, even with the classical inner-scale normalization shown in these figures, there are substantial remaining differences apparent among the pdfs from these seven cases. These differences result from incomplete resolution of the smallest-scale motions by the PIV measurements with increasing Re_δ. In these reacting flow cases the increased viscosity, due primarily to the higher temperatures, leads to a substantial increase in λ_ν, and as a consequence the resolution is substantially higher at the same Re_δ value than for the nonreacting cases in Chapter V. While the reacting flow cases corresponding to the two lowest Re_δ values in Figs. 6.8 – 6.13

appear to be fully resolved, as evidenced by the fact that the classical inner-scale normalization collapses these to a single curve in each figure, the remaining cases clearly reflect varying degrees of under-resolution, as can be seen from the fact that they do not match this same curve in the classical inner-scale normalization.

6.2.1 Resolution-Corrected Pdfs

The artificial resolution degradation strategy detailed in §5.4.1, is then applied to the reacting, inner scale data. A sample set of resolution plots obtained from the vorticity statistics is shown in Figs. 6.14 – 6.20, for cases *IR1* – *IR7*. Qualitatively these plots are similar in character to those obtained for the nonreacting inner scale results of Chapter V. However the plots indicate that the filtering scheme reveals less of the inertial range in the reacting flow fitting diagrams, as compared to the nonreacting cases. For example, only three of the seven reacting flow cases (*IR1*, *IR2* and *IR7*) cases yield a value of $(\mathrm{var}\{\omega_z\}_\Delta \,/\, \mathrm{var}\{\omega_z\}_{\mathrm{MAX}}) < 0.3$, (see rightmost data point in Figs. 6.14, 6.15 and 6.20). By comparison, all of the nonreacting cases (Figs. 5.17 – 5.22) display a value < 0.3 for their data points furthest into the inertial range (filtering at the largest values of Δ).

The parameters (p and Δ_R) and length scale ($\Delta^\star$) resulting from the reacting flow viscous roll-off model are shown in Table 6.1. As with the nonreacting data the values for these parameters have been averaged over four independently processed gradients: S_{xx}, S_{yy}, S_{xy} and ω_z; to produce one final value for each quantity.

The same inertial-range correction given by (5.23) was applied to the pdfs presented in Figs. 6.8 – 6.13 and the corrected pdfs are shown in Figs. 6.21 – 6.24, for the four accessible components of the velocity gradient tensor. As with the nonreacting data, a roughly similar level of collapse in the pdfs was observed across the seven reacting, inner scale data sets, *IR1* to *IR7*. The inertial-range correction manages to reconcile the lowest Reynolds number case (*IR1*) with the rest of the cases in a satisfactory manner. This lowest Reynolds number case was acquired at a nontrivial distance *beyond* the visible flame tip. The next case *IR2* was such that the PIV FOV was very near the visible flame tip. The behavior of these two conditions was markedly different from the other cases, when scaled on classical inner variables ν and λ_ν, see Figs. 6.8 and 6.9. The width of the *IR1* and *IR2* pdfs in these figures was at least twice as wide as the remaining reacting cases. However, by accounting for the changes in resolution, *IR1* and *IR2* fall in line with the other inner scale reacting conditions; although the degree of collapse is not quite as high as in the nonreacting data of Chapter V.

Of the four gradient components rescaled in Figs. 6.21 – 6.24, the $\partial u/\partial y$ component in Fig. 6.24 appears mildly pathological in its collapse. In the next section, both off-diagonal components ($\partial u/\partial y$ and $\partial v/\partial x$) of the velocity gradient tensor will be seen to exhibit unique behavior relative to the other gradients quantities.

The remaining pdfs normalized by $\mathcal{N}^\star$ are displayed in Figs. 6.30 – 6.37, including the same set of gradient quantities presented in Chapter V: strain rate quantities, S_{xx}, S_{yy}, S_{xy} and $S_{ij}S_{ij}$, vorticity and enstrophy ω_z, ϑ_z, along with $(\boldsymbol{\nabla}\cdot\mathbf{u})_{2D}$ and $\boldsymbol{\nabla}\mathbf{u} : \boldsymbol{\nabla}\mathbf{u}$. The detailed moment information for all the gradient pdfs is listed in detail in Tables 6.4 – 6.10. Defined in §5.6, the first four moments are tabulated: the mean μ, the *rms* value σ, the skewness γ and the kurtosis β.

The normalized pdfs in Figs. 6.30 – 6.37 exhibit a similar level of universality and collapse comparable to that found for the four velocity gradient gradient components discussed above and shown in Figs. 6.21 – 6.24. While the agreement between the pdfs is not quite as good as the nonreacting data of Chapter V, the agreement is far superior to that of the classically scaled pdfs using ν and λ_ν. Here again the two cases obtained beyond or near to the flame tip (*IR1* and *IR2*) appeared to be much different when scaled on classical inner variables. However, by accounting for the varying levels of resolution, they are brought into reasonable agreement with the remainder of the reacting flow cases.

6.2.2 Comparisons with Nonreacting Inner-Scale Results

Figures 6.25 – 6.28 now present comparisons of the nonreacting flow results from Figs. 5.26 – 5.29 of Chapter V with the corresponding reacting results from Figs. 6.21 – 6.24 to identify the true effects of heat release in these inner-scale quantities. Comparing the widths of the pdfs in a simplistic manner, the aggregate average value of the *rms* across the six nonreacting cases (*INR1* – *INR6*) for each gradient component is computed: 2.934, $(\partial u/\partial x)$; 4.173, $(\partial u/\partial y)$; 3.955, $(\partial v/\partial x)$; and 2.892, $(\partial v/\partial y)$. Similarly, for the seven reacting cases (*IR1* – *IR7*): 3.764, $(\partial u/\partial x)$; 5.689, $(\partial u/\partial y)$; 4.757, $(\partial v/\partial x)$; and 3.676, $(\partial v/\partial y)$. By taking the ratio of these aggregate *rms* values, the on-diagonal components increase by 28% $(\partial u/\partial x)$ and 27% $(\partial v/\partial y)$. The off-diagonal components are less well-behaved: 36% increase for $(\partial u/\partial y)$ and 20% for $(\partial v/\partial x)$.

In addition to the accessible velocity gradient components, the remaining gradients quantities are also shown in direct comparison to their nonreacting counterparts in Figs. 6.30 – 6.37. Focusing on the first order gradients, S_{xy}, ω_z and $(\boldsymbol{\nabla}\cdot\mathbf{u})_{2D} \equiv (-\partial w/\partial z + \boldsymbol{\nabla}\cdot\mathbf{u})$, the same level of agreement is observed between the reacting and nonreacting data as was seen in gradient components described above. The widths of the reacting pdfs increase only a modest amount over their nonreacting counterparts. The same aggregate averaging described above can be repeated to examine the changes in pdf width. The ratio of reacting over nonreacting gradient *rms* values: 29% for S_{xy}; 29% for ω_z; and 27% for $(\boldsymbol{\nabla} \cdot \mathbf{u})_{2D}$. While the $S_{xx} = 1/2\,(\partial u/\partial x + \partial u/\partial x)$, and $S_{yy} = 1/2\,(\partial v/\partial y + \partial v/\partial y)$ strain rate components do not provide any new information over the velocity gradient components, the remaining gradients S_{xy}, ω_z and $(\boldsymbol{\nabla} \cdot \mathbf{u})_{2D}$ agree quite well with the on-diagonal velocity gradients.

Setting aside the off-diagonal velocity gradients momentarily, the augmentation provided by exothermicity in the other first order gradients is between 27% and 29%. This increase appears to be quite consistent and systematic amongst the measured gradient quantities. The use of $\mathcal{N}^\star$ to account for resolution effects in the classical inner scaling with ν and λ_ν allows a *direct* comparison between the reacting and nonreacting gradients and thus reveals the impact of exothermicity on a turbulent shear flow. The effect of $\mathcal{N}^\star$ acts, is to correct for the effect of measurement resolution relative to the inner length scale of the flow. Additionally, by directly measuring the outer scales δ and u_c, the effects of buoyancy and coflow on the jet outer scale properties and thereby on the inner length scale λ_ν, is taken into account. This allows straightforward comparisons to be made between reacting and nonreacting flows.

6.2.3 Inner-Scale Effects of Heat Release

The goal of the effective length scale $\Delta^\star$ and the subsequent normalization $\mathcal{N}^\star$ is to remove the effects of the outer scales while simultaneously correcting for under-resolution. This provides an equal basis by which both the nonreacting and reacting data can be fairly compared. The remaining differences observed between the burning and nonburning flows can then be ascribed to the effect of heat release acting on the finest scales of the flow. Indeed, in Figs. 6.25 – 6.37, the reacting pdfs bear a distinct and systematic departure from their nonreacting counterparts. While the deviations are not profound, they are unmistakable.

To explore these differences more deeply, the following analysis is performed. Each of the independent first-order gradients is considered: $\partial u/\partial x$, $\partial u/\partial y$, $\partial v/\partial x$, $\partial v/\partial y$, S_{xy}, ω_z and $(\boldsymbol{\nabla} \cdot \mathbf{u})_{2D}$. Here the focus is on the change in width of the pdfs, from nonreacting to reacting. Beginning with the *rms* values of the nonreacting cases (*INR1* – *INR6*), the statistics are first normalized using $\mathcal{N}^{\star}$,

$$\sigma_q \equiv \left(\frac{\sigma}{\mathcal{N}^{\star}}\right)_q , \tag{6.1}$$

where σ is the *rms* value of the gradients and q is any of the aforementioned first order gradients.

Since the present interest is comparing the relative change from nonreacting to reacting, each of the selected gradients q are then reduced by their own aggregate average value, computed in the following manner:

$$\langle \sigma_q \rangle_{NR} \equiv \sum_{\text{all } Re_\delta} \sigma_q \left(Re_\delta\right) . \tag{6.2}$$

In this case, the brackets quantity $\langle \sigma_q \rangle_{NR}$ is the aggregate average *rms* value for the q-th gradient, across all nonreacting *NR* datasets (Re_δ cases).

Each of the normalized gradients σ_q is reduced via dividing by its aggregate average *rms* value, giving $\sigma_q/\langle \sigma_q \rangle_{NR}$. The result for these reduced *rms* values are then plotted against their Re_δ values, as shown in the upper panel of Fig. 6.38 for the nonreacting conditions. For these nonreacting cases the behavior of $\sigma_q/\langle \sigma_q \rangle_{NR}$

shows no discernable Reynolds number dependence as the response is flat across all measured values, for all gradients. The values of $\sigma_q/\langle\sigma_q\rangle_{NR}$ hover tightly about unity, as expected from the repeated normalization described above. The plot reaffirms that the $\mathcal{N}^{\star}$ scaling has properly scaled the nonreacting data in the expected manner.

Thus the results presented in the lower panel of Fig. 6.38 for the reacting data are processed in the same manner as the nonreacting data, where each of the normalized reacting *rms* values σ_q are reduced by the nonreacting aggregate average *rms* $\langle\sigma_q\rangle_{NR}$. In general, the results for the reacting hydrogen flames shown in the lower panel are more interesting than their nonreacting counterparts. Their response of $\sigma_q/\langle\sigma_q\rangle_{NR}$ as a function of Reynolds number is *not* flat. At first glance there appears to be an influence of Re_δ on the reduced gradients.

The results for both the nonreacting and reacting cases are combined and presented in Fig. 6.39 to provide the current interpretation. In addition to replotting both the nonreacting and reacting data, a heuristic diagram is supplied. Each of the "nozzles" shown schematically corresponds to an individual Re_δ condition of reacting measurements, e.g. one each of *IR1* – *IR7*. The location of the FOV is shown to scale as the green rectangle, relative to the nozzle position. As noted in Table 3.4, the streamwise location of the FOV is held constant for all the *IRX* cases at approximately 153 nozzle diameters downstream. The visible flames for each Re_δ case are then drawn schematically, giving an indication of the location of the visible flame tip relative to the FOV. Note that for the lowest Re_δ case (*IR1*), the FOV is *beyond* the visible flame tip.

As the exit momentum flux J_0 at the nozzle is increased, increasing the Reynolds number, the location of the visible flame tip moves further downstream. The increase of the flame length with increased momentum flux indicates that the flame is not yet momentum-driven and buoyancy cannot be neglected. The 's' shown schematically on the centerline of each jet indicates the approximate location of the stoichiometric mixture along the jet axis. The diagram here depicts this stoichiometric point starting out upstream of the FOV (low Re_δ's), passing through the FOV (near the $Re_\delta = 60\,600$ case) and then proceeding downstream of the FOV for the high Re_δ conditions.

The picture described is a conjecture based on the behavior observed in the reacting $\sigma_q/\langle\sigma_q\rangle_{NR}$ data shown along with each "jet flame" sketch. The lowest Reynolds number case (*IR1*), obtained where its PIV FOV is the furthest beyond the visible flame tip, shows the smallest departure from the nonreacting data. Note that the dashed horizontal line at $\sigma_q/\langle\sigma_q\rangle_{NR} = 1$, indicates the averaged position of the reduced nonreacting data. This difference between the $\sigma_q/\langle\sigma_q\rangle_{NR}$ values of the reacting data and the nonreacting values of $\sigma_q/\langle\sigma_q\rangle_{NR}$ is interpreted as the influence of exothermicity on the inner scale gradients of the turbulence. Based on this hypothesis, the *IR1* case (where the local averaged temperatures are the smallest) should produce the smallest amount of heat release effect. The averaged value of reduced gradients for *IR1* is $\sigma_q/\langle\sigma_q\rangle_{NR} = 1.117$, only an 11.7% above the baseline (nonreacting) value.

Increasing the flow rate and thus increasing the flame length, the PIV measurement location is near the visible flame tip for *IR2*. The stoichiometric point s has moved closer to the FOV and the local averaged temperatures are increased. The reduced gradients demonstrate a significant increase in the *IR2* as compared to the *IR2* condition. The change relative to the nonreacting data is significant. The apparent effect of increasing Re_δ on the reduced reacting gradients is not a true Reynolds number effect, but rather the result of moving the stoichiometric point s relative to the FOV. By increasing the momentum flux J_0, the averaged temperature profile along the jet centerline changes relative to a laboratory frame, due to the influence of buoyancy.

The reduced reacting gradients peak at the *IR3* case, suggesting that the FOV is coincident with the averaged centerline stoichiometric location s – based on the current interpretation of the data. Further increasing J_0 increases the flame length such that the FOV is no longer located in the fuel-lean portion of the jet flame, but is now fuel-rich, moving between the stoichiometric point s and the nozzle exit. Since the change in relative position of the FOV is now moving away from s, the averaged centerline temperatures are diminishing, and the impact on the reduced gradients is slightly less for the *IR4* case, relative to *IR3*.

Further increases in J_0 push the stoichiometric point s further downstream beyond the FOV and the averaged temperatures continue to drop, as evidence in the monotonic decay in the reduced gradients of cases *IR5* – *IR7*. The final two conditions at the highest nozzle exit velocities, indicate that the jet has begun to enter the asymptotic limit of a momentum-driven flow, where the role of buoyancy is diminished. Comparing these two, an increase of 38% in Re_δ is realized from *IR6* (145 300) to *IR7* (200 100), but the response of $\sigma_q/\langle\sigma_q\rangle_{NR}$ is only changed by 1%. This suggests that the flame length is now independent of Re_δ, as the temperature (hence the location of s) is unchanged between the two conditions.

The reacting data provide information regarding the maximum amount of change between the reacting and nonreacting flows. The data at $Re_\delta = 60\,600$, *IR3*, represent the peak values in the reduced gradients, approximately $\sigma_q/\langle\sigma_q\rangle_{NR} = 1.405$. This is a 40.5% increase over the nonreacting baseline. These results, obtained for hydrogen-air chemistry, provide insight regarding the maximum magnitude of impact due to exothermicity on the inner scale gradients of a turbulent flame. Other fuel/oxidizer combinations could provide different levels of change between nonreacting and reacting flows.

6.2.4 Effects of Heat Release on Isotropy

Identical tests of isotropy presented in §5.3 for the nonreacting, inner scale data, were applied to the reacting data and the results are listed in Tables 6.2 and 6.3. The results from (5.2), listed in Table 6.3 are remarkably similar in comparison of the reacting against the nonreacting cases. If the results from the reacting cases and those of the nonreacting were averaged together, the overall values are 1.950 for the nonreacting data, over all Re_δ values and 1.986 for all reacting cases.

Despite the similarity observed by summing the on-diagonal and off-diagonal components, the individual gradients display a non-trivial difference in behavior. The comparison of on/off-diagonal gradients within each velocity component in Table 6.2 are noticeably asymmetric – where the u-component ratio is significantly larger than the tranverse v-component ratio. Indeed, if the same averaging across all Re_δ cases is applied, the mean value of $\mathrm{var}\{\partial u/\partial y\}/\mathrm{var}\{\partial u/\partial x\}$ is 2.280 in contrast to 1.678 for the quantity of $\mathrm{var}\{\partial v/\partial x\}/\mathrm{var}\{\partial v/\partial y\}$ for the burning flow data. The disparity is larger for the reacting cases as compared to the nonreacting cases where the u-component ratio is 2.025 and the v-component ratio is 1.873.

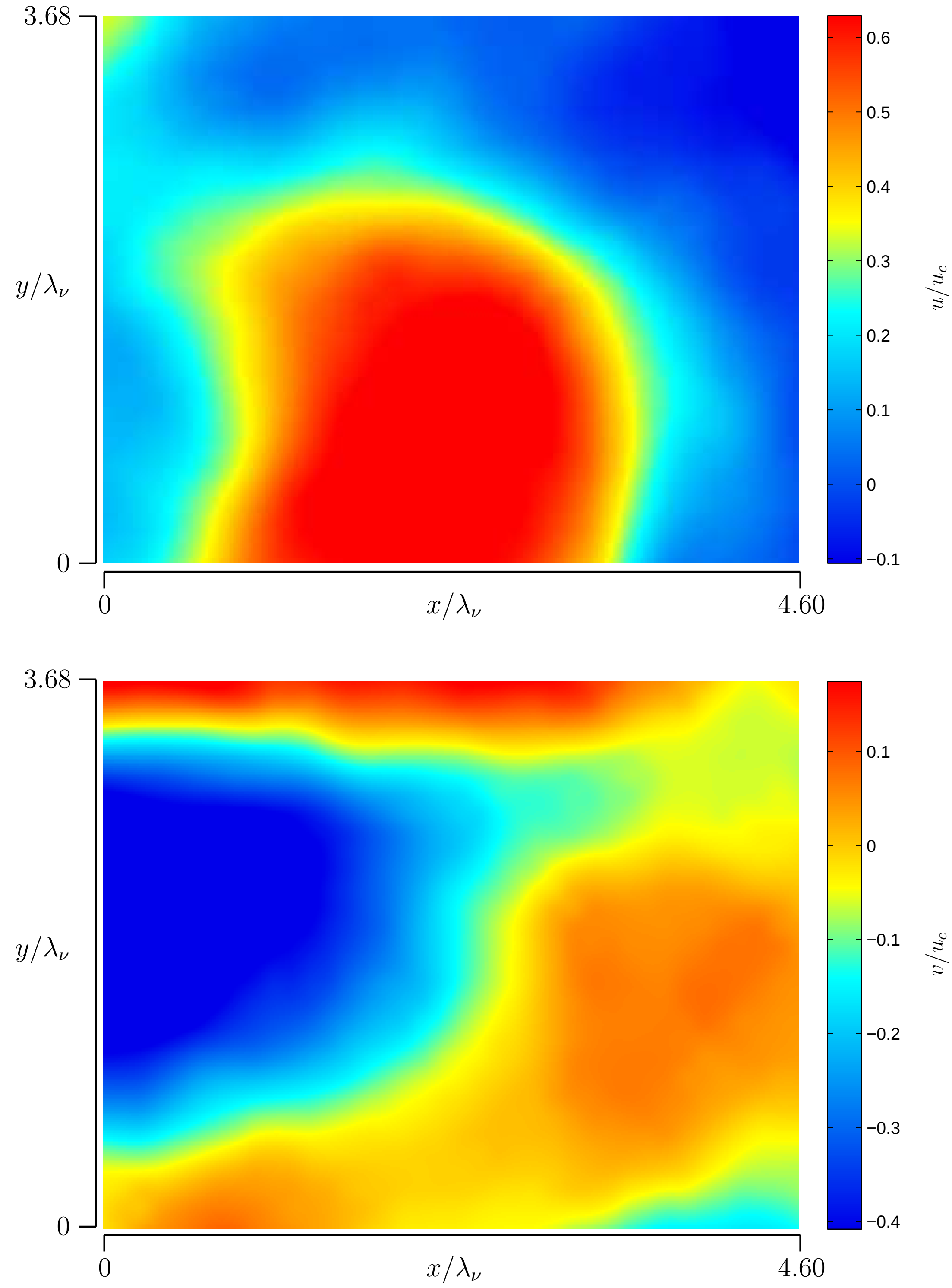

Figure 6.1: Sample velocity fields at $Re_\delta = 200\,100$. Instantaneous velocity fluctuations u *(top)* and v *(bottom)*, normalized by the centerline velocity u_c.

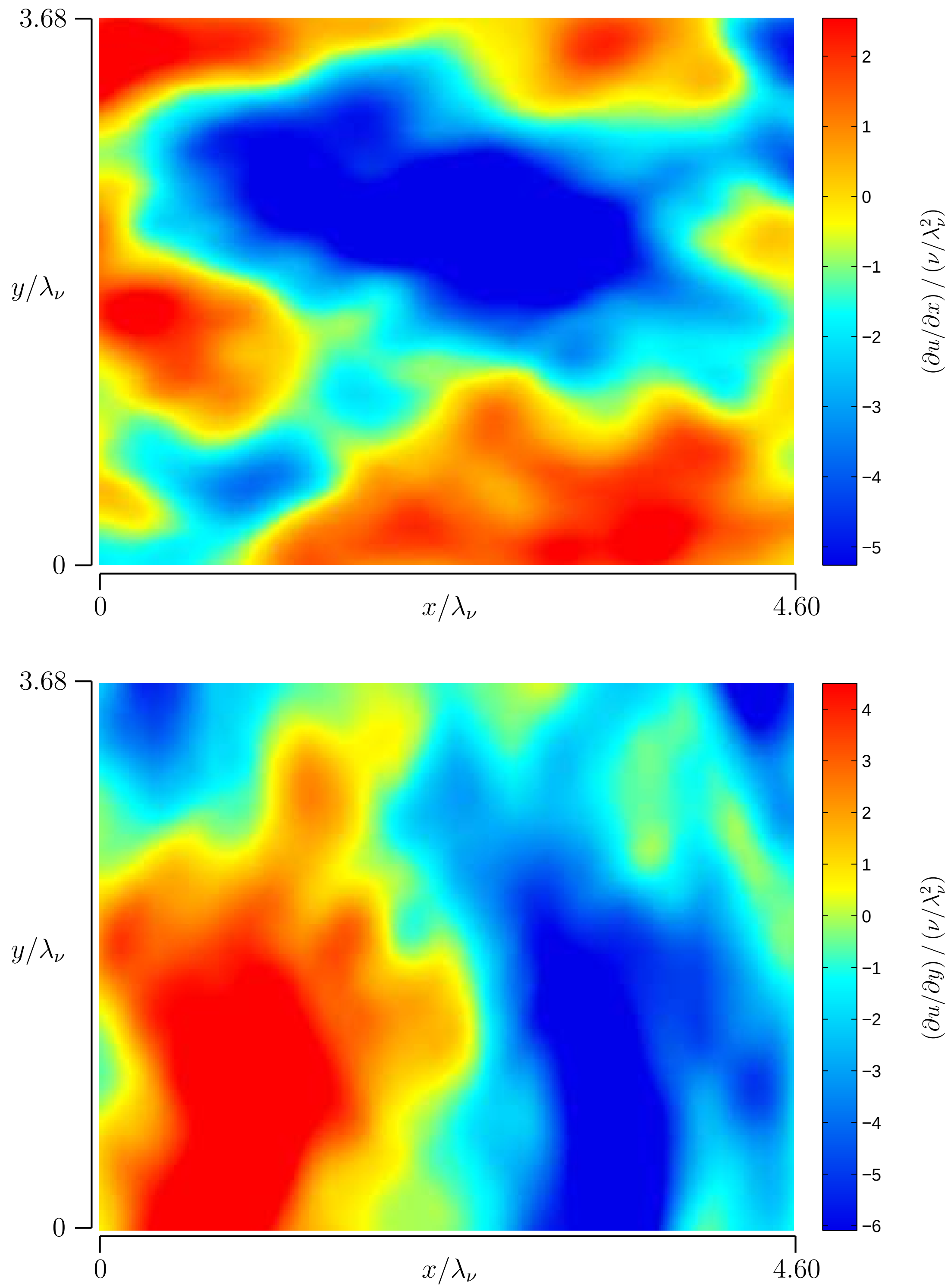

Figure 6.2: Sample velocity gradient fields at $Re_\delta = 200\,100$. Instantaneous velocity gradients $\partial u/\partial x$ *(top)* and $\partial u/\partial y$ *(bottom)*, normalized by inner variables ν/λ_ν^2 .

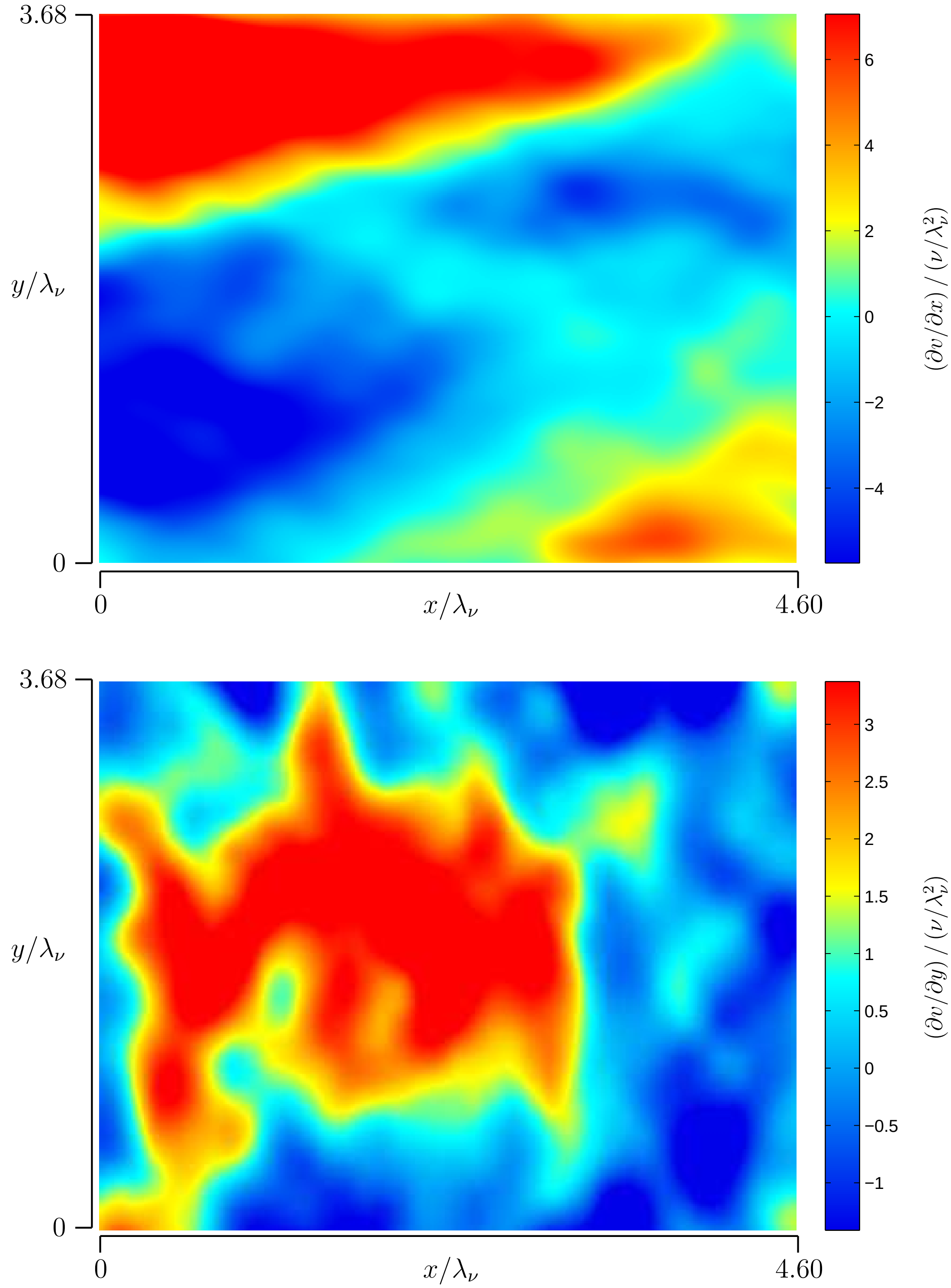

Figure 6.3: Sample velocity gradient fields at $Re_\delta = 200\,100$. Instantaneous velocity gradients $\partial v/\partial x$ *(top)* and $\partial v/\partial y$ *(bottom)*, normalized by inner variables ν/λ_ν^2 .

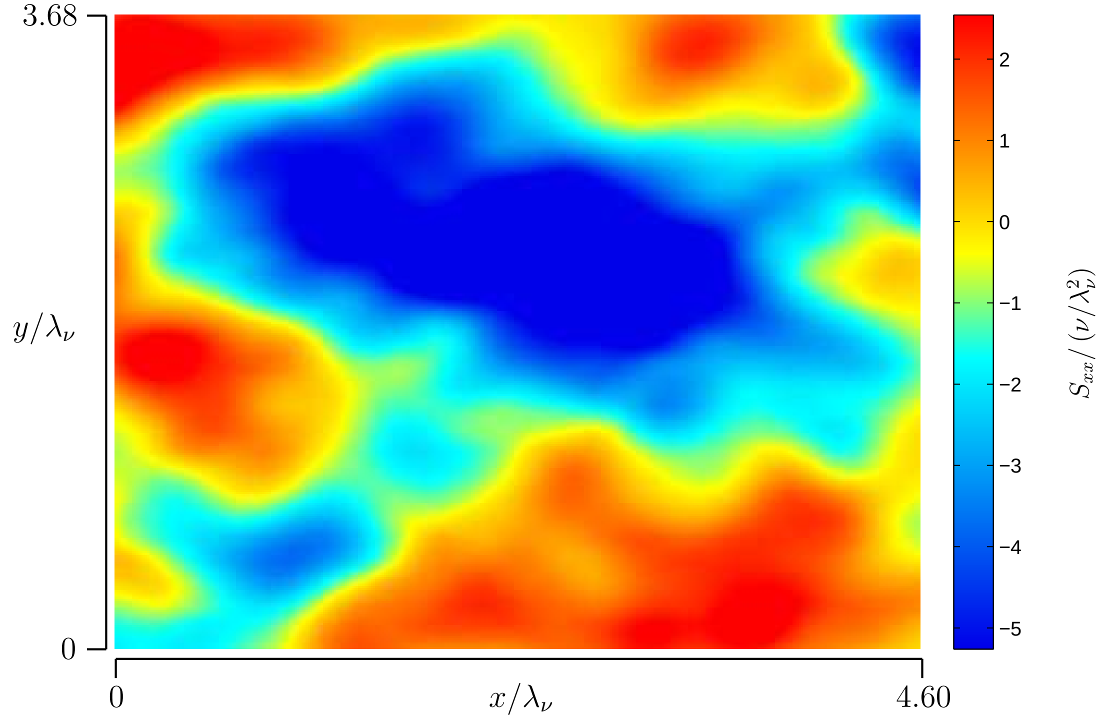

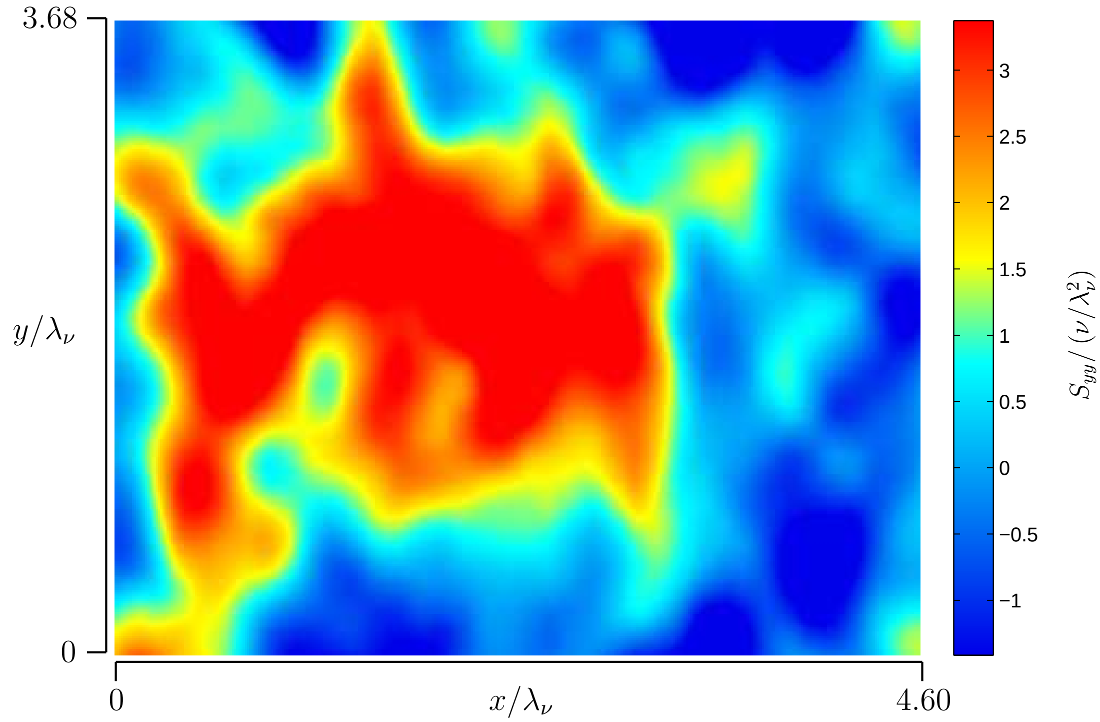

Figure 6.4: Sample velocity gradient fields at $Re_\delta = 200\,100$. Instantaneous strain rate components S_{xx} *(top)* and S_{yy} *(bottom)*, normalized by inner variables ν/λ_ν^2 .

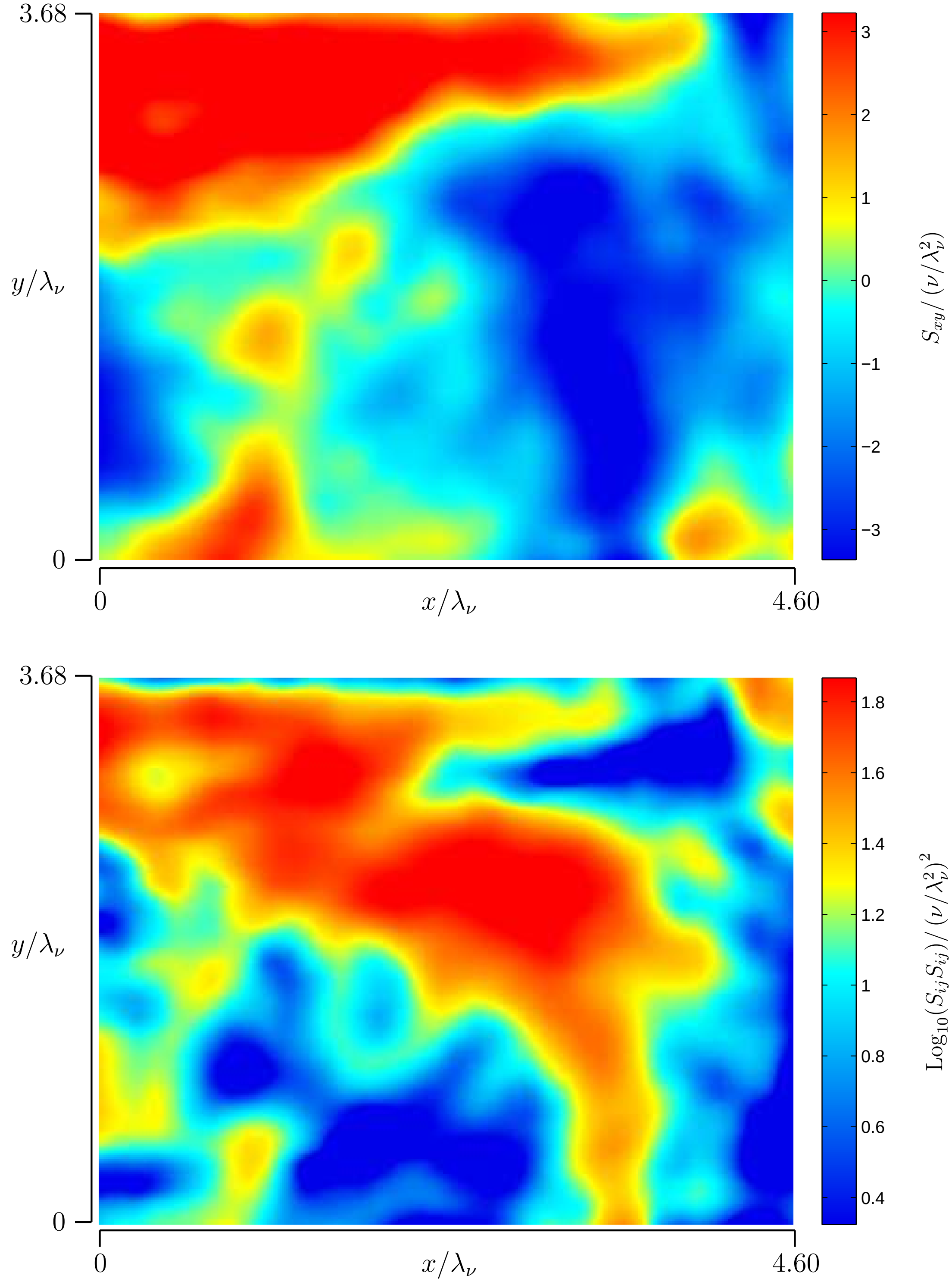

Figure 6.5: Sample velocity gradient fields at $Re_\delta = 200\,100$. Instantaneous strain rate component S_{xy} *(top)* and $\mathrm{Log}_{10}(S_{ij}S_{ij})$ *(bottom)*, normalized respectively by classical inner scaling ν/λ_ν^2 and $(\nu/\lambda_\nu^2)^2$. Here $S_{ij}S_{ij} \equiv S_{xx}^2 + S_{yy}^2 + 2\,S_{xy}^2$.

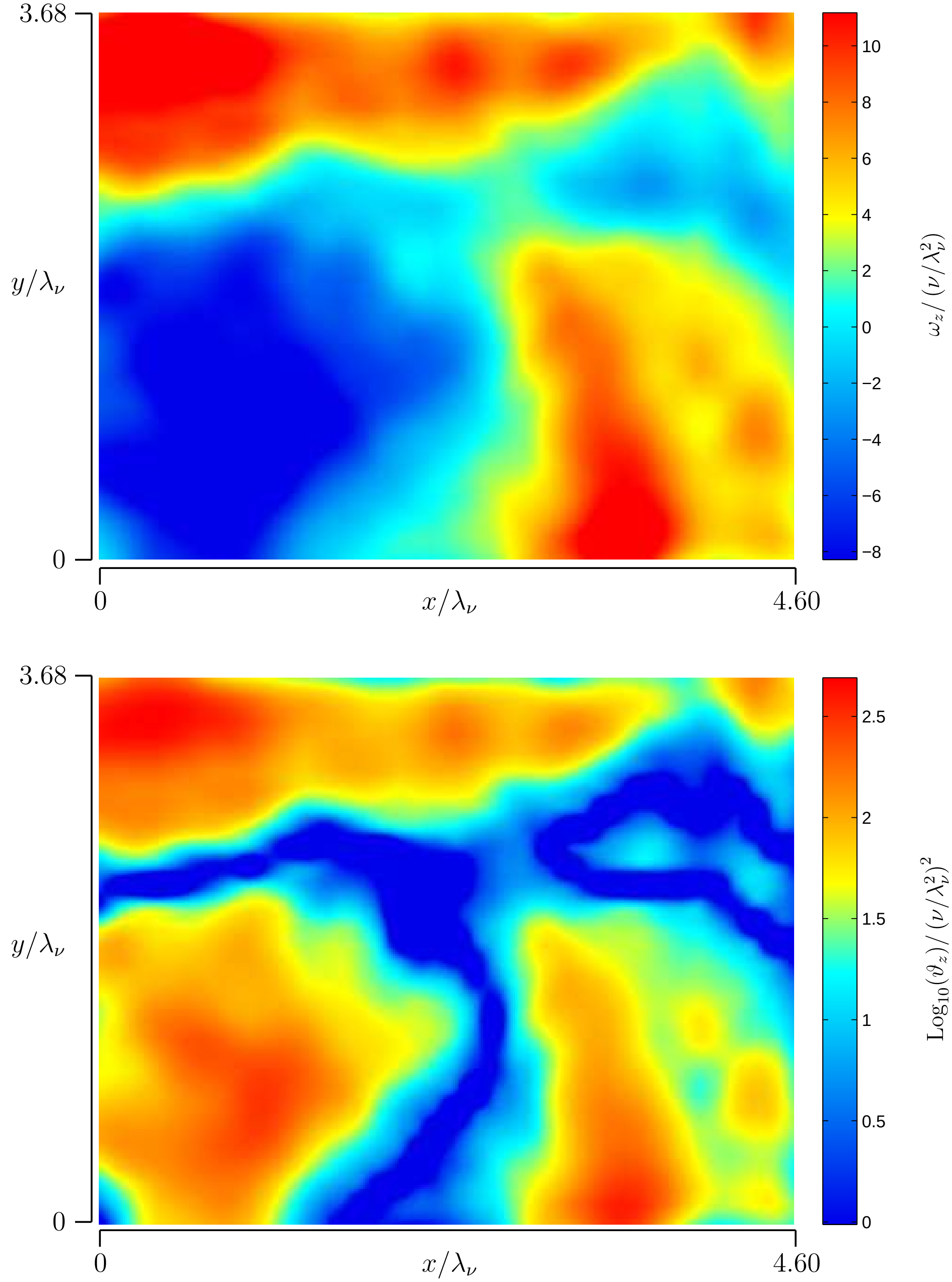

Figure 6.6: Sample velocity gradient fields at $Re_\delta = 200\,100$. Instantaneous in-plane vorticity ω_z *(top)* and enstrophy $\mathrm{Log}_{10}(\vartheta_z)$ *(bottom)*, normalized respectively by classical inner scaling ν/λ_ν^2 and $(\nu/\lambda_\nu^2)^2$. Here $\vartheta_z \equiv 3/2\,\omega_z^2$.

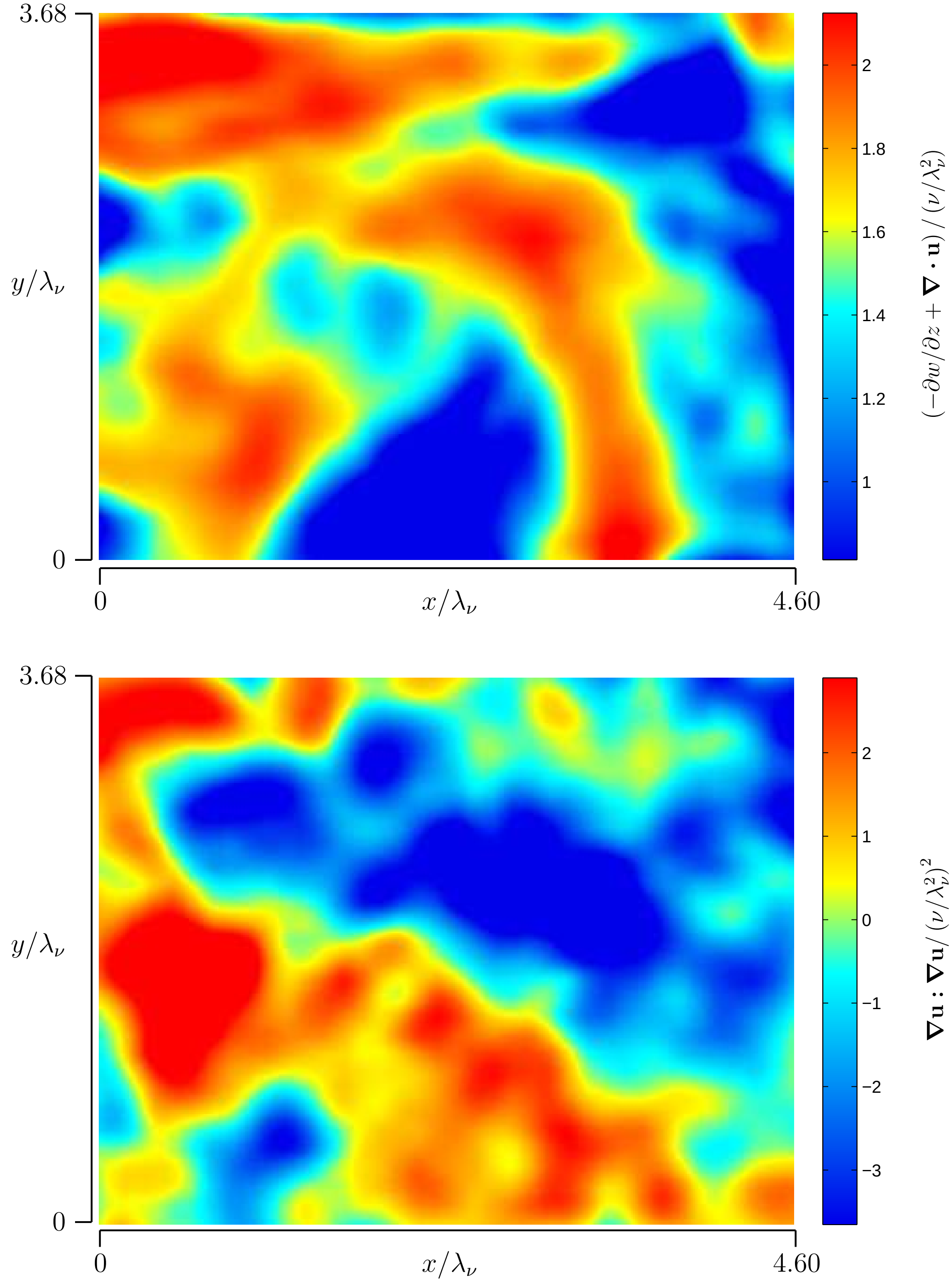

Figure 6.7: Sample velocity gradient fields at $Re_\delta = 200\,100$, showing contraction of instantaneous velocity gradient tensor $\mathrm{Log}_{10}(\boldsymbol{\nabla}\mathbf{u} : \boldsymbol{\nabla}\mathbf{u})$ *(top)* and two-dimensional divergence $(-\partial w/\partial z + \boldsymbol{\nabla}\cdot\mathbf{u})$ *(bottom)*, normalized respectively by classical inner scaling $(\nu/\lambda_\nu^2)^2$ and ν/λ_ν^2.

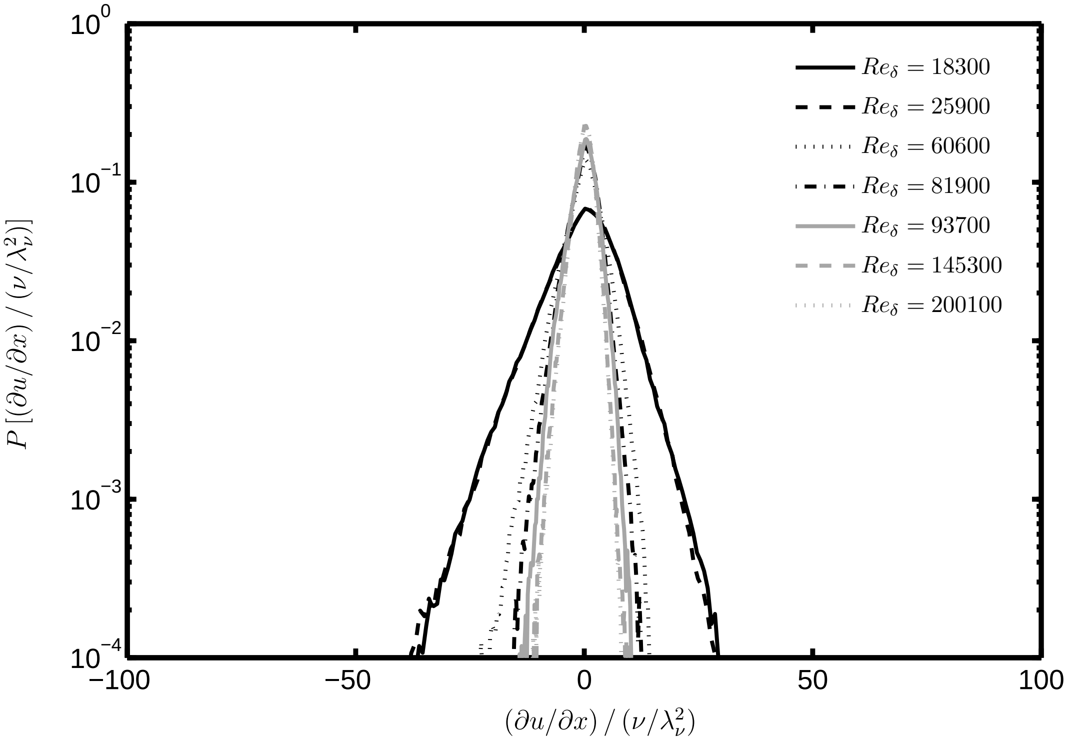

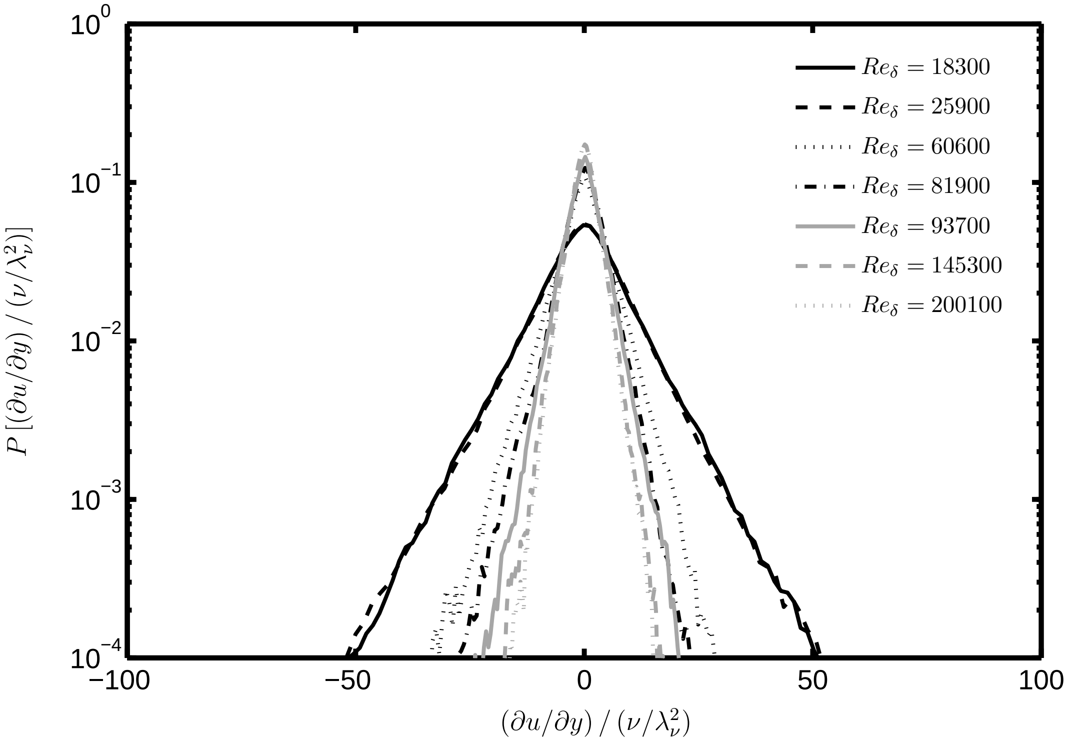

Figure 6.8: Pdfs from all reacting cases *IR1 – IR7* for velocity gradient $\partial u/\partial x$ *(top)* and $\partial u/\partial y$ *(bottom)* normalized by inner variables ν/λ_ν^2.

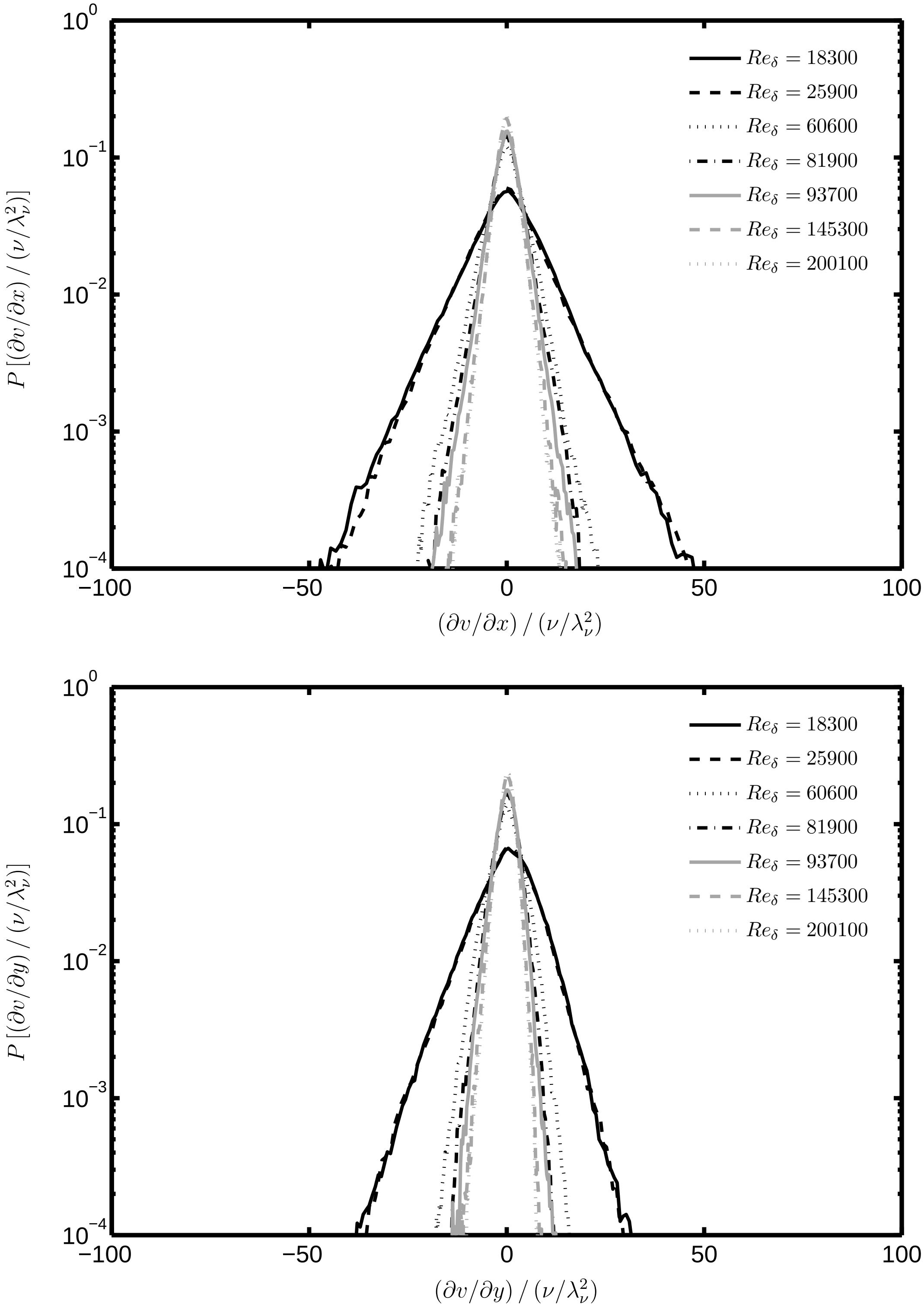

Figure 6.9: Pdfs from all reacting cases *IR1 – IR7* for velocity gradient $\partial v/\partial x$ *(top)* and $\partial v/\partial y$ *(bottom)* normalized by inner variables ν/λ_ν^2.

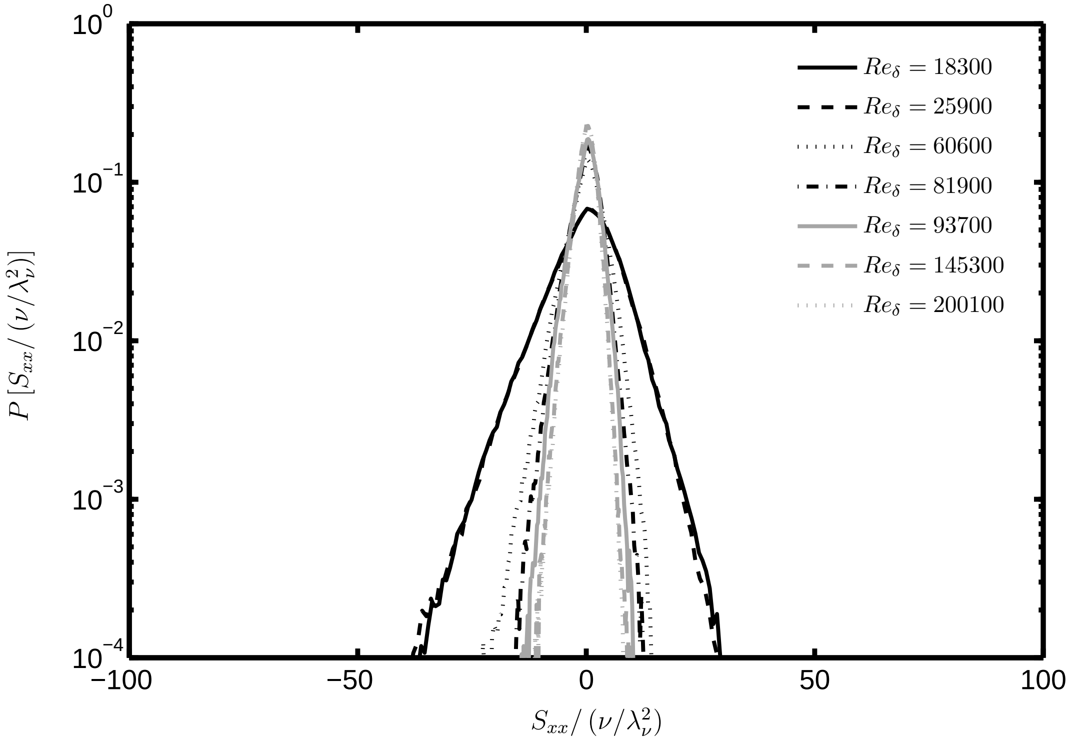

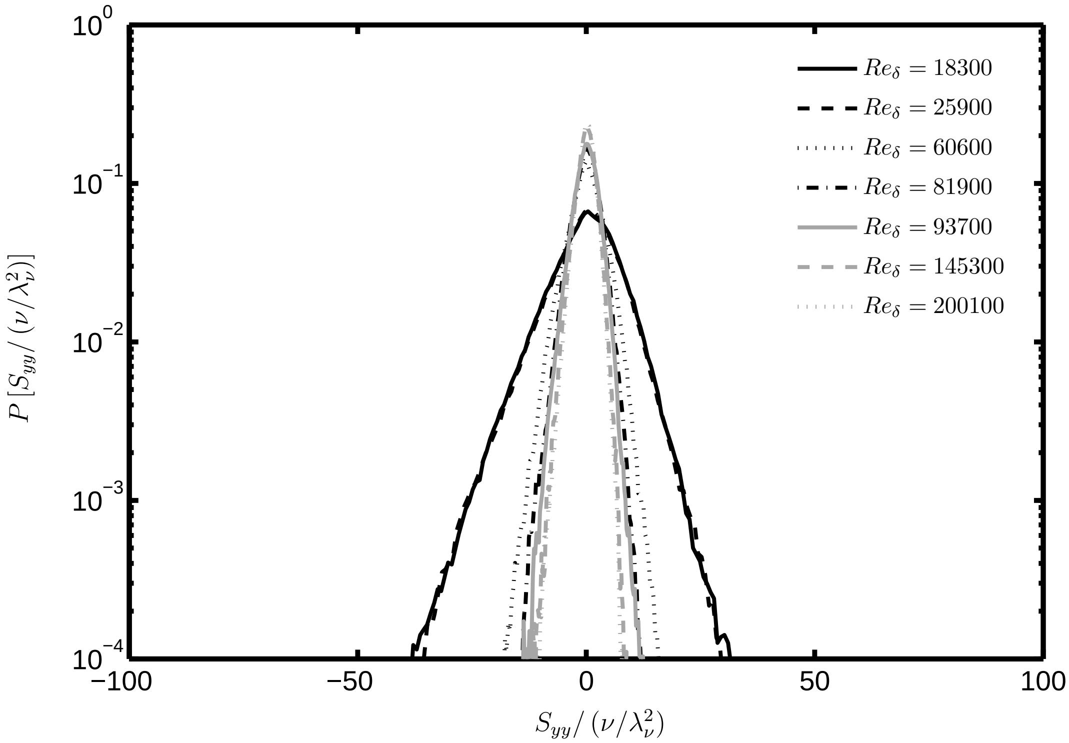

Figure 6.10: Pdfs from all reacting cases *IR1* − *IR7* for strain rate components S_{xx} *(top)* and S_{yy} *(bottom)* normalized by inner variables ν/λ_ν^2.

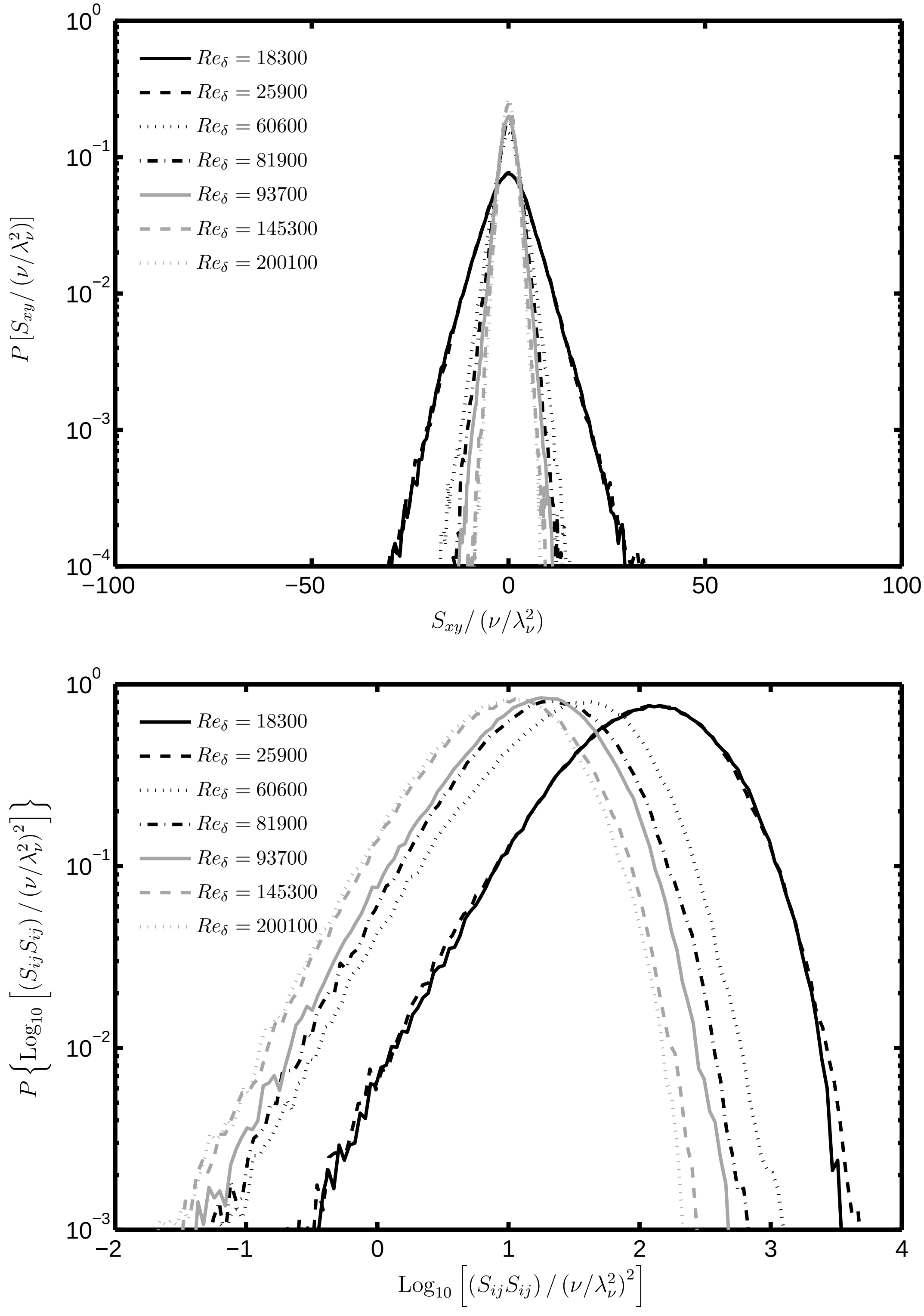

Figure 6.11: Pdfs from all reacting cases *IR1* – *IR7* for strain rate components S_{xy} *(top)* and $\mathrm{Log}_{10}\left(S_{ij}S_{ij}\right)$ *(bottom)* normalized by inner variables ν/λ_ν^2 and $\left(\nu/\lambda_\nu^2\right)^2$.

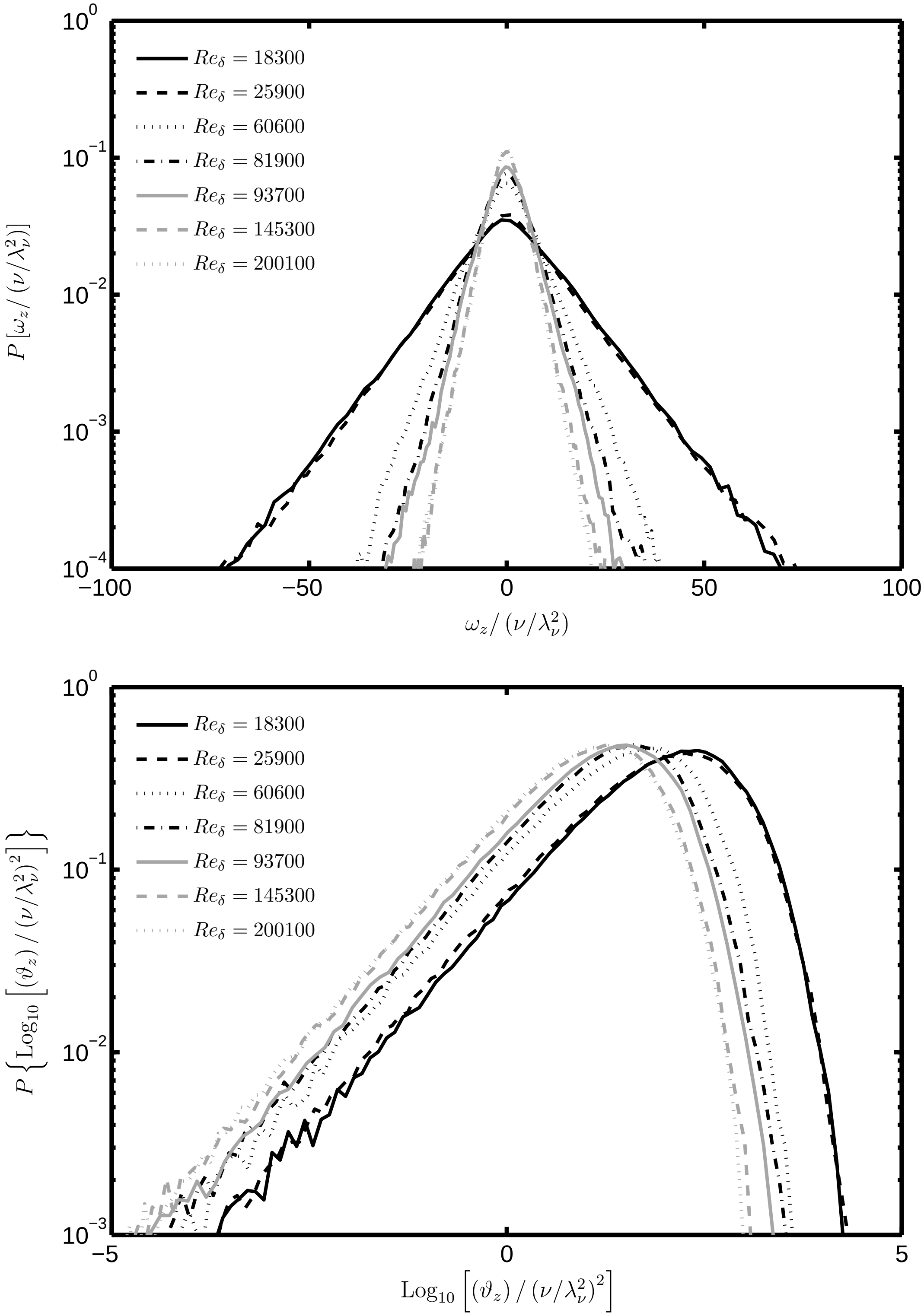

Figure 6.12: Pdfs from all reacting cases *IR1* − *IR7* for in-plane vorticity ω_z *(top)* and enstrophy $\mathrm{Log}_{10}\left(\vartheta_z\right)$ *(bottom)* normalized by inner variables ν/λ_ν^2 and $\left(\nu/\lambda_\nu^2\right)^2$.

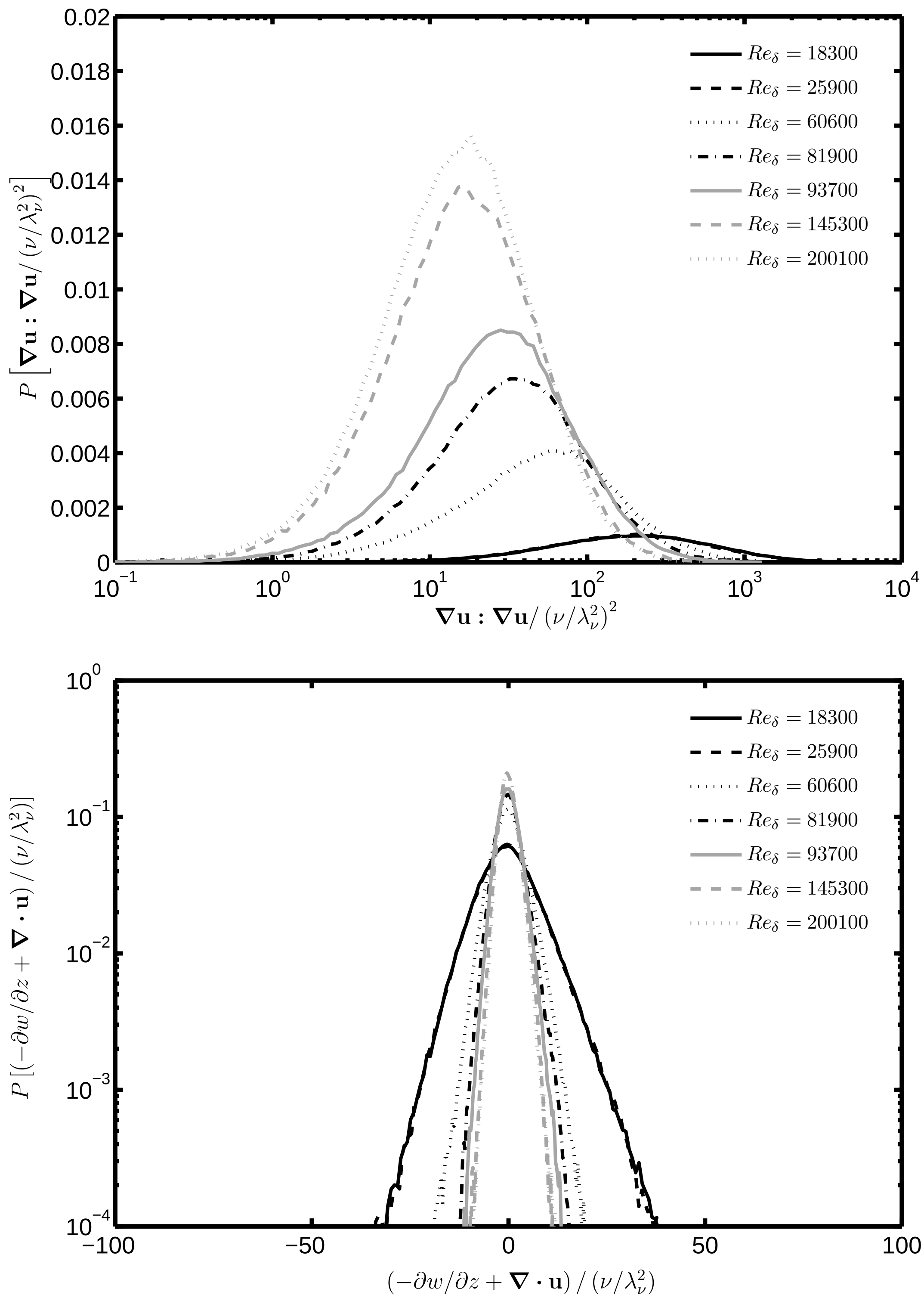

Figure 6.13: Pdfs from all reacting cases *IR1 – IR7* for contraction of the instantaneous velocity gradient tensor $\nabla\mathbf{u}:\nabla\mathbf{u}$ *(top)* and two-dimensional divergence $(-\partial w/\partial z + \nabla\cdot\mathbf{u})$ *(bottom)* normalized by inner variables $\left(\nu/\lambda_\nu^2\right)^2$ and ν/λ_ν^2.

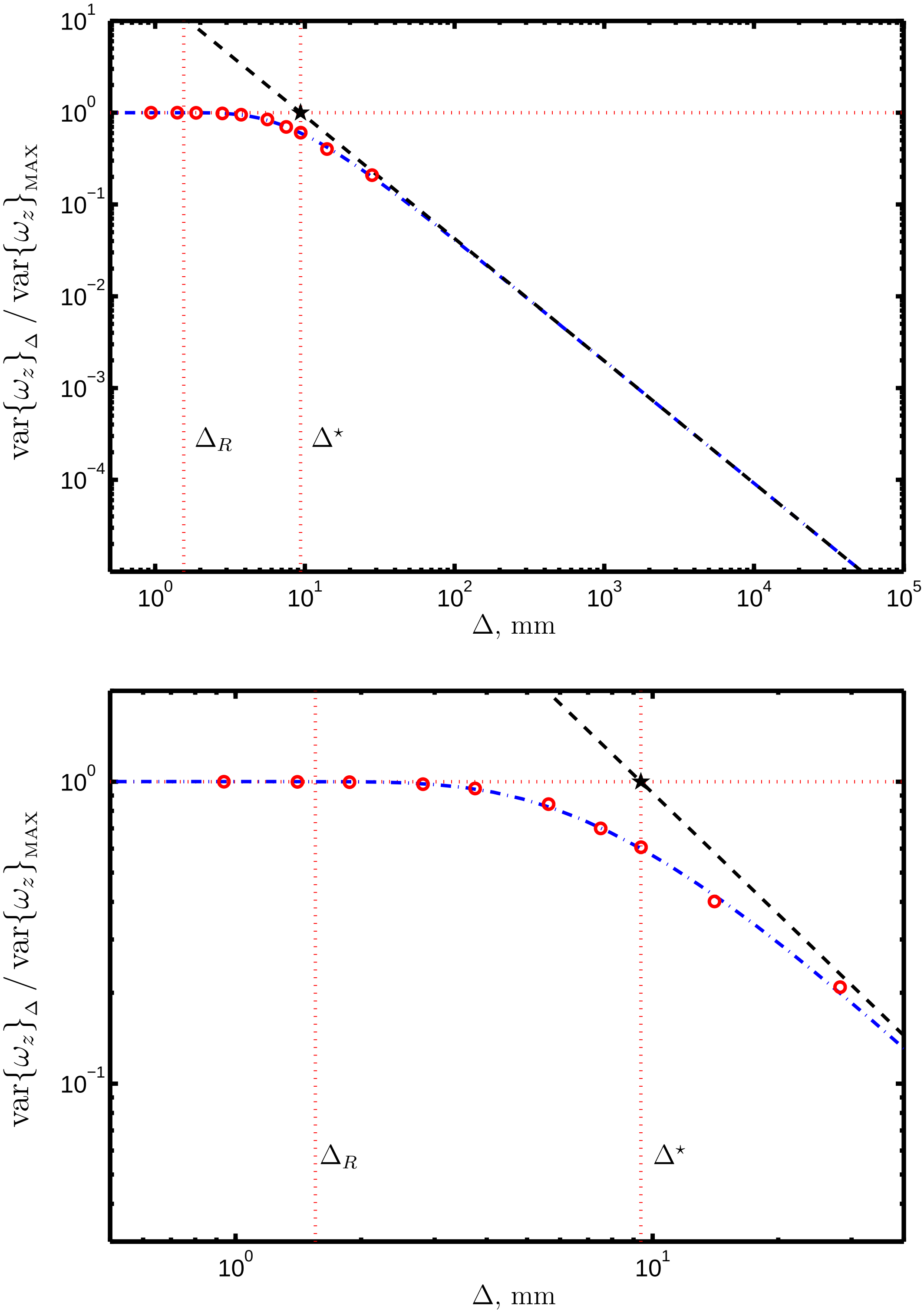

Figure 6.14: Results from low-pass filtering to determine effective length scale $\Delta^\star$ for case *IR1*, $Re_\delta = 18\,300$.

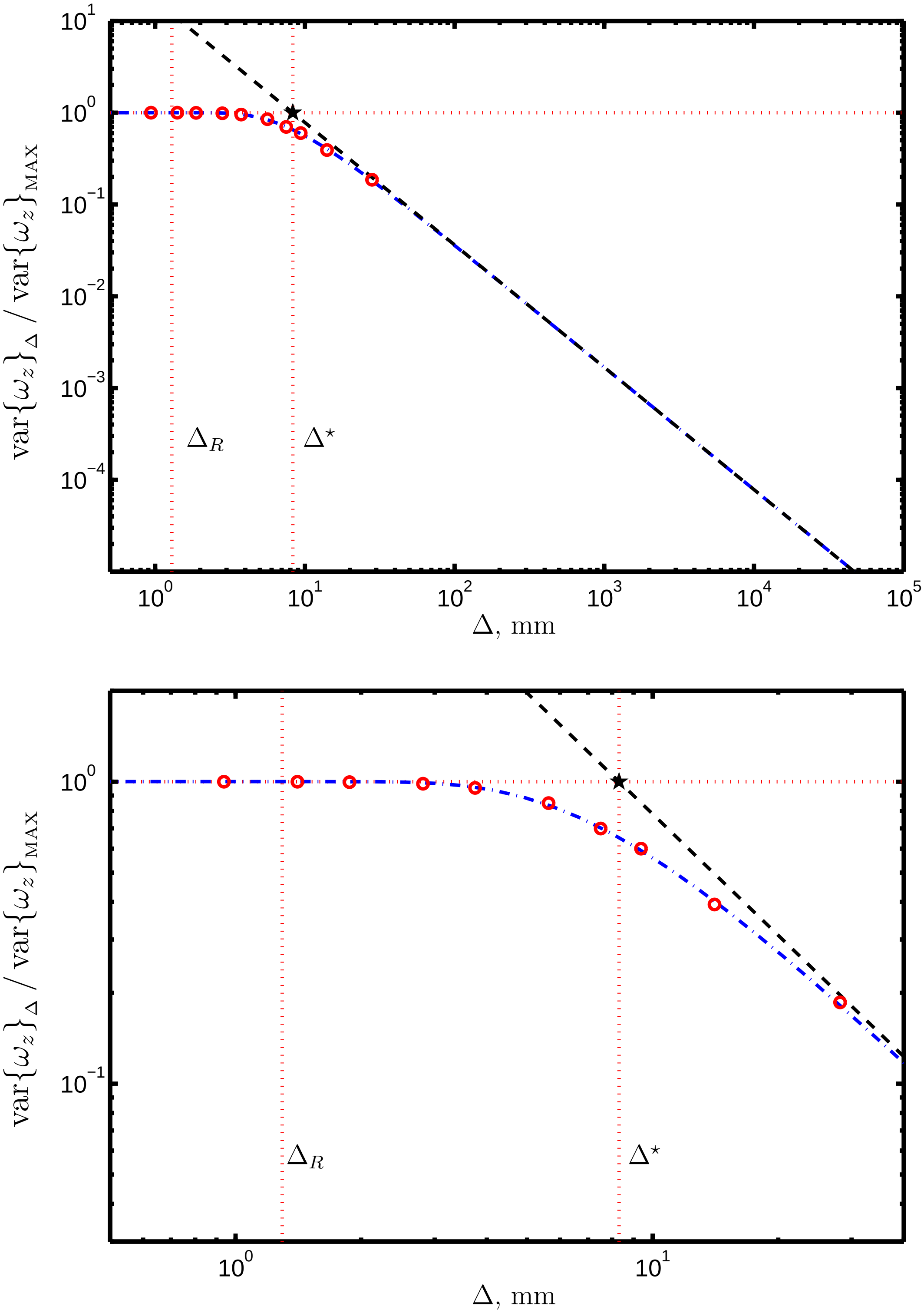

Figure 6.15: Results from low-pass filtering to determine effective length scale $\Delta^\star$ for case *IR2*, $Re_\delta = 25\,900$.

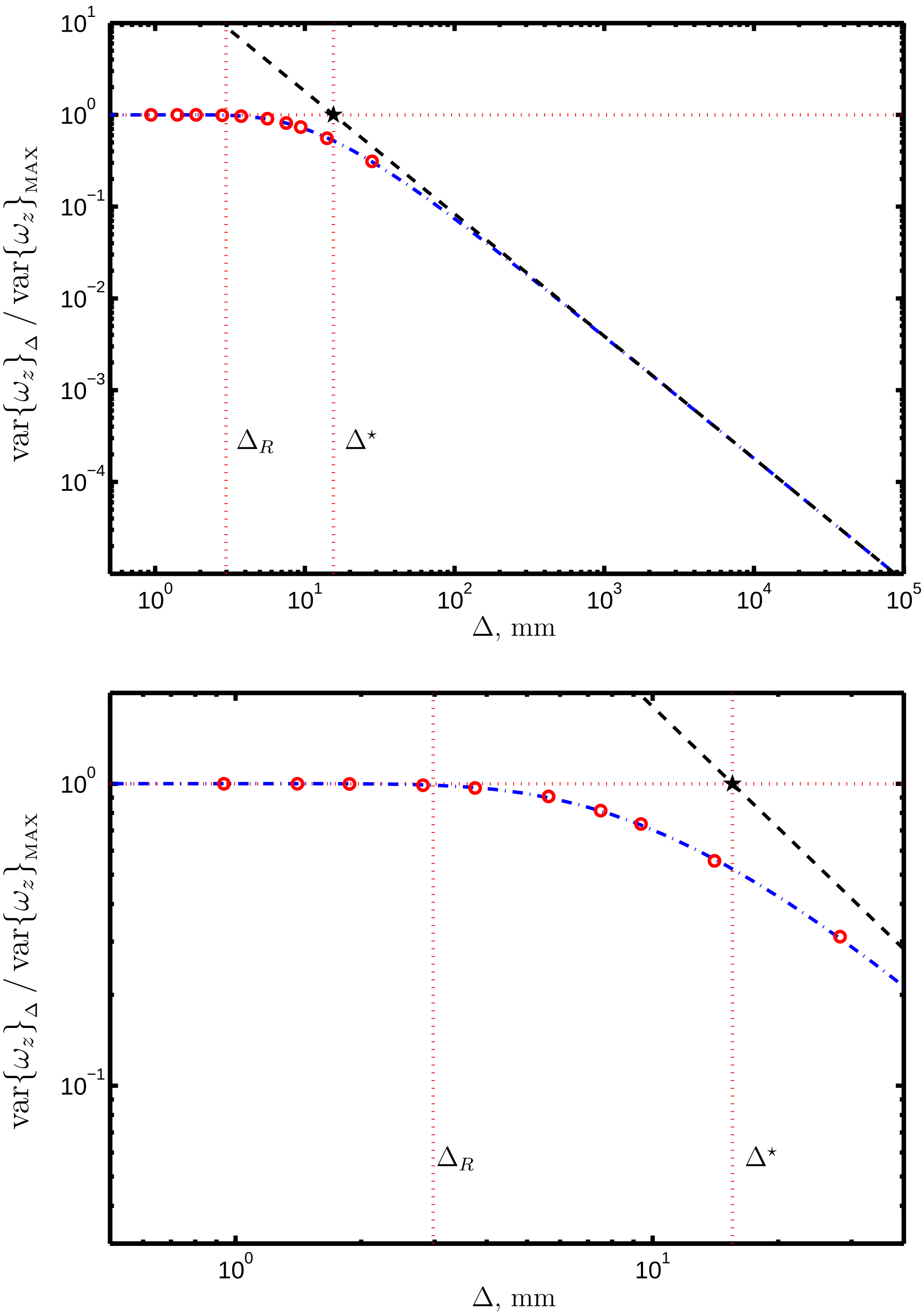

Figure 6.16: Results from low-pass filtering to determine effective length scale $\Delta^\star$ for case *IR3*, $Re_\delta = 60\,600$.

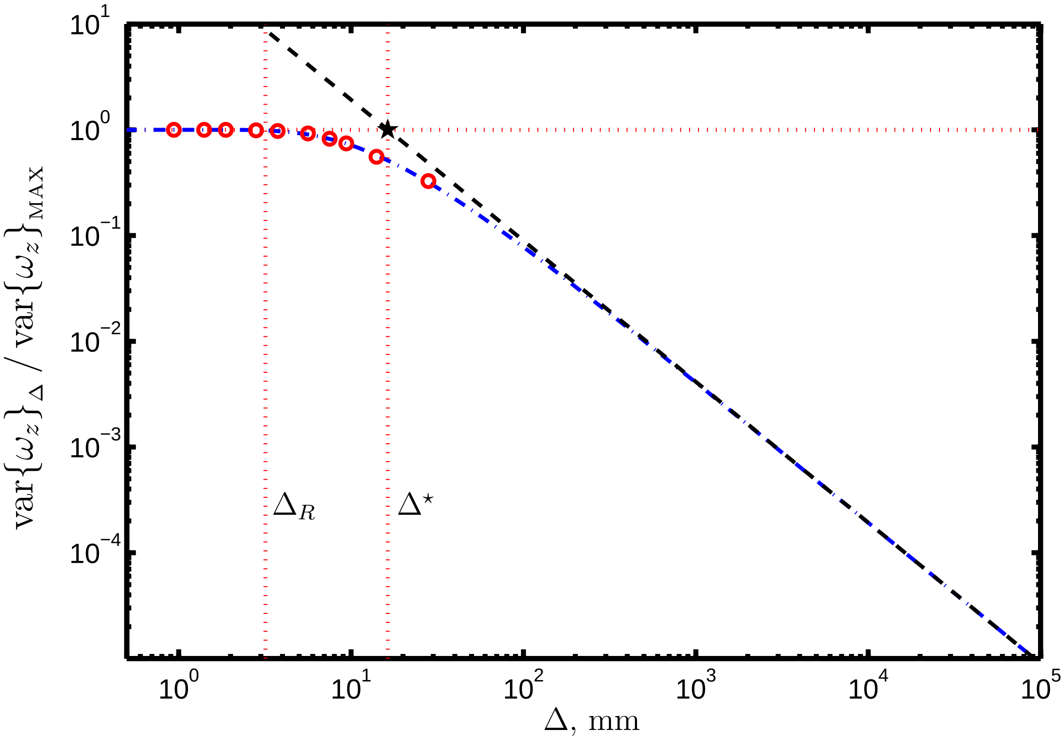

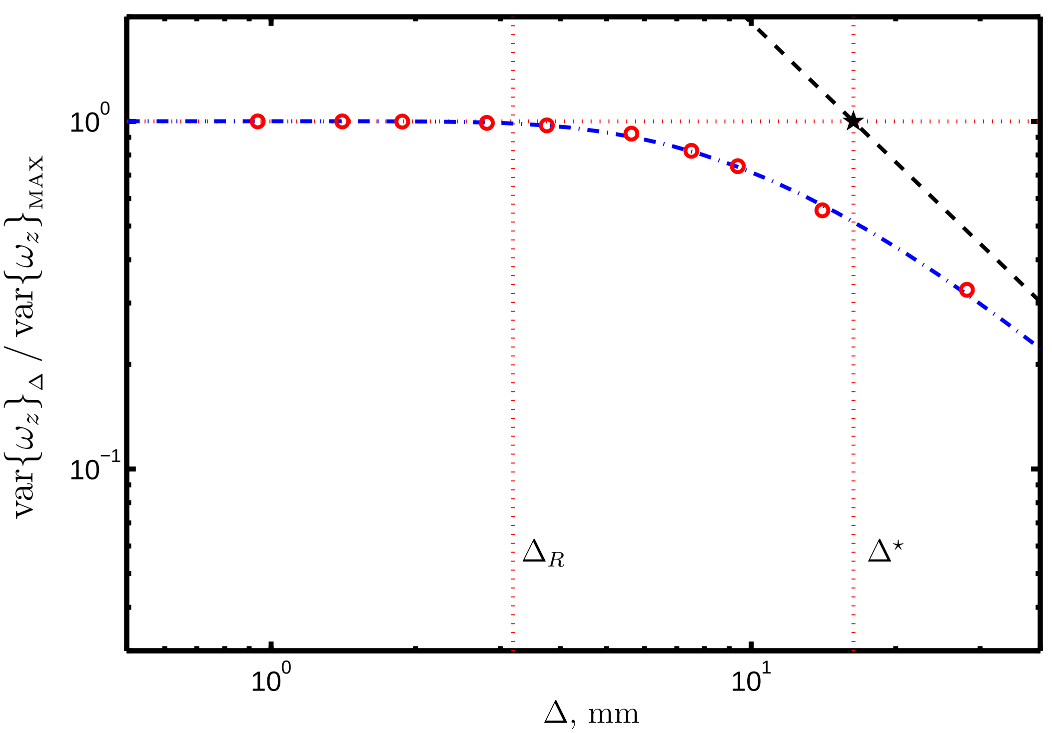

Figure 6.17: Results from low-pass filtering to determine effective length scale $\Delta^\star$ for case *IR4*, $Re_\delta = 81\,900$.

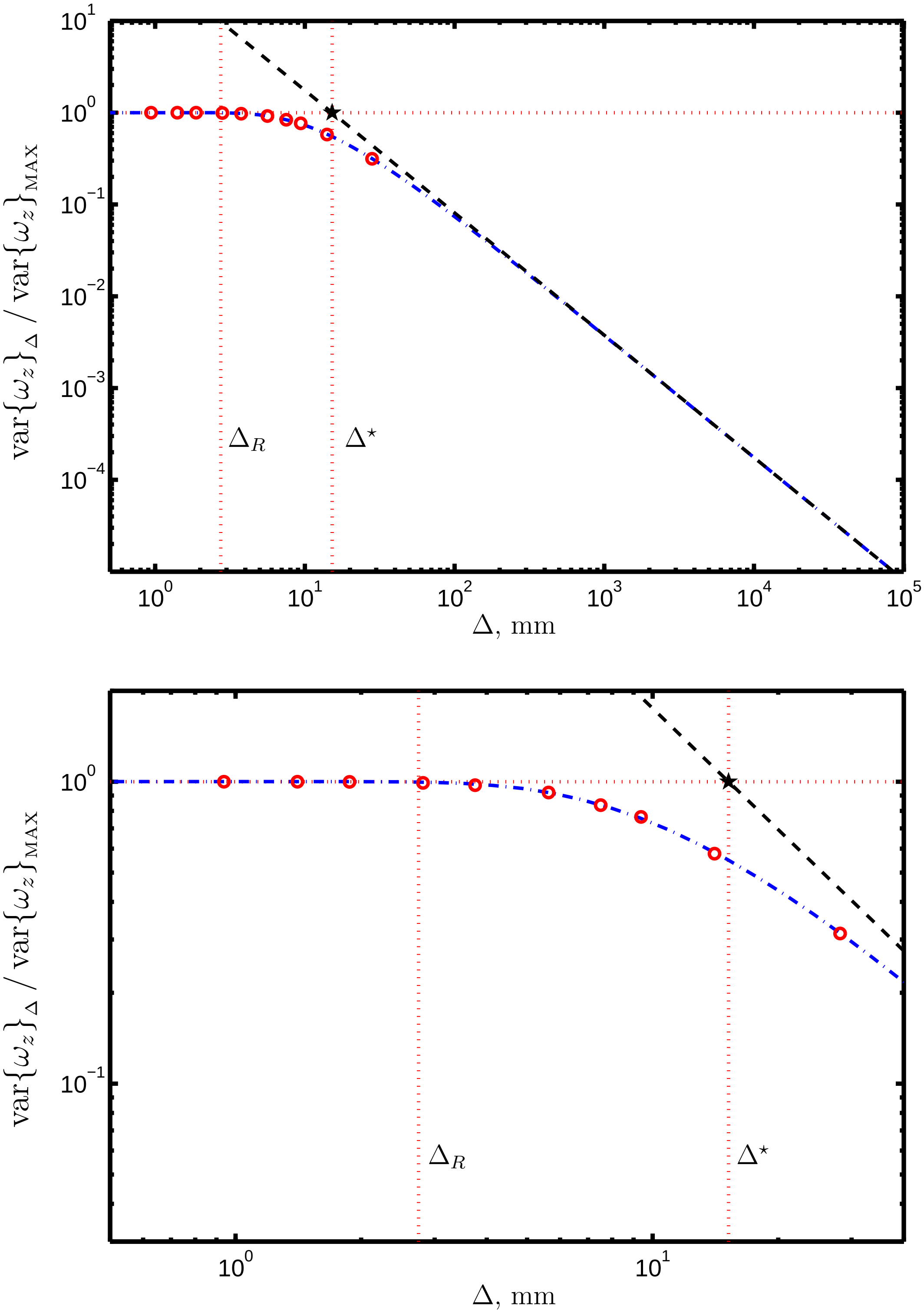

Figure 6.18: Results from low-pass filtering to determine effective length scale $\Delta^\star$ for case *IR5*, $Re_\delta = 93\,700$.

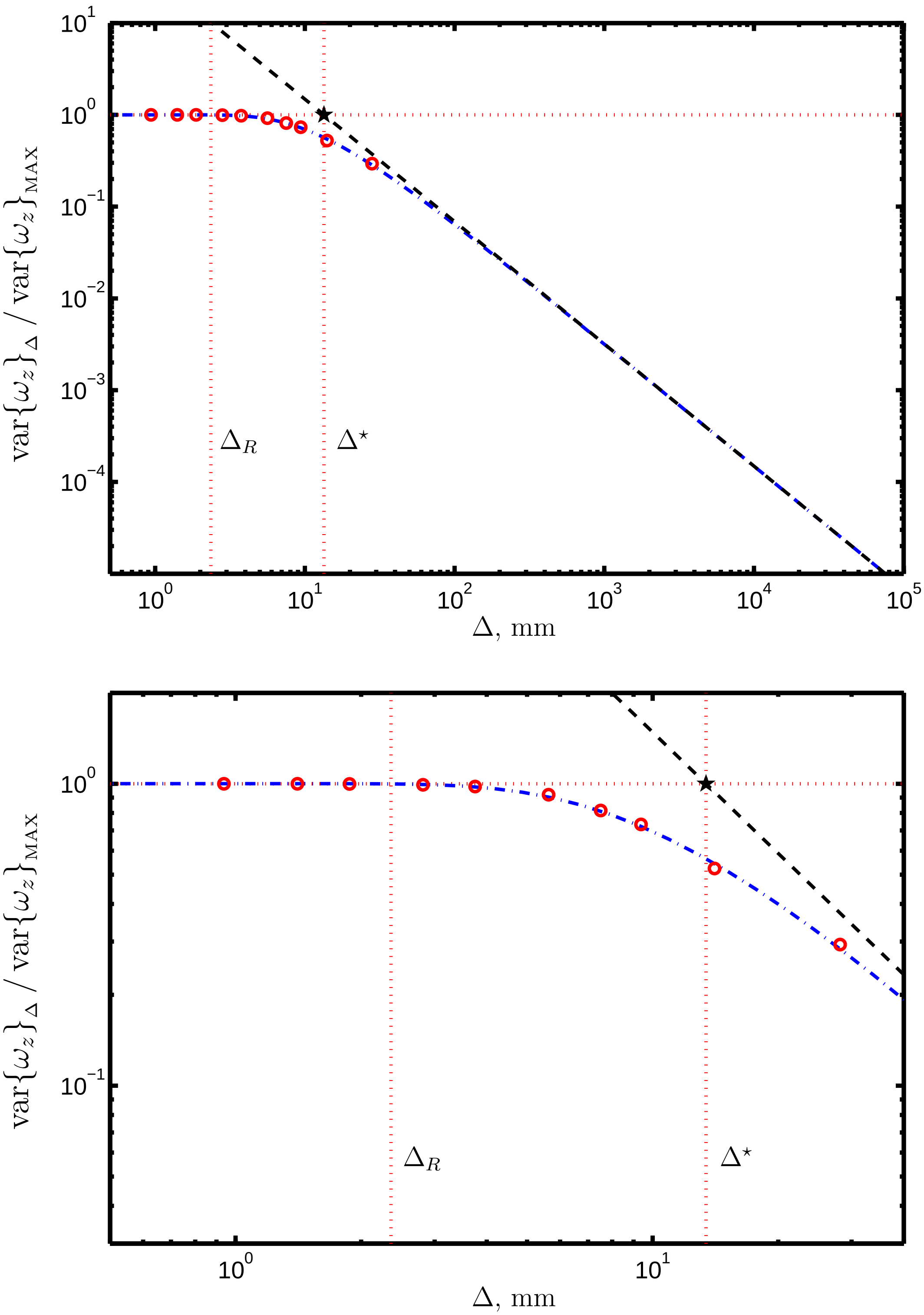

Figure 6.19: Results from low-pass filtering to determine effective length scale $\Delta^\star$ for case *IR6*, $Re_\delta = 145\,300$.

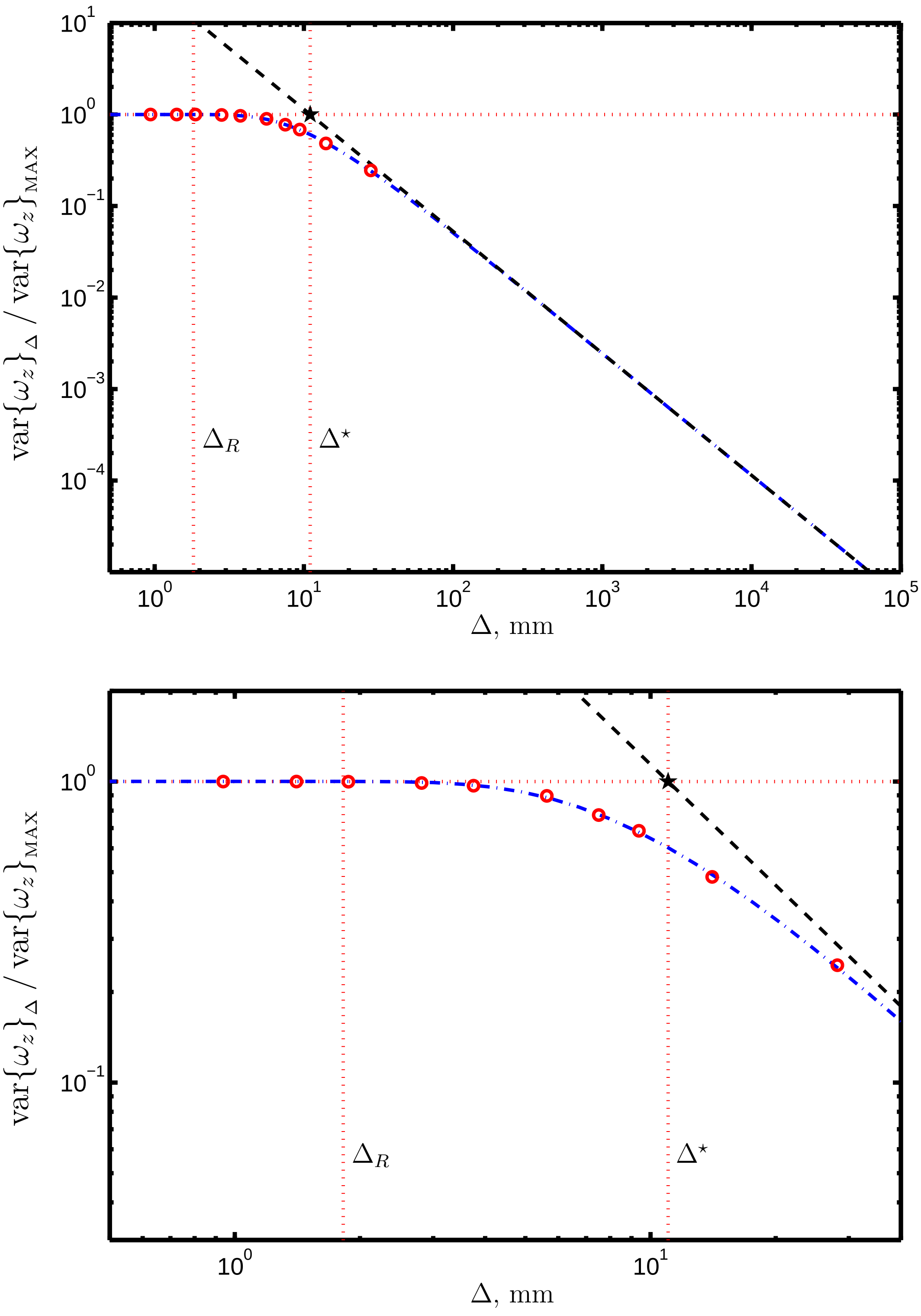

Figure 6.20: Results from low-pass filtering to determine effective length scale $\Delta^\star$ for case *IR7*, $Re_\delta = 200\,100$.

Re_δ	δ [m]	Δ_{IW} mm	Inertial- and dissipation-range spectral parameters and resulting factors							
			$\langle p \rangle$ [-]	$\langle \Delta_R \rangle$ mm	Λ_ν [-]	$\langle \Delta^\star \rangle$ mm	$\Lambda^\star$ [-]	$\langle \Delta^\star \rangle / \langle \Delta_R \rangle$	$D(p)$	$\mathcal{N}^\star$
18300†	0.230	0.469	1.151	1.640	11.223	9.617	65.825	5.87	0.0918	13.061
25900	0.230	0.469	1.260	1.501	13.306	9.187	81.449	6.12	0.0875	18.558
60600	0.247	0.469	0.881	2.998	51.108	14.747	251.409	4.92	0.1114	36.526
81900	0.216	0.469	0.892	3.288	75.447	16.053	368.292	4.88	0.1098	50.910
93700	0.197	0.469	0.918	2.998	82.064	15.357	420.362	5.12	0.1073	65.599
145300	0.191	0.469	1.051	2.367	92.225	13.360	520.498	5.64	0.0968	109.484
200100	0.193	0.469	1.172	1.864	91.374	10.925	535.634	5.86	0.0906	164.563

Table 6.1: Averaged spectral parameters $\langle p \rangle$, $\langle \Delta_R \rangle$ and $\langle \Delta^\star \rangle$ for all cases in Table 3.4 obtained by averaging over results from ω_z, S_{xx}, S_{yy} and S_{xy}. Here Λ_ν and $\Lambda^\star$ values are from $\Lambda_i \equiv (\Delta_i/\delta) Re_\delta^{3/4}$.

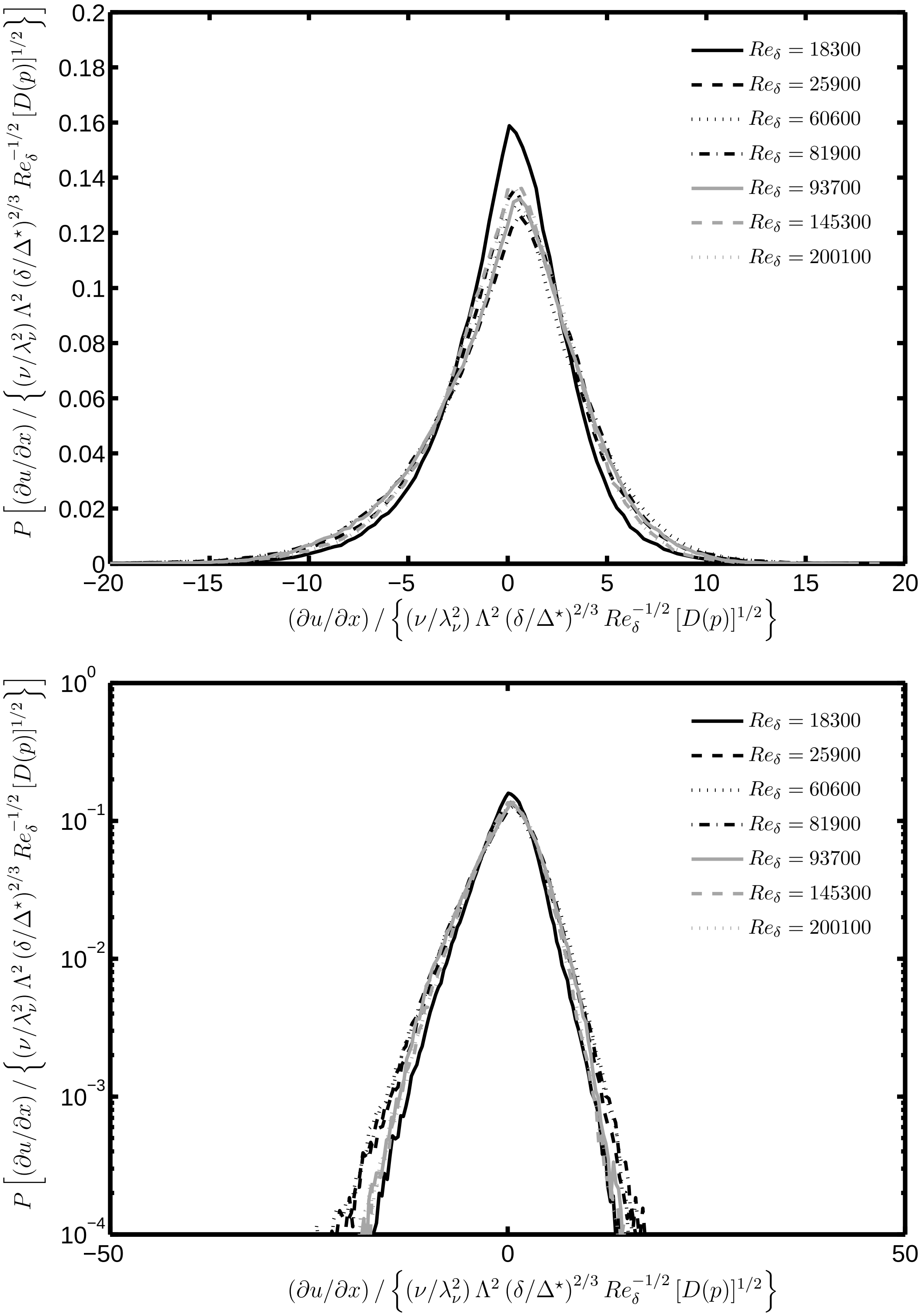

Figure 6.21: Pdfs from all nonreacting cases *IR1* – *IR7* for velocity gradient $\partial u/\partial x$ normalized by resolution-corrected inner scaling $(\nu/\lambda_\nu^2)\,\Lambda^2\,(\delta/\Delta^\star)^{2/3}\,Re_\delta^{-1/2}\,[D(p)]^{1/2}$, shown in linear axes *(top)* and semilogarithmic axes *(bottom)*.

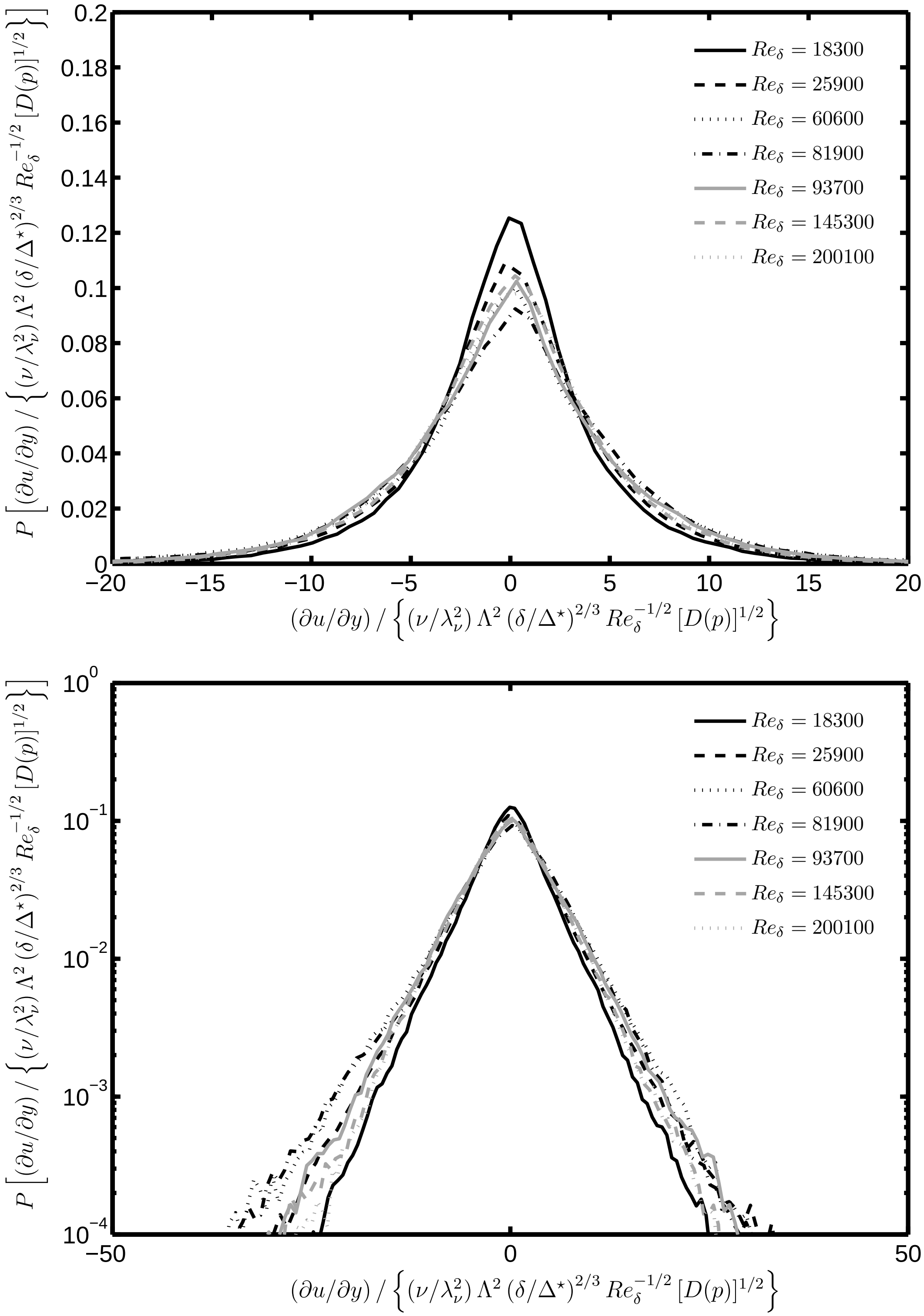

Figure 6.22: Pdfs from all nonreacting cases *IR1* – *IR7* for velocity gradient $\partial u/\partial y$ normalized by resolution-corrected inner scaling $(\nu/\lambda_\nu^2)\,\Lambda^2\,(\delta/\Delta^\star)^{2/3}\,Re_\delta^{-1/2}\,[D(p)]^{1/2}$, shown in linear axes *(top)* and semilogarithmic axes *(bottom)*.

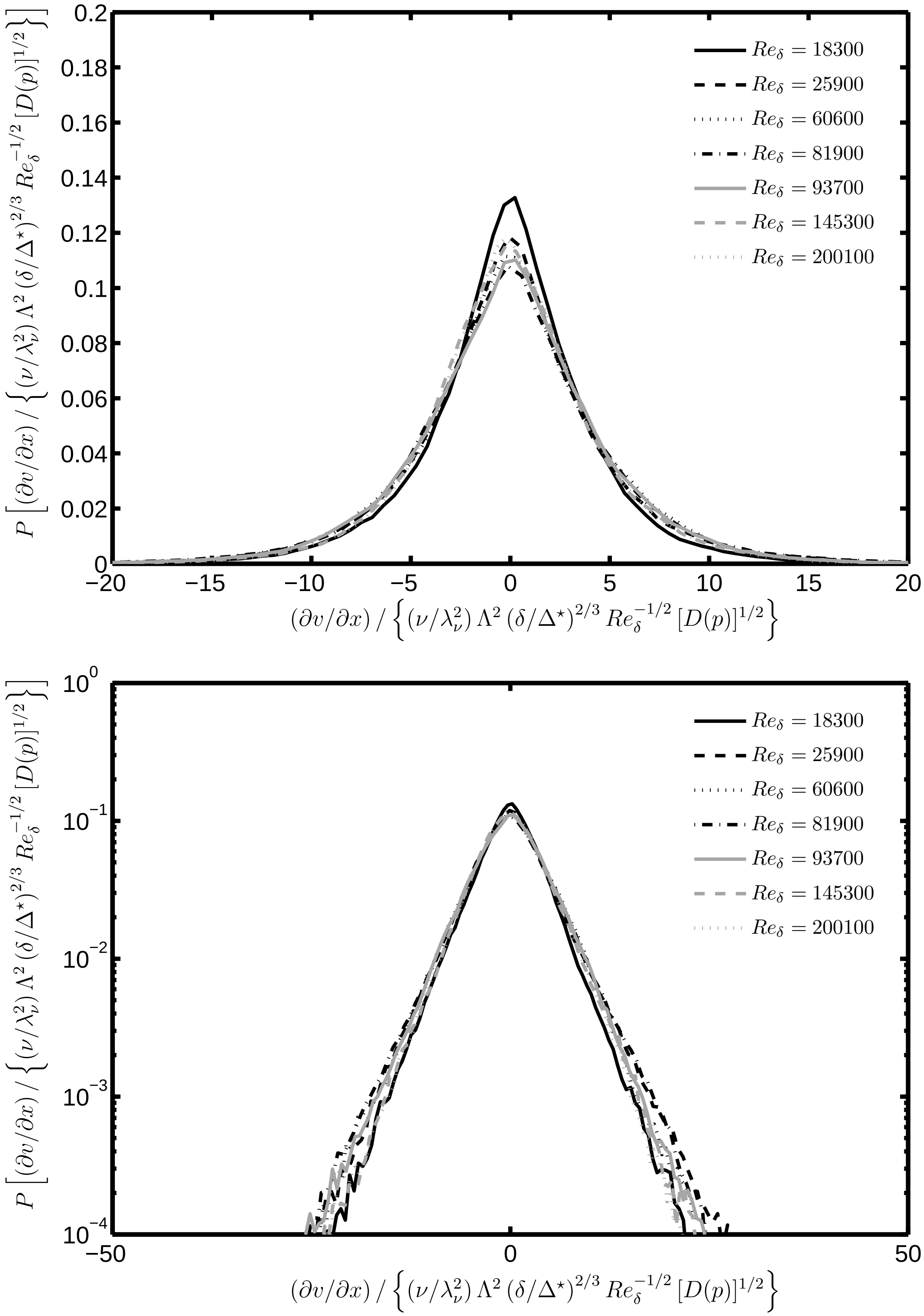

Figure 6.23: Pdfs from all nonreacting cases *IR1* – *IR7* for velocity gradient $\partial v/\partial x$ normalized by resolution-corrected inner scaling $(\nu/\lambda_\nu^2)\,\Lambda^2\,(\delta/\Delta^\star)^{2/3}\,Re_\delta^{-1/2}\,[D(p)]^{1/2}$, shown in linear axes *(top)* and semilogarithmic axes *(bottom)*.

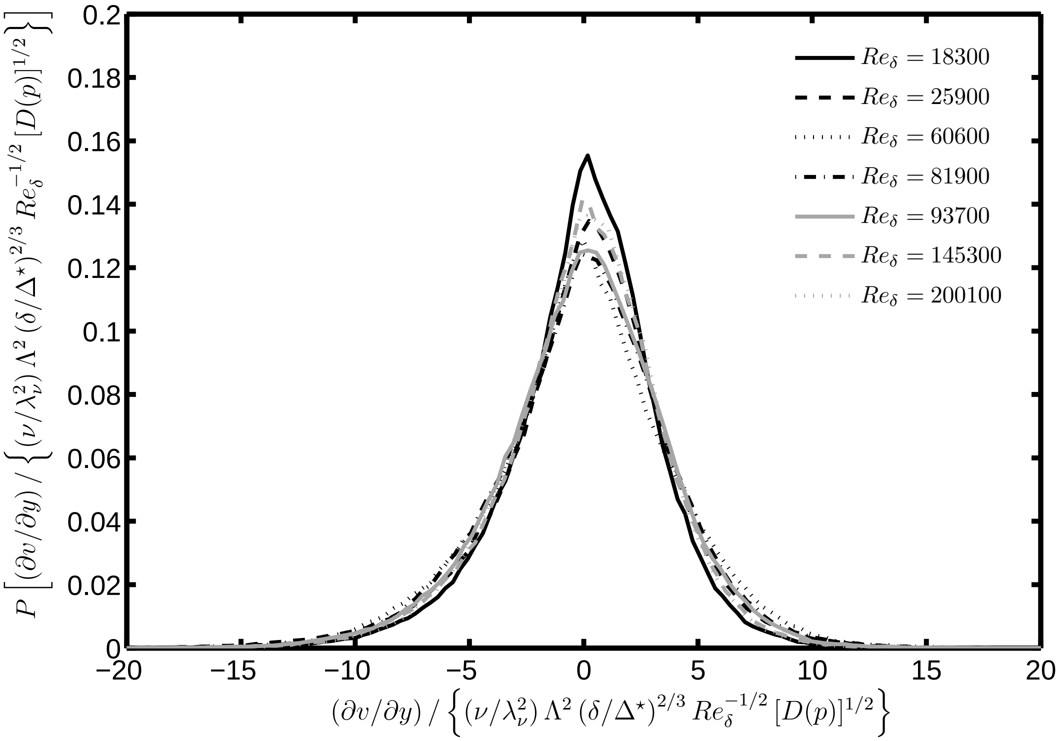

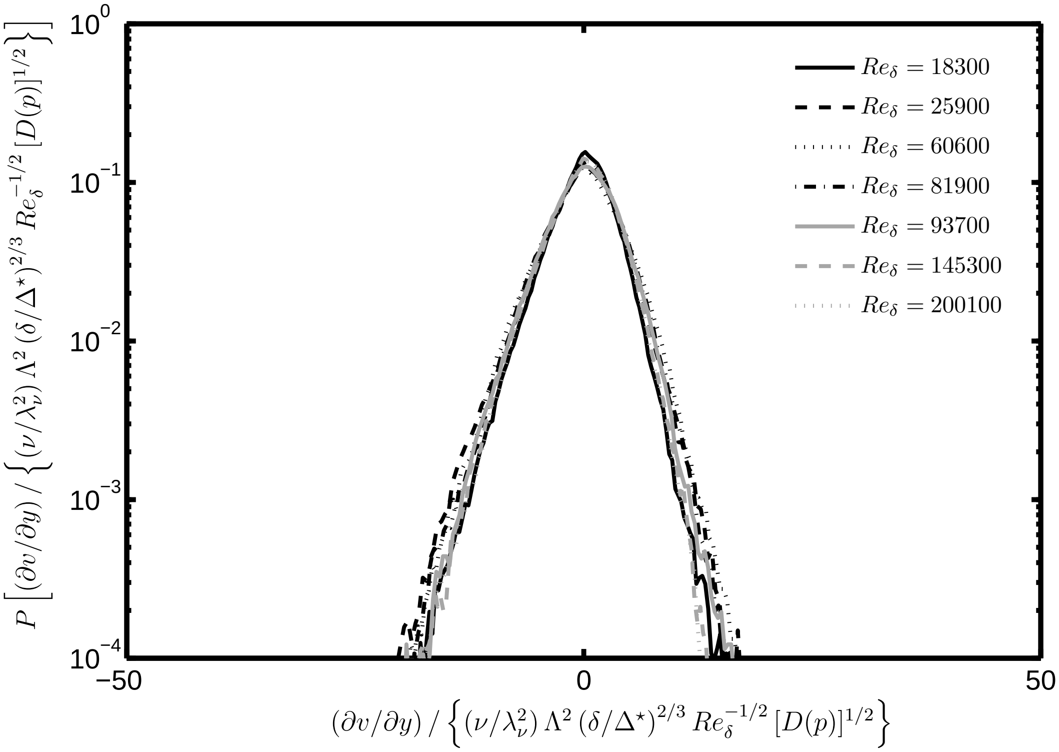

Figure 6.24: Pdfs from all nonreacting cases *IR1 – IR7* for velocity gradient $\partial v/\partial y$ normalized by resolution-corrected inner scaling $(\nu/\lambda_\nu^2)\,\Lambda^2\,(\delta/\Delta^\star)^{2/3}\,Re_\delta^{-1/2}\,[D(p)]^{1/2}$, shown in linear axes *(top)* and semilogarithmic axes *(bottom)*.

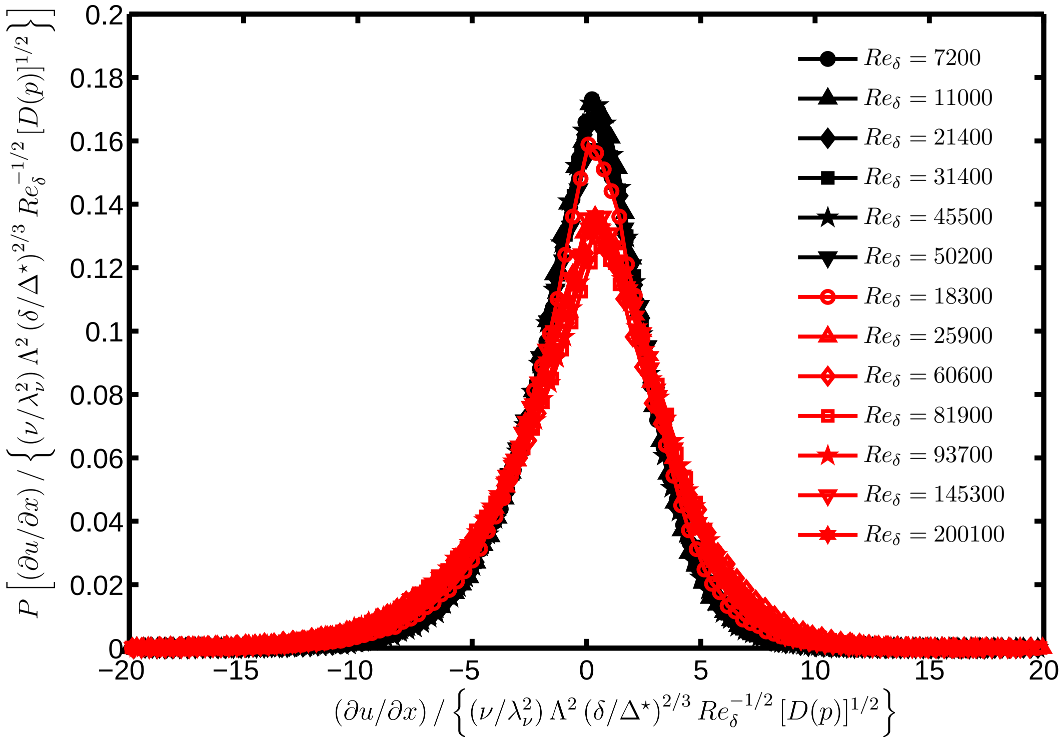

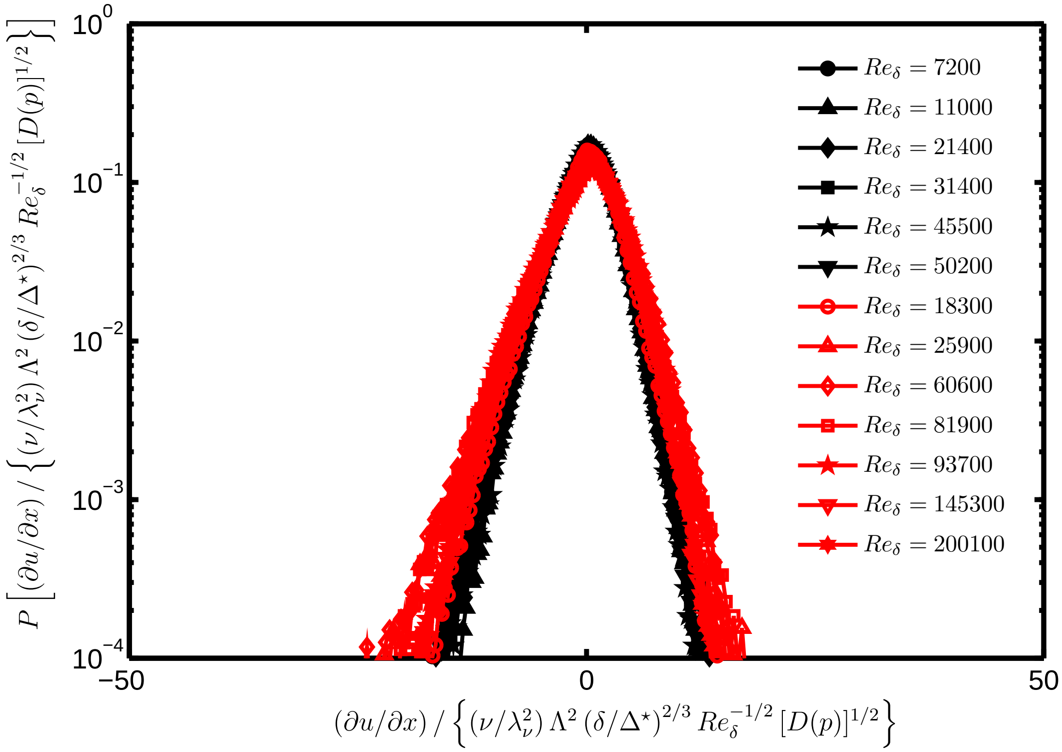

Figure 6.25: Pdfs from all on-axis cases, reacting (open, red symbols) and nonreacting (closed, black symbols) for velocity gradient $\partial u/\partial x$ normalized by resolution-corrected inner scaling $(\nu/\lambda_\nu^2)\,\Lambda^2\,(\delta/\Delta^\star)^{2/3}\,Re_\delta^{-1/2}\,[D(p)]^{1/2}$, shown in linear axes *(top)* and semilogarithmic axes *(bottom)*.

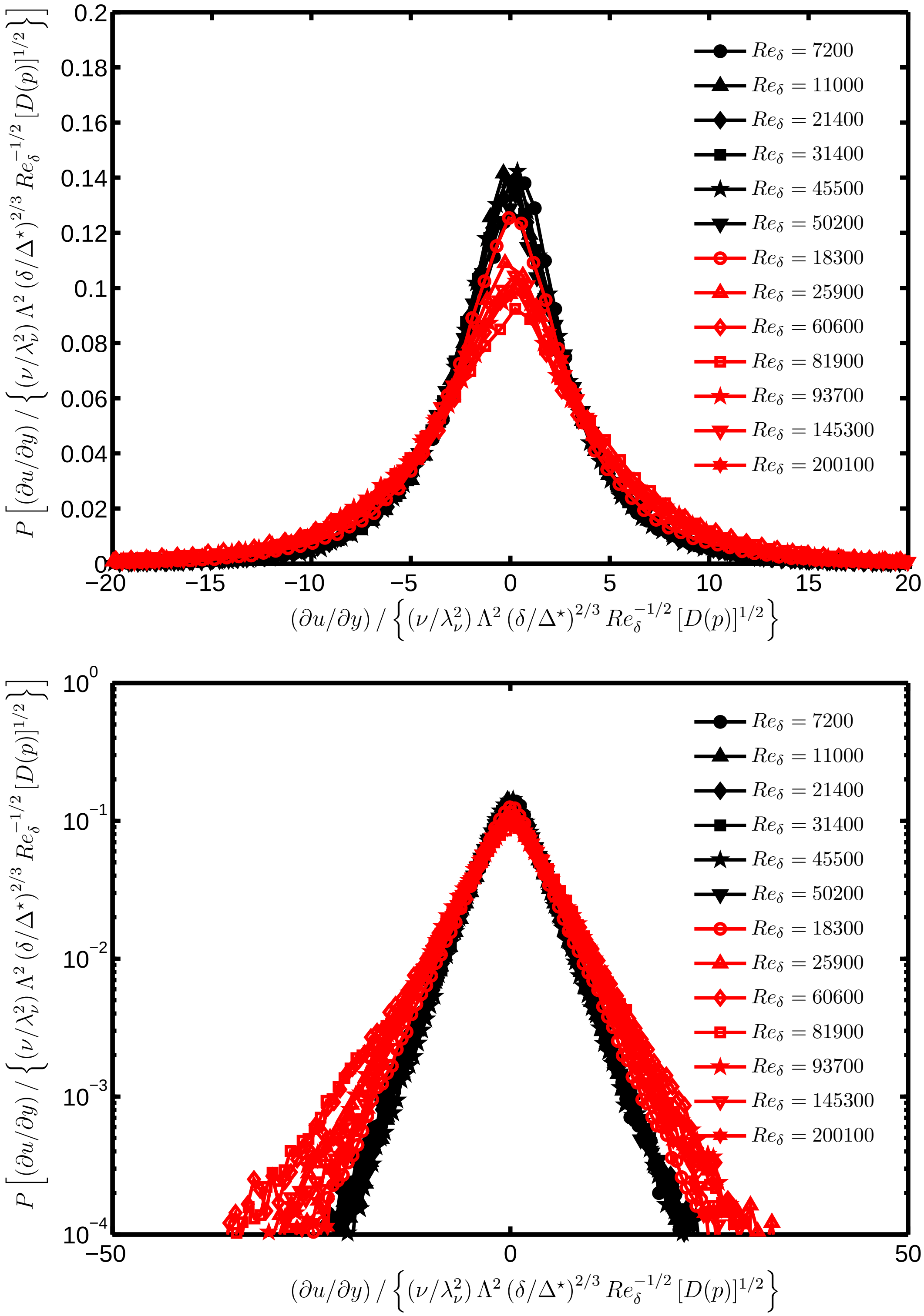

Figure 6.26: Pdfs from all on-axis cases, reacting (open, red symbols) and nonreacting (closed, black symbols) for velocity gradient $\partial u/\partial y$ normalized by resolution-corrected inner scaling $(\nu/\lambda_\nu^2)\,\Lambda^2\,(\delta/\Delta^\star)^{2/3}\,Re_\delta^{-1/2}\,[D(p)]^{1/2}$, shown in linear axes *(top)* and semilogarithmic axes *(bottom)*.

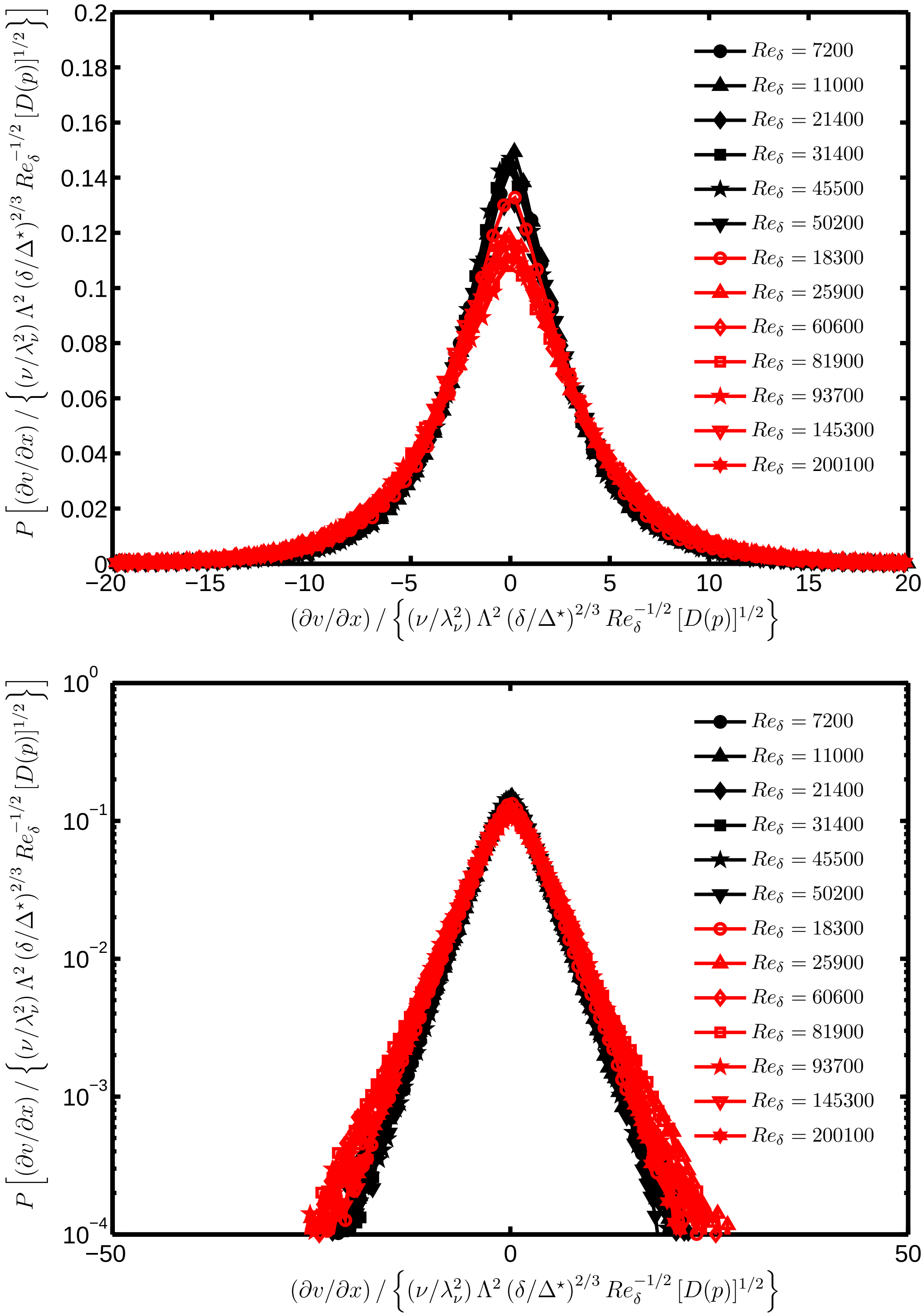

Figure 6.27: Pdfs from all on-axis cases, reacting (open, red symbols) and nonreacting (closed, black symbols) for velocity gradient $\partial v/\partial x$ normalized by resolution-corrected inner scaling $(\nu/\lambda_\nu^2)\,\Lambda^2\,(\delta/\Delta^\star)^{2/3}\,Re_\delta^{-1/2}\,[D(p)]^{1/2}$, shown in linear axes *(top)* and semilogarithmic axes *(bottom)*.

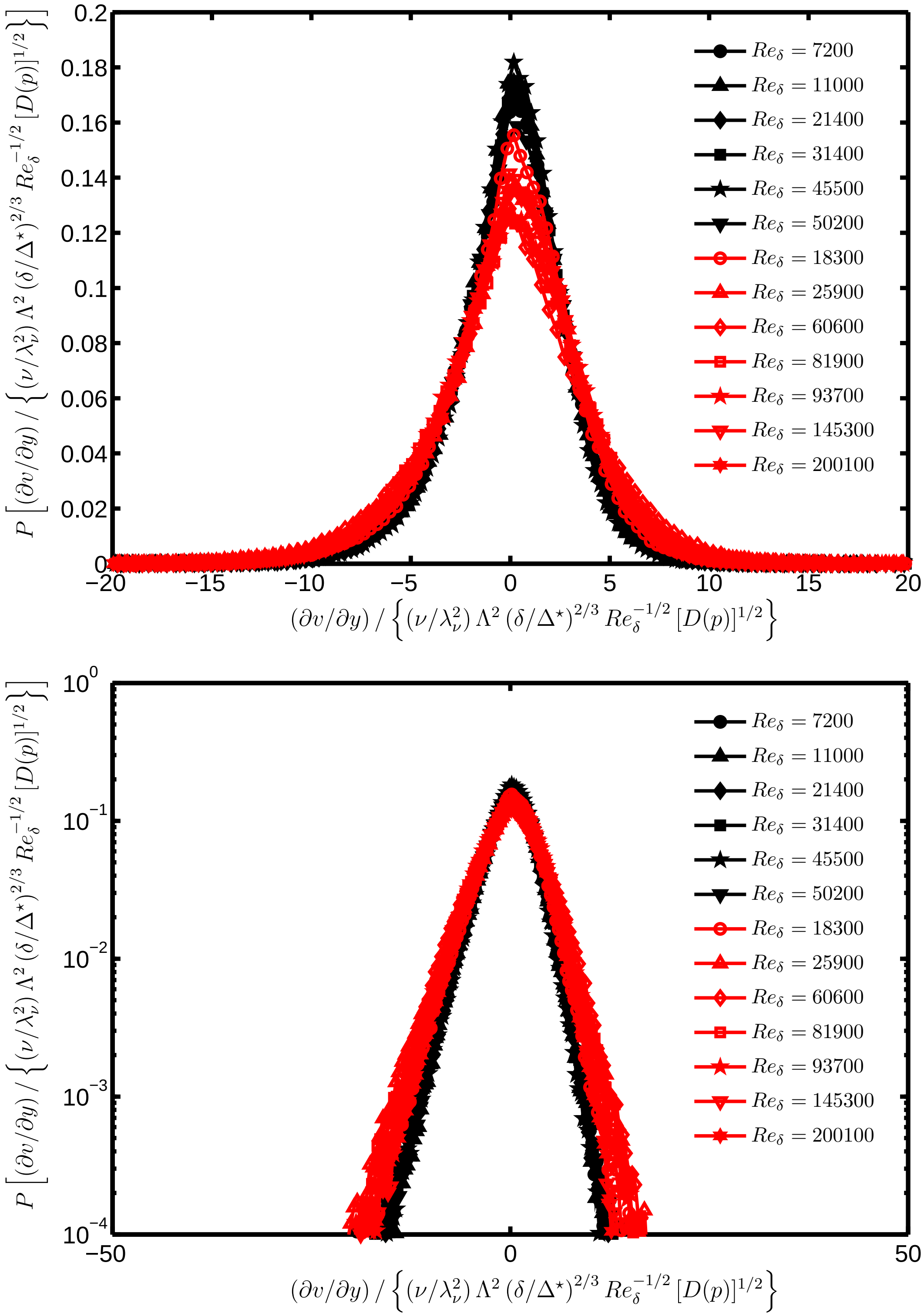

Figure 6.28: Pdfs from all on-axis cases, reacting (open, red symbols) and nonreacting (closed, black symbols) for velocity gradient $\partial v/\partial y$ normalized by resolution-corrected inner scaling $(\nu/\lambda_\nu^2)\,\Lambda^2\,(\delta/\Delta^\star)^{2/3}\,Re_\delta^{-1/2}\,[D(p)]^{1/2}$, shown in linear axes *(top)* and semilogarithmic axes *(bottom)*.

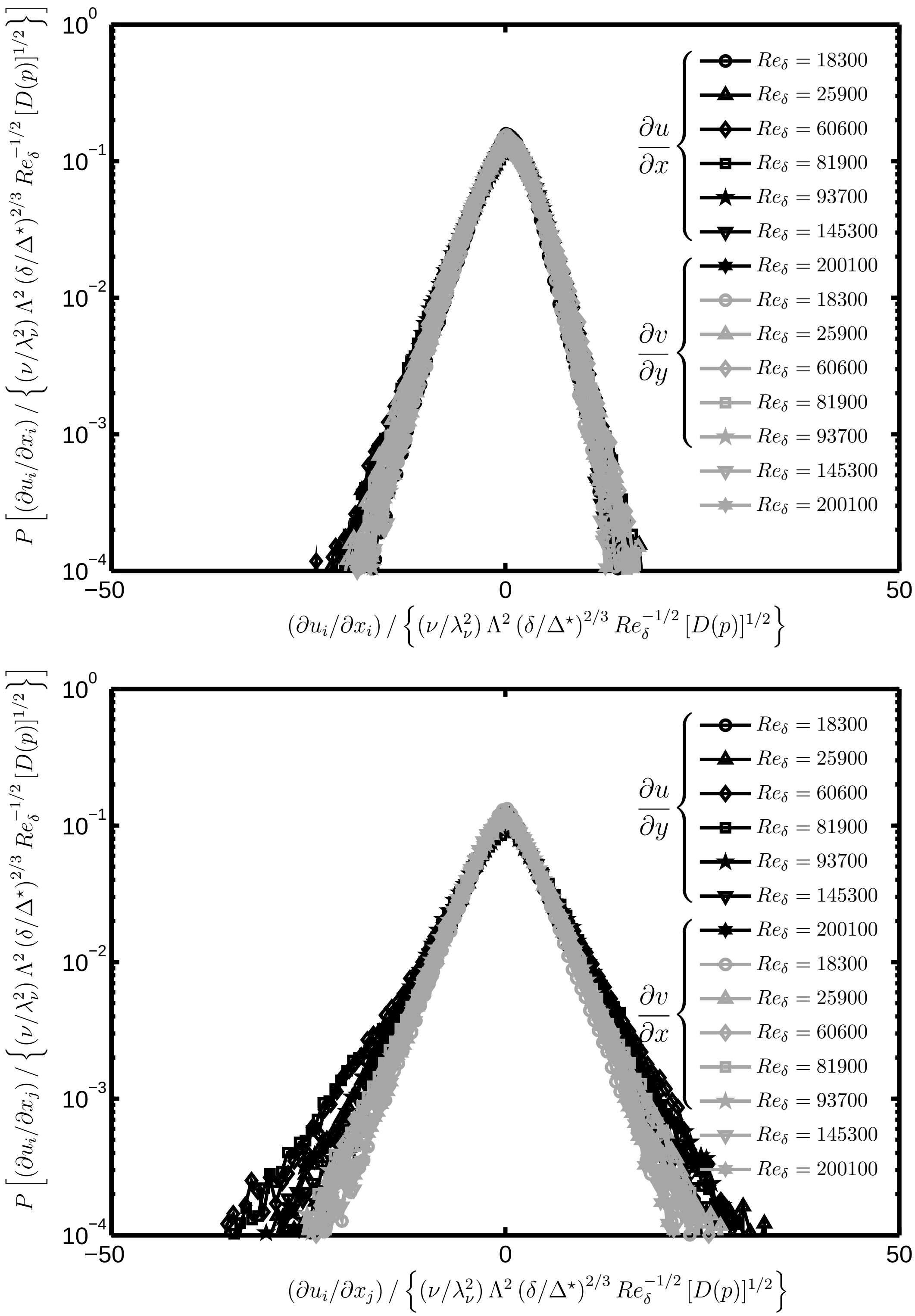

Figure 6.29: Pdfs from all reacting cases *IR1 – IR7*, normalized by resolution-corrected inner scaling. On-diagonal velocity gradients *(top)*, where the black symbols represent the $\partial u/\partial x$ component while the grey display $\partial v/\partial y$. Off-diagonal velocity gradients *(bottom)*, where the black symbols represent the $\partial u/\partial y$ component while the grey display $\partial v/\partial x$.

Re_δ	$\dfrac{\mathrm{var}\left(\dfrac{\partial u}{\partial y}\right)}{\mathrm{var}\left(\dfrac{\partial u}{\partial x}\right)}$	$\dfrac{\mathrm{var}\left(\dfrac{\partial v}{\partial x}\right)}{\mathrm{var}\left(\dfrac{\partial v}{\partial y}\right)}$
18300	2.129	1.678
25900	2.124	1.664
60600	2.399	1.484
81900	2.418	1.774
93700	2.353	1.736
145300	2.294	1.704
200100	2.243	1.703

Table 6.2: Ratios of the variances of the on-diagonal gradient components over the off-diagonal components. The analytical value obtained via the assumption of homogeneous isotropic turbulence is 2.

Re_δ	$\dfrac{\overline{\left(\dfrac{\partial u}{\partial y}\right)^2} + \overline{\left(\dfrac{\partial v}{\partial x}\right)^2}}{\overline{\left(\dfrac{\partial u}{\partial x}\right)^2} + \overline{\left(\dfrac{\partial v}{\partial y}\right)^2}}$
18300	1.899
25900	1.893
60600	1.955
81900	2.113
93700	2.055
145300	2.006
200100	1.984

Table 6.3: Ratios of the variances of the on-diagonal gradient components over the off-diagonal components. The analytical value obtained via the assumption of homogeneous isotropic turbulence is 2.

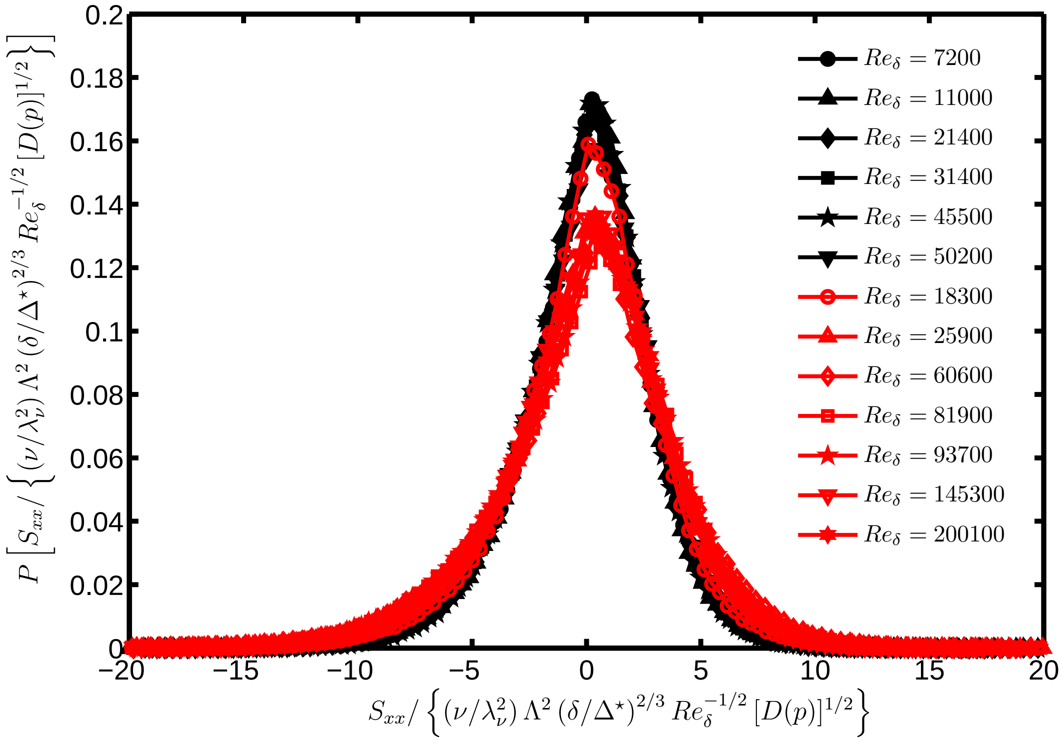

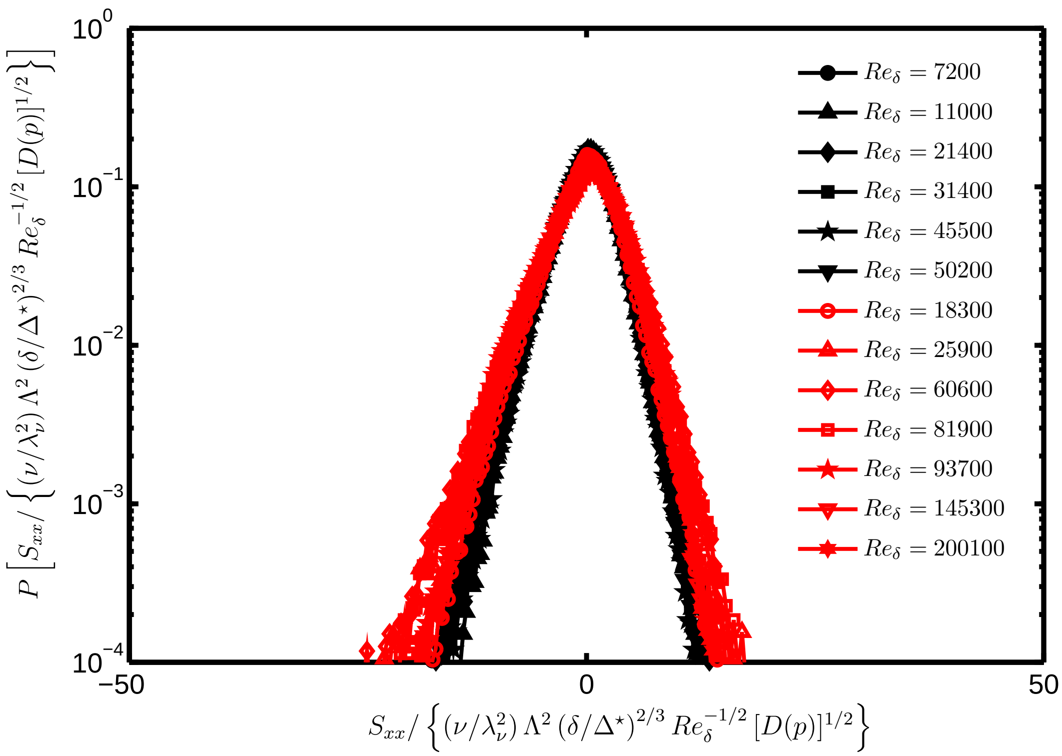

Figure 6.30: Pdfs from all on-axis cases, reacting (open, red symbols) and nonreacting (closed, black symbols) for strain rate S_{xx} normalized by resolution-corrected inner scaling $(\nu/\lambda_\nu^2)\,\Lambda^2\,(\delta/\Delta^\star)^{2/3}\,Re_\delta^{-1/2}\,[D(p)]^{1/2}$, shown in linear axes *(top)* and semilogarithmic axes *(bottom)*.

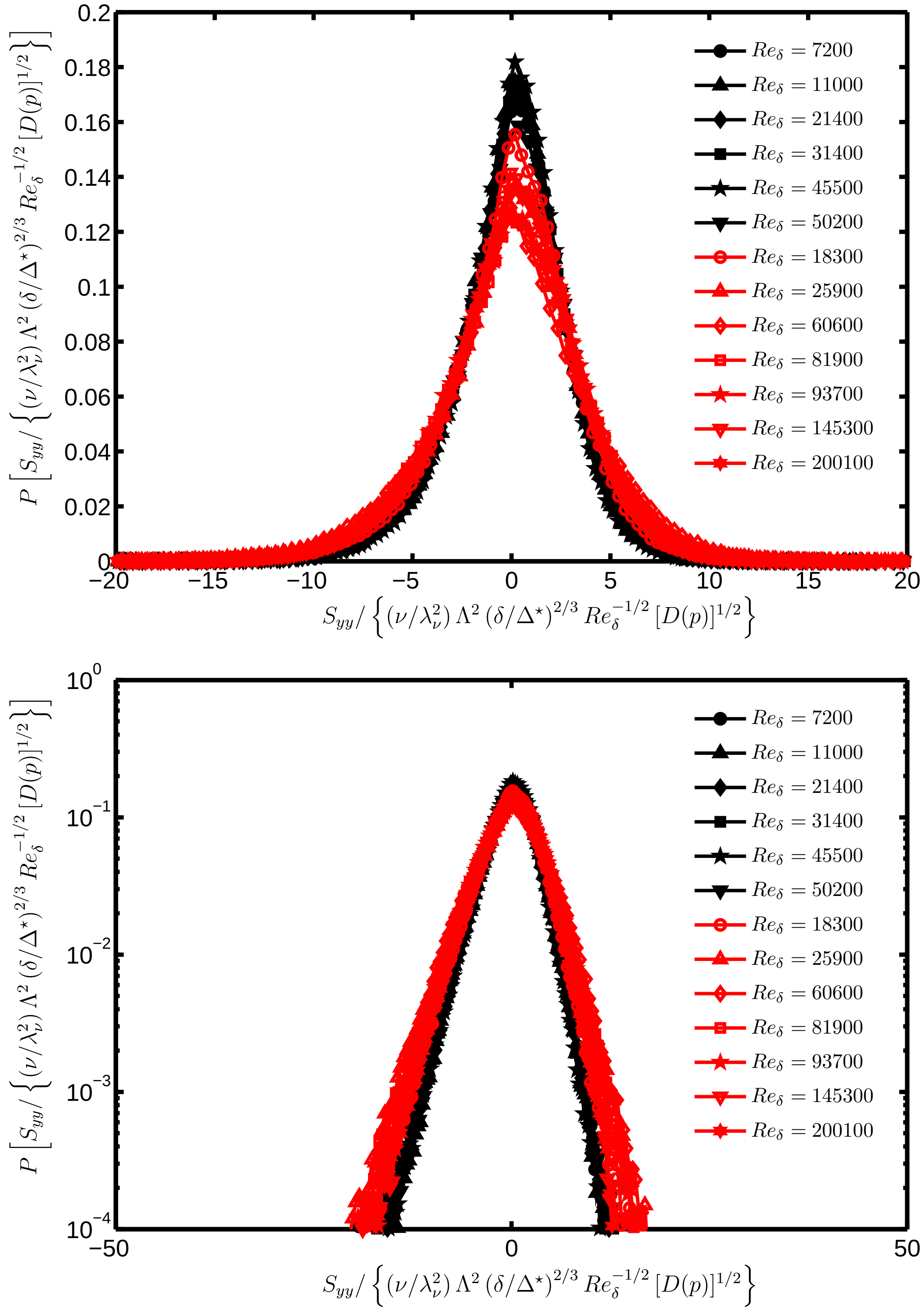

Figure 6.31: Pdfs from all on-axis cases, reacting (open, red symbols) and nonreacting (closed, black symbols) for strain rate S_{yy} normalized by resolution-corrected inner scaling $(\nu/\lambda_\nu^2)\,\Lambda^2\,(\delta/\Delta^\star)^{2/3}\,Re_\delta^{-1/2}\,[D(p)]^{1/2}$, shown in linear axes *(top)* and semilogarithmic axes *(bottom)*.

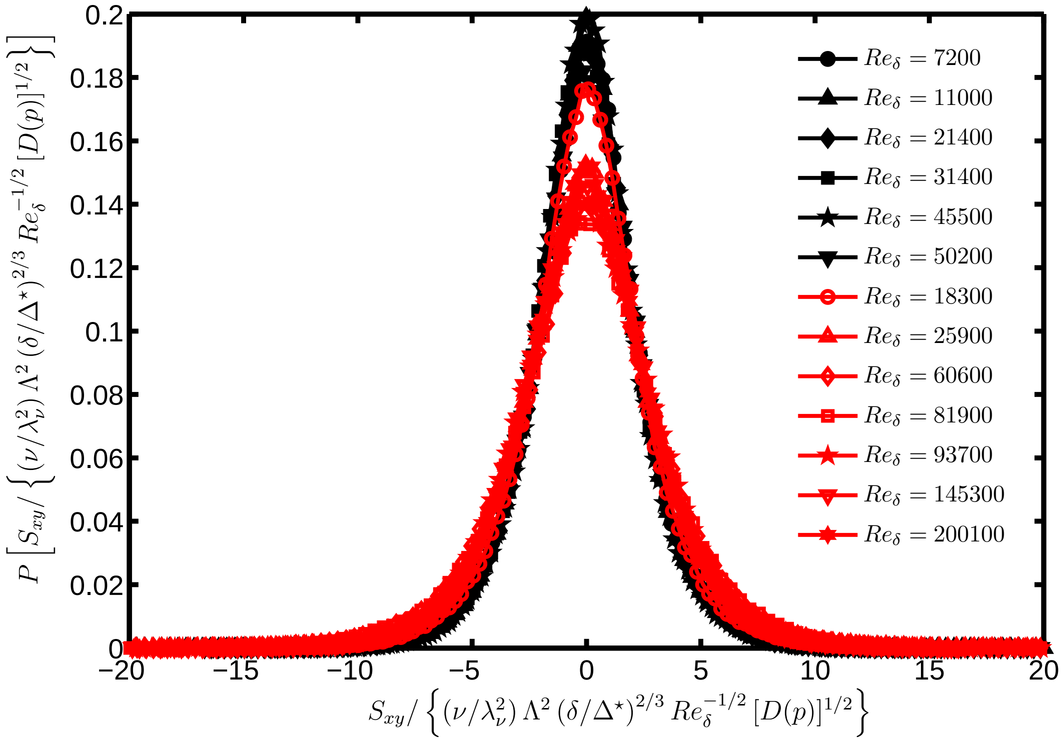

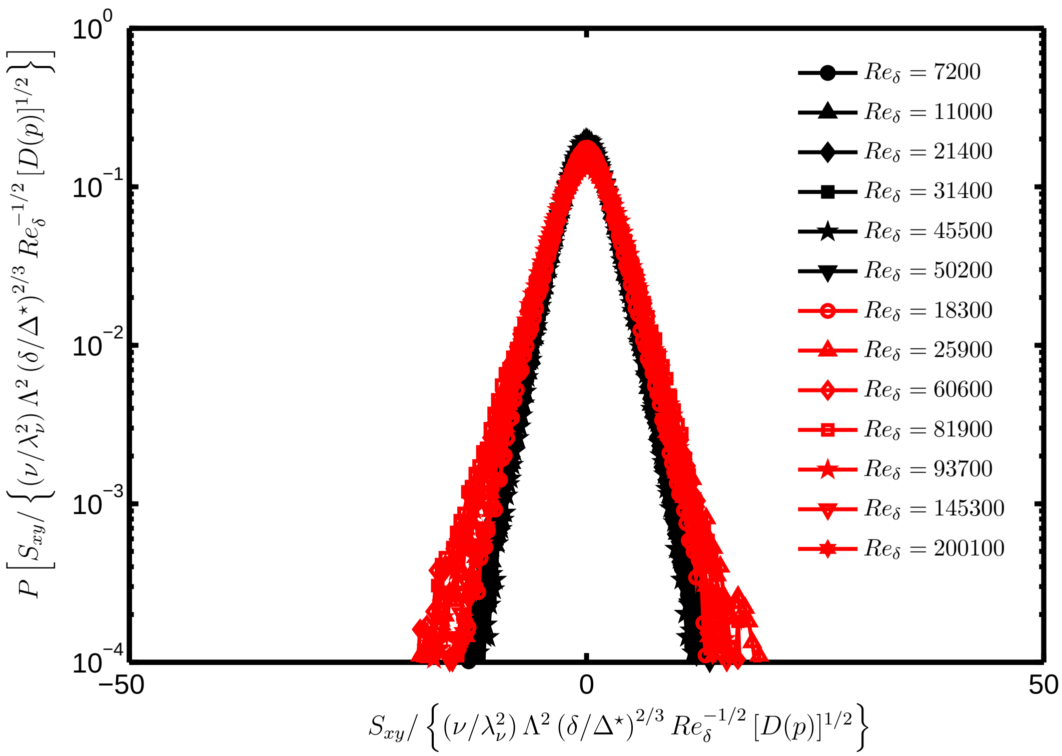

Figure 6.32: Pdfs from all on-axis cases, reacting (open, red symbols) and nonreacting (closed, black symbols) for strain rate S_{xy} normalized by resolution-corrected inner scaling $(\nu/\lambda_\nu^2)\,\Lambda^2\,(\delta/\Delta^\star)^{2/3}\,Re_\delta^{-1/2}\,[D(p)]^{1/2}$, shown in linear axes *(top)* and semilogarithmic axes *(bottom)*.

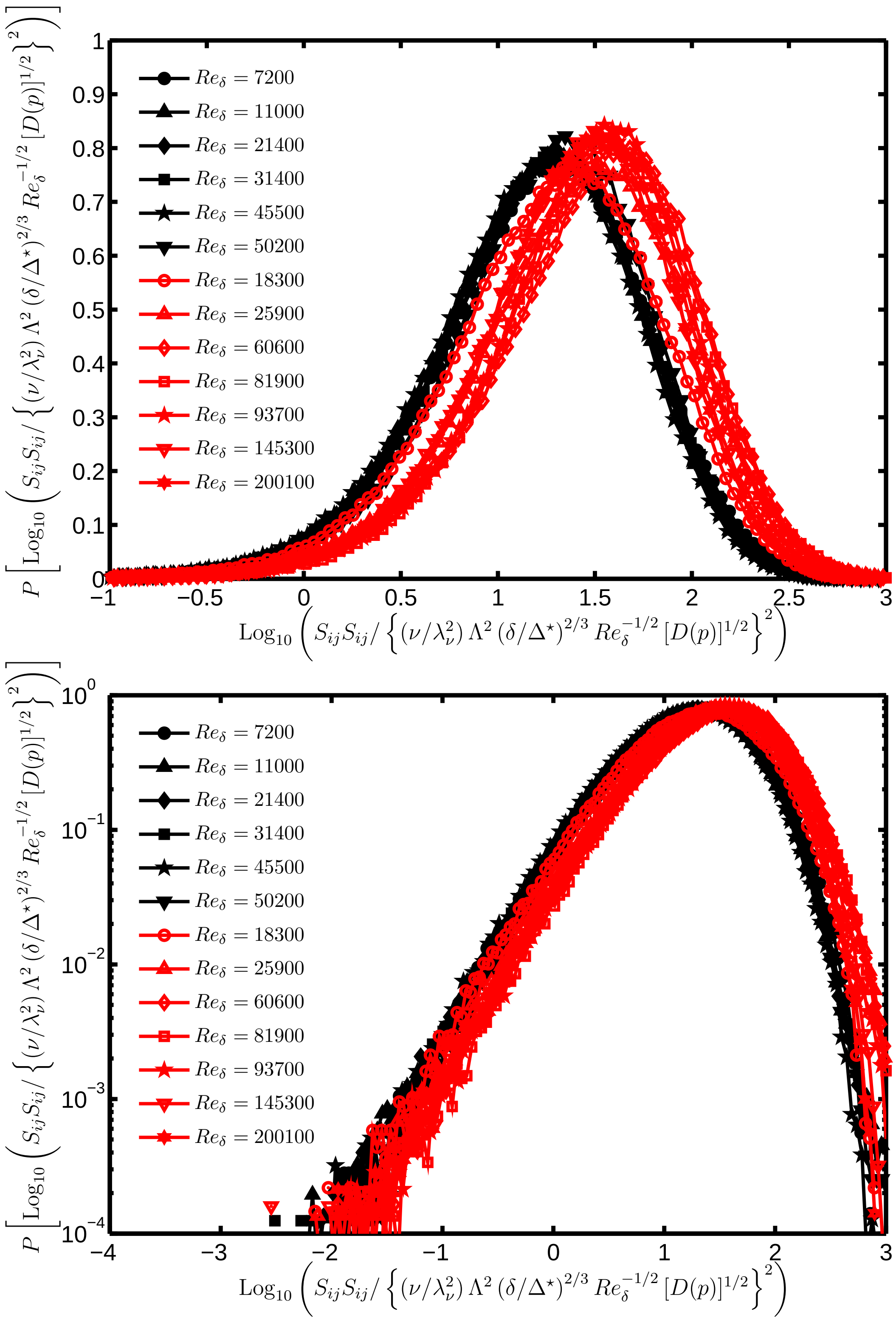

Figure 6.33: Pdfs from all on-axis cases, reacting (open, red symbols) and nonreacting (closed, black symbols) for pseudo-dissipation $\mathrm{Log}_{10}\,(S_{ij}S_{ij})$ normalized by resolution-corrected inner scaling $\{(\nu/\lambda_\nu^2)\,\Lambda^2\,(\delta/\Delta^\star)^{2/3}\,Re_\delta^{-1/2}\,[D(p)]^{1/2}\}^2$, shown in linear axes *(top)* and semilogarithmic axes *(bottom)*.

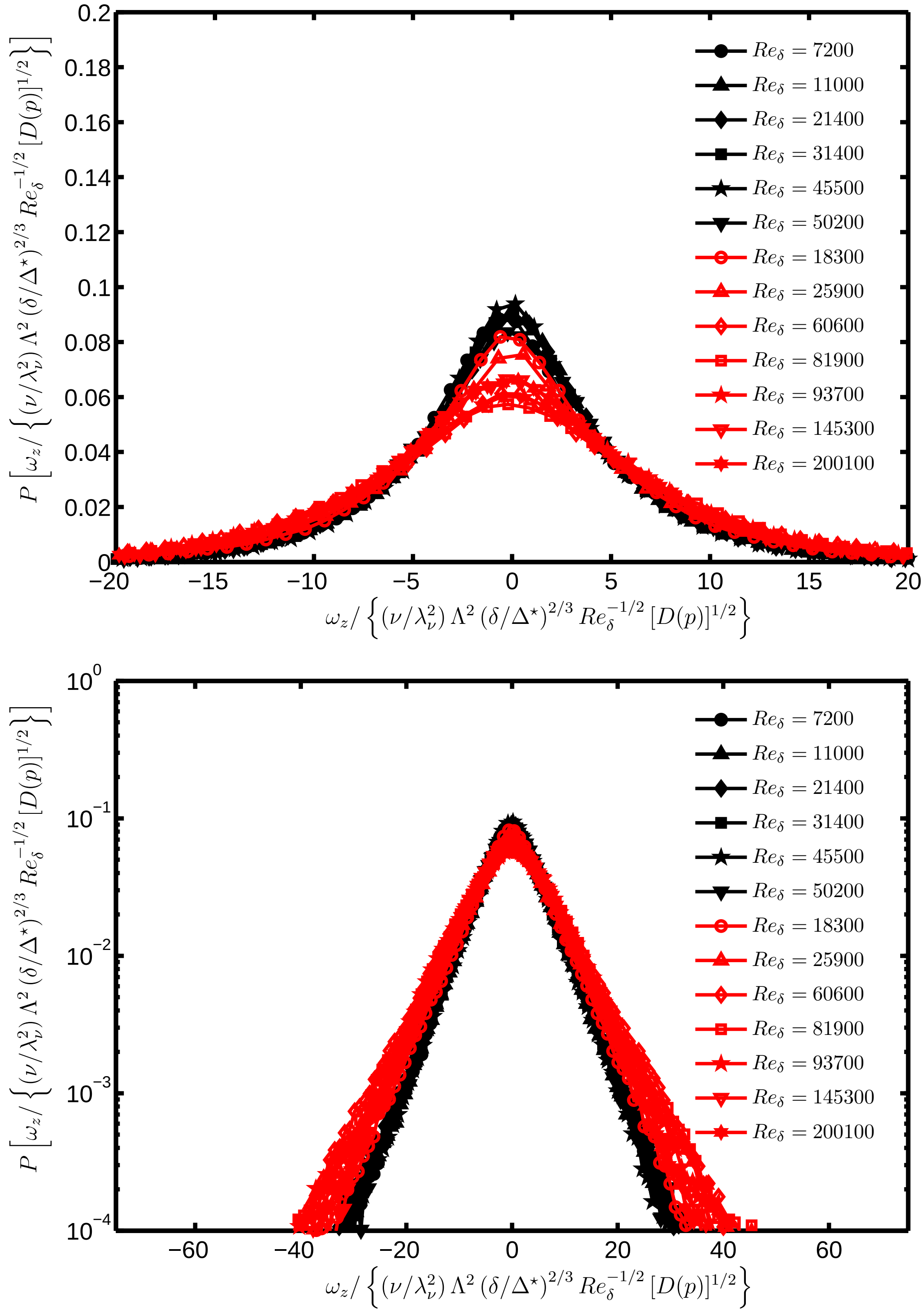

Figure 6.34: Pdfs from all on-axis cases, reacting (open, red symbols) and nonreacting (closed, black symbols) for vorticity ω_z normalized by resolution-corrected inner scaling $(\nu/\lambda_\nu^2)\,\Lambda^2\,(\delta/\Delta^\star)^{2/3}\,Re_\delta^{-1/2}\,[D(p)]^{1/2}$, shown in linear axes *(top)* and semilogarithmic axes *(bottom)*.

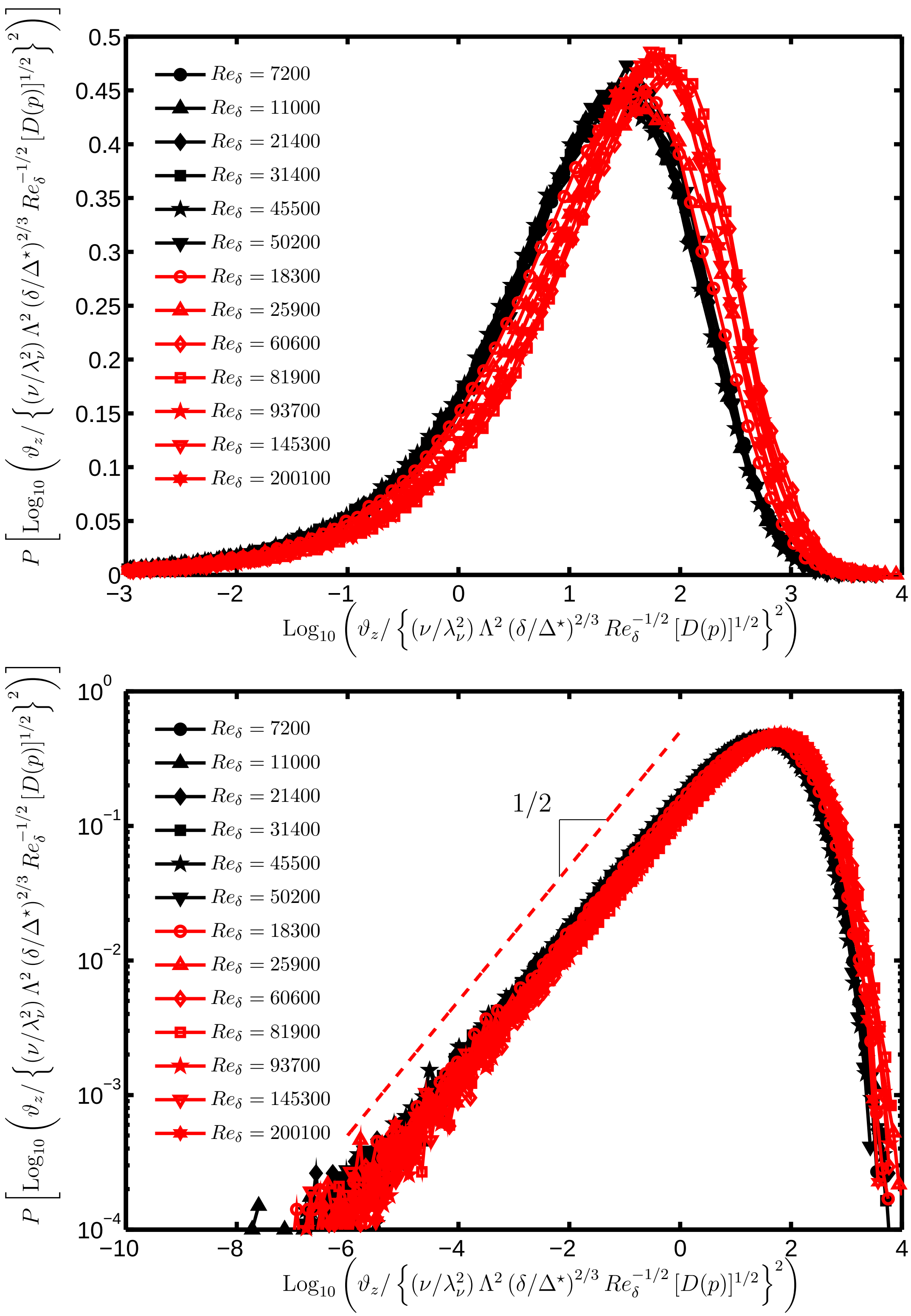

Figure 6.35: Pdfs from all on-axis cases, reacting (open, red symbols) and nonreacting (closed, black symbols) for enstrophy $\mathrm{Log}_{10}(\vartheta_z)$ normalized by resolution-corrected inner scaling $\{(\nu/\lambda_\nu^2)\,\Lambda^2\,(\delta/\Delta^\star)^{2/3}\,Re_\delta^{-1/2}\,[D(p)]^{1/2}\}^2$, shown in linear axes *(top)* and semilogarithmic axes *(bottom)*.

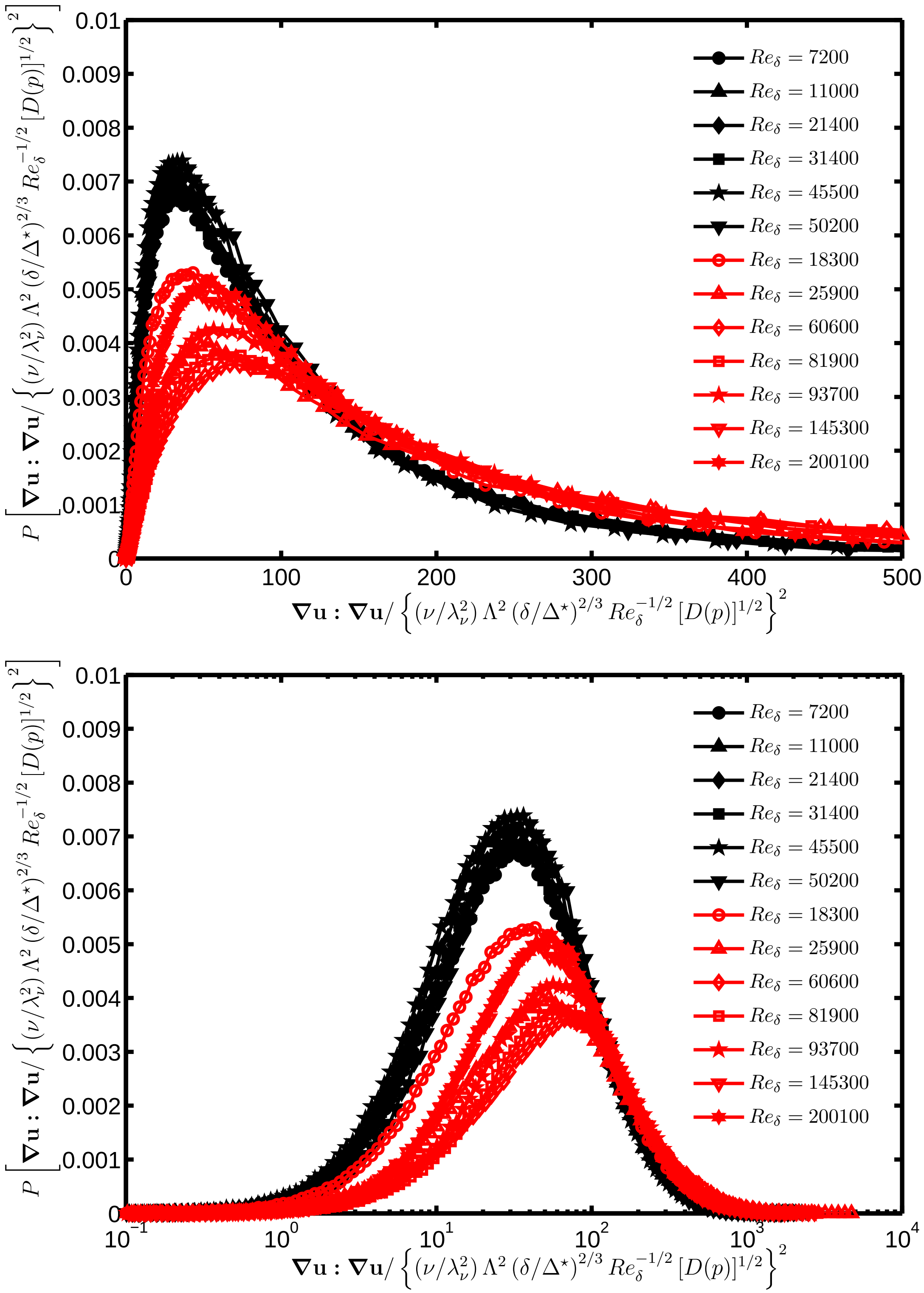

Figure 6.36: Pdfs from all on-axis cases, reacting (open, red symbols) and nonreacting (closed, black symbols) for contraction of the velocity gradient tensor $\nabla\mathbf{u} : \nabla\mathbf{u}$ normalized by resolution-corrected inner scaling $\{(\nu/\lambda_\nu^2)\,\Lambda^2\,(\delta/\Delta^\star)^{2/3}\,Re_\delta^{-1/2}\,[D(p)]^{1/2}\}^2$, shown in linear axes *(top)* and semilogarithmic axes *(bottom)*.

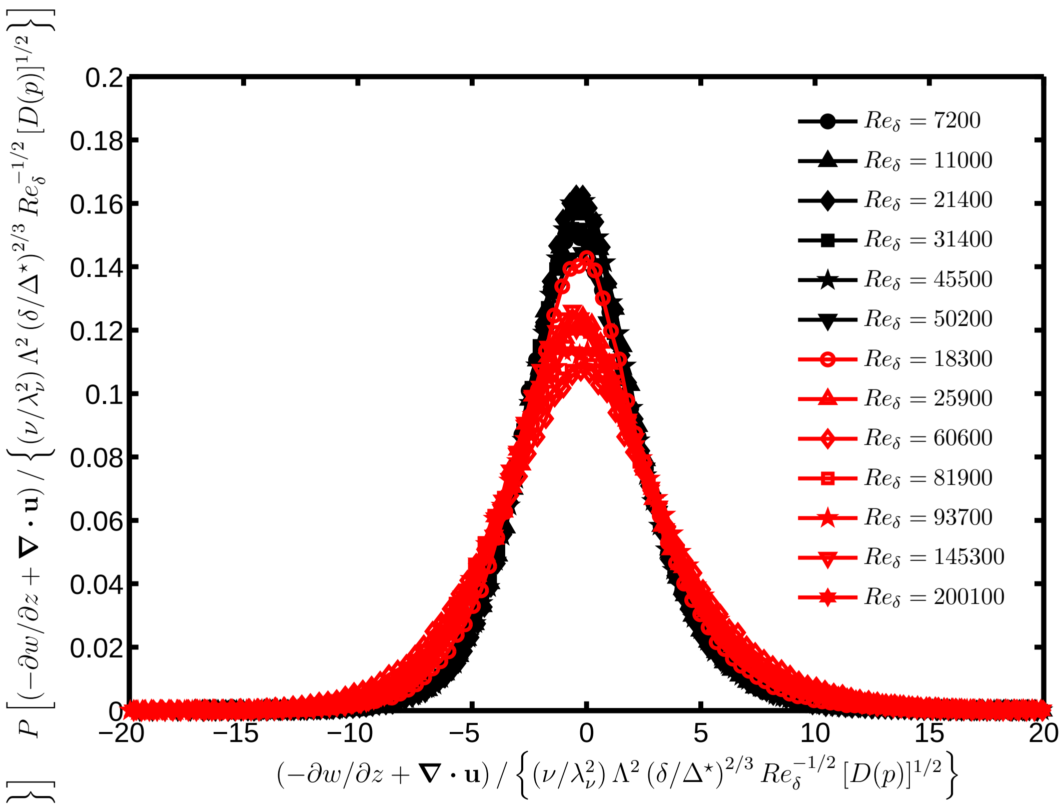

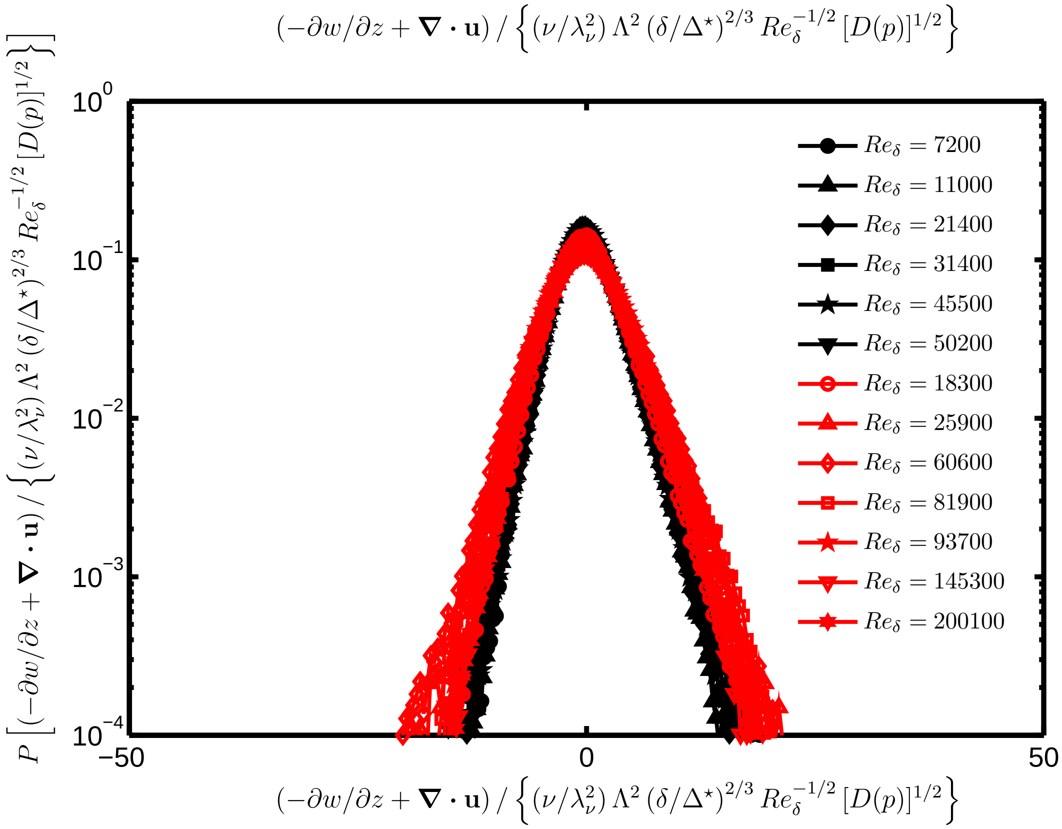

Figure 6.37: Pdfs from all on-axis cases, reacting (open, red symbols) and nonreacting (closed, black symbols) for two-dimensional divergence $(-\partial w/\partial z + \nabla\cdot\mathbf{u})$ normalized by resolution-corrected inner scaling $(\nu/\lambda_\nu^2)\,\Lambda^2\,(\delta/\Delta^\star)^{2/3}\,Re_\delta^{-1/2}\,[D(p)]^{1/2}$, shown in linear axes *(top)* and semilogarithmic axes *(bottom)*.

Quantity	μ	σ	γ	β
u/u_c	$3.995E-18$	$2.767E-01$	$1.351E-01$	$2.760E+00$
v/u_c	$-9.080E-18$	$2.321E-01$	$-1.396E-02$	$2.924E+00$
$\partial u/\partial x$	$4.888E-17$	$3.257E+00$	$-4.091E-01$	$4.658E+00$
$\partial u/\partial y$	$4.101E-16$	$4.752E+00$	$4.912E-02$	$6.146E+00$
$\partial v/\partial x$	$-4.303E-17$	$4.300E+00$	$-9.098E-02$	$5.883E+00$
$\partial v/\partial y$	$-7.703E-17$	$3.319E+00$	$-4.325E-01$	$4.720E+00$
S_{xx}	$4.888E-17$	$3.257E+00$	$-4.091E-01$	$4.658E+00$
S_{yy}	$-7.703E-17$	$3.319E+00$	$-4.325E-01$	$4.720E+00$
S_{xy}	$1.333E-16$	$2.793E+00$	$4.425E-03$	$4.541E+00$
ω_z	$-6.673E-16$	$7.138E+00$	$-5.901E-02$	$6.057E+00$
ε	$4.055E-01$	$5.584E-01$	$3.776E+00$	$2.611E+01$
$\mathrm{Log}_{10}\,[\varepsilon]$	$-7.031E-01$	$5.658E-01$	$-4.711E-01$	$3.522E+00$
$(-\partial w/\partial z + \boldsymbol{\nabla}\cdot\mathbf{u})$	$1.777E-16$	$3.410E+00$	$3.648E-01$	$4.737E+00$
$\boldsymbol{\nabla}\mathbf{u} : \boldsymbol{\nabla}\mathbf{u}$	$7.433E+01$	$9.620E+01$	$4.058E+00$	$3.287E+01$
$\left[\dfrac{(-\partial w/\partial z + \boldsymbol{\nabla}\cdot\mathbf{u})}{(\boldsymbol{\nabla}\mathbf{u} : \boldsymbol{\nabla}\mathbf{u})^{1/2}}\right]$	$2.041E-02$	$4.176E-01$	$1.905E-01$	$1.972E+00$
$S_{ij} : S_{ij}$	$3.722E+01$	$4.840E+01$	$3.428E+00$	$2.162E+01$
$\mathrm{Log}_{10}\,[S_{ij} : S_{ij}]$	$1.279E+00$	$5.497E-01$	$-5.066E-01$	$3.586E+00$
$3/2\,(\omega_z)^2$	$7.643E+01$	$1.719E+02$	$7.044E+00$	$9.540E+01$
$\mathrm{Log}_{10}\left[3/2\ (\omega_z)^2\right]$	$1.125E+00$	$1.071E+00$	$-1.179E+00$	$5.702E+00$

Table 6.4: Normalized central moments computed from pdfs for $Re = 18\,300$ case. The mean is μ, σ is the *rms* fluctuation, $\gamma = \mu_3/\sigma^3$ is the skewness and $\beta = \mu_4/\sigma^4$ is the kurtosis. All quantities normalized by resolution-corrected inner scaling $(\nu/\lambda_\nu^2)\,\Lambda^2\,(\delta/\Delta^\star)^{2/3}\,Re_\delta^{-1/2}\,[D(p)]^{1/2}$ as shown in Figs. 6.21 – 6.37.

Quantity	μ	σ	γ	β
u/u_c	$2.005E-17$	$3.358E-01$	$5.936E-01$	$3.388E+00$
v/u_c	$-1.350E-17$	$2.531E-01$	$-8.130E-03$	$2.967E+00$
$\partial u/\partial x$	$5.509E-16$	$3.857E+00$	$-4.766E-01$	$4.981E+00$
$\partial u/\partial y$	$8.207E-17$	$5.621E+00$	$-3.240E-02$	$7.789E+00$
$\partial v/\partial x$	$-3.290E-17$	$4.987E+00$	$1.364E-01$	$6.207E+00$
$\partial v/\partial y$	$1.361E-16$	$3.866E+00$	$-5.188E-01$	$5.147E+00$
S_{xx}	$5.509E-16$	$3.857E+00$	$-4.766E-01$	$4.981E+00$
S_{yy}	$1.361E-16$	$3.866E+00$	$-5.188E-01$	$5.147E+00$
S_{xy}	$8.675E-17$	$3.332E+00$	$5.610E-02$	$5.092E+00$
ω_z	$-2.468E-16$	$8.279E+00$	$8.970E-02$	$6.931E+00$
ε	$1.150E+00$	$1.700E+00$	$4.818E+00$	$4.397E+01$
$\mathrm{Log}_{10}[\varepsilon]$	$-2.590E-01$	$5.717E-01$	$-4.786E-01$	$3.596E+00$
$(-\partial w/\partial z + \boldsymbol{\nabla}\cdot\mathbf{u})$	$8.218E-16$	$4.012E+00$	$3.307E-01$	$4.677E+00$
$\boldsymbol{\nabla}\mathbf{u} : \boldsymbol{\nabla}\mathbf{u}$	$1.024E+02$	$1.444E+02$	$6.145E+00$	$9.599E+01$
$\left[\dfrac{(-\partial w/\partial z + \boldsymbol{\nabla}\cdot\mathbf{u})}{(\boldsymbol{\nabla}\mathbf{u} : \boldsymbol{\nabla}\mathbf{u})^{1/2}}\right]$	$2.793E-02$	$4.190E-01$	$1.997E-01$	$1.958E+00$
$S_{ij} : S_{ij}$	$5.203E+01$	$7.198E+01$	$4.341E+00$	$3.685E+01$
$\mathrm{Log}_{10}[S_{ij} : S_{ij}]$	$1.417E+00$	$5.555E-01$	$-5.145E-01$	$3.665E+00$
$3/2\,(\omega_z)^2$	$1.028E+02$	$2.504E+02$	$9.375E+00$	$1.931E+02$
$\mathrm{Log}_{10}\left[3/2\ (\omega_z)^2\right]$	$1.217E+00$	$1.092E+00$	$-1.120E+00$	$5.415E+00$

Table 6.5: Normalized central moments computed from pdfs for $Re = 25\,900$ case. The mean is μ, σ is the *rms* fluctuation, $\gamma = \mu_3/\sigma^3$ is the skewness and $\beta = \mu_4/\sigma^4$ is the kurtosis. All quantities normalized by resolution-corrected inner scaling $(\nu/\lambda_\nu^2)\,\Lambda^2\,(\delta/\Delta^\star)^{2/3}\,Re_\delta^{-1/2}\,[D(p)]^{1/2}$ as shown in Figs. 6.21 – 6.37.

Quantity	μ	σ	γ	β
u/u_c	$2.656E-18$	$3.623E-01$	$2.884E-01$	$3.033E+00$
v/u_c	$-1.042E-17$	$2.563E-01$	$4.071E-02$	$2.741E+00$
$\partial u/\partial x$	$1.773E-15$	$4.152E+00$	$-5.821E-01$	$5.109E+00$
$\partial u/\partial y$	$9.483E-16$	$6.430E+00$	$-1.977E-01$	$6.391E+00$
$\partial v/\partial x$	$9.727E-17$	$4.914E+00$	$-8.719E-02$	$5.099E+00$
$\partial v/\partial y$	$5.775E-17$	$4.034E+00$	$-1.947E-01$	$4.003E+00$
S_{xx}	$1.773E-15$	$4.152E+00$	$-5.821E-01$	$5.109E+00$
S_{yy}	$5.775E-17$	$4.034E+00$	$-1.947E-01$	$4.003E+00$
S_{xy}	$7.492E-16$	$3.511E+00$	$-1.438E-01$	$4.566E+00$
ω_z	$-1.378E-15$	$9.039E+00$	$7.633E-02$	$5.199E+00$
ε	$4.972E+00$	$6.839E+00$	$4.548E+00$	$4.088E+01$
$\mathrm{Log}_{10}[\varepsilon]$	$3.972E-01$	$5.609E-01$	$-5.708E-01$	$3.712E+00$
$(-\partial w/\partial z + \boldsymbol{\nabla}\cdot\mathbf{u})$	$1.684E-15$	$4.389E+00$	$1.655E-01$	$4.003E+00$
$\boldsymbol{\nabla}\mathbf{u} : \boldsymbol{\nabla}\mathbf{u}$	$1.183E+02$	$1.486E+02$	$4.282E+00$	$3.810E+01$
$\left[\dfrac{(-\partial w/\partial z + \boldsymbol{\nabla}\cdot\mathbf{u})}{(\boldsymbol{\nabla}\mathbf{u} : \boldsymbol{\nabla}\mathbf{u})^{1/2}}\right]$	$1.604E-02$	$4.265E-01$	$1.222E-01$	$1.912E+00$
$S_{ij} : S_{ij}$	$5.816E+01$	$7.460E+01$	$4.401E+00$	$4.196E+01$
$\mathrm{Log}_{10}[S_{ij} : S_{ij}]$	$1.487E+00$	$5.443E-01$	$-6.302E-01$	$3.805E+00$
$3/2\,(\omega_z)^2$	$1.225E+02$	$2.511E+02$	$5.742E+00$	$6.011E+01$
$\mathrm{Log}_{10}\left[3/2\ (\omega_z)^2\right]$	$1.367E+00$	$1.057E+00$	$-1.232E+00$	$5.830E+00$

Table 6.6: Normalized central moments computed from pdfs for $Re = 60\,600$ case. The mean is μ, σ is the *rms* fluctuation, $\gamma = \mu_3/\sigma^3$ is the skewness and $\beta = \mu_4/\sigma^4$ is the kurtosis. All quantities normalized by resolution-corrected inner scaling $(\nu/\lambda_\nu^2)\,\Lambda^2\,(\delta/\Delta^\star)^{2/3}\,Re_\delta^{-1/2}\,[D(p)]^{1/2}$ as shown in Figs. 6.21 – 6.37.

Quantity	μ	σ	γ	β
u/u_c	$-2.680E-17$	$3.475E-01$	$2.409E-01$	$2.822E+00$
v/u_c	$4.353E-18$	$2.475E-01$	$-1.605E-02$	$2.751E+00$
$\partial u/\partial x$	$1.198E-15$	$4.068E+00$	$-4.696E-01$	$4.405E+00$
$\partial u/\partial y$	$3.358E-16$	$6.326E+00$	$-3.554E-01$	$6.603E+00$
$\partial v/\partial x$	$3.522E-16$	$5.136E+00$	$-1.730E-01$	$6.533E+00$
$\partial v/\partial y$	$7.087E-17$	$3.856E+00$	$-2.891E-01$	$4.037E+00$
S_{xx}	$1.198E-15$	$4.068E+00$	$-4.696E-01$	$4.405E+00$
S_{yy}	$7.087E-17$	$3.856E+00$	$-2.891E-01$	$4.037E+00$
S_{xy}	$-3.053E-17$	$3.594E+00$	$-1.720E-01$	$4.783E+00$
ω_z	$6.978E-17$	$9.006E+00$	$8.757E-02$	$5.723E+00$
ε	$9.691E+00$	$1.375E+01$	$5.224E+00$	$6.147E+01$
$\mathrm{Log}_{10}\,[\varepsilon]$	$6.912E-01$	$5.452E-01$	$-4.607E-01$	$3.626E+00$
$(-\partial w/\partial z + \boldsymbol{\nabla}\cdot\mathbf{u})$	$7.434E-16$	$4.218E+00$	$3.989E-01$	$4.379E+00$
$\boldsymbol{\nabla}\mathbf{u} : \boldsymbol{\nabla}\mathbf{u}$	$1.156E+02$	$1.502E+02$	$5.029E+00$	$5.014E+01$
$\left[\dfrac{(-\partial w/\partial z + \boldsymbol{\nabla}\cdot\mathbf{u})}{(\boldsymbol{\nabla}\mathbf{u} : \boldsymbol{\nabla}\mathbf{u})^{1/2}}\right]$	$1.974E-02$	$4.144E-01$	$1.831E-01$	$1.985E+00$
$S_{ij} : S_{ij}$	$5.726E+01$	$7.376E+01$	$4.288E+00$	$3.979E+01$
$\mathrm{Log}_{10}\,[S_{ij} : S_{ij}]$	$1.489E+00$	$5.250E-01$	$-5.304E-01$	$3.733E+00$
$3/2\,(\omega_z)^2$	$1.217E+02$	$2.644E+02$	$7.227E+00$	$9.348E+01$
$\mathrm{Log}_{10}\left[3/2\ (\omega_z)^2\right]$	$1.388E+00$	$1.032E+00$	$-1.274E+00$	$6.063E+00$

Table 6.7: Normalized central moments computed from pdfs for $Re = 81\,900$ case. The mean is μ, σ is the *rms* fluctuation, $\gamma = \mu_3/\sigma^3$ is the skewness and $\beta = \mu_4/\sigma^4$ is the kurtosis. All quantities normalized by resolution-corrected inner scaling $(\nu/\lambda_\nu^2)\,\Lambda^2\,(\delta/\Delta^\star)^{2/3}\,Re_\delta^{-1/2}\,[D(p)]^{1/2}$ as shown in Figs. 6.21 – 6.37.

Quantity	μ	σ	γ	β
u/u_c	$-4.621E-18$	$3.313E-01$	$1.078E-01$	$2.760E+00$
v/u_c	$1.422E-18$	$2.538E-01$	$9.871E-02$	$2.897E+00$
$\partial u/\partial x$	$-8.555E-16$	$3.853E+00$	$-4.413E-01$	$3.908E+00$
$\partial u/\partial y$	$-3.728E-16$	$5.909E+00$	$-8.500E-02$	$5.754E+00$
$\partial v/\partial x$	$9.816E-17$	$4.910E+00$	$-6.366E-02$	$5.430E+00$
$\partial v/\partial y$	$7.151E-17$	$3.727E+00$	$-2.926E-01$	$4.099E+00$
S_{xx}	$-8.555E-16$	$3.853E+00$	$-4.413E-01$	$3.908E+00$
S_{yy}	$7.151E-17$	$3.727E+00$	$-2.926E-01$	$4.099E+00$
S_{xy}	$-2.534E-16$	$3.345E+00$	$-7.218E-02$	$4.433E+00$
ω_z	$-1.185E-17$	$8.562E+00$	$4.325E-02$	$5.401E+00$
ε	$1.423E+01$	$1.886E+01$	$4.310E+00$	$3.604E+01$
$\mathrm{Log}_{10}\,[\varepsilon]$	$8.745E-01$	$5.367E-01$	$-5.587E-01$	$3.792E+00$
$(-\partial w/\partial z + \boldsymbol{\nabla}\cdot\mathbf{u})$	$-8.048E-16$	$3.888E+00$	$2.777E-01$	$3.853E+00$
$\boldsymbol{\nabla}\mathbf{u} : \boldsymbol{\nabla}\mathbf{u}$	$1.029E+02$	$1.237E+02$	$4.235E+00$	$3.784E+01$
$\left[\dfrac{(-\partial w/\partial z + \boldsymbol{\nabla}\cdot\mathbf{u})}{(\boldsymbol{\nabla}\mathbf{u} : \boldsymbol{\nabla}\mathbf{u})^{1/2}}\right]$	$1.966E-02$	$4.110E-01$	$1.667E-01$	$1.996E+00$
$S_{ij} : S_{ij}$	$5.110E+01$	$6.172E+01$	$3.607E+00$	$2.619E+01$
$\mathrm{Log}_{10}\,[S_{ij} : S_{ij}]$	$1.453E+00$	$5.181E-01$	$-6.168E-01$	$3.891E+00$
$3/2\,(\omega_z)^2$	$1.100E+02$	$2.307E+02$	$6.726E+00$	$8.434E+01$
$\mathrm{Log}_{10}\left[3/2\;(\omega_z)^2\right]$	$1.347E+00$	$1.030E+00$	$-1.257E+00$	$6.017E+00$

Table 6.8: Normalized central moments computed from pdfs for $Re = 93\,700$ case. The mean is μ, σ is the *rms* fluctuation, $\gamma = \mu_3/\sigma^3$ is the skewness and $\beta = \mu_4/\sigma^4$ is the kurtosis. All quantities normalized by resolution-corrected inner scaling $(\nu/\lambda_\nu^2)\,\Lambda^2\,(\delta/\Delta^\star)^{2/3}\,Re_\delta^{-1/2}\,[D(p)]^{1/2}$ as shown in Figs. 6.21 – 6.37.

Quantity	μ	σ	γ	β
u/u_c	$-1.064E-17$	$2.974E-01$	$4.409E-02$	$2.779E+00$
v/u_c	$-7.828E-18$	$2.246E-01$	$-6.304E-02$	$2.844E+00$
$\partial u/\partial x$	$-5.638E-16$	$3.579E+00$	$-4.643E-01$	$4.259E+00$
$\partial u/\partial y$	$2.779E-16$	$5.421E+00$	$-1.153E-01$	$5.545E+00$
$\partial v/\partial x$	$3.042E-18$	$4.558E+00$	$8.422E-02$	$5.153E+00$
$\partial v/\partial y$	$1.344E-17$	$3.492E+00$	$-4.163E-01$	$4.163E+00$
S_{xx}	$-5.638E-16$	$3.579E+00$	$-4.643E-01$	$4.259E+00$
S_{yy}	$1.344E-17$	$3.492E+00$	$-4.163E-01$	$4.163E+00$
S_{xy}	$1.126E-16$	$3.135E+00$	$-1.768E-02$	$4.210E+00$
ω_z	$-7.920E-16$	$7.810E+00$	$1.053E-01$	$5.028E+00$
ε	$3.470E+01$	$4.545E+01$	$3.948E+00$	$3.148E+01$
$\mathrm{Log}_{10}[\varepsilon]$	$1.259E+00$	$5.358E-01$	$-4.980E-01$	$3.652E+00$
$(-\partial w/\partial z + \boldsymbol{\nabla}\cdot\mathbf{u})$	$-7.261E-16$	$3.733E+00$	$3.428E-01$	$3.989E+00$
$\boldsymbol{\nabla}\mathbf{u} : \boldsymbol{\nabla}\mathbf{u}$	$8.910E+01$	$1.040E+02$	$3.645E+00$	$2.711E+01$
$\left[\dfrac{(-\partial w/\partial z + \boldsymbol{\nabla}\cdot\mathbf{u})}{(\boldsymbol{\nabla}\mathbf{u} : \boldsymbol{\nabla}\mathbf{u})^{1/2}}\right]$	$1.554E-02$	$4.149E-01$	$2.202E-01$	$1.992E+00$
$S_{ij} : S_{ij}$	$4.467E+01$	$5.431E+01$	$3.385E+00$	$2.252E+01$
$\mathrm{Log}_{10}[S_{ij} : S_{ij}]$	$1.390E+00$	$5.177E-01$	$-5.427E-01$	$3.736E+00$
$3/2\,(\omega_z)^2$	$9.149E+01$	$1.836E+02$	$5.553E+00$	$5.304E+01$
$\mathrm{Log}_{10}\left[3/2\ (\omega_z)^2\right]$	$1.268E+00$	$1.035E+00$	$-1.265E+00$	$5.956E+00$

Table 6.9: Normalized central moments computed from pdfs for $Re = 145\,300$ case. The mean is μ, σ is the *rms* fluctuation, $\gamma = \mu_3/\sigma^3$ is the skewness and $\beta = \mu_4/\sigma^4$ is the kurtosis. All quantities normalized by resolution-corrected inner scaling $(\nu/\lambda_\nu^2)\,\Lambda^2\,(\delta/\Delta^\star)^{2/3}\,Re_\delta^{-1/2}\,[D(p)]^{1/2}$ as shown in Figs. 6.21 – 6.37.

Quantity	μ	σ	γ	β
u/u_c	$5.822E-17$	$3.215E-01$	$5.906E-02$	$2.626E+00$
v/u_c	$5.744E-18$	$2.256E-01$	$1.374E-02$	$2.901E+00$
$\partial u/\partial x$	$-9.236E-16$	$3.583E+00$	$-4.747E-01$	$4.227E+00$
$\partial u/\partial y$	$1.063E-15$	$5.366E+00$	$-4.769E-02$	$5.124E+00$
$\partial v/\partial x$	$-9.648E-17$	$4.489E+00$	$-2.462E-02$	$4.902E+00$
$\partial v/\partial y$	$1.552E-17$	$3.441E+00$	$-4.238E-01$	$4.150E+00$
S_{xx}	$-9.236E-16$	$3.583E+00$	$-4.747E-01$	$4.227E+00$
S_{yy}	$1.552E-17$	$3.441E+00$	$-4.238E-01$	$4.150E+00$
S_{xy}	$4.210E-16$	$3.061E+00$	$-1.422E-02$	$3.943E+00$
ω_z	$-9.526E-16$	$7.772E+00$	$-3.682E-02$	$4.897E+00$
ε	$7.575E+01$	$9.456E+01$	$3.478E+00$	$2.278E+01$
$\mathrm{Log}_{10}\,[\varepsilon]$	$1.609E+00$	$5.294E-01$	$-5.341E-01$	$3.658E+00$
$(-\partial w/\partial z + \boldsymbol{\nabla}\cdot\mathbf{u})$	$-1.051E-15$	$3.696E+00$	$3.996E-01$	$4.088E+00$
$\boldsymbol{\nabla}\mathbf{u} : \boldsymbol{\nabla}\mathbf{u}$	$8.728E+01$	$9.883E+01$	$3.369E+00$	$2.259E+01$
$\left[\dfrac{(-\partial w/\partial z + \boldsymbol{\nabla}\cdot\mathbf{u})}{(\boldsymbol{\nabla}\mathbf{u} : \boldsymbol{\nabla}\mathbf{u})^{1/2}}\right]$	$1.754E-02$	$4.171E-01$	$2.066E-01$	$1.990E+00$
$S_{ij} : S_{ij}$	$4.342E+01$	$5.098E+01$	$3.171E+00$	$1.918E+01$
$\mathrm{Log}_{10}\,[S_{ij} : S_{ij}]$	$1.388E+00$	$5.100E-01$	$-5.819E-01$	$3.793E+00$
$3/2\,(\omega_z)^2$	$9.061E+01$	$1.789E+02$	$5.170E+00$	$4.541E+01$
$\mathrm{Log}_{10}\left[3/2\ (\omega_z)^2\right]$	$1.268E+00$	$1.032E+00$	$-1.273E+00$	$6.017E+00$

Table 6.10: Normalized central moments computed from pdfs for $Re = 200\,100$ case. The mean is μ, σ is the *rms* fluctuation, $\gamma = \mu_3/\sigma^3$ is the skewness and $\beta = \mu_4/\sigma^4$ is the kurtosis. All quantities normalized by resolution-corrected inner scaling $(\nu/\lambda_\nu^2)\,\Lambda^2\,(\delta/\Delta^\star)^{2/3}\,Re_\delta^{-1/2}\,[D(p)]^{1/2}$ as shown in Figs. 6.21 – 6.37.

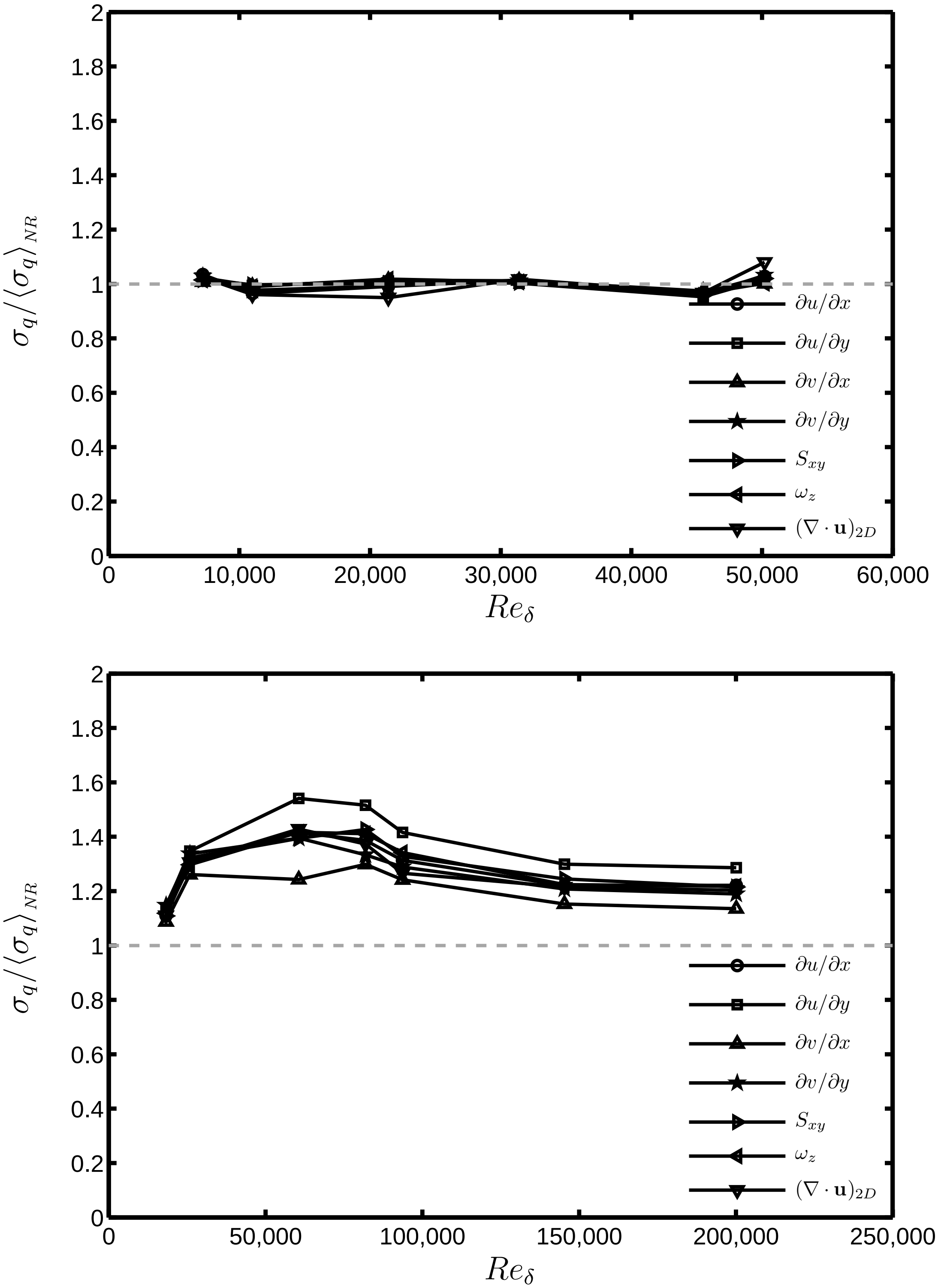

Figure 6.38: Reduced *rms* values for the four $\partial u_i/\partial x_j$ components, S_{xy}, ω_z and $(-\partial w/\partial z + \boldsymbol{\nabla}\cdot\mathbf{u})$. Here σ_q is normalized by $\mathcal{N}^\star$ and by the nonreacting ensemble value $\langle\sigma_q\rangle_{NR}$ for each of the aforementioned gradients q. Results for nonreacting gradient data *(top)* and reacting gradients *(bottom)*.

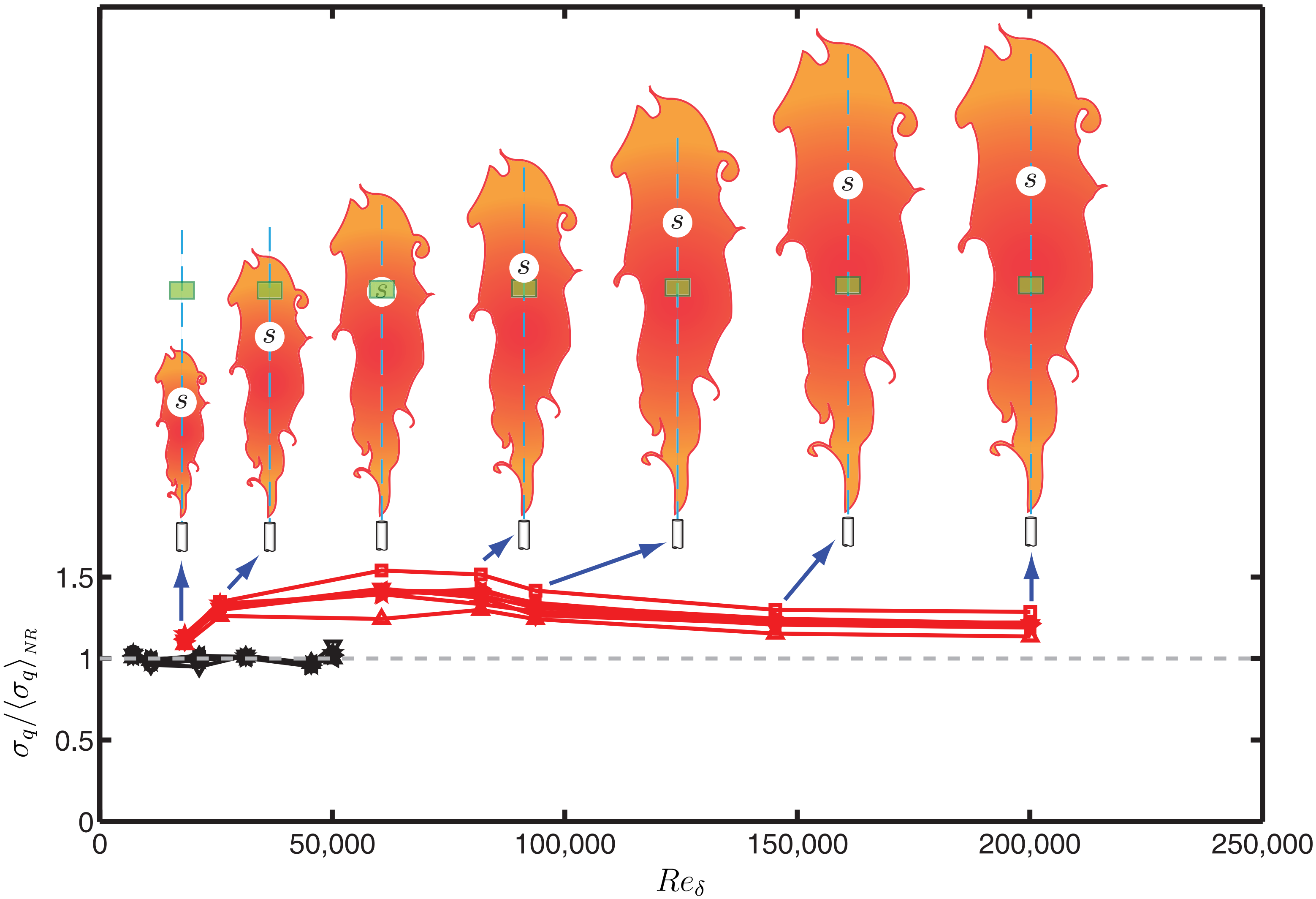

Figure 6.39: Data from Fig. 6.38 replotted according to relative magnitude. The global average of all nonreacting data (black symbols), is $\sigma_q/\langle\sigma_q\rangle_{NR} = 1$. Each reacting cases is represented schematically above it by to-scale sketches of flames depicting the PIV FOV (green rectangles) and averaged stoichiometric centerline location s. The influence of buoyancy is diminished moving from left-to-right, as jet momentum flux J_0 is increased.

CHAPTER VII

Inner-Scaling of Nonreacting Flows: Effects of Shear

Chapter V developed and demonstrated the proper inner scaling for velocity gradient quantities in turbulent shear flows in terms of the measurement resolution scale $\Delta^{\star}$. The self-similar forms of the resulting distributions for various inner-scaled velocity gradient quantities in a nonreacting turbulent shear flow then served as the basis in Chapter VI for comparisons with similarly-scaled distributions from a corresponding reacting turbulent shear flow, and thereby allowed effects of heat release on these quantities to be directly determined. Those comparisons involved velocity gradients measured around the centerline of an axisymmetric coflowing turbulent jet, where the mean shear $\mathcal{S} \equiv (S_{ij}S_{ij})^{1/2}$ is essentially zero. Since the inner scaling is fundamentally based on an approach to locally homogeneous and isotropic turbulence at increasingly smaller scales, the inner scaling should be most nearly valid on the jet centerline, since the mean shear $\mathcal{S}$ is zero there. At increasing radial distances r from the centerline, the mean shear $\mathcal{S}(r)$ initially increases, then peaks at about $r \approx \delta_{1/2}$ and returns to zero for $r \gtrsim 2\,\delta_{1/2}$. Where $\mathcal{S} > 0$ the mean shear induces anisotropy in the large scales of the local turbulence, and any anisotropy that remains at the smaller scales will lead to departures from the strict inner-scale similarity seen in Chapter V. In this chapter, inner-scaled distributions of velocity gradients quantities from PIV measurements at various radial locations in a nonreacting turbulent shear flow are investigated for such departures from strict similarity due to the local relative mean shear ($\mathcal{S}\delta/u_c$). These results then serve as the basis in Chapter VIII for comparisons with corresponding PIV measurements at the same radial locations in an exothermically reacting turbulent shear flow, to identify the combined effects of shear and heat release on the small scales of a turbulent shear flow.

7.1 Inner Scale PIV: Off-Axis Experiments

Table 3.5 lists the experimental conditions for each of the six radial nonreacting flow cases for which results are presented in this chapter. All measurements were made at $x/d = 154$ downstream of the jet exit, and correspond to the same flow condition but different radial positions in the flow. The six radial locations r ranged from the jet centerline ($r = 0$) to near the outer edge of the jet ($r = 1.45\,\delta_{1/2}$). At each radial location, 600 instantaneous inner-scale velocity fields were measured, each with a 13.2 mm $\times$ 16.5 mm field-of-view containing 32 $\times$ 40 instantaneous velocity vectors. At each location, the measurement resolution scale $\Delta^\star$ was obtained in the same manner as described for the measurements in Chapters V and VI. An additional 600 outer-scale velocity fields were measured, from which the local outer variables u_c and δ were obtained. The resulting outer-scale Reynolds number was $Re_\delta = 19\,000$.

7.2 Inner-Scale Velocity Gradients

Probability density functions for each of the resulting inner-scale velocity gradient components are given in Figs. 7.1 – 7.12. Each quantity is normalized by the proper form that accounts for both the inner scaling and the measurement resolution scale $\Delta^\star$. A separate curve in each figure panel corresponds to each of the six cases, denoted *RN0* – *RN5*. In each figure, the corresponding pdf is shown in linear form in the upper panel, where the distributions at small values of the quantity can be clearly seen, as well as in semi-logarithmic form in the lower panel, where the tails of the distributions can be more clearly discerned.

It is apparent in the pdfs in Figs. 7.1 – 7.12 that, unlike for the on-centerline nonreacting flow results in Chapter V, the inner-scaled pdfs from these differing radial locations do not fall onto a single curve, even when the resolution scale $\Delta^\star$ has been accounted for. There are clear differences apparent among the distributions for different radial locations. This is especially evident, for example, in Figs. 7.8 and 7.10, where the shape of the distributions can be seen to vary widely among the radial locations shown. In the upper panel in each of these figures, the two extreme curves corresponding to cases *RN0* and *RN5* give an indication of the nature of these differences. The distributions for case *RN0*, from measurements on the jet centerline, peak at values nearly two orders of magnitude larger than do the distributions for case *RN5*, from measurements nearer to the jet edge. Furthermore, comparing the distributions at increasing radial locations suggests that these are each a "blend" of the distribution from the jet centerline and a distribution corresponding to nearly-irrotational fluid, with the contribution from the latter becoming larger at increasing radial locations.

Moreover, close inspection shows that in all these figures the pdfs for cases *RN0*, *RN1* and *RN2*, which correspond to the jet centerline and the two smallest off-centerline radial locations, are very nearly identical. The differences become clearly apparent, however, at the three largest radial locations. These differences are not a result of anisotropy due to the local mean shear, since the mean shear $(\mathcal{S}\delta/u_c)$ increases for the first three cases, but then decreases again to similar values for the last three cases.

Instead, the reason for these differences becomes apparent when examining the velocity fields themselves. For the cases corresponding to the three largest radial locations off the jet centerline, namely *RN3*, *RN4* and *RN5*, these fields were found to include large regions of essentially-irrotational fluid that had been entrained into the turbulent shear flow from the surrounding coflowing stream. The size and frequency of appearance of such regions in these fields increases dramatically at larger radial locations, where most of the newly-entrained fluid is to be expected. These regions can be readily identified in the data by the fact that they contain essentially no vorticity, consistent with fluid that has been newly entrained from the nearly-irrotational coflow.

The presence of such large regions of newly-entrained irrotational fluid among the otherwise turbulent flow has often been referred to as "external intermittency" (Corrsin and Kistler 1955; Wygnanski and Fiedler 1969; Hinze 1975), and was the subject of considerable research on turbulent shear flows during the 1970's and 80's. Turbulence statistics obtained at locations where such irrotational regions occur with significant frequency are found be "contaminated" by contributions from this irrotational fluid. Since the present study seeks to investigate the effects of heat release only on the turbulence statistics, this newly-entrained fluid must be removed from the statistical ensemble.

7.3 Data Conditioning

The enstrophy field can in principle be used to identify and exclude such large irrotational regions from the statistical ensemble, yet doing this accurately is far more difficult than it might seem. A local condition based on the enstrophy field values over a small spatial stencil would indeed allow essentially-irrotational points to be excluded from the statistics, but would also exclude points in the interior of the flow where the vorticity happens to be below a threshold value. The goal is to only exclude the large regions that account for "external intermittency" due to newly-entrained irrotational fluid, without excluding smaller regions that account for the "internal intermittency" that characterizes fully turbulent flow. Yet there is no clear distinction between these two types of regions that would reliably allow only the former to be excluded, since even the newly-entrained fluid is not completely irrotational. Increasingly elaborate schemes could be devised to identify and exclude regions based on various criteria, but any such approach to data conditioning creates significant potential for introducing bias in the statistics beyond the original ill-defined goal of excluding only the newly-entrained fluid from the ensemble.

For this reason, the present study uses a very simple global approach for excluding such regions. Rather than developing complex local criteria for rejecting data on a point-by-point basis, entire data planes are rejected if the average enstrophy value in them is below a threshold value. This is done using the raw velocity fields, before any smoothing or filtering has been applied. Such a plane-by-plane exclusion approach necessarily rejects valid regions of fully turbulent flow in the discarded planes, but the principal effect of this is simply a reduction in the size of the remaining statistical ensemble. A sufficiently large ensemble can be maintained by choosing the rejection criterion accordingly, in this case setting the threshold value for the average enstrophy to be sufficiently low. This will necessarily admit at least some regions of essentially-irrotational flow into the ensemble, and evidence of these in the resulting probability density functions. The final threshold value represents a compromise between maintaining an adequate ensemble size and achieving adequate rejection of essentially-irrotational regions of the flow.

This data conditioning approach was applied to the original ensembles for each of the six cases in Table 3.5 and Figs. 7.1 – 7.12. For the three cases on or near the jet centerline – namely *RN0*, *RN1* and *RN2* – none of the 600 planes in each of these velocity fields was rejected. For case *RN3* just 4% of the 600 planes were rejected, while for cases *RN4* and *RN5* respectively 38.0% and 76.3% of the 600 planes were rejected.

7.4 Conditioned Inner-Scale Velocity Gradient Statistics

After data conditioning as described above to remove most of the effects of "external intermittency" from newly-entrained irrotational fluid near the jet edge, the remaining ensemble of velocity fields was processed in the same manner as before. This included determination of the measurement resolution scale $\Delta^\star$ from the conditioned data. The resulting spectral parameters p and Δ_R, as well as the corresponding $\Delta^\star$ and other associated information, are given for each case in Table 7.1. Note that changes in the inner-scale normalization factors $\mathcal{N}^\star$ due to the data conditioning process were essentially negligible. From the conditioned data and these $\mathcal{N}^\star$ values, the distributions for the same velocity gradient quantities shown previously in Figs. 7.1 – 7.12 are now shown in Figs. 7.13 – 7.24. Corresponding moments from each of these distributions are given in Tables 7.2 – 7.7.

Consistent with the fact that few or no planes were rejected for the four cases closest to the centerline, the distributions for cases *RN0* – *RN3* are essentially the same as before. However for the cases that correspond to the two outermost radial locations, namely *RN4* and *RN5*, the effect of removing the essentially-irrotational regions due to newly-entrained fluid is substantial. This can be most clearly seen by comparing the upper panels in Figs. 7.20 and 7.22 with the earlier Figs. 7.8 and 7.10. For the radially outermost case, *RN5*, the previous peak in each distribution at low values has essentially disappeared, verifying that this was indeed the result of "external intermittency" from newly-entrained fluid and not an effect of shear. A small peak remains in Fig. 7.22 for cases *RN4* and *RN5*, but this is now at larger enstrophy values and presumably results from the relatively simple global data conditioning approach used here due to the compromise between maintaining an adequate ensemble size and achieving adequate rejection.

In essentially all of Figs. 7.13 – 7.24, the distributions corresponding to the six radial locations in each figure panel fall onto two relatively distinct self-similar curves. The first corresponds to cases *RN0*, *RN1* and *RN2*, for which all three curves are relatively similar, and the second corresponds to cases *RN3*, *RN4* and *RN5*, for which all three curves are again essentially similar but substantially different from the first group. This is especially evident in Fig. 7.20, though the same grouping can generally be seen in the other figures as well. It is unlikely that the differences between these two groups is primarily due to the incomplete removal of "external intermittency" by the data conditioning approach, since the two cases in which 38% and 76% of the planes were rejected essentially agree with case *RN3*, in which just 4% of the planes were rejected. This suggests that these differences are real, though the reason why these distributions might fall into two such self-similar groups is not apparent. It is noteworthy that the first group corresponds to locations radially inward from the point of maximum shear, and the second group is radially outward from this point.

Even if the evidence for grouping these cases into two more or less distinct self-similar curves is regarded as insufficiently compelling, it is undeniable that in all of Figs. 7.13 – 7.24 there is a limiting form apparent for cases *RN0* and *RN1*, and a transition to a second limiting form that clearly applies for cases *RN4* and *RN5*. These two pairs of cases show distinctly different limiting forms even though the mean shear rates that correspond to them are essentially similar. Moreover, the transition between these two limiting forms occurs over a remarkably narrow range of shear rates. In general, while these distributions do not appear to correlate simply with the mean shear rate ($\mathcal{S}\delta/u_c$), there does appear to be a clear effect of the radial position within the shear profile on these inner-scale flow properties.

7.5 Effects of Shear on Inner-Scale Statistics

Relatively little is currently understood about the extent to which the local shear affects the inner-scale properties of turbulent shear flows. In broadest terms, what is known is based on the classical hypothesis of a universal approach to a locally homogeneous and isotropic state at sufficiently small scales. Beyond this local isotropy assumption, however, the precise extension of classical turbulence theory to turbulent shear flows is still a subject of considerable uncertainty. The approach to a universal, homogeneous, isotropic state at small scales is complicated in turbulent shear flows by the presence of organized large-scale structure, spatial inhomogeneity and anisotropy, as well as the comparatively small scale-range achievable at the moderate Reynolds numbers of most experimental studies and the limitations of measurement resolution in accessing the small-scale structure of the flow. To date, relatively little is known about the range of scales over which these characteristics of shear flow turbulence will create significant departures from the asymptotic state that is presumed to apply at sufficiently small scales.

The departures from isotropy in turbulent shear flows are generally believed to depend on how the local shear $\mathcal{S}$ compares with the local turbulence time scale k/ε, where $k \equiv 1/2\,\overline{u_i' u_i'}$ is the local turbulence kinetic energy and ε is the local dissipation rate of k, and with the local viscous time scale $(\nu/\varepsilon)^{1/2}$ or equivalently (λ_ν^2/ν). These provide two dimensionless parameters that characterize the extent of the anisotropy induced by the mean shear. The first of these is

$$\mathcal{S}^\star \equiv \left(\frac{\mathcal{S}k}{\varepsilon}\right), \tag{7.1}$$

and as $\mathcal{S}^\star$ increases the anisotropy induced at the large scales is believed to extend to increasingly smaller scales. Note that, since $\varepsilon \sim (u_c^3/\delta)$, the shear parameter $\mathcal{S}^\star$ above is proportional to $(\mathcal{S}\delta/u_c)$ given in the legends in Figs. 7.13 – 7.24. The second ratio, termed the Corrsin-Uberoi parameter (Corrsin 1958; Uberoi 1957), is

$$\mathcal{S}_c^\star \equiv \mathcal{S}\left(\frac{\nu}{\varepsilon}\right)^{\frac{1}{2}} \ll 1, \tag{7.2}$$

and when $\mathcal{S}$ is sufficiently large that $\mathcal{S}_c^\star$ approaches one then even the smallest scales will be affected by the shear. When this parameter is small, then the inner time scale is sufficiently fast compared to the shear time scale for the inner scales to maintain their natural isotropic state. The effects of $\mathcal{S}^\star$ and $\mathcal{S}_c^\star$ in characterizing the anisotropy in the velocity field is consistent with measurements in a large-scale turbulent boundary layer by Saddoughi and Veeravalli (1994). For the cases in Table 3.5 and Figs. 7.13 – 7.24, corresponding values of the Corrsin-Uberoi parameter based on the local shear are $\mathcal{S}_c^\star \leq 0.156$, with the maximum value occurring for case *RN3*. Here the dissipation ε is estimated from the measured gradient values as

$$\varepsilon = 15\nu \left[\frac{3}{2} \left(S_{xx}^2 + S_{yy}^2 \right) + 6\, S_{xy}^2 \right] \tag{7.3}$$

Since $\mathcal{S}_c^\star \ll 1$ these values suggest that the smallest scales in the flow should remain largely isotropic, and that the inner-scaled distributions in Figs. 7.13 – 7.24 might thus be largely unaffected by the local shear. This is partly consistent with the distributions in these figures, since the three cases *RN0*, *RN1* and *RN2* all have $\mathcal{S}_c^\star \leq 0.156$ and all fall onto essentially the same limiting curve. However, it is inconsistent with the transition to a different limiting curve in cases *RN3*, *RN4* and *RN5*, since these also all have $\mathcal{S}_c^\star \ll 1$.

Additional insights can be obtained by examining the moments in Tables 7.2 – 7.7 obtained from these distributions. Key ratios of these moments are shown as a function of the dimensionless shear $\mathcal{S}\delta/u_c$ in Figs. 7.25 and 7.26, where corresponding results from Mullin and Dahm (2005b) are shown for comparison. In Fig. 7.25, two moment ratios are used to indicate the degree of anisotropy in the velocity gradient fields and any correlation this may have with the mean shear. The upper panel compares the *rms* values of the on-diagonal strain rates S_{xx} and S_{yy}, for which the isotropic value is 1. The leftmost point, labeled *RN0*, is from the present measurements on the jet centerline, and proceeding rightward the measurement location moves from the centerline towards the jet edge. At the maximum shear value, the curve reverses and proceeds leftward as the measurement location further proceeds radially outward. It is apparent that there is essentially no variation in this anisotropy measure with increasing $\mathcal{S}\delta/u_c$, or equivalently with increasing $\mathcal{S}k/\varepsilon$. The lower panel presents a similar anisotropy measure based on a ratio *rms* values for the on-diagonal and off-diagonal components of the strain rates, for which the isotropic value is 0.25. Here, too, there is little variation in the degree of anisotropy with increasing $\mathcal{S}\delta/u_c$. The curves in both panels, however, show two distinct branches that correspond to the two distinctly different limiting forms of the distributions in Figs. 7.13 – 7.24.

Further such tests are shown in Fig. 7.26, where the upper panel is the ratio of the *rms* values of the u and v components velocity fluctuations, and the lower panel is ratio of the *rms* value of $-\partial w/\partial z$ inferred from continuity. The upper panel thus reflects the anisotropy at the large scales of the flow, while the measure in the lower panel is dominated by small-scale anisotropy. For these anisotropy measures as well, there is little consistent variation in the degree of anisotropy with increasing $\mathcal{S}\delta/u_c$. The upper panel does show a slightly larger departure from the isotropic value of 1 with increasing shear rate, as would be expected for a measure that is sensitive to large-scale anisotropy. However, the measure in the lower panel shows little effect of the shear rate on the level of small-scale anisotropy. The curves in both panels of both figures again show two distinct branches that correspond to the two distinctly different limiting forms of the distributions in Figs. 7.13 – 7.24.

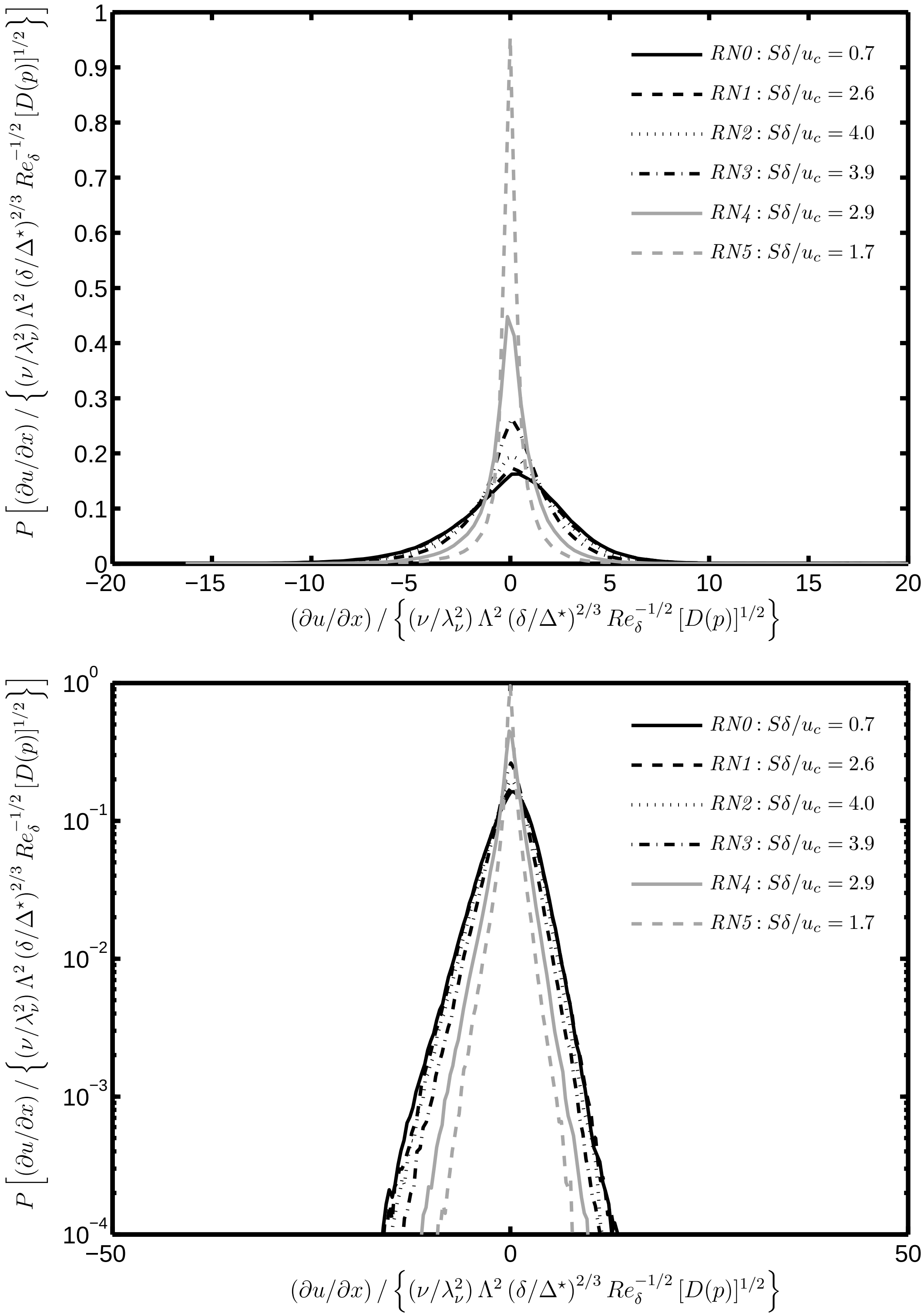

Figure 7.1: Pdfs from all nonreacting, off-centerline cases *RN0* – *RN5* for velocity gradient $\partial u/\partial x$ normalized by resolution-corrected inner scaling $(\nu/\lambda_\nu^2)\,\Lambda^2\,(\delta/\Delta^\star)^{2/3}\,Re_\delta^{-1/2}\,[D(p)]^{1/2}$, shown in linear axes *(top)* and semilogarithmic axes *(bottom)*.

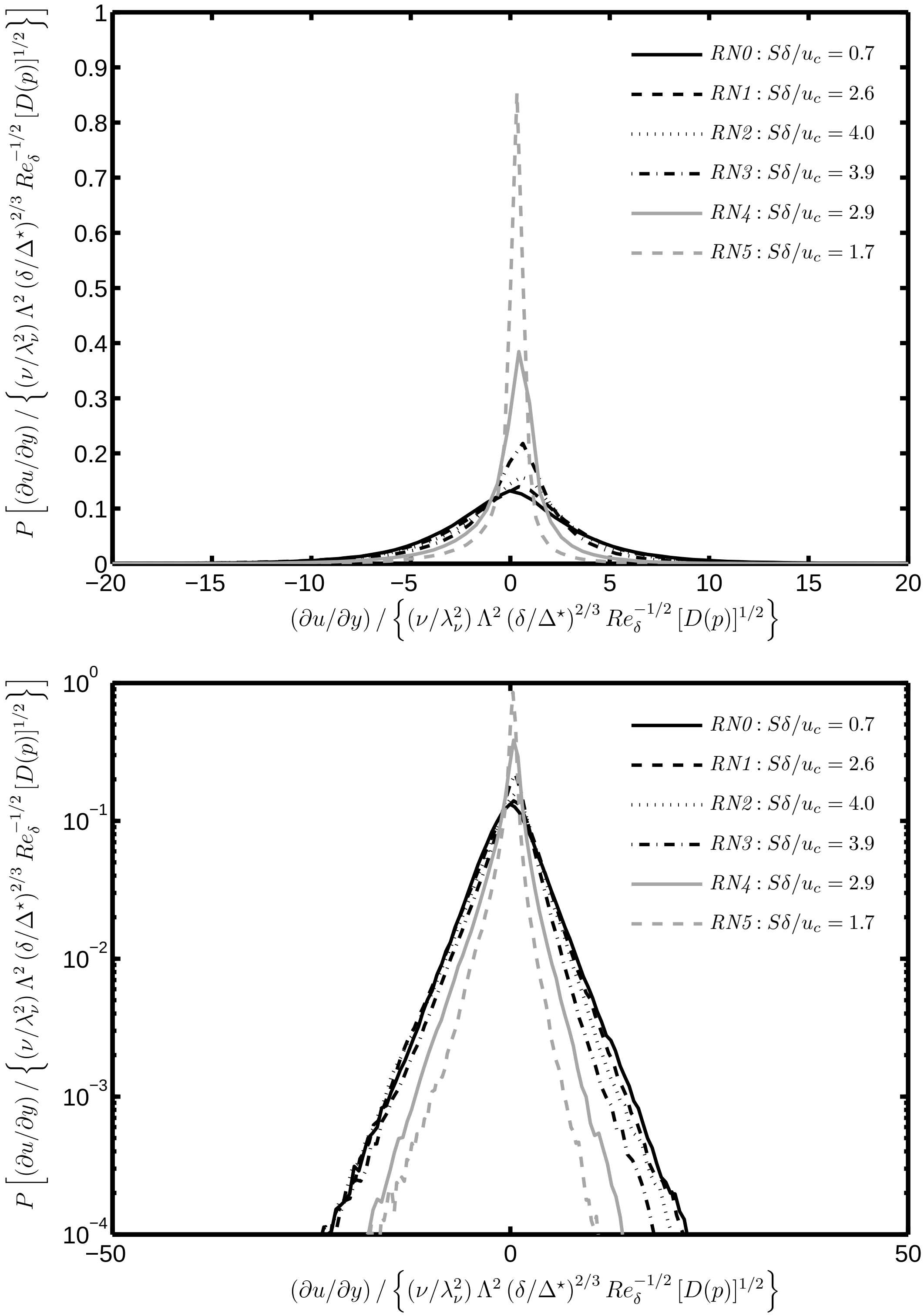

Figure 7.2: Pdfs from all nonreacting, off-centerline cases *RN0* – *RN5* for velocity gradient $\partial u/\partial y$ normalized by resolution-corrected inner scaling $(\nu/\lambda_\nu^2)\,\Lambda^2\,(\delta/\Delta^\star)^{2/3}\,Re_\delta^{-1/2}\,[D(p)]^{1/2}$, shown in linear axes *(top)* and semilogarithmic axes *(bottom)*.

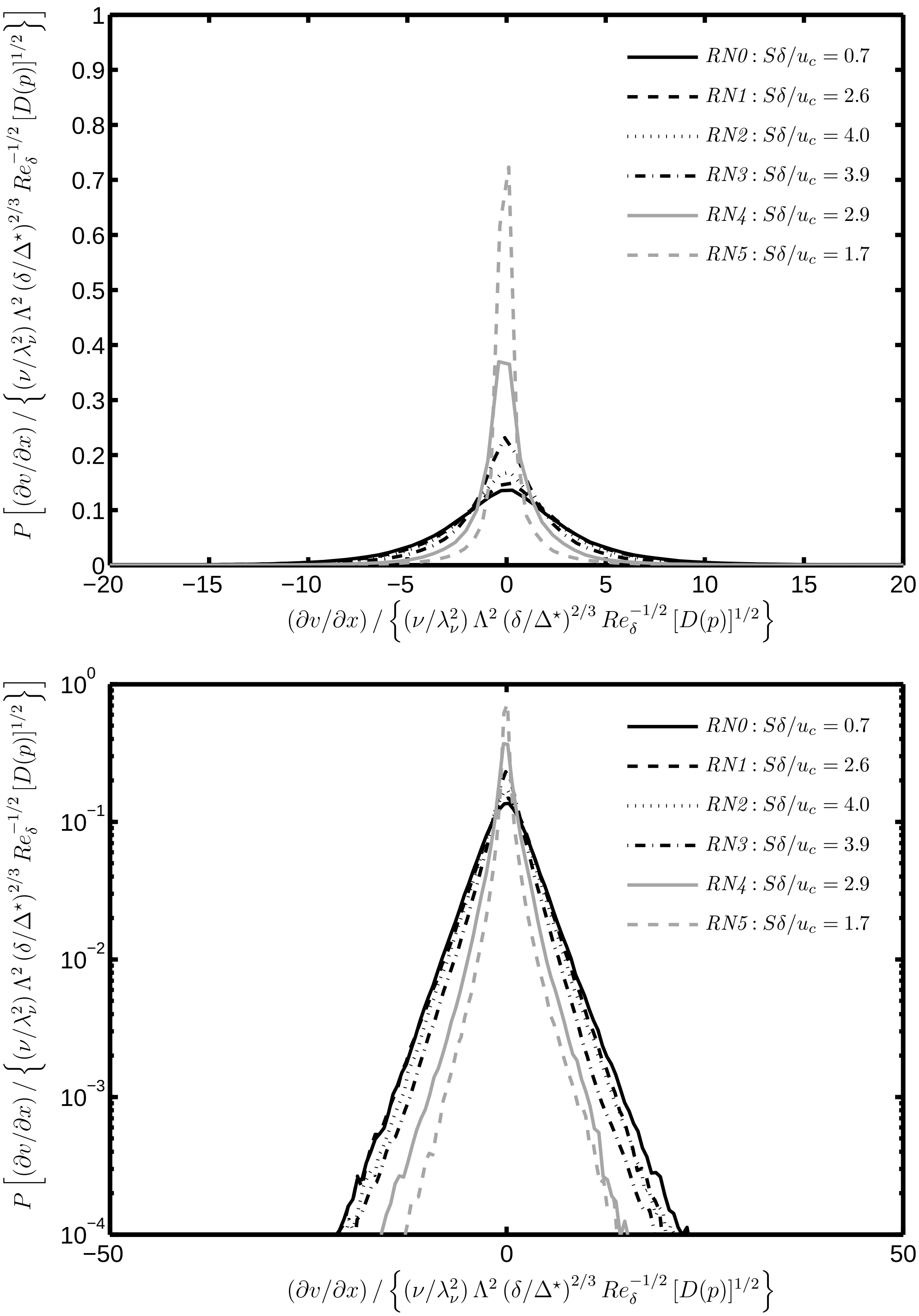

Figure 7.3: Pdfs from all nonreacting, off-centerline cases *RN0* – *RN5* for velocity gradient $\partial v/\partial x$ normalized by resolution-corrected inner scaling $(\nu/\lambda_\nu^2)\,\Lambda^2\,(\delta/\Delta^\star)^{2/3}\,Re_\delta^{-1/2}\,[D(p)]^{1/2}$, shown in linear axes *(top)* and semilogarithmic axes *(bottom)*.

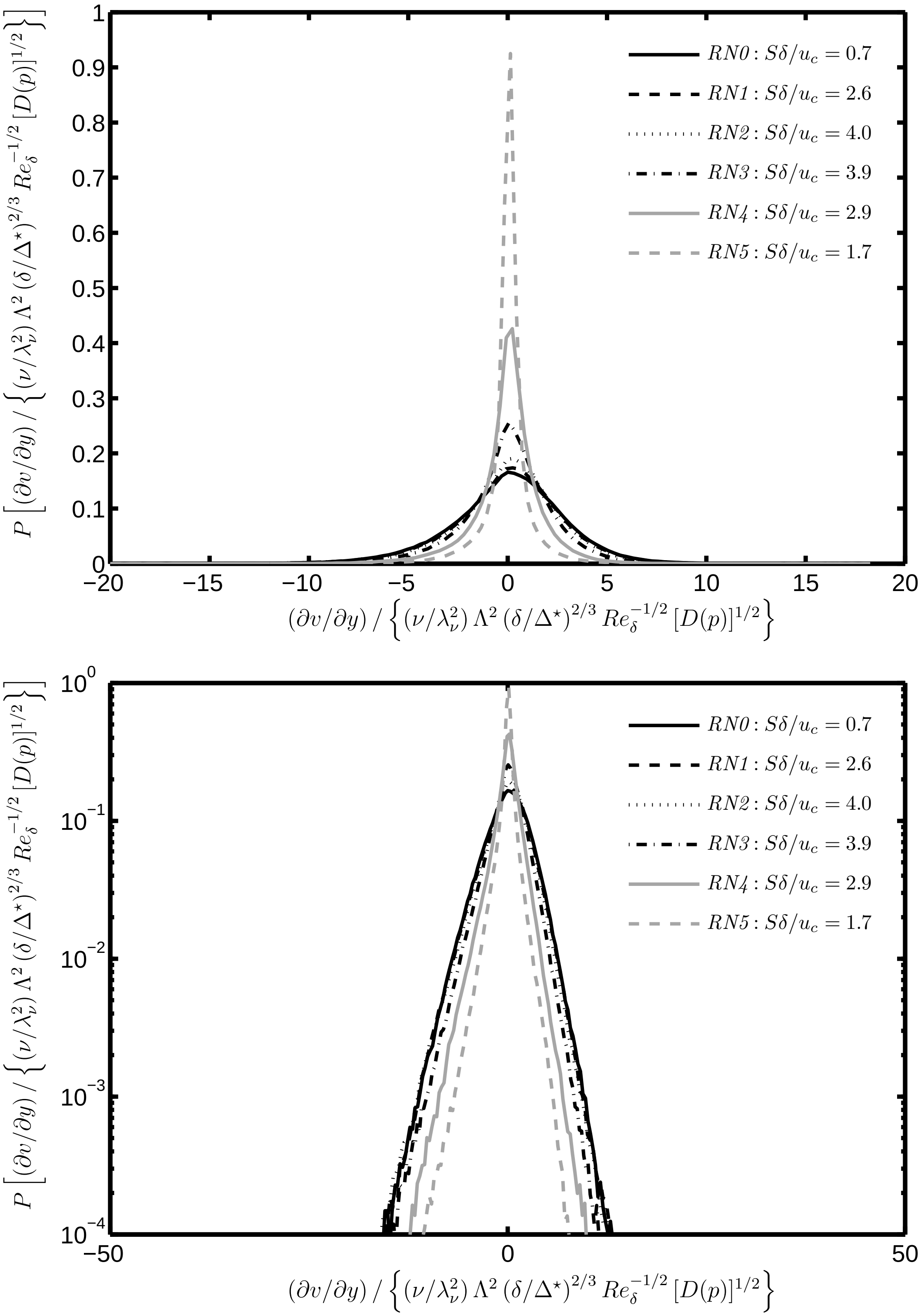

Figure 7.4: Pdfs from all nonreacting, off-centerline cases *RN0* – *RN5* for velocity gradient $\partial v/\partial y$ normalized by resolution-corrected inner scaling $(\nu/\lambda_\nu^2)\,\Lambda^2\,(\delta/\Delta^\star)^{2/3}\,Re_\delta^{-1/2}\,[D(p)]^{1/2}$, shown in linear axes *(top)* and semilogarithmic axes *(bottom)*.

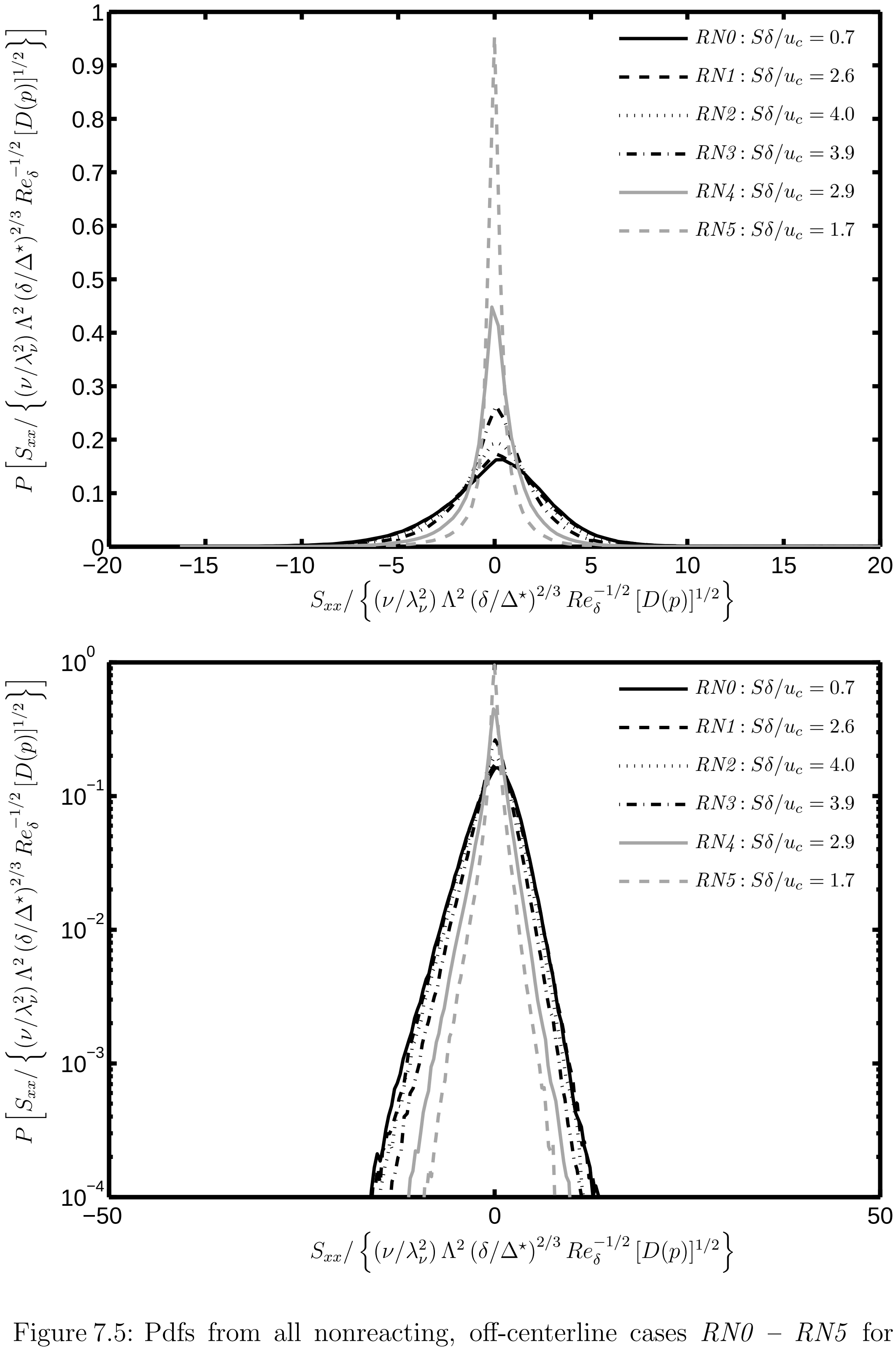

Figure 7.5: Pdfs from all nonreacting, off-centerline cases *RN0* – *RN5* for strain rate component S_{xx} normalized by resolution-corrected inner scaling $(\nu/\lambda_\nu^2)\,\Lambda^2\,(\delta/\Delta^\star)^{2/3}\,Re_\delta^{-1/2}\,[D(p)]^{1/2}$, shown in linear axes *(top)* and semilogarithmic axes *(bottom)*.

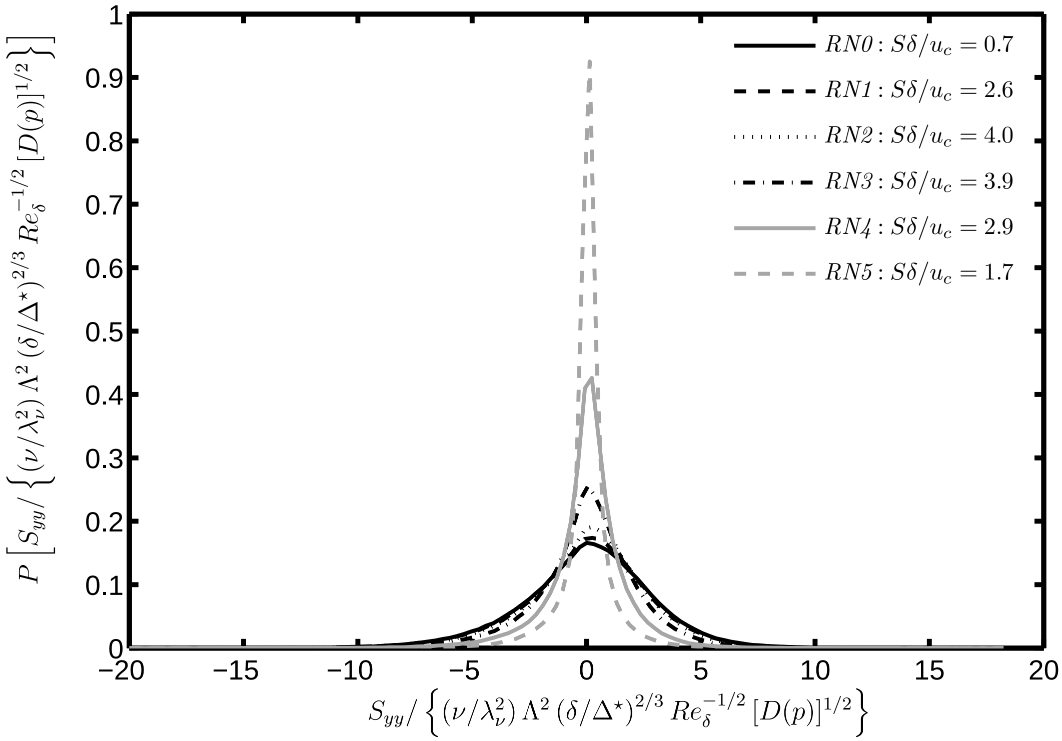

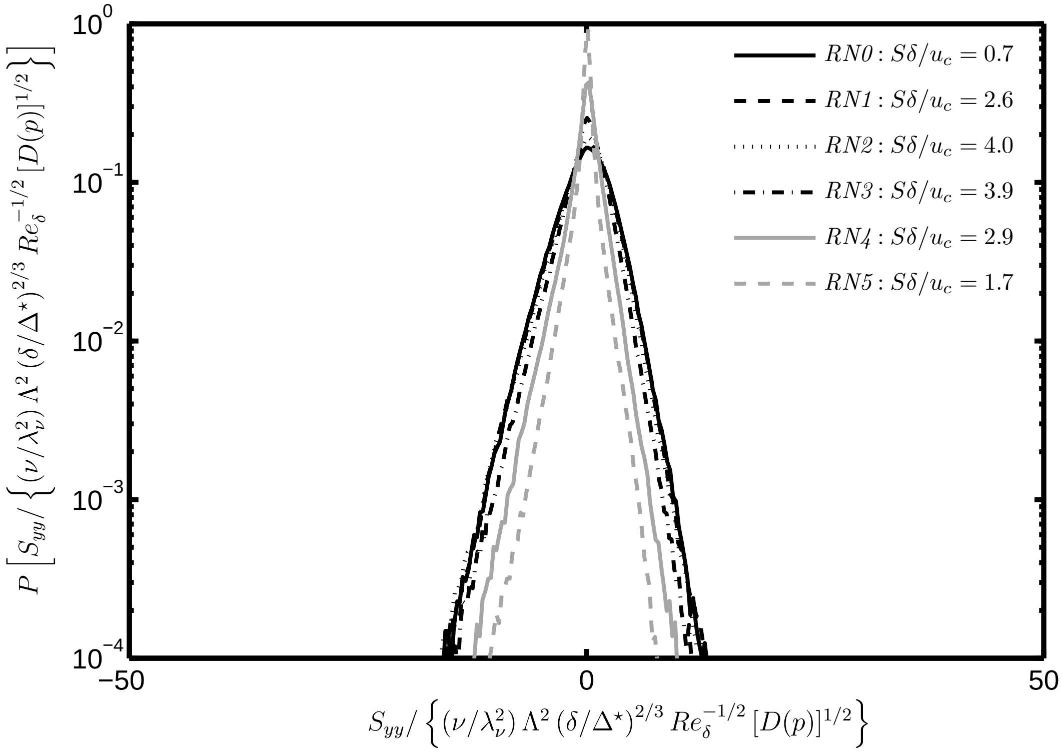

Figure 7.6: Pdfs from all nonreacting, off-centerline cases *RN0* – *RN5* for strain rate component S_{yy} normalized by resolution-corrected inner scaling $(\nu/\lambda_\nu^2)\,\Lambda^2\,(\delta/\Delta^\star)^{2/3}\,Re_\delta^{-1/2}\,[D(p)]^{1/2}$, shown in linear axes *(top)* and semilogarithmic axes *(bottom)*.

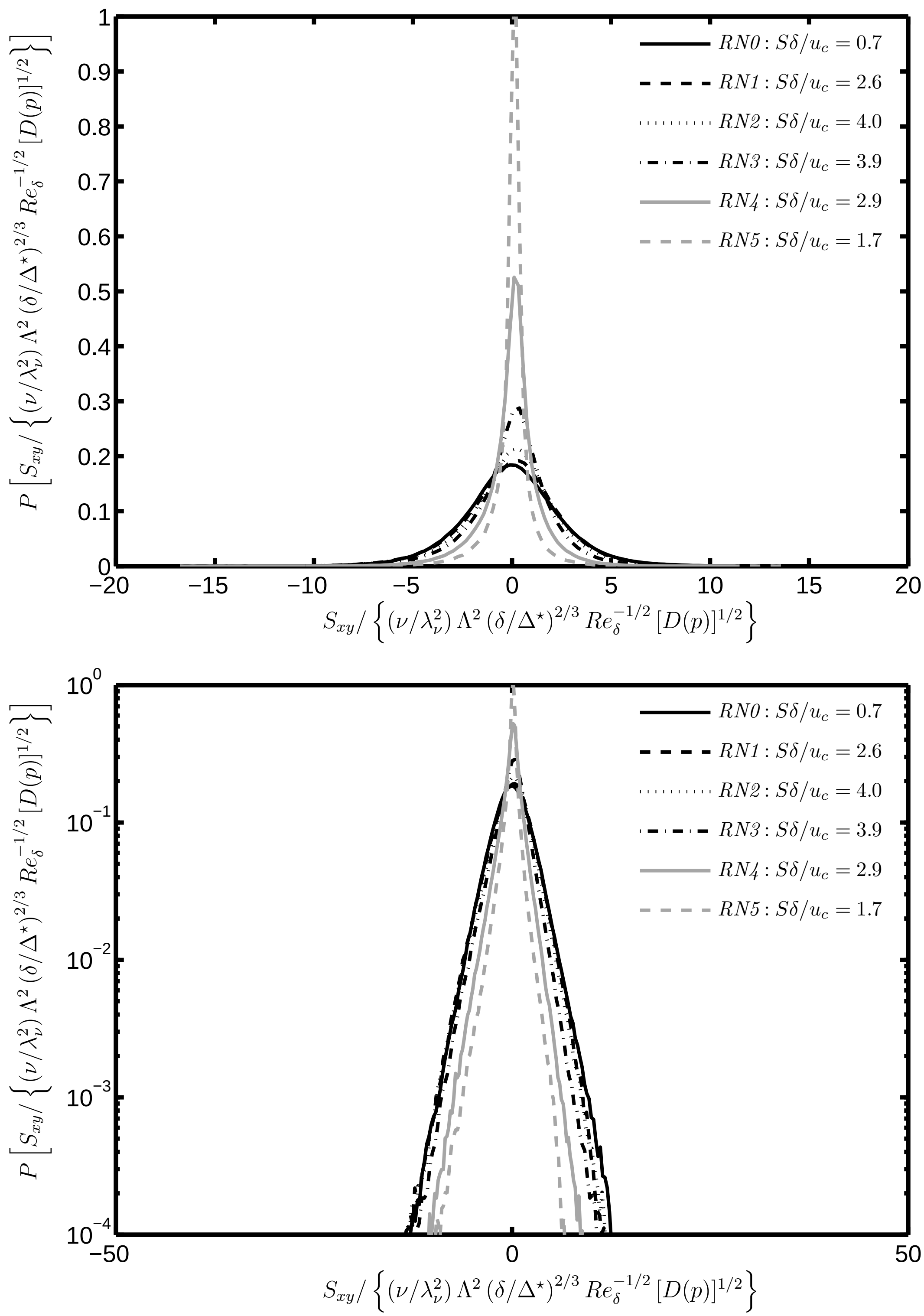

Figure 7.7: Pdfs from all nonreacting, off-centerline cases *RN0* − *RN5* for strain rate component S_{xy} normalized by resolution-corrected inner scaling $(\nu/\lambda_\nu^2)\,\Lambda^2\,(\delta/\Delta^\star)^{2/3}\,Re_\delta^{-1/2}\,[D(p)]^{1/2}$, shown in linear axes *(top)* and semilogarithmic axes *(bottom)*.

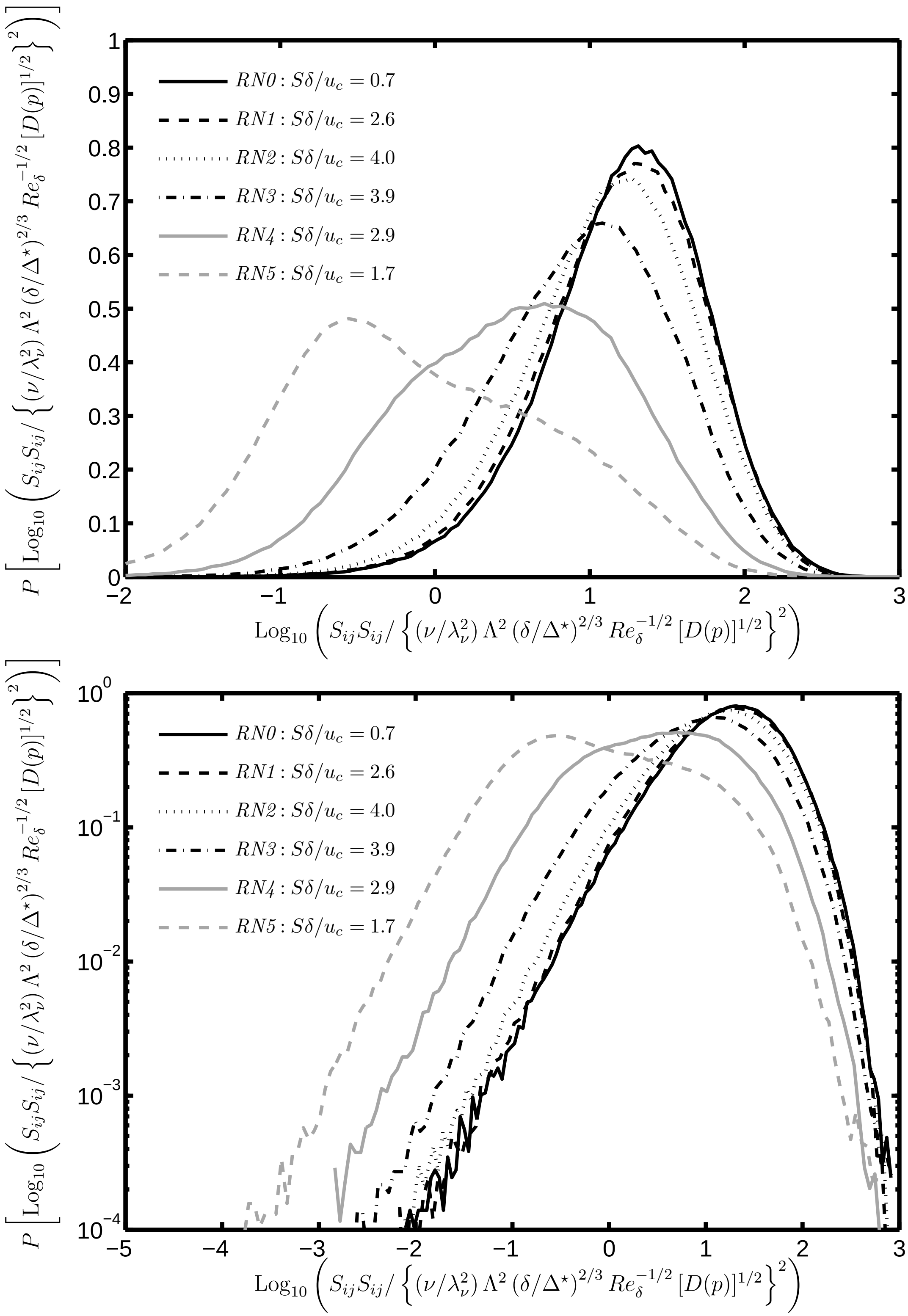

Figure 7.8: Pdfs from all nonreacting, off-centerline cases *RN0* – *RN5*, for dissipation $\mathrm{Log}_{10}(S_{ij}S_{ij})$ normalized by resolution-corrected inner scaling $\{(\nu/\lambda_\nu^2)\,\Lambda^2\,(\delta/\Delta^\star)^{2/3}\,Re_\delta^{-1/2}\,[D(p)]^{1/2}\}^2$, shown in linear axes *(top)* and semilogarithmic axes *(bottom)*.

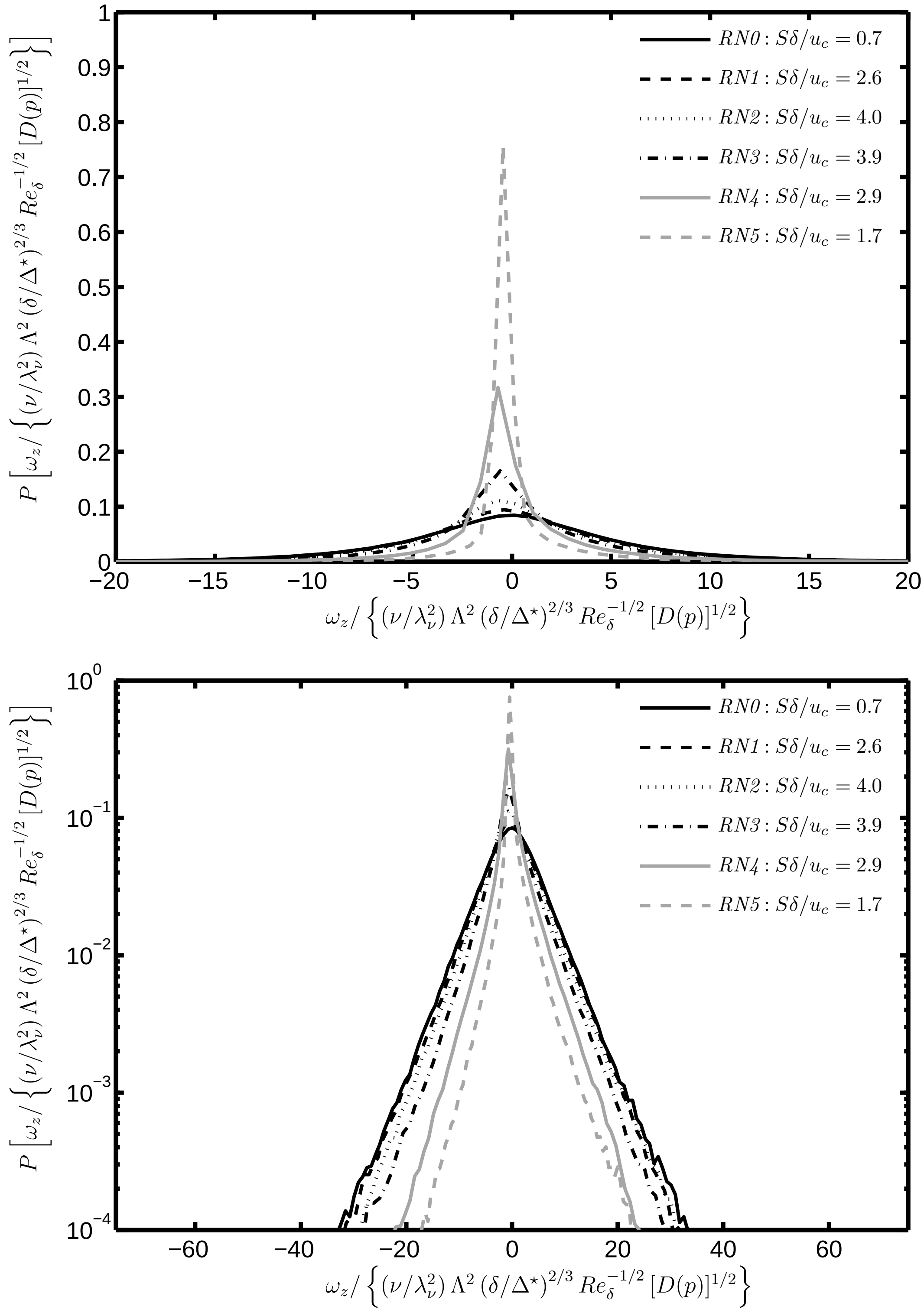

Figure 7.9: Pdfs from all nonreacting, off-centerline cases *RN0* – *RN5* for vorticity ω_z normalized by resolution-corrected inner scaling $(\nu/\lambda_\nu^2)\,\Lambda^2\,(\delta/\Delta^\star)^{2/3}\,Re_\delta^{-1/2}\,[D(p)]^{1/2}$, shown in linear axes *(top)* and semilogarithmic axes *(bottom)*.

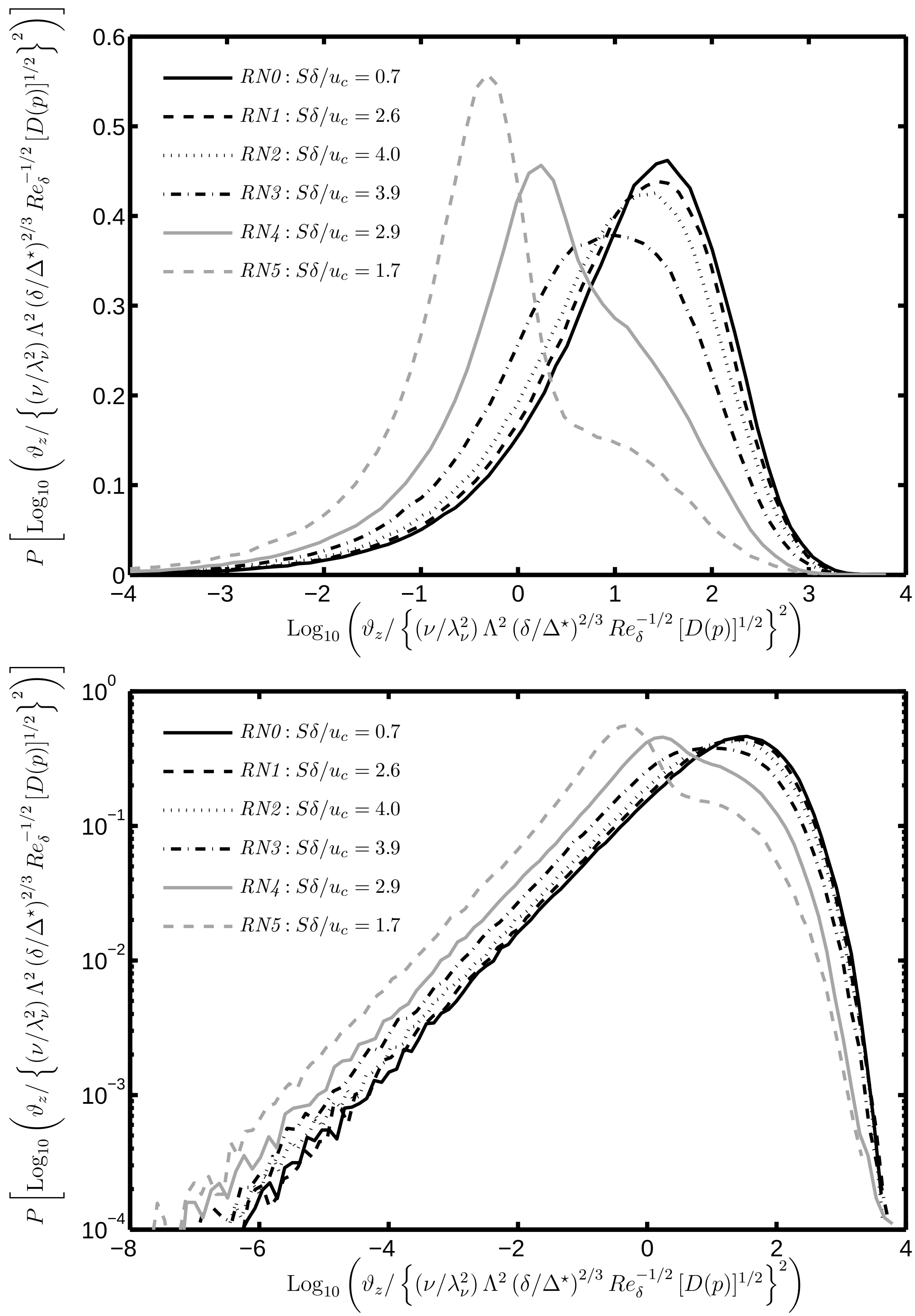

Figure 7.10: Pdfs from all nonreacting, off-centerline cases *RN0* – *RN5*, for enstrophy $\mathrm{Log}_{10}(\vartheta_z)$ normalized by resolution-corrected inner scaling, $\{(\nu/\lambda_\nu^2)\,\Lambda^2\,(\delta/\Delta^\star)^{2/3}\,Re_\delta^{-1/2}\,[D(p)]^{1/2}\}^2$, shown in linear axes *(top)* and semilogarithmic axes *(bottom)*.

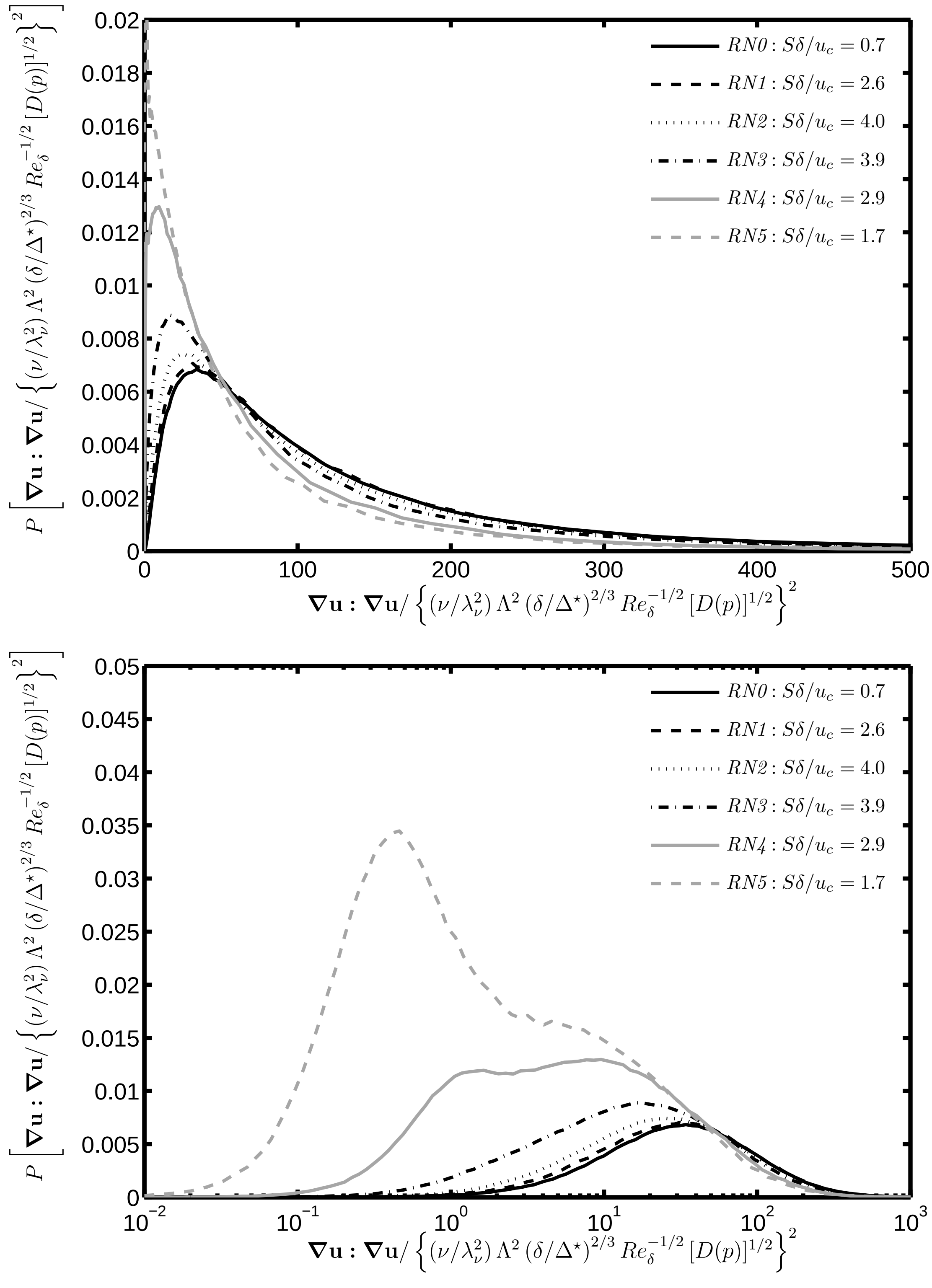

Figure 7.11: Pdfs from all nonreacting, off-centerline cases *RN0* – *RN5*, for contraction of the velocity gradient tensor $\nabla\mathbf{u} : \nabla\mathbf{u}$ normalized by resolution-corrected inner scaling, $\{(\nu/\lambda_\nu^2)\,\Lambda^2\,(\delta/\Delta^\star)^{2/3}\,Re_\delta^{-1/2}\,[D(p)]^{1/2}\}^2$, shown in linear axes *(top)* and semilogarithmic axes *(bottom)*.

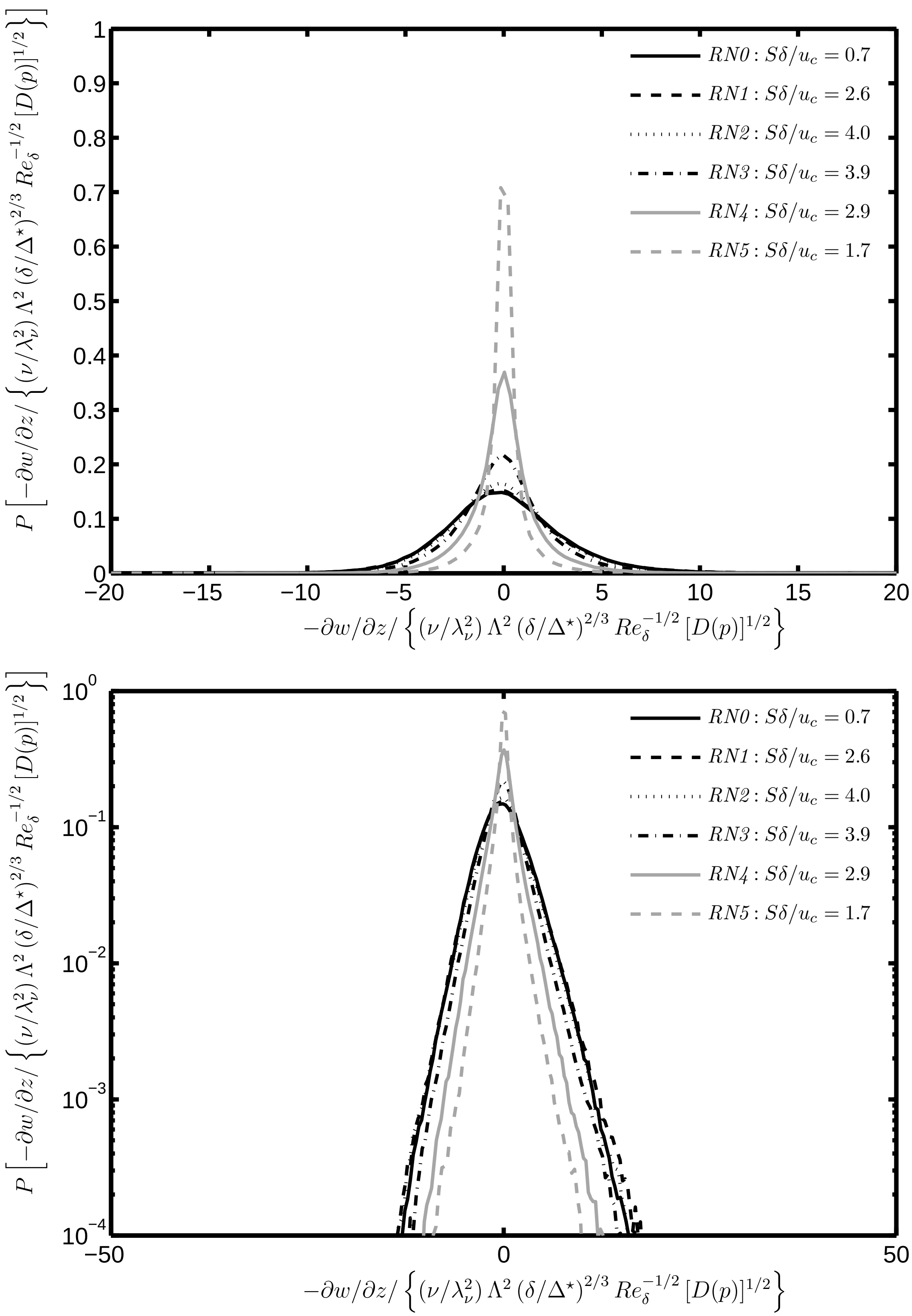

Figure 7.12: Pdfs from all nonreacting, off-centerline cases *RN0* − *RN5* for two-dimensional divergence $-\partial w/\partial z$ normalized by resolution-corrected inner scaling $(\nu/\lambda_\nu^2)\,\Lambda^2\,(\delta/\Delta^\star)^{2/3}\,Re_\delta^{-1/2}\,[D(p)]^{1/2}$, shown in linear axes *(top)* and semilogarithmic axes *(bottom)*.

Case	$r/\delta_{1/2}$	$\mathcal{S}\delta/u_c$ [-]	Δ_{IW} mm	Inertial- and dissipation-range spectral parameters and resulting factors							
				$\langle p\rangle$ [-]	$\langle\Delta_R\rangle$ mm	Λ_ν [-]	$\langle\Delta^\star\rangle$ mm	$\Lambda^\star$ [-]	$\langle\Delta^\star\rangle/\langle\Delta_R\rangle$	$D(p)$	$\mathcal{N}^\star$
RN0	0.00	0.708	0.413	1.448	0.910	7.272	5.834	46.650	6.41	0.0829	21.307
RN1	0.16	2.582	0.413	1.522	0.879	7.029	5.699	45.569	6.48	0.0816	21.473
RN2	0.48	3.999	0.413	1.370	0.996	7.967	6.271	50.139	6.29	0.0845	20.505
RN3	0.81	3.948	0.413	1.402	1.034	8.267	6.567	52.506	6.35	0.0837	19.790
RN4	1.13	2.929	0.413	1.353	1.180	9.434	7.365	58.885	6.24	0.0848	18.446
RN5	1.45	1.721	0.413	1.150	1.502	12.009	8.845	70.719	5.89	0.0917	16.978
RN4†	1.13	2.929	0.413	1.446	1.121	8.960	7.108	56.832	6.34	0.0827	18.660
RN5†	1.45	1.721	0.413	1.269	1.340	10.718	8.182	65.423	6.10	0.0871	17.426

Table 7.1: Averaged spectral parameters $\langle p\rangle$, $\langle\Delta_R\rangle$ and $\langle\Delta^\star\rangle$ for all cases in Table 3.5 obtained by averaging over results from ω_z, S_{xx}, S_{yy} and S_{xy}. Here Λ_ν and $\Lambda^\star$ values are from $\Lambda_i \equiv (\Delta_i/\delta)Re_\delta^{3/4}$. The quantity $r/\delta_{1/2}$ is the radius normalized by the half width at the half-maximum point. The mean outer shear is $\mathcal{S} \equiv \sqrt{2}\,|\partial\langle u\rangle/\partial r|$. For all cases, $Re_\delta = 19\,000$ and $\delta = 0.202$ m. The final two cases, indicated by a †, are the cases reprocessed with the data conditioning strategy.

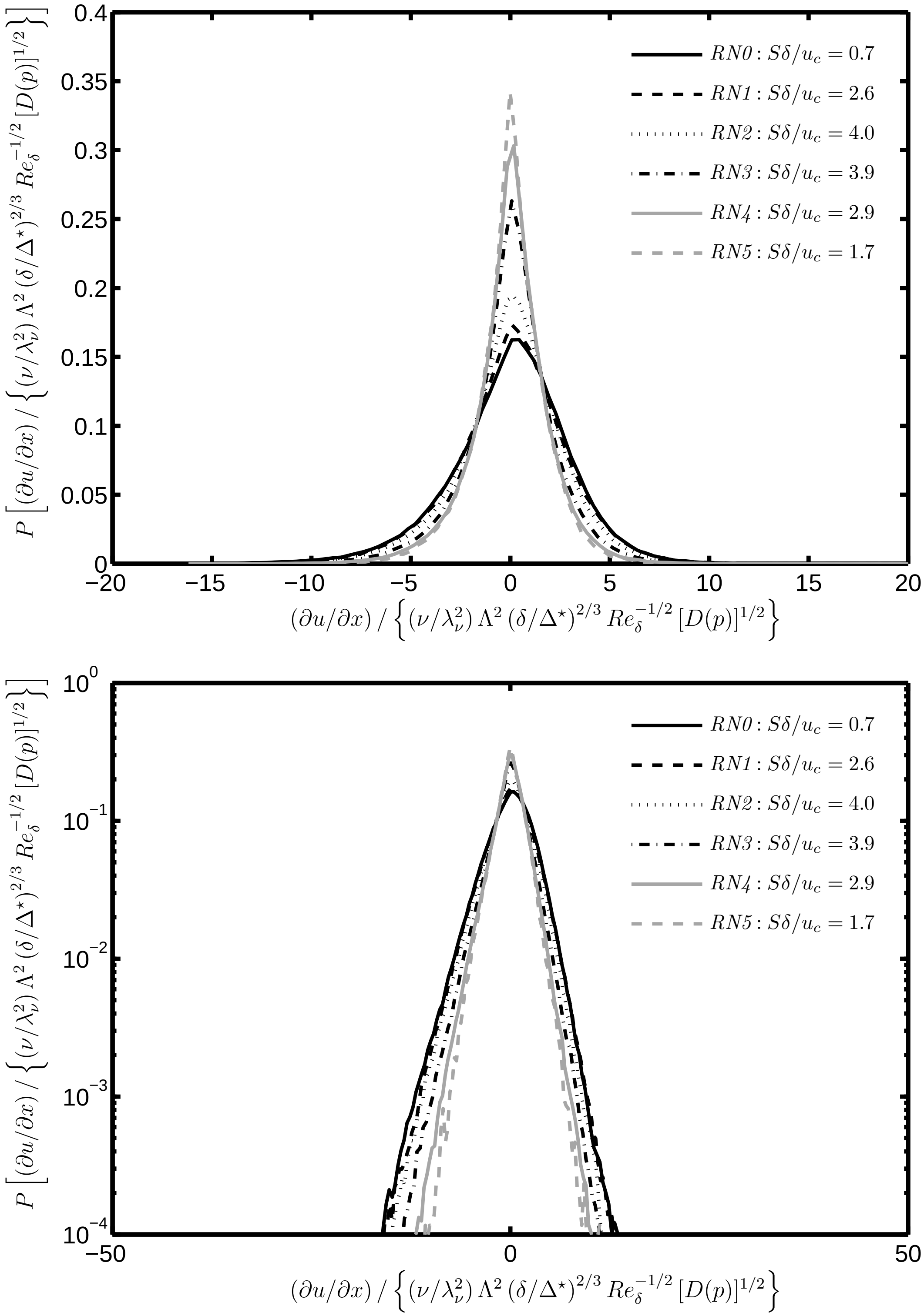

Figure 7.13: Pdfs from all nonreacting, off-centerline cases *RN0* – *RN5* for velocity gradient $\partial u/\partial x$ normalized by resolution-corrected inner scaling $(\nu/\lambda_\nu^2)\,\Lambda^2\,(\delta/\Delta^\star)^{2/3}\,Re_\delta^{-1/2}\,[D(p)]^{1/2}$, shown in linear axes *(top)* and semilogarithmic axes *(bottom)*.

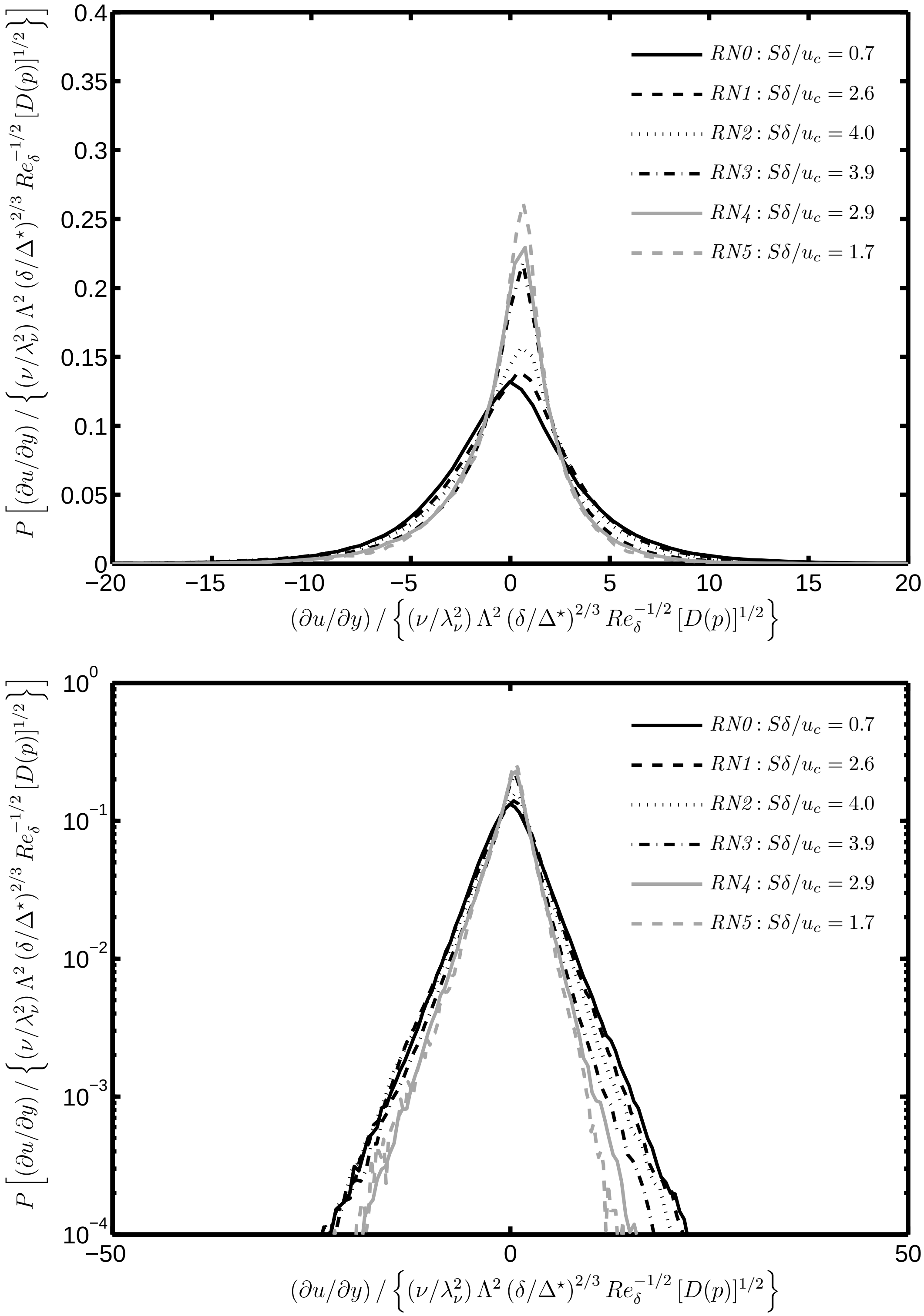

Figure 7.14: Pdfs from conditioned data for all nonreacting, off-centerline cases *RN0* – *RN5* for velocity gradient $\partial u/\partial y$ normalized by resolution-corrected inner scaling $(\nu/\lambda_\nu^2)\, \Lambda^2\, (\delta/\Delta^\star)^{2/3}\, Re_\delta^{-1/2}\, [D(p)]^{1/2}$, shown in linear axes *(top)* and semilogarithmic axes *(bottom)*.

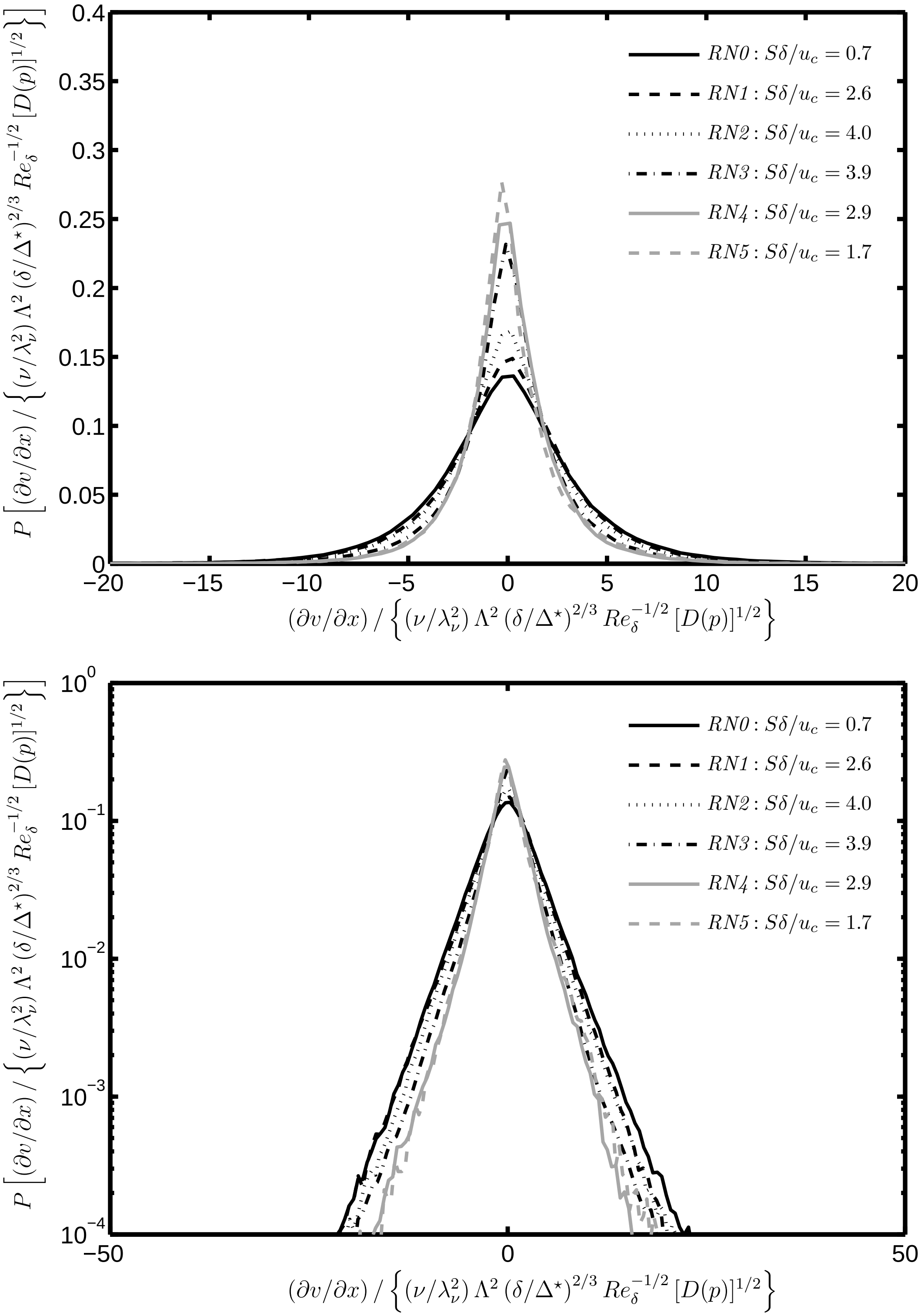

Figure 7.15: Pdfs from conditioned data for all nonreacting, off-centerline cases *RN0* – *RN5* for velocity gradient $\partial v/\partial x$ normalized by resolution-corrected inner scaling $(\nu/\lambda_\nu^2)\,\Lambda^2\,(\delta/\Delta^\star)^{2/3}\,Re_\delta^{-1/2}\,[D(p)]^{1/2}$, shown in linear axes *(top)* and semilogarithmic axes *(bottom)*.

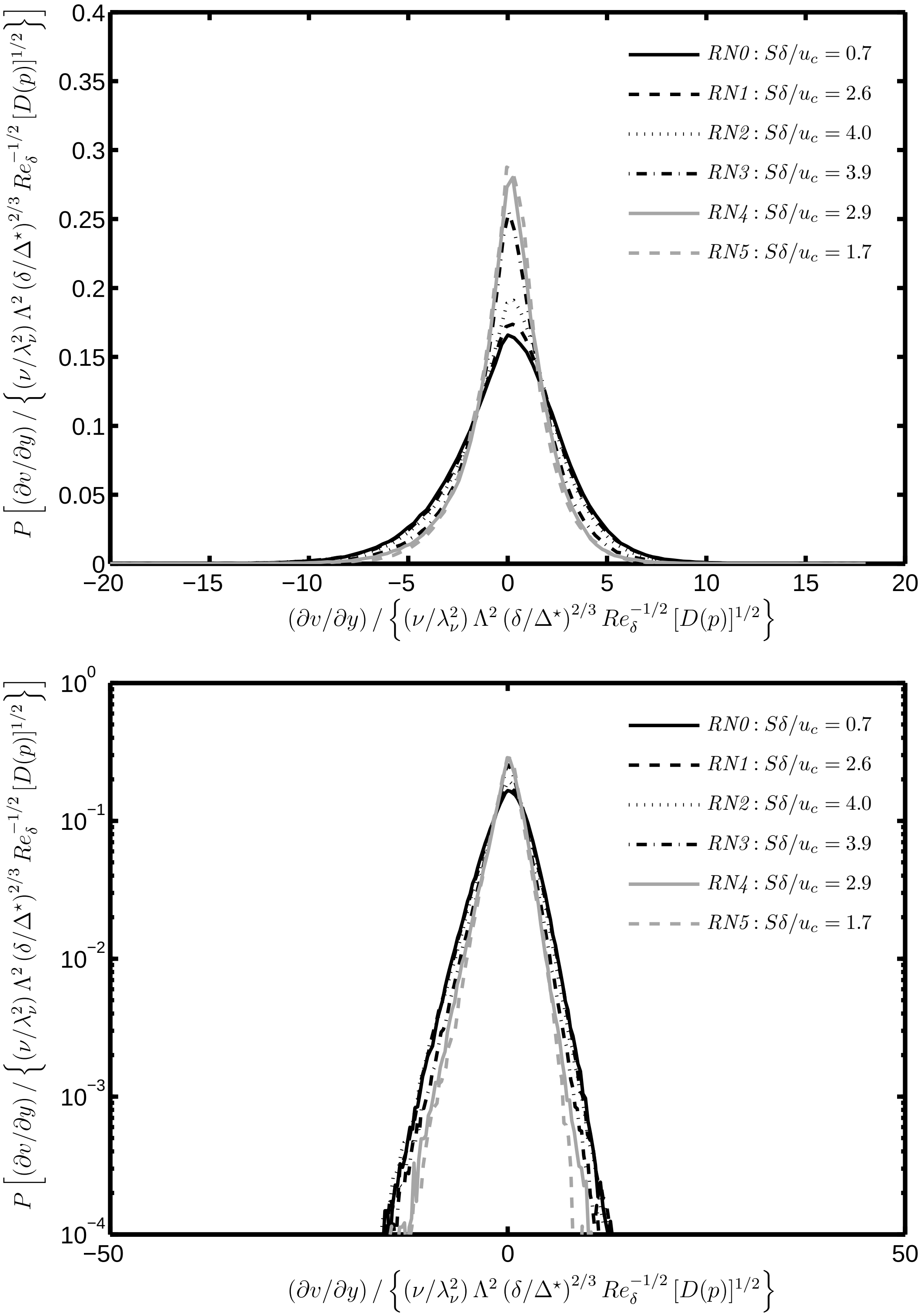

Figure 7.16: Pdfs from conditioned data for all nonreacting, off-centerline cases *RN0* – *RN5* for velocity gradient $\partial v/\partial y$ normalized by resolution-corrected inner scaling $(\nu/\lambda_\nu^2)\,\Lambda^2\,(\delta/\Delta^\star)^{2/3}\,Re_\delta^{-1/2}\,[D(p)]^{1/2}$, shown in linear axes *(top)* and semilogarithmic axes *(bottom)*.

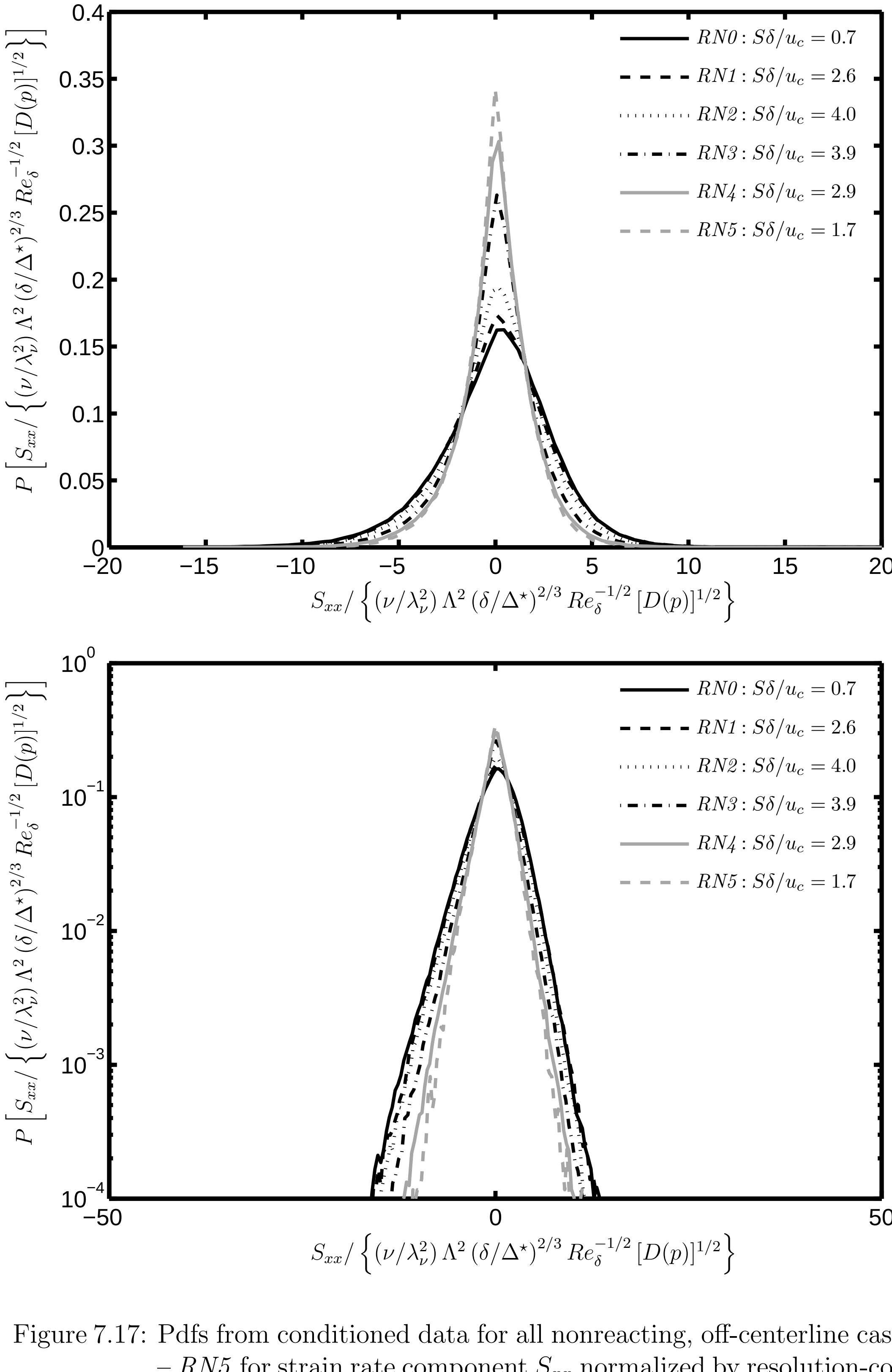

Figure 7.17: Pdfs from conditioned data for all nonreacting, off-centerline cases *RN0* – *RN5* for strain rate component S_{xx} normalized by resolution-corrected inner scaling $(\nu/\lambda_\nu^2)\,\Lambda^2\,(\delta/\Delta^\star)^{2/3}\,Re_\delta^{-1/2}\,[D(p)]^{1/2}$, shown in linear axes *(top)* and semilogarithmic axes *(bottom)*.

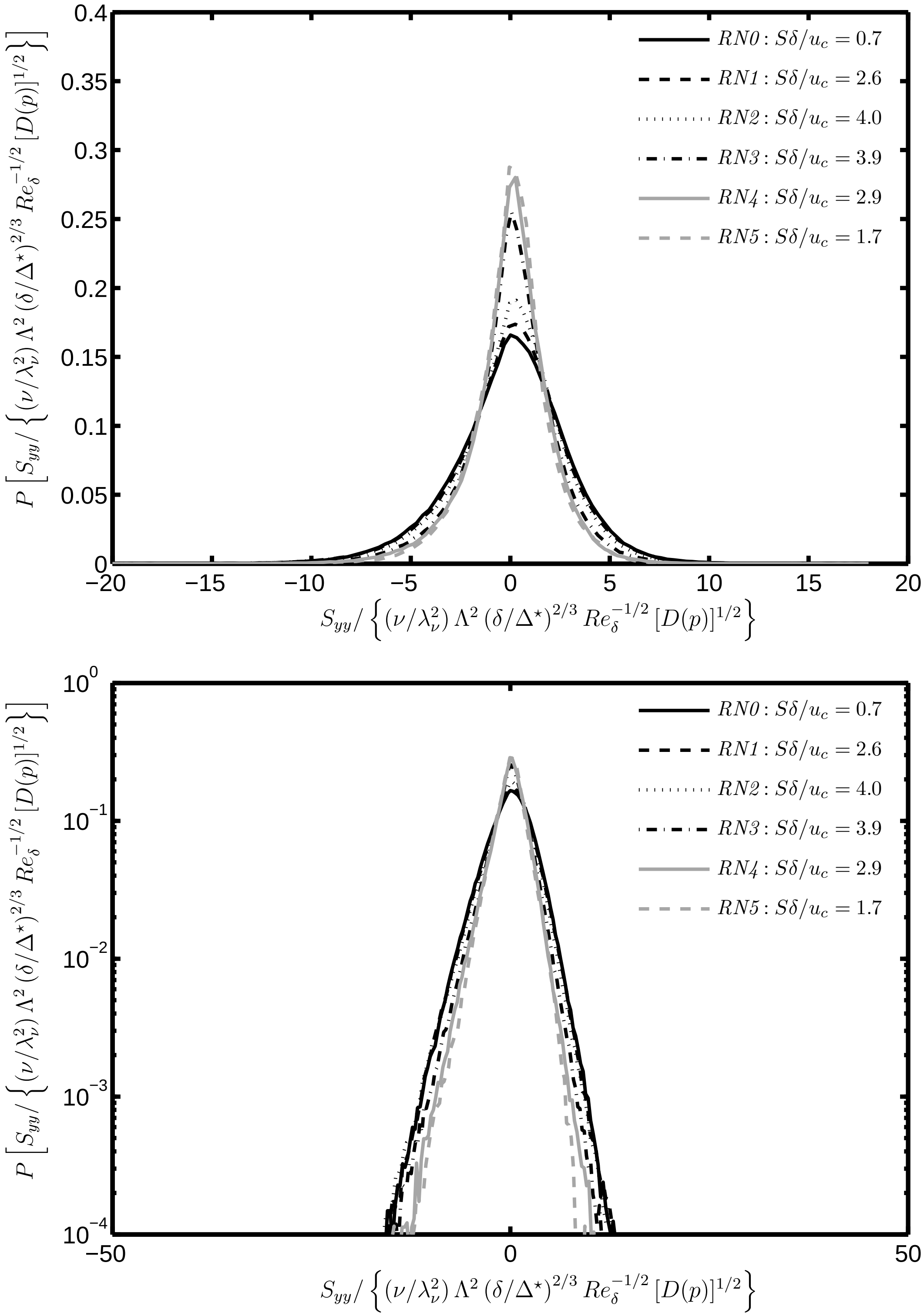

Figure 7.18: Pdfs from conditioned data for all nonreacting, off-centerline cases *RN0* – *RN5* for strain rate component S_{yy} normalized by resolution-corrected inner scaling $(\nu/\lambda_\nu^2)\,\Lambda^2\,(\delta/\Delta^\star)^{2/3}\,Re_\delta^{-1/2}\,[D(p)]^{1/2}$, shown in linear axes *(top)* and semilogarithmic axes *(bottom)*.

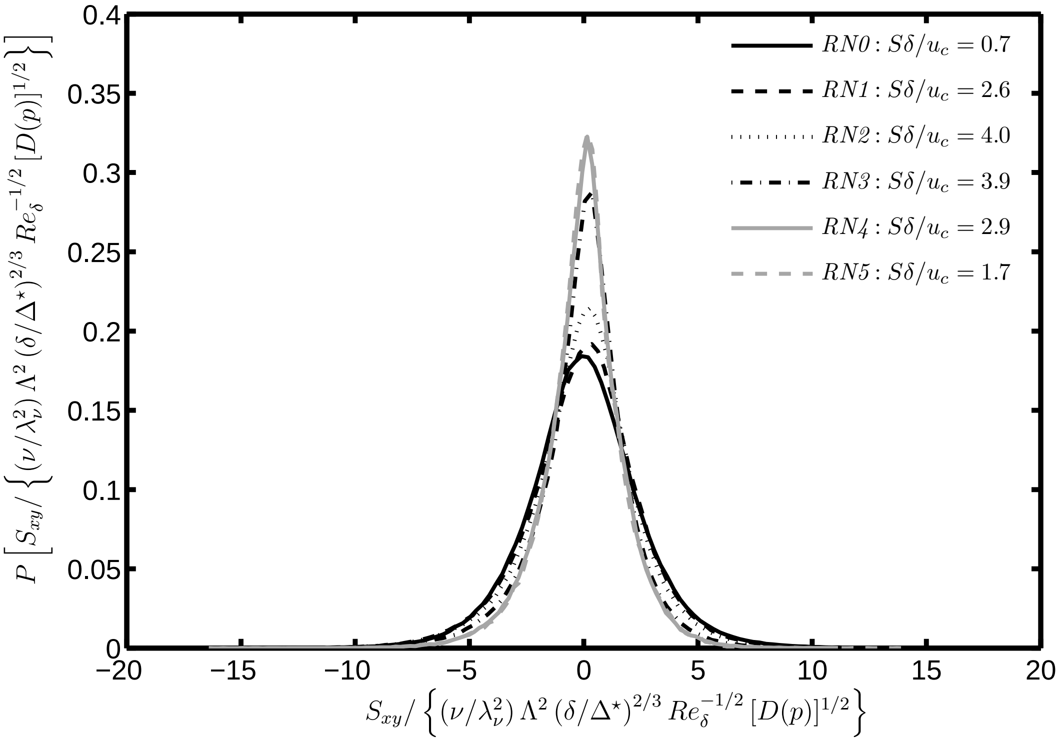

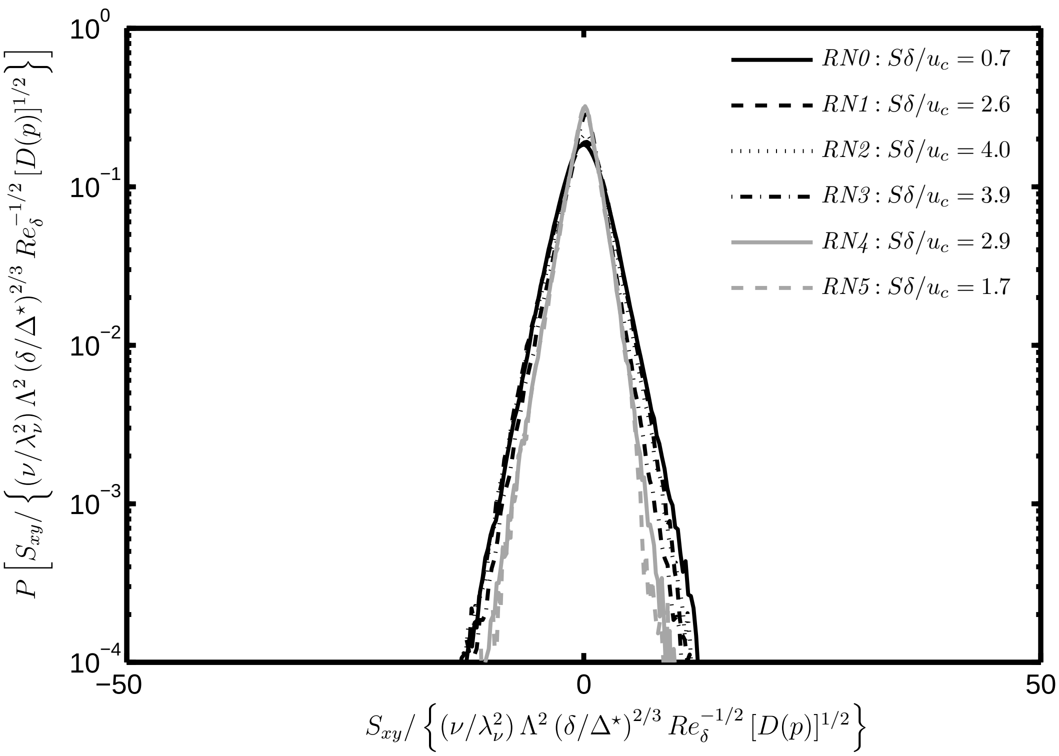

Figure 7.19: Pdfs from conditioned data for all nonreacting, off-centerline cases *RN0* – *RN5* for strain rate component S_{xy} normalized by resolution-corrected inner scaling $(\nu/\lambda_\nu^2)\,\Lambda^2\,(\delta/\Delta^\star)^{2/3}\,Re_\delta^{-1/2}\,[D(p)]^{1/2}$, shown in linear axes *(top)* and semilogarithmic axes *(bottom)*.

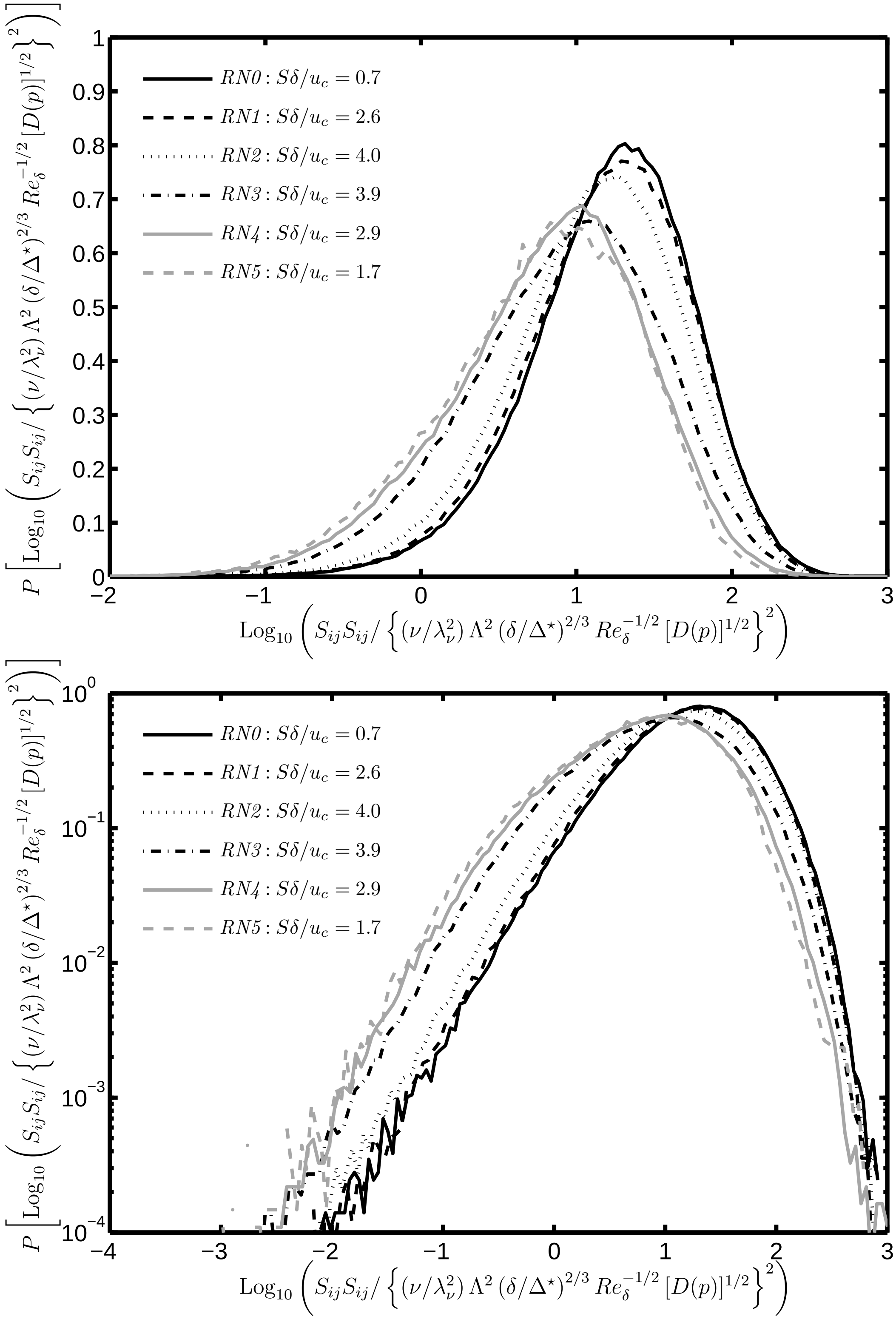

Figure 7.20: Pdfs from conditioned data for all nonreacting, off-centerline cases *RN0* – *RN5*, for the pseudo-dissipation $\mathrm{Log}_{10}(S_{ij}S_{ij})$ normalized by resolution-corrected inner scaling $\{(\nu/\lambda_\nu^2)\,\Lambda^2\,(\delta/\Delta^\star)^{2/3}\,Re_\delta^{-1/2}\,[D(p)]^{1/2}\}^2$, shown in linear axes *(top)* and semilogarithmic axes *(bottom)*.

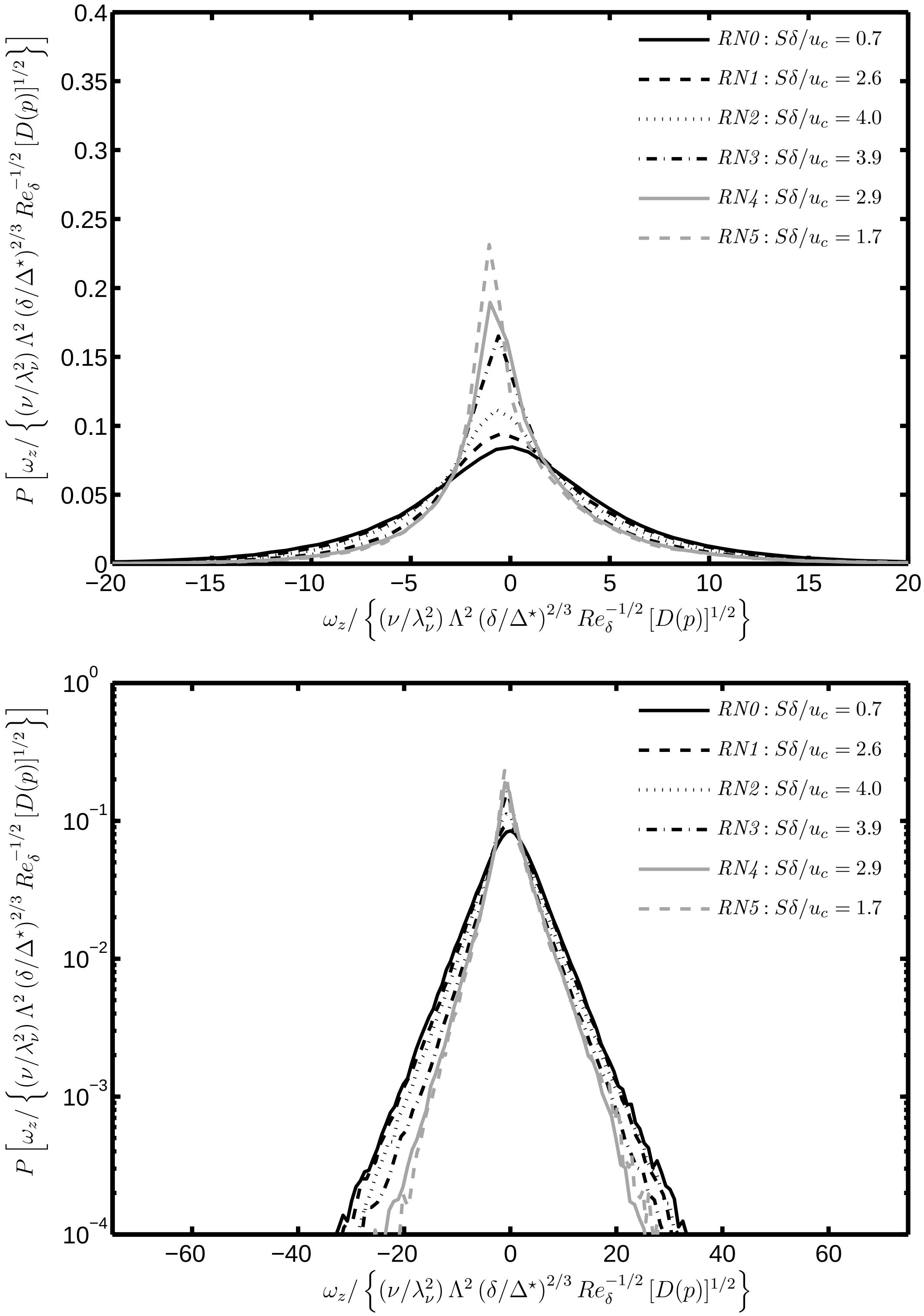

Figure 7.21: Pdfs from conditioned data for all nonreacting, off-centerline cases *RN0* – *RN5* for the vorticity ω_z normalized by resolution-corrected inner scaling $(\nu/\lambda_\nu^2)\,\Lambda^2\,(\delta/\Delta^\star)^{2/3}\,Re_\delta^{-1/2}\,[D(p)]^{1/2}$, shown in linear axes *(top)* and semilogarithmic axes *(bottom)*.

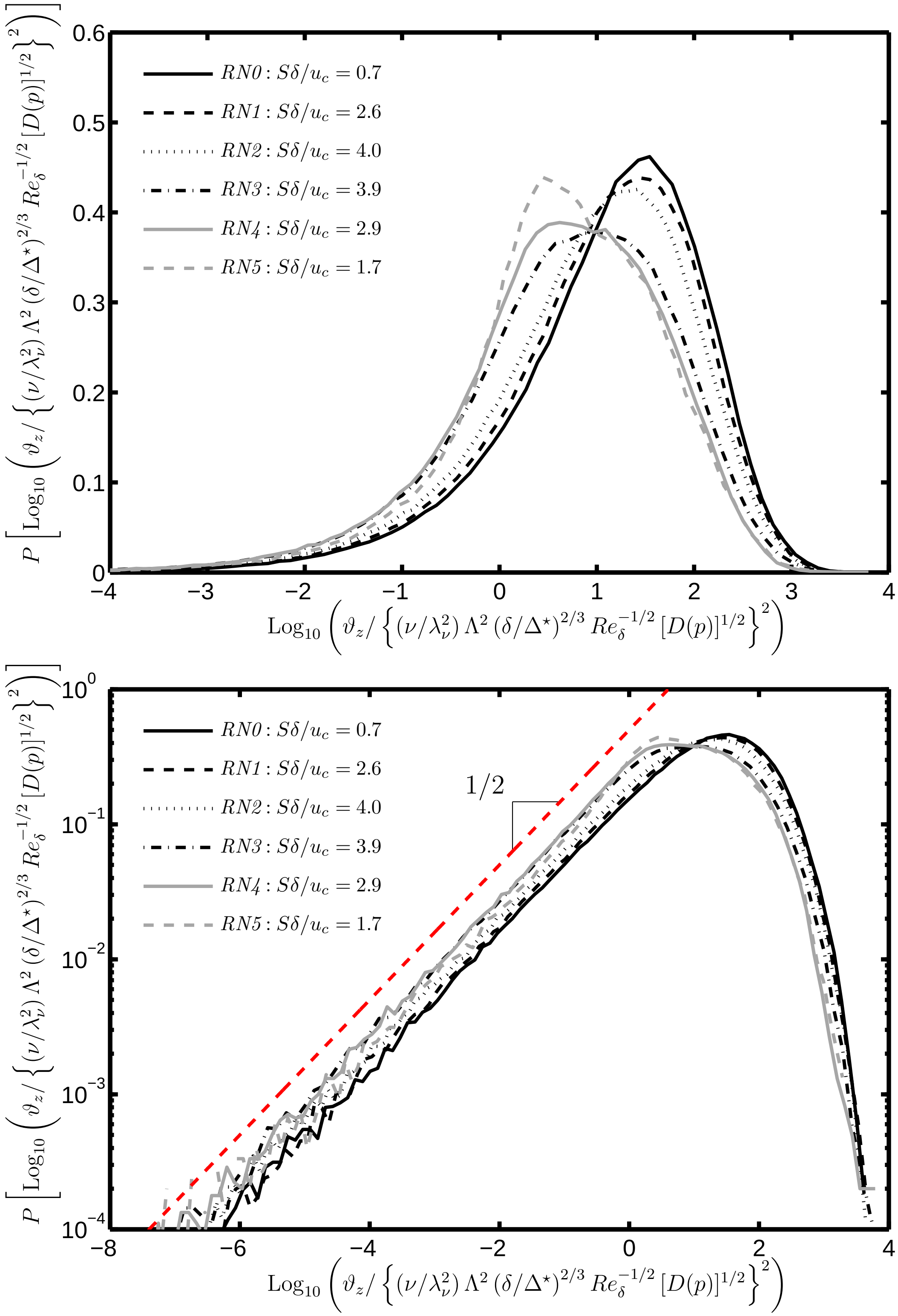

Figure 7.22: Pdfs from conditioned data for all nonreacting, off-centerline cases *RN0* – *RN5*, for pseudo-enstrophy $\mathrm{Log}_{10}(\vartheta_z)$ normalized by resolution-corrected inner scaling, $\{(\nu/\lambda_\nu^2)\,\Lambda^2\,(\delta/\Delta^\star)^{2/3}\,Re_\delta^{-1/2}\,[D(p)]^{1/2}\}^2$, shown in linear axes *(top)* and semilogarithmic axes *(bottom)*.

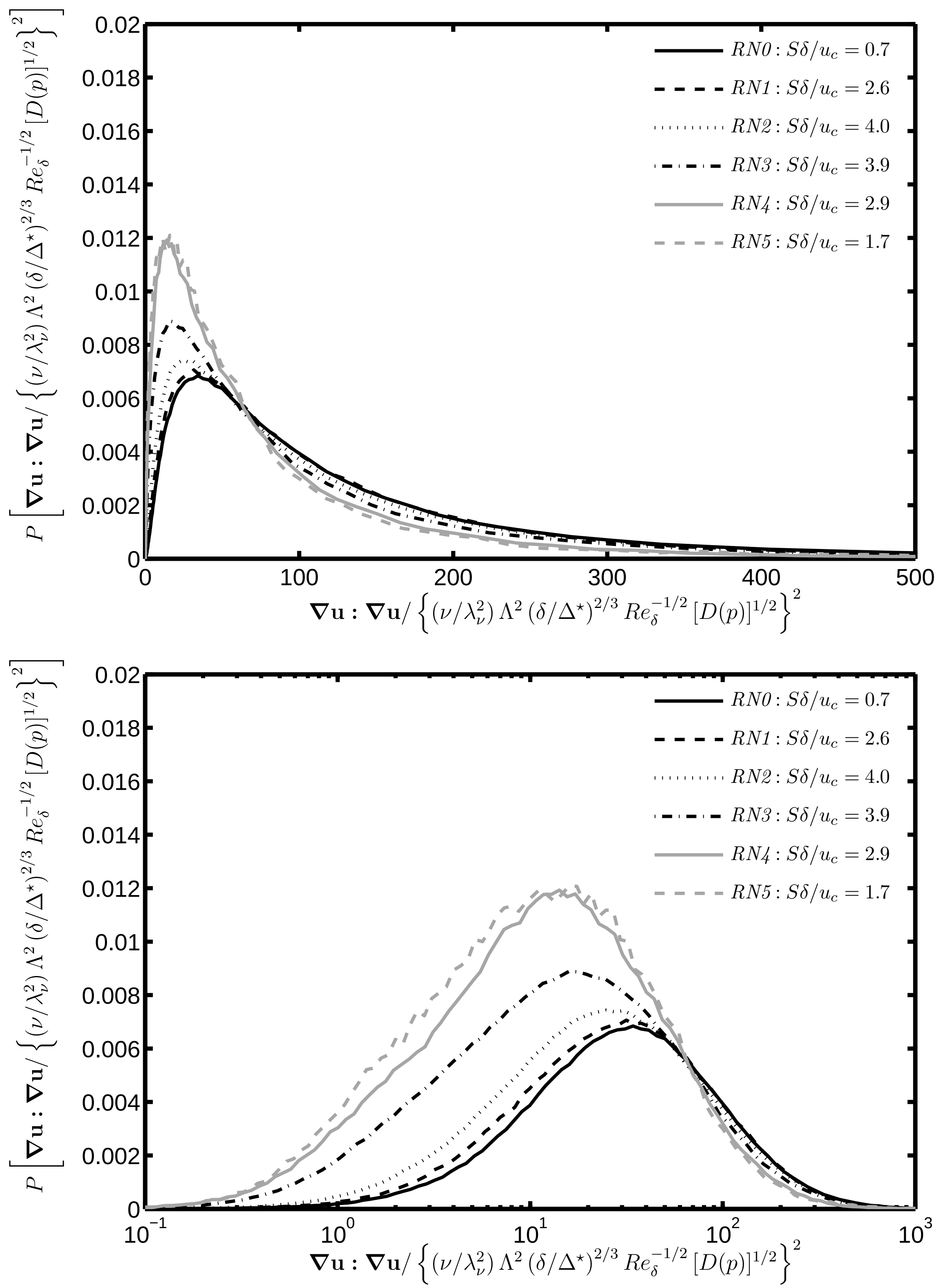

Figure 7.23: Pdfs from conditioned data for all nonreacting, off-centerline cases *RN0* – *RN5*, for contraction of the velocity gradient tensor $\nabla\mathbf{u} : \nabla\mathbf{u}$ normalized by resolution-corrected inner scaling, $\{(\nu/\lambda_\nu^2)\,\Lambda^2\,(\delta/\Delta^\star)^{2/3}\,Re_\delta^{-1/2}\,[D(p)]^{1/2}\}^2$, shown in linear axes *(top)* and semilogarithmic axes *(bottom)*.

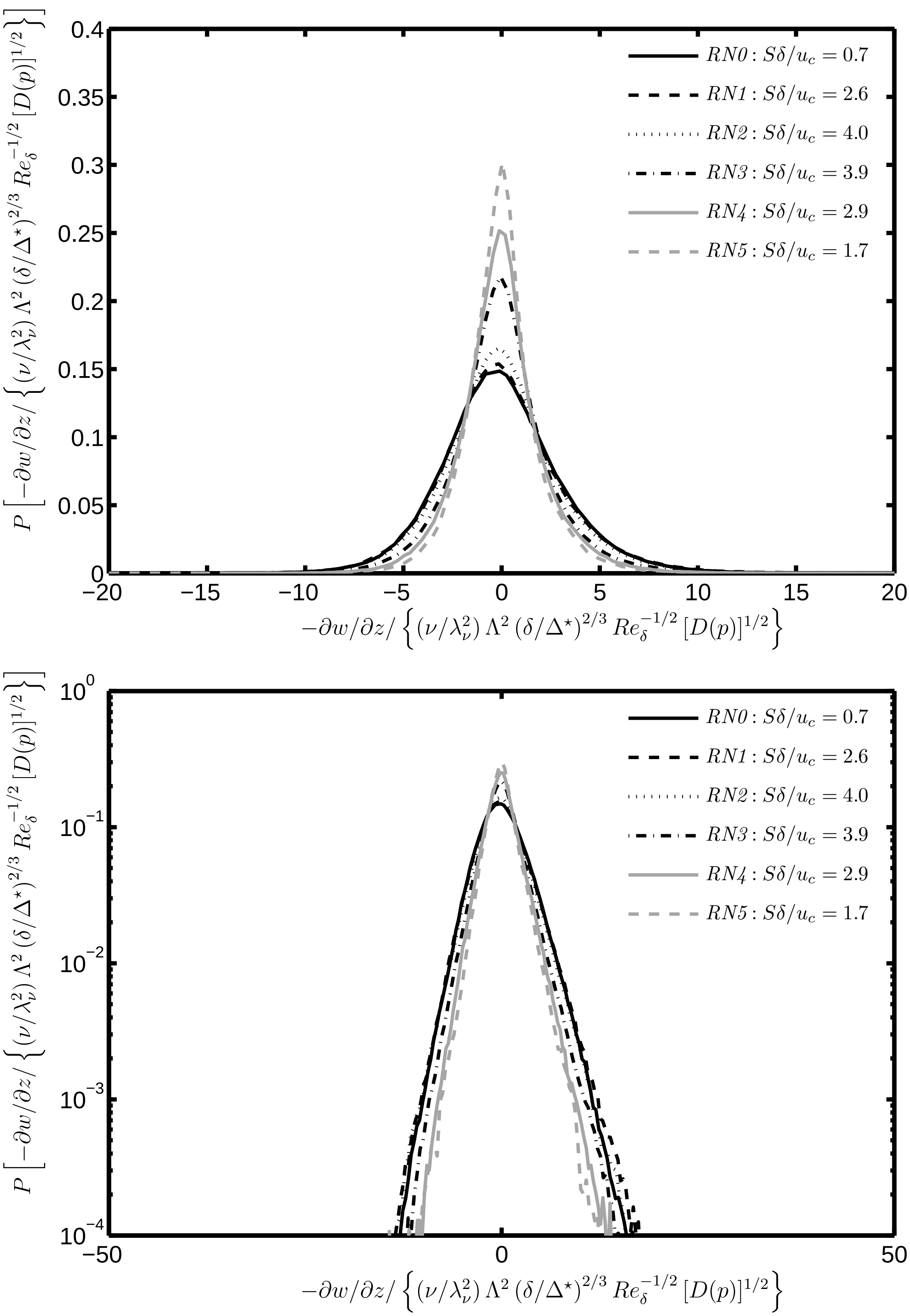

Figure 7.24: Pdfs from conditioned data for all nonreacting, off-centerline cases *RN0* – *RN5* for two-dimensional divergence $-\partial w/\partial z$ normalized by resolution-corrected inner scaling $(\nu/\lambda_\nu^2)\,\Lambda^2\,(\delta/\Delta^\star)^{2/3}\,Re_\delta^{-1/2}\,[D(p)]^{1/2}$, shown in linear axes *(top)* and semilogarithmic axes *(bottom)*.

Quantity	μ	σ	γ	β
u/u_c	$-6.820E-18$	$2.526E-01$	$9.158E-02$	$2.818E+00$
v/u_c	$-1.534E-18$	$2.172E-01$	$7.718E-03$	$2.847E+00$
$\partial u/\partial x$	$-7.643E-16$	$3.016E+00$	$-4.640E-01$	$4.544E+00$
$\partial u/\partial y$	$3.240E-16$	$4.280E+00$	$3.320E-02$	$6.152E+00$
$\partial v/\partial x$	$1.612E-17$	$4.053E+00$	$5.213E-02$	$5.970E+00$
$\partial v/\partial y$	$-2.913E-17$	$2.928E+00$	$-3.641E-01$	$4.382E+00$
S_{xx}	$-7.643E-16$	$3.016E+00$	$-4.640E-01$	$4.544E+00$
S_{yy}	$-2.913E-17$	$2.928E+00$	$-3.641E-01$	$4.382E+00$
S_{xy}	$1.728E-16$	$2.560E+00$	$3.999E-02$	$4.503E+00$
ω_z	$-2.371E-16$	$6.579E+00$	$3.875E-02$	$5.912E+00$
ε	$8.965E-01$	$1.215E+00$	$4.383E+00$	$4.100E+01$
$\mathrm{Log}_{10}\left[\varepsilon\right]$	$-3.377E-01$	$5.449E-01$	$-4.950E-01$	$3.638E+00$
$-\partial w/\partial z$	$-6.601E-16$	$3.096E+00$	$3.380E-01$	$4.296E+00$
$\boldsymbol{\nabla}\mathbf{u} : \boldsymbol{\nabla}\mathbf{u}$	$6.200E+01$	$7.835E+01$	$4.349E+00$	$3.899E+01$
$\left[\dfrac{-\partial w/\partial z}{(\boldsymbol{\nabla}\mathbf{u} : \boldsymbol{\nabla}\mathbf{u})^{1/2}}\right]$	$1.847E-02$	$4.162E-01$	$1.912E-01$	$1.968E+00$
$S_{ij} : S_{ij}$	$3.078E+01$	$3.886E+01$	$3.765E+00$	$2.872E+01$
$\mathrm{Log}_{10}\left[S_{ij} : S_{ij}\right]$	$1.219E+00$	$5.275E-01$	$-5.419E-01$	$3.734E+00$
$3/2\,(\omega_z)^2$	$6.492E+01$	$1.439E+02$	$6.679E+00$	$8.084E+01$
$\mathrm{Log}_{10}\left[3/2\ (\omega_z)^2\right]$	$1.076E+00$	$1.052E+00$	$-1.198E+00$	$5.839E+00$

Table 7.2: Normalized central moments computed from pdfs of conditioned data for *RN0* case. The mean is μ, σ is the *rms* fluctuation, $\gamma = \mu_3/\sigma^3$ is the skewness and $\beta = \mu_4/\sigma^4$ is the kurtosis. All quantities normalized by resolution-corrected inner scaling $(\nu/\lambda_\nu^2)\,\Lambda^2\,(\delta/\Delta^\star)^{2/3}\,Re_\delta^{-1/2}\,[D(p)]^{1/2}$ as shown in Figs. 7.13 – 7.24.

Quantity	μ	σ	γ	β
u/u_c	$-2.867E-17$	$2.679E-01$	$6.893E-02$	$2.665E+00$
v/u_c	$7.022E-18$	$2.072E-01$	$3.742E-02$	$2.801E+00$
$\partial u/\partial x$	$-1.279E-15$	$2.939E+00$	$-3.747E-01$	$4.557E+00$
$\partial u/\partial y$	$-9.341E-16$	$4.174E+00$	$-2.872E-01$	$6.248E+00$
$\partial v/\partial x$	$3.038E-17$	$3.828E+00$	$-1.140E-01$	$6.232E+00$
$\partial v/\partial y$	$-2.407E-17$	$2.875E+00$	$-4.183E-01$	$4.628E+00$
S_{xx}	$-1.279E-15$	$2.939E+00$	$-3.747E-01$	$4.557E+00$
S_{yy}	$-2.407E-17$	$2.875E+00$	$-4.183E-01$	$4.628E+00$
S_{xy}	$-5.233E-16$	$2.508E+00$	$-2.016E-01$	$4.413E+00$
ω_z	$8.971E-16$	$6.245E+00$	$7.236E-02$	$6.359E+00$
ε	$8.728E-01$	$1.170E+00$	$4.048E+00$	$3.410E+01$
$\mathrm{Log}_{10}\left[\varepsilon\right]$	$-3.561E-01$	$5.535E-01$	$-4.867E-01$	$3.533E+00$
$-\partial w/\partial z$	$-1.260E-15$	$3.150E+00$	$4.135E-01$	$4.664E+00$
$\boldsymbol{\nabla}\mathbf{u} : \boldsymbol{\nabla}\mathbf{u}$	$5.890E+01$	$7.524E+01$	$4.307E+00$	$4.072E+01$
$\left[\dfrac{-\partial w/\partial z}{(\boldsymbol{\nabla}\mathbf{u} : \boldsymbol{\nabla}\mathbf{u})^{1/2}}\right]$	$1.655E-02$	$4.239E-01$	$1.902E-01$	$1.931E+00$
$S_{ij} : S_{ij}$	$2.948E+01$	$3.698E+01$	$3.504E+00$	$2.464E+01$
$\mathrm{Log}_{10}\left[S_{ij} : S_{ij}\right]$	$1.192E+00$	$5.370E-01$	$-5.268E-01$	$3.600E+00$
$3/2\,(\omega_z)^2$	$5.850E+01$	$1.354E+02$	$7.520E+00$	$1.084E+02$
$\mathrm{Log}_{10}\left[3/2\ (\omega_z)^2\right]$	$1.005E+00$	$1.063E+00$	$-1.143E+00$	$5.599E+00$

Table 7.3: Normalized central moments computed from pdfs of conditioned data for *RN1* case. The mean is μ, σ is the *rms* fluctuation, $\gamma = \mu_3/\sigma^3$ is the skewness and $\beta = \mu_4/\sigma^4$ is the kurtosis. All quantities normalized by resolution-corrected inner scaling $(\nu/\lambda_\nu^2)\,\Lambda^2\,(\delta/\Delta^\star)^{2/3}\,Re_\delta^{-1/2}\,[D(p)]^{1/2}$ as shown in Figs. 7.13 – 7.24.

Quantity	μ	σ	γ	β
u/u_c	$3.028E-17$	$2.626E-01$	$3.276E-01$	$2.831E+00$
v/u_c	$4.392E-18$	$2.045E-01$	$2.771E-01$	$3.083E+00$
$\partial u/\partial x$	$-2.343E-16$	$2.705E+00$	$-4.395E-01$	$4.840E+00$
$\partial u/\partial y$	$-1.322E-15$	$3.977E+00$	$-4.453E-01$	$6.832E+00$
$\partial v/\partial x$	$-7.517E-17$	$3.589E+00$	$2.845E-02$	$6.573E+00$
$\partial v/\partial y$	$-4.636E-17$	$2.777E+00$	$-5.546E-01$	$5.260E+00$
S_{xx}	$-2.343E-16$	$2.705E+00$	$-4.395E-01$	$4.840E+00$
S_{yy}	$-4.636E-17$	$2.777E+00$	$-5.546E-01$	$5.260E+00$
S_{xy}	$-6.091E-16$	$2.397E+00$	$-2.546E-01$	$4.874E+00$
ω_z	$1.361E-15$	$5.865E+00$	$2.791E-01$	$7.151E+00$
ε	$7.192E-01$	$1.050E+00$	$4.410E+00$	$3.799E+01$
$\mathrm{Log}_{10}\,[\varepsilon]$	$-4.719E-01$	$5.808E-01$	$-4.524E-01$	$3.486E+00$
$-\partial w/\partial z$	$-2.174E-16$	$3.004E+00$	$3.024E-01$	$4.830E+00$
$\boldsymbol{\nabla}\mathbf{u} : \boldsymbol{\nabla}\mathbf{u}$	$5.275E+01$	$7.250E+01$	$4.481E+00$	$4.014E+01$
$\left[\dfrac{-\partial w/\partial z}{(\boldsymbol{\nabla}\mathbf{u} : \boldsymbol{\nabla}\mathbf{u})^{1/2}}\right]$	$2.224E-02$	$4.295E-01$	$1.700E-01$	$1.901E+00$
$S_{ij} : S_{ij}$	$2.652E+01$	$3.624E+01$	$3.929E+00$	$3.003E+01$
$\mathrm{Log}_{10}\,[S_{ij} : S_{ij}]$	$1.116E+00$	$5.639E-01$	$-4.927E-01$	$3.545E+00$
$3/2\,(\omega_z)^2$	$5.160E+01$	$1.280E+02$	$7.857E+00$	$1.120E+02$
$\mathrm{Log}_{10}\left[3/2\ (\omega_z)^2\right]$	$9.060E-01$	$1.086E+00$	$-1.096E+00$	$5.445E+00$

Table 7.4: Normalized central moments computed from pdfs of conditioned data for *RN2* case. The mean is μ, σ is the *rms* fluctuation, $\gamma = \mu_3/\sigma^3$ is the skewness and $\beta = \mu_4/\sigma^4$ is the kurtosis. All quantities normalized by resolution-corrected inner scaling $(\nu/\lambda_\nu^2)\,\Lambda^2\,(\delta/\Delta^\star)^{2/3}\,Re_\delta^{-1/2}\,[D(p)]^{1/2}$ as shown in Figs. 7.13 – 7.24.

Quantity	μ	σ	γ	β
u/u_c	$-1.703E-17$	$2.371E-01$	$4.633E-01$	$2.922E+00$
v/u_c	$2.370E-18$	$1.817E-01$	$5.530E-01$	$3.387E+00$
$\partial u/\partial x$	$5.084E-16$	$2.306E+00$	$-4.161E-01$	$6.005E+00$
$\partial u/\partial y$	$1.325E-16$	$3.431E+00$	$-8.452E-01$	$9.804E+00$
$\partial v/\partial x$	$-4.979E-17$	$3.045E+00$	$-1.878E-01$	$8.591E+00$
$\partial v/\partial y$	$4.348E-17$	$2.364E+00$	$-5.424E-01$	$5.763E+00$
S_{xx}	$5.084E-16$	$2.306E+00$	$-4.161E-01$	$6.005E+00$
S_{yy}	$4.348E-17$	$2.364E+00$	$-5.424E-01$	$5.763E+00$
S_{xy}	$4.628E-17$	$2.050E+00$	$-4.499E-01$	$6.070E+00$
ω_z	$-1.455E-17$	$5.029E+00$	$4.108E-01$	$9.394E+00$
ε	$4.883E-01$	$8.183E-01$	$7.851E+00$	$2.281E+02$
$\mathrm{Log}_{10}[\varepsilon]$	$-7.049E-01$	$6.432E-01$	$-4.394E-01$	$3.289E+00$
$-\partial w/\partial z$	$5.203E-16$	$2.522E+00$	$3.851E-01$	$5.668E+00$
$\boldsymbol{\nabla}\mathbf{u} : \boldsymbol{\nabla}\mathbf{u}$	$3.831E+01$	$6.256E+01$	$8.778E+00$	$2.441E+02$
$\left[\dfrac{-\partial w/\partial z}{(\boldsymbol{\nabla}\mathbf{u} : \boldsymbol{\nabla}\mathbf{u})^{1/2}}\right]$	$2.265E-02$	$4.308E-01$	$1.513E-01$	$1.892E+00$
$S_{ij} : S_{ij}$	$1.931E+01$	$3.012E+01$	$6.016E+00$	$1.132E+02$
$\mathrm{Log}_{10}[S_{ij} : S_{ij}]$	$9.138E-01$	$6.283E-01$	$-4.716E-01$	$3.319E+00$
$3/2\,(\omega_z)^2$	$3.793E+01$	$1.099E+02$	$1.335E+01$	$4.546E+02$
$\mathrm{Log}_{10}\left[3/2\ (\omega_z)^2\right]$	$6.798E-01$	$1.125E+00$	$-9.560E-01$	$5.086E+00$

Table 7.5: Normalized central moments computed from pdfs of conditioned data for *RN3* case. The mean is μ, σ is the *rms* fluctuation, $\gamma = \mu_3/\sigma^3$ is the skewness and $\beta = \mu_4/\sigma^4$ is the kurtosis. All quantities normalized by resolution-corrected inner scaling $(\nu/\lambda_\nu^2)\,\Lambda^2\,(\delta/\Delta^\star)^{2/3}\,Re_\delta^{-1/2}\,[D(p)]^{1/2}$ as shown in Figs. 7.13 – 7.24.

Quantity	μ	σ	γ	β
u/u_c	$1.052E-17$	$1.873E-01$	$4.867E-01$	$3.132E+00$
v/u_c	$6.367E-18$	$1.503E-01$	$2.661E-01$	$3.292E+00$
$\partial u/\partial x$	$5.224E-16$	$2.007E+00$	$-3.011E-01$	$6.418E+00$
$\partial u/\partial y$	$4.262E-16$	$3.053E+00$	$-5.758E-01$	$7.728E+00$
$\partial v/\partial x$	$-1.051E-17$	$2.679E+00$	$-2.343E-01$	$1.112E+01$
$\partial v/\partial y$	$1.776E-17$	$2.121E+00$	$-5.835E-01$	$6.176E+00$
S_{xx}	$5.224E-16$	$2.007E+00$	$-3.011E-01$	$6.418E+00$
S_{yy}	$1.776E-17$	$2.121E+00$	$-5.835E-01$	$6.176E+00$
S_{xy}	$1.853E-16$	$1.811E+00$	$-3.275E-01$	$5.435E+00$
ω_z	$-2.538E-16$	$4.459E+00$	$2.654E-01$	$1.015E+01$
ε	$3.393E-01$	$5.502E-01$	$5.864E+00$	$8.207E+01$
$\mathrm{Log}_{10}\,[\varepsilon]$	$-8.562E-01$	$6.444E-01$	$-5.008E-01$	$3.338E+00$
$-\partial w/\partial z$	$4.793E-16$	$2.213E+00$	$4.543E-01$	$5.934E+00$
$\boldsymbol{\nabla}\mathbf{u} : \boldsymbol{\nabla}\mathbf{u}$	$2.993E+01$	$4.990E+01$	$9.713E+00$	$2.448E+02$
$\left[\dfrac{-\partial w/\partial z}{(\boldsymbol{\nabla}\mathbf{u} : \boldsymbol{\nabla}\mathbf{u})^{1/2}}\right]$	$1.996E-02$	$4.222E-01$	$1.655E-01$	$1.927E+00$
$S_{ij} : S_{ij}$	$1.509E+01$	$2.351E+01$	$6.170E+00$	$1.051E+02$
$\mathrm{Log}_{10}\,[S_{ij} : S_{ij}]$	$8.114E-01$	$6.294E-01$	$-5.272E-01$	$3.380E+00$
$3/2\,(\omega_z)^2$	$2.982E+01$	$9.022E+01$	$1.966E+01$	$9.261E+02$
$\mathrm{Log}_{10}\left[3/2\ (\omega_z)^2\right]$	$6.017E-01$	$1.096E+00$	$-9.497E-01$	$5.173E+00$

Table 7.6: Normalized central moments computed from pdfs of conditioned data for *RN4* case. The mean is μ, σ is the *rms* fluctuation, $\gamma = \mu_3/\sigma^3$ is the skewness and $\beta = \mu_4/\sigma^4$ is the kurtosis. All quantities normalized by resolution-corrected inner scaling $(\nu/\lambda_\nu^2)\,\Lambda^2\,(\delta/\Delta^\star)^{2/3}\,Re_\delta^{-1/2}\,[D(p)]^{1/2}$ as shown in Figs. 7.13 – 7.24.

Quantity	μ	σ	γ	β
u/u_c	$-2.105E-17$	$1.686E-01$	$6.619E-01$	$3.722E+00$
v/u_c	$2.358E-17$	$1.462E-01$	$3.196E-01$	$3.147E+00$
$\partial u/\partial x$	$-3.448E-16$	$1.849E+00$	$-4.373E-02$	$6.862E+00$
$\partial u/\partial y$	$-1.003E-16$	$2.858E+00$	$-1.037E+00$	$7.950E+00$
$\partial v/\partial x$	$-9.358E-17$	$2.800E+00$	$3.855E-01$	$9.038E+00$
$\partial v/\partial y$	$1.911E-17$	$1.983E+00$	$-5.870E-01$	$6.586E+00$
S_{xx}	$-3.448E-16$	$1.849E+00$	$-4.373E-02$	$6.862E+00$
S_{yy}	$1.911E-17$	$1.983E+00$	$-5.870E-01$	$6.586E+00$
S_{xy}	$-2.806E-17$	$1.767E+00$	$-3.594E-01$	$5.408E+00$
ω_z	$1.601E-16$	$4.418E+00$	$9.112E-01$	$8.707E+00$
ε	$2.711E-01$	$4.463E-01$	$6.408E+00$	$8.961E+01$
$\mathrm{Log}_{10}[\varepsilon]$	$-9.635E-01$	$6.573E-01$	$-5.085E-01$	$3.259E+00$
$-\partial w/\partial z$	$-2.469E-16$	$2.000E+00$	$2.873E-01$	$8.732E+00$
$\boldsymbol{\nabla}\mathbf{u} : \boldsymbol{\nabla}\mathbf{u}$	$2.735E+01$	$4.692E+01$	$8.196E+00$	$1.447E+02$
$\left[\dfrac{-\partial w/\partial z}{(\boldsymbol{\nabla}\mathbf{u} : \boldsymbol{\nabla}\mathbf{u})^{1/2}}\right]$	$1.892E-02$	$3.978E-01$	$1.757E-01$	$2.064E+00$
$S_{ij} : S_{ij}$	$1.359E+01$	$2.139E+01$	$6.615E+00$	$9.747E+01$
$\mathrm{Log}_{10}[S_{ij} : S_{ij}]$	$7.595E-01$	$6.407E-01$	$-5.447E-01$	$3.299E+00$
$3/2\,(\omega_z)^2$	$2.928E+01$	$8.127E+01$	$8.207E+00$	$1.113E+02$
$\mathrm{Log}_{10}\left[3/2\ (\omega_z)^2\right]$	$6.284E-01$	$1.040E+00$	$-9.302E-01$	$5.515E+00$

Table 7.7: Normalized central moments computed from pdfs of conditioned data for *RN5* case. The mean is μ, σ is the *rms* fluctuation, $\gamma = \mu_3/\sigma^3$ is the skewness and $\beta = \mu_4/\sigma^4$ is the kurtosis. All quantities normalized by resolution-corrected inner scaling $(\nu/\lambda_\nu^2)\,\Lambda^2\,(\delta/\Delta^\star)^{2/3}\,Re_\delta^{-1/2}\,[D(p)]^{1/2}$ as shown in Figs. 7.13 – 7.24.

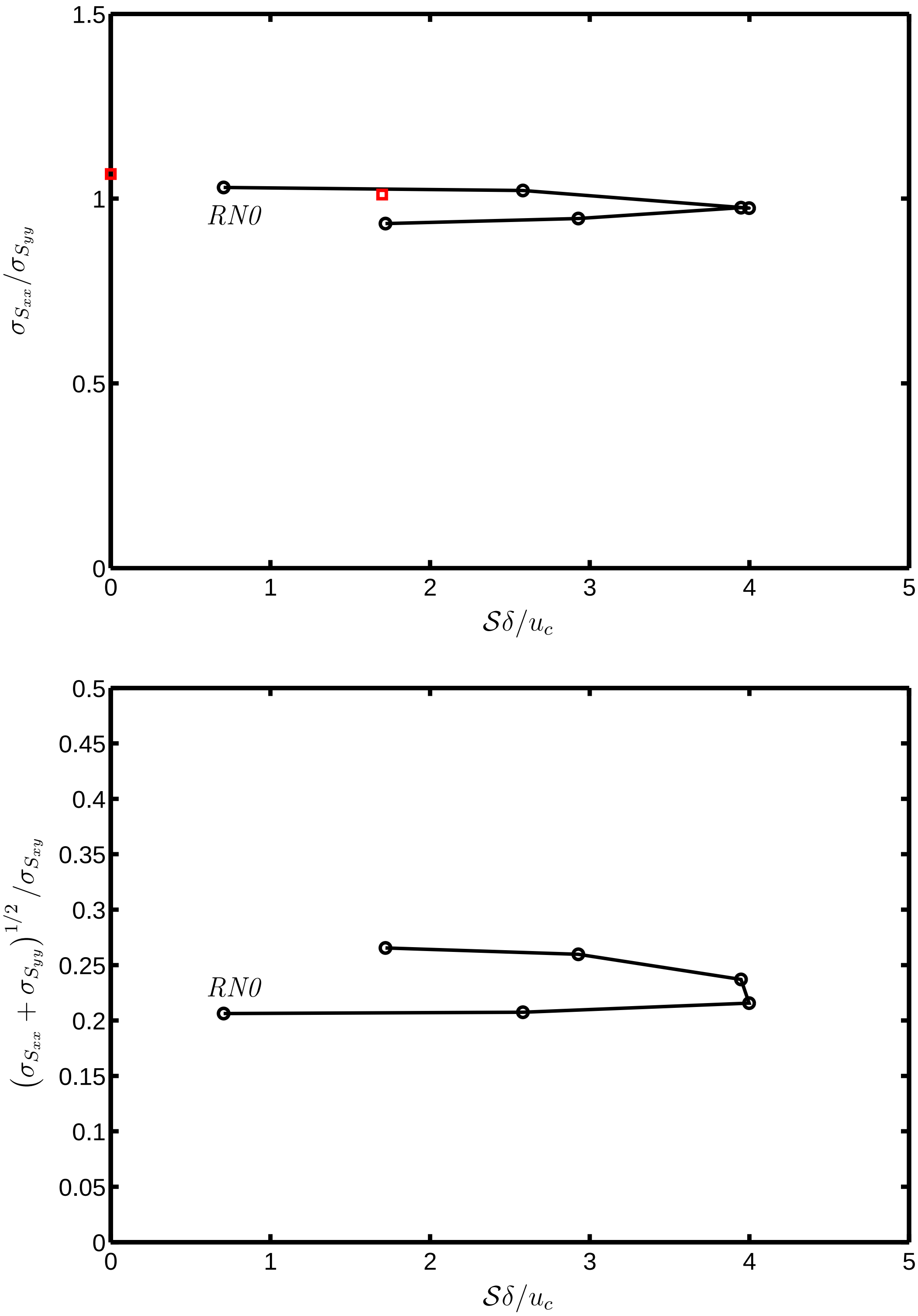

Figure 7.25: *Rms* values of the strain rate components as a function of shear $\mathcal{S}$ nondimensionalized on outer variables. The ratio of the *rms* of the on-diagonal strain rates S_{xx}/S_{yy}, *(top)*, is shown with the ratio $(\sigma_{S_{xx}} + \sigma_{S_{xx}})^{1/2}/\sigma_{S_{xy}}$, *(bottom)*. The black circles are data from the present study, the red squares are from the data of Mullin and Dahm (2005b).

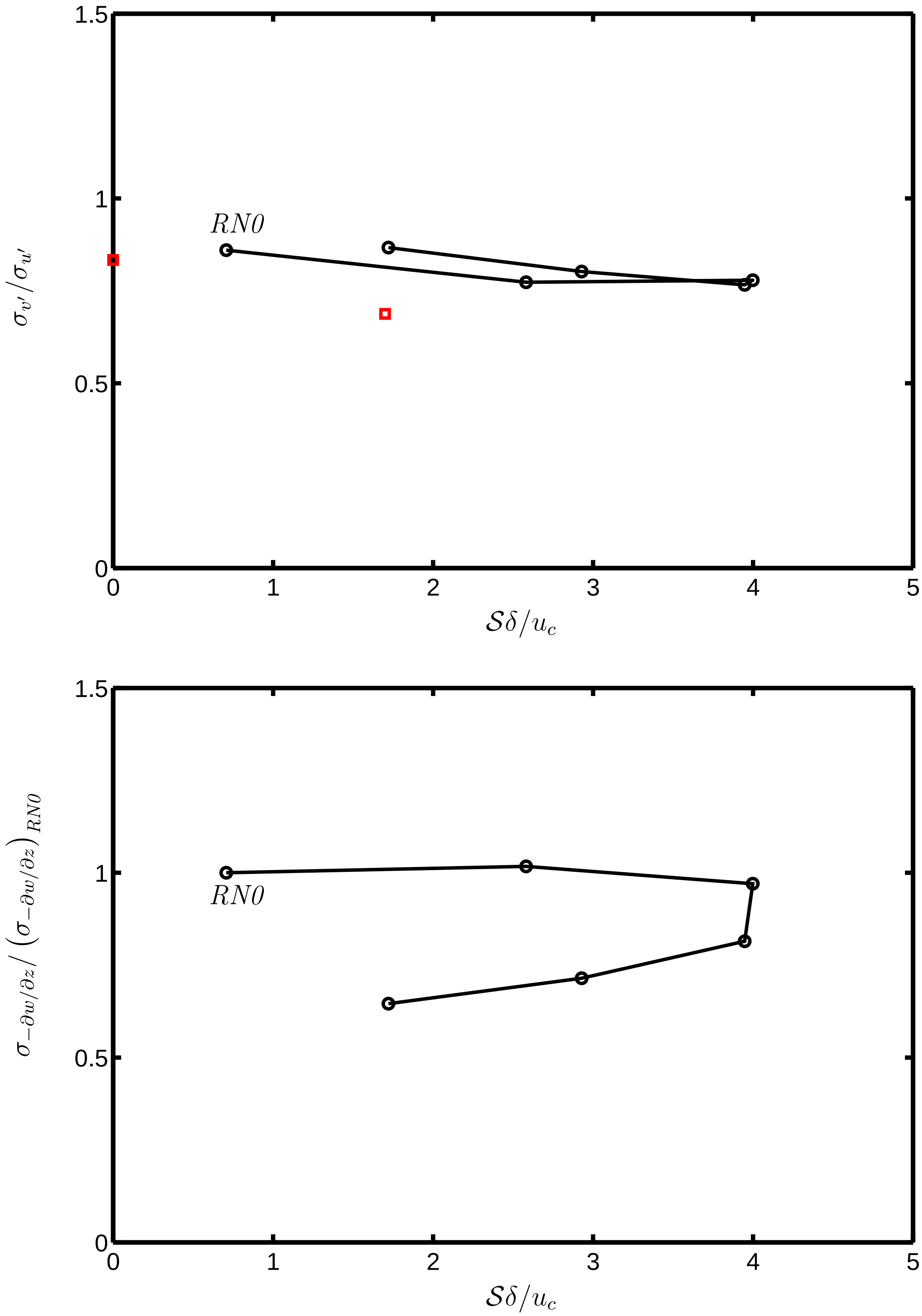

Figure 7.26: *Rms* values of the velocity fluctuation ratio $\sigma_{v'}/\sigma_{u'}$ as a function of shear $\mathcal{S}$ nondimensionalized on outer variables, *(top)*. The *rms* of the divergence, normalized by its centerline (*RN0*) value $\sigma_{-\partial w/\partial z}/\left(\sigma_{-\partial w/\partial z}\right)_{RN0}$, is also plotted against the dimensionless shear, *(bottom)*. The black circles are data from the present study, the red squares are the data of Mullin and Dahm (2005b).

CHAPTER VIII

Inner-Scaling of Nonreacting Flows: Effects of Shear and Heat Release

In Chapters V and VI, results for nonreacting and reacting inner scale gradients were presented. The measurement resolution scale $\Delta^\star$ permitted the comparison across both flow conditions to be on an equal basis. Chapter VII explored the effect of mean flow shear on the inner scales of a nonreacting flow by relaxing the $\mathcal{S} \approx 0$ constraint. While the mean shear was introducing anisotropic tendencies into the local outer scales, the inner scales were largely unaffected – as corroborated by the Corrsin-Uberoi criteria.

In the present chapter, the simultaneous presence of exothermicity and nonzero mean shear are investigated. Following the established pattern of Chapters V – VII, the reacting data have been corrected with their measurement resolution scale $\Delta^\star$ via the extended inner normalization $\mathcal{N}^\star$ described in §5.4.5. Secondly, the off-centerline reacting data were conditioned according to the strategy outlined in §7.3. These results for chemically reacting exothermic flows are then able to be directly compared to their nonreacting counterparts from Chapter VII. From these comparisons, the combined effects of heat release and shear on the small scales of a turbulent shear flow are identified.

8.1 Inner Scale PIV: Off-Axis Reacting Flow Experiments

The experimental conditions for each of the six radial nonreacting flow cases for which results are presented in this chapter are listed in Table 3.6. All measurements were made at the same axial location, $x/d = 153$ downstream of the jet exit, and correspond to the same flow condition but different radial positions in the flow. The six radial locations r ranged from the jet centerline ($r = 0$) to near the outer edge of the jet ($r = 1.45\,\delta_{1/2}$). At each radial station, 600 instantaneous inner-scale velocity fields were measured, each with a 13.5 mm$\times$16.8 mm field-of-view containing 32×40 instantaneous velocity vectors. At each location, the measurement resolution scale $\Delta^\star$ was obtained in the same manner as described for the measurements in Chapters V and VI. An additional 600 outer-scale velocity fields were measured, from which the local outer variables u_c and δ were obtained. Based on these measurements, the resulting outer-scale Reynolds number was $Re_\delta = 65\,000$.

8.2 Inner Scale Velocity Gradients

For each of the off-centerline reacting flow cases, pdfs are shown in Figs. 8.1 – 8.12. Each of the selected gradients are normalized by the proper $\mathcal{N}^\star$ value which corrects for both measurement resolution while accounting for inner scaling. In each of the figures, individual curves are presented, corresponding to each of the six cases *RR0* – *RR5* listed in Table 3.6. The figures are shown in the typical fashion with linearly plotted pdfs in the upper panels and the same pdfs plotted in a semilogarithmic manner in the lower panels. The spectral parameters from the $\mathcal{N}^{\star}$ corrections are tabulated in Table 8.1. Note that similar to the off-centerline, nonreacting results of Chapter VII, the measurement resolution correction provides little impact on the final gradient values – a difference of only 20% by comparing the most disparate cases, *RR0* and *RR3*. This change between the extrema is nearly identical to the differences observed in the nonreacting cases reported in the previous chapter. The detailed moment information for each of the reacting, off-centerline cases is reported in Tables 8.2 – 8.7, where the first four central moments are presented.

8.3 Inner Scale, Off-Axis: Reacting & Nonreacting

Similar to the nonreacting off-centerline results of Chapter VII, the statistics for the reacting cases do not collapse onto a single curve. Although two groups of "self-similar" curves were noted in §7.4, for the nonreacting cases – the same behavior is not easily identified in the reacting cases. However, for reasons that are again not readily apparent, cases *RR0* and *RR1* agree well across the gradients in Figs. 8.1 – 8.12. Similarly, *RR3* and *RR4* have generally high levels of self-similarity. The remaining two cases, *RR2* and *RR5*, are more ambiguous and do not *clearly* find themselves in one of the two groups.

Direct comparison between the reacting and nonreacting off-centerline cases is shown in Figs. 8.13 – 8.15. In these plots, both upper and lower panels are shown in linear axes. The upper panels reproduce the nonreacting data from Figs. 7.20, 7.22 and 7.24, while the lower panels reproduce the reacting data from Figs. 8.8, 8.10 and 8.12. Three gradients were selected for these comparisons, the pseudo-dissipation, $S_{ij}S_{ij}$, the pseudo-enstrophy ϑ_z and the apparent two-dimensional divergence $(\boldsymbol{\nabla} \cdot \mathbf{u})_{2D}$. As stated in Chapter VI, the apparent two-dimensional divergence in these reacting flow cases now includes both the additional velocity gradient component $\partial w/\partial z \equiv -(\partial u/\partial x + \partial v/\partial y)$ as well as the true divergence $\boldsymbol{\nabla} \cdot \mathbf{u}$ induced by heat release as described in § 2.5. Direct comparison between the two panels for each gradient is permitted as the pdfs have been corrected by $\mathcal{N}^\star$ and the data conditioned according to §7.3. Note that care has been taken to display each respective pdf on the same axes scales for both the upper and lower panels. At first glance, the overall comparison between the reacting and nonreacting cases is generally similar. The combined effects of shear and exothermicity do not dramatically alter the statistics as compared to the sheared, nonreacting conditions. The spread amongst the pdfs, moving from one radial station to the next, is comparable from nonreacting to reacting. That is, the differences observed between the *RN0* and *RN5* cases are similar to the corresponding differences exhibited between *RR0* and *RR5*.

The differences between the reacting and nonreacting conditions, while not profound, are noticeable. The apparent two-dimensional divergence pdfs in Fig. 8.15 are wider for the reacting cases. This is consistent with the behavior noted in Chapter VI for data obtained on the jet centerline. Examination of the 2nd-order gradients in Figs. 8.13 and 8.14 reveal a systematic trend. The squared gradients of $S_{ij}S_{ij}$ and ϑ_z are more sharply peaked for the reacting pdfs than their nonreacting counterparts. This is most noticeable for radial positions *RN3* – *RN5* and *RR3* – *RR5*. This observation is consistent with the noted widening in the apparent two-dimensional divergence pdfs.

Another observation is noted in Fig. 8.14. Here the pseudo-enstrohpy reveals the lingering signature of entrained coflow fluid evident in the *RN5* pdf of the nonreacting, off-centerline results *(top)*. Furthermore, a less pronounced impact on the *RN3* and *RN4* pdfs is also visible. By comparison, the *RR5* case in the lower panel reveals only the slightest perturbation in its pdf – the type of perturbation due to the freshly entrained, irrotational coflow fluid. Similarly, in the *RR3* and *RR4* cases there is a reduced signature of irrotational fluid as compared to their nonreacting *RN3* and *RN4* radial counterparts. This observation is consistent with the reduced entrainment levels widely reported in jet flames, over nonreacting jets, (Ricou and Spalding, 1961). The jet-scaling entrainment relationship, (Diez and Dahm, 2007),

$$m(x) = I_1 \left(c_u\right)_j \left(c_\delta\right)_j^2 \left(\rho_\infty J_0\right)^{\frac{1}{2}} x, \tag{8.1}$$

where I_1, $(c_u)_j$ and $(c_\delta)_j^2$ are constants identified in §2.2. The entrainment rate, $E(x)$ is,

$$E(x) \equiv \frac{\mathrm{d}m}{\mathrm{d}x} = I_1 \left(c_u\right)_j \left(c_\delta\right)_j^2 \left(\rho_\infty J_0\right)^{\frac{1}{2}}. \tag{8.2}$$

For jet-like scaling, the entrainment depends explicitly on the coflow density ρ_∞. According to the Equivalence Principle outlined in Chapter II, this ρ_∞ is replaced by $\rho_\infty^{\mathit{eff}}$ to obtain the corresponding entrainment rate for an otherwise equivalent reacting flow. From (2.8), and taking $T_\infty^{\mathit{eff}} \approx 3259$ K, (Tacina and Dahm, 2000), this gives a reduction in entrainment for a hydrogen-air reacting jet of,

$$\frac{[E(x)]_R}{[E(x)]_{NR}} = \left(\frac{\rho_\infty^{\mathit{eff}}}{\rho_\infty}\right)^{\frac{1}{2}} \approx 0.30, \tag{8.3}$$

where $[E(x)]_R$ is the entrainment rate for a reacting flow and $[E(x)]_{NR}$ is for a nonreacting flow.

8.4 Effects of Shear and Exothermicity on Local Isotropy

The Corrsin-Uberoi parameter defined in (7.2), is used to measure the degree of local (an)isotropy present at the small scales of a turbulent shear flow. (Recall that for $\mathcal{S}_c^\star \ll 1$ the smallest scales in the flow should remain largely isotropic). For the off-centerline reacting data, the maximum Corrsin-Uberoi parameter based on the local shear $\mathcal{S}$ (listed in Table 3.6) is $\mathcal{S}_c^\star = 0.185$, occurring for case *RR3*. This is only a small departure from the maximum value admitted by the nonreacting off-centerline data from Chapter VII, $\mathcal{S}_c^\star = 0.156$, at *RN3*. This suggests that, similar to the nonreacting results of the previous chapter, the smallest scales in the flow should remain largely isotropic, and that the inner-scaled statistics presented as pdfs in Figs. 8.1 – 8.12 might be largely unaffected by the local shear.

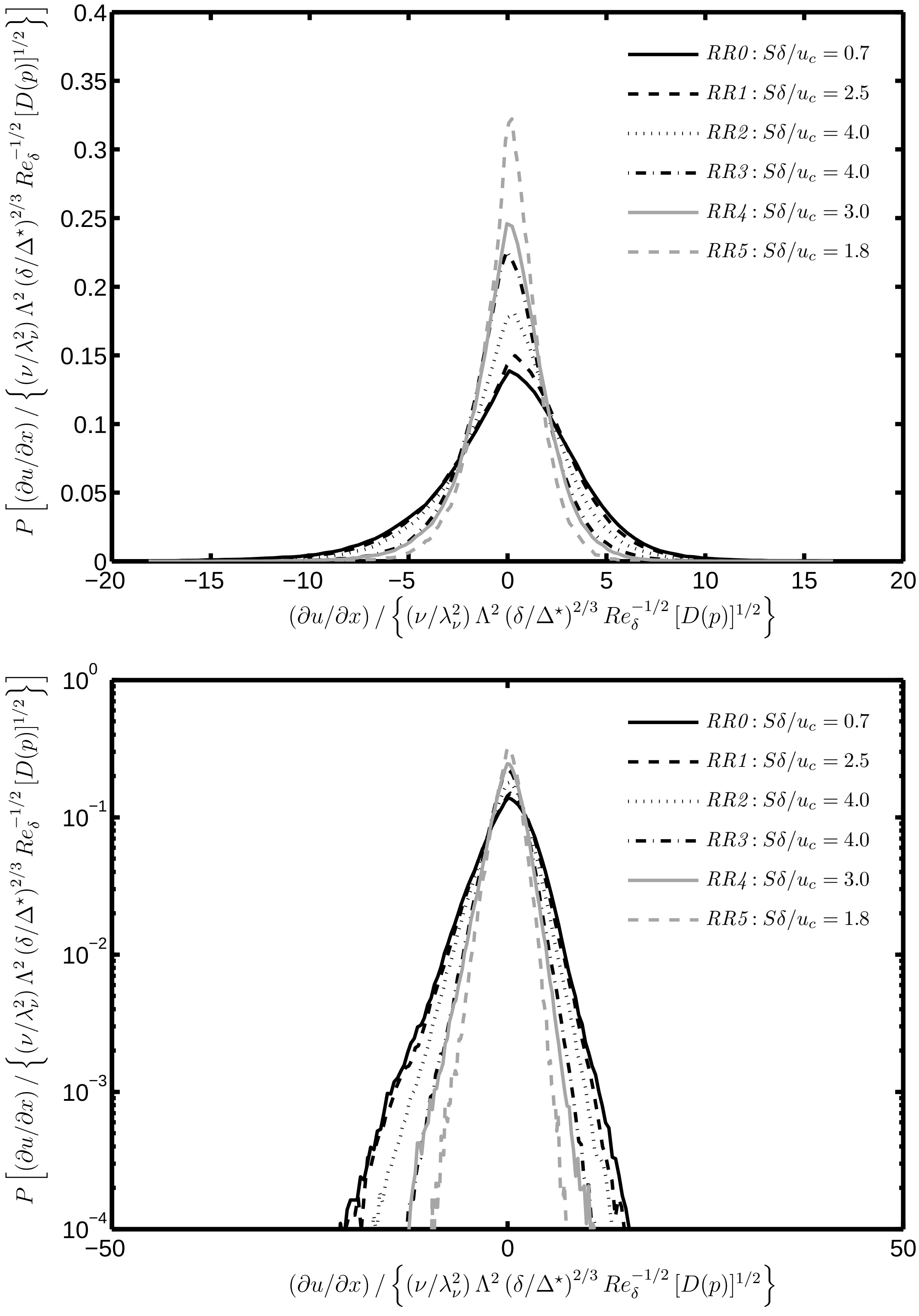

Figure 8.1: Pdfs from all reacting, off-centerline cases *RR0* – *RR5* for velocity gradient $\partial u/\partial x$ normalized by resolution-corrected inner scaling $(\nu/\lambda_\nu^2)\,\Lambda^2\,(\delta/\Delta^\star)^{2/3}\,Re_\delta^{-1/2}\,[D(p)]^{1/2}$, shown in linear axes *(top)* and semilogarithmic axes *(bottom)*.

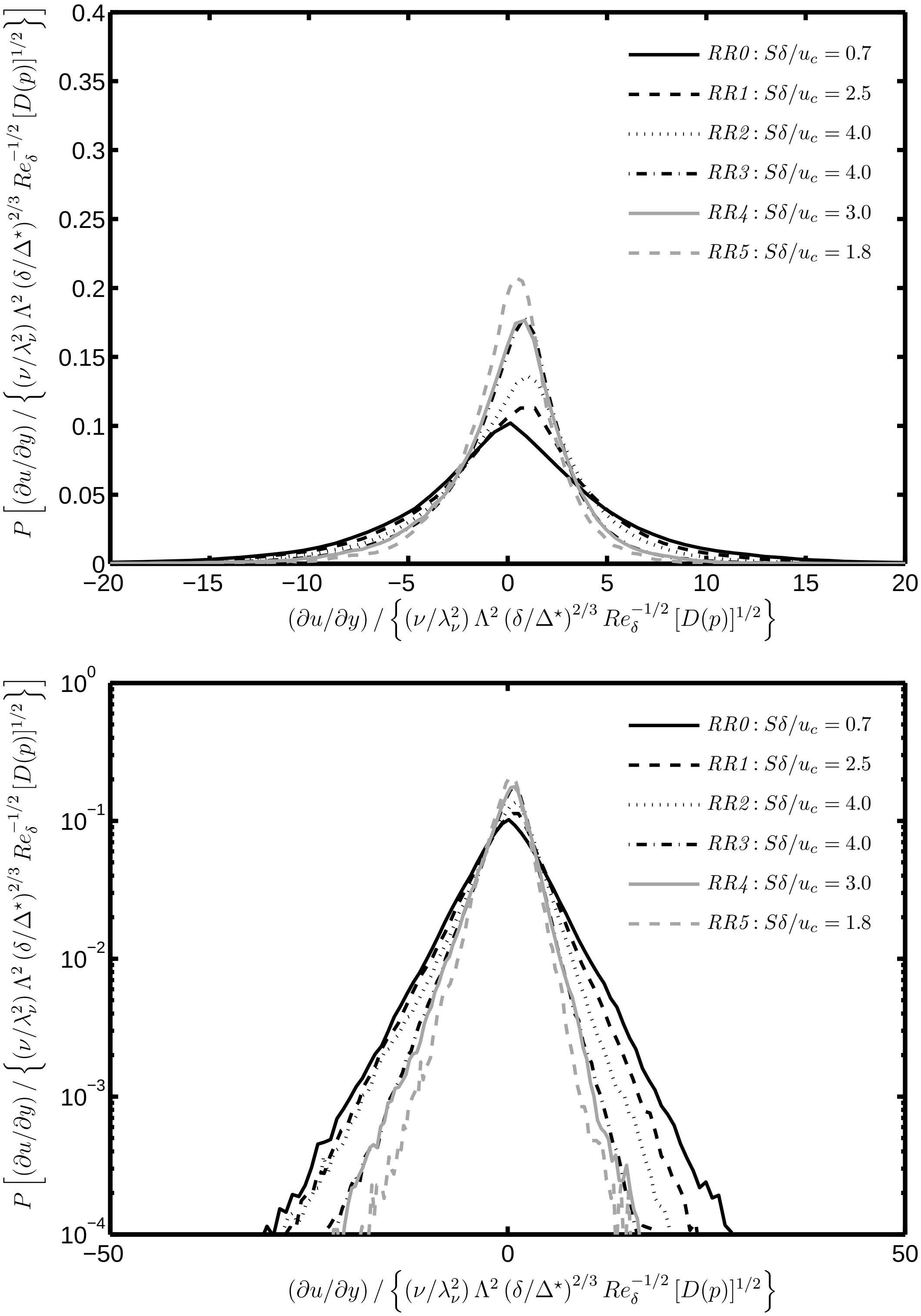

Figure 8.2: Pdfs from all reacting, off-centerline cases *RR0* – *RR5* for velocity gradient $\partial u/\partial y$ normalized by resolution-corrected inner scaling $(\nu/\lambda_\nu^2)\,\Lambda^2\,(\delta/\Delta^\star)^{2/3}\,Re_\delta^{-1/2}\,[D(p)]^{1/2}$, shown in linear axes *(top)* and semilogarithmic axes *(bottom)*.

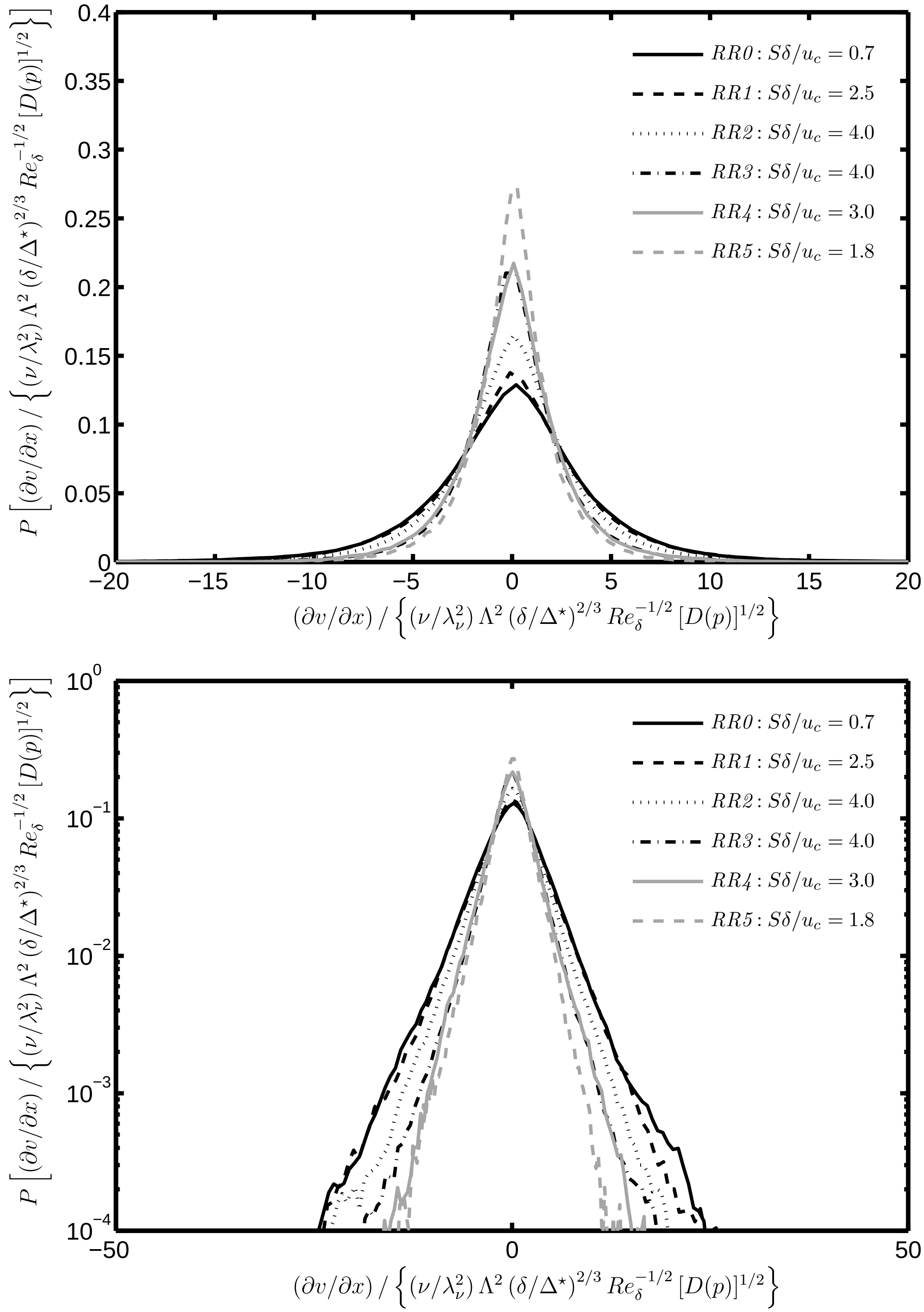

Figure 8.3: Pdfs from all reacting, off-centerline cases *RR0* – *RR5* for velocity gradient $\partial v/\partial x$ normalized by resolution-corrected inner scaling $(\nu/\lambda_\nu^2)\,\Lambda^2\,(\delta/\Delta^\star)^{2/3}\,Re_\delta^{-1/2}\,[D(p)]^{1/2}$, shown in linear axes *(top)* and semilogarithmic axes *(bottom)*.

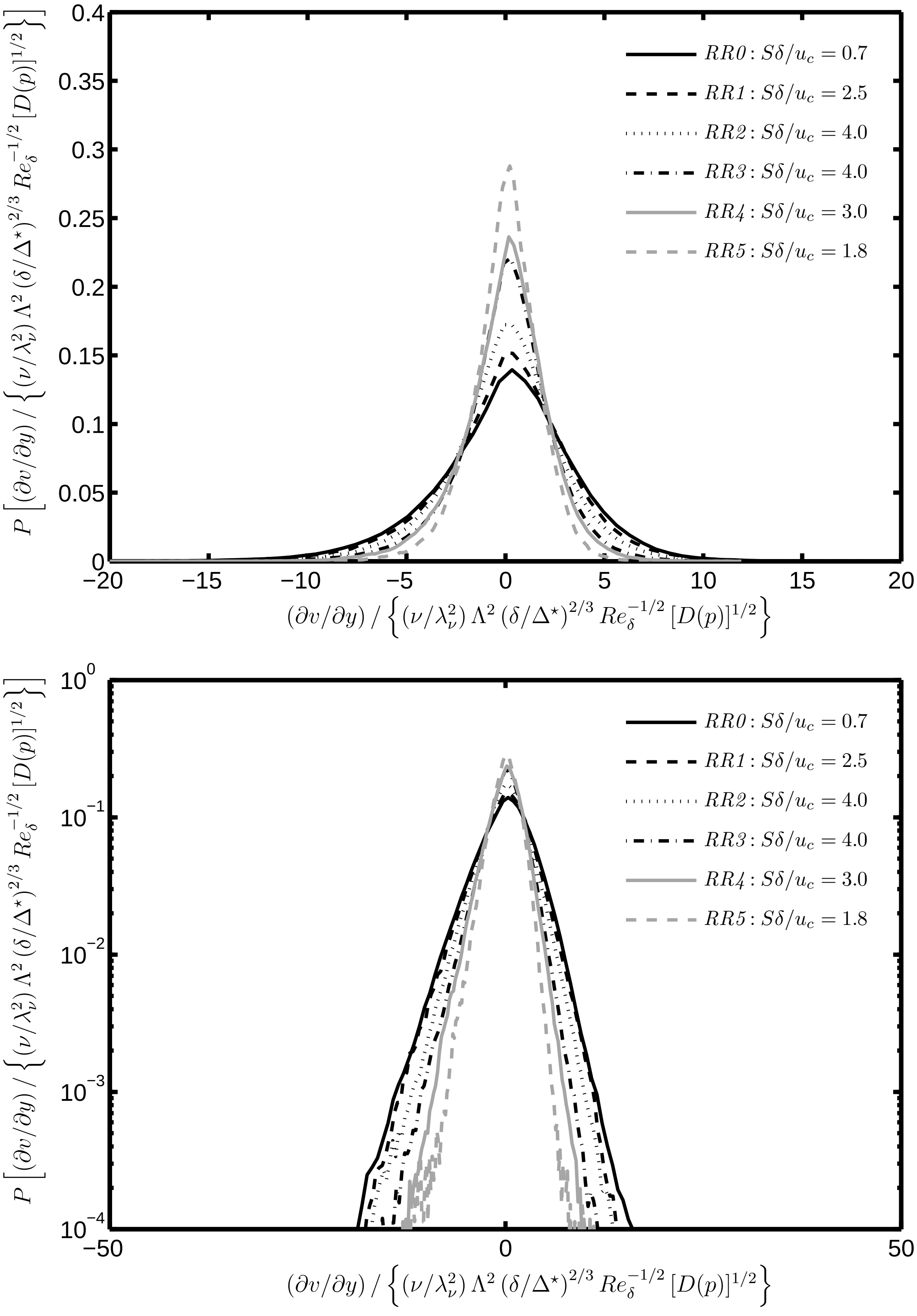

Figure 8.4: Pdfs from all reacting, off-centerline cases *RR0* – *RR5* for velocity gradient $\partial v/\partial y$ normalized by resolution-corrected inner scaling $(\nu/\lambda_\nu^2)\,\Lambda^2\,(\delta/\Delta^\star)^{2/3}\,Re_\delta^{-1/2}\,[D(p)]^{1/2}$, shown in linear axes *(top)* and semilogarithmic axes *(bottom)*.

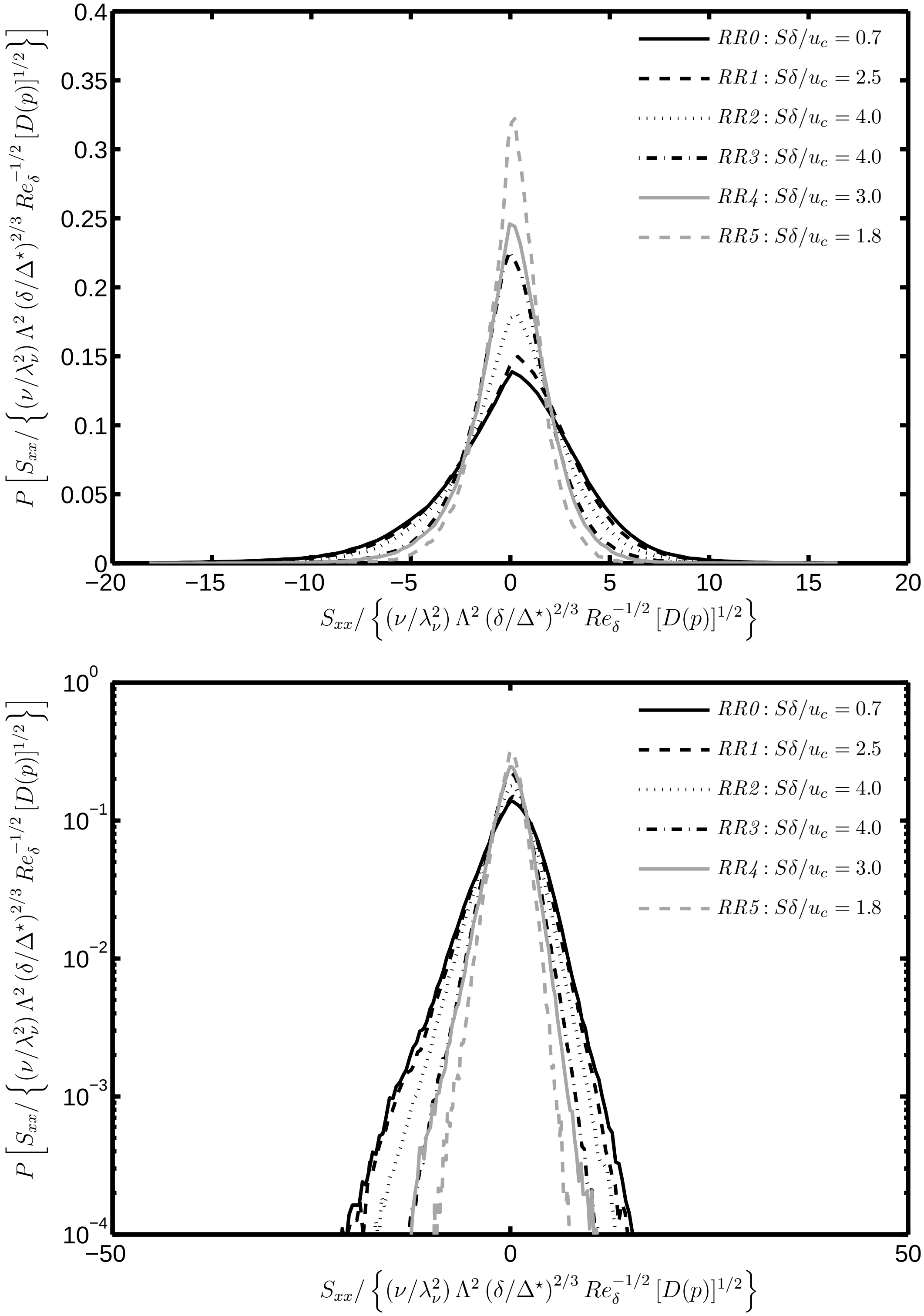

Figure 8.5: Pdfs from conditioned data for all reacting, off-centerline cases *RR0* – *RR5* for strain rate component S_{xx} normalized by resolution-corrected inner scaling $(\nu/\lambda_\nu^2)\,\Lambda^2\,(\delta/\Delta^\star)^{2/3}\,Re_\delta^{-1/2}\,[D(p)]^{1/2}$, shown in linear axes *(top)* and semilogarithmic axes *(bottom)*.

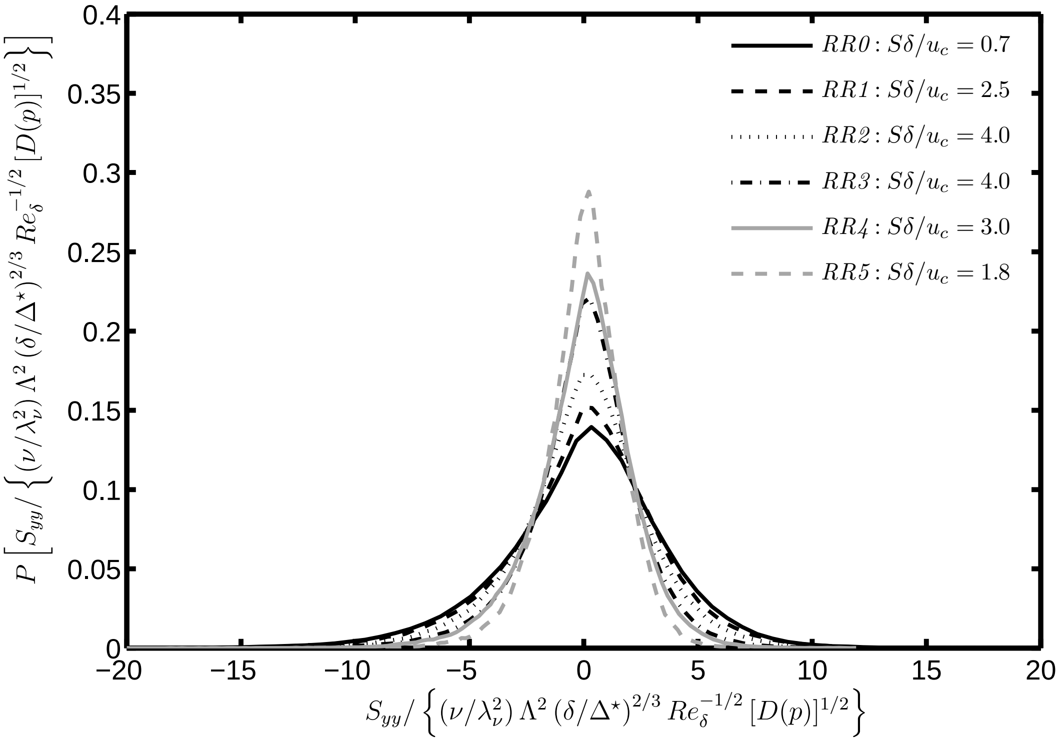

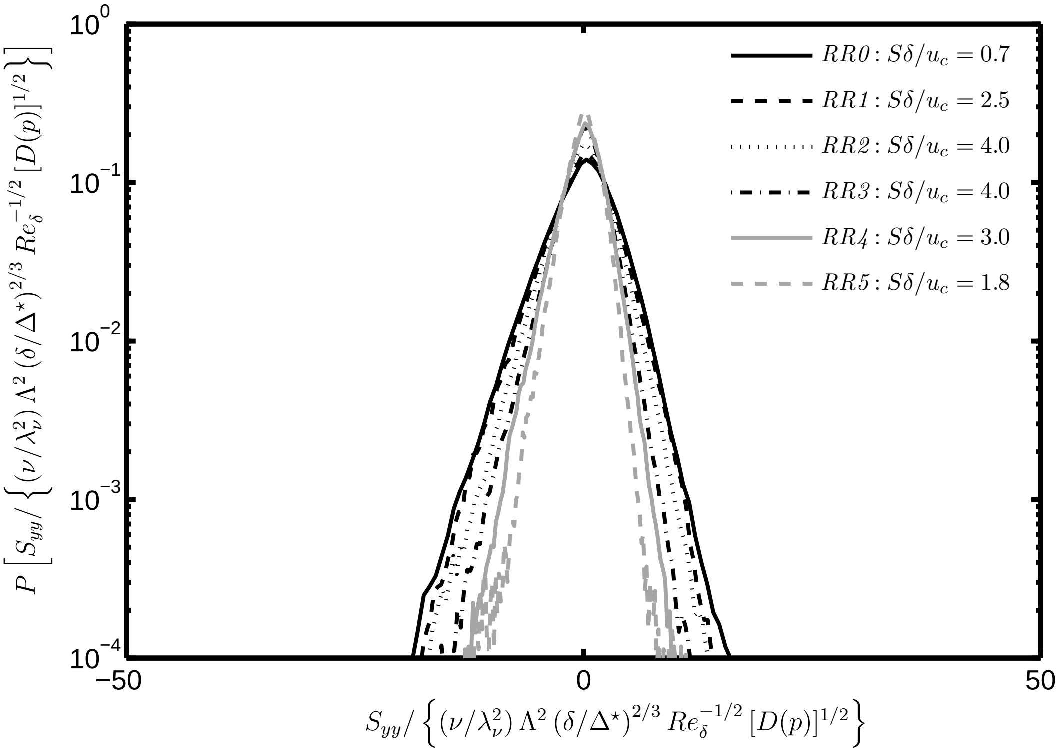

Figure 8.6: Pdfs from conditioned data for all reacting, off-centerline cases *RR0* – *RR5* for strain rate component S_{yy} normalized by resolution-corrected inner scaling $(\nu/\lambda_\nu^2)\,\Lambda^2\,(\delta/\Delta^\star)^{2/3}\,Re_\delta^{-1/2}\,[D(p)]^{1/2}$, shown in linear axes *(top)* and semilogarithmic axes *(bottom)*.

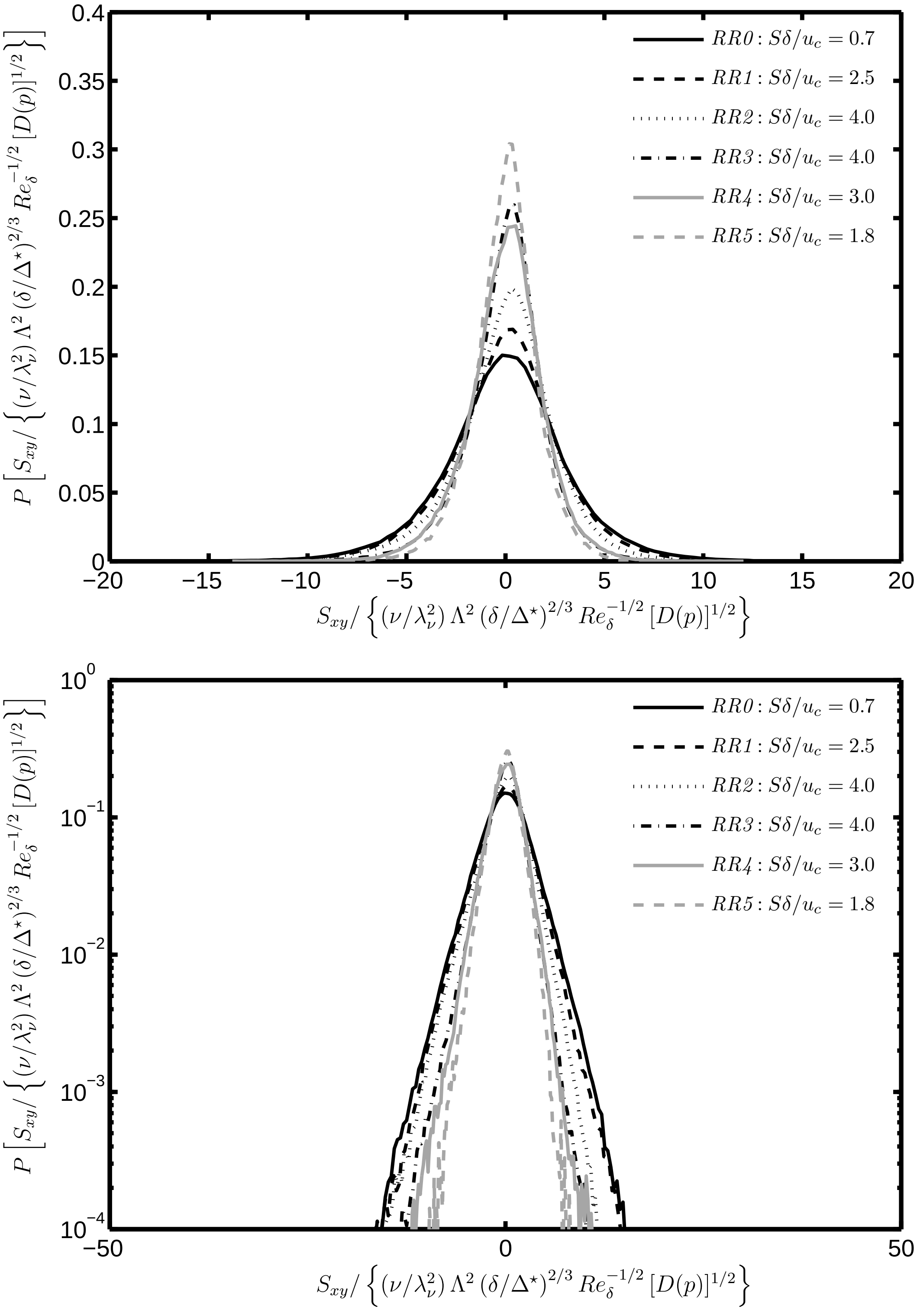

Figure 8.7: Pdfs from conditioned data for all reacting, off-centerline cases *RR0* – *RR5* for strain rate component S_{xy} normalized by resolution-corrected inner scaling $(\nu/\lambda_\nu^2)\,\Lambda^2\,(\delta/\Delta^\star)^{2/3}\,Re_\delta^{-1/2}\,[D(p)]^{1/2}$, shown in linear axes *(top)* and semilogarithmic axes *(bottom)*.

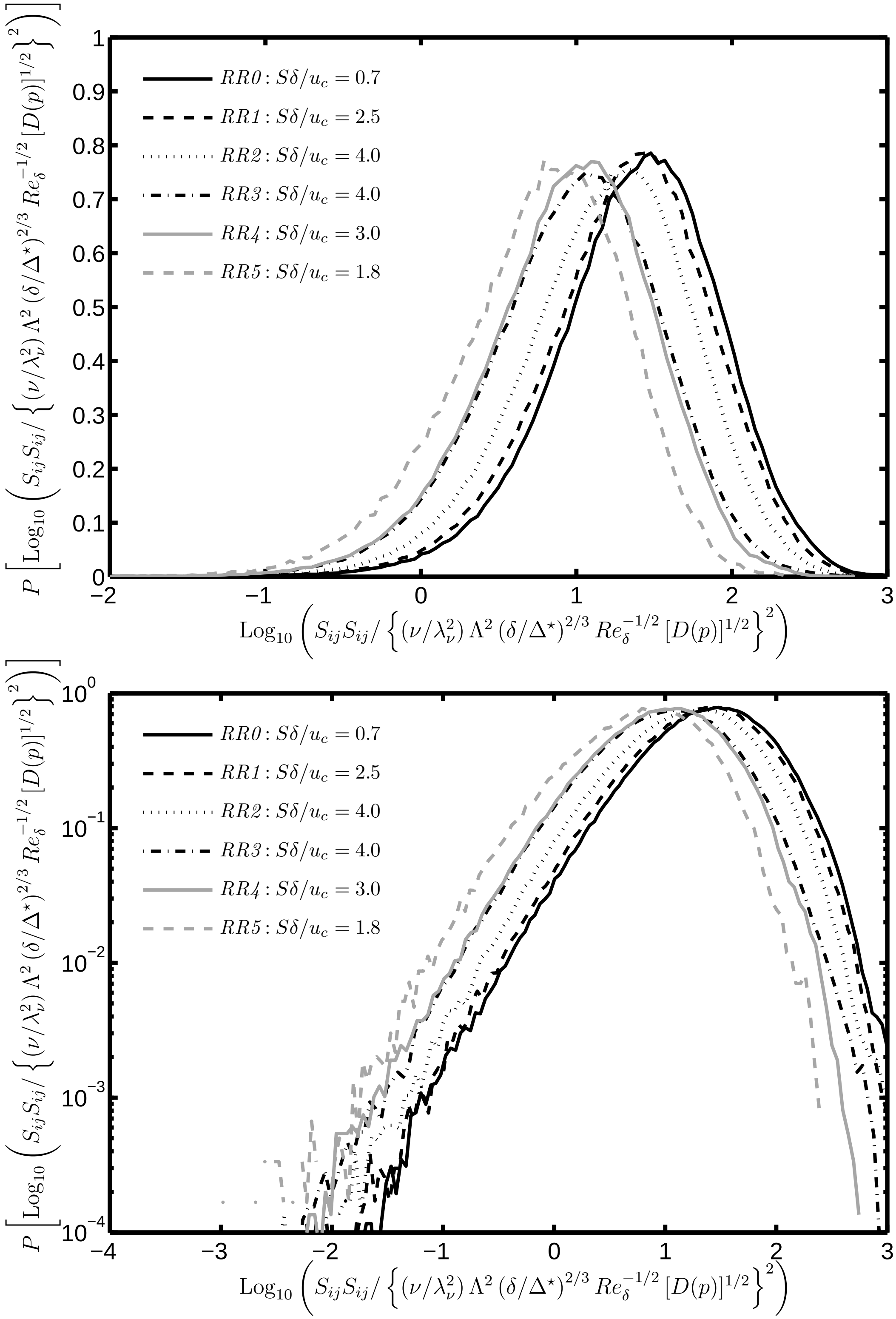

Figure 8.8: Pdfs from conditioned data for all reacting, off-centerline cases *RR0* – *RR5*, for pseudo-dissipation $\mathrm{Log}_{10}\,(S_{ij}S_{ij})$ normalized by resolution-corrected inner scaling $\{(\nu/\lambda_\nu^2)\,\Lambda^2\,(\delta/\Delta^\star)^{2/3}\,Re_\delta^{-1/2}\,[D(p)]^{1/2}\}^2$, shown in linear axes *(top)* and semilogarithmic axes *(bottom)*.

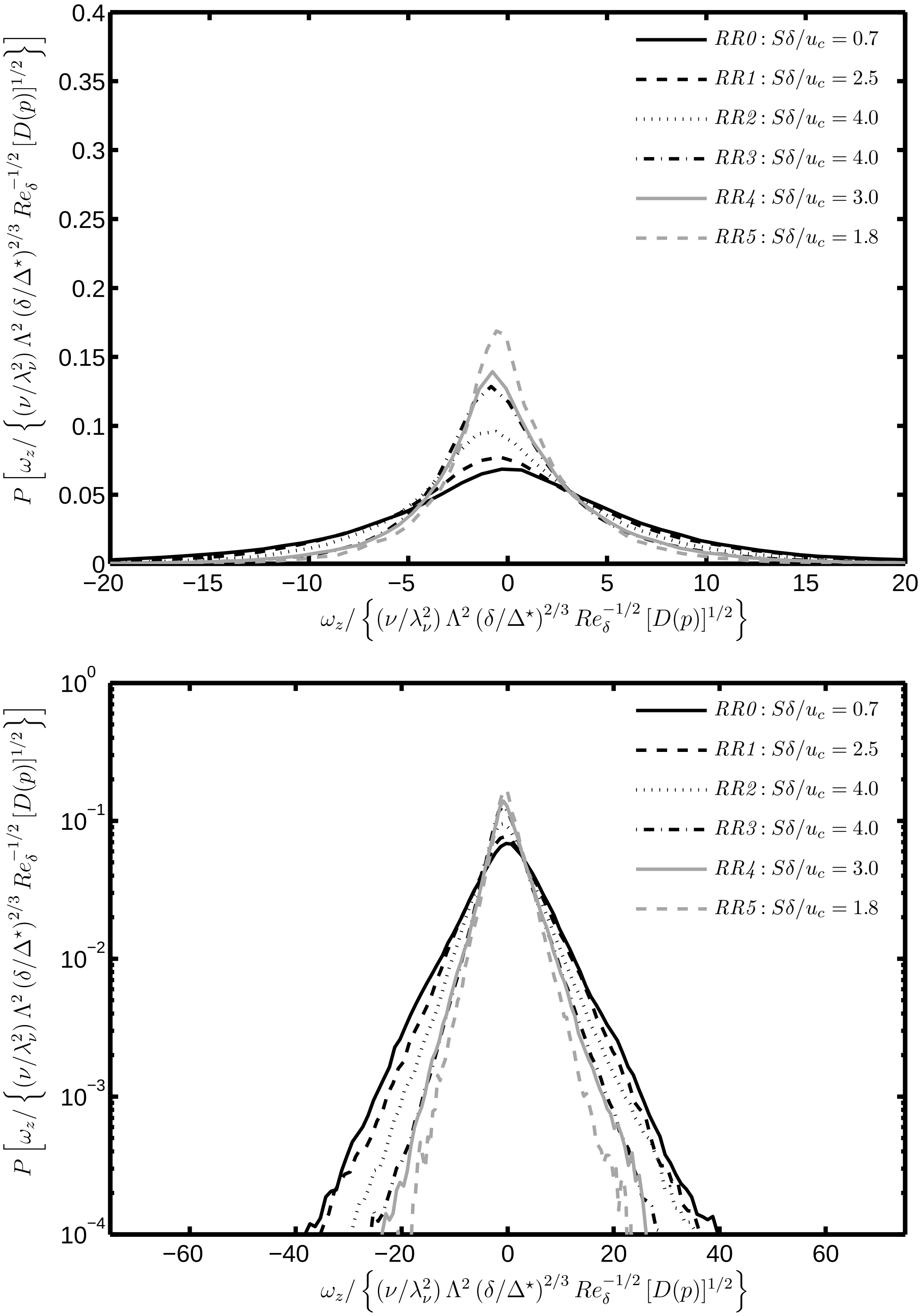

Figure 8.9: Pdfs from conditioned data for all reacting, off-centerline cases *RR0* – *RR5* for vorticity ω_z normalized by resolution-corrected inner scaling $(\nu/\lambda_\nu^2)\,\Lambda^2\,(\delta/\Delta^\star)^{2/3}\,Re_\delta^{-1/2}\,[D(p)]^{1/2}$, shown in linear axes *(top)* and semilogarithmic axes *(bottom)*.

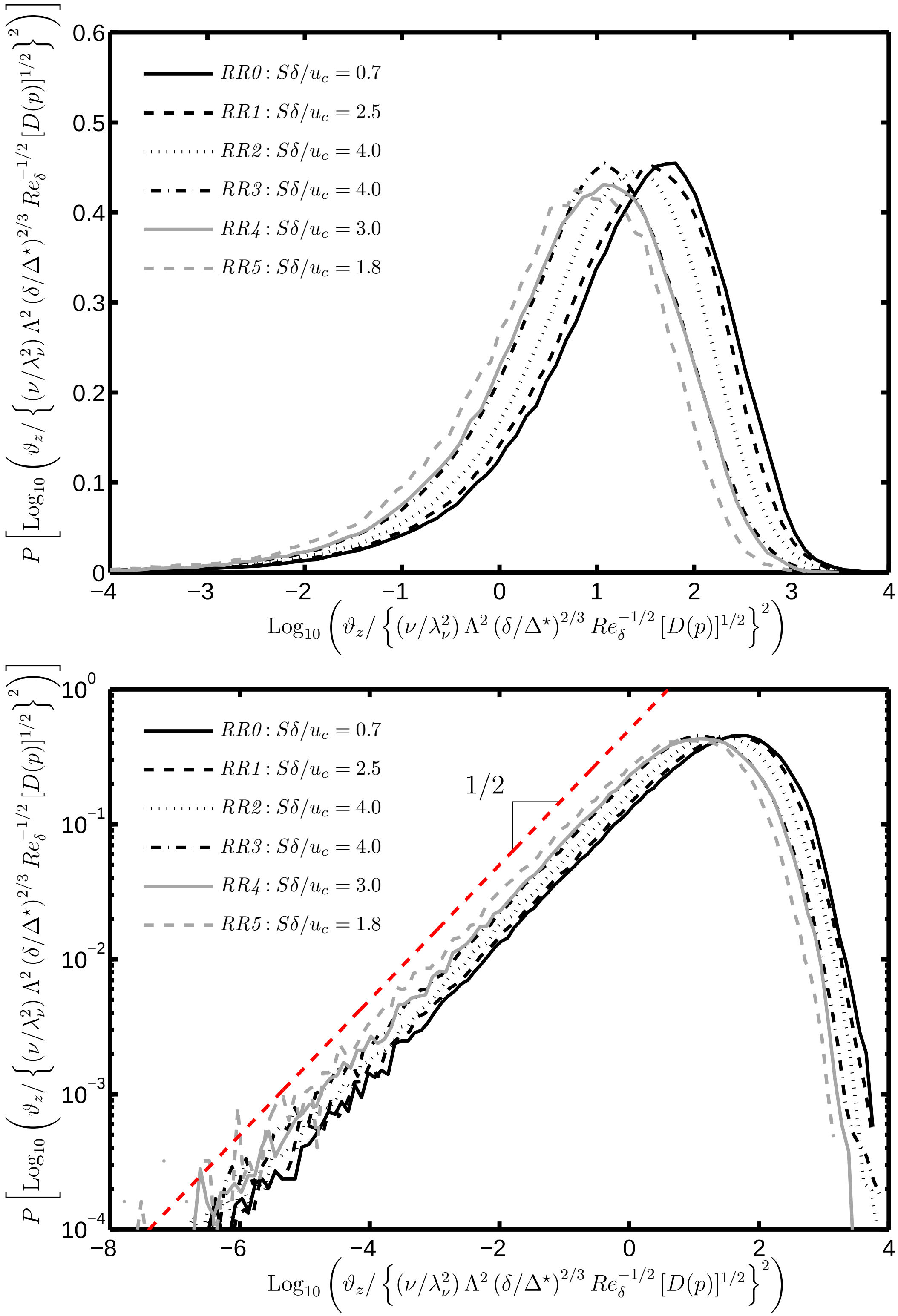

Figure 8.10: Pdfs from conditioned data for all reacting, off-centerline cases *RR0* – *RR5*, for pseudo-enstrophy $\mathrm{Log}_{10}(\vartheta_z)$ normalized by resolution-corrected inner scaling, $\{(\nu/\lambda_\nu^2)\,\Lambda^2\,(\delta/\Delta^\star)^{2/3}\,Re_\delta^{-1/2}\,[D(p)]^{1/2}\}^2$, shown in linear axes *(top)* and semilogarithmic axes *(bottom)*.

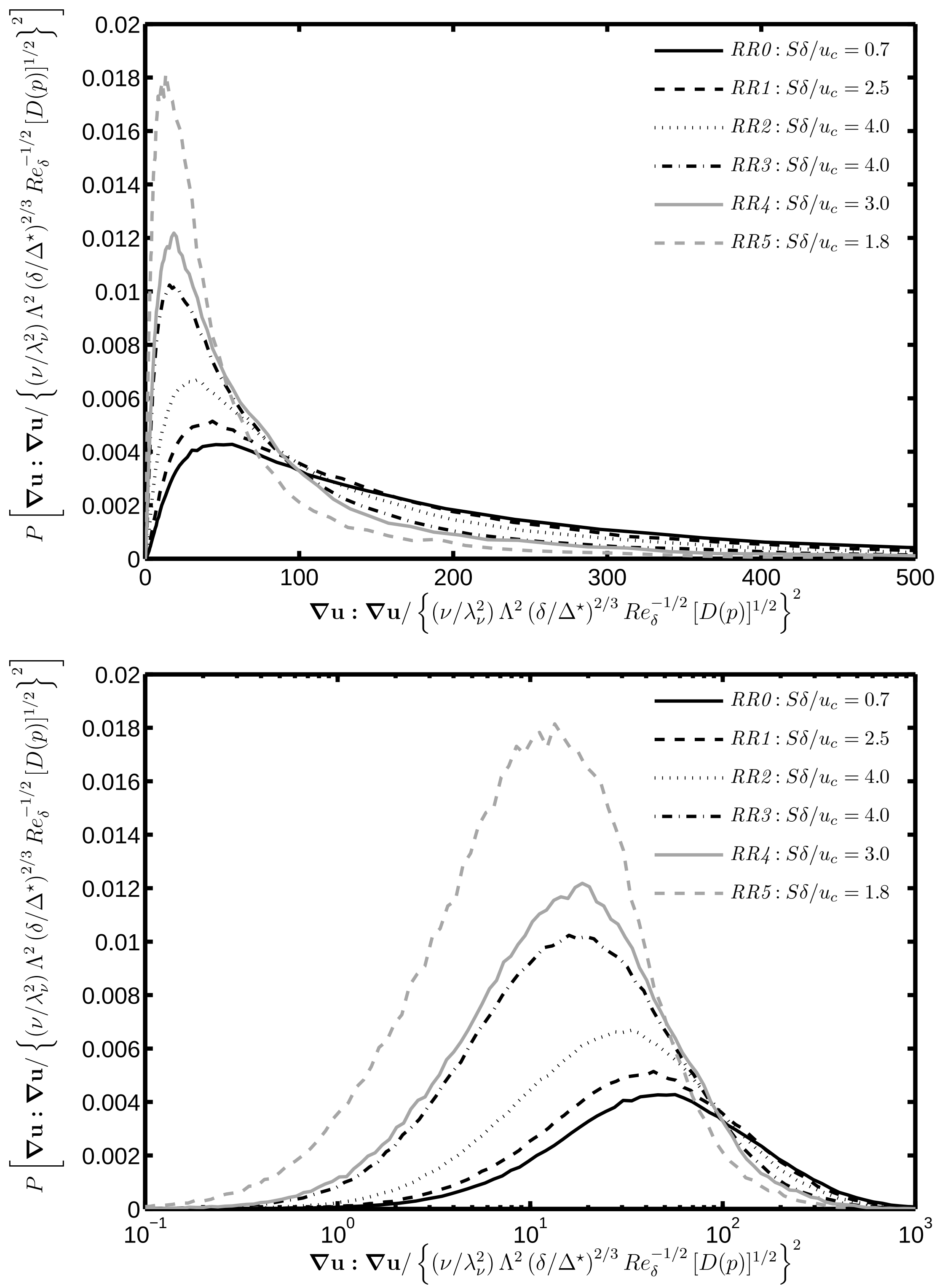

Figure 8.11: Pdfs from conditioned data for all reacting, off-centerline cases *RR0* – *RR5*, for contraction of the velocity gradient tensor $\nabla\mathbf{u} : \nabla\mathbf{u}$ normalized by resolution-corrected inner scaling, $\{(\nu/\lambda_\nu^2)\,\Lambda^2\,(\delta/\Delta^\star)^{2/3}\,Re_\delta^{-1/2}\,[D(p)]^{1/2}\}^2$, shown in linear axes *(top)* and semilogarithmic axes *(bottom)*.

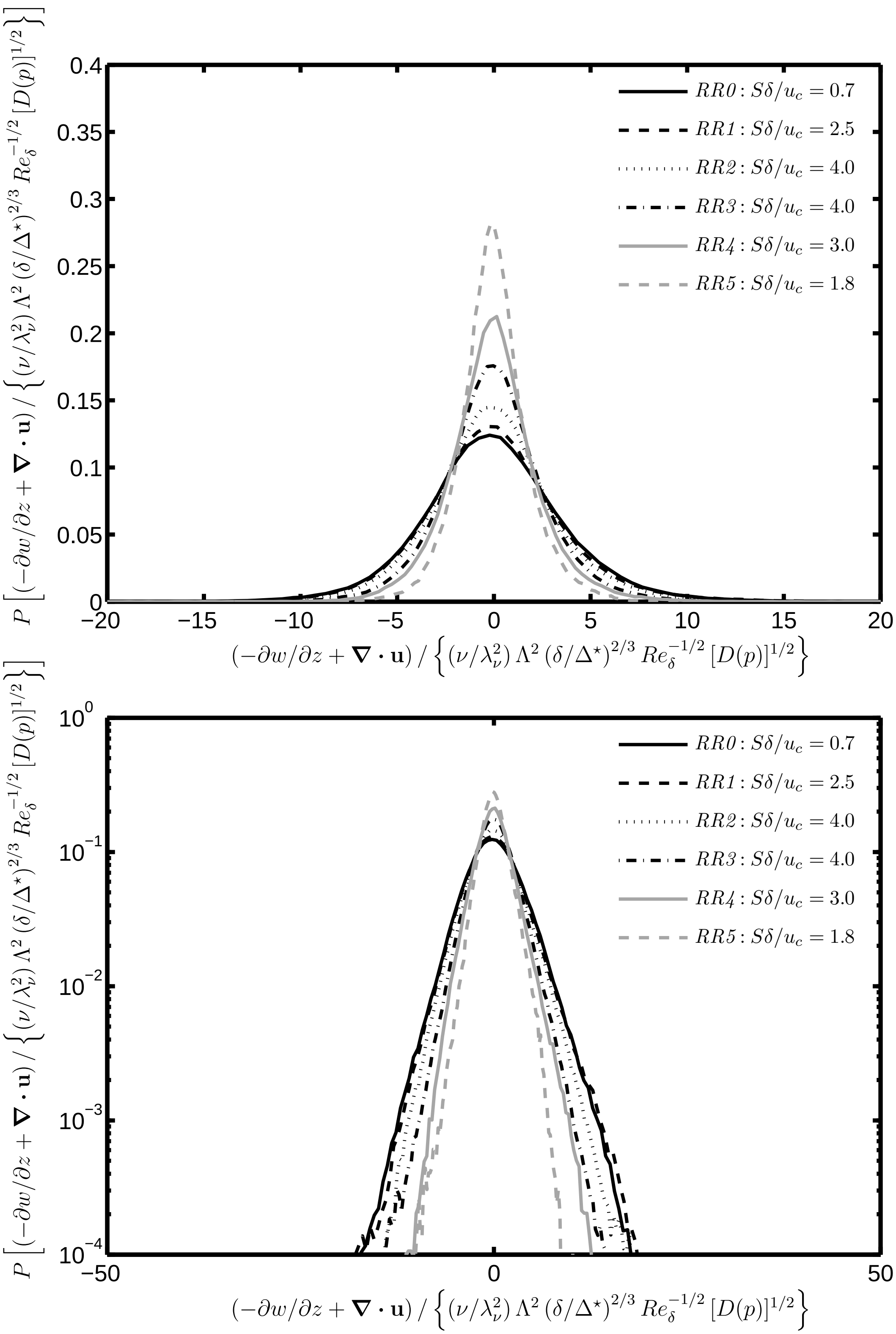

Figure 8.12: Pdfs from conditioned data for all reacting, off-centerline cases *RR0* – *RR5* for two-dimensional divergence $(-\partial w/\partial z + \boldsymbol{\nabla}\cdot\mathbf{u})$ normalized by resolution-corrected inner scaling $(\nu/\lambda_\nu^2)\,\Lambda^2\,(\delta/\Delta^\star)^{2/3}\,Re_\delta^{-1/2}\,[D(p)]^{1/2}$, shown in linear axes *(top)* and semilogarithmic axes *(bottom)*.

Case	$r/\delta_{1/2}$	$\mathcal{S}\delta/u_c$ [-]	Δ_{IW} mm	Inertial- and dissipation-range spectral parameters and resulting factors							
				$\langle p \rangle$ [-]	$\langle \Delta_R \rangle$ mm	Λ_ν [-]	$\langle \Delta^\star \rangle$ mm	$\Lambda^\star$ [-]	$\langle \Delta^\star \rangle / \langle \Delta_R \rangle$	$D(p)$	$\mathcal{N}^\star$
RR0	0.00	0.697	0.421	0.862	3.168	62.745	15.482	306.611	4.89	0.1127	43.447
RR1	0.16	2.536	0.421	0.860	2.997	59.357	14.599	289.124	4.87	0.1133	45.290
RR2	0.47	3.972	0.421	0.836	2.866	56.751	13.334	264.073	4.65	0.1164	48.764
RR3	0.79	3.978	0.421	0.818	2.387	47.265	11.065	219.136	4.64	0.1194	55.930
RR4	1.11	3.014	0.421	0.980	2.105	41.680	11.132	220.471	5.29	0.1020	51.479
RR5	1.42	1.824	0.421	1.011	1.827	36.181	10.044	198.916	5.50	0.0998	54.543
RR4†	1.11	3.014	0.421	1.034	2.055	40.696	11.028	218.413	5.37	0.0978	50.743
RR5†	1.42	1.824	0.421	1.138	1.601	31.706	9.377	185.710	5.86	0.0922	54.879

Table 8.1: Averaged spectral parameters $\langle p \rangle$, $\langle \Delta_R \rangle$ and $\langle \Delta^\star \rangle$ for all cases in Table 3.6 obtained by averaging over results from ω_z, S_{xx}, S_{yy} and S_{xy}. Here Λ_ν and $\Lambda^\star$ values are from $\Lambda_i \equiv (\Delta_i/\delta) Re_\delta^{3/4}$. The quantity $r/\delta_{1/2}$ is the radius normalized by the half width at the half-maximum point. The mean outer shear is $\mathcal{S} \equiv \sqrt{2}\ |\partial\langle u \rangle/\partial r|$. For all cases, $Re_\delta = 65\,000$ and $\delta = 0.226$ m. The final two cases, indicated by a †, are the cases reprocessed with the data conditioning strategy.

Quantity	μ	σ	γ	β
u/u_c	$-7.313E-19$	$3.319E-01$	$3.907E-01$	$3.190E+00$
v/u_c	$1.092E-17$	$2.421E-01$	$-9.903E-02$	$2.779E+00$
$\partial u/\partial x$	$-2.463E-16$	$3.697E+00$	$-6.207E-01$	$5.474E+00$
$\partial u/\partial y$	$-1.080E-15$	$5.849E+00$	$-1.607E-01$	$6.961E+00$
$\partial v/\partial x$	$5.877E-17$	$4.445E+00$	$1.214E-02$	$6.649E+00$
$\partial v/\partial y$	$4.983E-17$	$3.627E+00$	$-4.011E-01$	$5.241E+00$
S_{xx}	$-2.463E-16$	$3.697E+00$	$-6.207E-01$	$5.474E+00$
S_{yy}	$4.983E-17$	$3.627E+00$	$-4.011E-01$	$5.241E+00$
S_{xy}	$-5.766E-16$	$3.199E+00$	$-1.100E-01$	$5.016E+00$
ω_z	$1.067E-15$	$8.186E+00$	$5.734E-02$	$5.958E+00$
ε	$5.756E+00$	$8.537E+00$	$5.570E+00$	$6.751E+01$
$\mathrm{Log}_{10}\,[\varepsilon]$	$4.515E-01$	$5.548E-01$	$-4.221E-01$	$3.567E+00$
$(-\partial w/\partial z + \boldsymbol{\nabla}\cdot\mathbf{u})$	$-3.506E-16$	$3.716E+00$	$2.183E-01$	$4.885E+00$
$\boldsymbol{\nabla}\mathbf{u} : \boldsymbol{\nabla}\mathbf{u}$	$9.461E+01$	$1.318E+02$	$6.233E+00$	$9.921E+01$
$\left[\dfrac{(-\partial w/\partial z + \boldsymbol{\nabla}\cdot\mathbf{u})}{(\boldsymbol{\nabla}\mathbf{u} : \boldsymbol{\nabla}\mathbf{u})^{1/2}}\right]$	$2.700E-02$	$4.125E-01$	$1.693E-01$	$1.983E+00$
$S_{ij} : S_{ij}$	$4.730E+01$	$6.631E+01$	$5.386E+00$	$7.335E+01$
$\mathrm{Log}_{10}\,[S_{ij} : S_{ij}]$	$1.387E+00$	$5.368E-01$	$-4.600E-01$	$3.652E+00$
$3/2\,(\omega_z)^2$	$1.005E+02$	$2.238E+02$	$7.302E+00$	$9.673E+01$
$\mathrm{Log}_{10}\left[3/2\,(\omega_z)^2\right]$	$1.263E+00$	$1.057E+00$	$-1.190E+00$	$5.715E+00$

Table 8.2: Normalized central moments computed from pdfs of conditioned data for *RR0* case. The mean is μ, σ is the *rms* fluctuation, $\gamma = \mu_3/\sigma^3$ is the skewness and $\beta = \mu_4/\sigma^4$ is the kurtosis. All quantities normalized by resolution-corrected inner scaling $(\nu/\lambda_\nu^2)\,\Lambda^2\,(\delta/\Delta^\star)^{2/3}\,Re_\delta^{-1/2}\,[D(p)]^{1/2}$ as shown in Figs. 8.1 – 8.12.

Quantity	μ	σ	γ	β
u/u_c	$3.474E-18$	$3.461E-01$	$2.499E-01$	$2.777E+00$
v/u_c	$-4.925E-18$	$2.330E-01$	$2.602E-01$	$3.002E+00$
$\partial u/\partial x$	$-6.864E-17$	$3.475E+00$	$-6.497E-01$	$5.497E+00$
$\partial u/\partial y$	$0.000E+00$	$5.120E+00$	$-3.875E-01$	$6.220E+00$
$\partial v/\partial x$	$-8.090E-17$	$4.322E+00$	$-1.250E-01$	$7.174E+00$
$\partial v/\partial y$	$4.841E-17$	$3.389E+00$	$-4.265E-01$	$4.645E+00$
S_{xx}	$-6.864E-17$	$3.475E+00$	$-6.497E-01$	$5.497E+00$
S_{yy}	$4.841E-17$	$3.389E+00$	$-4.265E-01$	$4.645E+00$
S_{xy}	$-1.324E-16$	$2.956E+00$	$-1.714E-01$	$4.780E+00$
ω_z	$2.390E-16$	$7.406E+00$	$9.662E-02$	$6.273E+00$
ε	$5.400E+00$	$7.851E+00$	$4.855E+00$	$4.810E+01$
$\mathrm{Log}_{10}[\varepsilon]$	$4.223E-01$	$5.575E-01$	$-4.201E-01$	$3.513E+00$
$(-\partial w/\partial z + \boldsymbol{\nabla}\cdot\mathbf{u})$	$-3.513E-16$	$3.638E+00$	$2.843E-01$	$4.879E+00$
$\boldsymbol{\nabla}\mathbf{u} : \boldsymbol{\nabla}\mathbf{u}$	$8.169E+01$	$1.119E+02$	$5.076E+00$	$5.235E+01$
$\left[\dfrac{(-\partial w/\partial z + \boldsymbol{\nabla}\cdot\mathbf{u})}{(\boldsymbol{\nabla}\mathbf{u} : \boldsymbol{\nabla}\mathbf{u})^{1/2}}\right]$	$2.393E-02$	$4.225E-01$	$1.592E-01$	$1.941E+00$
$S_{ij} : S_{ij}$	$4.103E+01$	$5.653E+01$	$4.571E+00$	$4.375E+01$
$\mathrm{Log}_{10}[S_{ij} : S_{ij}]$	$1.324E+00$	$5.401E-01$	$-4.587E-01$	$3.609E+00$
$3/2\,(\omega_z)^2$	$8.227E+01$	$1.889E+02$	$8.105E+00$	$1.268E+02$
$\mathrm{Log}_{10}\left[3/2\ (\omega_z)^2\right]$	$1.172E+00$	$1.058E+00$	$-1.193E+00$	$5.761E+00$

Table 8.3: Normalized central moments computed from pdfs of conditioned data for *RR1* case. The mean is μ, σ is the *rms* fluctuation, $\gamma = \mu_3/\sigma^3$ is the skewness and $\beta = \mu_4/\sigma^4$ is the kurtosis. All quantities normalized by resolution-corrected inner scaling $(\nu/\lambda_\nu^2)\,\Lambda^2\,(\delta/\Delta^\star)^{2/3}\,Re_\delta^{-1/2}\,[D(p)]^{1/2}$ as shown in Figs. 8.1 – 8.12.

Quantity	μ	σ	γ	β
u/u_c	$-8.776E-18$	$3.116E-01$	$7.594E-01$	$3.600E+00$
v/u_c	$8.959E-18$	$2.088E-01$	$5.174E-01$	$3.391E+00$
$\partial u/\partial x$	$2.869E-16$	$2.976E+00$	$-4.827E-01$	$5.248E+00$
$\partial u/\partial y$	$1.233E-15$	$4.511E+00$	$-7.853E-01$	$7.108E+00$
$\partial v/\partial x$	$-7.456E-17$	$3.602E+00$	$-1.948E-01$	$7.244E+00$
$\partial v/\partial y$	$-8.296E-17$	$2.979E+00$	$-4.166E-01$	$5.262E+00$
S_{xx}	$2.869E-16$	$2.976E+00$	$-4.827E-01$	$5.248E+00$
S_{yy}	$-8.296E-17$	$2.979E+00$	$-4.166E-01$	$5.262E+00$
S_{xy}	$6.483E-16$	$2.609E+00$	$-5.001E-01$	$5.330E+00$
ω_z	$-1.411E-15$	$6.278E+00$	$5.003E-01$	$7.026E+00$
ε	$4.810E+00$	$7.454E+00$	$5.718E+00$	$6.610E+01$
$\text{Log}_{10}[\varepsilon]$	$3.562E-01$	$5.706E-01$	$-4.113E-01$	$3.518E+00$
$(-\partial w/\partial z + \boldsymbol{\nabla}\cdot\mathbf{u})$	$3.666E-16$	$3.249E+00$	$2.240E-01$	$4.464E+00$
$\boldsymbol{\nabla}\mathbf{u} : \boldsymbol{\nabla}\mathbf{u}$	$6.160E+01$	$8.851E+01$	$5.811E+00$	$7.854E+01$
$\left[\dfrac{(-\partial w/\partial z + \boldsymbol{\nabla}\cdot\mathbf{u})}{(\boldsymbol{\nabla}\mathbf{u} : \boldsymbol{\nabla}\mathbf{u})^{1/2}}\right]$	$1.992E-02$	$4.326E-01$	$1.176E-01$	$1.878E+00$
$S_{ij} : S_{ij}$	$3.134E+01$	$4.540E+01$	$5.359E+00$	$6.064E+01$
$\text{Log}_{10}[S_{ij} : S_{ij}]$	$1.193E+00$	$5.535E-01$	$-4.539E-01$	$3.579E+00$
$3/2\,(\omega_z)^2$	$5.913E+01$	$1.451E+02$	$9.140E+00$	$1.883E+02$
$\text{Log}_{10}\left[3/2\ (\omega_z)^2\right]$	$1.006E+00$	$1.058E+00$	$-1.161E+00$	$5.792E+00$

Table 8.4: Normalized central moments computed from pdfs of conditioned data for *RR2* case. The mean is μ, σ is the *rms* fluctuation, $\gamma = \mu_3/\sigma^3$ is the skewness and $\beta = \mu_4/\sigma^4$ is the kurtosis. All quantities normalized by resolution-corrected inner scaling $(\nu/\lambda_\nu^2)\,\Lambda^2\,(\delta/\Delta^\star)^{2/3}\,Re_\delta^{-1/2}\,[D(p)]^{1/2}$ as shown in Figs. 8.1 – 8.12.

Quantity	μ	σ	γ	β
u/u_c	$2.875E-17$	$2.512E-01$	$7.938E-01$	$3.917E+00$
v/u_c	$2.148E-18$	$1.834E-01$	$7.636E-01$	$4.260E+00$
$\partial u/\partial x$	$-4.989E-16$	$2.290E+00$	$-2.905E-01$	$5.229E+00$
$\partial u/\partial y$	$-1.190E-16$	$3.532E+00$	$-8.140E-01$	$7.755E+00$
$\partial v/\partial x$	$-4.615E-17$	$2.883E+00$	$1.697E-01$	$1.016E+01$
$\partial v/\partial y$	$1.774E-17$	$2.474E+00$	$-6.267E-01$	$6.429E+00$
S_{xx}	$-4.989E-16$	$2.290E+00$	$-2.905E-01$	$5.229E+00$
S_{yy}	$1.774E-17$	$2.474E+00$	$-6.267E-01$	$6.429E+00$
S_{xy}	$-4.162E-17$	$2.048E+00$	$-4.952E-01$	$5.873E+00$
ω_z	$2.238E-16$	$4.980E+00$	$7.550E-01$	$9.594E+00$
ε	$3.961E+00$	$6.506E+00$	$6.247E+00$	$7.262E+01$
$\text{Log}_{10}\,[\varepsilon]$	$2.618E-01$	$5.752E-01$	$-3.798E-01$	$3.490E+00$
$(-\partial w/\partial z + \boldsymbol{\nabla}\cdot\mathbf{u})$	$-5.010E-16$	$2.736E+00$	$1.219E-01$	$4.790E+00$
$\boldsymbol{\nabla}\mathbf{u} : \boldsymbol{\nabla}\mathbf{u}$	$3.963E+01$	$6.200E+01$	$8.315E+00$	$1.759E+02$
$\left[\dfrac{(-\partial w/\partial z + \boldsymbol{\nabla}\cdot\mathbf{u})}{(\boldsymbol{\nabla}\mathbf{u} : \boldsymbol{\nabla}\mathbf{u})^{1/2}}\right]$	$1.738E-02$	$4.483E-01$	$8.301E-02$	$1.817E+00$
$S_{ij} : S_{ij}$	$1.975E+01$	$3.049E+01$	$6.137E+00$	$7.555E+01$
$\text{Log}_{10}\,[S_{ij} : S_{ij}]$	$9.814E-01$	$5.590E-01$	$-4.182E-01$	$3.545E+00$
$3/2\,(\omega_z)^2$	$3.720E+01$	$1.090E+02$	$1.932E+01$	$8.594E+02$
$\text{Log}_{10}\left[3/2\ (\omega_z)^2\right]$	$7.788E-01$	$1.062E+00$	$-1.132E+00$	$5.744E+00$

Table 8.5: Normalized central moments computed from pdfs of conditioned data for *RR3* case. The mean is μ, σ is the *rms* fluctuation, $\gamma = \mu_3/\sigma^3$ is the skewness and $\beta = \mu_4/\sigma^4$ is the kurtosis. All quantities normalized by resolution-corrected inner scaling $(\nu/\lambda_\nu^2)\,\Lambda^2\,(\delta/\Delta^\star)^{2/3}\,Re_\delta^{-1/2}\,[D(p)]^{1/2}$ as shown in Figs. 8.1 – 8.12.

Quantity	μ	σ	γ	β
u/u_c	$-1.472E-17$	$1.958E-01$	$4.150E-01$	$3.446E+00$
v/u_c	$-7.908E-18$	$1.483E-01$	$5.712E-01$	$3.717E+00$
$\partial u/\partial x$	$-3.391E-17$	$2.131E+00$	$-4.610E-01$	$5.363E+00$
$\partial u/\partial y$	$-7.548E-17$	$3.398E+00$	$-7.784E-01$	$6.885E+00$
$\partial v/\partial x$	$-3.884E-17$	$2.774E+00$	$1.018E-01$	$6.960E+00$
$\partial v/\partial y$	$-9.299E-18$	$2.218E+00$	$-4.773E-01$	$4.769E+00$
S_{xx}	$-3.391E-17$	$2.131E+00$	$-4.610E-01$	$5.363E+00$
S_{yy}	$-9.299E-18$	$2.218E+00$	$-4.773E-01$	$4.769E+00$
S_{xy}	$-6.646E-17$	$1.988E+00$	$-3.166E-01$	$4.884E+00$
ω_z	$1.400E-16$	$4.761E+00$	$5.040E-01$	$6.816E+00$
ε	$2.927E+00$	$4.364E+00$	$5.138E+00$	$5.025E+01$
$\mathrm{Log}_{10}[\varepsilon]$	$1.502E-01$	$5.650E-01$	$-4.461E-01$	$3.561E+00$
$(-\partial w/\partial z + \boldsymbol{\nabla}\cdot\mathbf{u})$	$-1.012E-17$	$2.365E+00$	$2.693E-01$	$4.857E+00$
$\boldsymbol{\nabla}\mathbf{u} : \boldsymbol{\nabla}\mathbf{u}$	$3.429E+01$	$4.831E+01$	$5.188E+00$	$5.525E+01$
$\left[\dfrac{(-\partial w/\partial z + \boldsymbol{\nabla}\cdot\mathbf{u})}{(\boldsymbol{\nabla}\mathbf{u} : \boldsymbol{\nabla}\mathbf{u})^{1/2}}\right]$	$2.490E-02$	$4.190E-01$	$1.482E-01$	$1.933E+00$
$S_{ij} : S_{ij}$	$1.736E+01$	$2.407E+01$	$4.545E+00$	$4.029E+01$
$\mathrm{Log}_{10}[S_{ij} : S_{ij}]$	$9.463E-01$	$5.466E-01$	$-4.902E-01$	$3.647E+00$
$3/2\,(\omega_z)^2$	$3.400E+01$	$8.200E+01$	$7.748E+00$	$1.183E+02$
$\mathrm{Log}_{10}\left[3/2\ (\omega_z)^2\right]$	$7.459E-01$	$1.068E+00$	$-1.099E+00$	$5.477E+00$

Table 8.6: Normalized central moments computed from pdfs of conditioned data for *RR4* case. The mean is μ, σ is the *rms* fluctuation, $\gamma = \mu_3/\sigma^3$ is the skewness and $\beta = \mu_4/\sigma^4$ is the kurtosis. All quantities normalized by resolution-corrected inner scaling $(\nu/\lambda_\nu^2)\,\Lambda^2\,(\delta/\Delta^\star)^{2/3}\,Re_\delta^{-1/2}\,[D(p)]^{1/2}$ as shown in Figs. 8.1 – 8.12.

Quantity	μ	σ	γ	β
u/u_c	$1.335E-17$	$1.491E-01$	$3.529E-01$	$3.067E+00$
v/u_c	$6.811E-18$	$1.246E-01$	$4.686E-01$	$3.572E+00$
$\partial u/\partial x$	$6.271E-17$	$1.634E+00$	$-4.595E-01$	$4.754E+00$
$\partial u/\partial y$	$4.046E-17$	$2.756E+00$	$-5.802E-01$	$6.426E+00$
$\partial v/\partial x$	$8.800E-17$	$2.286E+00$	$-2.578E-01$	$6.596E+00$
$\partial v/\partial y$	$3.692E-17$	$1.771E+00$	$-5.249E-01$	$5.264E+00$
S_{xx}	$6.271E-17$	$1.634E+00$	$-4.595E-01$	$4.754E+00$
S_{yy}	$3.692E-17$	$1.771E+00$	$-5.249E-01$	$5.264E+00$
S_{xy}	$2.630E-17$	$1.647E+00$	$-2.725E-01$	$4.384E+00$
ω_z	$-1.500E-16$	$3.846E+00$	$3.463E-01$	$6.736E+00$
ε	$2.257E+00$	$3.221E+00$	$4.410E+00$	$3.674E+01$
$\text{Log}_{10}[\varepsilon]$	$3.271E-02$	$5.782E-01$	$-4.937E-01$	$3.469E+00$
$(-\partial w/\partial z + \boldsymbol{\nabla}\cdot\mathbf{u})$	$9.104E-18$	$1.815E+00$	$9.746E-02$	$4.793E+00$
$\boldsymbol{\nabla}\mathbf{u} : \boldsymbol{\nabla}\mathbf{u}$	$2.192E+01$	$3.008E+01$	$4.810E+00$	$4.195E+01$
$\left[\dfrac{(-\partial w/\partial z + \boldsymbol{\nabla}\cdot\mathbf{u})}{(\boldsymbol{\nabla}\mathbf{u} : \boldsymbol{\nabla}\mathbf{u})^{1/2}}\right]$	$2.116E-02$	$4.084E-01$	$1.576E-01$	$1.997E+00$
$S_{ij} : S_{ij}$	$1.123E+01$	$1.499E+01$	$4.213E+00$	$3.389E+01$
$\text{Log}_{10}[S_{ij} : S_{ij}]$	$7.562E-01$	$5.566E-01$	$-5.502E-01$	$3.566E+00$
$3/2\,(\omega_z)^2$	$2.219E+01$	$5.314E+01$	$7.575E+00$	$1.004E+02$
$\text{Log}_{10}\left[3/2\ (\omega_z)^2\right]$	$5.555E-01$	$1.085E+00$	$-1.130E+00$	$5.497E+00$

Table 8.7: Normalized central moments computed from pdfs of conditioned data for *RR5* case. The mean is μ, σ is the *rms* fluctuation, $\gamma = \mu_3/\sigma^3$ is the skewness and $\beta = \mu_4/\sigma^4$ is the kurtosis. All quantities normalized by resolution-corrected inner scaling $(\nu/\lambda_\nu^2)\,\Lambda^2\,(\delta/\Delta^\star)^{2/3}\,Re_\delta^{-1/2}\,[D(p)]^{1/2}$ as shown in Figs. 8.1 – 8.12.

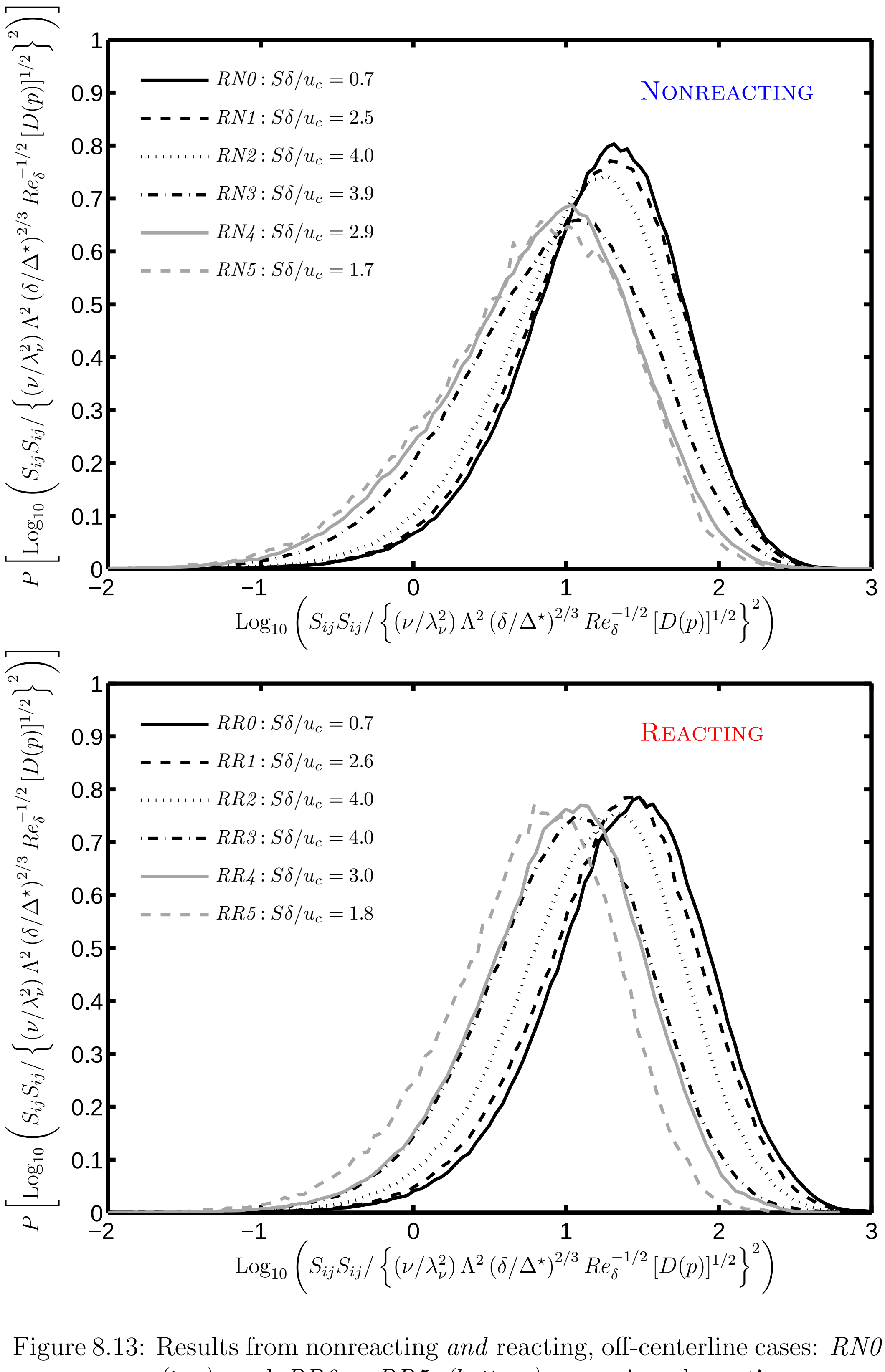

Figure 8.13: Results from nonreacting *and* reacting, off-centerline cases: *RN0* – *RN5* *(top)*, and *RR0* – *RR5* *(bottom)*, spanning the entire range of shear values $\mathcal{S}$ investigated. Pdfs of dissipation $\mathrm{Log}_{10}\,(S_{ij}S_{ij})$ normalized by $(\mathcal{N}^\star)^2$. Statistics are shown *with* application of the enstrophy rejection strategy.

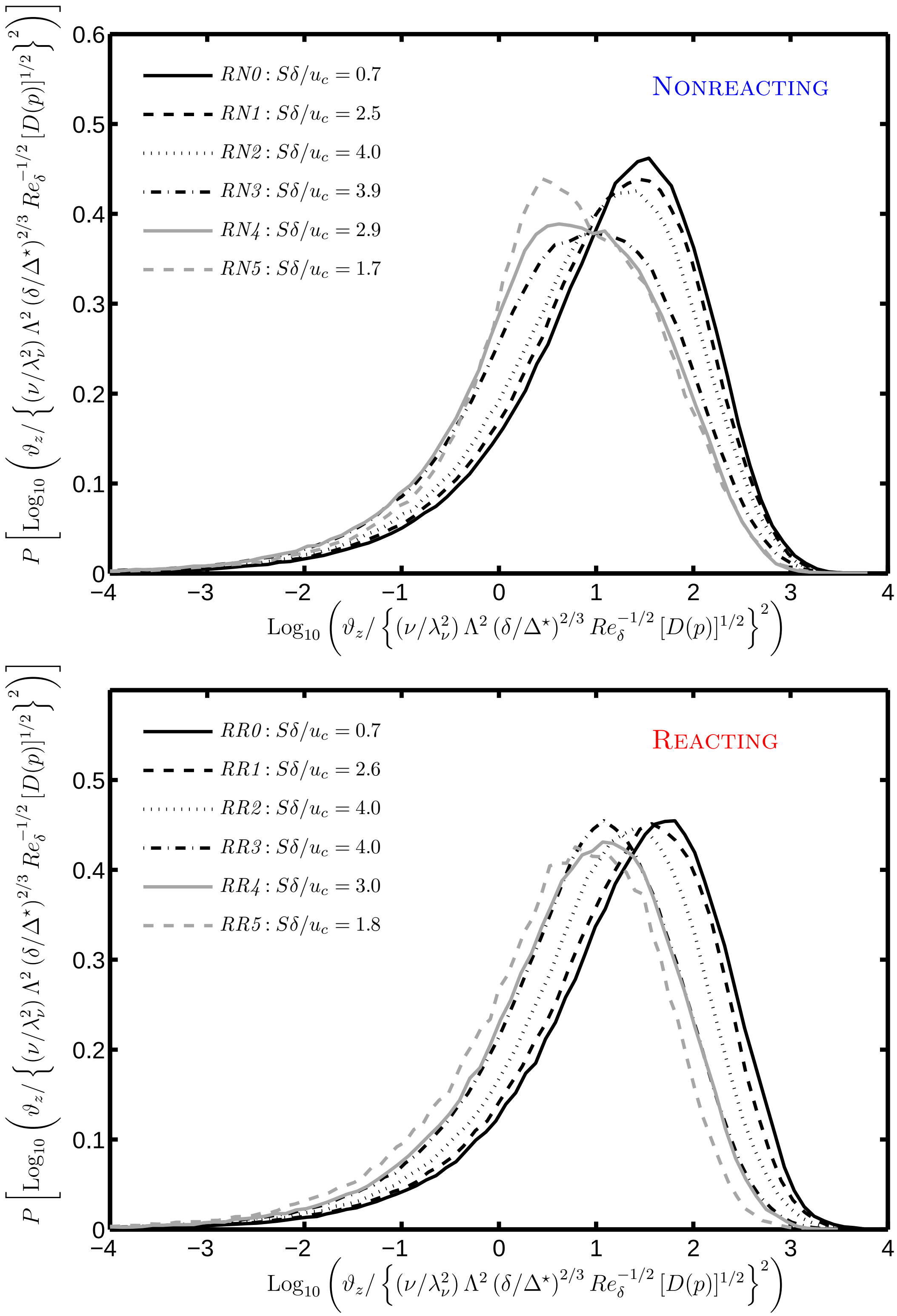

Figure 8.14: Results from nonreacting *and* reacting, off-centerline cases: *RN0* – *RN5* *(top)*, and *RR0* – *RR5* *(bottom)*, spanning the entire range of shear values $\mathcal{S}$ investigated. Pdfs of enstrophy $\mathrm{Log}_{10}\,(\vartheta_z)$ normalized by $(\mathcal{N}^\star)^2$. Statistics are shown *with* application of the enstrophy rejection strategy.

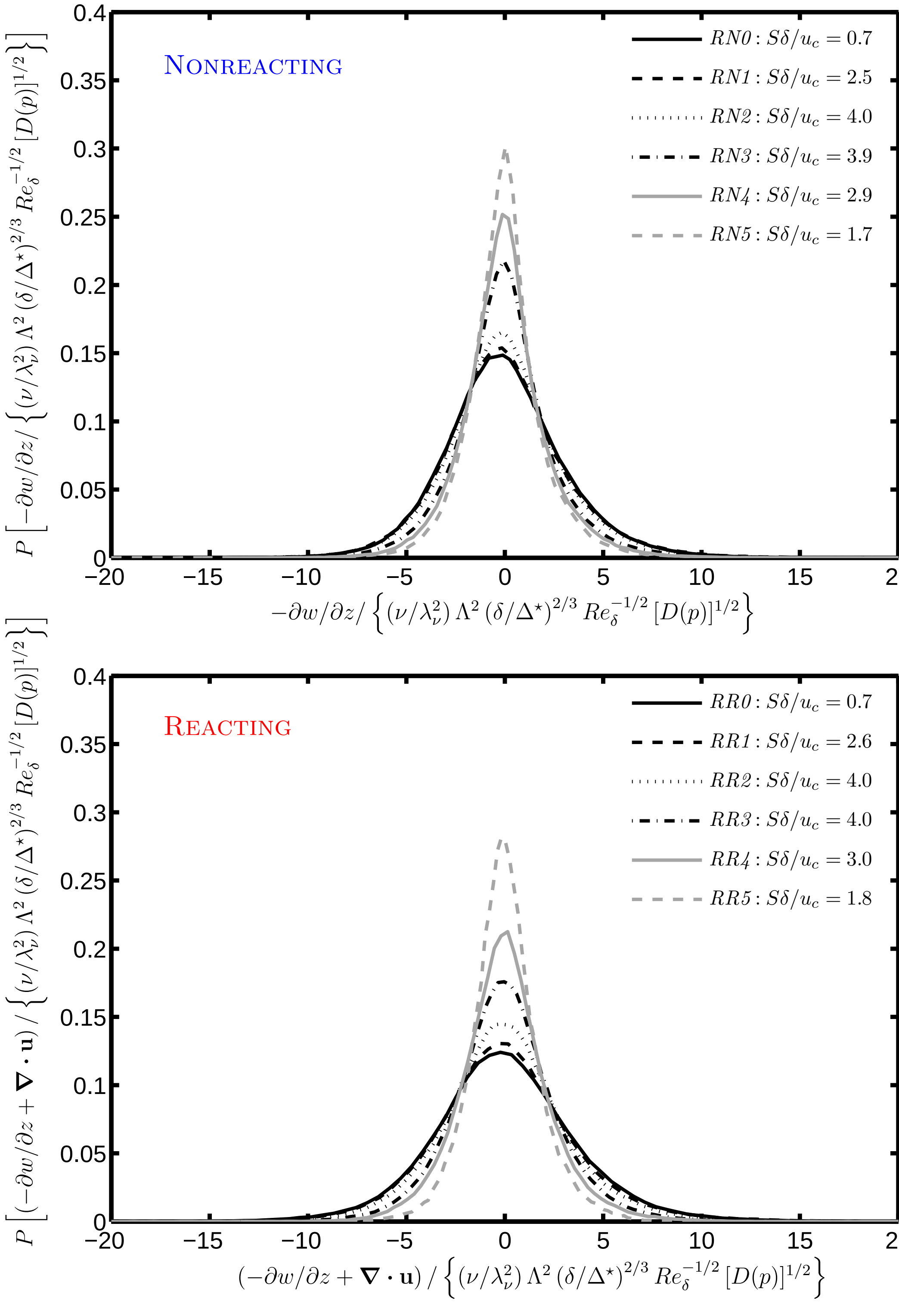

Figure 8.15: Results from nonreacting *and* reacting, off-centerline cases: *RN0* – *RN5 (top)*, and *RR0* – *RR5 (bottom)*, spanning the entire range of shear values $\mathcal{S}$ investigated. Pdfs of the two-dimensional divergence $(-\partial w/\partial z + \boldsymbol{\nabla}\cdot\mathbf{u})$ normalized by $\mathcal{N}^\star$. Statistics are shown *with* application of the enstrophy rejection strategy.

CHAPTER IX

Conclusions

The overarching conclusion from the theoretical considerations and experimental results in this dissertation is that differences observed between otherwise equivalent reacting and nonreacting turbulent shear flows are accounted for by changes in the local outer scales to within the level of agreement seen in the figures. Specifically, these changes in the local outer length δ and velocity u_c scales are due primarily to inertial effects and the influence of buoyancy – the physics of which are both widely understood. Subsequently, these two principle mechanisms dictate the behavior of the local inner scales by means of physical processes that are well-established for nonreacting turbulent shear flows. In this respect, principles which hold true for nonreacting turbulent shear flows can be directly extended to otherwise equivalent reacting turbulent shear flows.

Furthermore, the individual findings presented in Chapters V – VIII lead to the following additional major conclusions from this study:

(1) Classical inner scaling must be corrected as shown herein to account for resolution effects, and the analysis presented herein gives the expression that "recovers" the unresolved portions of a given gradient's spectrum by means of

a combined inertial- and dissipation-range model.

(*2*) Essentially near-perfect similarity is demonstrated in perfect collapse of the nonreacting, on-centerline results of Chapter V – verifying conclusion *(1)*.

(*3*) When the inner-scale resolution $\mathcal{N}^{\star}$ is applied to the on-centerline reacting data of Chapter VI, it provides strong similarity of the data. This verifies (as suggested by Chapter II) that this is also the correct scaling for reacting flow.

(*4*) While these results were obtained from a coflowing jet, the care taken to properly scale the inner-scale results renders them universally applicable to any turbulent shear flow, reacting or nonreacting.

(*5*) Small differences between the nonreacting (Chapters V and VII) and reacting (Chapters VI and VIII) results are the influence of exothermicity at the small scales. The aforementioned overarching conclusion asserts the primacy of inertia and body forces acting on the local outer scales – implying that the influence of dilation and exothermically altered viscosity are second-order effects. Furthermore, the influence of viscosity can be readily accounted for via a mixture-fraction averaged viscosity, as described in (2.21). These second-order effects are observed at the finest scales of the turbulence, shown in the nonreacting/reacting comparisons of Chapters VI and VIII.

(*6*) Changes in the local outer length scale δ of turbulent reacting jets have been widely cited as an effect of heat release. Theoretical considerations of Chapter II and experimental verification in Chapter IV demonstrate that modulation of the local outer length scale is due solely to inertial effects. Exothermicity has no direct impact on the local outer length scale, apart from its *indirect* influence on the ambient density – which using the Equivalence Principle can be produced in an otherwise equivalent *nonreacting* jet with fictitious effective density $\rho_\infty^{\mathit{eff}}$.

(*7*) Consistent with the fact that the Corrsin-Uberoi parameter $\mathcal{S}_c^\star$ is sufficiently small, there should be no shear effects at the inner scales for the nonreacting results of Chapter VII, nor for the reacting results of Chapter VIII.

(*8*) By application of $\mathcal{N}^\star$ to different radial locations, two self-similar groups emerge for the nonreacting results for Chapter VII. Following conclusion *(7)*, little evidence exists which would suggest that this is the influence of mean shear. The mechanism for this apparent self-similar clustering is not immediately obvious.

(*9*) The results in Fig. 6.39 show an increase over the nonreacting baseline values in the *rms* of the velocity gradients due to effect of exothermicity at the inner scales, with a maximum observed level of increase of 42 %, for hydrogen-air chemistry.

These results are directly relevant to nonpremixed and partially-premixed combustion and following *(4)* above, are generally applicable to turbulent shear flows. Moreover, while the heat release effects presently studied are from a hydrogen-air flame, the heat release levels (T_s/T_∞) represent and upper bound for most hydrocarbon combustion systems.

Collectively the findings in this study have provided the first rigorous theoretical foundations, strongly supported by experimental verifications presented herein, of the changes that are produced by heat release in essentially any reacting turbulent shear flow.

Based on these results, distributions of essentially any quantity derived from the velocities u_i or the velocity gradients $\partial u_i/\partial x_j$ in any exothermically reacting turbulent shear flow, can be inferred *a priori* from corresponding quantities in an otherwise equivalent nonreacting turbulent shear flow.

APPENDICES

APPENDIX A

Index of Refraction Effects in a Reacting Flow

The statistical character of randomly oriented sheet-like structures and their effect on beam deflection is investigated. Via a Monte-Carlo (MC) simulation, probability distribution functions (Pdfs) are obtained and found to have an analytical basis. Furthermore, summation of a large number of statistically independent interfaces yields an unexpected result, contrary to the naïve expectations of Central Limit Theorem (CLT). Yet, this result is found to be entirely consistent with probability theory.

Experimental results agree with the predictions made by the MC simulations and a Reynolds number scaling is found in the positional uncertainty of the beam deflections.

> "*Now in the further development of science, we want more than just a formula. First we have an observation, then we have numbers that we measure, then we have a law which summarizes all the numbers. But the real* glory *of science is that* we can find a way of thinking *such that the law is* evident."
>
> —Richard P. Feynman, *The Feynman Lectures on Physics, vol. I.*

A.1 Concept

Based upon the known character of the fine-scale structure of turbulent shear flows where scalar gradients are highly-concentrated into thin sheet-like structures, a physically based model is developed to predict the effect of flow exothermicity on the propagation of laser light. The scalar jump across these structures can be related to the index of refraction (IoR) and the structure treated as an IoR interface to a first-order approximation. If the orientation of the interface is known, the deflection of the beam from its unperturbed path can be readily determined from Snell's law of refraction. In order to estimate the overall uncertainty of a beam passing through an exothermic flow, the beam path can be modeled as a series of discrete interfaces through which the beam passes. The sum of the individual deflections from each of the interfaces yields the overall positional uncertainty of the beam.

The two main challenges lie in first modeling the scalar jump across each interface and relating to the refractive index and second in determining the orientation of each interface. The first challenge will be dealt with later, but the second will be attacked via a Monte Carlo (MC) simulation. The MC simulation will allow the interfaces to be randomly oriented and the statistics of their orientations will be then collected. With the statistics understood, the character of the interface orientations can be predicted and used to obtain the overall uncertainty of the beam's position.

A.2 Formulation

Consider a spherical coordinate system as shown in Fig. A.1. Now let the radius ρ denote the unit normal $\hat{\mathbf{n}}$ vector associated with a plane which defines the IoR interface. Since these interfaces (or unit processes) are assumed to be statistically independent, the plane is taken to be infinite. In order to use Snell's Law:

$$n_1 \sin(\theta_1) = n_2 \sin(\theta_2), \tag{A.1}$$

to determine the beam steering effects, the orientation of the plane (unit normal) must be known (NOTE: the angles in (A.1) are defined in Fig. A.2; also, n_1 & n_2 are the refractive indicies on either side of the interface). Since it is not possible to know

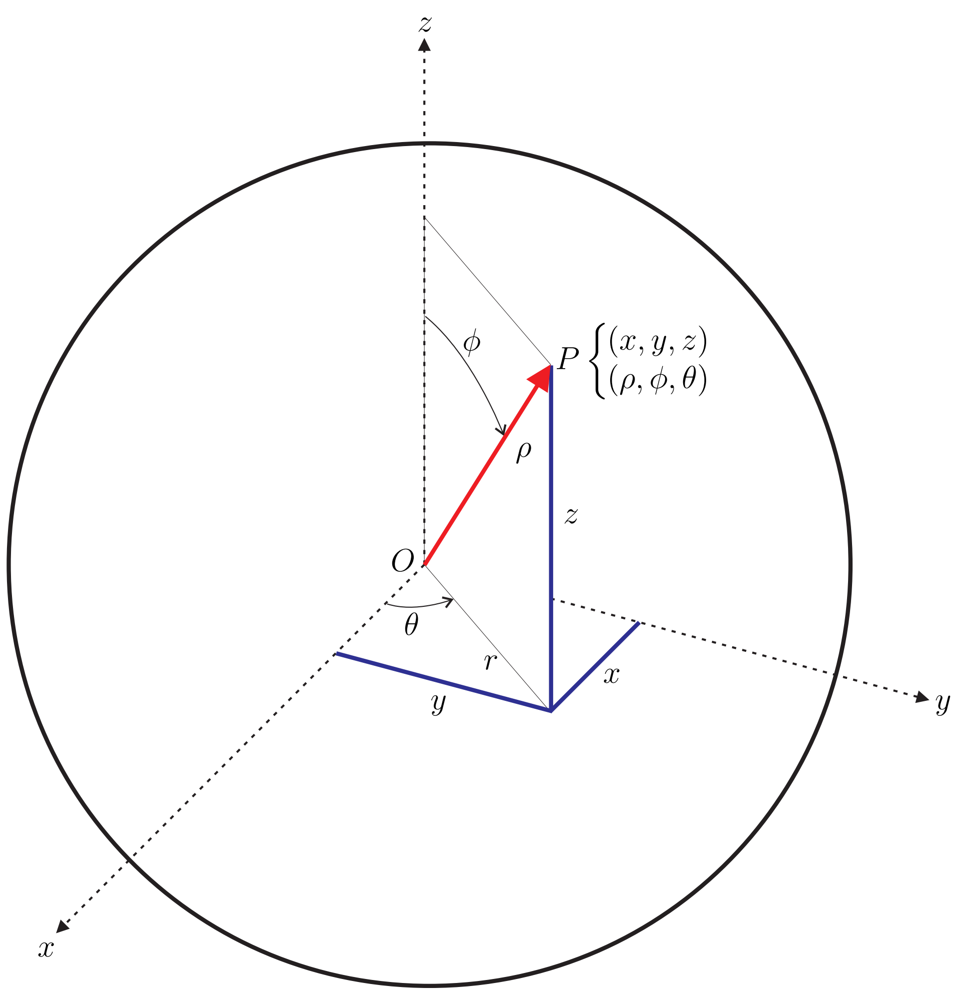

Figure A.1: Spherical coordinate system.

the precise, instantaneous orientation of the plane, it is assumed that each plane is randomly oriented in an isotropic manner. Returning to the spherical coordinate system, the radius ($\hat{\mathbf{n}}$) is arbitrarily fixed at $\rho = 1$, the angle ϕ is varied through $\phi \in [0, \pi/2]$ and $\theta \in [0, 2\pi]$. Conventionally, ϕ is allowed in the domain $\phi \in [0, \pi]$, however since the plane is infinite, all *unique* orientations of the plane (thus $\hat{\mathbf{n}}$) are obtained by defining a *hemisphere* with the radius ($\hat{\mathbf{n}}$). Due to mathematical considerations which will arise later, ϕ is limited to the domain $\phi \in [0, \pi/2]$.

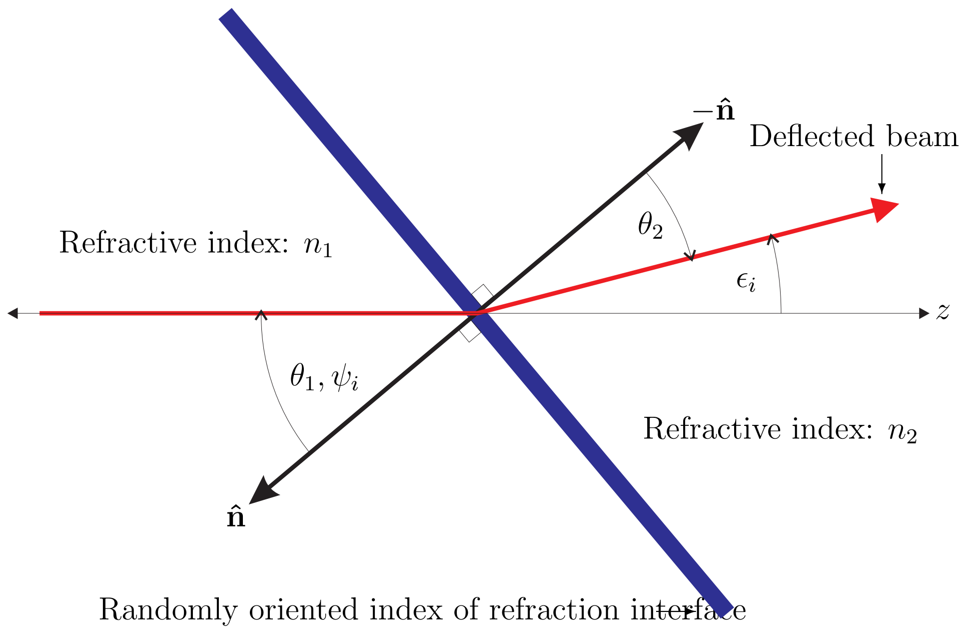

Figure A.2: Nomenclature for Snell's law applied to randomly oriented index of refraction interface.

Since the aim is to employ an MC technique to obtain solutions, ϕ and θ must be cast in statistical terms. Statistically, ϕ and θ are described by their respective probability distribution functions (Pdfs): $\beta(\phi)$ and $\beta(\theta)$. To determine these functions consider spherical coordinates and a differential surface element dS on the sphere of radius ρ, see Fig. A.3. The size and location of dS describe the probability that $\hat{\mathbf{n}}$ will be oriented in a given manner.

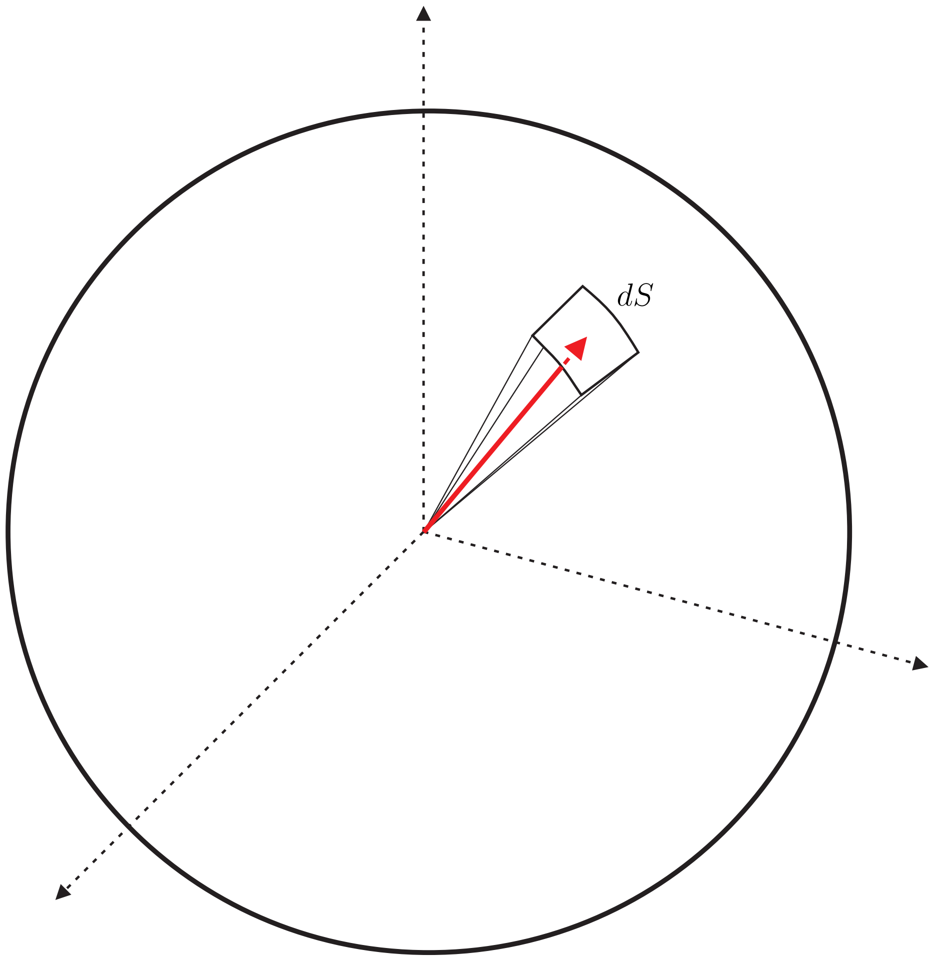

Figure A.3: Differential surface element in spherical coordinates.

This surface element is known in terms of ρ, ϕ and θ:

$$dS = \rho^2 \sin\phi \, d\phi \, d\theta. \tag{A.2}$$

Probability theory states that the only two necessary and sufficient conditions for a function to be a PDF are that it must be positive everywhere and that the probability of an event occuring somewhere within the domain is unity; or (letting $f(x)$ represent an arbitrary PDF):

$$f(x) \geq 0, \quad -\infty < x < \infty, \tag{A.3}$$

$$\int_{-\infty}^{\infty} f(x')dx' = 1. \tag{A.4}$$

Since ρ is fixed as the unit normal $\hat{\mathbf{n}}$, (i.e. $\rho = 1$), the surface area of such a hemisphere is $A = 2\pi$. Thus by normalizing (A.2) by 2π it is found for $\phi \in [0, \pi/2]$ and $\theta \in [0, 2\pi]$ that the normalized form of (A.2) satisfies the conditions in (A.3),(A.4), giving:

$$\beta(\phi, \theta)\, d\phi\, d\theta = \frac{1}{2\pi} \sin\phi\, d\phi\, d\theta. \tag{A.5}$$

Thus, by inspection, the joint PDF is found: $\beta(\phi, \theta) = \frac{1}{2\pi} \sin\phi$. Since ϕ and θ are statistically independent, (A.5) can be decomposed into the Pdfs of ϕ and θ:

$$\beta(\phi, \theta) = \beta(\phi)\beta(\theta). \tag{A.6}$$

To obtain the specific form of the individual Pdfs, it is noted that $\beta(\theta)$ is constant over its entire domain for fixed ϕ. Thus to satisfy (A.4),

$$\beta(\theta) = \frac{1}{2\pi}, \tag{A.7}$$

and by inspection with (A.5),

$$\beta(\phi) = \sin\phi. \tag{A.8}$$

Now that the orientation of $\hat{\mathbf{n}}$ is completely described in statistical terms (i.e. the Pdfs of ϕ and θ are known and ρ is fixed), the Pdfs must be sampled and recreated to perform an MC Simulation. At this point the cumulative distribution function (CDF) is introduced. The CDF gives the probability that a random variable x' is less than or equal to x:

$$CDF \equiv \text{prob}(x' \leq x) \equiv F(x), \tag{A.9}$$

$$F(x) = \int_{-\infty}^{x} f(x')\, dx'. \tag{A.10}$$

The CDF is characterized by a few useful properties:

(a). $F(x)$ increases monotonically.

(b). $F(-\infty) = 0$.

(c). $F(\infty) = 1$.

An elegant methodology for efficient sampling was proposed by von Neumann; it utilizes the CDF and is sometimes called the *The Golden Rule of Sampling*, von Neumann (1946), see Fig. A.4:

(i). Sample a random number ξ from the uniform distribution $U[0, 1]$.

(ii). Equate ξ with the CDF: $F(x) = \xi$.

(iii). Invert the CDF and solve for x: $x = F^{-1}(\xi)$.

Thus for the Pdfs of ϕ and θ:

Quantity	ϕ	θ
PDF	$\beta(\phi) = \sin(\phi)$	$\beta(\theta) = \frac{1}{2\pi}$
CDF	$B(\phi) = 1 - \cos\phi$	$B(\theta) = \frac{\theta}{2\pi}$
Sampling Function (SF)	$\phi = B^{-1}(\xi) = \cos^{-1}(1 - \xi)$	$\theta = B^{-1}(\xi) = 2\pi\xi$
Range	$\phi \in [0, \pi/2]$	$\theta \in [0, 2\pi]$

Table A.1: Sampling functions for ϕ and θ: $\beta(\phi)$ and $\beta(\theta)$.

In order to apply Snell's Law and sum the deflections from the IoR interfaces over M interfaces, it is necessary to project ϕ and θ onto the xz and yz-planes and define the angles ψ_x and ψ_y, see Fig. A.5.

Where ψ_x and ψ_y are given in terms of ϕ and θ by:

$$\psi_x = \sin^{-1}\left(\frac{\sin\phi\,\cos\theta}{\sqrt{\sin^2\phi\,\cos^2\theta + \cos^2\phi}}\right), \tag{A.11}$$

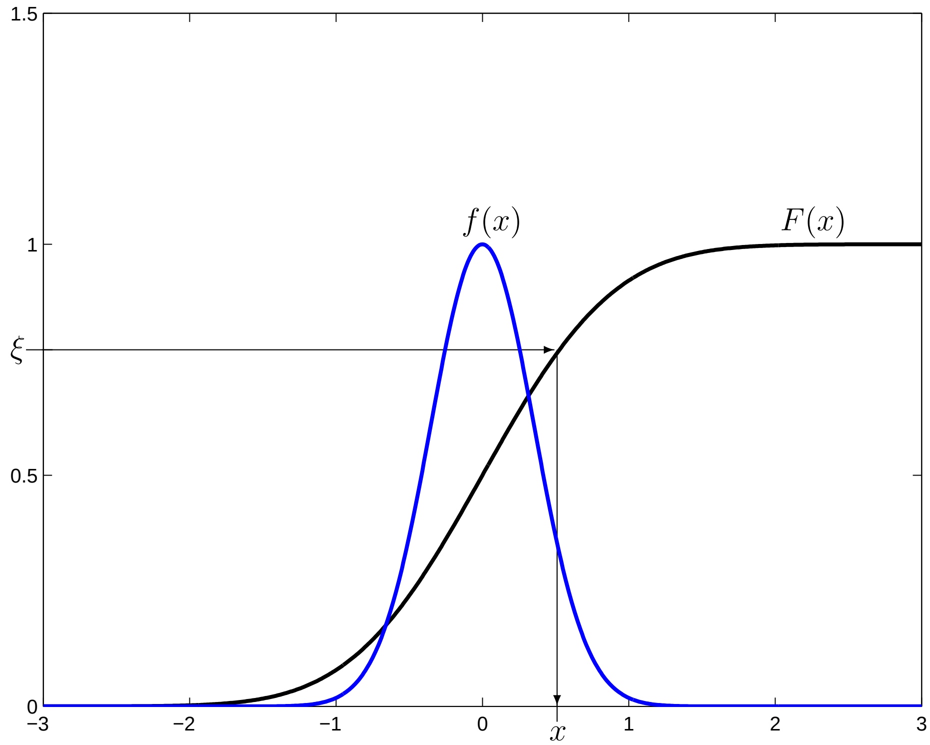

Figure A.4: von Neumann's Golden Rule for sampling a distribution.

$$\psi_y = \sin^{-1}\left(\frac{\sin\phi\,\sin\theta}{\sqrt{\sin^2\phi\,\sin^2\theta+\cos^2\phi}}\right). \tag{A.12}$$

Here it is seen that the judicious choice of domain for ϕ keeps (A.11) and (A.12) finite and well-defined $\forall\ \phi \in [0,\pi/2]$, $\theta \in [0,2\pi]$. The range of both ψ_x and ψ_y is $[-\pi/2,\pi/2]$, which is consistent and well-defined for Snell's Law as applied to this problem.

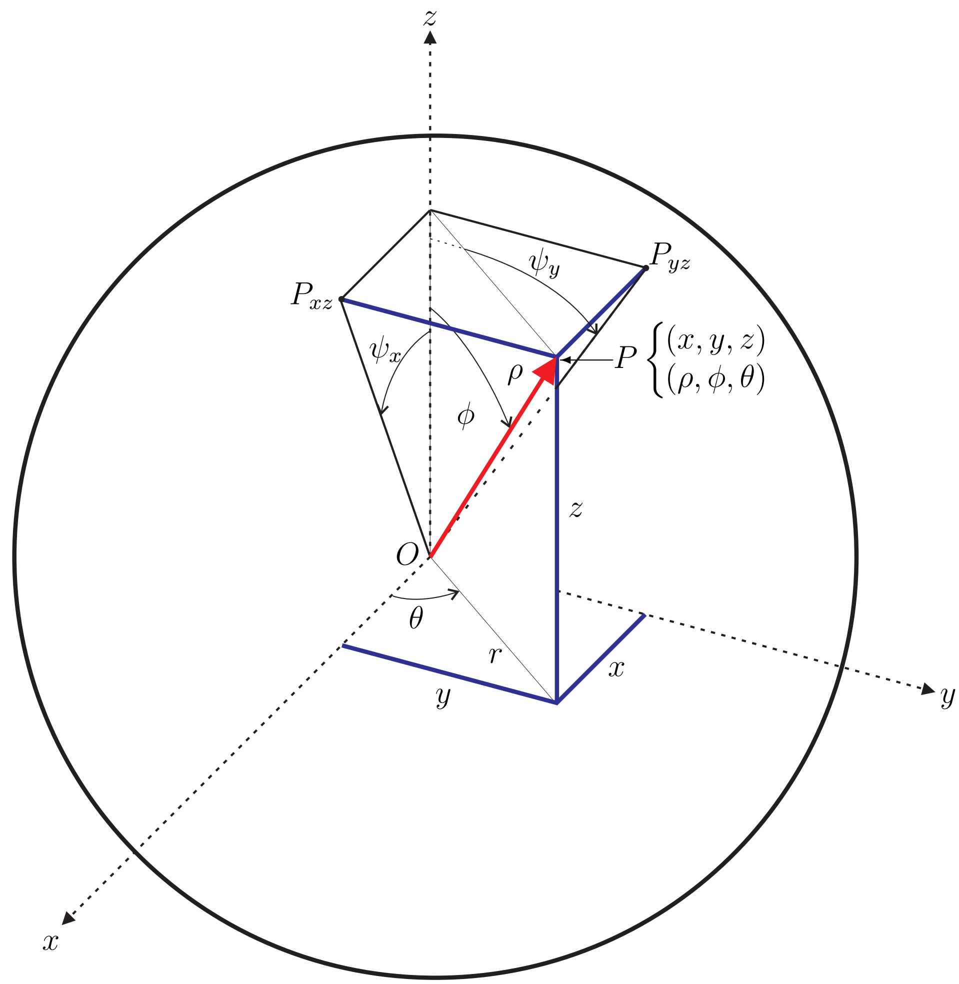

Figure A.5: Projection of ϕ and θ onto ψ_x and ψ_y.

A.3 Index of Refraction Interface Deflections

The deflections caused by an IoR interface can be calculated using Snell's Law, see Fig. A.2. The angles associated with these deflections are given by,

$$\epsilon_i = \psi_i - \sin^{-1}(\eta \sin \psi_i), \quad i = x, y, \tag{A.13}$$

where η is defined as $\eta \equiv \frac{n_1}{n_2}$, which is ratio of the IoR before the interface over the IoR after the interface. Employing the small angle approximation:

$$\tan \alpha \approx \alpha, \tag{A.14}$$

the deflections are simply given by,

$$\delta_i = \epsilon_i l, \tag{A.15}$$

where l is the path traveled by the ray after the IoR interface until it reaches the next IoR interface. NOTE: the quantities η and l are taken as constant as a first-order approximation to the solution.

Thus from the Pdfs of ϕ and θ the statistics of the IoR interface orientations can be determined; from those statistics the Pdfs of ψ_x and ψ_y are known and finally the statistics describing the deflections and deflection angles are found.

A.4 First-Order Approximation Results

The MC simulation was programmed in FORTRAN to improve the speed of the numerical algorithm. As a validation for the sampling algorithm outlined above, the results for the PDF sampling of ϕ and θ are presented in Figs. A.6-A.8 for various samples sizes: $N = 1000$, 1×10^6, and number of discrete histogram bins: 100, 1000. Each figure plots the sampling function (see Table A.1) vs. N in the upper graph and the sampled & analytical Pdfs in the lower graph for both ϕ and θ. The sampled results are plotted on top of the analytical form of the Pdfs at the same ϕ and θ values. All the Pdfs have been numerically integrated to verify unity area.

Having a high N/bins ratio yields a smoother (more accurate) reproduction of the PDF, but sacrifices the fidelity of the result by having fewer bins. Overall the sampling scheme appears to perform quite well in reproducing the shape of the PDF, especially at high sample sizes.

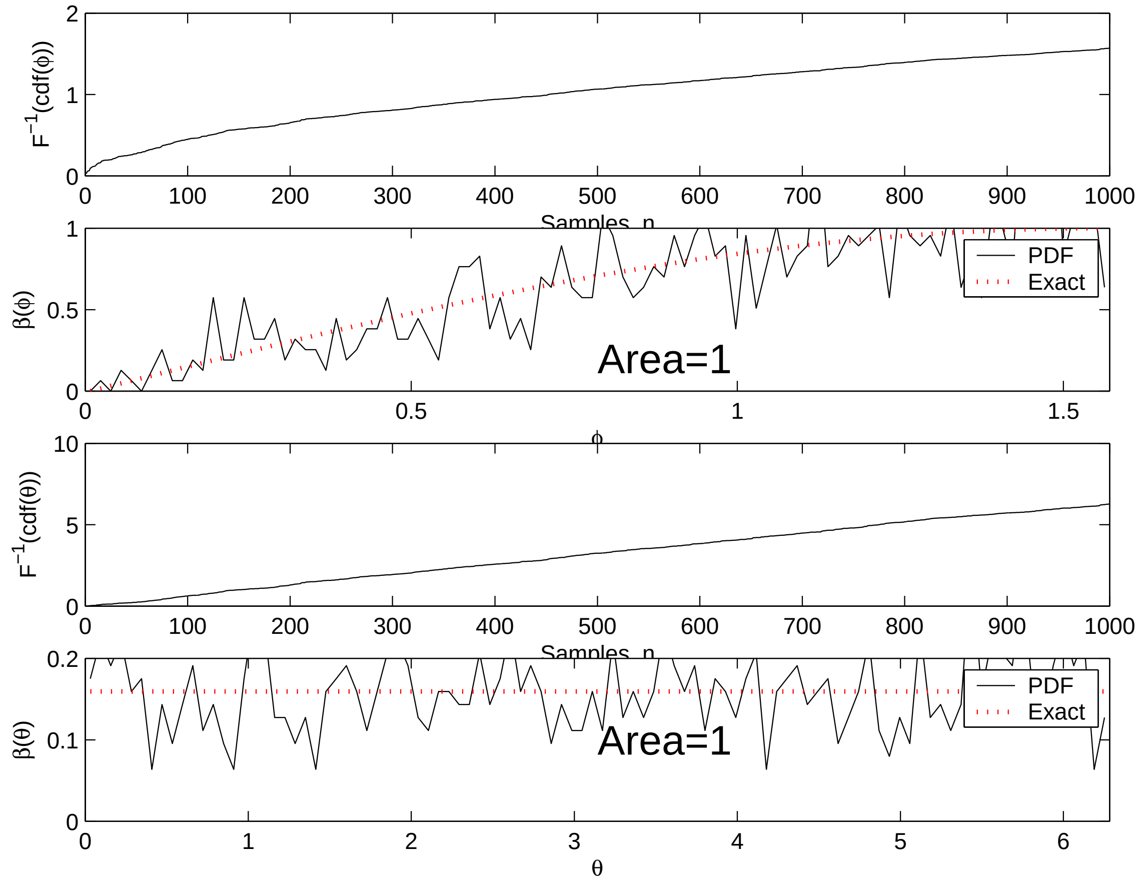

Figure A.6: Sampling of $\beta(\phi)$ and $\beta(\theta)$: $N = 1000$, bins $= 100$.

A.5 Random Number Generator

A random number generator (RNG) routine was implemented into the Monte-Carlo (MC) simulation in order to improve the uniformity of the sampling on the unit interval $U[0,1]$. This was motivated by the implicit assumption that no self-respecting MC simulator would use the intrinsic RNG function provided by *any* programming language to form the basis of the algorithm. Thus a new RNG was selected as described Press, Teukolsky, Vetterling, and Flannery (1989) The intrinsic

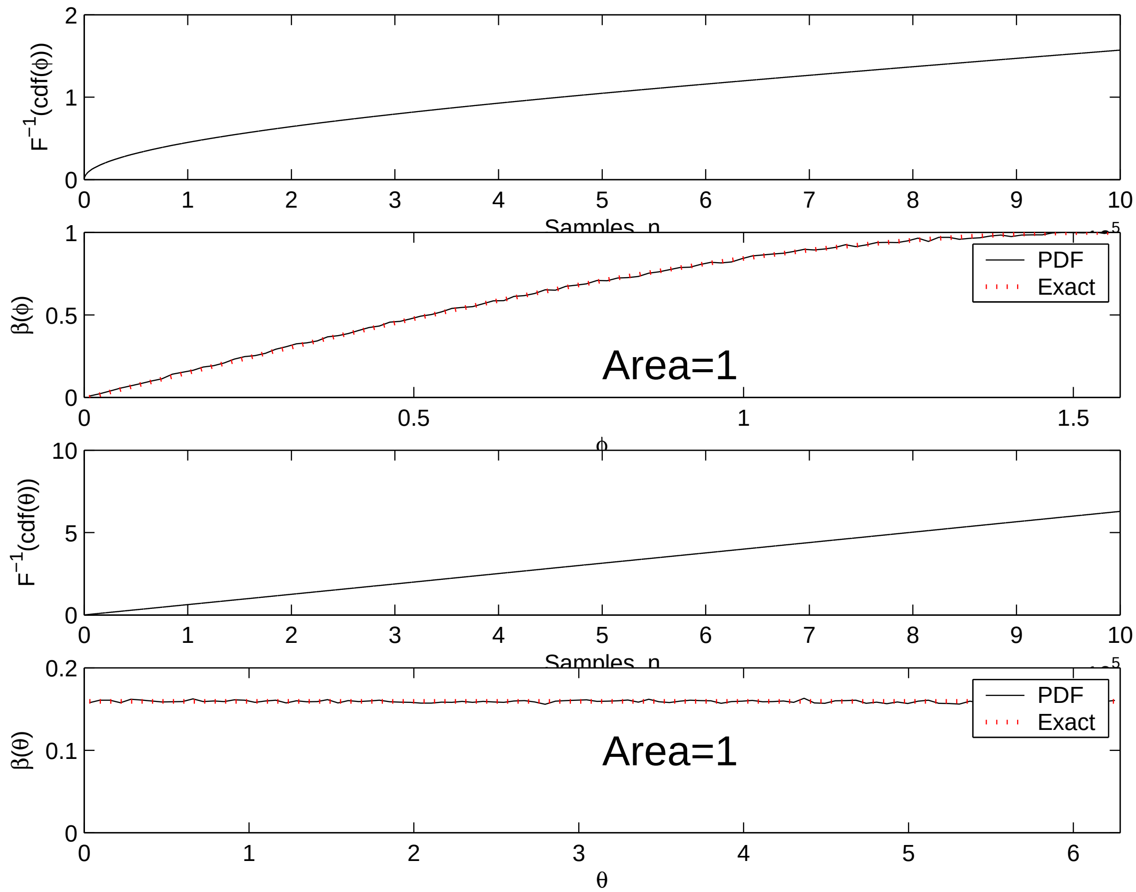

Figure A.7: Sampling of $\beta(\phi)$ and $\beta(\theta)$: $N = 1 \times 10^6$, bins $= 100$.

RNG within FORTRAN has an effective period of 2^{32}; thus, approximately 4.29 billion samples will be obtained before the RNG begins to "recycle" values. The RNG suggested by Flannery *et al.* has an effective period of 2^{64}, or 18.4 quintillion (1.84×10^{19}). A reasonable MC simulation sums over $\mathcal{N} = 100$ interfaces $\mathcal{M} = 10^8$ times requires 10^{10} random samples. This typical simulation exceeds the intrinsic period by a factor of two. Half of the simulation is effectively rendered redundant and wasteful. Furthermore, this imposes a restrictive limit on the accuracy of the simulation by limiting the sample size to a relatively meager proportion. Thus the need for a new RNG function is readily justified.

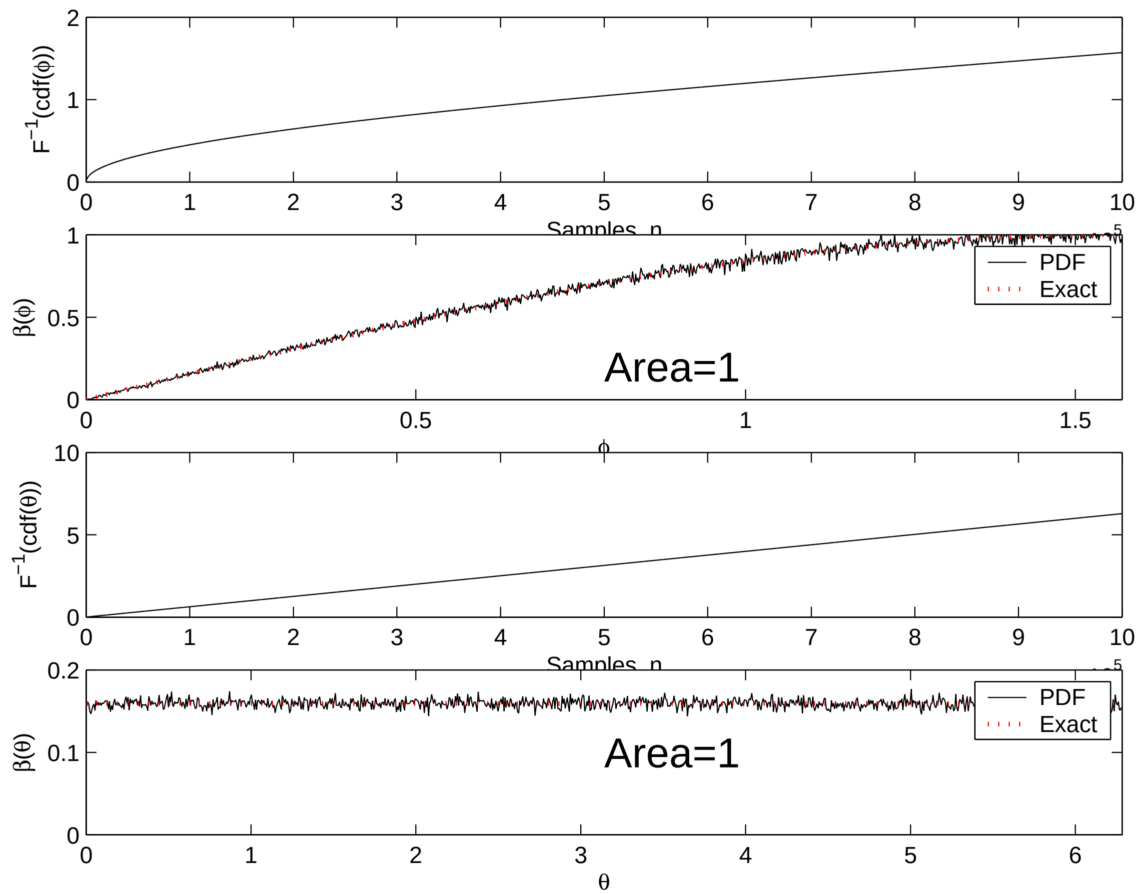

Figure A.8: Sampling of $\beta(\phi)$ and $\beta(\theta)$: $N = 1 \times 10^6$, bins $= 1000$.

A.6 Probability Distribution of Individual Interfaces

Initial results from this MC simulation indicate that the beam deflections due to interaction with a single interface (unit process) are governed by a Cauchy (or Lorentzian) distribution, given by the general form

$$\beta(x) = \frac{1}{\pi} \frac{\frac{1}{2}\Gamma}{(x-m)^2 + \left(\frac{1}{2}\Gamma\right)^2}, \tag{A.16}$$

where Γ is defined as the full-width at the half-maximum (FWHM) value and m is the statistical median. The the Cauchy or Lorentzian distribution is a two-parameter distribution which is interpreted as having two-degrees of freedom.

As an aside, it should be noted that the Cauchy distribution is a "pathological"

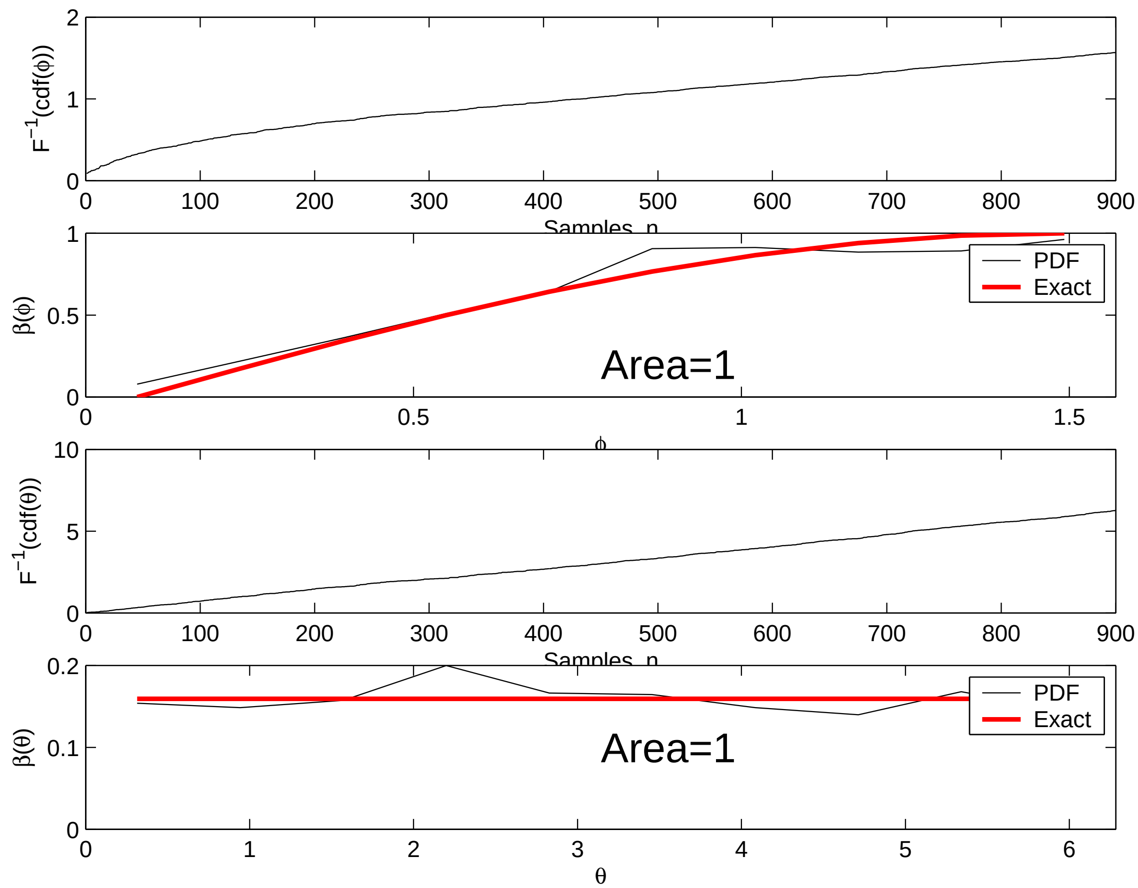

Figure A.9: Sampling of $\beta(\phi)$ and $\beta(\theta)$: $N = 900$, $\text{bins}_{\phi,\theta} = 10$, $\text{bins}_{\epsilon_{x,y}} = 100$.

distribution in that it has no moments for $n \geq 1$. It is able only to be normalized, which satisfies one of the key requirements for it to be a valid distribution.

In general, the moments of the Cauchy distribution μ_n are undefined for $n \geq 1$ since the corresponding integrals diverge,

$$\mu_n = \int_{-\infty}^{\infty} \frac{\Gamma}{2\pi} \frac{x^n}{(x-m)^2 + \left(\frac{1}{2}\Gamma\right)^2}. \tag{A.17}$$

Thus it has no definable mean and its variance is infinite.

One interpretation of the practical implications of the Cauchy distribution's lack of a finite variance is to examine the history of the running average of a sample set. If the running average is plotted against the samples size, it is found that regardless of how large the sample size is, the mean never converges, see Fig. A.11.

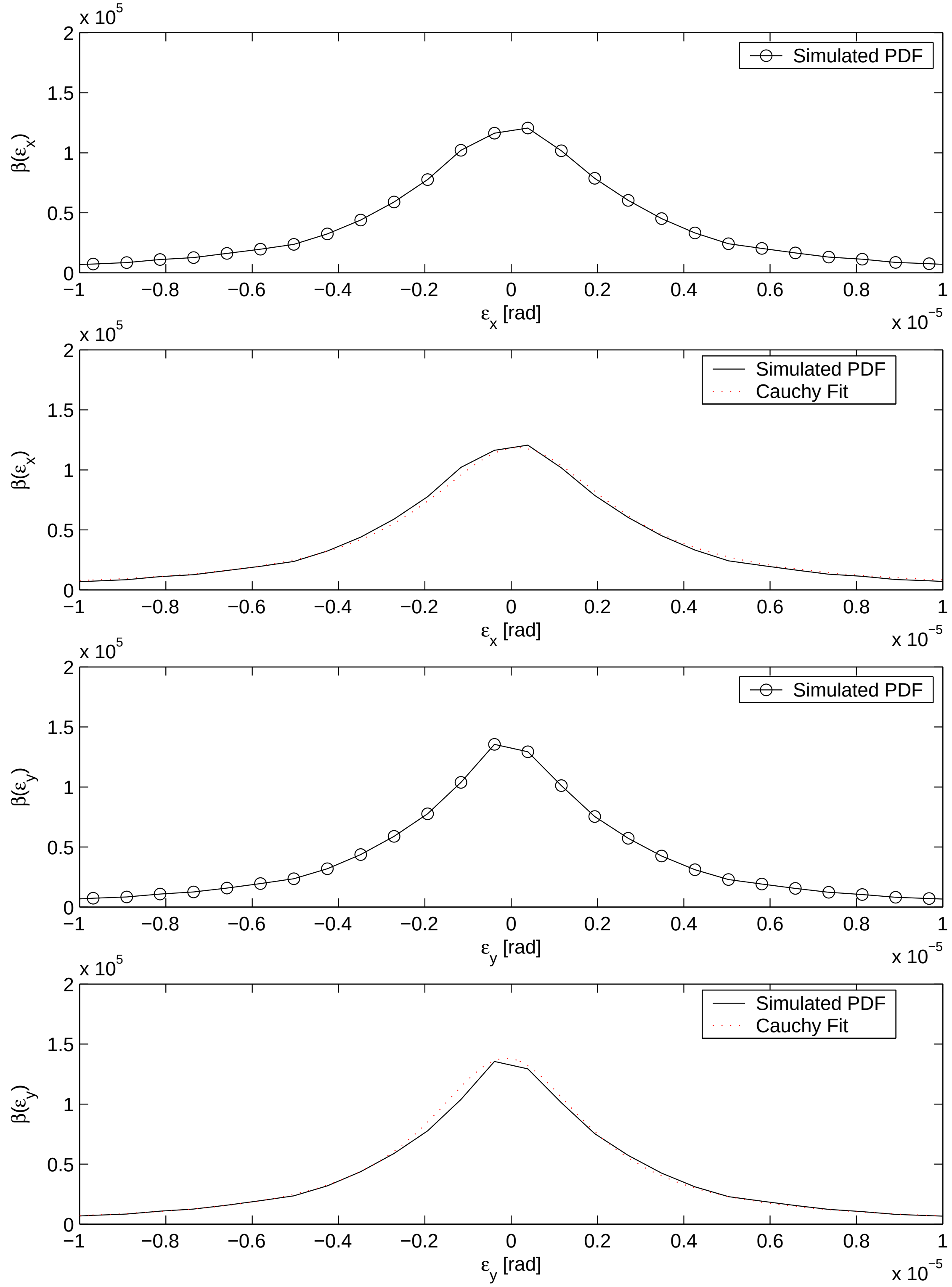

Figure A.10: Sampling of $\beta(\epsilon_x)$ and $\beta(\epsilon_y)$ for $N = 2000$, $\text{bins}_{\phi,\theta} = 50$, $\text{bins}_{\epsilon_{x,y}} = 1000$.

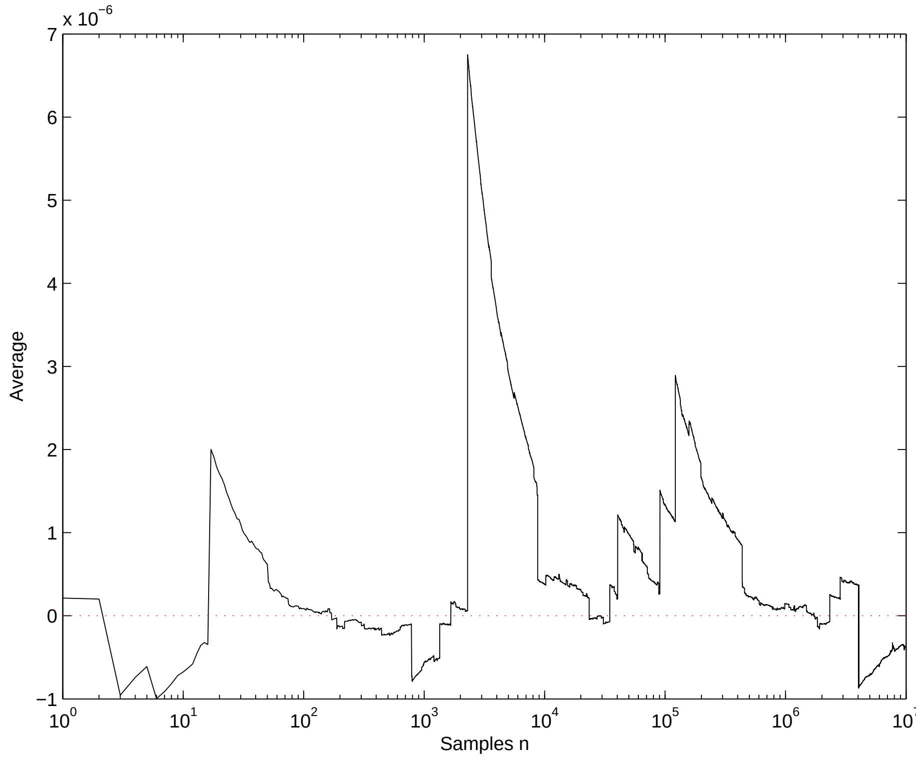

Figure A.11: History of running average plotted against sample size for a record length of $n = 10^7$ samples.

A.6.1 Geometric Interpretation

One interesting geometric interpretation of the Cauchy distribution arises from the definition of the distribution itself. Consider a Cartesian plane with the point b fixed along the ordinate some arbitrary distance from the abscissa. Now let the angle θ describe the angle between the ordinate and a line segment extending from the point b and intersecting the abscissa, (see Fig. A.12). If θ is allowed to vary randomly within its range $[-\pi/2, \pi/2]$, then the probability of realizing a given length x is described by the Cauchy distribution. The following derivation provides such a proof:

$$\tan(\theta) = \frac{x}{b} \tag{A.18}$$

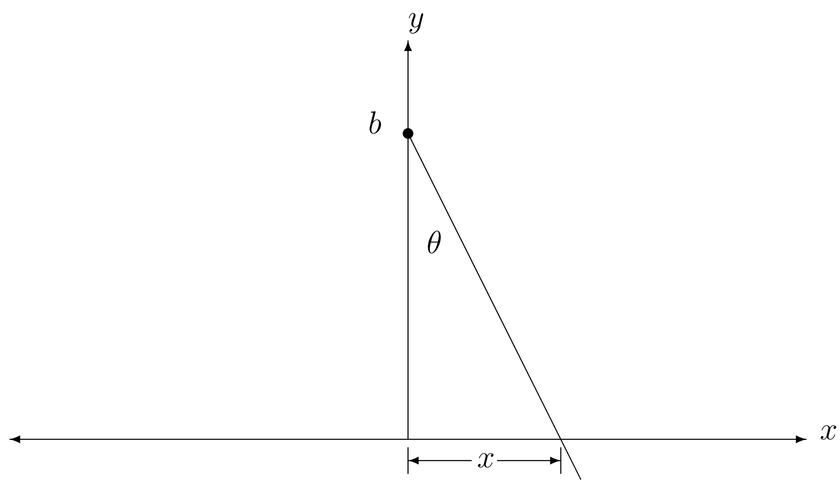

Figure A.12: Geometric origin of Cauchy distribution.

$$\theta = \tan^{-1}\left(\frac{x}{b}\right) \tag{A.19}$$

$$\begin{aligned} d\theta &= -\frac{1}{1+\frac{x^2}{b^2}}\frac{dx}{b} && \text{(A.20)} \\ &= -\frac{bdx}{b^2+x^2}, && \text{(A.21)} \end{aligned}$$

The distribution of the angle θ is given by,

$$\frac{d\theta}{\pi} = -\frac{1}{\pi}\frac{bdx}{b^2+x^2} \tag{A.22}$$

This expression is normalized over all angles since

$$\int_{-\pi/2}^{\pi/2} \frac{d\theta}{\pi} = 1 \tag{A.23}$$

and

$$\begin{aligned} -\int_{-\infty}^{\infty} \frac{1}{\pi}\frac{bdx}{b^2+x^2} &= \frac{1}{\pi}\left[\tan^{-1}\frac{b}{x}\right]_{-\infty}^{\infty} && \text{(A.24)} \\ &= \frac{1}{\pi}\left[\frac{1}{2}\pi - (-\frac{1}{2}\pi)\right] && \text{(A.25)} \\ &= 1. && \text{(A.26)} \end{aligned}$$

Thus interpreting x as the beam deflection from its unperturbed path and θ as the deflection angle $\epsilon_{x,y}$ the analogy is clear.

A.7 Probability Distribution of a Sum over $\mathcal{N}$ Individual Interfaces

From Central Limit Theorem (CLT) it is expected that any sum over a large number of statistically independent random variables should result in a Gaussian distribution of the resultant sum's values. However, CLT theorem also requires that the mean and variance of the distribution(s) which govern these individual processes be defined and finite. The Cauchy distribution which *does* govern the individual interfaces fails both these criteria: it has no definable mean and its variance is infinite. However, given a large number of statistically independent processes which are governed by a Cauchy distribution, the sum of these processes it itself distributed in a Cauchy manner. This result is born out in the MC simulations (Fig. A.10) as well as experimentally, see Fig. B.1.

APPENDIX B

Experimental Results for Index of Refraction Effects in a Reacting Flow

Monte-Carlo simulations predicted the same Reynolds number scaling of the beam position uncertainty as was found experimentally, see Fig. B.2.

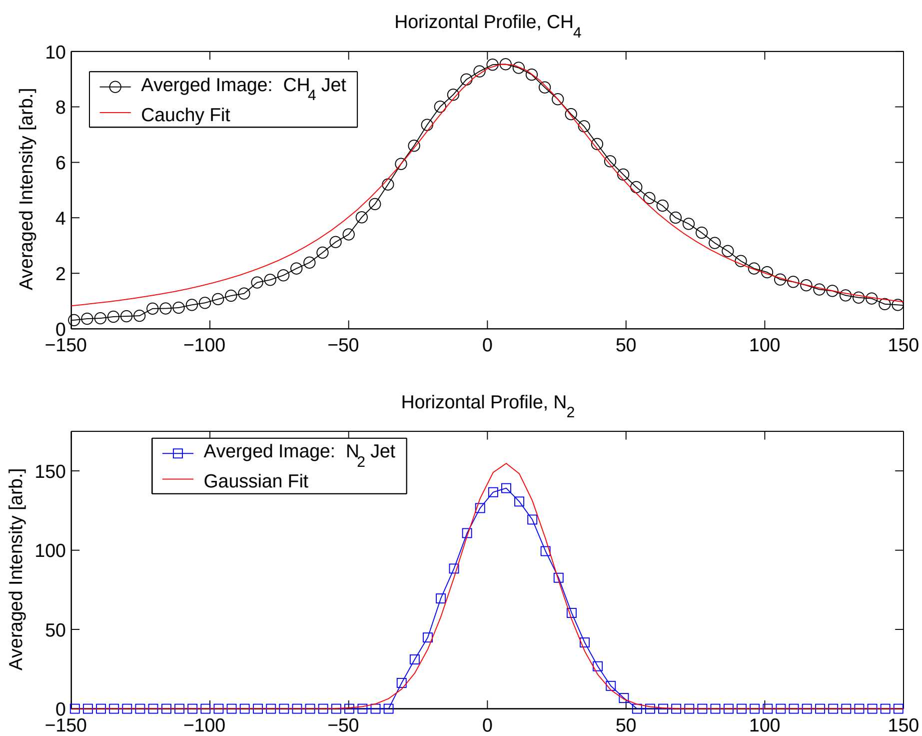

Figure B.1: Profiles of the beam position uncertainty and the analytical Cauchy fit using the experimentally determined parameters. Upper panel: positional uncertainty for a reacting jet flame; lower panel: uncertainty for nonreacting Nitrogen jet.

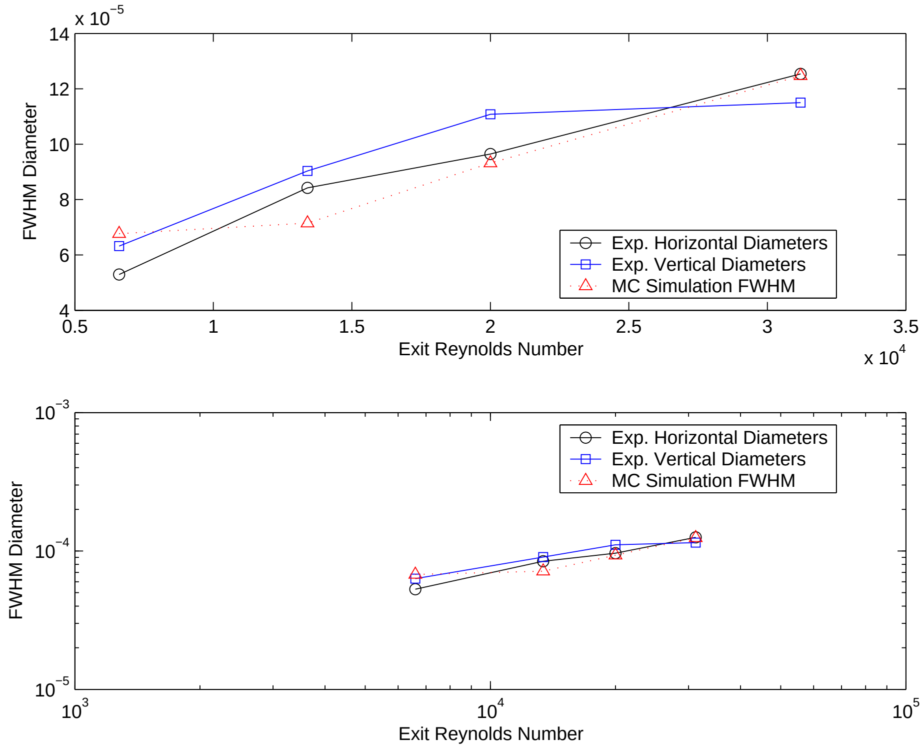

Figure B.2: Reynolds number scaling of beam position uncertainty. Plotted on linear axes in the upper panel and log-log in the lower panel. The squares and circles indicate experimental data and the red triangles are the results from corresponding MC simulations.

B.1 Conclusions

Employing knowledge of the fine-scale structure of the scalar fields in shear driven turbulent flows, a model is developed to predict the positional uncertainty of a laser beam propagating through an exothermic flow field. A Monte Carlo simulation was created to determine the statistical character of randomly oriented scalar jump interfaces corresponding to gradients in the index of refraction field in a turbulent reacting shear flow. The interface orientations are distributed in a Cauchy manner. Central Limit Theorem does not apply due to the pathological nature of the Cauchy distribution. However, sums of Cauchy random variables *are* distributed in a Cauchy manner. This theoretical (and numerical) result for the overall positional uncertainty of the beam is supported by experimental data with reasonable agreement. Reynolds number scaling is apparent in the preliminary experimental results and this finding is also in accord with the concomitant MC simulations.

BIBLIOGRAPHY

BIBLIOGRAPHY

Antonia, R. A., Bilger, R. W., 1973. An experimental investigation of an axisymmetric jet in a co–flowing air stream. *Journal of Fluid Mechanics* **61** (4), 805–822.

Antonia, R. A., Mi, J., 1993. Corrections for velocity and temperature derivatives in turbulent flows. *Experiments in Fluids* **14**, 203–208.

Bard, 1974. Nonlinear Parameter Estimation. Academic Press.

Becker, H. A., Yamazaki, S., 1978. Entrainment, momentum flux and temperature in vertical free turbulent diffusion flames. *Combustion and Flame* **33**, 123–149.

Beér, J. M., Chigier, N. A., 1983. Combustion Aerodynamics. Robert E. Krieger Publ.

Biringen, S., 1975. An experimental study of a turbulent axisymmetric jet issuing into a coflowing airstream. Tech. Rep. *VKI Technical Note 110*, von Karman Institute.

Blake, T. R., Coté, J. B., 1999. Similitude and the interpretation of turbulent diffusion flames. *Combustion and Flame* **117**, 589–599.

Blake, T. R., McDonald, M., 1995. Similitude and the interpretation of turbulent diffusion flames. *Combustion and Flame* **101**, 175–184.

Buch, K. A., Dahm, W. J. A., 1996. Experimental study of the fine-scale structure of conserved scalar mixing in turbulent flows. Part 1. Sc $\gg$ 1. *Journal of Fluid Mechanics* **317**, 21–71.

Buch, K. A., Dahm, W. J. A., 1998. Experimental study of the fine-scale structure of conserved scalar mixing in turbulent shear flows. Part 2. Sc $\approx$ 1. *Journal of Fluid Mechanics* **364**, 1–29.

Cetegen, B. M., Zukoski, E. E., Kubota, T., 1984. Entrainment in the near and far field of fire plumes. *Combustion Sci. Technol.* **39**, 305–331.

Chapman, D. R., 1979. Computational aerodynamics development and outlook. *AIAA Journal* **17** (12), 1293–1313.

Chen, C. J., Rodi, W., 1980. Vertical Turbulent Buoyant Jets. A Review of Experimental Data. Pergamon.

Chigier, N. A., Strokin, V., 1974. Mixing processes in a free turbulent diffusion flame. *Combustion Science and Technology* **9** (3-4), 111–118.

Clemens, N. T., Mungal, M. G., 1991. A planar mie scattering technique for visualizing supersonic mixing flows. *Experiments in Fluids* **11**, 175–185.

Corrsin, S., 1958. On local isotropy in turbulent shear flow. Tech. Rep. R&M 58B11, NACA.

Corrsin, S., Kistler, A. L., 1955. Free–stream boundaries of turbulent flows. Tech. Rep. TR–1244, NACA.

Dahm, W. J. A., 2005. Effects of heat release on turbulent shear flows. Part 2. Turbulent mixing layers and the equivalence principle. *Journal of Fluid Mechanics* **540**, 1–19.

Dahm, W. J. A., Dibble, R. W., 1988. Coflowing turbulent jet diffusion flame blowout. In: *Proceedings of the Twenty-Second International Symposium on Combustion.* The Combustion Institute, Pittsburgh, pp. 801–808.

Davidson, M. J., Wang, H. J., 2002. Strongly advected jet in a coflow. *Journal of Hydraulic Engineering*, 742–752.

Delichatsios, M., 1993. Transition from momentum to buoyancy-controlled turbulent jet diffusion flames and flame height relationships. *Combustion and Flame* **92**, 349–364.

Diez, F. J., Dahm, W. J. A., 2007. Effects of heat release on turbulent shear flows. Part 3. Buoyancy effects due to heat release in jets and plumes. *Journal of Fluid Mechanics* **575**, 221–255.

Draper, Smith, 1981. Applied Regression Analysis. John Wiley and Sons.

Elsner, J. W., Domagala, P., Elsner, W., 1993. Effect of finite spatial resolution of hot-wire anemometry on measurements of turbulence energy dissipation. *Meas. Sci. Technol.* **4**, 517–523.

Ewing, D., Hussein, H. J., George, W. K., 1995. Spatial resolution of parallel hot-wire probes for derivative measurements. *Exp. Therm. Fluid Sci.* **11**, 155–173.

Foucaut, J. M., Stanislas, M., 2002. Some considerations on the accuracy and frequency response of some derivative filters applied to particle image velocimetry vector fields. *Measurement Science and Technology* **13**, 1058–1071.

Gotoh, T., Fukayama, D., Nakano, T., 2002. Velocity field statistics in homogeneous steady turbulence obtained using a high-resolution direct numerical simulation. *Physics of Fluids* **14** (3), 1065–1081.

Han, D., Mungal, M. G., 2001. Direct measurement of entrainment in reacting/non-reacting turbulent jets. *Combustion and Flame* **124**, 370–386.

Hawthorne, W. R., Hottel, D. S. W. H. C., 1949. Mixing and combustion in turbulent gas jets. In: *Proc. 3rd Intl Symp. on Combustion, Flame, and Experimental Phenomena*. Williams & Wilkins, Co., Baltimore, pp. 266–288.

Hermanson, J. C., Dimotakis, P. E., 1989. Effects of heat release in a turbulent, reacting shear layer. *Journal of Fluid Mechanics* **199**, 333–375.

Heskestad, G., 1981. Peak gas velocities and flame heights of buoyancy–controlled turbulent diffusion flames. In: Proceedings of the Eighteenth International Symposium on Combustion. The Combustion Institute, Pittsburgh, pp. 951–960.

Hinze, J. O., 1975. Turbulence. McGraw–Hill, Inc.

Hottel, H. C., Hawthorne, W. R., 1949. Diffusion in laminar flame jets. In: *Proc. 3rd Intl Symp. on Combustion, Flame, and Experimental Phenomena*. Williams & Wilkins, Co., Baltimore, pp. 254–266.

Jiménez, J., Wray, A. A., Saffman, P. G., Rogallo, R. S., 1993. The structure of intense vorticity in isotropic turbulence. *Journal of Fluid Mechanics* **255**, 65–90.

Kolmogorov, A. N., 1941. Local structure of turbulence in an incompressible fluid at very high reynolds numbers. C. R. Acad. Sci. URSS **30**, 301–304.

Kremer, H., 1967. Mixing in a plane free–turbulent–jet diffusion flame. In: Proceedings of the Eleventh Internation Symposium on Combustion. The Combustion Institute, Pittsburgh, pp. 799–806.

Maczyński, J. F. J., 1962. A round jet in an ambient co–axial stream. *Journal of Fluid Mechanics* **13** (4), 597–608.

McBride, B. J., Reno, M. A., Gordon, S., 1994. Cet93 and cetpc. an interim updated version of the nasa lewis computer program for calculating complex chemical equilibrium with applications. Nasa report tm–4557, National Aeronautics and Space Administration.

Melling, A., 1997. Tracer particles and seeding for particle image velocimetry. *Measurement Science and Technology* **8**, 1406–1416.

Mi, J., Nathan, G. J., 2003. The influence of probe resolution on the measurement of a passive scalar and its derivatives. *Experiments in Fluids* **34**, 687–696.

Morton, B. R., 1959. Forced plumes. *Journal of Fluid Mechanics* **5**, 151–163.

Muñiz, L., 2002. Particle image velocimetry studies of turbulent nonpremixed flames. Ph.D. thesis, Stanford University.

Muñiz, L., Mungal, M. G., 1995. A piv investigation of turbulent diffusion flames. In: *Fall Mtg., Western States Section of the Combustion Institute*. The Combustion Institute, Pittsburgh, pp. WSS/CI–95F–206.

Muñiz, L., Mungal, M. G., 2001. Effects of heat release and buoyancy on flow structure and entrainment in turbulent nonpremixed flames. *Combustion and Flame* **126**, 1402–1420.

Mullin, J. A., 2004. A study of velocity gradient fields at intermediate and small scales of turbulent shear flows via dual-plane particle image velocimetry. Ph.D. thesis, University of Michigan.

Mullin, J. A., Dahm, W. J. A., 2005a. Dual-plane stereo particle image velocimetry measurements of velocity gradient tensor fields in turbulent shear flow. I. accuracy assessments. *Physics of Fluids* **18** (035101).

Mullin, J. A., Dahm, W. J. A., 2005b. Dual-plane stereo particle image velocimetry measurements of velocity gradient tensor fields in turbulent shear flow. II. experimental results. *Physics of Fluids* **18** (035102).

Nickels, T. B., Perry, A. E., 1996. An experimental and theoretical study of the turbulent coflowing jet. *Journal of Fluid Mechanics* **309**, 157–182.

Pao, Y.-H., 1965. Structure of turbulent velocity and scalar fields at large wavenumbers. The Physics of Fluids **8** (6), 1063–1075.

Papanicolaou, P., List, E. J., 1988. Investigations of round vertical turbulent buoyant jets. *Journal of Fluid Mechanics* **195**, 341–391.

Peters, N., Göttgens, J., 1991. Scaling of buoyant turbulent jet diffusion flames. *Combustion and Flame* **85**, 206–214.

Press, W. H., Teukolsky, S. A., Vetterling, W. T., Flannery, B. P., 1989. Numerical Recipes, The Art of Scientific Computing (FORTRAN). Cambridge Press.

Raffel, M., Willert, C., Kompenhans, J., 1998. Particle Image Velocimetry. Springer.

Rehm, J. E., Clemens, N. T., 1998. The large-scale turbulent structure of nonpremixed planar jet flames. *Combustion and Flame* **116**, 615–626.

Reuss, D. L., Rosalik, M. E., 1998. Piv measurements during combustion in a reciprocating internal combustion engine. In: 8th Int. Symp. on Applic. Laser Technol. to Fluid Mech. Lisbon, Portugal, pp. 37.1.1–37.1.17.

Ricou, F. P., Spalding, D. B., 1961. Measurements of entrainment and mixing by axisymmetrical turbulent jets. *Journal of Fluid Mechanics* **11**, 21–32.

Saddoughi, S. G., Veeravalli, S. V., 1994. Local isotropy in turbulent boundary layers at high Reynolds number. *Journal of Fluid Mechanics* **268**, 333–372.

Southerland, K. B., 1994. A four-dimensional experimental study of passive scalar mixing in turbulent flows. Ph.D. thesis, University of Michigan.

Stella, A., Guj, G., Kompenhans, J., Raffel, M., Richard, H., 2001. Application of particle image velocimetry to combusting flows: Design considerations and uncertainty assessments. *Experiments in Fluids* **30**, 167–180.

Steward, F. R., 1970. Prediction of the height of turbulent diffusion buoyant flames. *Combustion Sci. Technol.* **2**, 203–212.

Sung, C. J., Law, C. K., Axelbaum, R. L., 1994. Thermophoretic effects on seeding particles in LDV measurements of flames. *Combustion Science and Technology* **99** (1-3), 119–132.

Tacina, K. M., Dahm, W. J. A., 2000. Effects of heat release on turbulent shear flows. Part 1. A general equivalence principle for non-buoyant flows and its application to turbulent jet flames. *Journal of Fluid Mechanics* **415**, 23–44.

Takagi, T., Shin, H.-D., Ishio, A., 1981. Properties of turbulence in turbulent diffusion flames. *Combustion and Flame* **40**, 121–140.

Thring, M. W., Newby, M. P., 1953. Combustion length of enclosed turbulent jet flames. In: Proc. 4th Intl. Symp. on Combustion. pp. 789–796.

Uberoi, M. S., 1957. Equipartition of energy and local isotropy in turbulent flows. *J. Appl. Phys.* **28**, 1165–1170.

von Neumann, J., 1946. Letter to Stan Ulam. LANL Science Magazine **23**.

Wallace, A. K., 1981. Experimental investigation on the effect of chemical heat release in the reacting turbulent plane shear layer. Ph.D. thesis, University of Adelaide.

Wang, H. J., Davidson, M. J., 2001. A profile tracking system for investigating the behaviour of discharges in moving environments. *Experiments in Fluids* **31**, 533–541.

Wygnanski, I., Fiedler, H., 1969. Some measurements in the self–preserving jet. *Journal of Fluid Mechanics* **38** (3), 577–612.

Wyngaard, J. C., 1968. Measurement of small-scale turbulence structure with hot wires. *Journal of Scientific Instruments (Journal of Physics E)* **1**, 1105–1108.

Zhou, T., Antonia, R. A., Chua, L. P., 2002. Performance of a probe for measuring turbulent energy and temperature dissipation rates. *Exp. Fluids* **33**, 334–345.

Zukoski, E. E., Kubota, T., Cetegen, B., 1981. Entrainment in fire plumes. *Fire Safety* **3**, 107–121.